NUMERICAL MODELLING OF TIDE-INDUCED CIRCULATION

by

Lida Mardapitta-Hadjipandeli B.Sc.

A thesis submitted for the degree of Doctor of Philosophy

Department of Civil Engineering
Faculty of Engineering
The University of Birmingham

November 1985

SYNOPSIS

A finite difference computational model has been enhanced and refined to simulate tide-induced circulatory flows, with special reference to eddies shed in the lee of headlands and tidal circulation and flushing in narrow entranced coastal basins. The model is of the two-dimensional depth-integrated type and includes a relatively simple "zero-equation" turbulence model. In the turbulence model particular emphasis has been placed on the representation of the free shear layer turbulence, occurring in the mixing zone of eddying flows. This component of turbulent structure has been expressed in terms of a constant eddy viscosity across the shear layer and a semi-empirical velocity distribution.

The finite difference representation of the hydrodynamic and mass transport equations was based on the Alternating Direction Implicit scheme, with the hydrodynamic equations involving a double iteration to represent the advective acceleration terms in a time-centred form. The solution of the governing equations yielded the depth-mean velocity, water elevation and concentration fields throughout the computational domain.

The model's ability to simulate tide-induced circulatory flows was tested against field measurements from around Rattray Island, and laboratory model studies of idealised rectangular harbours. The agreement between numerical predictions and measurements proved to be encouraging in both cases. The one-way interaction nesting technique has been adopted and applied with success to the harbour simulations. A final application of the numerical model to prototype harbours, enabled comparisons to be made between prototype and laboratory model predictions, an exercise which highlighted the problems associated with scaling effects in distorted physical models.

To my mother

ACKNOWLEDGEMENTS

I acknowledge with gratitude my supervisor Dr R.A.Falconer for his continuing help and encouragement throughout the project. Thanks are also due to Mr C.Beaton for his advice on computer problems, and to Mr R.Preston, Peter and Philip for the useful discussions we had on the subject. My thanks also go to members of the technical staff, namely Mr R.Cooper and Mr A.Fitzgerald, for their assistance with the laboratory tests. I am also grateful to Professor M.J.Hamlin, the head of Civil Engineering department, for his support since my undergraduate years.

My appreciation goes to the Australian Institute of Marine Science for providing the data for the Rattray Island study. The research has been partly suported by an SERC grant, an ORS award and the Caroline Harrold fund.

Thanks are also due to the research students with whom I was fortunate to share a room and my fellow tutors at Mason Hall. To Sian for insisting that physical torture was equally as important as mental torture and dragging me to our lunch-time runs. To Chara and Dimitris for the pleasant hours we spent over the two years at Mason Hall. To Wendy for helping me with the typing of equations in the thesis.

Finally I would like to express my gratitude to my family. To my husband George for his unfailing support throughout the period of the research, for bearing with me the last few months of writing up and for his help towards the preparation of the thesis. To my father Savvas for being always very supportive and my brothers Chris and Alecos.

LIST OF SYMBOLS

A	wave amplitude, plan-form area
A_i	Fourier series component
a	wave amplitude
B	breadth of harbour, constant in shear stress term
C	Chezy coefficient
C^*	resistance coefficient
C_n	numerical wave celerity
C_p, c	physical wave celerity ($\sqrt{gh}$)
D_{ij}	tensor of dispersion coefficient
D'_{ij}	tensor of shear-induced dispersion coefficient
D_ℓ	coefficient of longitudinal dispersion
D_t	coefficient of transverse dispersion
E	exchange coefficient
E_c	Coriolis scaling number
Fr	Froude scaling number
f	bed friction coefficient
f_c	Coriolis parameter
g	gravitational acceleration
H	total depth
h	mean depth
i, j	grid point co-ordinates in the x- and y-direction respectively
j	square root of -1
k	kinetic energy, von Karman constant
k_s	bed roughness parameter
L	wavelength of standing wave, length of harbour, length scale

ℓ_m	length scale
n	Grid point co-ordinate on time axis
P	time-averaged pressure
$\hat{P}$	instantaneous pressure
P'	fluctuating pressure
Pa	atmospheric pressure
q_x, q_y	Discharge per unit width in the x- and y-direction respectively
R	hydraulic radius
Re	Reynolds number
R_e	bed generated turbulence scaling number
Ro	Rossby number
R_s	dispersion scaling number
s	time-averaged concentration
$\hat{s}$	instantaneous concentration
s'	fluctuating concentration
S	depth-averaged concentration
T	wave period
T_{ij}	effective depth-mean stress tensor
T'_{xy}	depth-mean shear stress
$T_{xy\|b}$	depth-mean bed generated shear stress component
$T_{xy\|f}$	depth-mean free shear layer stress component
TPR	tidal prism ratio
t	time
u_i	time-averaged velocity components (u, v, w)
$\hat{u}_i$	instantaneous velocity components
u'_i	fluctuating velocity components
U, V	depth-averaged u and v velocity components respectively

U_*, V_*	shear velocities in the x- and y-direction respectively
U_*	line of errors for velocity U
U_o	constant local U velocity
U_1	free stream velocity
W	harbour entrance width, wind speed
W_x,W_y	wind velocity components
X_i	external body force
x_i	Cartesian co-ordinate tensor (x, y, z)
x', y'	longitudinal and lateral co-ordinates in the mixing zone
α	coefficient relating hydraulic radius to mean depth, amplification factor
β	wave number ($2\pi/L$)
γ	molecular diffusivity
Δx	grid spacing
Δt	timestep
ε	dissipation rate of turbulent kinetic energy
ε_{ij}	eddy diffusivity tensor
ε_h	horizontal diffusivity
η	water surface elevation, flushing efficiency
η_*	line of errors of water surface elevation
λ	amplification factor, friction scaling number
μ	Courant number ($\sqrt{gh}\,\frac{\Delta t}{\Delta x}$)
ν	kinematic viscosity
ν_t	eddy viscosity
$\nu_t\|_b$	eddy viscosity for bed generated shear stress component
$\nu_t\|_f$	eddy viscosity for free shear layer stress component

ρ	fluid density
ρ_a	density of the atmosphere
σ	wave frequency ($2\pi/T$)
σ_{xx} σ_{yy}	Reynolds direct stress components in the x- and y-direction respectively
τ_{ij}	Reynolds stress tensor
τ_{xb}, τ_{xy}	bed shear stress components
τ_{xw}, τ_{yz}	wind shear stress components
ϕ	phase angle, geographical lattitude
Ω	angular velocity of the earth's rotation
ω	tidal frequency
$\| \|$	Magnitude
$O( )$	Order of approximation

LIST OF CONTENTS

LIST OF FIGURES

LIST OF TABLES

CHAPTER 1

INTRODUCTION

The prediction and understanding of tide-induced currents in coastal waters represent an intriquing and complex area of research. Such currents are of particular significance in the vicinity of boundary irregularities, such as headlands and tidal inlets, where large scale circulation patterns can be generated with important hydro-ecological and morphological implications.

Recently, there have been serious attempts in understanding the tidal physics of headland flows (see Pingree and Maddock(1979), Wolanski et al(1984), Wolanski(1985)). The eddies formed in the wake of headlands are very important locally because of their potential for trapping water and particulates as well as leading to enhanced mixing in the region. Such processes influence the determination of sitings of waste outfalls or the location of fisheries. For example, it is acknowledged that judicious sitings of sewage outfalls or radioactive discharges may take advantage of the strong flows that occur off headlands. Rapid dilution of the discharged material would then occur in the stronger tidal flow seaward of the headland, which is a characteristic of tides in the neighbourhood of promontories. Headland circulating flows are also important in determining sediment transport and appear to play a key role in the dynamics of offshore tidal bank formation (see Pingree and Maddock(1980)).

Tidal inlets to coastal basins, on the other hand, often serve as conduits through which the interior waters communicate, mix and exchange with the open sea. Consequently, they can affect water mass distributions as well as coastal sediment transport, with both processes being of particular interest to the hydraulic engineer. The domain of influence of flow and mass transport phenomena associated with tidal inlets extends from the confined areas of basin waters to waters on the continental shelf region. In fact, the presence of a narrow entrance can give rise to large scale circulation patterns on both the basin interior and the local ambient regions. The ever increasing concern on the water quality implications of coastal engineering works has led to detail model studies of the tidal flushing for many proposed and existing harbours. Water exchange, by tidal flushing, is assumed to be the dominant flow factor in governing the water quality characteristics within such basins, particularly with respect to that of ambient external flow field. Physical model tests, performed by Nece and Richey(1972,1975), Nece et al(1980), Nece(1984) and Jiang and Falconer(1983) on various, site specific, small boat basins and on generalised basin geometries, have provided some qualitative understandings of the tidal flushing characteristics and internal circulation patterns of such harbours.

The tide-induced circulatory flows in the lee of headlands and in narrow entranced coastal basins, find their origin in the separation mechanism occurring at the headland perimeter and the harbour entrance respectively. Separated flows are a common occurrence in engineering hydraulics. A computational model capable of predicting such flows, coupled with a scalar field - such as, temperature or constituent concentrations - would therefore find an abundance of important

engineering applications.

In view of the complexity, large computer storage and computational costs involved in simulating three-dimensional unsteady flows of large water bodies, flow problems of the nature outlined are usually reduced to two dimensions. Tidal flows in shallow waters, generally have good vertical uniformity of the horizontal components of their velocities and regarded as nearly horizontal flows. This property allows the reduction of the three-dimensional physical problem to one of the depth-integrated two-dimensional type. Because of the assumptions involved, such a model can only be expected to predict the gross characteristics of the physical flow processes, with stratification effects and the vertical mixing associated with secondary currents being ignored. Nevertheless, the modelling of flows that are two-dimensional in plan is widely practiced and its results are accepted for many predictive purposes. In addition, there is accumulating evidence, see Abbott et al(1985), to support the physically realistic prediction of flows by such models.

The main objective of this research study has been to develop and test a depth-integrated two-dimensional model capable of predicting tide-induced horizontal circulatory flows and the associated transport of conservative constituents, with special reference to flows in the lee of headlands and in narrow entranced coastal basins. The first stage of the research involved the formulation of the governing differential equations to represent the physical processes being modelled; they include the continuity, momentum and advective-diffusion equations. The momentum diffusion operator, representing the turbulent transfer of momentum mechanism, was introduced in view of its theoretically long-established significance in generating and sustaining circulation. Existing

turbulence models were reviewed before deciding on the adoption of a simple "zero-equation" closure, generally employed in the modelling of tidal flows. In this turbulence model, particular emphasis has been placed on the representation of shear layer turbulence - a significant momentum transfer mechanism in the mixing zone of eddying flows. For the formulation of this component of turbulence structure, use was made of semi-empirical concepts and approaches developed from extensive experimental studies of velocity field characteristics in wakes and jets - reviewed by Townsend(1956).

In proceeding with the numerical solution, the governing equations were discretised on a finite difference grid. The numerical properties of the basic finite difference schemes were investigated, followed by numerical experiments which enabled the choice of the most appropriate finite difference representation of the governing differential equations. A scheme based on the central implicit difference representation was chosen, with a double iteration method that expressed, explicitly, the advective and diffusive terms of the momentum equations in a time-centred form. Solution of the finite difference equations, using the method of Gauss elimination and back-substitution, yielded the depth-averaged velocity components U and V, the water elevation η, and the constituent consentration S throughout the computational domain.

The model's ability to simulate tide-induced circulatory flows was tested against field measurements from around Rattray Island, Australia, and laboratory model studies of idealised model harbours. In the first application, the predicted velocity field was compared with existing data from a field study on the re-circulating flows around the island - undertaken by the Australian Institute of Marine Science. Measurements

and observations had shown the existence of a strong, stable, clockwise-rotating eddy in the south eastern lee of the island, which was predicted by the numerical model with an encouraging degree of accuracy. In the second application, direct comparisons were made between laboratory and mathematical flow field results and tidal exchange coefficients, for model rectangular harbours with similar physical and geometric properties and dynamic boundary conditions. An experimental programme was carried out on a range of model harbours with different aspect (or length to breadth) ratios, each with a horizontal bed and asymmetric entrance. Laboratory model studies on similar harbour configurations, performed by Jiang and Falconer(1983), provided the data on the tidal flushing characteristics.

In view of the complexity of the flow at the harbour entrance, the numerical model boundaries were located beyond the immediate vicinity of the entrance and the "one-way interaction nesting technique" was adopted in order to achieve the required grid resolution in the harbour basins. Because the boundaries are remote from the region of interest, the use of large-sized domains reduces the sensitivity of the numerical results to the quality of the boundary conditions. As a result, large-sized domains have the advantage of not requiring knowledge of detail boundary data. The nesting technique, being widely used in the modelling of tide-induced flows (see Fisher(1981)), combines the advantages of using large-sized domains with adequate grid resolution in the domain of interest - achieved by the nesting of grids with increasing grid resolution. The numerically predicted results from the harbour model simulations share an encouraging degree of similarity with measurements, with all of the indications being that the model is capable of accurately predicting

tide-induced circulatoty flows and thereby providing useful information to the hydraulic engineer.

A final application of the numerical model to idealised prototype harbours enabled comparisons to be made between prototype and physical model predictions, an exercise which highlighted the problems associated with scaling effects in distorted physical models.

CHAPTER 2

DERIVATION OF THE GOVERNING EQUATIONS FOR DEPTH-AVERAGED TIDAL FLOWS

2.1 Formulation of the Basic Hydrodynamic Equations.

The partial differential equations governing the fluid motion described by the numerical model, are derived from the three-dimensional hydrodynamic equations obtained from Newton's second law for the motion of an arbitrary volume of a deformable continuum. Using Cartesian tensor notation, the basic equations representing an incompressible, Newtonian fluid on a rotating earth, known as the Navier-Stokes equations (see Lamb(1932), Schlichting(1960)), can be written in a "conservation" form to give:

$$\frac{\partial \hat{u}_i}{\partial t} + \frac{\partial \hat{u}_i \hat{u}_j}{\partial x_j} + \frac{1}{\rho}\frac{\partial \hat{P}}{\partial x_i} = X_i + \nu \frac{\partial}{\partial x_j}\left[\frac{\partial \hat{u}_i}{\partial x_j}\right] \tag{2.1}$$

where x_i = Cartesian co-ordinate system in tensor notation = (x,y,z)

$\hat{u}_i$ = instantaneous velocity components

t = time

ρ = fluid density

ν = kinematic viscosity

$\hat{P}$ = instantaneous pressure

X_i = external force components

Likewise, the continuity equation for an incompressible flow can be expressed as (see Lamb(1932)):

$$\frac{\partial \hat{u}_i}{\partial x_i} = 0 \tag{2.2}$$

If it were possible to solve the above equations directly, there would be no need to go further. However, engineering flows in general are almost invariably turbulent and possess scales of motion spanning over a range of several orders of magnitude. Given the need to represent all scales of flow, and the present computational time constraints, it still remains a futile task to seek the true solution of these equations.

The difficulty can be overcome by replacing the instantaneous dependent variables with new "averaged" dependent variables, with a reduced range of scales of flow. The most common "averaging" process is that of Reynolds, see Lamb(1932), who introduced the concept of first replacing an instantaneous value of a dependent variable with a mean and fluctuating component, and then averaging over time. Unfortunately, because of the non-linear character of the Navier-Stokes equations, the averaging process gives rise to additional dependent variables in the form of correlations of the fluctuating components (turbulent fluxes) of the velocity vector. The resulting equations do not constitute a closed system, and the requirement to specify or determine these turbulent fluxes in terms of known or determinable properties already in the equation, and avoid proliferation of higher order correlations is the classical "closure" problem of turbulence. The time averaging process filters the explicit behaviour of certain scales from the turbulent motion, the extent of filtering being set by the length of averaging. A reasonable time scale needs to be large compared with the time scales of turbulence - Dronkers(1964) describes the time length in channel flows as being of the order of minutes, and the r.m.s. of turbulent velocities in tidal currents to be of the order of 15% of the mean velocity. The modelling of the unknown turbulent fluxes must recover to some degree the

lost information, that is, the problem has to be "closed" at a chosen level of recovery. The present work is concerned with modelling first order correlations and it therefore deals with a first order "closure".

The derivation proceeds by substituting the Reynolds decomposition, $\hat{u}_i = u_i + u_i'$ and $\hat{P} = P + P'$, into the Navier-Stokes equations and time-averaging to give the so called Reynolds equations (see Hinze(1975)):

$$\frac{\partial u_i}{\partial t} + \frac{\partial u_i u_j}{\partial x_j} - \frac{1}{\rho}\frac{\partial \tau_{ij}}{\partial x_j} + \frac{1}{\rho}\frac{\partial P}{\partial x_i} = \bar{X}_i + \nu \frac{\partial}{\partial x_j}\left(\frac{\partial u_i}{\partial x_j}\right) \qquad (2.3)$$

where u_i = time-averaged velocity components

P = time-averaged pressure

$\tau_{ij} = -\rho\overline{u_i' u_j'}$ known as the Reynolds stress tensor

u_i' = fluctuating velocity components

and the overbar denotes time-average. For the type of flows being considered in this work the viscous stresses are generally negligible compared to the turbulent Reynolds stresses.

The Reynolds decomposition theory is also applied to the continuity eqn.(2.2) to give:

$$\frac{\partial u_i}{\partial x_i} = 0 \qquad (2.4)$$

The external or body force acting on the fluid includes the effects due to gravity and the earth's rotation - giving rise to the Coriolis force. For a right-hand set of axes, see fig.(2.1), the external forces are included in the Reynolds equations in the following form (see Dronkers(1964)):

(a) The gravitational force is included on the "acceleration" side of the equations in the form of the acceleration due to gravity, g:

$$g_i = 0 \quad \text{for} \quad i=1,2$$
$$= -g \qquad i=3$$

(b) The Coriolis force is also included with the accelerative terms of the equations:

$$f_c u_j \text{ for motion in the direction } (i) = -f_c u_2 \text{ for } i=1$$
$$= +f_c u_1 \qquad i=2$$
$$= 0 \qquad i=3$$

where $f_c = 2\,\Omega \sin\phi$

with Ω = angular velocity of the earth's rotation

and ϕ = geographical latitude

Hence, eqn.(2.3) becomes:

$$\frac{\partial u_i}{\partial t} + \frac{\partial u_i u_j}{\partial x_j} - g_i + f_c u_j + \frac{1}{\rho}\frac{\partial P}{\partial x_i} = \frac{1}{\rho}\frac{\partial \tau_{ij}}{\partial x_j} \tag{2.5}$$

In estuarine and coastal flow systems, the flow is predominantly horizontal and the vertical accelerations associated with the hydrodynamic processes are usually small. Therefore the vertical acceleration and turbulent diffusion are generally neglected so that the equation of motion in the vertical direction (i=3) can be simplified to give the hydrostatic equation:

$$\frac{\partial p}{\partial z} + \rho g = 0 \tag{2.6}$$

This is an important step towards two-dimensionality. In deriving the two-dimensional shallow water equations, Benque et al(1982) made the assumption of a linear variation of the vertical component of velocity

over the depth. As a result the pressure was not hydrostatic, but included effects of the curvature of fluid trajectories. However, when modelling tidal flows, they reverted to a hydrostatic pressure distribution, since tidal heights are very small compared with the tidal wavelengths.

For homogeneous fluids, the integration of eqn.(2.6) gives a linear pressure distribution with depth of the form:

$$P(z) = \int - \rho g \, dz = - \rho g z + c \qquad (2.7)$$

where c is a constant of integration. Using the boundary condition that the pressure at the free surface is atmospheric (Pa) and with reference to the definition sketch of fig.(2.2), the eqn.(2.7) becomes:

$$P(z) = \rho g \, (\eta - z) + Pa \qquad (2.8)$$

The pressure derivatives in the horizontal plane can now be expressed in terms of the water surface elevation as:

$$\frac{\partial P}{\partial x_i} = \rho g \frac{\partial \eta}{\partial x_i} \qquad (2.9)$$

for any horizontal direction x_i and assuming that the atmospheric pressure is uniform over the domain - for the scale of models being investigated, the variations in atmospheric pressure are small. With this simplification of a hydrostatic pressure distribution, the Reynold's equations for the two horizontal directions (i=1,2) become, in Cartesian co-ordinate form:

Momentum in x-direction:

$$\frac{\partial u}{\partial t} + \frac{\partial u^2}{\partial x} + \frac{\partial uv}{\partial y} + \frac{\partial uw}{\partial z} - f_c v + g \frac{\partial \eta}{\partial x} - \frac{1}{\rho} \left(\frac{\partial \sigma_{xx}}{\partial x} + \frac{\partial \tau_{xy}}{\partial y} + \frac{\partial \tau_{xz}}{\partial z}\right) = 0 \qquad (2.10)$$

Momentum in y-direction:

$$\frac{\partial v}{\partial t} + \frac{\partial uv}{\partial x} + \frac{\partial v^2}{\partial y} + \frac{\partial vw}{\partial z} + f_c u + g \frac{\partial \eta}{\partial y} - \frac{1}{\rho} \left(\frac{\partial \tau_{yx}}{\partial x} + \frac{\partial \sigma_{yy}}{\partial y} + \frac{\partial \tau_{yz}}{\partial z}\right) = 0 \qquad (2.11)$$

For completeness, the continuity equation is also given in Cartesian co-ordinate form:

$$\frac{\partial u}{\partial x} + \frac{\partial v}{\partial y} + \frac{\partial w}{\partial z} = 0 \qquad (2.12)$$

In determining the two-dimensional depth-averaged equations of motion, use is made of the kinematic boundary conditions, see Lamb(1932). The free surface is a moving impermeable boundary and its motion is determined by the kinematic condition that no water particles cross the surface, described by:

$$\frac{\partial \eta}{\partial t} + u_\eta \frac{\partial \eta}{\partial x} + v_\eta \frac{\partial \eta}{\partial y} - w_\eta = 0 \qquad (2.13)$$

Likewise, the corresponding boundary condition at the bed, also considered to be an impermeable boundary, becomes:

$$u_{-h} \frac{\partial (-h)}{\partial x} + v_{-h} \frac{\partial (-h)}{\partial y} - w_{-h} = 0 \qquad (2.14)$$

where u_η, v_η and w_η are the velocity components at the water surface, and u_{-h}, v_{-h} and w_{-h} are the velocity components at the bed.

2.2 The Two-Dimensional Depth-Averaged Equations

The two-dimensional depth-averaged hydrodynamic equations can be derived by integrating the three-dimensional eqns.(2.10), (2.11) and (2.12) over the depth, thereby defining the depth-mean velocities in the horizontal plane. Referring to fig.(2.2) the integration limits are $Z = -h(x,y)$ at the bed, and $Z = \eta(x,y)$ at the surface. The momentum equation in the x-direction then becomes:

$$\int_{-h}^{\eta} [\frac{\partial u}{\partial t} + \frac{\partial u^2}{\partial x} + \frac{\partial uv}{\partial y} + \frac{\partial uw}{\partial z} - f_c v + g \frac{\partial \eta}{\partial x} - \frac{1}{\rho}(\frac{\partial \sigma xx}{\partial x} + \frac{\partial \tau_{xy}}{\partial y} + \frac{\partial \tau_{xz}}{\partial z})]dz = 0 \quad (2.15)$$

The integrals may be expanded using Leibnitz's rule, as given by Sokolnikoff and Redheffer(1966):

$$\int_a^b \frac{\partial f(x,\alpha)}{\partial \alpha} dx = \frac{\partial}{\partial \alpha} \int_a^b f(x, \alpha) dx - f(b, \alpha) \frac{\partial b}{\partial \alpha} + f(a,\alpha) \frac{\partial a}{\partial \alpha} \quad (2.16)$$

Use of Leibnitz's rule gives, for eqn.(2.15):

$$\frac{\partial}{\partial t} \int_{-h}^{\eta} u \, dz + \frac{\partial}{\partial x} \int_{-h}^{\eta} u^2 \, dz + \frac{\partial}{\partial y} \int_{-h}^{\eta} uv \, dz - f_c \int_{-h}^{\eta} v \, dz +$$

$$g(h + \eta) \frac{\partial \eta}{\partial x} - \frac{1}{\rho} \frac{\partial}{\partial x} \int_{-h}^{\eta} \sigma_{xx} \, dz - \frac{1}{\rho} \frac{\partial}{\partial y} \int_{-h}^{\eta} \tau_{xy} \, dz - [u_\eta \frac{\partial \eta}{\partial t} + u_\eta^2 \frac{\partial \eta}{\partial x} +$$

$$u_\eta v_\eta \frac{\partial \eta}{\partial y} - u_\eta w_\eta] + [u^2_{-h} \frac{\partial(-h)}{\partial x} + u_{-h} v_{-h} \frac{\partial(-h)}{\partial y} - u_{-h} w_{-h}] + \frac{1}{\rho}$$

$$(\sigma_{xx_\eta} \frac{\partial \eta}{\partial x} + \tau_{xy_\eta} \frac{\partial \eta}{\partial y} - \tau_{xz_\eta} - \sigma_{xx_{-h}} \frac{\partial(-h)}{\partial x} - \tau_{xy_{-h}} \frac{\partial(-h)}{\partial y} + \tau_{xz_{-h}}) = 0 \quad (2.17)$$

In simplifying this equation it is now possible to define the depth-mean velocity components as:

$$U = \frac{1}{(h + \eta)} \int_{-h}^{\eta} u \, dz \tag{2.18}$$

$$V = \frac{1}{(h + \eta)} \int_{-h}^{\eta} v \, dz \tag{2.19}$$

and to express the wind and bottom shear stress components, see Kuipers and Vreugdenhil(1973), as:

$$\tau_{xw} = - \sigma_{xx_\eta} \frac{\partial \eta}{\partial x} - \tau_{xy_\eta} \frac{\partial \eta}{\partial y} + \tau_{xz_\eta} \tag{2.20}$$

$$\tau_{xb} = -\sigma_{xx_{-h}} \frac{\partial (-h)}{\partial x} - \tau_{xy_{-h}} \frac{\partial (-h)}{\partial y} + \tau_{xz_{-h}} \tag{2.21}$$

The velocity components u and v in the advective acceleration terms, may be expressed in terms of the depth-averaged velocities U and V respectively:

$$u = U + (u - U) \tag{2.22}$$

$$v = V + (v - V) \tag{2.23}$$

These equivalences are introduced (see Kuipers and Vreugdenhil(1973)) to treat the non-linear terms and allow the basic equation form of the time-averaged quantities (eqns.(2.10) and (2.11)) to be retained for the depth-averaged quantities. Using, in addition, the kinematic boundary conditions described by eqns.(2.13) and (2.14), eqn.(2.17) is transformed to:

$$\frac{\partial U(h+\eta)}{\partial t} + \frac{\partial U^2(h+\eta)}{\partial x} + \frac{\partial UV(h+\eta)}{\partial y} - f_c(h+\eta)V +$$

$$g(h+\eta)\frac{\partial \eta}{\partial x} - \frac{1}{\rho}(\tau_{xw} - \tau_{xb}) - \frac{1}{\rho}\left\{\frac{\partial}{\partial x}\int_{-h}^{\eta}[\sigma_{xx} - \rho(u-U)^2]\,dz\right.$$

$$\left. + \frac{\partial}{\partial y}\int_{-h}^{\eta}[\tau_{xy} - \rho(u-U)(v-V)]\,dz\right\} = 0 \qquad (2.24)$$

The square bracketed terms constitute the effective stresses which include, in addition to the turbulent Reynolds stresses, extra stress type (dispersion) terms generated by the depth-averaging process. These dispersion terms are momentum transfer terms compensating for the vertical momentum transfer that is being lost once the structure of vertical profiles is depth-averaged out. Any closure attempt on them therefore should be kept separate from the closure on the Reynolds stresses representing momentum transfer due to turbulent motion.

The wind-induced surface shear stress τ_{xw} and the bed friction shear stress τ_{xb} may be simplified using the quadratic friction laws and defined as, for wind-induced stress (see Neumann and Pierson(1966)):

$$\tau_{xw} = C^*\rho_a W W_x \qquad (2.25)$$

and, similarly for bed friction (see Dronkers(1964)):

$$\tau_{xb} = \frac{\rho g U\sqrt{U^2 + V^2}}{C^2} \qquad (2.26)$$

where ρ_a = density of air

W = absolute wind velocity

W_x, W_y = components of wind velocity

C^* = resistance coefficient

C = Chezy coefficient

Using these modifications, eqn.(2.24) becomes:

$$\frac{\partial UH}{\partial t} + \frac{\partial U^2H}{\partial x} + \frac{\partial UVH}{\partial y} - f_c VH + g\,H\frac{\partial \eta}{\partial x} - \frac{C^*\rho_a\, WW_x}{\rho}$$

$$+ \frac{gU\sqrt{U^2+V^2}}{C^2} - \frac{1}{\rho}\left\{\frac{\partial H\,T_{xx}}{\partial x} + \frac{\partial H\,T_{xy}}{\partial y}\right\} = 0 \qquad (2.27)$$

where H = total depth = $(h+\eta)$

T_{xx} = effective depth-mean direct stress

$$= \frac{1}{H}\int_{-h}^{\eta} [\sigma_{xx} - \rho(u-U)^2]\, dz$$

T_{xy} = effective depth-mean shear stress

$$= \frac{1}{H}\int_{-h}^{\eta} [\tau_{xy} - \rho\,(u-U)\,(v-V)]\, dz$$

Likewise, following a similar treatment, the depth-averaged momentum equation in the y-direction becomes:

$$\frac{\partial VH}{\partial t} + \frac{\partial UVH}{\partial x} + \frac{\partial V^2H}{\partial y} + f_c UH + g\,H\frac{\partial \eta}{\partial y} - \frac{C^*\rho_a\, W\,W_y}{\rho}$$

$$+ \frac{gV\sqrt{U^2+V^2}}{C^2} - \frac{1}{\rho}\left\{\frac{\partial\, H\,T_{yx}}{\partial x} + \frac{\partial\, H\,T_{yy}}{\partial y}\right\} = 0 \qquad (2.28)$$

Finally, integration of the continuity eqn.(2.12) over the depth leads to:

$$\frac{\partial \eta}{\partial t} + \frac{\partial UH}{\partial x} + \frac{\partial VH}{\partial y} = 0 \qquad (2.29)$$

2.3 Representation of the Effective Stresses

As already mentioned, the final closure of the two-dimensional depth-averaged hydrodynamic equations requires separate consideration of the turbulent Reynolds stresses and the dispersion terms. A description of the closures chosen and employed in this model follows in this section.

2.3.1 The Turbulent Reynolds Stresses

The set of equations introduced to determine the turbulent transport terms may be of algebraic or differential form, and is known as the "turbulence model". Turbulence models require empirical imput and introduce assumptions which limit the universality of any such numerical models, and preclude the possibility of accurate solutions for all turbulent flows.

2.3.1.1 A Review of Existing Turbulence Models

A number of turbulence models, with variable degrees of complexity, have been proposed over the years. One of the earliest turbulence models is the mixing length hypothesis suggested by Prandtl, see Goldstein(1938). Prandtl based his hypothesis on the kinetic theory of gases and assumed a direct relationship between the Reynolds stresses and the mean velocity field of the following form:

$$\tau_{ij} = -\rho \overline{u_i' u_j'} = -\rho \ell_m^2 \left|\frac{\partial u_i}{\partial x_j}\right| \left(\frac{\partial u_i}{\partial x_j} + \frac{\partial u_j}{\partial x_i}\right) \qquad (2.30)$$

where ℓ_m = a mixing length

Prandtl's hypothesis describes the distribution of Boussinesq's eddy viscosity ν_t, and assumes it to be equal to the product of the mean

velocity gradient and the mixing length squared. Equation(2.30) refers to two-dimensional flows; an expression for general flows has also been proposed, see Goldstein(1938). The mixing length hypothesis involves as a single unknown parameter, the mixing length ℓ_m. However, difficulties in determining ℓ_m in complex flows, restrict the model's use to relatively simple flows. In addition, the mixing length model assumes that turbulence is in local equilibrium and does not account for the transport of turbulence quantities. Therefore apart from the limitations imposed by ν_t and the need to specify ℓ_m, the mixing length model is not suitable when processes of advective or diffusive transport of turbulence are important, see Tennekes and Lumley(1977).

In order to overcome the limitations of the mixing length hypothesis and broaden the general applicability of turbulence models, several authors gave up the idea of a direct relationship between Reynolds stresses and the mean velocity field and tried to account for the transport of turbulence quantities by solving differential transport equations for them.

The earlier investigations in this direction were proposed by Kolmogorov(1942) and Prandtl(1945), who independently proposed a relationship between the eddy viscosity and the intensity of turbulence (known as the Kolmogorov-Prandtl expression):

$$\nu_t = C'_\mu \, L \, \sqrt{k} \tag{2.31}$$

where L = an appropriate length scale

$k = \frac{1}{2}(\overline{u'_i \, u'_i})$ = kinetic energy per unit mass

C'_μ = empirical constant

Using this relationship, the closure problem is shifted to the

determination of k and L. The distribution of k can be determined by solving a transport equation for this quantity - as suggested by Kolmogorov and Prandtl. Such a transport equation can be derived in an exact form, from the Navier-Stokes equation, see Reynolds(1974). For high Reynolds numbers, the equation in its modelled form reads (Rodi(1980)):

$$\underset{(1)}{\frac{\partial k}{\partial t} + u_i \frac{\partial k}{\partial x_i}} = \underset{(2)}{\nu_t \left(\frac{\partial u_i}{\partial x_j} + \frac{\partial u_j}{\partial x_i}\right) \frac{\partial u_i}{\partial x_j}} + \underset{(3)}{\frac{\partial}{\partial x_i}\left(\frac{\nu_t}{\sigma_k} \frac{\partial k}{\partial x_i}\right)} \underset{(4)}{- \varepsilon} \qquad (2.32)$$

where σ_k = empirical constants

and ε = viscous dissipation rate, given by:

$$\varepsilon = C_\Delta \, k^{\frac{3}{2}} / L \qquad (2.33)$$

with C_Δ = empirical constant

Eqn.(2.32), known as the k-equation, expresses the rate of change of k by advection due to the mean flow (term 1), production due to interaction of Reynolds stresses and mean flow (term 2), diffusion due to pressure and velocity fluctuations (term 3) and viscous dissipation (term 4). The model is classified as a "one-equation" turbulence model as it only requires one transport equation for the turbulence quantities. Similar "one-equation" models have been proposed more recently by other workers in this field, most notably among them: Bradshaw et al(1967), Vager and Kagan(1971), Gawain and Pritchett(1970) and Spalding(1967). The first authors did not employ the eddy viscosity concept; instead they obtained from the k-equation a transport equation for the turbulent shear stresses. A major disadvantage of the "one-equation" turbulence models is that the length scale L does not have a very precise definition and, like the mixing length ℓ_m, it is difficult to specify empirically in

complex flows. In addition, the algebraic formulae proposed for its specification in general flows are rather complex and expensive in terms of computing time. However, these models account for advective and diffusive transport of the turbulence velocity scale, and are therefore superior to the mixing length hypothesis when this transport is important.

The difficulties in finding widely valid formulae for calculating the length scale L, have stimulated the use of a further transport equation to determine the distribution of L, since L is subject to transport processes in a similar manner to the kinetic energy k. Models that employ transport equations for both k and L are categorised as "two-equation" turbulence models, some of the most notable being proposed by: Rodi and Spalding(1970), Ng and Spalding(1972), Harlow and Nakayama(1967), Jones and Launder(1972), and Launder and Spalding(1972). Most of the proposed transport equations for the length scale L do not use L as a variable; instead, a second variable Z, of the form $Z = k^m L^n$, is used from which L can be deduced. The modelled form of the transport equation for Z is given as (Rodi(1980)):

$$\underset{(1)}{\frac{\partial Z}{\partial t} + u_i \frac{\partial Z}{\partial x_i}} = \underset{(2)}{\frac{\partial}{\partial x_i}\left(\frac{\sqrt{k}L}{\sigma_Z} \frac{\partial Z}{\partial x_i}\right)} + \underset{(3)}{\frac{Z}{k}\left(C_1 \nu_t \left(\frac{\partial u_i}{\partial x_j} + \frac{\partial u_j}{\partial x_i}\right) \frac{\partial u_i}{\partial x_j}\right)} - \underset{(4)}{C_2 Z \frac{\sqrt{k}}{L}} + \underset{(5)}{S} \qquad (2.34)$$

where C_1, C_2 = empirical constants depending on the form of Z

σ_Z = diffusivity ratio

Eqn.(2.34) expresses the rate of change of the property Z by advection of the mean flow (term 1), diffusion (term 2), interaction of turbulence with the mean flow (term 3), the turbulent energy (term 4) and a secondary source S (term 5).

Several forms of the transported property Z have been suggested and the most frequently used form is when Z is assumed to be the dissipation rate ε. The transport equation for the dissipation rate is known as the ε-equation, and its advantage over the transport equations of all other forms of Z is that it does not require a secondary source S (see Launder and Spalding(1974)). Because of its relative simplicity, the ε-equation has become considerably more popular than any other length scale transport equations, and when used in combination with the k-equation (eqn.(2.32)) and the Kolmogorov-Prandtl expression (eqn.(2.31)) it forms the two-equation "k-ε" turbulence model.

The k-ε model is one of the most widely used and tested turbulence models and its predictive capabilities for shear-layer and confined re-circulating flows are well established. It has been used successfully by many investigators, including: Jones and Launder(1972), Singhal and Spalding(1975), Stephenson(1976), and Naot and Rodi(1982). The k-ε model has also been adapted for use in depth-averaged calculations (see Rodi(1980)), and has been successfully tested by, among others, Rastogi and Rodi(1978), McGuirk and Rodi(1978) and Tong(1982).

In general the "two-equation" models are more universally applicable than the "one-equation" models as they allow the determination of the length scale distribution even in complex flows. However, even if the models describe accurately the transport of the velocity scale assumed to characterize the local state of turbulence, they do not account adequately for the transport of the individual Reynolds stresses as they assume an arbitrary relationship between the stresses and the velocity scale. As a consequence, in order to allow for the different development of the various Reynolds stresses in complex flows and account properly

for their transport, models have been developed which employ transport equations for the individual stresses. These "multi-equation" models offer a direct solution to the closure problem but, are computationally very expensive. Because of their complexity, the models have not been sufficiently tested to-date. However, they have great potential and provide the most useful approach to problems of compex flow situations. Two typical "multi-equation" models were proposed by: Launder, Reece and Rodi(1975), and Hanjalic and Launder(1972). The Reynolds stress equations are derived from the Navier-Stokes equations in a similar manner to the turbulent kinetic energy equation, see Reynolds(1974). They contain equivalent terms to those of the kinetic energy equation, plus an additional term. This term involves correlations between fluctuating pressure and strain rates and acts to re-distribute the energy among its components and reduce the shear stresses, but has no contribution to the total energy balance.

This short review indicates that the more universal turbulence models are generally more complex. However, in practical applications, the choice of the most suitable model involves optimising the usually conflicting demands of universality versus simplicity and accuracy versus economy.

2.3.1.2 Representation of the Reynolds Stresses

In the modelling of large water bodies like ocean waters, simple closures of the "zero-equation" type have been adopted, in general, for the turbulent Reynolds stresses. The simplest closure is the complete neglection of the depth-averaged Reynolds stresses, e.g. Leendertse(1967) and Kuipers and Vreugdenhil(1973)), on the grounds that

these terms are small in comparison with the other terms of the momentum eqns.(2.27) and(2.28). With such closure, the only influence of turbulence is then through the bottom shear stress. However, in the computation of horizontal re-circulating flows, these terms are required to be present as they are vorticity sources (see Flokstra(1977)). Other popular turbulence closures in large scale modelling include the use of a constant eddy viscosity, e.g. Chiu and van de Kreeke(1980) and HRS(1980), empirical eddy viscosity formulae, e.g. Fisher(1976), and Prandtl's mixing-length theory, e.g. Falconer(1977). In some models the eddy viscosity approximation is used to improve numerical stability (see Leendertse(1967)).

The more advanced turbulence models discussed earlier, in section 2.3.1.1, may also be applicable to the modelling of tidal flows. However, the horizontal dimensions of such unsteady water flow problems are so large that grid-independent numerical solutions cannot normally be obtained and, numerical diffusion may influence significantly the numerical predictions and obscure the effects of turbulent diffusion (see Rodi(1980)). Refined modelling of horizontal turbulent transport processes in such flows therefore appears not to be worthwhile, and a "zero-equation" closure has been used in this research study which is described herewith.

Firstly, the direct Reynolds stresses σ_{xx} and σ_{yy} have been neglected as these terms are generally small in re-circulating flows in comparison with the lateral shear stresses τ_{xy} and τ_{yx}, see Kuipers and Vreugdenhil(1973).

In adopting a formulation for the lateral shear stresses, the turbulence in the mixing zone of the re-circulating flows in consideration was separated into its two components, namely: (1) Shear layer turbulence occurring between the main flow and the eddy as a result of the relatively large velocity gradients, and (2) bed generated turbulence. That is, the lateral shear stresses can be represented as:

$$T'_{xy} = T_{xy}|_f + T_{xy}|_b$$

where T'_{xy} = depth-mean turbulent shear stress

$$= \frac{1}{H} \int_{-h}^{\eta} \tau_{xy} \, dz$$

$T_{xy}|_f$ = depth-mean free shear layer stress component

$T_{xy}|_b$ = depth-mean bed generated shear stress component

The eddy viscosity concept has been employed in modelling both components of the shear stresses.

In establishing a formulation for the shear layer turbulence component, use has been made of some semi-empirical concepts and approaches developed from extensive experimental studies of the velocity field characteristics in wakes and jet flows. These investigations have been undertaken by a number of authors and are reviewed in Townsend(1956).

The pronounced horizontal velocity gradients occurring in the mixing zone were approximated in the evaluation of the free shear layer stress components by firstly assuming that the depth-mean velocity distribution could be adequately represented by:

$$U = U_1 \sqrt{\frac{R}{2\pi}} \int_{\gamma}^{\infty} e^{-\frac{1}{2} R (s-\gamma_o)^2} \, ds \qquad (2.35)$$

where U_1 = free stream velocity

R = experimental constant

$\gamma = y'/x'$

$\gamma_o = y_o/l_o$

y_o, l_o = representative scales of flow

x', y' = longitudinal and lateral co-ordinates in the mixing zone as illustrated in fig.(2.3).. In eqn.(2.35) $y' = 0 \rightarrow -\infty$

This composite distribution is in fair agreement with the measurements of Liepmann and Laufer(1947) if $R \cong 288$ and is valid in the range (Townsend(1956)):

$$-2R^{-\frac{1}{2}} \leq \gamma - \gamma_o \leq 2R^{-\frac{1}{2}} \tag{2.36}$$

Eqn.(2.35) can be re-written in an error function form by making the substitution:

$$t = \sqrt{\frac{R}{2}}\,(s-\gamma_o)$$

to give:

$$U = \frac{U_1}{2}\,\frac{2}{\sqrt{\pi}} \int_{\sqrt{\frac{R}{2}}\,(\gamma-\gamma_o)}^{\infty} e^{-t^2}\,dt$$

$$= \frac{U_1}{2}\left[1 + \operatorname{erf}\left\{\sqrt{\frac{R}{2}}\,(\gamma-\gamma_o)\right\}\right] \quad \text{for} \quad y' = 0 \rightarrow +\infty \tag{2.37}$$

However, $\gamma_o = 0$ for a free shear layer (see Lean and Weare(1979), Tong(1982)), and the velocity distribution reduces to:

$$U = U_1 f(\gamma) = \frac{U_1}{2}\left[1 + \operatorname{erf}\left(\sqrt{\frac{R}{2}}\,\gamma\right)\right] \tag{2.38}$$

The mean velocity distribution given by eqn.(2.38) corresponds to an eddy viscosity distribution of the following form (Townsend(1956)):

$$\nu_t\,(y')\Big|_f = \frac{U_1 x'\, f(\gamma)}{R} \tag{2.39}$$

where $\nu_t(y')\Big|_f$ = laterally varying eddy viscosity due to shear layer turbulence

However, Townsend(1956) suggests that a mean eddy viscosity may be applied across the mixing layer, which can be approximated to the value at the centreline ($y'=0$), giving:

$$\nu_t\Big|_f = \frac{U_1 x'}{2R} \tag{2.40}$$

where $\nu_t\Big|_f$ = mean eddy viscosity across mixing layer

Using the Boussinesq representation for the shear stress, the resulting shear layer stress component becomes:

$$T_{xy}\Big|_f = \rho\, \nu_t\Big|_f \frac{\partial U}{\partial y'} = \rho\, \frac{U_1 x'}{2R} \frac{\partial U}{\partial y'} \tag{2.41}$$

The lateral velocity gradient ($\partial U|\partial y'$) can be evaluated from the velocity distribution assumed in eqn.(2.38) by simple application of the chain-rule and the derivative of an error function, expressed as a Hermite polynomial (Abramowitz and Stegun(1966)). Thus the resulting velocity gradient can be written as:

$$\frac{\partial U}{\partial y'} = \frac{U_1}{2} \frac{\partial}{\partial y'} \left[\operatorname{erf} \left(\sqrt{\frac{R}{2}}\, \gamma \right) \right] = U_1 \sqrt{\frac{R}{2\pi}} \frac{1}{x'} e^{-\frac{R}{2}\gamma^2} \tag{2.42}$$

which, on substitution in eqn.(2.41) gives the shear layer stress component in the circulation zone as:

$$T_{xy}\Big|_f = \rho \frac{U_1^2}{2\sqrt{2\pi R}} e^{-\frac{R}{2}\left(\frac{y'}{x'}\right)^2} \tag{2.43}$$

For the bed generated turbulence component, an experimentally determined lateral eddy viscosity, $\nu_{t|b}$, was employed. Numerous investigators have determined $\nu_{t|b}$ by observing the dispersion of marked fluid in uniform conditions and assuming an analogy between the exchange of mass and momentum. Fisher(1973) indicates that the depth-mean lateral eddy viscosity is related to the shear velocity at the bed by the approximate empirical relationship:

$$\nu_t\Big|_b = 0.15\ U_* H \tag{2.44}$$

where U_* = the shear velocity

$= \sqrt{\tau_o/\rho}$

$= \sqrt{g}\ U/C$ (see McDowell and O'Connor(1977))

τ_o = bed shear stress

This equation is a result of a compilation of experiments performed by various researchers. Substitution of eqn.(2.44) into the Boussinesq representation for the shear stress, yields the bed generated component as adopted in this study:

$$T_{xy}\Big|_b = \rho \left(\frac{0.15\ \sqrt{g}\ UH}{C}\right) \frac{\partial U}{\partial y} \tag{2.45}$$

Mixing due to shear layer turbulence dominates when $\nu_t\Big|_f > \nu_t\Big|_b$, which on comparing eqns.(2.40) and (2.44), yields:

$$\frac{1}{2}\ U_1\ \frac{x'}{R} > 0.15\ \frac{1}{2}\ U_1\ \frac{\sqrt{g}}{C}\ H$$

$$\text{or } x' > \frac{43\ \sqrt{g}\ H}{C} \tag{2.46}$$

where $U=\frac{1}{2}U_1$ has been assumed.

For a Chezy coefficient, $C=50\ m^{\frac{1}{2}}/s$, eqn(2.46) indicates that, as far as

turbulent mixing is concerned, the shear layer will begin to dominate within a distance of a few depths downstream of its origin (Lean and Weare(1979)). Hence, eqn(2.46) provides a lower bound for x'.

Shear layer conditions do not, however, prevail indefinitely and an upper bound of x' can be estimated. Lean and Weare(1979), in comparing the rate of production of turbulence energy in the free shear layer with that due to the bed, have estimated the distance x' at which bed generated turbulence is re-established. For a unit mass, invoking eqns.(2.40) and (2.42), the maximum production rate in the shear layer - occurring at the centreline ($y'=0$) - can be expressed as:

$$P_{\text{shear layer}} = \rho\, \nu_t\Big|_f \left[\frac{\partial U}{\partial y'}\right]^2$$

$$= \rho\, \frac{1}{4\pi}\, U_J{}^3\, \frac{1}{x'} \qquad (2.47)$$

On the other hand, the production rate of turbulence energy due to the bed is of the form:

$$P_{\text{bed}} = \tau_o\, \frac{1}{H}\, U$$

$$= \frac{1}{H}\, \rho\, U_*^2\, U$$

$$= \rho\, \frac{1}{8}\, \frac{1}{H}\, U_1^3\, \frac{g}{C^2} \qquad (2.48)$$

where $U = \frac{1}{2}U_1$ has again been assumed at $y'=0$

Hence, the mixing due to bed generated turbulence will be re-established as the dominant mechanism when:

$$P_{\text{bed}} > P_{\text{shear layer}}$$

or

$$x' > \frac{2}{\pi}\, \frac{C^2}{g}\, H \qquad (2.49)$$

which, again for $C=50\ m^{\frac{1}{2}}/s$, indicates that the shear layer will dominate

for up to a few hundred depths downstream.

Therefore, combining both the shear layer and bed generated turbulence within the area of shear layer dominance defined by the limits set in eqns.(2.46) and (2.49), the resulting lateral shear stress representations used in the mathematical model can be summarised as follows:

$$T'_{xy} = \rho \left\{ \frac{U_1^2}{2\sqrt{2\pi R}} e^{-\frac{R}{2}\left(\frac{y'}{x'}\right)^2} + \frac{0.15\sqrt{g}\,UH}{C}\frac{\partial U}{\partial y} \right\} \qquad (2.50)$$

Outside the mixing zone, the turbulent shear stress is simply defined by the bed generated turbulence as:

$$T'_{xy} = \rho \left\{ \frac{0.15\sqrt{g}\,UH}{C}\frac{\partial U}{\partial y} \right\} \qquad (2.51)$$

2.3.2 The Dispersion Terms

A closure of the dispersion terms - occurring as a result of the depth-averaging process - is also required to enable the solution of the depth-averaged equations of motion. A number of investigators have adopted the simplest closure, the complete neglection of the dispersion terms on the assumption that they are small compared with the other terms of the momentum equations (Leendertse(1967), Kuipers and Vreugdenhil(1973), McGuirk and Rodi(1980), Tong(1982)). Kuipers and Vreugdenhil have investigated the importance of these terms by assuming a power-law velocity profile and estimating the relative magnitudes of the various terms in the depth-averaged momentum equations. Their analysis has shown that their contribution relative to the Reynolds shear stresses is of the order of only a few percent.

Flokstra(1977) suggests, however, that the dispersion terms are similar to the Reynolds stresses in that they are also vorticity sources and can be important in the modelling of horizontal circulation. Flokstra deduces a closure model from an assumed power-law velocity profile, which Lean and Weare(1979) suggest can be improved by assuming a logarithmic velocity profile since the latter leads to a better agreement with observations. Lean and Weare have therefore expressed the dispersion terms in the form:

$$\rho \frac{1}{H} \int_{-h}^{\eta} \rho(u-U)(v-V)dz \cong -\rho \frac{H}{r} \frac{U^2}{k^3} \frac{g^{\frac{1}{2}}}{C} (0.8 - 0.4 \frac{g^{\frac{1}{2}}}{kC}) \qquad (2.52)$$

where r = radius of curvature of mean streamline

k = von Karman's constant

In comparing the relative magnitudes of the effective stresses Lean and Weare deduced that, in circulating flows, free shear layer Reynolds stresses dominate when:

$$\frac{L}{H} > 250 \frac{g^{\frac{1}{2}}}{C} \qquad \text{for } r \sim L$$

$$\text{or} \quad \frac{L}{H} > 12.5 \qquad \text{for } C = 50 \text{ m}^{\frac{1}{2}}/\text{s}$$

For shallow water coastal flows typical values of the ratio (L/H) are of the order of 100 (Tong(1982)).

Falconer(1984), on the other hand, employed a seventh power-law velocity profile in the closure of the dispersion terms which may be expressed as:

$$\begin{aligned} \int_{-h}^{\eta} (u-U)^2 \, dz &= 0.016 \, U^2 H \\ \int_{-h}^{\eta} (u-U)(v-V) \, dz &= 0.016 \, UVH \\ \int_{-h}^{\eta} (v-V)^2 \, dz &= 0.016 \, V^2 H \end{aligned} \qquad (2.53)$$

This is the approach adopted in establishing a formulation for the dispersion terms in this model, because of its simplicity and the minimum additional modelling effort involved. That is, the dispersion terms in the form of eqns.(2.53) can de directly included in the advective acceleration terms, which results in this acceleration being multiplied by the coefficient 1.016.

2.4 The Depth-Averaged Vorticity Transport

Before attempting to solve the equations of motion to predict tide-induced circulation, it is worthwhile analysing the transport equation for the vorticity of the depth-mean flow and therefore obtaining a better understanding of the hydrodynamic mechanism by which circulation can be both generated and maintained. The equation of vorticity can be obtained as follows:

Vorticity eqn. = [{eqn.(2.27) - U x eqn.(2.29)}/H]

- [{eqn.(2.28) - V x eqn.(2.29)}/H]

Neglecting the wind stresses, as wind effects have not been included in this research, the vorticity transport equation becomes (Flokstra(1977)):

$$\underbrace{\frac{\partial \omega}{\partial t}}_{(1)} + \underbrace{\frac{\partial (U\omega)}{\partial x} + \frac{\partial (V\omega)}{\partial y}}_{(2)} \underbrace{- f_c \left[\frac{\partial U}{\partial x} + \frac{\partial V}{\partial y}\right]}_{(3)} + \underbrace{\frac{\partial}{\partial y}\left[\frac{\tau_{xb}}{\rho H}\right] - \frac{\partial}{\partial x}\left[\frac{\tau_{yb}}{\rho H}\right]}_{(4)} \underbrace{- \frac{\partial}{\partial y}\left[\frac{1}{\rho H}\frac{\partial}{\partial y}(H\,T_{xy}) + \frac{1}{\rho H}\frac{\partial}{\partial x}(H\,T_{xx})\right] + \frac{\partial}{\partial x}\left[\frac{1}{\rho H}\frac{\partial}{\partial x}(H\,T_{yx}) + \frac{1}{\rho H}\frac{\partial}{\partial y}(H\,T_{yy})\right]}_{(5)} = 0 \qquad (2.54)$$

where ω = depth-mean vorticity = $\frac{\partial U}{\partial y} - \frac{\partial V}{\partial x}$

The terms in eqn.(2.54) refer to: the local change of vorticity (term 1), the advection of vorticity by the mean flow (term 2), production of vorticity by convergence or divergence of the mean flow on

a rotating earth (term 3), the effects of bottom friction (term 4), and moments of the lateral effective stresses relative to a vertical axis (term 5).

In the presence of a circulating flow, there exists a region S bounded by a closed streamline α. Integration of eqn.(2.54) over the bounded area S and application of the divergence theorem (see Weatherburn(1966)) to term 2, term 3 and term 4 yields the following equation in vector form (Flokstra(1977)):

$$\int_S \frac{\partial \omega}{\partial t}\, ds + \oint_\alpha (\underline{v}.\underline{n})\, \omega d\alpha - f_c \oint_\alpha (\underline{v}.\underline{n})\, d\alpha + \oint_\alpha \frac{(\underline{\tau}_b.\underline{t})}{\rho H}\, d\alpha + \int_S E\, ds = 0 \qquad (2.55)$$

where E represents the effective stress terms (term 5)

$\underline{v}$ = the velocity vector

$\underline{\tau}_b$ = the bottom stress vector

$\underline{n},\underline{t}$ = the normal and tangential unit vectors respectively

Since $(\underline{v}.\underline{n}) = 0$ and for a steady flow, the equation reduces to:

$$\oint_\alpha \frac{\underline{\tau}_b.\underline{t}}{\rho H}\, d\alpha + \int_S E\, ds = 0 \qquad (2.56)$$

Substitution of the Chezy quadratic law for $\underline{\tau}_b$ yields an integrant for the first term of eqn.(2.56) of $(g\,(U^2+V^2)/C^2H)$. This expression, always positive, ensures the existence of E, the effective stresses, for circulating flows. Omission of these stresses in this case results in an inconsistent eqn.(2.56). This analysis on steady circulating flows shows and confirms the importance of the effective stresses on vorticity generation.

Equation (2.56) also stresses the importance of bed friction on vorticity transport. Although the overall effect of bed fricton on vorticity is dissipation, an analysis of this term shows that the bed frictional effects are not straightforward. The use of the well established quadratic friction law, gives rise to both sinks and sources of vorticity. This can be explained more fully by expanding the components of term 4 of the vorticity transport eqn.(2.54), see Pingree and Maddock(1980), to give:

$$\frac{\partial}{\partial y}\left[\frac{\tau_{xb}}{\rho H}\right] - \frac{\partial}{\partial x}\left[\frac{\tau_{yb}}{\rho H}\right] = \frac{g}{C^2 H}\left(\underset{(1)}{\bar{V}\omega} - \underset{(2)}{\left\{U\frac{\partial \bar{V}}{\partial y} - V\frac{\partial \bar{V}}{\partial x}\right\}} + \underset{(3)}{\frac{\bar{V}}{H}\left[U\frac{\partial H}{\partial y} - V\frac{\partial H}{\partial x}\right]}\right) \quad (2.57)$$

where $\bar{V}$ = depth-mean velocity speed and the terms of eqn.(2.57) can be thought of as: dissipation of vorticity (term 1), production of vorticity due to quadratic friction (term 2), and production due to bathymetric effects (term 3).

The advection of vorticity by the mean flow - term 2 of eqn.(2.54) - is also an important vorticity source, as argued by Flokstra(1977) on purely theoretical grounds and demonstrated numerically by Kuipers and Vreugdenhil(1973), Lean and Weare(1979) and Falconer et al(1984).

The above analysis of the vorticity transport equation has therefore identified the important vorticity sources and, as this research is concerned with the numerical modelling of circulating flows, particular care has been taken in their numerical representation.

2.5 Formulation of the Advective-Diffusion Equation

The advective-diffusion equation represents conservation of matter for a constituent introduced into a fluid media. For a conservative substance the governing equation can be written, in tensor notation, as (Fisher(1973)):

$$\frac{\partial \hat{s}}{\partial t} + \hat{u}_i \frac{\partial \hat{s}}{\partial x_i} = \gamma \frac{\partial^2 \hat{s}}{\partial x_i \partial x_i} \tag{2.58}$$

where $\hat{s}$ = instantaneous concentration of a conservative substance

γ = molecular diffusivity

However, at high Reynolds numbers, characteristic of engineering flows, the random concentration field has, like the velocity field, spatial structure over a vast range of length scales. As a result, essentially all mathematical models of constituent transport deal with some sort of average concentrations, see Chatwin and Allen(1985), with the time-average approach being most widely employed. Thus, after time-averaging, eqn.(2.58) becomes of the form:

$$\frac{\partial s}{\partial t} + u_i \frac{\partial s}{\partial x_i} = \frac{\partial}{\partial x_i} (-\overline{u_i' s'}) + \gamma \frac{\partial^2 s}{\partial x_i \partial x_i} \tag{2.59}$$

where s = time-averaged concentration

s' = fluctuation in concentration

Chatwin and Allen(1985) argue that eqn.(2.59) cannot be derived rigorously from eqn.(2.58). However, eqn.(2.59) is regarded as an acceptable model equation for the concentration s. The addition of the product of the continuity eqn.(2.4) and the scalar concentration s to eqn.(2.59) gives rise to the "conservation" form of the

advective-diffusion equation which may be expressed as:

$$\frac{\partial s}{\partial t} + \frac{\partial\, su_i}{\partial x_i} = \frac{\partial}{\partial x_i}\,(-\overline{u_i' s'}) \tag{2.60}$$

The molecular diffusion term has been ignored in eqn.(2.60) as in turbulent flows the turbulent diffusion represented by $\frac{\partial}{\partial x_i}\,(-\overline{u_i' s'})$ is generally much more significant than molecular diffusion.

Before eqn.(2.60) can be used to estimate the constituent transport, a description of the turbulent correlations $\overline{u_i' s'}$ in terms of determinable properties is necessary. Closures employing differential transport equations for $\overline{u_i' s'}$, analogous to the transport equations for the Reynolds stresses, have been adopted by various investigators, see Rodi(1980). However, the most common approach is based on the eddy diffusivity concept where, in direct analogy to the turbulent momentum transport, the turbulent mass transport is assumed to be proportional to the gradient of the transported quantity. The resulting equation becomes (Fisher(1973)):

$$\frac{\partial s}{\partial t} + \frac{\partial\, u_i s}{\partial x_i} = \frac{\partial}{\partial x_i}\left(\epsilon_{ij}\,\frac{\partial s}{\partial x_j}\right) \tag{2.61}$$

in which ϵ_{ij} is a tensor of turbulent mixing, called "eddy diffusivity".

Elder(1959) has shown that, provided the time scale for vertical diffusion is short compared to the time scales associated with motion in the horizontal plane (vertically well-mixed flows), often the case in coastal and oceanic waters, constituent transport in a fluid flowing with a free surface may be described in terms of depth-averaged quantities. However, the depth-averaging process leads to an additional diffusion-like term known as the shear-induced dispersion, arising from the

vertical shear and acting in the direction of flow. Therefore, integrating eqn.(2.61) over the depth and imposing the condition that contaminant fluxes through the surface and into the bed are zero, yields the depth integrated advective-diffusion equation, expressed in Cartesian co-ordinates as (see Preston(1985)):

$$\frac{\partial(HS)}{\partial t} + \frac{\partial(HUS)}{\partial x} + \frac{\partial(HVS)}{\partial y} = \frac{\partial}{\partial x}\left[H < \varepsilon_h > \frac{\partial S}{\partial x}\right] + \frac{\partial}{\partial y}\left[H < \varepsilon_h > \frac{\partial S}{\partial y}\right]$$
$$- \frac{\partial}{\partial x}\left[H < (u-U)\ (s-S) >\right] - \frac{\partial}{\partial y}\left[H < (v-V)\ (s-S) >\right]$$
$$+ \frac{\partial}{\partial x}\left[H < \varepsilon_h \frac{\partial(s-S)}{\partial x} >\right] + \frac{\partial}{\partial y}\left[H < \varepsilon_h \frac{\partial(s-S)}{\partial y} >\right] \qquad (2.62)$$

where the angle brackets < > denote depth-averaging

S = depth-averaged concentration

$$= \frac{1}{H} \int_{-h}^{\eta} s\ dz$$

ε_h = horizontal eddy diffusivity on the assumption of isotropic turbulence in the horizontal plane

Preston(1985) went on to approximate eqn.(2.62) to the form:

$$\frac{\partial(HS)}{\partial t} + \frac{\partial(HUS)}{\partial x} + \frac{\partial(HVS)}{\partial y} = \frac{\partial}{\partial x}\left[H(D'_{xx} + < \varepsilon_h >) \frac{\partial S}{\partial x}\right.$$
$$\left. + H\ D'_{xy} \frac{\partial S}{\partial y}\right] + \frac{\partial}{\partial y}\left[H\ D'_{yx} \frac{\partial S}{\partial x} + H\ (D'_{yy} + < \varepsilon_h >) \frac{\partial S}{\partial y}\right] \qquad (2.63)$$

where the quantities D'_{xx}, D'_{xy}, D'_{yx} and D'_{yy} are the coefficients of shear-induced dispersion. Eqn.(2.63) can be expressed in terms of the total dispersion coefficients D_{xx}, D_{xy}, D_{yx} and D_{yy} to give:

$$\frac{\partial(HS)}{\partial t} + \frac{\partial(HUS)}{\partial x} + \frac{\partial(HUS)}{\partial y} = \frac{\partial}{\partial x}\left[H\ D_{xx} \frac{\partial S}{\partial x} + H\ D_{xy} \frac{\partial S}{\partial y}\right]$$
$$+ \frac{\partial}{\partial y}\left[H\ D_{yx} \frac{\partial S}{\partial x} + H\ D_{yy} \frac{\partial S}{\partial y}\right] \qquad (2.64)$$

In cases where it is possible to choose one of the co-ordinates (say x-axis) to be parallel to the direction of flow, it is a consequence of the work by Elder(1959), that the depth-averaged advective-diffusion eqn.(2.64) may be written as:

$$\frac{\partial(HS)}{\partial t} + \frac{\partial(HUS)}{\partial x} = \frac{\partial}{\partial x}\left[D_\ell \, H \, \frac{\partial S}{\partial x}\right] + \frac{\partial}{\partial y}\left[D_t \, H \, \frac{\partial S}{\partial y}\right] \qquad (2.65)$$

where D_ℓ is the longitudinal dispersion coefficient due to both shear-induced dispersion and turbulent diffusion, and D_t is the transverse turbulent diffusion coefficient.

Elder(1959) obtained expressions for both D_ℓ and D_t of the form:

$$D_\ell = k_\ell \, U_* \, H$$

$$D_t = k_t \, U_* \, H \qquad (2.66)$$

where k_ℓ and k_t are constants of proportionality. k_ℓ is larger than k_t as the shear-induced dispersion is normally much larger than the diffusion due to turbulent motion.

Fisher(1978) extended Elder's analysis to the general case when neither of the co-ordinate axes lies parallel to the direction of flow and obtained expressions for the coefficients D_{xx}, D_{xy}, D_{yx} and D_{yy}. However, these expressions require knowledge of the variation of flow with depth, and detailed information of this type may not be available in many practical situations. Subsequently, Preston(1985) went on to suggest a method of obtaining appropriate values for the dispersion coefficients directly from eqns.(2.66), without considering the three-dimensional character of the flow. The resulting expressions are of the form:

$$D_{xx} = \frac{k_\ell U^2 + k_t V^2}{C \bar{V}} \sqrt{g} H$$

$$D_{yy} = \frac{k_\ell V^2 + k_t U^2}{C \bar{V}} \sqrt{g} H \qquad (2.67)$$

$$D_{xy} = D_{xy} = \frac{(k_\ell - k_t) UV}{C \bar{V}} \sqrt{g} H$$

where $\bar{V}$ is the depth mean speed.

It is unclear precisely what values ought to be assigned to the constants of proportionality k_ℓ and k_t as there is considerable disagreement within the literature. A brief review on the investigations and disagreements of longitudinal and transverse dispersion is given by Preston(1985), which reflects the sensitivity of the dispersion coefficients to the way flow and turbulent diffusivity vary with depth.

In this study, the constants k_ℓ and k_t have assumed values of 5.93 after Elder(1959) and 0.15 after Fisher(1973), respectively. Elder(1959) computed the coefficient of longitudinal dispersion on the assumption of a logarithmic profile, and the value of $D_\ell = 5.93 U_* H$ has arisen from a combination of the transverse turbulent diffusion ($D_t = 0.07 U_* H$) and shear-induced dispersion ($D_s = 5.86 U_* H$). He also obtained experimentally that the transverse diffusion coefficient was given by $D_t = 0.23 U_* H$. However, his experiments were restricted to boundary layer flows with Reynolds numbers not exceeding 4500, and consequently his results are unlikely to be universally applicable. Fisher(1973), on the other hand, reviewed a number of experiments to determine the coefficient of transverse diffusion and the value $D_t = 0.15 U_* H$ is the obtained average relation.

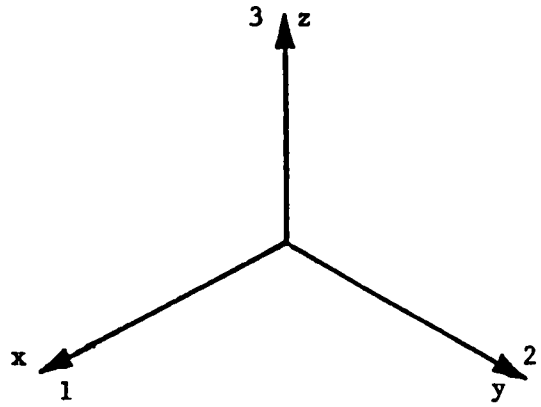

Figure 2.1 Orientation of a right-hand set of axes

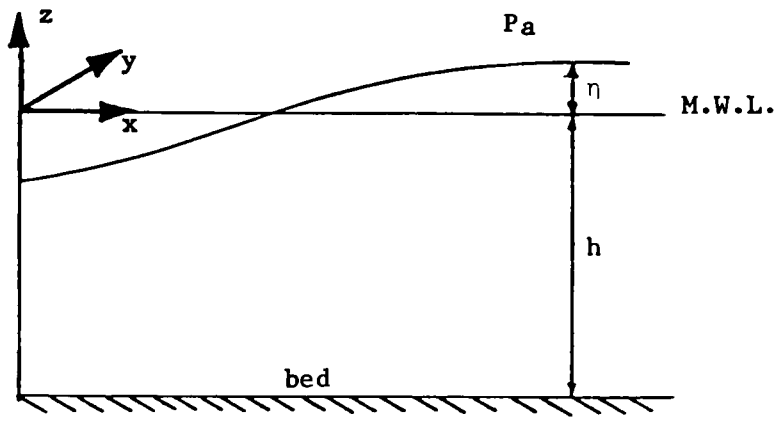

Figure 2.2 Definition diagram for nearly horizontal flow

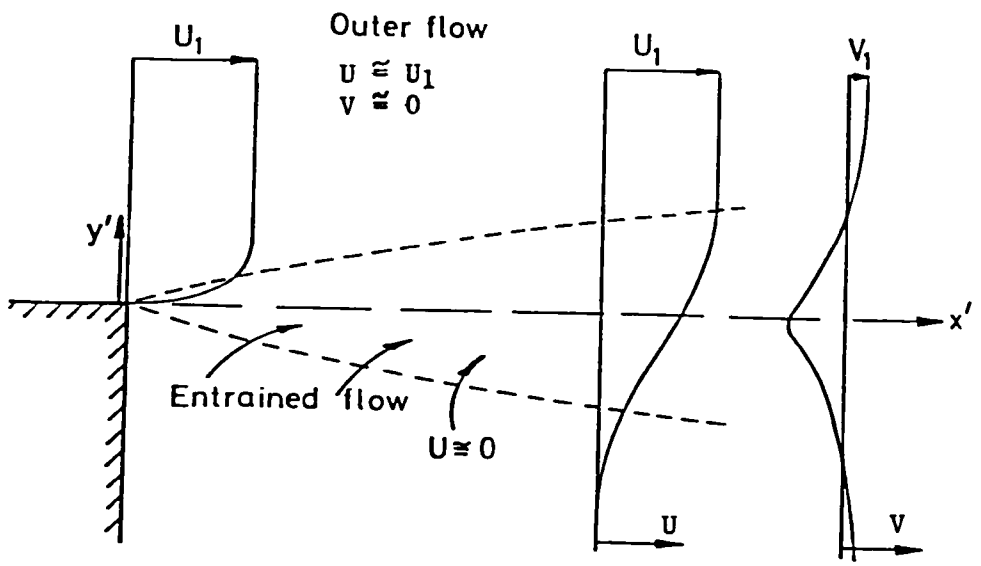

Figure 2.3 Notation for depth-mean velocity profile in the mixing zone of separated flows

CHAPTER 3

NUMERICAL PROPERTIES OF FINITE DIFFERENCE SCHEMES

3.1 Analysis of Finite Difference Schemes

Having established the governing equations for the two-dimensional depth-integrated flow problem, it is a logical sequel to attempt and choose the procedure of their numerical solution.

The finite difference technique has been widely used for the solution of tide-induced flows (see Leendertse(1967), Abbott(1979), Fisher(1981)) and has been adopted in this study. This numerical procedure involves the discretisation of a continuum description in both the space and time dimensions, with the partial differential equations being replaced by difference equations that operate in spatial and time co-ordinates on definite points on the grid system. As a result, the numerical solution produces a finite amount of information at representative points of the continuum problem area, the grid points. The horizontal set of grid points is usually equally spaced (Δx and Δy) with the adjacent time grid points being separated by a chosen timestep, Δt, and the behaviour of a variable at each grid point is described by a function of the variables at other grid points.

The solution of the finite difference equations requires the prescription of initial and boundary conditions. The initial conditions specify a state at the boundary of the time domain from which the solution evolves, and the boundary conditions close the system of equations algebraically and influence the solution at all times. The numerical model is complete when the appropriate finite difference scheme

is chosen to represent the governing equations and the initial and boundary conditions are defined. This chapter deals with the factors affecting the choice of the appropriate finite difference scheme.

In choosing the most suitable finite difference scheme, it is desirable to analyse and compare the numerical properties of the various possible schemes. Each difference scheme may have different numerical properties which may be categorised as:

(1) approximation,

(2) consistency,

(3) convergence,

(4) stability,

(5) accuracy.

The mathematical foundations for the analytical treatment of the above properties of finite difference schemes are well developed for linear systems only, with the results then being used as indication of the behaviour of non-linear systems. To investigate the properties of each scheme, a linearised form of the one-dimensional wave and mass transport equations have been considered herein. These equations may be expressed as, for the continuity:

$$\frac{\partial \eta}{\partial t} + h \frac{\partial U}{\partial x} = 0 \qquad (3.1)$$

the momentum:

$$\frac{\partial U}{\partial t} + U_o \frac{\partial U}{\partial x} + g \frac{\partial \eta}{\partial x} + \frac{g|U|U}{HC^2} - \nu_t \frac{\partial^2 U}{\partial x^2} = 0 \qquad (3.2)$$

and advective-diffusion:

$$\frac{\partial S}{\partial t} + U_o \frac{\partial S}{\partial x} - D\frac{\partial^2 S}{\partial x^2} = 0 \qquad (3.3)$$

where Uo = local depth-mean velocity

$|U|$ = depth-mean velocity speed

D = dispersion coefficient

ν_t = eddy viscosity

The coefficients Uo, $|U|$, D and ν_t have been assumed constant within the domain of the local variables.

The development and comparison of the fundamental difference schemes may be illustrated more readily with the idealised flow wave equations, where the momentum equation may be assumed to be of the form (see Ippen(1966)):

$$\frac{\partial U}{\partial t} + g \frac{\partial \eta}{\partial x} = 0 \qquad (3.4)$$

The analysis of the basic numerical properties of the difference schemes has therefore been performed with special reference to the idealised flow shallow water wave eqns.(3.1) and (3.4).

3.2 Approximation

The discretisation of the governing differential equations introduces truncation errors into the finite difference equations, with the magnitude of such errors reflecting the degree of approximation between the finite difference and differential equations. The Taylor series expansion of the derivatives of the differential equations can be used to determine how well the finite difference equations approximate to the original differential equations.

When a function f(x) and its derivatives are single-valued, finite and continuous functions of x, then Taylor's theorem gives:

$$f(x+\Delta x) = f(x) + \Delta x f'(x) + \frac{1}{2}\Delta x^2 f''(x) + \frac{1}{6}\Delta x^3 f'''(x) + \ldots \qquad (3.5)$$

and

$$f(x-\Delta x) = f(x) - \Delta x f'(x) + \frac{1}{2}\Delta x^2 f''(x) - \frac{1}{6}\Delta x^3 f'''(x) + \ldots . \qquad (3.6)$$

From eqns.(3.5) and (3.6) the first derivative can be approximated in any of the following three forms:

$$f'(x) = \frac{df(x)}{dx} \cong \frac{1}{\Delta x}[f(x+\Delta x) - f(x)] \qquad (3.7)$$

$$f'(x) = \frac{df(x)}{dx} \cong \frac{1}{\Delta x}[f(x) - f(x-\Delta x)] \qquad (3.8)$$

$$f'(x) = \frac{df(x)}{dx} \cong \frac{1}{2\Delta x}[f(x+\Delta x) - f(x-\Delta x)] \qquad (3.9)$$

these being the forward, backward and central difference approximations respectively. The second and higher order derivatives have been ignored which has introduced errors of the order h, or O(h) in eqns.(3.7) and (3.8) and an error $O(h^2)$ in eqn.(3.9). This indicates that in any finite difference scheme, central differences are preferable to either forward or backward differences since they normally give rise to smaller truncation errors. Figure(3.1) gives a graphical representation of the approximation to the tangential slope at a point P on the curve f(x), given by these three different schemes.

Further to the three basic finite difference approximations given by eqns.(3.7) to (3.9), it is now possible to establish four finite difference schemes for the shallow water wave eqns.(3.1) and (3.4), namely:

(i) Forward Explicit:

$$\frac{1}{\Delta t}\left(\eta_i^{n+1} - \eta_i^n\right) + \frac{h}{\Delta x}\left(U_{i+\frac{1}{2}}^n - U_{i-\frac{1}{2}}^n\right) = 0 \tag{3.10}$$

$$\frac{1}{\Delta t}\left(U_{i+\frac{1}{2}}^{n+1} - U_{i+\frac{1}{2}}^n\right) + \frac{g}{\Delta x}\left(\eta_{i+1}^n - \eta_i^n\right) = 0 \tag{3.11}$$

(ii) Central Explicit:

$$\frac{1}{\Delta t}\left(\eta_i^{n+1} - \eta_i^n\right) + \frac{h}{\Delta x}\left(U_{i+\frac{1}{2}}^{n+\frac{1}{2}} - U_{i-\frac{1}{2}}^{n+\frac{1}{2}}\right) = 0 \tag{3.12}$$

$$\frac{1}{\Delta t}\left(U_{i+\frac{1}{2}}^{n+\frac{1}{2}} - U_{i+\frac{1}{2}}^{n-\frac{1}{2}}\right) + \frac{g}{\Delta x}\left(\eta_{i+1}^n - \eta_i^n\right) = 0 \tag{3.13}$$

(iii) Backward Implicit:

$$\frac{1}{\Delta t}\left(\eta_i^{n+1} - \eta_i^n\right) + \frac{h}{\Delta x}\left(U_{i+\frac{1}{2}}^{n+1} - U_{i-\frac{1}{2}}^{n+1}\right) = 0 \tag{3.14}$$

$$\frac{1}{\Delta t}\left(U_{i+\frac{1}{2}}^{n+1} - U_{i+\frac{1}{2}}^n\right) + \frac{g}{\Delta x}\left(\eta_{i+1}^{n+1} - \eta_i^{n+1}\right) = 0 \tag{3.15}$$

and (iv) Central Implicit:

$$\frac{1}{\Delta t}\left(\eta_i^{n+1} - \eta_i^n\right) + \frac{h}{2\Delta x}\left(U_{i+\frac{1}{2}}^{n+1} + U_{i+\frac{1}{2}}^n - U_{i-\frac{1}{2}}^{n+1} - U_{i-\frac{1}{2}}^n\right) = 0 \tag{3.16}$$

$$\frac{1}{\Delta t}\left(U_{i+\frac{1}{2}}^{n+1} - U_{i+\frac{1}{2}}^n\right) + \frac{g}{2\Delta x}\left(\eta_{i+1}^{n+1} + \eta_{i+1}^n - \eta_i^{n+1} - \eta_i^n\right) = 0 \tag{3.17}$$

where the water level η and the velocity U are defined at the grid points i and $i+\frac{1}{2}$ respectively for a space staggered grid.

In an explicit method the unknown value is calculated directly from known values. In the more complex implicit method, however, one unknown is represented in terms of the surrounding unknown values and the difference equations therefore need to be solved simultaneously, requiring greater computational effort in the solution procedure than the explicit method.

The equations of the forward explicit scheme, eqns.(3.10) and (3.11), and the the backward implicit scheme, eqns.(3.14) and (3.15), are not fully time-centred although they are centred in space. Consequently the schemes only have a first order accuracy in time with a leading truncation error $O(\Delta t)$. On the other hand, the central explicit scheme, eqns.(3.12) and (3.13), and the central implicit scheme, eqns.(3.16) and (3.17), are fully centred in both time and space, giving a second order accuracy and a truncation error $O(\Delta t^2, \Delta x^2)$. This observation therefore indicates that the central difference implicit and explicit schemes represent the shallow water wave eqns.(3.1) and (3.4) more accurately.

Diagrammatic representations of the four finite difference schemes, showing clearly the time and space structure of each scheme, are given in Weare(1975) and Falconer(1977).

3.3 Consistency

For the finite difference equations to be consistent with the partial differential equations, the truncation errors introduced by the discretisation of the partial differential equations should tend to zero

in the limit as Δx and Δt both tend to zero. That is, a finite difference equation with a centre point should contract about that point to the original differential equation as Δx and Δt both tend to zero. If this occurs, regardless of how Δx and Δt tend to zero, then the finite difference equations are said to be unconditionally consistent. However, if the truncation errors do not disappear as Δx and Δt tend to zero, the scheme is inconsistent and the solution to the finite difference equations represents the solution to some other differential equations. Inconsistent schemes may sometimes be deliberately chosen in cases where the differential equations do not adequately represent the physical problem, such as where high energy losses occur. An inconsistent scheme may be used in such a way that the residual truncation errors may act as a dissipating force on the energy in the system. An example of frequent use of inconsistent difference schemes is the classic dam break problem, see Mahmood and Yevjevich(1975).

In the case of the shallow water wave eqns.(3.1) and (3.4), where energy losses are generally small, it is important that a consistent scheme is used in order that mass and momentum are conserved. The central implicit scheme is used as an example of checking for consistency. The central time and space points of eqns.(3.16) and (3.17) are at i and $n+\frac{1}{2}$ respectively for the continuity equation and at $i+\frac{1}{2}$ and $n+\frac{1}{2}$ for the momentum equation. The individual terms of the equations do not correspond to the centre points and it is therefore necessary to expand each term about the centre point of the equation, using Taylor's theorem for functions of one or two variables as derived by Zeldovich and Myskis(1976). Taking the continuity eqn.(3.16) and expanding the terms about the centre point $(i,n+\frac{1}{2})$, it can be expressed after re-arranging

the terms as:

$$\left[\frac{\partial \eta}{\partial t} + h\frac{\partial U}{\partial x}\right] + \left[\frac{\partial^3 \eta}{\partial t^3}\frac{\Delta t^2}{24} + \frac{\partial^3 U}{\partial x^3}\frac{h\Delta x^2}{24} + \frac{\partial^3 U}{\partial x \partial t^2}\frac{h\Delta t^2}{4} + \ldots\ldots\right] = 0 \qquad (3.18)$$

The first square bracketed term contains the original partial differential eqn.(3.1) and the second square bracket contains the truncation error. In the limit as Δx and Δt tend to zero all the terms in the second square bracket will tend to zero regardless of the manner in which Δx and Δt diminish. A similar analysis of the momentum equation shows that this too converges about the centre point of the partial differential eqn.(3.4), as Δx and Δt tend to zero. The central implicit scheme therefore satisfies the requirements for unconditional consistency with the original shallow water wave eqns.(3.1) and (3.4). It can also be shown that the three other finite difference schemes are unconditionally consistent with the original equations of motion - see Falconer(1977), where a detailed analysis of the central explicit scheme is given.

3.4 Convergence

Having shown that a particular finite difference scheme is consistent with the original partial differential equations, it is also necessary to check that the solution of the former converges to the solution of the latter as Δx and Δt both tend to zero. Consistency in itself does not necessarily imply convergence, as a scheme may only be convergent for a limited range of Δx and Δt values, and become unstable or even converge to an incorrect solution for values outside this range. It is therefore important that the convergence properties of the solution to a scheme are also known.

In the case of the shallow water wave eqns.(3.1) and (3.4), if the exact solutions of the partial differential equations are denoted by $H(x,T)$ and $u(x,T)$ at some fixed time T, and the exact solutions of the finite difference equations are denoted by $\{\eta(i\Delta x, N\Delta t);\ i=1,2...I,\ n=1,2...N\}$ and $U((i+\frac{1}{2})\Delta x, N\Delta t)$ at time T, so that $N\Delta t=T$, then the finite difference scheme will be convergent if (see Abbott(1979)):

$$\Delta x \sum_{i=1}^{I} \left| \eta\ (i\Delta x,\ N\Delta t) - H(x,\ T) \right| \rightarrow 0$$

$$\Delta x \sum_{i=1}^{I} \left| U((i+\tfrac{1}{2})\ \Delta x,\ N\Delta t) - u\ (x,\ T) \right| \rightarrow 0 \qquad (3.19)$$

for every choice of $N\Delta t=T$ as $\Delta x \rightarrow 0$ and $\Delta t \rightarrow 0$.

Convergence is a difficult problem to investigate analytically because the final expressions derived for the discretisation error, defined as the difference between the exact solutions of the partial differential and finite difference equations, are usually in terms of unknown derivatives for which no bounds can be estimated, see Smith(1978). However, for linear systems with constant coefficients, operating on uniformly continuous initial and boundary data, convergence can be investigated in terms of stability and consistency by making use of Lax's equivalence theorem. This states that (see Richtmyer and Morton(1967), Ames(1969)): "Given a properly posed initial value problem and a finite difference approximation to it that satisfies the consistency condition, stability is the necessary and sufficient condition for convergence".

3.5 Stability

In the previous section on convergence, the exact solutions to the finite difference equations, $U^n_{i+\frac{1}{2}}$ and η^n_i were mentioned. These exact numerical solutions would, in theory, be obtained only if all the calculations were carried out to an infinite number of decimal places. However, in practice, each calculation is carried out to a finite number of decimal places by the computer, a procedure that introduces a rounding error during each calculation step. As a result, the calculated solution is different to the exact numerical solution because of the cumulative effect of the rounding errors. The study of stability in a finite difference scheme is the determination of the behaviour of the cumulative rounding errors as the calculation progresses, as defined by O'Brien et al(1951). A finite difference scheme will be stable if the cumulative effect of the rounding errors is negligible. If, on the other hand, the rounding errors are amplified in an unlimited manner as the computation progresses, then the scheme is said to be unstable and the correct solution is usually swamped by the growth of these errors. A more general definition of stability, see Richtmyer and Morton(1967), requires that the set of computed solutions are always uniformly bounded - otherwise the difference scheme is found to be unstable. It is therefore important that the stability of any numerical scheme is checked before undertaking any solution procedure.

A number of methods of analytically investigating the boundedness of the solution of a finite difference scheme exist, see Roache(1976). Two standard methods of stability analysis include the matrix method which involves expressing the equations in matrix form and examining the eigenvalues of an associated matrix, and the Fourier series method which

involves the use of a finite Fourier series leading to the evaluation of an amplification factor which reflects the time dependent behaviour of the rounding errors. The Fourier method is generally the easiest and most straightforward, in that it requires no knowledge of matrix algebra, but it is less rigorous in that it neglects the boundary conditions. Because of its simplicity the Fourier method has been adopted in this study.

The Fourier stability analysis, developed by von Neumann (see O'Brien et al(1951)) will be illustrated by applying it to the central implicit scheme defined by eqns.(3.16) and (3.17). The first step in determining the stability of a scheme is to assume that at t=0 there is an initial line of errors, for both U and η, at every grid point within the flow field, and that these errors are propagated through time by the calculation. These initial error lines U_* and η_* may be represented in the form of a finite, complex exponential Fourier series as follows:

$$\eta_{*_i} = \sum_{p=0}^{N} A_p \, e^{j \beta_p i \Delta x} \tag{3.20}$$

where $i = 0, 1, 2, \ldots I$

I = total number of grid points

A_p = coefficients of the Fourier series

β_p = wave numbers = $i\pi / I\Delta x$

$j = \sqrt{-1}$

Since the finite difference eqns.(3.16) and (3.17) are linear, with additive solutions, it is possible to consider the propagation of the error due to a single term from the series, giving:

$$\eta_{*i} = \eta_* \, e^{j\beta i\Delta x} \tag{3.21}$$

where $\beta = 2\pi/L$

L = wavelength

The error η_{*i} is also time dependent and can therefore be expressed as:

$$\eta^n_{*i} = \eta_* \, \lambda^n \, e^{j\beta i\Delta x} \tag{3.22}$$

where $\lambda = |\lambda| \, e^{j\sigma\Delta t}$

$n = 0, 1, 2, \ldots N$

N = number of timesteps considered

σ = wave frequency = $2\pi/T$

T = wave period

A similar expression can be derived for the error in the velocity field U.

The error functions η^n_{*i} defined by eqn.(3.22), and U^n_{*i}, will not grow with time if the modulus of the amplification factor λ does not exceed unity, i.e.:

$$|\lambda| \leqslant 1 \tag{3.23}$$

This is the von Neumann stability condition, which is necessary and sufficient for two time-level finite difference equations, but is not always sufficient for three or more time-level equations - although it is always necessary (see Smith(1978)).

The error functions η^n_{*i} and U^n_{*i} will satisfy the same difference equation as η^n_i and U^n_i and their substitution into the central implicit difference eqns.(3.16) and (3.17) therefore gives:

$$\eta_* \left[\lambda^{n+1} e^{j\beta i\Delta x} - \lambda^n e^{j\beta i\Delta x} \right] + U_* \frac{h\Delta t}{2\Delta x} \left[\lambda^{n+1} e^{j\beta(i+\frac{1}{2})\Delta x} + \lambda^n e^{j\beta(1+\frac{1}{2})\Delta x} \right.$$

$$\left. - \lambda^{n+1} e^{j\beta(i-\frac{1}{2})\Delta x} - \lambda^n e^{j\beta(i-\frac{1}{2})\Delta x} \right] = 0 \qquad (3.24)$$

$$U_* \left[\lambda^{n+1} e^{j\beta(i+\frac{1}{2})\Delta x} - \lambda^n e^{j\beta(i+\frac{1}{2})\Delta x} \right] + \eta_* \frac{g\Delta t}{2\Delta x} \left[\lambda^{n+1} e^{j\beta(i+1)\Delta x} \right.$$

$$\left. + \lambda^n e^{j\beta(i+1)\Delta x} - \lambda^{n+1} e^{j\beta i\Delta x} - \lambda^n e^{j\beta i\Delta x} \right] = 0 \qquad (3.25)$$

Dividing eqn.(3.24) by $\lambda^n e^{j\beta i\Delta x}$ and eqn.(3.25) by $\lambda^n e^{j\beta(i+\frac{1}{2})\Delta x}$ gives:

$$\eta_* (\lambda - 1) + U_* \frac{h\Delta t}{2\Delta x} (\lambda + 1)\, 2j \sin\theta = 0 \qquad (3.26)$$

$$U_* (\lambda - 1) + \eta_* \frac{g\Delta t}{2\Delta x} (\lambda + 1)\, 2j \sin\theta = 0 \qquad (3.27)$$

where $\theta = \frac{1}{2}\beta\Delta x$. Elimination of U_* from eqns.(3.26) and (3.27) yields the following quadratic equation for λ :

$$\lambda^2 (1 + \mu^2 \sin^2\theta) - 2\lambda (1 - \mu^2 \sin^2\theta) + (1 + \mu^2 \sin^2\theta) = 0 \qquad (3.28)$$

where $\mu = \sqrt{gh}\, \frac{\Delta t}{\Delta x}$ and is defined as the Courant number. Solution of eqn.(3.28) gives the following complex values for λ:

$$\lambda = \frac{(1 - \mu^2 \sin^2\theta) \pm 2j\mu \sin\theta}{(1 + \mu^2 \sin^2\theta)} \qquad (3.29)$$

Hence, the stability requirement is that the modulus of λ of eqn.(3.29) must be less than or equal to one. Using complex algebra, it can be shown that the modulus of λ in eqn.(3.29) is equal to one for all values of μ and θ . The central implicit scheme is therefore unconditionally stable, with the original rounding errors neither growing nor decaying with time.

A similar stability analysis for the three other finite difference schemes yields the following equations for λ and $|\lambda|$ respectively:

Forward Explicit:

$$\lambda = 1 \pm 2j\mu\sin\theta$$

$$|\lambda| = (1 + 4\mu^2\sin^2\theta)^{\frac{1}{2}} \tag{3.30}$$

Central Explicit:

$$\lambda = (1 - 2\mu^2\sin^2\theta) \pm 2j\mu\sin\theta\ (1 - \mu^2\sin^2\theta)^{\frac{1}{2}}$$

$$|\lambda| = 1 \text{ if } \mu\sin\theta < 1 \tag{3.31}$$

Backward Implicit:

$$\lambda = (1 + 2j\mu\sin\theta)^{-1}$$

$$|\lambda| = (1 + 4\mu^2\sin^2\theta)^{-\frac{1}{2}} \tag{3.32}$$

Equation(3.30) shows that the modulus of λ is always greater than one since the term $4\mu^2\sin^2\theta$ is always positive. Consequently, the forward explicit scheme is always unstable.

The stability condition for the central explicit scheme is given by eqn.(3.31), where it is shown that the scheme is stable only for a limited range of Δx and Δt. The maximum constraint comes from $\theta = \frac{\pi}{2}$, which corresponds to a wavelength $L=2\Delta x$ i.e. the shortest representable wavelength. The stability condition is then simplified to:

$$\mu \leqslant 1 \quad \text{or} \quad \sqrt{gh}\,\frac{\Delta t}{\Delta x} \leqslant 1 \tag{3.33}$$

This stability constraint is rather severe for the type of flow fields being modelled, see Falconer(1977). Severe restrictions on the timestep tend to make the scheme computationally expensive.

The backward implicit scheme has an amplification factor whose modulus is always less than unity, since the term $4\mu^2\sin^2\theta$ is always positive. It therefore follows that the backward implicit scheme is unconditionally stable with the added advantage that rounding errors are inherently dissipated by the scheme.

From a comparison of the stability properties of the four finite difference schemes, it is clear that the forward explicit scheme should be disregarded on the grounds of unconditional instability. The central explicit scheme is also unattractive for many small scale civil engineering applications since the severe restrictions on the timestep can make it computationally uneconomical when compared with the implicit schemes and their theoretically unlimited timestep size. Either of the implicit schemes may be chosen as they are both unconditionally stable. The central implicit scheme, however, is usually preferred because of its second order accuracy as compared with the first order accuracy of the backward implicit scheme.

So far, the stability analysis has only been applied to the simplified wave eqns.(3.1) and (3.4). However, it is also desirable to study the effects on the stability of difference schemes as a result of the advective and diffusive terms of the shallow water wave equations. To investigate these effects each term can be individually introduced into the momentum eqn.(3.4) and a Fourier stability analysis undertaken. The Fourier stability analysis described above, based on the propagation of one Fourier component, applies only to linear systems of equations since in non-linear systems each term in a Fourier series can no longer propagate independently as different components interact with one another through the non-linear terms. However, it is possible to get some indication of the stability properties of a non-linear finite difference scheme by analysing the linearised system of equations obtained by considering part of the non-linear term to be constant within the locality of the dependent variable, as illustrated in eqn.(3.2). A similar procedure may be followed to examine the effects on the stability of difference schemes as a result of the advective and diffusive terms of the advective-diffusion eqn.(3.3).

In considering the stability effect of the advective acceleration term on the scheme, the term can be introduced, in a quasi-linear form, into the momentum eqn.(3.4) to give:

$$\frac{\partial U}{\partial t} + U_o \frac{\partial U}{\partial x} + g \frac{\partial \eta}{\partial x} = 0 \qquad (3.34)$$

Using the central implicit scheme with the advective accelerations expressed in a time-centred form, see Falconer(1977), the momentum eqn.(3.34) can be expressed as:

$$U_{i+\frac{1}{2}}^{n+1} - U_{i+\frac{1}{2}}^{n} + \frac{U_o \Delta t}{\Delta x}(U_{i+\frac{3}{2}}^{n+\frac{1}{2}} - U_{i-\frac{1}{2}}^{n+\frac{1}{2}}) + \frac{g\Delta t}{2\Delta x}(\eta_{i+1}^{n+1} + \eta_{i+1}^{n} - \eta_{i}^{n+1} - \eta_{i}^{n}) = 0 \quad (3.35)$$

When a Fourier stability analysis is applied to eqns.(3.35) and (3.16), the solution of a quartic equation is required for the determination of the amplification factor. A further simplification can be made by eliminating the water surface elevation term - particularly since this term has already been shown to be stable. Equation(3.35) is therefore only expressed in terms of the velocity U, and the use of eqn.(3.16) is not required. A stability analysis on the resulting momentum equation yields the following quadratic equation for the amplification factor α:

$$\alpha^2 + (2\, j\, \gamma \sin\theta)\, \alpha - 1 = 0 \quad (3.36)$$

where $\alpha = \lambda^{\frac{1}{2}}$

and $\gamma = \frac{U_o \Delta t}{\Delta x}$

Solving eqn.(3.36) for α, gives:

$$\alpha = \pm \sqrt{1 - \gamma^2 \sin^2\theta} - j\gamma\sin\theta \quad (3.37)$$

Provided that $\gamma^2 \sin^2 \theta < 1$ the modulus of α can be shown to be equal to one. For the limiting case when $\theta = \pi/2$ the stability constraint reduces to:

$$\frac{U_o\, \Delta t}{\Delta x} \leqslant 1 \qquad \text{or} \qquad |U| \leqslant \frac{\Delta x}{\Delta t} \quad (3.38)$$

which for the type of flows being modelled is not a severe constraint (see Falconer(1977)). The constraint is removed when the double iteration method is used to express the advective acceleration term in a time centred form. This method first expresses the advective acceleration term in an explicit form, at the lower timestep n, to obtain

a first estimate of $\dot{U}_i^{n+1}$, while for the second iteration the advection term is time-centred as a result of the average $U_i^{n+\frac{1}{2}} = \frac{1}{2}(U_i^n + \dot{U}_i^{n+1})$, and appears to be unconditionally stable (see Pearson(1965)).

If the advective acceleration term is not fully time-centred, non-linear instabilities are fed into the system. A physical explanation of non-linear instabilities, given by Phillips(1959), is based on the mechanism of energy transfer: Energy is transferred by non-linear interactions from large scales towards smaller and smaller scales until it is eventually dissipated by friction. The dissipation scales are generally much smaller than the grid size used in numerical models and, as scales smaller than twice the grid size cannot be reproduced numerically, the energy transfer is interrupted at that scale with the result of an energy "pile-up" at the wavelength of twice the grid size. Weare(1976) has shown both numerically and analytically that an imperfect time-centering of the non-linear terms introduces such instabilities into the scheme, which may be controlled by the friction term. Similarly, the advection term of the advective-diffusion eqn(3.3) is required to be time-centred to avoid introducing instabilities into the scheme.

The stability effect of the bed friction on the scheme, may be determined by analysing the following momentum equation:

$$\frac{\partial U}{\partial t} + g \frac{\partial \eta}{\partial x} + g \frac{|U|U}{H\, C^2} = 0 \qquad (3.39)$$

Expressing the friction term in a fully centred implicit form, the corresponding central difference representation of eqn.(3.39) can be shown to be:

$$U_{i+\frac{1}{2}}^{n+1} - U_{i+\frac{1}{2}}^{n} + \frac{g\Delta t}{2\Delta x}(\eta_{i+1}^{n+1} + \eta_{i+1}^{n} - \eta_{i}^{n+1} - \eta_{i}^{n}) + \frac{Q\Delta t|U|}{2}(U_{i+\frac{1}{2}}^{n+1} + U_{i+\frac{1}{2}}^{n}) = 0 \quad (3.40)$$

where $Q = \frac{g}{HC^2}$

A stability analysis of eqns.(3.40) and (3.16) leads to the following quadratic equation for λ:

$$(1 + \mu^2 \sin^2\theta + \delta)\lambda^2 + (2\mu^2 \sin^2\theta - 2)\lambda + (1 + \mu^2 \sin^2\theta - \delta) = 0 \quad (3.41)$$

where $2\delta = Q\Delta t\,|U|$

The solution of eqn.(3.41) yields the following expressions for λ and $|\lambda|$:

$$\lambda = \frac{(1-\mu^2 \sin^2\theta) \pm \sqrt{\delta^2 - 4\mu^2 \sin^2\theta}}{(1+\mu^2 \sin^2\theta+\delta)} \quad (3.42)$$

$$|\lambda| = \left(\frac{1+\mu^2 \sin^2\theta - \delta}{1+\mu^2 \sin^2\theta + \delta}\right)^{\frac{1}{2}} < 1 \qquad \text{for } \delta^2 < 4\mu^2 \sin^2\theta \quad (3.43)$$

$$|\lambda| = \left|1 - \frac{\delta+2\mu^2 \sin^2\theta \pm (\delta^2 - 4\mu^2 \sin^2\theta)^{\frac{1}{2}}}{\delta+\mu^2 \sin^2\theta + 1}\right| < 1 \quad (3.44)$$

$$\text{for } \delta^2 > 4\mu^2 \sin^2\theta$$

The scheme is therefore unconditionally stable, with the bed friction improving the stability properties of the scheme's damping capacity. This damping effect of the friction term may also counteract instabilities introduced into the scheme through other terms, such as the wind stress (see Falconer(1977)).

The stability effect of the Reynolds stress can be determined by analysing the following momentum equation:

$$\frac{\partial U}{\partial t} + g\frac{\partial \eta}{\partial x} - \nu_t \frac{\partial^2 U}{\partial x^2} = 0 \quad (3.45)$$

Because of the second order derivative in the Reynolds stress term, its finite difference representation is not straightforward. If it is expressed in a fully centred implicit manner, like the friction term, it complicates the solution procedure and increases the computational costs because it requires the setting up of a five-diagonal matrix array of coefficients rather than a three-diagonal matrix as required by the other terms (see Falconer(1977)). On the other hand, the dispersion term of the advective-diffusion eqn.(3.3) - of the same form as the Reynolds stress - can be expressed in an implicit time-centred form without imposing such implications on the solution. This is because the solution procedure for this equation involves the constituent concentration S as the only unknown variable, unlike the shallow water wave equations where both U and η are the unknown variables. The expression of the dispersion term in an implicit time-centred form imposes no stability constraints on the difference schemes (see Leendertse(1970)).

Although the Reynolds stress can be represented explicitly, at the lower timestep n, it imposes a stability constraint on the scheme. This constraint, though not severe for the flows considered here, requires that (see Roache(1976)):

$$\nu_t \frac{\Delta t}{\Delta x^2} \leq \tfrac{1}{2} \tag{3.46}$$

A well-known explicit method for removing this constraint is the Du-Fort and Frankel difference representation. This representation leads to the following equation:

$$U_{i+\frac{1}{2}}^{n+1} - U_{i+\frac{1}{2}}^{n} + \frac{g\Delta t}{2\Delta x}(\eta_{i+1}^{n+1} + \eta_{i+1}^{n} - \eta_{i}^{n+1} - \eta_{i}^{n}) +$$

$$\nu_t \frac{\Delta t}{\Delta x^2}(U_{i+\frac{3}{2}}^{n+\frac{1}{2}} - 2\,(U_{i+\frac{1}{2}}^{n+1} + U_{i+\frac{1}{2}}^{n}) + U_{i-\frac{1}{2}}^{n+\frac{1}{2}}) = 0 \tag{3.47}$$

When a Fourier stability analysis is applied to eqns.(3.47) and (3.16), a quartic equation for the amplification factor results and, like the stability analysis of the advective acceleration term, the analysis is performed on the simplified momentum eqn.(3.47) with the water elevation ignored. A quadratic equation for the amplification factor α is deduced, which is:

$$(1+\phi)\,\alpha^2 - (2\phi\,\cos 2\theta)\,\alpha + (\phi-1) = 0 \qquad (3.48)$$

where $\phi = \nu_t \dfrac{\Delta t}{\Delta x^2}$

Solving eqn.(3.48) for α and $|\alpha|$ gives:

$$\alpha = \frac{\phi\,\cos 2\theta \pm \sqrt{1-\phi^2\,\sin^2 2\theta}}{(1+\phi)} \qquad (3.49)$$

$$|\alpha| = \frac{\phi-1}{\phi+1} < 1 \quad \text{for } \phi^2 \sin^2\theta > 1 \qquad (3.50)$$

$$|\alpha| = \left| 1 - \frac{1+\phi-\phi\,\cos 2\theta \pm (1-\phi^2\,\sin^2 2\theta)^{\frac{1}{2}}}{1+\phi} \right| < 1 \text{ for } \phi^2 \sin^2\theta \leq 1 \qquad (3.51)$$

Consequently, since ϕ is always positive, the moduli of the amplification factors are always less than one and the stability condition is therefore always met. The disadvantage of this representation is that it is not unconditionally consistent and requires $\Delta t/\Delta x \to 0$ in the limit as $\Delta t, \Delta x \to 0$ for consistency, see Roache(1976). The consistency condition may be avoided when use is made of the double iteration method, where the Reynolds stress is represented explicitly, at the lower timestep n, during the first iteration, and time-centred during the second iteration.

The stability analysis presented for the one-dimensional wave equations can be extended to two dimensions in a straightforward manner, see Roache(1976), Ramming and Kowalic(1980). A stability analysis on the two-dimensional shallow water wave equations gives rise to the following stability constraints, see Weare(1975):

The central explicit scheme stability condition becomes:

$$\sqrt{2}\ \sqrt{gh}\ \frac{\Delta t}{\Delta x} \leqslant 1 \tag{3.52}$$

The non-linear advective acceleration terms, when expressed in the form of eqn.(3.35), impose a constraint of the form:

$$|U| + |V| \leqslant \frac{\Delta x}{\Delta t} \tag{3.53}$$

The Coriolis terms give rise to a weak constraint on the timestep by the condition:

$$f_c\ \Delta t \leqslant 1 \tag{3.54}$$

3.6 Accuracy

The analysis used to study the stability of difference schemes may be extended to give a useful description for their accuracy. Although a finite difference scheme may be both stable and consistent with the original differential equations, the sum of the truncation errors may be large enough to provide a relatively inaccurate numerical solution. For the shallow water wave eqns.(3.1) and (3.4), a measure of accuracy may be obtained by comparing the celerities of the numerical and physical waves, see Leendertse(1967). To illustrate this method of analysis for the accuracy, the central implicit scheme - eqns.(3.16) and (3.17) - is used. The scheme has already been shown to be consistent and unconditionally

stable, with an amplification factor λ of:

$$\lambda = \frac{(1 - \mu^2 \sin^2\theta) \pm 2j\mu\sin\theta}{(1 + \mu^2 \sin^2\theta)} \tag{3.55}$$

Defining the numerical wave celerity as:

$$C_n = \frac{L}{T} = \frac{\sigma}{\beta} \tag{3.56}$$

and with the shallow water celerity being:

$$C_p = \sqrt{gh} \tag{3.57}$$

the numerical accuracy of the scheme is then given by the ratio:

$$\frac{C_n}{C_p} = \frac{\sigma}{\beta\sqrt{gh}} \tag{3.58}$$

From the definition of the amplification factor, $\lambda = |\lambda| e^{j\sigma\Delta t}$, it can be shown that the complex number λ has an argument of $\sigma\Delta t$ and, therefore the wave frequency σ can be expressed as:

$$\sigma = \frac{1}{\Delta t} \arg.\lambda \tag{3.59}$$

and eqn.(3.58) becomes:

$$\frac{C_n}{C_p} = \frac{\arg.\lambda}{2\mu\theta} \tag{3.60}$$

where $\theta = \frac{1}{2}\beta\Delta x$

and $\mu = \sqrt{gh}\ \frac{\Delta t}{\Delta x}$

Using eqn.(3.55) it can be shown that the argument of λ is given by:

$$\arg.\lambda = \sigma\Delta t = \tan^{-1}\left[\frac{2\mu\sin\theta}{1 - \mu^2\sin^2\theta}\right] \tag{3.61}$$

When the division within the bracket is carried out and the trigonometric functions replaced by the corresponding series expansions, eqn.(3.61) becomes (see Cox(1981)):

$$\arg.\lambda = \tan^{-1}\left[2\mu\left(\theta - \frac{\theta^3}{3!} + \frac{\theta^5}{5!} - \frac{\theta^7}{7!} + \ldots\ldots\right)\left\{1 + \mu^2\left(\theta - \frac{\theta^3}{3!} + \frac{\theta^5}{5!} - \ldots\ldots\right)^2 + \mu^4\left(\theta - \frac{\theta^3}{3!} + \frac{\theta^5}{5!} - \ldots\ldots\right)^4 + \ldots\ldots\right\}\right] \tag{3.62}$$

which reduces to:

$$\arg.\lambda = 2\mu\theta\left(1 - \frac{\theta^2}{6} - \frac{\theta^2\mu^2}{3} - \ldots\ldots\right) \text{ for } \mu\theta \leqslant \tfrac{1}{2} \tag{3.63}$$

and

$$\arg.\lambda = \frac{\pi}{2} - \frac{1}{2\mu\theta\left(1 - \frac{\theta^2}{6} + \mu^2\theta^2 + \ldots\ldots\right)} + \frac{1}{3\left[2\mu\theta\left(1 - \frac{\theta^2}{6} + \mu^2\theta^2 + \ldots\right)\right]^3} - \ldots\ldots \text{ for } \mu\theta > \tfrac{1}{2} \tag{3.64}$$

This gives, for the measure of accuracy:

$$\frac{C_n}{C_p} = \left(1 - \frac{\theta^2}{6}\left(1 + 2\mu^2 + \ldots\ldots\right)\right) \text{ for } \mu\theta \leqslant \tfrac{1}{2} \tag{3.65}$$

and

$$\frac{C_n}{C_p} = \frac{\pi}{4\mu\theta} - \frac{1}{4\mu^2\theta^2\left(1 - \frac{\theta^2}{6} + \mu^2\theta^2 + \ldots\right)} + \frac{1}{48\mu^4\theta^4\left(1 - \frac{\theta^2}{6} + \mu^2\theta^2 + \ldots\right)^3} - \ldots$$

for $\mu\theta > \frac{1}{2}$ (3.66)

The numerical accuracy for the central explicit and backward implicit schemes may similarly be described as (see Falconer(1977)):

Central Explicit:

$$\frac{C_n}{C_p} = \left[1 - \frac{\theta^2}{6}\left(1 - \mu^2 + \ldots\right)\right] \tag{3.67}$$

Backward Implicit:

$$\frac{C_n}{C_p} = [1 - \frac{\theta^2}{6}(1 + 8\mu^2 + ...)] \text{ for } \mu\theta \ll \tfrac{1}{2} \qquad (3.68)$$

and

$$\frac{C_n}{C_p} = \frac{\pi}{4\mu\theta} - \frac{1}{4\mu^2\theta^2(1 - \frac{\theta^2}{6} + ...)} + ... \text{ for } \mu\theta > \tfrac{1}{2} \qquad (3.69)$$

The accuracy of each of the three schemes is represented graphically in figs.(3.2), (3.3) and (3.4), which have been reproduced from Falconer(1977).

It is clear from the equations describing the accuracy of schemes and their graphical representations, that the backward implicit scheme is the least accurate. Another feature is that as the grid spacing decreases, the accuracy of all schemes increases, for all values of μ. On the other hand, as the timestep increases, the accuracy of the implicit schemes deteriorates but not that of the central explicit scheme which is improved as μ increases from zero to one. An important property that can also be deduced from the graphs is that for all schemes the ratio C_n/C_p is always less than one - except at $\mu=1$ for the central explicit scheme - indicating that the numerical wave always travels slower than the physical wave.

A comparison of the eqns.(3.65) and (3.66) with (3.67), which give the ratio of the numerical and physical wave celerities for the central implicit and explicit schemes respectively, shows that the explicit scheme is more accurate than the implicit scheme for all values of μ and $\Delta x/L$. Also at the stability limit of the explicit scheme, $\mu=1$, the ratio

C_n/C_p is equal to one for all wavelengths and therefore the explicit scheme is 100% accurate under these conditions (see also figs.(3.2) and (3.3)).

The analysis on the accuracy of finite difference schemes has so far been applied to the simplified linear shallow water wave equations for ideal fluids. Numerical experiments have been performed to assess the accuracy of difference schemes for the non-linear wave equations and are described in the next Chapter.

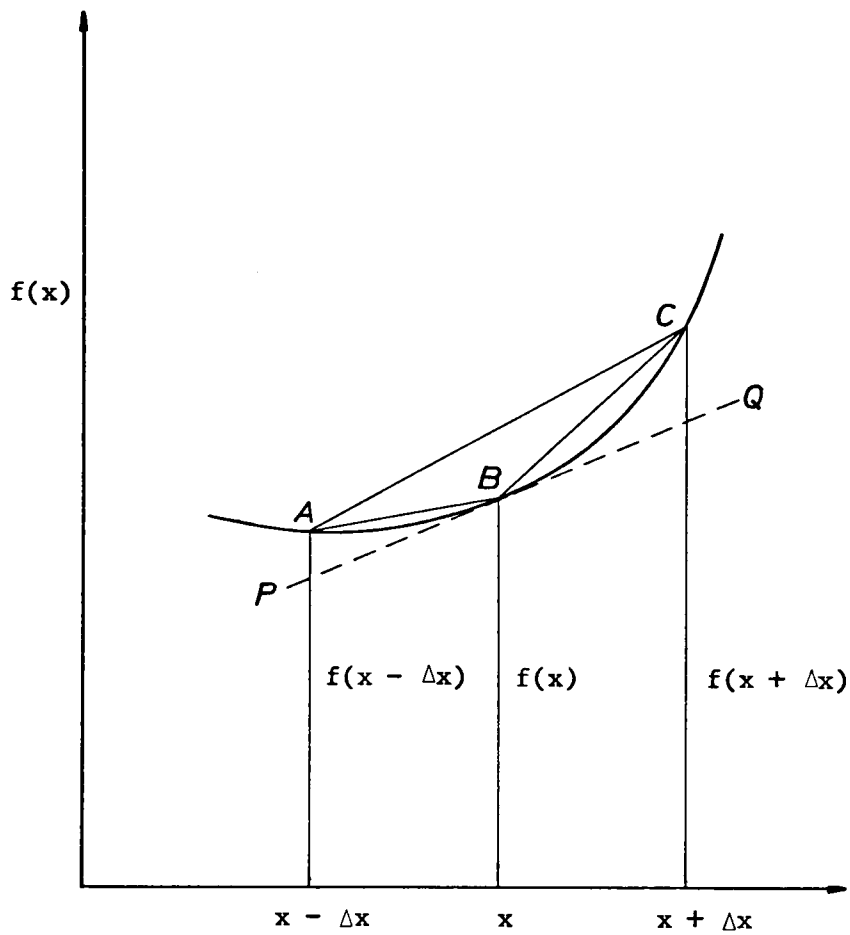

Figure 3.1 Diagram to Illustrate the Principle Finite Difference Forms

Chords AB, BC and AC represent the backward, forward and central difference approximations to the tangential slope at B

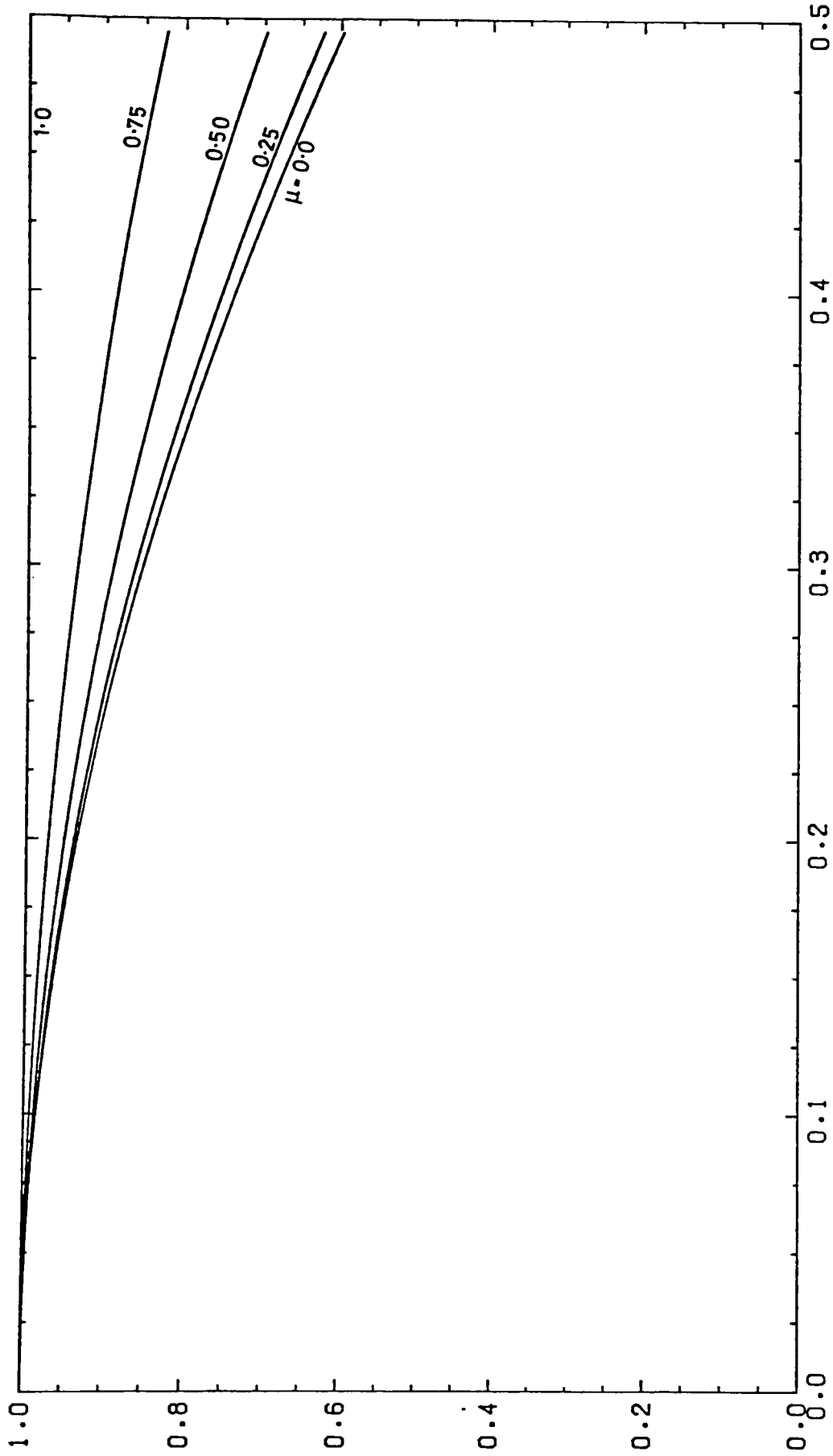

FIGURE 3.2 Measure of Accuracy for the Central Difference Explicit Scheme

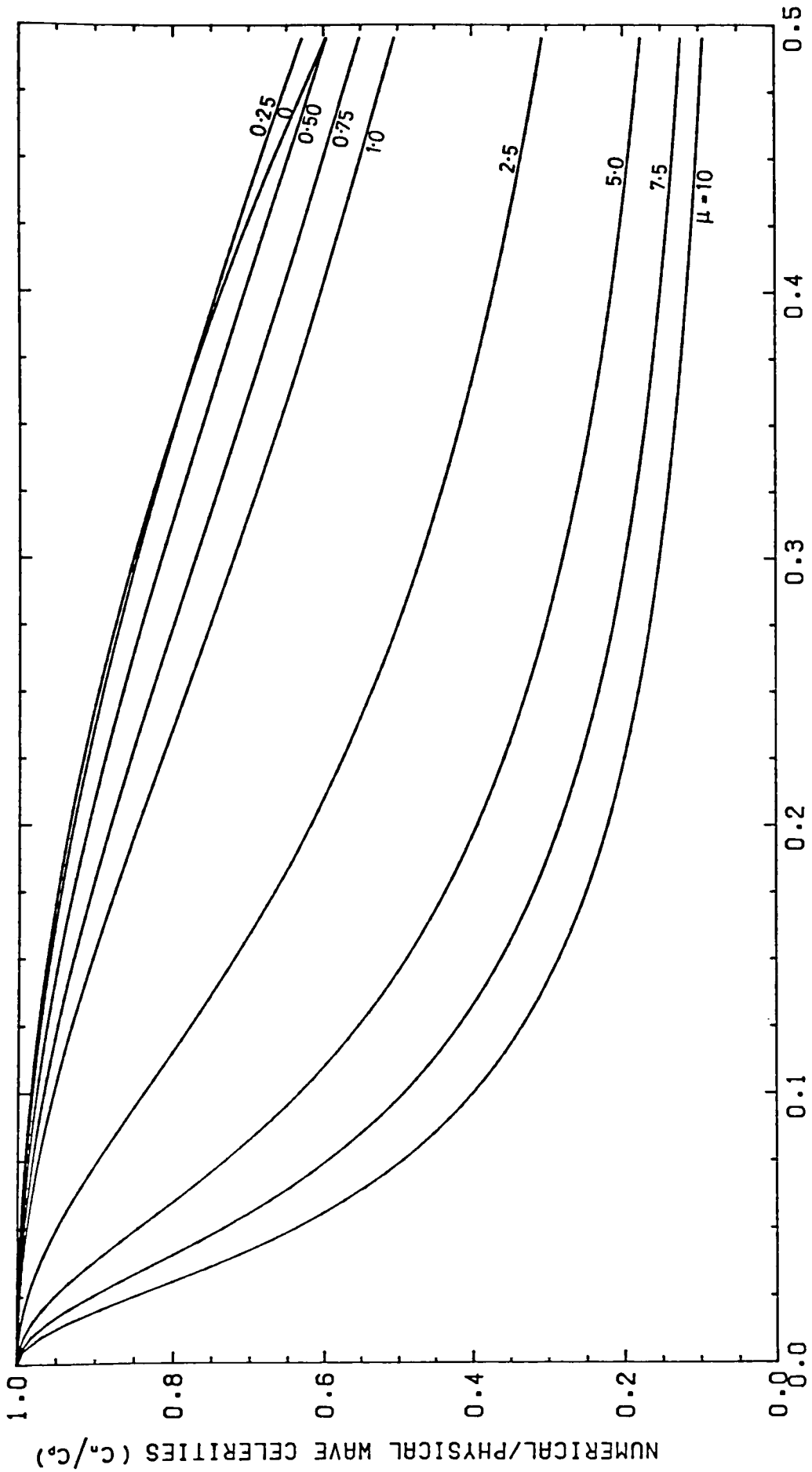

FIGURE 3.3 Measure of Accuracy for the Central Difference Implicit Scheme

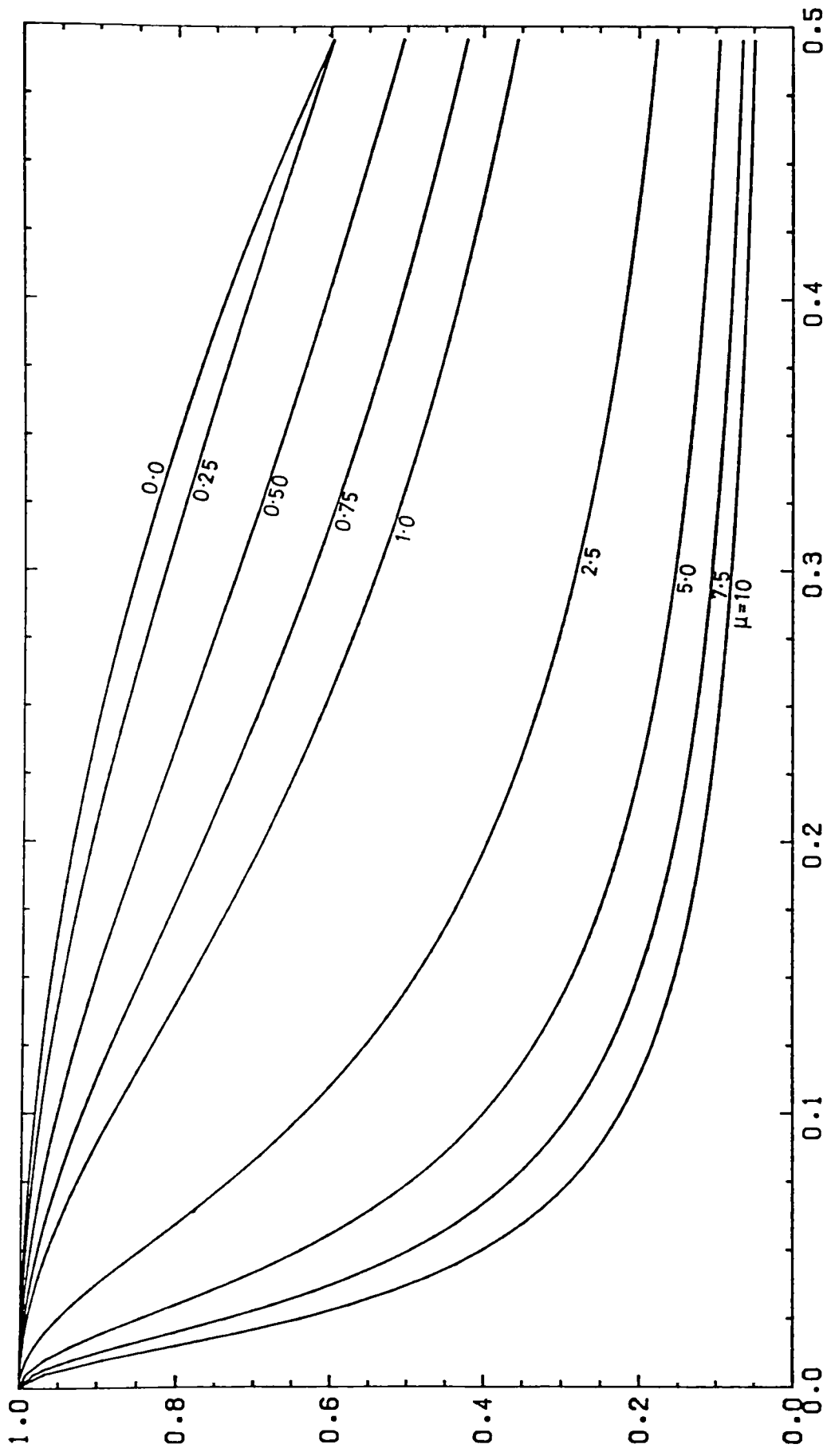

FIGURE 3.4 Measure of Accuracy for the Backward Difference Implicit Scheme

CHAPTER 4

NUMERICAL MODEL EXPERIMENTS

4.1 Introduction

A number of analytical solutions to the shallow water wave equations exist. Because of the complex nature of the governing equations, all analytical solutions known to date involve their simplification to a considerable degree. In practice, analytical solutions are only applicable to idealised estuaries of simple geometry and therefore, their direct application to natural estuaries is limited.

However, analytical solutions may be of great use in assessing the accuracy of numerical methods. If numerical solutions are obtained for idealised estuaries, they may be compared with the appropriate analytical solutions and, depending upon the degree of agreement, useful conclusions may be drawn regarding the validity of the numerical methods.

Many of the proposed analytical solutions neglect or simplify some of the second order terms. For example, a number of analytical solutions have been developed for estuaries of varying cross-section by linearising the friction term and ignoring the advective accelerations (see Ippen(1966), McDowell and O'Connor(1977), Lynch and Gray(1978), Prandle and Rahman(1980)). Proudman(1955a,1955b) also developed analytical solutions for estuaries of varying cross-section. In his earlier paper, severe restrictions were imposed on the height of the wave and the distance from the open sea, while in his subsequent paper the range of the validity of the analytical solutions was widely extended by ignoring

the advective acceleration terms in the governing equations.

This chapter presents a study of one of the analytical solutions due to Proudman(1957). Proudman's analytical solution applies to an estuary of uniform cross-section, open to the sea at one end, and closed at the other. The non-linear advective acceleration and quadratic friction terms have been included in the momentum equation and the analytical solution has therefore been used to investigate the numerical treatment of these terms in particular. Similarly, the numerical representation of the linear form of the governing equations has been studied by comparing the predictions with the analytical results for linear wave theory.

4.2 The Second Order Analytical Solution.

The second order analytical solution by Proudman(1957) is based on the following one-dimensional shallow water equations:

$$\frac{\partial \eta}{\partial t} + \frac{\partial}{\partial x}\left[U(h + \eta)\right] = 0 \qquad (4.1)$$

$$\frac{\partial U}{\partial t} + U\frac{\partial U}{\partial x} + g\frac{\partial \eta}{\partial x} + \frac{fU|U|}{2h\alpha} = 0 \qquad (4.2)$$

where f is the Darcy-Weisbach bed resistance coefficient and α is a coefficient relating the hydraulic radius to the mean depth. Thus:

$$\alpha = \frac{R}{h} = 1/(1 + 2h/b) \qquad (4.3)$$

Proudman's approximate solution to the eqns.(4.1) and (4.2) is of the following form, for elevation:

$$\frac{\eta}{h} = F(t + \tfrac{x}{c}) + F(t - \tfrac{x}{c}) + \tfrac{1}{8} F^2(t + \tfrac{x}{c}) + \tfrac{1}{8} F^2(t - \tfrac{x}{c}) - \tfrac{1}{8} F^2(t + \tfrac{x}{c} - \tfrac{2\ell}{c})$$

$$- \tfrac{1}{8} F^2(t - \tfrac{x}{c} - \tfrac{2\ell}{c}) + \tfrac{1}{2} F(t + \tfrac{x}{c}) F(t - \tfrac{x}{c}) - \tfrac{1}{4} f(t + \tfrac{x}{c}) F(t + \tfrac{x}{c} - \tfrac{2\ell}{c})$$

$$- \tfrac{1}{4} F(t - \tfrac{x}{c}) F(t - \tfrac{x}{c} - \tfrac{2\ell}{c}) + \tfrac{3}{2} (\tfrac{\ell - x}{c}) F(t + \tfrac{x}{c}) F'(t + \tfrac{x}{c})$$

$$+ \tfrac{3}{2} (\tfrac{\ell + x}{c}) F(t - \tfrac{x}{c}) F'(t - \tfrac{x}{c}) - \tfrac{1}{4} F'(t + \tfrac{x}{c}) \int_{t + \frac{x}{c} - \frac{2\ell}{c}}^{t - \frac{x}{c}} F(\theta)\, d\theta$$

$$- \tfrac{1}{4} F'(t - \tfrac{x}{c}) \int_{t - \frac{x}{c} - \frac{2\ell}{c}}^{t + \frac{x}{c}} F(\theta)\, d\theta$$

$$- \frac{fc}{8h\alpha} \int_{t + \frac{x}{c} - \frac{2\ell}{c}}^{t - \frac{x}{c}} |F(t + \tfrac{x}{c}) - F(\theta)| \{F(t + \tfrac{x}{c}) - F(\theta)\}\, d\theta$$

$$+ \frac{fc}{8h\alpha} \int_{t - \frac{x}{c} - \frac{2\ell}{c}}^{t + \frac{x}{c}} |F(\theta) - F(t - \tfrac{x}{c})| \{F(\theta) - F(t - \tfrac{x}{c})\}\, d\theta \qquad (4.4)$$

and, likewise for the longitudinal velocity distribution:

$$\frac{U}{c} = - F(t + \tfrac{x}{c}) + F(t - \tfrac{x}{c}) + \frac{3x}{4c} \{[F^2(t + \tfrac{x}{c})]' + [F^2(t - \tfrac{x}{c})]'\}$$

$$- \tfrac{1}{4} \{F'(t + \tfrac{x}{c}) + F'(t - \tfrac{x}{c})\} \int_{t - \frac{x}{c}}^{t + \frac{x}{c}} F(\theta) d\theta - \frac{fc}{8h\alpha} \int_{t - \frac{x}{c}}^{t + \frac{x}{c}} \{|F(t + \tfrac{x}{c}) - F(\theta)|$$

$$(F(t + \tfrac{x}{c}) - F(\theta)) - |F(\theta) - F(t - \tfrac{x}{c})| \quad (F(\theta) - F(t - \tfrac{x}{c}))\}\, d\theta$$

$$- f(t + \tfrac{x}{c}) + f(t - \tfrac{x}{c}) \qquad (4.5)$$

where the function $f(t)$ is given by:

$$f(t) = -\frac{1}{8}\left[F(t) + F(t-\frac{2\ell}{c})\right]^2 + F(t)\left[\frac{3\ell}{2c}F(t) - \frac{1}{4}\int_{t-\frac{2\ell}{c}}^{t} F(\theta)\,d\theta\right]$$
$$-\frac{fc}{8h\alpha}\int_{t-\frac{2\ell}{c}}^{t}\left|F(t)-F(\theta)\right|\{F(t)-F(\theta)\}\,d\theta \qquad (4.6)$$

The function F(t) is any physically interpretable function and $F'(t)$ is the first partial derivative.

Clearly, as the second order terms in the equations of motion have been retained, Proudman's solution is very complicated compared to other analytical solutions which ignore or simplify these terms. However, although the second order terms are retained, there is a limitation to the validity of Proudman's solution. Proudman himself indicates in his paper (Proudman(1957)) that his solution is only valid when the second order terms are small in comparison with the first order terms. He does not, however, give any indication of the proposed limits of this approximation.

Proudman(1957) obtained, in addition, expressions for the tidal elevation and time of the high water at the head of the estuary and are given as, for elevation:

$$\frac{\eta}{h} = 2F(0) + \frac{3}{4}F^2(0) - \frac{1}{4}F^2(-\frac{2\ell}{c}) - \frac{1}{2}F(0)\,F(-\frac{2\ell}{c})$$
$$-\frac{fc}{4h\alpha}\int_{-\frac{2\ell}{c}}^{0}\left|F(0)-F(\theta)\right|\{F(0)-F(\theta)\}\,d\theta \qquad (4.7)$$

and for time:

$$t = -\frac{3}{2}\frac{\ell}{c}F(0) + \frac{1}{4}\frac{F'(-2\ell/c)}{F''(0)}\{F(0) + F(-\frac{2\ell}{c})\}$$

$$+\frac{1}{4}\int_{-\frac{2\ell}{c}}^{0} F(\theta)\,d\theta - \frac{fc}{8h\alpha}\frac{1}{F''(0)}|F(0) - F(-\frac{2\ell}{c})|$$

$$\{F(0) - F(-\frac{2\ell}{c})\} \qquad (4.8)$$

Equation(4.7) is a second order approximation in F, which results in the tidal elevation at high water being approximated to that at time t=0. The true value of the tidal elevation at high water can be obtained by substituting t=t(high water) - given by eqn.(4.8) - into eqn.(4.7) instead of t=0. Equation(4.8) is a first order approximation in F.

Using the eqns.(4.7) and (4.8), Proudman(1957) developed expressions for the height and time of high water at the head of the estuary, in the case where the first order tide is harmonic, of amplitude 2hA and period $2\pi/\sigma$, see fig.(4.1), as given by:

$$F(t) = A\cos\sigma t \qquad (4.9)$$

Similar expressions for the height and time of low water at the head of the estuary were later obtained by Knight(1973a). However, although the expressions are only approximations to the water elevations at high or low tide, they clearly show the effects of the second order terms on the tidal flow. The expressions for high and low tide are therefore in terms of water elevation as:

$$\left(\frac{\eta}{h}\right)_{High} = 2A + A^2 \left\{\frac{5}{8} - \frac{1}{2}\cos\left(\frac{2\sigma\ell}{c}\right) - \frac{1}{8}\cos\left(\frac{4\sigma\ell}{c}\right)\right.$$

$$\left. - \frac{fc}{4h\sigma\alpha}\left[\frac{3\sigma\ell}{c} - 2\sin\left(\frac{2\sigma\ell}{c}\right) + \frac{1}{4}\sin\left(\frac{4\sigma\ell}{c}\right)\right]\right\} \qquad (4.10)$$

$$\left(\frac{\eta}{h}\right)_{Low} = -2A + A^2 \left\{\frac{5}{8} - \frac{1}{2}\cos\left(\frac{2\sigma\ell}{c}\right) - \frac{1}{8}\cos\frac{4\sigma\ell}{c}\right\}$$

$$+ \frac{fc}{4h\sigma\alpha}\left[\frac{3\sigma\ell}{c} - 2\sin\left(\frac{2\sigma\ell}{c}\right) + \frac{1}{4}\sin\left(\frac{4\sigma\ell}{c}\right)\right]\right\} \qquad (4.11)$$

and in terms of time as:

$$t_{Low} = \frac{A}{\sigma}\left\{\frac{3\sigma\ell}{2c} + \frac{1}{8}\sin\left(\frac{4\sigma\ell}{c}\right) + \frac{fc}{16h\sigma\alpha}\left[3 - 4\cos\left(\frac{2\sigma\ell}{c}\right) + \cos\left(\frac{4\sigma\ell}{c}\right)\right]\right\} \qquad (4.12)$$

$$t_{High} = \frac{A}{\sigma}\left\{-\frac{3\sigma\ell}{2c} - \frac{1}{8}\sin\left(\frac{4\sigma\ell}{c}\right) + \frac{fc}{16h\sigma\alpha}\left[3 - 4\cos\left(\frac{2\sigma\ell}{c}\right) + \cos\left(\frac{4\sigma\ell}{c}\right)\right]\right\} \qquad (4.13)$$

The effect of the friction term is to make the high water lower and later in comparison to the first order solution and, conversely, low water higher and later. The effect of the "shallow water" terms, which include the advective accelarations and the contribution from the non-linear continuity equation, is to make the high water higher and earlier and low water higher and later.

Knight(1973b) also developed for the first order harmonic tide, expressions giving the tidal height and velocity at any time and chainage along the estuary, using Proudman's eqns.(4.4) and (4.5). These expressions are as follows:

$$\frac{\eta}{h}=2A\cos\sigma t\cos\frac{\sigma x}{c}+\frac{A^2}{8}\{\cos^2(\sigma t+\frac{\sigma x}{c})+\cos^2(\sigma t-\frac{\sigma x}{c})$$

$$-\cos^2(\sigma t+\frac{\sigma x}{c}-\frac{2\sigma\ell}{c})-\cos^2(\sigma t-\frac{\sigma x}{c}-\frac{2\sigma\ell}{c})\}$$

$$-\frac{3A^2}{4}\frac{\sigma(\ell-x)}{c}\sin(2\sigma t+\frac{2\sigma x}{c})-\frac{3A^2}{4}\frac{\sigma(\ell+x)}{c}\sin(2\sigma t-\frac{2\sigma x}{c})$$

$$-\frac{A^2}{2}\cos\frac{2\sigma\ell}{c}+\frac{A^2}{2}\cos\frac{2\sigma x}{c}-\frac{fcA^2}{8h\alpha}\{\int_{t+\frac{x}{c}-\frac{2\ell}{c}}^{t-\frac{x}{c}}|\cos(\sigma t+\frac{\sigma x}{c})$$

$$-\cos\sigma\theta|[\cos(\sigma t+\frac{\sigma x}{c})-\cos\sigma\theta]\,d\theta+\int_{t-\frac{x}{c}-\frac{2\ell}{c}}^{t+\frac{x}{c}}|\cos(\sigma t-\frac{\sigma x}{c})$$

$$-\cos\sigma\theta|[\cos(\sigma t-\frac{\sigma x}{c})-\cos\sigma\theta]\,d\theta\} \qquad (4.14)$$

and

$$\frac{U}{c}=2A\sin\sigma t\sin\frac{\sigma x}{c}+\frac{A^2}{8}[\cos^2(\sigma t+\frac{\sigma x}{c})-\cos^2(\sigma t-\frac{\sigma x}{c})$$

$$+\cos^2(\sigma t+\frac{\sigma x}{c}-\frac{2\sigma\ell}{c})-\cos^2(\sigma t-\frac{\sigma x}{c}-\frac{2\sigma\ell}{c})]$$

$$+\frac{3A^2}{4}\frac{\sigma(\ell-x)}{c}\sin(2\sigma t+\frac{2\sigma x}{c})-\frac{3A^2}{4}\frac{\sigma(\ell+x)}{c}\sin(2\sigma t-\frac{2\sigma x}{c})$$

$$+\frac{fcA^2}{8h\alpha}\{\int_{t+\frac{x}{c}-\frac{2\ell}{c}}^{t-\frac{x}{c}}|\cos(\sigma t+\frac{\sigma x}{c})-\cos\sigma\theta|[\cos(\sigma t+\frac{\sigma x}{c})-\cos\sigma\theta]d\theta$$

$$-\int_{t-\frac{x}{c}-\frac{2\ell}{c}}^{t+\frac{x}{c}}|\cos(\sigma t-\frac{\sigma x}{c})-\cos\sigma\theta|[\cos(\sigma t-\frac{\sigma x}{c})-\cos\sigma\theta]\,d\theta\} \qquad (4.15)$$

Equations(4.14) and (4.15) give the solution to the idealised estuary problem, provided that analytical expressions are obtained for the integral terms present in both equations. The integration of these terms is given in detail by Knight(1973b).

The first term in both eqns.(4.14) and (4.15) represents the first order solution in which the advective acceleration and friction terms are ignored and both momentum and continuity equations are of linear form, that is:

$$\frac{\partial \eta}{\partial t} + h \frac{\partial U}{\partial x} = 0 \qquad (4.16)$$

$$\frac{\partial U}{\partial t} + g \frac{\partial \eta}{\partial x} = 0 \qquad (4.17)$$

The first order solution describes a standing wave formed by the superposition of an incident wave and its reflection from the closed end. Since the second order terms have been ignored, the solution is symmetrical about mean depth. There is also no phase difference between water elevations or velocities at the head and mouth. The first order solution is an exact solution to the linear equations of continuity and momentum and no theoretical limitations are imposed on its validity. Detailed derivations of similar first order solutions are given by Lamb(1932) and Ippen(1966).

Knight(1973a) showed graphical representations of the eqns.(4.14) and (4.15) and illustrated the influence of the four dimensionless groups of $\frac{\sigma \ell}{c}$, $\frac{c}{h\sigma}$, $\frac{a}{h}$ and $\frac{f}{\alpha}$. He also suggested, for practical purposes, the likely ranges of the four groups:

$$0 < \frac{\sigma \ell}{c} < 1.3 \qquad 2000 < \frac{c}{h\sigma} < 10{,}000 \qquad 0.05 < \frac{a}{h} < 0.25$$

$$0.005 < \frac{f}{\alpha} < 0.05$$

The precise values of these dimensionless groups at which Proudman's solution breaks down are difficult to determine. However, Knight(1973b) presented in a graphical form, see fig.(4.2), a tentative assessment of the limits of Proudman's solution, based on a number of practical solutions to the eqns.(4.14) and (4.15). The criterion for failure was taken to be at the point where the shape of the tidal curve becomes very distorted. The solution breaks down at the estuary mouth first, and then progressively up the estuary. The form of the graph is consistent with the theoretical limitations to Proudman's solution, namely that the second order terms must be small in comparison to the first order terms. It should be realised, however, that the graph can only be used as a tentative guideline.

4.3 Numerical Experiments

A series of numerical experiments have been performed to assess the practical behaviour of the implicit finite difference schemes discussed in Chapter 3, with respect to accuracy, and in particular its dependence on the Courant number, μ. This is an extension of the work done by Wallis(1982).

4.3.1 First Order Waves

The accuracy of the linear finite difference schemes was theoretically investigated in Chapter 3, where it was shown that it is primarily dependent on the dimensionless numbers:

$$\theta\ (=\beta\Delta x/2) \quad \text{and} \quad \mu\ (=\Delta t\sqrt{gh}/\Delta x)$$

To assess the practical behaviour of the schemes, the numerical models were set up in a one-dimensional form to obtain numerical solutions for an idealised estuary. These solutions were then compared to the corresponding first order analytical solution. Of the two implicit schemes mentioned in Chapter 3, namely the central and backward schemes, the central implicit scheme could not be used in these first order wave experiments because of the non-dissipative nature of the scheme, which prevented the numerical solution from converging to a harmonic solution. The numerical errors introduced into the model via the initial and boundary conditions and round-off errors, were not damped and therefore continued to influence the solution for all timesteps after their introduction into the model, see Wallis(1982). Only the behaviour of the backward implicit scheme was therefore studied, as it is a dissipative scheme and converges to a repetitive solution.

Wallis(1982) performed his numerical experiments using a backward implicit scheme based on the following one-dimensional first order equations of motion:

$$W \frac{\partial \eta}{\partial t} + \frac{\partial Q}{\partial x} = 0 \qquad (4.18)$$

$$\frac{\partial Q}{\partial t} + Ag \frac{\partial \eta}{\partial x} = 0 \qquad (4.19)$$

where W = width

A = cross-sectional area

and Q = flow rate

The eqns.(4.18) and (4.19) are not strictly linear as the discharge depends on both h and η. When the assumption that $\eta << h$ is made, these equations reduce to the linear equations of motion, eqns.(4.16) and(4.17). The first order analytical solution is an exact solution to the linear eqns.(4.16) and (4.17) and comparison between the numerical results from Wallis's first order model and the analytical solution are valid only when the assumption $\eta << h$ is true. However, as shown by Wallis, even a small degree of non-linearity in the eqns.(4.18) and (4.19) gave rise to an asymmetric numerical wave with respect to the mean water level.

Wallis(1982) carried out a series of experiments where both μ and θ were varied. The trends illustrated by his results were in agreement with the form of the theoretical relationship, as depicted in fig.(3.4). As Wallis varied μ over a limited range ($0.5 < \mu < 2.0$), it was felt that more information was needed on the influence of the Courant number on the accuracy of the scheme. Since implicit finite difference schemes are

unconditionally stable, with no theoretical restraints on μ, it is preferable to use high values of μ, and hence large timesteps, to reduce the computational time and cost.

The model (coded 1A) was first set up, using the backward implicit difference form of the equations of motion - given by eqns.(3.14) and (3.15). A sinusoidal tide of amplitude a (where $a=2hA\cos\frac{\sigma\ell}{c}$) at the mouth of the estuary and zero velocities at the head were the seaward and landward boundary conditions, respectively. The initial conditions were that η was defined at high tide throughout the domain, enabling U to be defined as zero. The finite difference equations were then solved using the method of Gauss elimination and back substitution, as described in Appendix A. The value of $\frac{\sigma\ell}{c}$ was set at 0.672 (ℓ=47.25 km, h=10 m, T=12.4 hr) and the amplitude of the sinusoidal wave at the mouth was assumed to be 1.0 m (giving a/h=0.1). A space staggered grid of 14 nodal points was chosen, with a grid spacing of 3500 m, and a value of θ of $\pi/126.3$. The Courant number μ was varied between 1 and 16, by increasing the timestep only. The model was run for 20 tidal cycles to ensure that the numerical results had converged to repetitive solutions, and the results were then compared with the analytical solution. The high and low water elevations at the final elevation grid point in the numerical model were compared with the corresponding high and low levels for the analytical solution, and the maximum and minimum velocities at the seventh velocity grid point (about midway along the estuary) were compared with the corresponding analytical velocities. These values were compared for a range of Courant mumbers, with the percentage difference between the analytical and the theoretical results being determined for each case. The corresponding results are presented in Table(4.1). As

both the numerical and analytical waves are symmetrical with respect to mean water level, only the results for high water and maximum velocity are presented in a graphical form in figs.(4.3) and (4.4) respectively.

The model behaved as expected, that is, its accuracy deteriorated as the Courant number increased. Both curves in figs.(4.3) and (4.4) are smooth, without any sudden changes in trend that would suggest an upper limit for μ. Vreugdenhil and Voogt(1975) suggest that $\mu=5$ is a reasonable upper limit for the implicit schemes. The results above, however, imply that the upper limit for μ depends on the degree of accuracy required for any particular study.

Figure(4.5) illustrates the quality of agreement between the numerical and analytical solutions at $\mu=4.21$. It shows that the numerical wave is slower than the analytical wave, and that the overall shape of the tide is very closely simulated by the model 1A.

When experimenting with the number of tidal cycles that the model 1A needed to run for before repetitive solutions were obtained for all μ, it was found that the model took longer to converge when Δt, and therefore μ was small. This is because the dissipative ability of the backward implicit scheme is reduced when μ decreases, which leads to values of the amplification factor λ being closer to unity, see eqn.(3.32). When $|\lambda|=1$ a repetitive solution is not achieved, as the numerical errors are not dissipated for this particular case. As $|\lambda|$ decreases, the degree of numerical damping increases causing a convergence of the solution after fewer tidal cycles.

4.3.2 Second Order Waves

In Chapter 3, no attempt was made to determine theoretically the accuracy characteristics of non-linear finite difference schemes. This is because the Fourier series method employed in the analysis of the accuracy of finite difference schemes, applies only to linear schemes.

Wallis(1982) performed a number of numerical experiments with one-dimensional non-linear implicit schemes, where he showed that their accuracy depended upon the dimensionless numbers μ and θ. This dependency was essentially the same as that for the linear backward implicit scheme, in that as both the timestep and grid spacing decreased, a limiting solution was reached. He also showed that the numerical results diverted from Proudman's analytical solution as both $\frac{\sigma \ell}{c}$ and $\psi (= \frac{a}{h} \frac{c}{h\sigma} \frac{f}{\alpha})$ increased. This deterioration in agreement between the numerical and analytical results occurred because the assumptions on which Proudman's solution is based were violated as $\frac{\sigma \ell}{c}$ and ψ increased.

In this study, the influence of μ on the accuracy of non-linear schemes was studied in greater detail. Three different numerical models were examined and compared against Proudman's analytical solution. Useful information has been obtained from such comparisons about the accuracy of the models with respect to μ, and in relation to each other.

The three numerical models are described below:

Model 2B: A central implicit scheme which involves a double iteration to represent the advective acceleration term in a time-centred form, in order to avoid the introduction of non-linear instabilities into the scheme. The finite difference equations are of the form :-

1st Iteration:

$$\eta_i^{n+1} - \eta_i^n + \frac{\Delta t}{2\Delta x} \{ U_{i+\frac{1}{2}}^{n+1} (h + \overline{\overline{\eta}}_{i+\frac{1}{2}}^{x\,n}) - U_{i-\frac{1}{2}}^{n+1} (h + \overline{\overline{\eta}}_{i-\frac{1}{2}}^{x\,n})$$

$$+ U_{i+\frac{1}{2}}^{n} (h + \overline{\overline{\eta}}_{i+\frac{1}{2}}^{x\,n}) - U_{i-\frac{1}{2}}^{n} (h + \overline{\overline{\eta}}_{i-\frac{1}{2}}^{x\,n}) \} = 0 \qquad (4.20)$$

$$U_{i+\frac{1}{2}}^{n+1} - U_{i+\frac{1}{2}}^{n} + \frac{\Delta t}{2\Delta x} U_{i+\frac{1}{2}}^{n} (U_{i+\frac{3}{2}}^{n} - U_{i-\frac{1}{2}}^{n}) +$$

$$\frac{g\Delta t}{2\Delta x} (\eta_{i+1}^{n+1} - \eta_i^{n+1} + \eta_{i+1}^{n} - \eta_i^{n}) + \frac{\Delta t\, f(U_{i+\frac{1}{2}}^{n+1} + U_{i+\frac{1}{2}}^{n}) \, |U_{i+\frac{1}{2}}^{n}|}{4h\alpha} = 0 \qquad (4.21)$$

2nd Iteration:

$$\eta_i^{n+1} - \eta_i^n + \frac{\Delta t}{2\Delta x} \{ U_{i+\frac{1}{2}}^{n+1} (h + \overline{\overline{\eta}}_{i+\frac{1}{2}}^{x\,n+1}) - U_{i-\frac{1}{2}}^{n+1} (h + \overline{\overline{\eta}}_{i-\frac{1}{2}}^{x\,n+1})$$

$$+ U_{i+\frac{1}{2}}^{n} (h + \overline{\overline{\eta}}_{i+\frac{1}{2}}^{x\,n}) - U_{i-\frac{1}{2}}^{n} (h + \overline{\overline{\eta}}_{i-\frac{1}{2}}^{x\,n}) \} = 0 \qquad (4.22)$$

$$U_{i+\frac{1}{2}}^{n+1} - U_{i+\frac{1}{2}}^{n} + \frac{\Delta t}{8\Delta x} (U_{i+\frac{1}{2}}^{n} + \dot{U}_{i+\frac{1}{2}}^{n+1}) \{ (U_{i+\frac{3}{2}}^{n} + \dot{U}_{i+\frac{3}{2}}^{n+1})$$

$$- (U_{i-\frac{1}{2}}^{n} + \dot{U}_{i-\frac{1}{2}}^{n+1}) \} + \frac{g\Delta t}{2\Delta x} (\eta_{i+1}^{n+1} - \eta_i^{n+1} + \eta_{i+1}^{n} - \eta_i^{n}) +$$

$$\frac{\Delta t\, f(U_{i+\frac{1}{2}}^{n+1} + U_{i+\frac{1}{2}}^{n}) \, |U_{i+\frac{1}{2}}^{n}|}{4h\alpha} = 0 \qquad (4.23)$$

where $\dot{\eta}^{n+1}$ and $\dot{U}^{n+1}$ are respectively the elevations and velocities obtained at the end of the first iteration,

and $\overline{\overline{\eta}}_{i+\frac{1}{2}}^{x\,n} = \frac{1}{2} (\eta_{i+1}^{n} + \eta_i^{n})$

Model 2C: A central implicit scheme which involves three time levels to represent the advective acceleration in a time-centred form. It is described by the following finite difference equations:

$$\eta_i^{n+1} - \eta_i^{n-1} + \frac{\Delta t}{\Delta x} \{ U_{i+\frac{1}{2}}^{n+1} (h + \overline{\eta}^{x,n}_{i+\frac{1}{2}}) - U_{i-\frac{1}{2}}^{n+1} (h + \overline{\eta}^{x,n}_{i-\frac{1}{2}}) +$$

$$U_{i+\frac{1}{2}}^{n-1} (h + \overline{\eta}^{x,n-1}_{i+\frac{1}{2}}) - U_{i-\frac{1}{2}}^{n-1} (h + \overline{\eta}^{x,n-1}_{i-\frac{1}{2}}) \} = 0 \qquad (4.24)$$

$$U_{i+\frac{1}{2}}^{n+1} - U_{i+\frac{1}{2}}^{n-1} + \frac{\Delta t}{\Delta x} U_{i+\frac{1}{2}}^{n} (U_{i+\frac{3}{2}}^{n} - U_{i-\frac{1}{2}}^{n}) + \frac{g\Delta t}{\Delta x} (\eta_{i+1}^{n+1} - \eta_i^{n+1} +$$

$$\eta_{i+1}^{n-1} - \eta_i^{n-1}) + \frac{\Delta t \, f (U_{i+\frac{1}{2}}^{n+1} + U_{i+\frac{1}{2}}^{n-1}) \, |U_{i+\frac{1}{2}}^{n}|}{4h\alpha} = 0 \qquad (4.25)$$

Model 1B: A backward implicit scheme with a double iteration, as in model 2B. The finite difference equations are as follows:

1st Iteration:

$$\eta_i^{n+1} - \eta_i^{n} + \frac{\Delta t}{\Delta x} \{ U_{i+\frac{1}{2}}^{n+1} (h + \overline{\eta}^{x,n}_{i+\frac{1}{2}}) - U_{i-\frac{1}{2}}^{n+1} (h + \overline{\eta}^{x,n}_{i-\frac{1}{2}}) \} = 0 \qquad (4.26)$$

$$U_{i+\frac{1}{2}}^{n+1} - U_{i+\frac{1}{2}}^{n} + \frac{\Delta t}{2\Delta x} U_{i+\frac{1}{2}}^{n} (U_{i+\frac{3}{2}}^{n} - U_{i-\frac{1}{2}}^{n}) +$$

$$\frac{g\Delta t}{\Delta x} (\eta_{i+1}^{n+1} - \eta_i^{n+1}) + \frac{\Delta t \, f \, U_{i+\frac{1}{2}}^{n+1} \, |U_{i+\frac{1}{2}}^{n}|}{2h\alpha} = 0 \qquad (4.27)$$

2nd Iteration:

$$\eta_i^{n+1} - \eta_i^n + \frac{\Delta t}{\Delta x} \{ U_{i+\frac{1}{2}}^{n+1} (h + \overset{x}{\eta}{}_{i+\frac{1}{2}}^{n+1}) - U_{i-\frac{1}{2}}^{n+1} (h + \overset{x}{\eta}{}_{i-\frac{1}{2}}^{n+1}) \} = 0 \qquad (4.28)$$

$$U_{i+\frac{1}{2}}^{n+1} - U_{i+\frac{1}{2}}^{n} + \frac{\Delta t}{8\Delta x} (U_{i+\frac{1}{2}}^{n} + \dot{U}_{i+\frac{1}{2}}^{n+1}) \{ (U_{i+\frac{3}{2}}^{n} + \dot{U}_{i+\frac{3}{2}}^{n+1}) - (U_{i-\frac{1}{2}}^{n} + \dot{U}_{i-\frac{1}{2}}^{n+1})$$

$$+ \frac{g\Delta t}{\Delta x} (\eta_{i+1}^{n+1} - \eta_i^{n+1}) + \frac{\Delta t \, f U_{i+\frac{1}{2}}^{n+1} |U_{i+\frac{1}{2}}^{n}|}{2h\alpha} = 0 \qquad (4.29)$$

The first series of numerical experiments were essentially the same as the series conducted for the first order tides. The estuary geometry was as before, with the dimensionless groups $\frac{\sigma \ell}{c}$ and $\frac{a}{h}$ being equal to 0.672 and 0.1, respectively. In addition, the two other dimensionless groups that influence Proudman's analytical solution were taken to be:

$$\frac{f}{\alpha} = 0.002 \qquad \text{and} \qquad \frac{c}{h\sigma} = 7035.7$$

All the above dimensionless numbers are within the recommended ranges given by Knight(1973a), except for the friction term which is below the suggested lower limit. The numerical grid and boundary conditions were the same as those adopted in the tests for model 1A, with the exception of the seaward boundary condition which was specified by the second order wave at the mouth of the estuary, i.e. as given by Proudman's solution and described by eqn.(4.14) for $x=\ell$.

Referring to fig.(4.2), the above data are in the safe region where Proudman's solution is expected to be well conditioned. Proudman's analytical wave for this set of data is pictured in fig.(4.6) and compared to the first order wave. The analytical wave is indeed well conditioned as can be seen by the undistorted tidal elevation curves at the mouth and head of the estuary, and the velocity curve in the middle of the estuary. When a larger friction factor was used (i.e. $f/\alpha=0.005$ - Knight's recommended lower limit), the analytical solution was noticeably distorted, see fig.(4.7). Although the analytical wave at the head showed no distortion, that at the mouth showed signs of breaking down and it was decided to resort to a lower friction factor. Since the analytical wave at the mouth of the estuary is the seaward boundary of the model, any distortions of this wave are fed into the model affecting the entire domain of the flow field. Thus a comparison between numerical and analytical solutions is not possible although the analytical solution may still be well conditioned at other parts of the estuary.

Fig.(4.6) also illustrates the effects of the second order terms on the tidal flow. Low water is raised and delayed whereas no difference is found for the position of high water. This is due to the effect of the shallow water and friction terms tending to cancel each other out at high water, but reinforcing one another at low water.

The three models were set up and run for increasing μ values from about 1 to 16. The backward implicit model 1B was run for 20 tidal cycles giving sufficient time for all numerical solutions to converge to repetitive solutions, and with the rate of convergence increasing with larger μ values. On the other hand, the central implicit models 2B and 2C, reached a repetitive solution earlier for small μ values, with the

rate of convergence being markedly reduced as μ increased. For this case repetitive solutions were fully achieved, after 60 tidal cycles, up to μ=7.894, with the numerical solutions for larger values of μ not converging even after 100 tidal cycles. The numerical results given by model 1B at the 20th tidal cycle and by models 2B and 2C at the 60th tidal cycle were compared with Proudman's analytical solution with the results being tabulated in Tables(4.2) to (4.4).

As expected, the accuracy of model 1B deteriorated with increasing μ, see Table(4.2). Although the individual parameters of the numerical wave did not follow the general trend of deterioration of agreement with the corresponding analytical parameters, the distortion of the numerical wave when compared with the analytical wave became more and more pronounced as μ increased.

The models 2B and 2C behaved in an almost identical manner, see Tables(4.3) and (4.4). The agreement between the numerical results of both models and Proudman's solution deteriorated as μ increased from 0.820 to 7.894. For larger values of μ, the numerical results not only failed to converge, but also showed a marked change in the trend followed by the results of smaller μ. However, since convergence of the numerical results was not achieved above the value of μ=7.894 no conclusions could be drawn about the behaviour of the models above this value and, in consequence, these results were disregarded.

The linear stability analysis performed on the central implicit scheme in Chapter 3, for the first order equations of motion with a linearised friction term, showed that the ability of the scheme to dissipate numerical errors comes entirely from the friction term. For

the flows considered here $\delta < \mu$ and, as illustrated by eqn.(3.43), the scheme's dissipative power decreases with increasing μ. The numerical experiments showed that as μ increased the models took longer to converge, also suggesting a decrease in the scheme's dissipative capacity with increasing μ. The friction term for the set of data chosen in this exercise is a very small term. It therefore limits the dissipative power of the central implicit models, and may be insufficient at high values of μ, to damp out the numerical errors. A similar stability analysis on the backward implicit scheme showed that its dissipative capacity is reinforced by the friction term and by increasing μ values. The numerical results were in agreement with the stability analysis, that is, model 1B reached a repetitive solution faster as μ increased, suggesting that the dissipative power of the scheme is more than sufficient for the damping of all numerical errors.

Figures(4.8) to (4.11) show graphical representations of the results from Tables(4.2) to (4.4) for the range $0.820 < \mu < 7.894$. The numerical results suggest that the value of $\mu=7.894$ is the upper limit of μ for the central implicit schemes for this particular set of data, which seems to have been imposed by the very small friction term. The numerical results of the backward implicit scheme, on the other hand, do not suggest an upper limit for μ and imply that it depends on the required degree of accuracy. The upper Courant number limit of 5, suggested by Vreugdenhil and Voogt(1975), is therefore a very conservative though safe upper limit, and should not be a rule for numerical modelling. It is deduced from the numerical experiments performed in this exercise that the choice of μ depends on the particular flow conditions being modelled and the degree of accuracy required, which may be determined from

numerical experiments on the particular flow study.

It is clear from figs.(4.8) to (4.11) that overall the model 2B is the most accurate. The second most accurate is model 2C with the least accurate model being 1B. The results therefore confirm that the central implicit schemes are more accurate than the backward implicit scheme. Also, the double iteration method adopted in model 2B gives better agreement with Proudman's solution than the three-time-level method of Falconer(1977) adopted in model 2C. Figs.(4.12) to (4.14) illustrate the degree of agreement between the numerical and analytical waves at μ=4.210. The overall shape of Proudman's second order wave is closely simulated by all three models, but is undoubtedly simulated more accurately by model 2B. This is in agreement with the findings of Aziz and Hellums(1967) who examined a number of methods for treating the non-linear terms and found that the double iteration procedure was the most accurate. Although model 2B involves two iterations per timestep, its computational cost is comparable with that of model 2C which only involves one iteration per timestep since, for the same value of μ, the number of timesteps per tidal cycle in model 2C is twice that of 2B.

The effects of the individual non-linear terms on the tidal wave were studied in the series of experiments described below. Although model 1B is less accurate than the central implicit schemes, it was chosen for this particular exercise because of its dissipative nature which permitted the study of the individual non-linear terms. A first order wave was fed into the model at the open boundary and the timestep was chosen to be Δt=1488s with a resulting value of μ=4.210. Firstly the effect of the non-linear continuity equation on the first order wave was studied and the resulting numerical wave was compared with the first

order wave given by model 1A, see fig.(4.15). An asymmetry was introduced into the numerical wave, high water became lower and earlier, and low water became lower and later. Also the maximum velocity was larger and earlier, whereas the minimum velocity was smaller and later. It is therefore evident that the non-linear term in the continuity equation contributes towards the second order solution given by eqns.(4.14) and (4.15), a factor that was overlooked by Knight(1973a) and Wallis(1982). Figs.(4.16) and(4.17) respectively show the effects of the advective acceleration and the friction terms on the first order wave solution. The advective acceleration made high water higher and earlier and low water higher and later. It also made the maximum velocity larger and earlier and the minimum velocity smaller and later. On the other hand, the friction term made high water lower and later, low water higher and later, with both the maximum and minimum velocities being smaller and later. Therefore the effects of the second order terms on the tidal wave given by the numerical results from this exercise are in agreement with their description by Proudman's analytical solution. The second order terms, however, were very small compared to the first order terms and their effect on the tidal wave was very small, as can be seen from figs.(4.15) to (4.17)

Courant Number	High Water (m)		% Age Difference	Low Water (m)		% Age Difference	Maximum Velocity (m/s)		% Age Difference	Minimum Velocity (m/s)		% Age Difference
	Model 1A	Analytical		Model 1A	Analytical		Model 1A	Analytical		Model 1A	Analytical	
0.820	1.277	1.277	0.030	-1.277	-1.277	0.031	0.432	0.432	0.025	-0.432	-0.432	0.025
1.617	1.275	1.277	0.135	-1.275	-1.277	0.135	0.431	0.432	0.141	-0.431	-0.432	0.141
2.429	1.273	1.277	0.308	-1.273	-1.277	0.308	0.430	0.432	0.338	-0.430	-0.432	0.338
3.324	1.270	1.277	0.579	-1.270	-1.277	0.579	0.429	0.432	0.637	-0.429	-0.432	0.637
4.210	1.265	1.277	0.925	-1.265	-1.277	0.925	0.427	0.432	1.024	-0.427	-0.432	1.024
4.858	1.261	1.277	1.225	-1.261	-1.277	1.225	0.426	0.432	1.360	-0.426	-0.432	1.360
6.315	1.251	1.277	2.037	-1.251	-1.277	2.037	0.422	0.432	2.331	-0.422	-0.432	2.331
7.894	1.237	1.277	3.108	-1.237	-1.277	3.108	0.416	0.432	3.609	-0.416	-0.432	3.609
10.525	1.210	1.277	5.251	-1.210	-1.277	5.251	0.405	0.432	6.275	-0.405	-0.432	6.275
12.630	1.185	1.277	7.198	-1.185	-1.277	7.198	0.396	0.432	8.163	-0.396	-0.432	8.163
15.788	1.145	1.277	10.320	-1.145	-1.277	10.320	0.374	0.432	13.290	-0.374	-0.432	13.290

Table 4.1 First order tides. Comparison of analytical and numerical results.

Courant Number	High Water (m)		% Age Difference	Low Water (m)		% Age Difference	Tidal Range (m)		% Age Difference	Maximum Velocity (m/s)		% Age Difference	Minimum Velocity (m/s)		% Age Difference
	Model 1B	Proudman		Model 1B	Proudman		Model 1B	Proudman		Model 1B	Proudman		Model 1B	Proudman	
0.820	1.299	1.277	-1.706	-1.172	1.237	5.227	2.514	2.514	1.705	0.440	0.432	-1.885	-0.390	-0.386	-1.110
1.619	1.289	1.277	-0.921	-1.160	1.237	6.211	2.449	2.514	2.588	0.438	0.432	-1.463	-0.394	-0.386	-2.138
2.429	1.279	1.277	-0.112	-1.151	1.237	6.952	2.430	2.514	3.364	0.435	0.432	-0.651	-0.397	-0.386	-2.804
3.324	1.267	1.277	0.767	-1.142	1.237	7.711	2.409	2.514	4.185	0.431	0.432	0.331	-0.397	-0.386	-2.947
4.210	1.256	1.277	1.632	-1.132	1.237	8.454	2.389	2.514	4.990	0.424	0.432	1.836	-0.398	-0.386	-3.032
4.858	1.248	1.277	2.262	-1.125	1.237	9.024	2.374	2.514	5.589	0.418	0.432	3.155	-0.397	-0.386	-2.925
6.315	1.230	1.277	3.692	-1.108	1.237	10.437	2.338	2.514	7.010	0.413	0.432	4.452	-0.392	-0.386	-1.630
7.894	1.210	1.277	5.260	-1.085	1.237	12.268	2.295	2.514	8.708	0.402	0.432	6.990	-0.386	-0.386	-0.029
10.525	1.177	1.277	7.885	-1.053	1.237	14.887	2.229	2.514	11.330	0.383	0.432	11.380	-0.373	-0.386	3.449
12.630	1.150	1.277	9.961	-1.030	1.237	16.702	2.180	2.514	13.278	0.372	0.432	13.786	-0.375	-0.386	2.785
15.788	1.112	1.277	12.951	-0.998	1.237	19.299	2.110	2.514	16.074	0.344	0.432	20.393	-0.341	-0.386	11.639

Table 4.2 Second order tides. Comparison of analytical and Model 1B results. (Numerical results from 20th tidal cycle)

Courant Number	High Water (m)		% Age Difference	Low Water (m)		% Age Difference	Tidal Range (m)		% Age Difference	Maximum Velocity (m/s)		% Age Difference	Minimum Velocity (m/s)		% Age Difference
	Model 2B	Proudman		Model 2B	Proudman		Model 2B	Proudman		Model 2B	Proudman		Model 2B	Proudman	
0.820	1.309	1.277	-2.466	-1.188	1.237	3.984	2.497	2.514	0.707	0.440	0.432	-1.902	-0.384	-0.386	0.364
1.619	1.309	1.277	-2.480	-1.188	1.237	3.959	2.497	2.514	0.688	0.440	0.432	-1.964	-0.384	-0.386	0.414
2.429	1.310	1.277	-2.572	-1.188	1.237	3.965	2.498	2.514	0.644	0.441	0.432	-2.101	-0.384	-0.386	0.524
3.324	1.311	1.277	-2.647	-1.187	1.237	4.081	2.498	2.514	0.663	0.442	0.432	-2.264	-0.383	-0.386	0.775
4.210	1.314	1.277	-2.870	-1.183	1.237	4.341	2.497	2.514	0.678	0.443	0.432	-2.596	-0.383	-0.386	0.738
4.858	1.316	1.277	-3.064	-1.183	1.237	4.396	2.499	2.514	0.606	0.445	0.432	-3.001	-0.383	-0.386	0.857
6.315	1.321	1.277	-3.447	-1.182	1.237	4.477	2.503	2.514	0.452	0.445	0.432	-2.947	-0.381	-0.386	1.235
7.894	1.325	1.277	-3.762	-1.175	1.237	5.009	2.500	2.514	0.553	0.449	0.432	-3.997	-0.377	-0.386	2.211
10.525	1.353	1.277	-5.954	-1.169	1.237	5.470	2.523	2.514	-0.333	0.473	0.432	-9.386	-0.384	-0.386	0.453
12.630	1.392	1.277	-8.951	-1.144	1.237	7.551	2.535	2.514	-0.832	0.456	0.432	-5.470	-0.413	-0.386	-7.048
15.788	1.368	1.277	-7.075	-1.210	1.237	2.217	2.577	2.514	-2.503	0.421	0.432	2.531	-0.460	-0.386	-19.078

Table 4.3 Second order tides. Comparison of analytical and Model 2B results. (Numerical results from 60th tidal cycle)

Courant Number	High Water (m)		% Age Difference	Low Water (m)		% Age Difference	Tidal Range (m)		% Age Difference	Maximum Velocity (m/s)		% Age Difference	Minimum Velocity (m/s)		% Age Difference
	Model 2C	Proudman		Model 2C	Proudman		Model 2C	Proudman		Model 2C	Proudman		Model 2C	Proudman	
0.820	1.310	1.277	-2.541	-1.187	1.237	4.013	2.497	2.514	0.683	0.441	0.432	-2.119	-0.384	-0.386	0.604
1.619	1.311	1.277	-2.661	-1.187	1.237	4.035	2.498	2.514	0.633	0.443	0.432	-2.437	-0.382	-0.386	0.883
2.429	1.313	1.277	-2.775	-1.187	1.237	4.067	2.499	2.514	0.591	0.444	0.432	-2.772	-0.382	-0.386	1.111
3.324	1.315	1.277	-2.926	-1.186	1.237	4.089	2.501	2.514	0.526	0.447	0.432	-3.396	-0.380	-0.386	1.564
4.210	1.319	1.277	-3.253	-1.187	1.237	4.062	2.506	2.514	0.346	0.448	0.432	-3.788	-0.378	-0.386	2.054
4.858	1.322	1.277	-3.485	-1.186	1.237	4.087	2.508	2.514	0.241	0.452	0.432	-4.523	-0.377	-0.386	2.403
6.315	1.329	1.277	-4.016	-1.186	1.237	4.087	2.515	2.514	-0.030	0.458	0.432	-5.975	-0.375	-0.386	2.725
7.894	1.335	1.277	-4.527	-1.177	1.237	4.880	2.512	2.514	0.101	0.462	0.432	-6.925	-0.371	-0.386	3.756
10.525	1.370	1.277	-7.287	-1.157	1.237	6.507	2.527	2.514	-0.500	0.494	0.432	-14.298	-0.390	-0.386	-1.190
12.630	1.425	1.277	-11.562	-1.128	1.237	8.846	2.553	2.514	-1.521	0.494	0.432	-14.472	-0.411	-0.386	-6.556
15.788	1.413	1.277	-10.636	-1.176	1.237	4.949	2.589	2.514	-2.968	0.445	0.432	-3.043	0.478	-0.386	-23.759

Table 4.4 Second order tides. Comparison of analytical and Model 2C results.
(Numerical results from 60th tidal cycle)

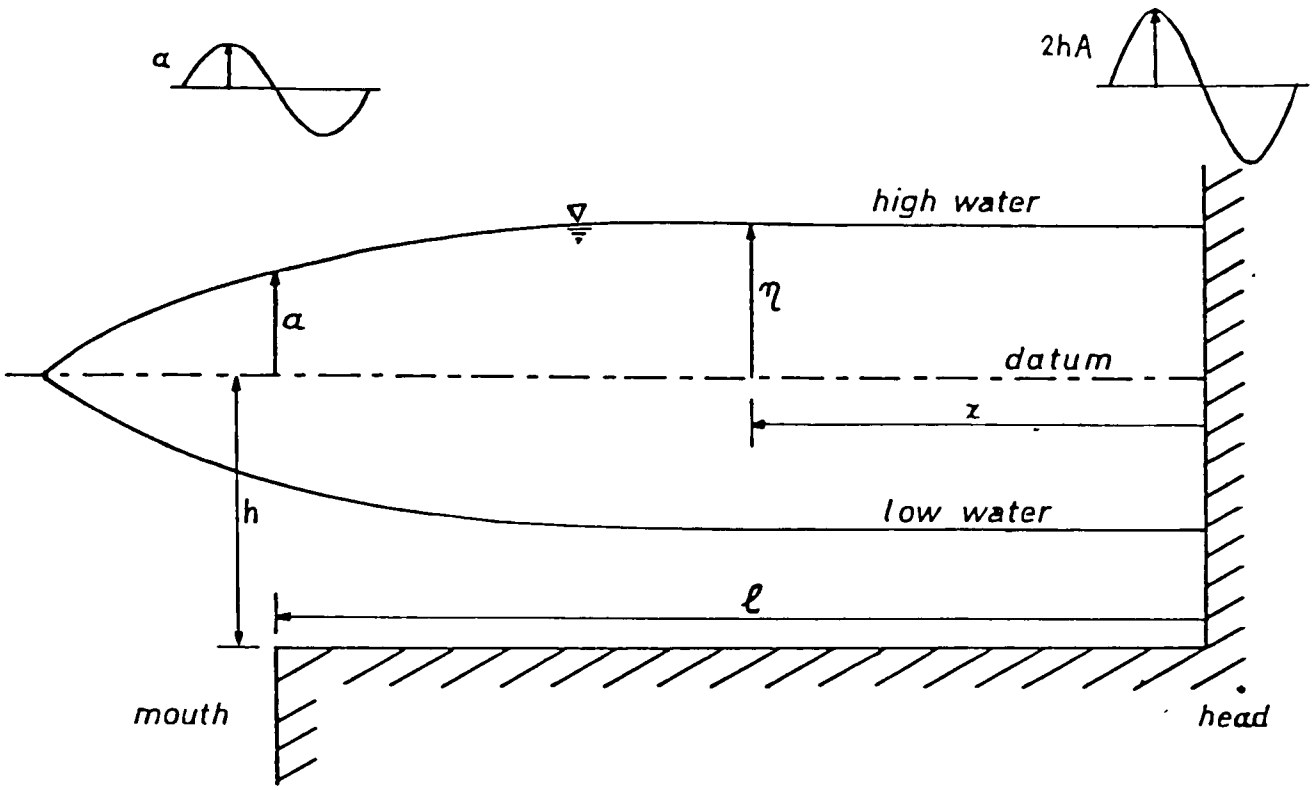

Figure 4.1 First order tides in an idealised estuary

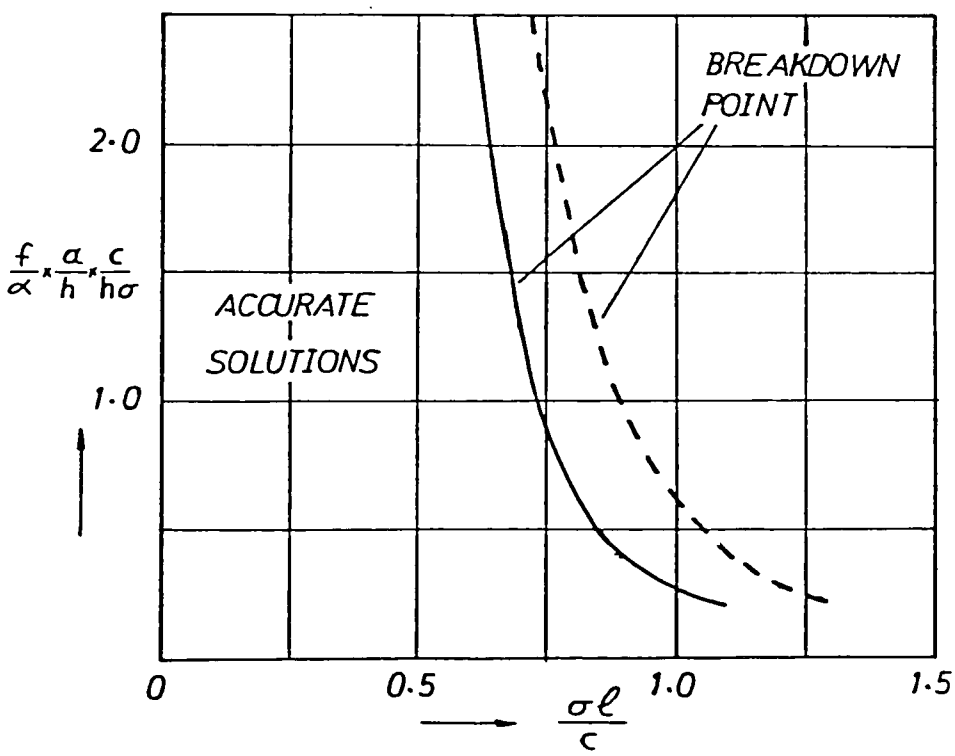

Figure 4.2 Limits of application of Proudman's solution

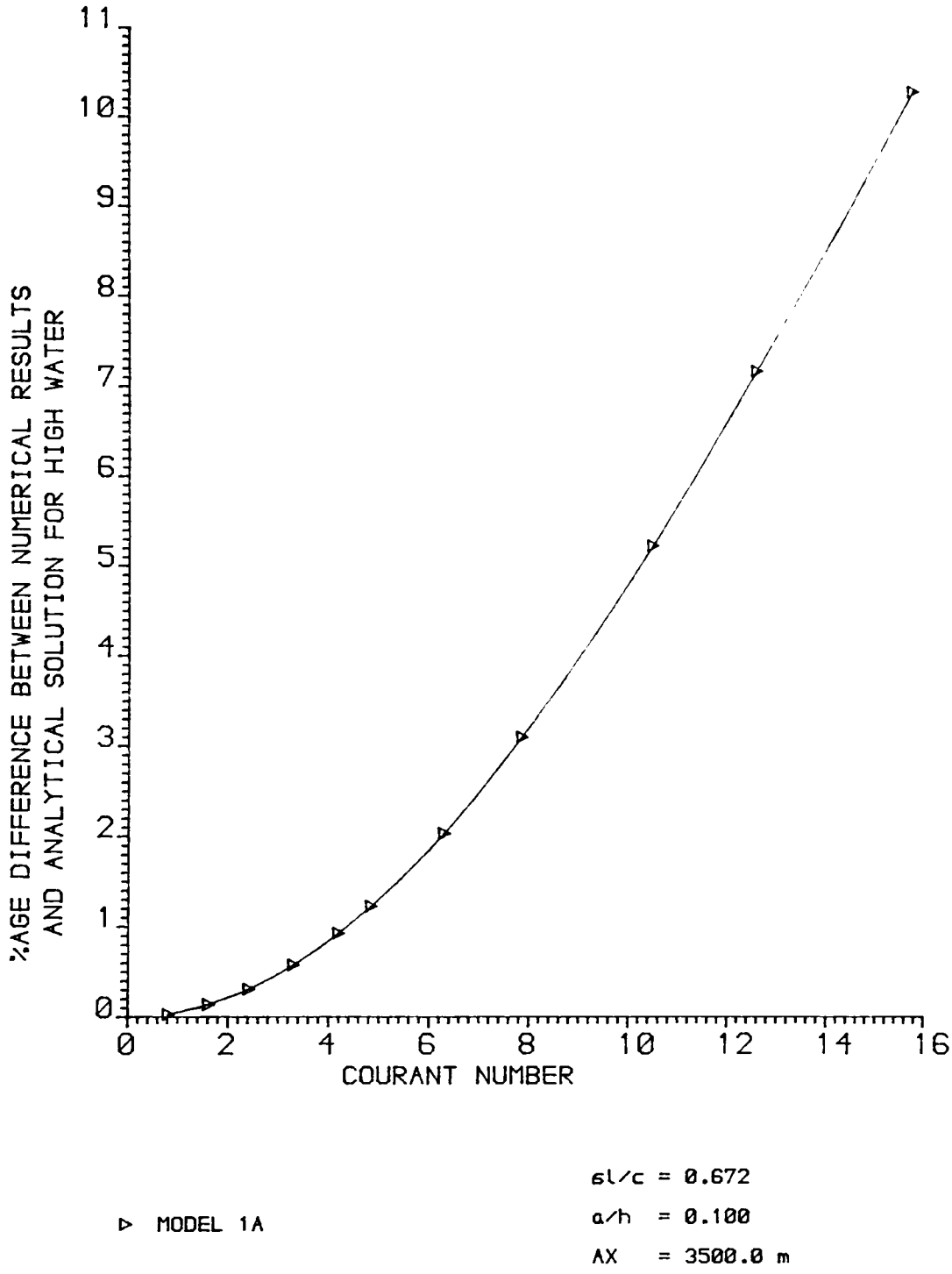

Figure 4.3 Variation of agreement between numerical and analytical high water results with the Courant number

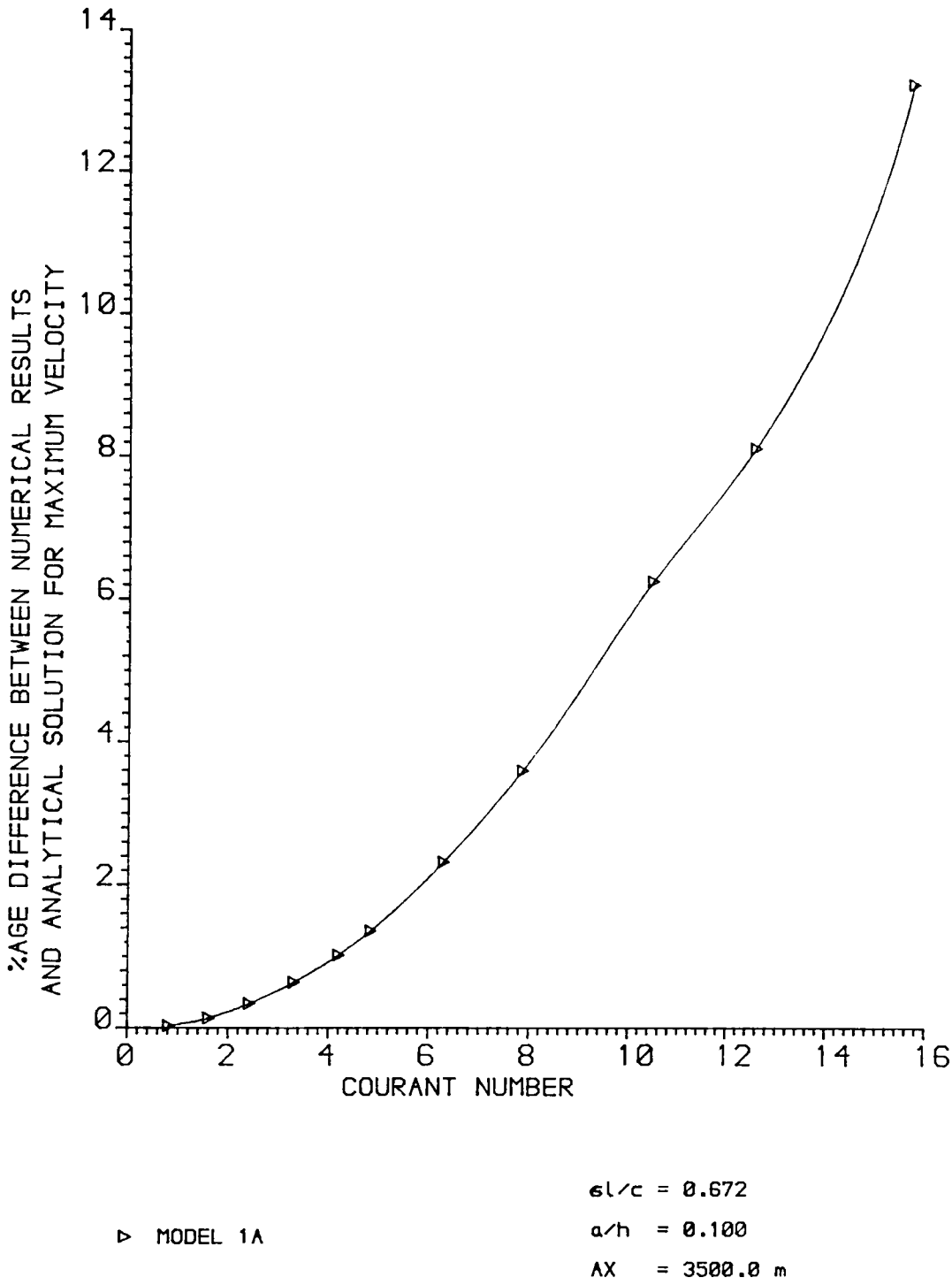

Figure 4.4 Variation of agreement between numerical and analytical maximum velocity results with the Courant number

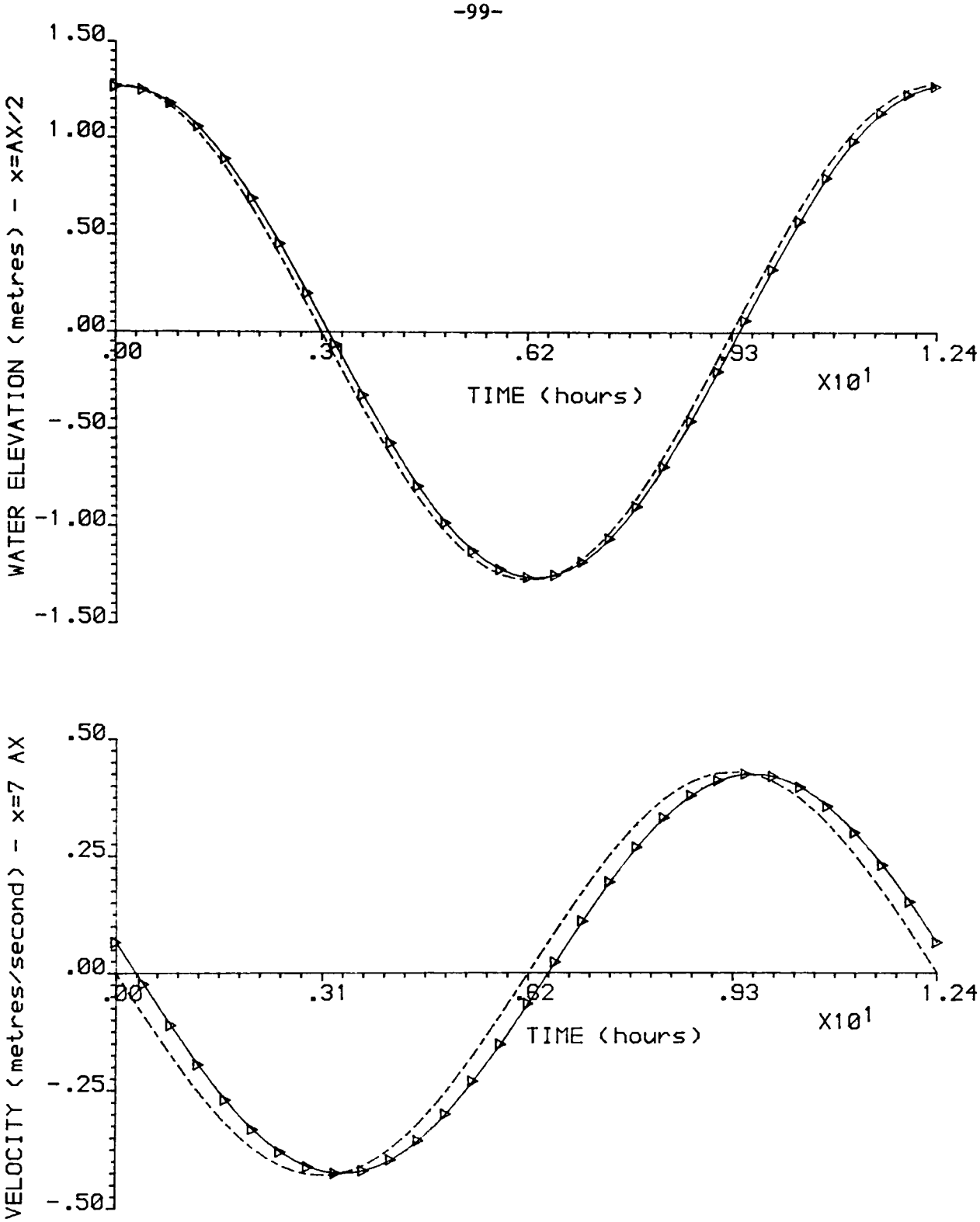

Figure 4.5 Comparison of analytical and numerical waves

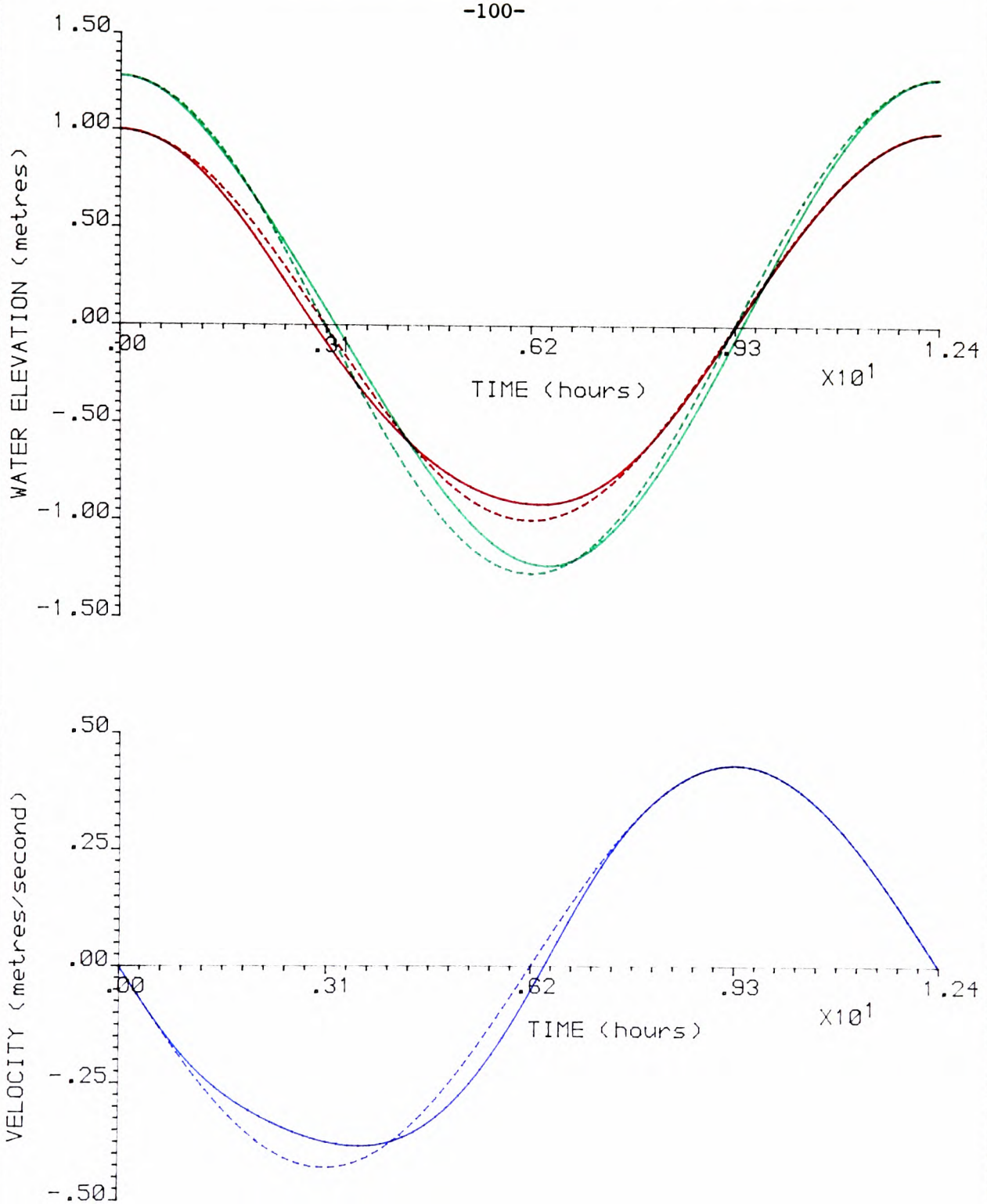

Figure 4.6 Proudman's analytical wave at f/α =0.002

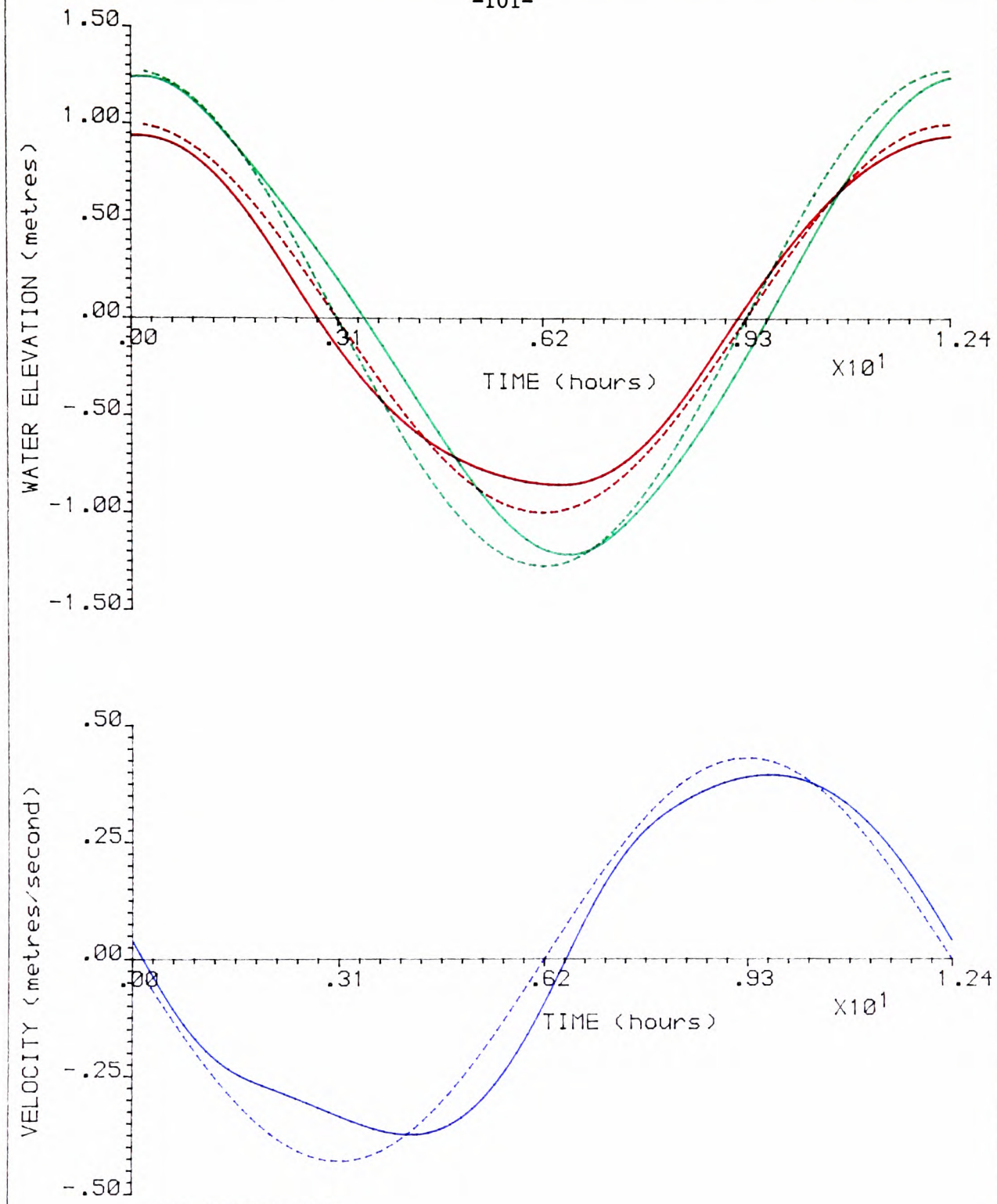

Figure 4.7 Proudman's analytical wave at f/α =0.005

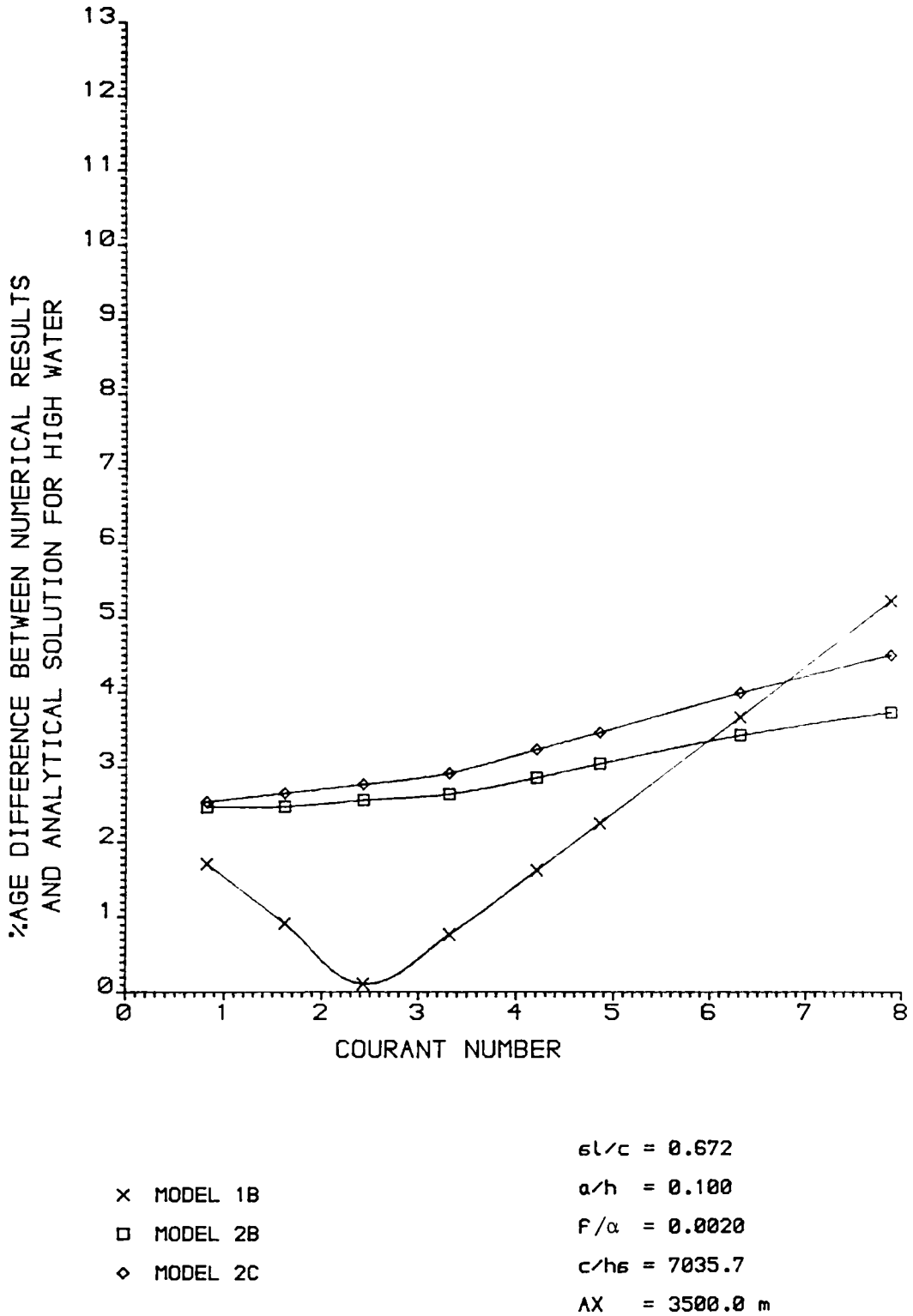

Figure 4.8 Variation of agreement between numerical and analytical high water results with the Courant number

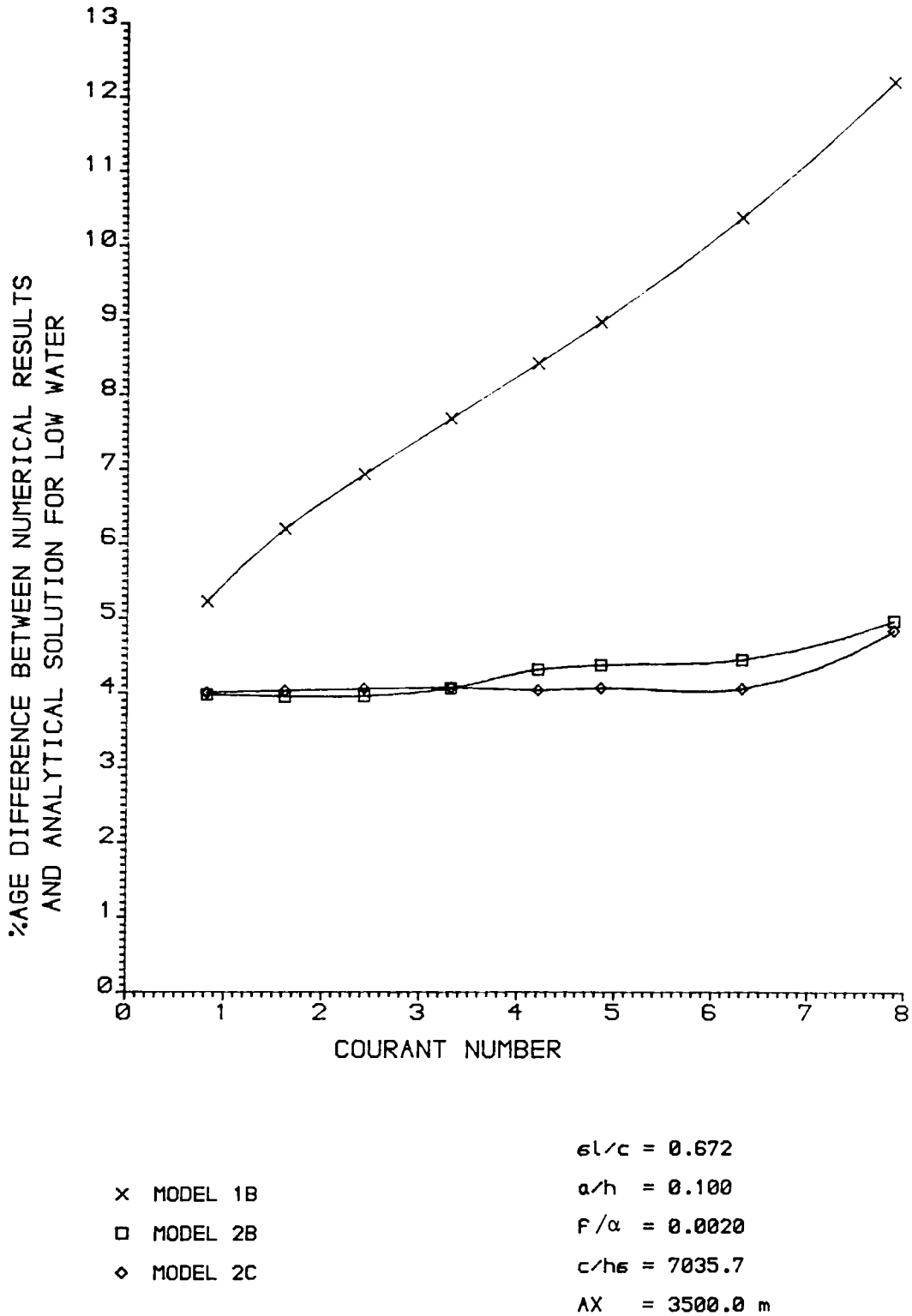

Figure 4.9 Variation of agreement between numerical and analytical low water results with the Courant number

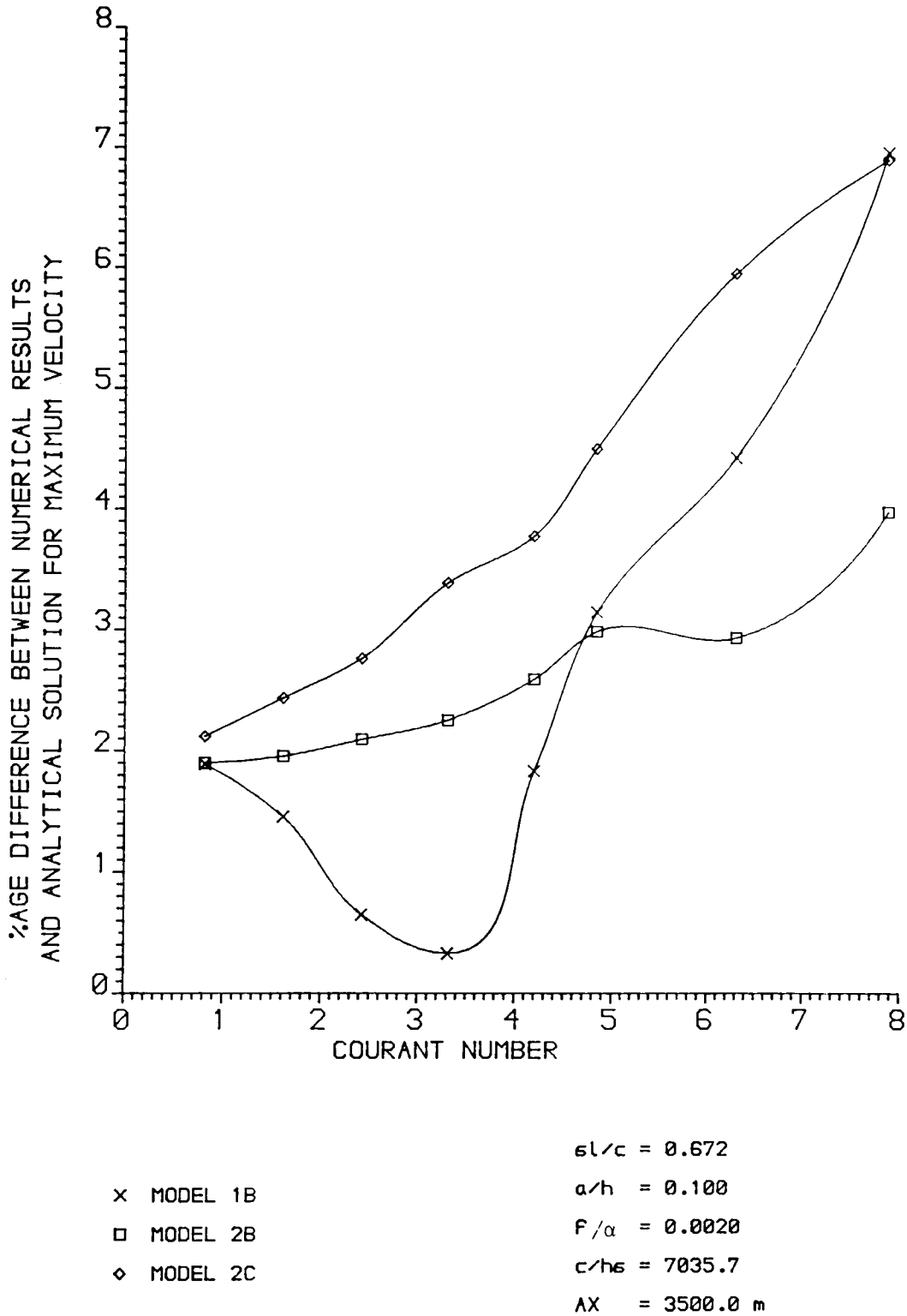

Figure 4.10 Variation between numerical and analytical maximum velocity results with the Courant number

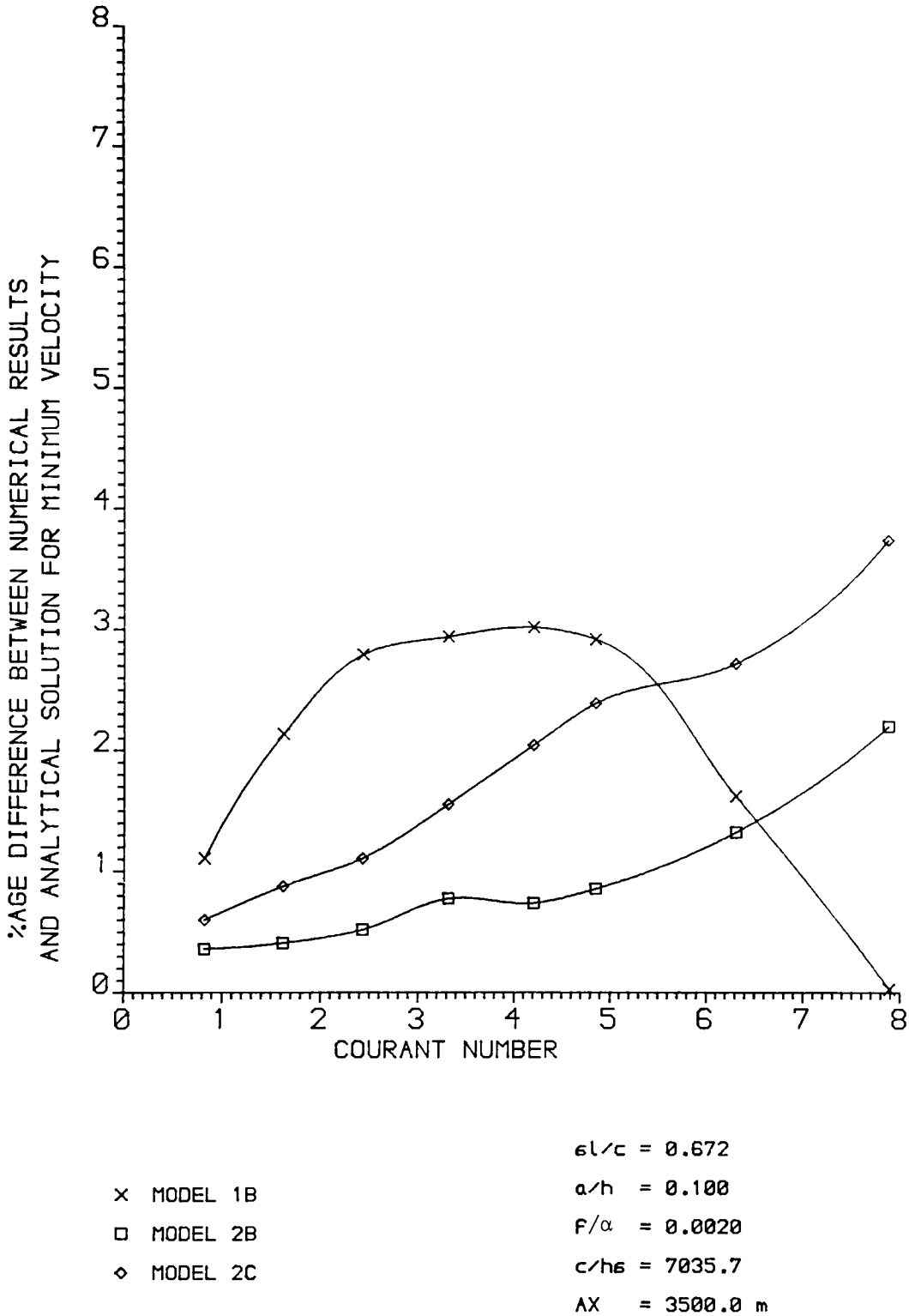

Figure 4.11 Variation agreement between numerical and analytical minimum velocity results with the Courant number

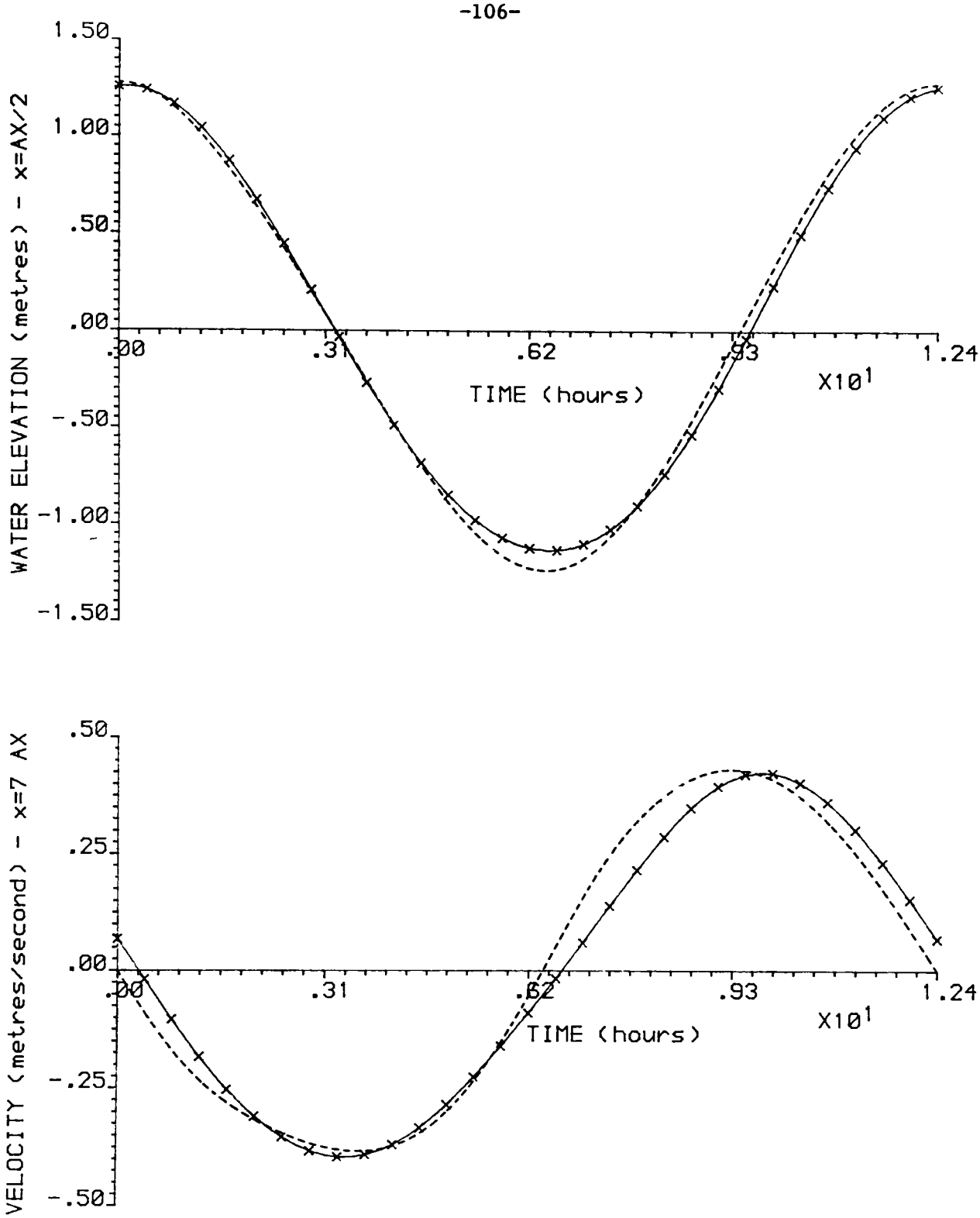

Figure 4.12 Comparison of the numerical wave of Model 1B and Proudman's solution

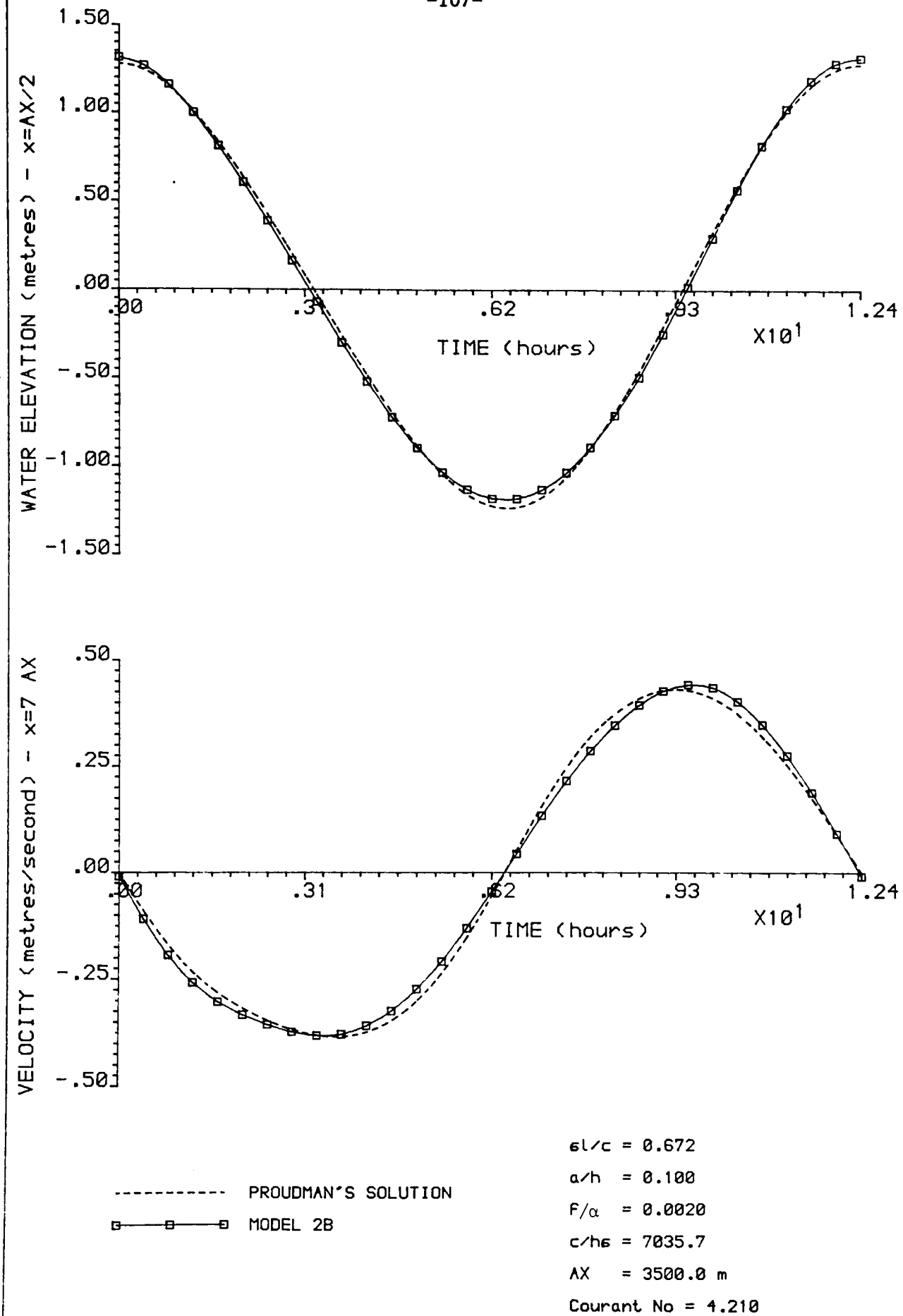

Figure 4.13 Comparison of the numerical wave of Model 2B and Proudman's solution

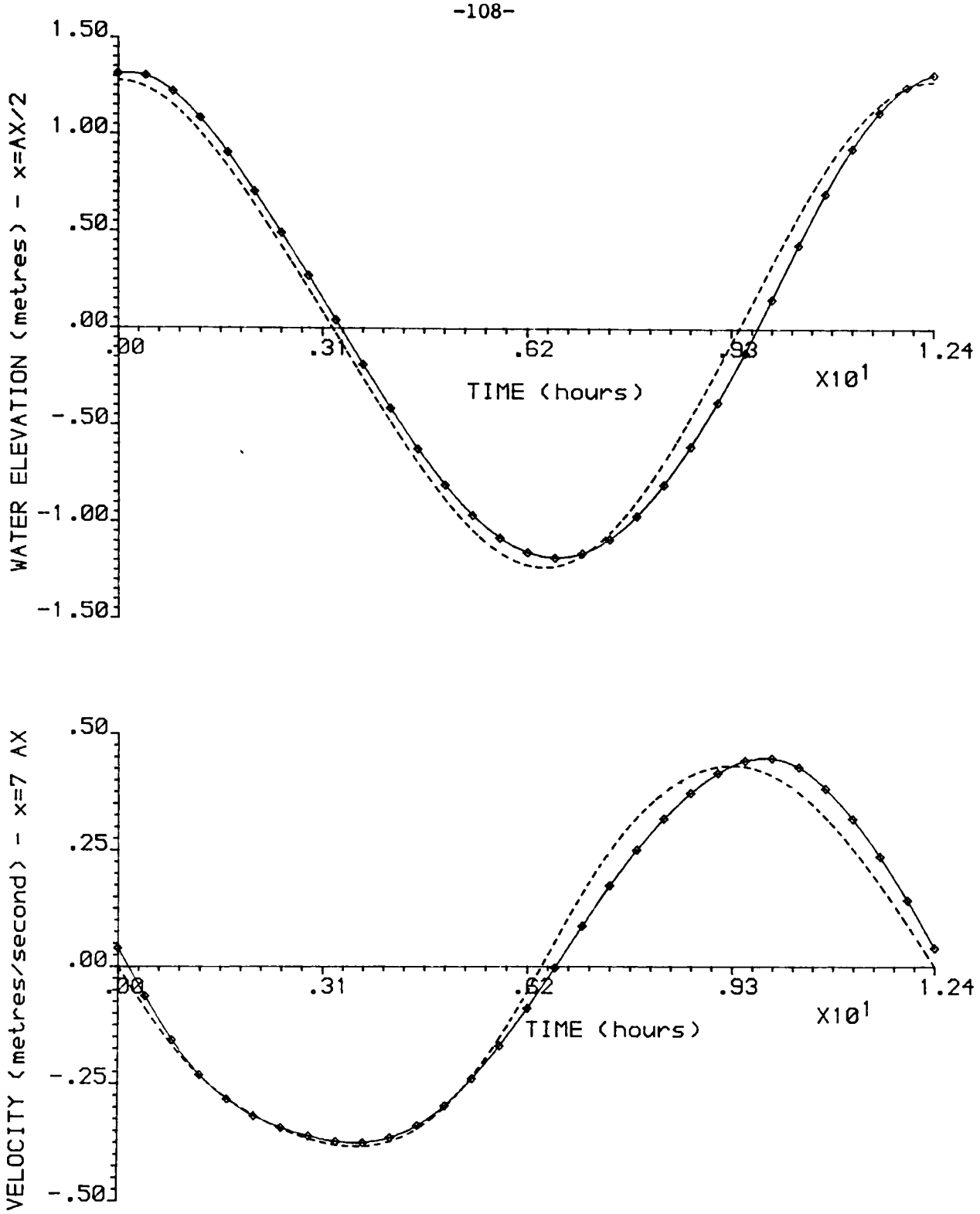

Figure 4.14 Comparison of the numerical wave of Model 2C and Proudman's solution

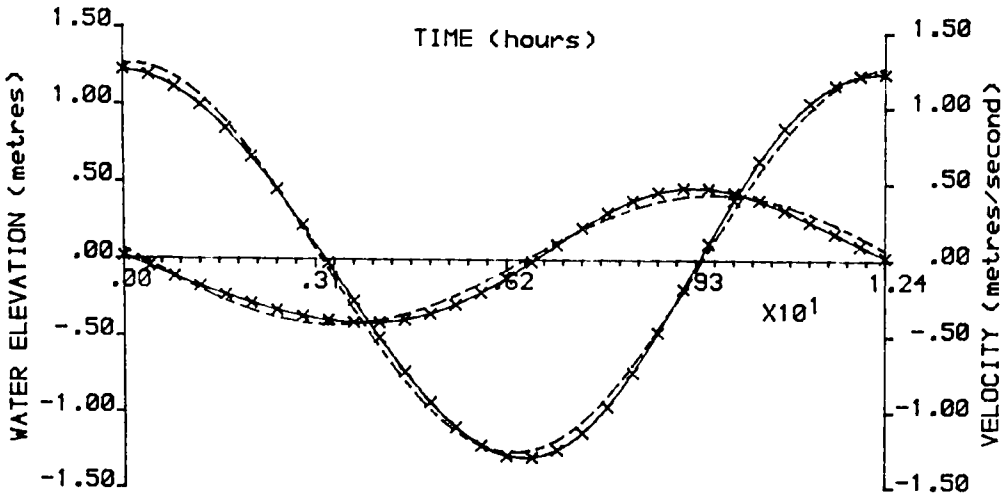

Figure 4.15 Effects of non-linear continuity equation on the first order wave

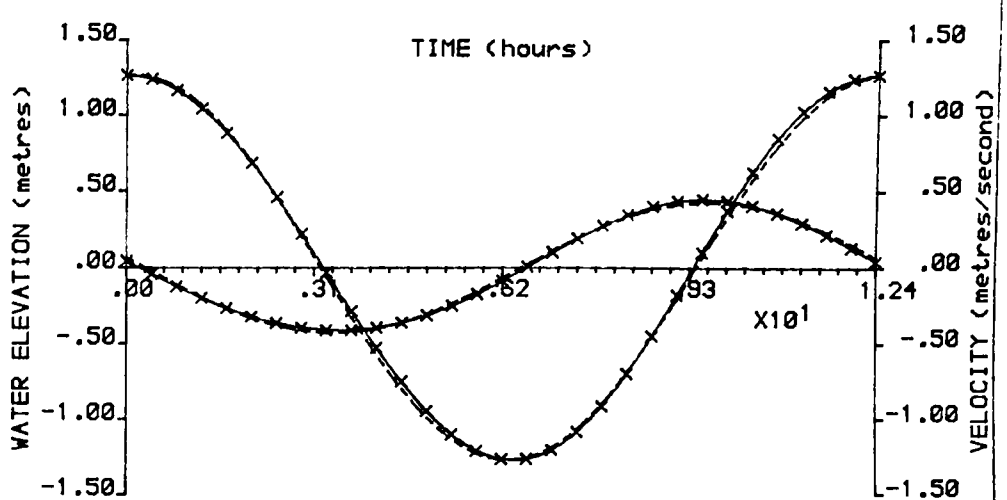

Figure 4.16 Effects of the convective acceleration on the first order wave

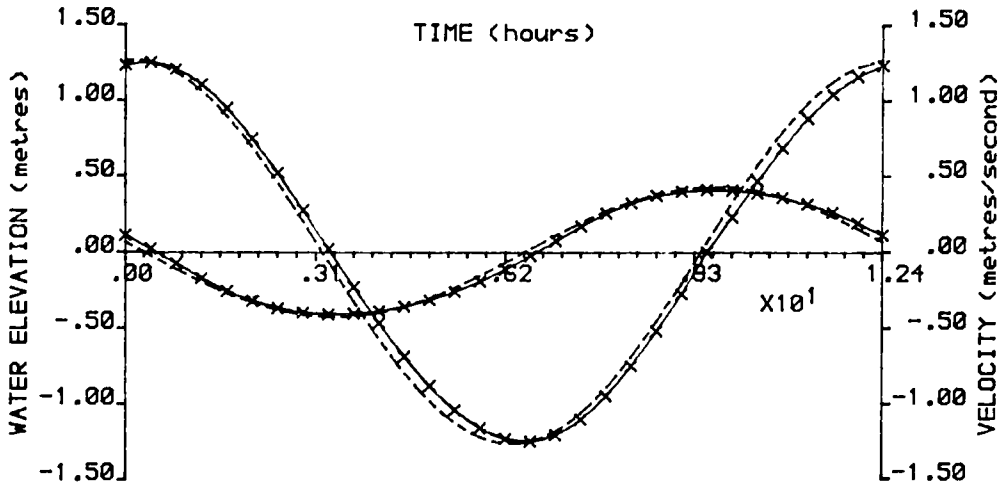

Figure 4.17 Effects of the friction term on the first order wave

---------- MODEL 1A

×——×——× MODEL 1B

ELEVATION AT x=AX/2

VELOCITY AT x=7.0 (AX)

$\epsilon l/c$ = 0.672

a/h = 0.100

f/α = 0.0020

AX = 3500.0 m

Courant No = 4.210

CHAPTER 5

PROCEDURE FOR SOLVING THE FINITE DIFFERENCE EQUATIONS

5.1 The Two-Dimensional Finite Difference Shallow Water Wave Equations.

The numerical analyses on the properties of the basic finite difference schemes, as outlined in Chapter 3, have indicated that the central implicit scheme is probably the most advantageous scheme for solving the first order shallow water wave equations, in that it is second order accurate and unconditionally stable. In addition, it has been shown that when the complete non-linear wave equations are considered, the advection terms must be centred in time in order to avoid problems associated with non-linear instabilities. In Chapter 4, two methods of expressing the advection terms in a time-centred form were considered, namely the three-time-level and the double iteration schemes. The numerical experiments outlined in Chapter 4 have demonstrated that the central implicit scheme involving a double iterative technique is the most accurate of the schemes considered, and this scheme has therefore been chosen for the basic two-dimensional numerical model. This approach is similar to that described by Pearson(1965) and subsequently used by many investigators including Leendertse(1984).

Application of this difference scheme to the two-dimensional shallow water wave eqns.(2.27) to (2.29), yields a set of finite difference equations which allow the prediction of the velocity field throughout the model domain. The solution procedure makes use of the Alternating Direction Implicit (ADI) approach, see Rychtmyer and Morton(1967) and Roache(1976), where, for each computing cycle, two successive time level operations are performed. During the first operation, from time $n\Delta t$ to

$(n+\frac{1}{2})\Delta t$, all components involving U and η of eqns.(2.27) and (2.29) are expressed in an implicit form while those relating to V are expressed explicitly. Similarly, during the second operation, from time $(n+\frac{1}{2})\Delta t$ to $(n+1)\Delta t$, all the components involving V and η of eqns.(2.28) and (2.29) are expressed implicitly, while the previous implicit U values are now expressed explicitly. The position of the different variables on the computational grid is illustrated in fig.(5.1).

Referring to fig.(5.1) each variable can be represented uniquely by a set of subscripts and superscripts of the following form:

$$\eta^{n}_{i,j} = \eta(i\Delta x,\ j\Delta y,\ n\Delta t),\ \Delta y = \Delta x$$

where $(i\Delta x, j\Delta y)$ is a spatial grid point. For average values at the grid points the following notation has been used:

$$\overline{\eta}^{x}_{i+\frac{1}{2},j} = \frac{1}{2}\,(\eta^{n}_{i+1,j} + \eta^{n}_{i,j})$$

$$\overline{\eta}^{y}_{i,j+\frac{1}{2}} = \frac{1}{2}\,(\eta^{n}_{i,j+1} + \eta^{n}_{i,j})$$

$$\overline{\overline{\eta}}^{n}_{i+\frac{1}{2},j+\frac{1}{2}} = \frac{1}{4}\,(\eta^{n}_{i+1,j+1} + \eta^{n}_{i,j+1} + \eta^{n}_{i+1,j} + \eta^{n}_{i,j})$$

In addition, the products UH and VH may be expressed in terms of the flow rate components per unit width, i.e. q_x and q_y respectively which, in finite difference form, may be written as:

$$q^{n}_{xi+\frac{1}{2},j} = U^{n}_{i+\frac{1}{2},j}\,(\overline{h}^{y}_{i+\frac{1}{2},j} + \overline{\eta}^{x}_{i+\frac{1}{2},j})$$

$$q^{n}_{yi,j+\frac{1}{2}} = V^{n}_{i,j+\frac{1}{2}}\,(\overline{h}^{x}_{i,j+\frac{1}{2}} + \overline{\eta}^{y}_{i,j+\frac{1}{2}})$$

Using the above notation the depth-averaged continuity and momentum equations may be re-written in the following finite difference form, for the first operation:

$$(\eta^{n+\frac{1}{2}}_{i,j} - \eta^{n}_{i,j}) + \frac{\Delta t}{2\Delta x}\,(q^{n+\frac{1}{2}}_{xi+\frac{1}{2},j} - q^{n+\frac{1}{2}}_{xi-\frac{1}{2},j}) + \frac{\Delta t}{2\Delta x}(q^{n}_{yi,j+\frac{1}{2}} - q^{n}_{yi,j-\frac{1}{2}}) = 0 \quad (5.1)$$

$$(q^{n+\frac{1}{2}}_{xi+\frac{1}{2},j} - q^{n-\frac{1}{2}}_{xi+\frac{1}{2},j}) + \alpha\,\frac{\Delta t}{\Delta x}\,(\overline{UM}^{x}_{i+1,j}\,\overline{QXM}^{x}_{i+1,j} - \overline{UM}^{x}_{i,j}\,\overline{QXM}^{x}_{i,j})$$

$$+ \alpha\,\frac{\Delta t}{\Delta x}\,(\overline{q}^{xn}_{yi+\frac{1}{2},j+\frac{1}{2}}\,UM_{i+\frac{1}{2},r} - \overline{q}^{xn}_{yi+\frac{1}{2},j+\frac{1}{2}}\,UM_{i+\frac{1}{2},s})$$

$$+ \frac{g\Delta t}{2\Delta x}\,(\overline{h}^{y}_{i+\frac{1}{2},j} + \overline{\eta}^{xn}_{i+\frac{1}{2},j})\,(\eta^{n+\frac{1}{2}}_{i+1,j} + \eta^{n-\frac{1}{2}}_{i+1,j} - \eta^{n+\frac{1}{2}}_{i,j} - \eta^{n-\frac{1}{2}}_{i,j})$$

$$- f\,\overline{\overline{q}}^{n}_{yi+\frac{1}{2},j} + \frac{g\Delta t\;(q^{n+\frac{1}{2}}_{xi+\frac{1}{2},j} + q^{n-\frac{1}{2}}_{xi+\frac{1}{2},j})\;[(QXM_{i+\frac{1}{2},j})^2 + (\overline{\overline{q}}^{n}_{yi+\frac{1}{2},j})^2]^{\frac{1}{2}}}{2(\overline{h}^{y}_{i+\frac{1}{2},j} + \overline{\eta}^{xn}_{i+\frac{1}{2},j})^2\;(\overline{C}^{x}_{i+\frac{1}{2},j})^2}$$

$$- \frac{\Delta t\;B\;\sqrt{g}\;\;[(QXM_{i+\frac{1}{2},j})^2 + (\overline{\overline{q}}^{n}_{yi+\frac{1}{2},j})^2]^{\frac{1}{2}}(\overline{h}^{y}_{i+\frac{1}{2},j} + \overline{\eta}^{xn}_{i+\frac{1}{2},j})}{\Delta x^2\;\overline{C}^{x}_{i+\frac{1}{2},j}}$$

$$(UM_{i+\frac{1}{2},j+1} - 2UM_{i+\frac{1}{2},j} + UM_{i+\frac{1}{2},j-1}) - C_f\,\Delta t\left[\overline{h}^{y}_{i+\frac{1}{2},j} + \overline{\eta}^{xn}_{i+\frac{1}{2},j}\right]$$

$$\left[\left(\frac{T_{xy|f}}{\rho}\right)^{n}_{i+\frac{1}{2},j+\frac{1}{2}} - \left(\frac{T_{xy|f}}{\rho}\right)^{n}_{i+\frac{1}{2},j-\frac{1}{2}}\right] = 0 \quad (5.2)$$

where $B = 0.15$

$C_f = 1$ inside a mixing zone
$= 0$ elsewhere

$$\left(\frac{T_{xy|f}}{\rho}\right)^{n}_{i+\frac{1}{2},j+\frac{1}{2}} = K^n\,e^{-\frac{R}{2}\left(\frac{I'}{J'}\right)^2}$$

I' = number of grid points downstream of shear layer origin

J' = number of grid points transverse to shear layer origin

$K = U_1^2/(2\sqrt{2\pi R})$

$\alpha = 1.016$

and likewise for the second operation:

$$(\eta^{n+1}_{i,j} - \eta^{n+\frac{1}{2}}_{i,j}) + \frac{\Delta t}{2\Delta x}\left(q^{n+\frac{1}{2}}_{xi+\frac{1}{2},j} - q^{n+\frac{1}{2}}_{xi-\frac{1}{2},j}\right) + \frac{\Delta t}{2\Delta x}\left(q^{n+1}_{yi,j+\frac{1}{2}} - q^{n+1}_{yi,j-\frac{1}{2}}\right) = 0 \quad (5.3)$$

$$\left(q^{n+1}_{yi,j+\frac{1}{2}} - q^{n}_{yi,j+\frac{1}{2}}\right) + \alpha\,\frac{\Delta t}{\Delta x}\left(\frac{\underline{y}_{n+\frac{1}{2}}}{q_{xi+\frac{1}{2},j+\frac{1}{2}}}\,VM_{p,j+\frac{1}{2}} - \frac{\underline{y}_{n+\frac{1}{2}}}{q_{xi+\frac{1}{2},j+\frac{1}{2}}}\,VM_{t,j+\frac{1}{2}}\right)$$

$$+\alpha\,\frac{\Delta t}{\Delta x}\left(\underline{VM}_{i,j+1}\,\underline{QYM}_{i,j+1} - \underline{VM}_{i,j}\,\underline{QYM}_{i,j}\right) + \frac{g\Delta t}{2\Delta x}\left(\underline{h}_{i,j+\frac{1}{2}} + \underline{\eta}^{n+\frac{1}{2}}_{i,j+\frac{1}{2}}\right)$$

$$\left(\eta^{n+1}_{i,j+1} + \eta^{n}_{i,j+1} - \eta^{n+1}_{i,j} - \eta^{n}_{i,j}\right) + f\,\bar{q}^{n+\frac{1}{2}}_{xi,j+\frac{1}{2}}$$

$$+\frac{g\Delta t\,\left(q^{n+1}_{yi,j+\frac{1}{2}} + q^{n}_{yi,j+\frac{1}{2}}\right)\left[\left(\bar{q}^{n+\frac{1}{2}}_{xi,j+\frac{1}{2}}\right)^2 + \left(QYM_{i,j+\frac{1}{2}}\right)^2\right]^{\frac{1}{2}}}{2\left(\underline{h}_{i,j+\frac{1}{2}} + \underline{\eta}^{n+\frac{1}{2}}_{i,j+\frac{1}{2}}\right)^2\left(\underline{C}_{i,j+\frac{1}{2}}\right)^2}$$

$$-\frac{\Delta t\;B\;\sqrt{g}\left[\left(\bar{q}^{n+\frac{1}{2}}_{x\,i,j+\frac{1}{2}}\right)^2 + \left(QYM_{i,j+\frac{1}{2}}\right)^2\right]^{\frac{1}{2}}\left(\underline{h}_{i,j+\frac{1}{2}} + \underline{\eta}^{n+\frac{1}{2}}_{i,j+\frac{1}{2}}\right)}{\Delta x^2\;\underline{C}_{i,j+\frac{1}{2}}}$$

$$\left(VM_{i+1,j+\frac{1}{2}} - 2VM_{i,j+\frac{1}{2}} + VM_{i-1,j+\frac{1}{2}}\right) - C_f\,\Delta t\left(\frac{\underline{x}}{h_{i,j+\frac{1}{2}}} + \underline{\eta}^{n+\frac{1}{2}}_{i,j+\frac{1}{2}}\right)$$

$$\left[\left(\frac{T_{xy|f}}{\rho}\right)^{n+\frac{1}{2}}_{i+\frac{1}{2},j+\frac{1}{2}} - \left(\frac{T_{xy|f}}{\rho}\right)^{n+\frac{1}{2}}_{i-\frac{1}{2},j+\frac{1}{2}}\right] = 0 \quad (5.4)$$

As already mentioned each operation involves a double iteration. During the first iteration the components UM, QXM, VM and QYM describe the corresponding terms at the lower time level, giving:

$$UM_{i+\frac{1}{2},j} = U^{n-\frac{1}{2}}_{i+\frac{1}{2},j}$$

$$QXM_{i+\frac{1}{2},j} = UM_{i+\frac{1}{2}j}\left(\underline{h}^{y}_{i+\frac{1}{2},j} + \underline{\eta}^{x}_{n\,i+\frac{1}{2},j}\right)$$

$$VM_{i,j+\frac{1}{2}} = V^{n}_{i,j+\frac{1}{2}}$$

$$QYM_{i,j+\frac{1}{2}} = VM_{i,j+\frac{1}{2}}\left(\frac{\underline{x}}{h_{i,j+\frac{1}{2}}} + \underline{\eta}^{n+\frac{1}{2}}_{i,j+\frac{1}{2}}\right)$$

whereas during the second iteration these components represent the terms in the form:

$$UM_{i+\frac{1}{2},j} = \frac{1}{2}\,(U^{n-\frac{1}{2}}_{i+\frac{1}{2},j} + \dot{U}^{n+\frac{1}{2}}_{i+\frac{1}{2},j})$$

$$QXM_{i+\frac{1}{2},j} = UM_{i+\frac{1}{2},j}\,(\frac{x}{h}_{i+\frac{1}{2},j} + \frac{y_n}{\eta}_{i+\frac{1}{2},j})$$

$$VM_{i,j+\frac{1}{2}} = \frac{1}{2}\,(V^{n}_{i,j+\frac{1}{2}} + \dot{V}^{n+1}_{i,j+\frac{1}{2}})$$

$$QYM_{i,j+\frac{1}{2}} = VM_{i,j+\frac{1}{2}}\,(\frac{x}{h}_{i,j+\frac{1}{2}} + \frac{y_{n+\frac{1}{2}}}{\eta}_{i,j+\frac{1}{2}})$$

where $\dot{U}^{n+\frac{1}{2}}_{i+\frac{1}{2},j}$ and $\dot{V}^{n+1}_{i,j+\frac{1}{2}}$ are the implicit velocities obtained at the end of the first iteration of the first and second operations respectively. Concerning the subscripts r and s in eqn.(5.2) and p and t in eqn.(5.4), these variables can be defined accordingly:

$$r = j \text{ if } \frac{x_n}{q}_{yi+\frac{1}{2},j+\frac{1}{2}} > 0 \quad \text{otherwise} \quad r = j+1$$

$$s = j \text{ if } \frac{x_n}{q}_{yi+\frac{1}{2},j-\frac{1}{2}} < 0 \quad \text{otherwise} \quad s = j-1$$

$$p = i \text{ if } \frac{y_{n+\frac{1}{2}}}{q}_{xi+\frac{1}{2},j+\frac{1}{2}} > 0 \quad \text{otherwise} \quad p = i+1$$

$$t = i \text{ if } \frac{y_{n+\frac{1}{2}}}{q}_{xi-\frac{1}{2},j+\frac{1}{2}} < 0 \quad \text{otherwise} \quad t = i-1$$

The use of this representation for the advective acceleration components $\frac{\partial UV(h+\eta)}{\partial x}$ and $\frac{\partial UV(h+\eta)}{\partial y}$, allows momentum to be conserved as accurately as possible, with the scheme being similar to that of upwind differencing (see Roache(1976)). The spatial location of the velocity products depends upon the direction of the velocity component perpendicular to the axis being considered. Hence, the momentum flux is calculated as near as possible to the point where it originates, see Williams and Holmes(1974).

Another advantage of this scheme is that it includes sufficient damping to counteract the occurrence of any grid scale oscillations, see Edwards and Preston(1985). In addition, as will be demonstrated in Chapter 6, it was found necessary to express the cross-product advection terms in the model as $\frac{\partial Uq_y}{\partial y}$ and $\frac{\partial q_x V}{\partial x}$, as opposed to $\frac{\partial q_x V}{\partial y}$ and $\frac{\partial Uq_y}{\partial x}$ employed by Falconer(1983,1984). Considering the cross-product advection term of the x-direction momentum equation, the first representation ($\frac{\partial Uq_y}{\partial y}$) involves the off-centering of the velocity component U, whereas the second representation ($\frac{\partial q_x V}{\partial y}$) involves the off-centering of the discharge component q_x - implying the off-centering of all U, h and η. The additional off-centering of h and η, in comparison to the first representation, may be introducing large inaccuracies that give rise to errors in the velocity field prediction where these terms are important.

The inclusion of wind action has not been considered in this study and therefore wind stresses have been omitted in the difference eqns.(5.2) and (5.4). Also the direct stresses, or Reynolds stresses, have been ignored on the grounds that they are negligible for the type of flows considered. Furthermore their representation using the Boussinesq approximation is dubious since the positive nature of these stresses cannot be guaranteed using this representation.

All terms of the finite difference eqns.(5.1) to (5.4) are centred in space with a truncation error of $O(\Delta x^2)$, with the exception of the cross-product advection terms which have a truncation error of $O(\Delta x)$. In addition, the difference scheme is second order accurate with respect to time, that is, all terms have a truncation error of $O(\Delta t^2)$.

5.2 Boundary and Initial Conditions for the Hydrodynamic Model.

In order to solve the shallow water wave eqns.(5.1) to (5.4) and determine the velocity field in the problem area, the prescription of initial and boundary conditions is necessary. A prime requirement of the mathematical formulation of a physical process is that it should be well-posed (see Rychtmyer and Morton(1967)), that is, a unique solution should exist and depend upon the boundary conditions.

With regard to the boundary conditions, guidelines as to their specification come from a number of studies on the well-posedness of initial boundary value problems. These studies are based on the Classical Energy Method (see Elvius and Sundstrom(1973), Gustaffsson and Sundstrom(1978), Abbott and Cunge(1982)) and the Normal Mode Analysis (see Oliger and Sundstrom(1978), Edwards et al(1983)). Their main findings are summarised in table(5.1), where the required number of boundary conditions to ensure well-posedness of the system of two-dimensional shallow water equations is shown to be dependent on the type of equations as well as the actual flow conditions. The governing equations are of a hyperbolic form when the turbulent shear stresses are ignored and advective transport is assumed to be the dominant mechanism. When the turbulent stresses are included the governing equations are of an incompletely parabolic form, with the equations of motion becoming of a parabolic type while the continuity equation remains of a hyperbolic type.

In addition to being correct in number, the boundary conditions need to be correct in type for the mathematical problem to be well-posed. The type of boundary conditions has been intensively researched and at

present there appears to be no "best" treatment of the boundaries.

5.2.1 Open Boundaries.

For the hyperbolic system of equations the inflow and outflow boundaries may be given by a combination of characteristic variables (Riemann invariants), which represent a combination of incoming and outgoing waves (see Abbott and Cunge(1982), Edwards et al(1983)).
(a) At inflow boundaries, two possible conditions are common practice in numerical models. These conditions prescribe either (i) the normal and tangential velocity components to the boundary, or (ii) the water elevation and tangential velocity component to the boundary. The well-posedness of these boundary conditions has been proved with the Normal Mode Analysis technique whereas the Classical Energy Method failed to do so, see Oliger and Sundstrom(1978) and Edwards et al(1983).
(b) At the outflow boundaries, the prescription of either (i) the normal velocity component to the boundary, or (ii) the water elevation are acceptable and well-posed conditions, see Oliger and Sundstrom(1978).

For the incompletely parabolic system of equations, the conditions for well-posedness are, as yet, difficult to understand physically or be applied in numerical practice, see Gustaffsson and Sundstrom(1978).

A second condition imposed on open boundaries, in addition to providing a well-posed mathematical problem, is to minimize the reflections of disturbances. Since the nature of open boundaries is non-physical, they should not include effects which are not present in the physical system. Therefore, disturbances generated in the interior of the model and propagated outwards should be allowed to cross these non-existing boundaries unhampered. In the literature, weakly-reflective

boundary conditions, of various degrees of complexity and accuracy, have been derived for the shallow water wave equations (see Engquist and Majda(1977), Abbott and Cunge(1982), Verboom and Slob(1984)) - non-reflective boundary conditions do exist for very elementary cases such as the one-dimensional shallow water equations without friction, see Abbott and Cunge(1982). The prescription of water elevation as a boundary condition in the hyperbolic system of shallow water equations - a common practice in numerical modelling - was shown by Engquist and Majda(1977) to be highly reflective. Other combinations of Riemann invariants give less-reflective boundaries, see Abbott and Cunge(1982).

Finally it must be remarked that, in practice, computations often survive and give useful information using a combination of boundary conditions different from those dictated by the theoretical requirements. Such a boundary treatment, not uncommon in numerical applications, is to set the advection terms at the boundary to zero and, hence, prescribe only the water elevation at the boundary, e.g. Leendertse(1967,1984), Flather and Heaps(1975) - the theoretical status of such a boundary treatment is, however, not clear. In practical computations, it is often the case of using whatever boundary conditions are available.

The open boundary conditions adopted in the numerical model reported herein, include the prescription of either (i) the normal and tangential velocity components, or (ii) the water elevation η and the tangential velocity component. Detailed descriptions of the open boundary specifications are given with each case study in Chapters 6 and 7.

5.2.2 Closed Boundaries.

The closed boundary corresponds to a physical situation which requires the normal velocity component to vanish at the boundary. For the hyperbolic system of shallow water wave equations only one boundary condition is necessary and well-posedness follows directly for this physical boundary condition. The incompletely parabolic system, on the other hand, requires in addition to the obvious condition of zero normal velocity components, one other boundary condition. This additional boundary condition requires that either (i) the tangential velocity component vanishes, representing a no-slip condition, or (ii) the tangential velocity gradient normal to the boundary vanishes, representing a free-slip boundary. Both the free-slip and no-slip boundary conditions have been proven to be well-posed by the Classical Energy Method, see Oliger and Sundstrom(1978).

The implementation of the free-slip or no-slip boundary condition in the numerical model of an incompletely parabolic system, such as the shallow water wave eqns.(5.1) to (5.4), can be achieved in the following way: Velocity values outside the boundary, included in the differential quotients in eqns.(5.2) and (5.4), need to be determined and this is achieved by equating these velocities to values from within the domain. The relationship used depends on whether the boundary is assumed to be no-slip or free-slip, see Welch et al(1966), Williams and Holmes(1974). For a free-slip boundary the exterior tangential velocity component is assumed to have the same value as the corresponding interior image velocity component, and the exterior normal velocity component is the negative of the interior image value. For a no-slip boundary, on the other hand, the exterior tangential velocity component is the negative of

the interior image velocity component, and the exterior normal velocity component has the same value as the interior image velocity component. For a schematic representation of the free-slip and no-slip boundary conditions see Falconer(1977).

In the numerical model presented herein, the no-slip boundary condition has been adopted, since this is believed to be a necessary requirement for accurate vorticity generation in re-circulating flows (see Flokstra(1977)).

5.2.3 Initial Conditions

With time dependent problems, the prescription of initial conditions is necessary, with all variables being defined at the start of the computation. For tidal flows it is usual to specify the initial conditions at either high or low tide, where the water elevation η is equated to the high or low water level and is assumed to be constant throughout the domain. This enables the initial velocity components U and V to be approximated to zero everywhere.

In a shallow water system which includes friction in a finite region with prescribed periodic boundary data, it is found that the ultimate periodic tide to which the solution converges is independent of the initial conditions (Edwards(1983)). As a consequence, the precise prescription of the initial data is not necessary because the error introduced into the model by the initial data is gradually dissipated by friction.

Once the boundary and initial conditions are specified, the finite difference eqns.(5.1) to (5.4) can be solved. The method of Gauss elimination and back substitution have been adopted in the solution of eqns.(5.1) to (5.4) and described fully in section A.1 of Appendix A.

5.3 The Two-Dimensional Finite Difference Advective-Diffusion Equation.

The advective-diffusion eqn.(2.64) may be added to the hydrodynamic model, to determine the distribution of a conservative substanse S (e.g. constituent concentration) in addition to the velocity field. The ADI representation has been used for the solution of eqn.(2.64). As before, this involves two successive time level operations, for each computing cycle, with each operation being performed at the end of the corresponding operation for the solution of the shallow water wave equations, see Leendertse and Gritton(1971), Falconer(1984).

Referring to fig.(5.1), and using the notations defined earlier in section 5.1, the advective - diffusion eqn.(2.64) may be re-written in finite difference form, for the first operation, as follows:

$$\left(\bar{\bar{h}}_{i,j} + \eta^{n+\frac{1}{2}}_{i,j}\right) S^{n+\frac{1}{2}}_{i,j} - \left(\bar{\bar{h}}_{i,j} + \eta^{n}_{i,j}\right) S^{n}_{i,j} + \frac{\Delta t}{2\Delta x}\left[\bar{\bar{S}}^{x\,n+\frac{1}{2}}_{i+\frac{1}{2},j} q^{n+\frac{1}{2}}_{xi+\frac{1}{2},j}\right.$$

$$\left. - \bar{\bar{S}}^{x\,n+\frac{1}{2}}_{i-\frac{1}{2},j} q^{n+\frac{1}{2}}_{xi-\frac{1}{2},j} + \bar{\bar{S}}^{y\,n}_{i,j+\frac{1}{2}} q^{n}_{yi,j+\frac{1}{2}} - \bar{\bar{S}}^{y\,n}_{i,j-\frac{1}{2}} q^{n}_{yi,j-\frac{1}{2}}\right]$$

$$= \frac{\Delta t}{2\Delta x^2}\left[\left(S^{n+\frac{1}{2}}_{i+1,j} - S^{n+\frac{1}{2}}_{i,j}\right)\left(\bar{h}^{y}_{i+\frac{1}{2},j} + \bar{\eta}^{x\,n+\frac{1}{2}}_{i+\frac{1}{2},j}\right) D^{n+\frac{1}{2}}_{xxi+\frac{1}{2},j} - \left(S^{n+\frac{1}{2}}_{i,j} - S^{n+\frac{1}{2}}_{i-1,j}\right)\right.$$

$$\left(\bar{h}^{y}_{i-\frac{1}{2},j} + \bar{\eta}^{x\,n+\frac{1}{2}}_{i-\frac{1}{2},j}\right) D^{n+\frac{1}{2}}_{xxi-\frac{1}{2},j} + \left(S^{n}_{i,j+1} - S^{n}_{i,j}\right)\left(\bar{h}^{x}_{i,j+\frac{1}{2}} + \bar{\eta}^{y\,n}_{i,j+\frac{1}{2}}\right) D^{n}_{yyi,j+\frac{1}{2}}$$

$$\left. - \left(S^{n}_{i,j} - S^{n}_{i,j-1}\right)\left(\bar{h}^{x}_{i,j-\frac{1}{2}} + \bar{\eta}^{y\,n}_{i,j-\frac{1}{2}}\right) D^{n}_{yyi,j-\frac{1}{2}} + \left(\bar{\bar{S}}^{n}_{i+\frac{1}{2},j+\frac{1}{2}} - \bar{\bar{S}}^{n}_{i+\frac{1}{2},j-\frac{1}{2}}\right)\right.$$

$$\left(\underline{\underline{h}}^{y}_{i+\frac{1}{2},j} + \underline{\underline{\eta}}^{x\,n+\frac{1}{2}}_{i+\frac{1}{2},j}\right) D^{n+\frac{1}{2}}_{xyi+\frac{1}{2},j} - \left(\underline{\underline{\bar{S}}}^{n}_{i-\frac{1}{2},j+\frac{1}{2}} - \underline{\underline{\bar{S}}}^{n}_{i-\frac{1}{2},j-\frac{1}{2}}\right) \left(\underline{\underline{h}}^{y}_{i-\frac{1}{2},j} + \underline{\underline{\eta}}^{x\,n+\frac{1}{2}}_{i-\frac{1}{2},j}\right) D^{n+\frac{1}{2}}_{xyi-\frac{1}{2},j}$$

$$+\left(\underline{\underline{\bar{S}}}^{n}_{i+\frac{1}{2},j+\frac{1}{2}} - \underline{\underline{\bar{S}}}^{n}_{i-\frac{1}{2},j+\frac{1}{2}}\right) \left(\underline{\underline{h}}^{x}_{i,j+\frac{1}{2}} + \underline{\underline{\eta}}^{y\,n}_{i,j+\frac{1}{2}}\right) D^{n}_{yxi,j+\frac{1}{2}} - \left(\underline{\underline{\bar{S}}}^{n}_{i+\frac{1}{2},j-\frac{1}{2}} - \underline{\underline{\bar{S}}}^{n}_{i-\frac{1}{2},j-\frac{1}{2}}\right)$$

$$\left(\underline{\underline{h}}^{x}_{i,j-\frac{1}{2}} + \underline{\underline{\eta}}^{y\,n}_{i,j-\frac{1}{2}}\right) D^{n}_{yxi,j-\frac{1}{2}}\Bigg] \tag{5.5}$$

and likewise for the second operation:

$$\left(\underline{\underline{h}}_{i,j} + \eta^{n+1}_{i,j}\right) S^{n+1}_{i,j} - \left(\underline{\underline{h}}_{i,j} + \eta^{n}_{i,j}\right) S^{n+\frac{1}{2}}_{i,j} + \frac{\Delta t}{2\Delta x}\left(\underline{\underline{S}}^{x\,n+\frac{1}{2}}_{i+\frac{1}{2},j} \; q^{n+\frac{1}{2}}_{xi+\frac{1}{2},j} - \right.$$

$$\left.\underline{\underline{S}}^{x\,n+\frac{1}{2}}_{i-\frac{1}{2},j} \; q^{n+\frac{1}{2}}_{xi-\frac{1}{2},j} + \underline{\underline{S}}^{y\,n+1}_{i,j+\frac{1}{2}} \; q^{n+1}_{yi,j+\frac{1}{2}} - \underline{\underline{S}}^{y\,n+1}_{i,j-\frac{1}{2}} \; q^{n+1}_{yi,j-\frac{1}{2}}\right)$$

$$= \frac{\Delta t}{2\Delta x^2}\Bigg[\left(S^{n+\frac{1}{2}}_{i+1,j} - S^{n+\frac{1}{2}}_{i,j}\right)\left(\underline{\underline{h}}^{y}_{i+\frac{1}{2},j} - \underline{\underline{\eta}}^{x\,n+\frac{1}{2}}_{i+\frac{1}{2},j}\right) D^{n+\frac{1}{2}}_{xxi+\frac{1}{2},j} - \left(S^{n+\frac{1}{2}}_{i,j} - S^{n+\frac{1}{2}}_{i-1,j}\right)$$

$$\left(\underline{\underline{h}}^{y}_{i-\frac{1}{2},j} + \underline{\underline{\eta}}^{x\,n+\frac{1}{2}}_{i-\frac{1}{2},j}\right) D^{n+\frac{1}{2}}_{xxi-\frac{1}{2},j} + \left(S^{n+1}_{i,j+1} - S^{n+1}_{i,j}\right)\left(\underline{\underline{h}}^{x}_{i,j+\frac{1}{2}} + \underline{\underline{\eta}}^{y\,n+1}_{i,j+\frac{1}{2}}\right) D^{n+1}_{yyi,j+\frac{1}{2}}$$

$$- \left(S^{n+1}_{i,j} - S^{n+1}_{i,j-1}\right)\left(\underline{\underline{h}}^{y}_{i,j-\frac{1}{2}} + \underline{\underline{\eta}}^{x\,n}_{i,j-\frac{1}{2}}\right) D^{n+1}_{yyi,j-\frac{1}{2}} + \left(\underline{\underline{\bar{S}}}^{n+\frac{1}{2}}_{i+\frac{1}{2},j} - \underline{\underline{\bar{S}}}^{n+\frac{1}{2}}_{i+\frac{1}{2},j-\frac{1}{2}}\right)$$

$$\left(\underline{\underline{h}}^{y}_{i+\frac{1}{2},j} + \underline{\underline{\eta}}^{x\,n+\frac{1}{2}}_{i+\frac{1}{2},j}\right) D^{n+\frac{1}{2}}_{xyi+\frac{1}{2},j} - \left(\underline{\underline{\bar{S}}}^{n+\frac{1}{2}}_{i-\frac{1}{2},j+\frac{1}{2}} - \underline{\underline{\bar{S}}}^{n+\frac{1}{2}}_{i-\frac{1}{2},j-\frac{1}{2}}\right)\left(\underline{\underline{h}}^{y}_{i-\frac{1}{2},j} + \underline{\underline{\eta}}^{x\,n+\frac{1}{2}}_{i-\frac{1}{2},j}\right)$$

$$D^{n+\frac{1}{2}}_{xyi-\frac{1}{2},j} + \left(\underline{\underline{\bar{S}}}^{n+\frac{1}{2}}_{i+\frac{1}{2},j+\frac{1}{2}} - \underline{\underline{\bar{S}}}^{n+\frac{1}{2}}_{i-\frac{1}{2},j+\frac{1}{2}}\right)\left(\underline{\underline{h}}^{x}_{i,j+\frac{1}{2}} + \underline{\underline{\eta}}^{y\,n+1}_{i,j+\frac{1}{2}}\right) D^{n+1}_{yx\,i,j+\frac{1}{2}} -$$

$$\left(\underline{\underline{\bar{S}}}^{n+\frac{1}{2}}_{i+\frac{1}{2},j-\frac{1}{2}} - \underline{\underline{\bar{S}}}^{n+\frac{1}{2}}_{i-\frac{1}{2},j-\frac{1}{2}}\right)\left(\underline{\underline{h}}^{x}_{i,j-\frac{1}{2}} + \underline{\underline{\eta}}^{y\,n+1}_{i,j-1}\right) D^{n+1}_{yx\,i,j-\frac{1}{2}}\Bigg] \tag{5.6}$$

where

$$D^{n+\frac{1}{2}}_{xxi+\frac{1}{2},j} = \frac{\left[k_\ell \left(q^{n+\frac{1}{2}}_{xi+\frac{1}{2},j}\right)^2 + k_t \left(\bar{q}^{n}_{yi+\frac{1}{2},j}\right)^2\right] \sqrt{g}}{\left\{\left(q^{n+\frac{1}{2}}_{xi+\frac{1}{2},j}\right)^2 + \left(\bar{q}^{n}_{yi+\frac{1}{2},j}\right)^2\right\}^{\frac{1}{2}} \bar{\bar{C}}^{x}_{i+\frac{1}{2},j}}$$

$$D^{n+1}_{yyi,j+\frac{1}{2}} = \frac{\left[k_\ell \left(q^{n+1}_{yi,j+\frac{1}{2}}\right)^2 + k_t \left(\bar{q}^{n+\frac{1}{2}}_{xi,j+\frac{1}{2}}\right)^2\right] \sqrt{g}}{\left\{\left(\bar{q}^{n+\frac{1}{2}}_{xi,j+\frac{1}{2}}\right)^2 + \left(q^{n+1}_{yi,j+\frac{1}{2}}\right)^2\right\}^{\frac{1}{2}} \bar{\bar{C}}^{y}_{i,j+\frac{1}{2}}}$$

$$D^{n+\frac{1}{2}}_{xyi+\frac{1}{2},j} = \frac{\sqrt{g}\ (k_\ell - k_t)\ q^{n+\frac{1}{2}}_{xi+\frac{1}{2},j}\ \bar{q}^{n}_{yi+\frac{1}{2},j}}{\left\{\left(q^{n+\frac{1}{2}}_{xi+\frac{1}{2},j}\right)^2 + \left(\bar{q}^{n}_{yi+\frac{1}{2},j}\right)^2\right\}^{\frac{1}{2}} \bar{\bar{C}}^{x}_{i+\frac{1}{2},j}}$$

$$D^{n+1}_{yxi,j+\frac{1}{2}} = \frac{\sqrt{g}\ (k_\ell - k_t)\ \bar{q}^{n+\frac{1}{2}}_{xi,j+\frac{1}{2}}\ q^{n+1}_{yi,j+\frac{1}{2}}}{\left\{\left(\bar{q}^{n+\frac{1}{2}}_{xi,j+\frac{1}{2}}\right)^2 + \left(q^{n+1}_{yi,j+\frac{1}{2}}\right)^2\right\}^{\frac{1}{2}} \bar{\bar{C}}^{y}_{i,j+\frac{1}{2}}}$$

The finite difference eqns.(5.5) and (5.6) are centred in both space and time with a truncation error of $O(\Delta x^2, \Delta t^2)$.

5.4 Boundary and Initial Conditions for the Advective-Diffusion Equation.

Before the solution of eqns.(5.5) and (5.6) is attempted, the prescription of the boundary and initial conditions is necessary. This requires the specification of the constituent concentration S along the boundaries at all times and throughout the computational domain at the start of the computation.

At open boundaries, in the absence of data, the concentrations S need to be specified as a function of time. During outflow, the boundary concentrations may be obtained by linearly extrapolating from the values computed within the computational field and assuming the tangential velocity components and dispersive transport to be negligible at the

boundary, see Leendertse(1970). Thus for an upper open boundary in the x-direction (x=I), extrapolation gives the following expression:

$$S^{n+\frac{1}{2}}_{I,j} = S^{n}_{I,j} - \frac{\Delta t}{2\Delta x} U^{n+\frac{1}{2}}_{I-\frac{1}{2},j} \left[S^{n}_{I,j} - S^{n}_{I-1,j} \right] \qquad (5.7)$$

During inflow the boundary concentrations can no longer be determined by extrapolation from values within the domain. In this case, it may be assumed that the boundary concentration decreases to a preset input value - usually assumed to be zero - over a specified period of time and remains constant over the rest of the incoming tide, see Leendertse(1970). The functional relationship desribing this variation in concentration is arbitrary - Falconer(1981) assumed a half-sinusoidal variation over a period of one hour. Falconer(1983) employed a different treatment to the inflow boundary, where a mean concentration was assumed throughout the incoming tide, assumed to be proportional to the mean outflow boundary concentration. Detail descriptions of the open boundary specifications used in the model are given in Chapter 7, where the flushing characteristics of rectangular harbours have been assessed using nested models.

At closed boundaries the constituent flux across the boundaries must be zero, i.e. at an x-direction boundary $\partial S/\partial x = 0$, see Fisher(1981). This is achieved in the model by setting the relevant dispersion coefficients to zero.

At the start of the computation, a common practice is to assume that a constant initial concentration So exists throughout the area of interest, a procedure similar to that usually adopted in laboratory model studies, see Nece and Richey(1975).

Once the initial and boundary conditions are known, the finite difference eqns.(5.5) and (5.6) can be solved using the method of Gauss elimination and back substitution, presented in section A.2 of Appendix A.

5.5 The Computer Program.

The computer program NESTH1 used to solve the finite difference eqns.(5.1) to (5.6) is fully listed in Appendix B. This particular listing describes the computation of the velocity field, water elevation and constituent concentration distribution in a physical model of a square harbour with an asymmetric narrow entrance and horizontal bed, under the influence of tidal flows. NESTH1 consists of two nested models, the technique being elaborated in Chapter 7, where a large-area coarse-grid model provides the boundary conditions for a more detailed fine-grid model of the laboratory harbour model.

The program sets out to solve the finite difference equations by following the solution procedure outlined in this Chapter. Firstly, the geometrical properties of the computational domain, dimensions of the numerical grid and initial conditions are defined by specifying a number of constants and calling the subroutines BOUND, DIVE1, FIND1 and DEPTH1 for the coarse-grid model, and DIVE2, FIND2 and DEPTH2 for the fine-grid model. The subroutines have the following functions:

BOUND defines the time dependent open boundary conditions for the coarse-grid model which, in this example, are described in terms of a sinusoidally varying water elevation η.

DIVE1 (or DIVE2) and FIND1 (or FIND2) define the boudaries of the computational domain and, except for some minor modifications, are

essentially the same as those used by Leendertse(1967). DIVE1 (or DIVE2) defines the physical boundaries by introducing integer numbers to each grid point, where 1 indicates that the position of the grid point is within the computational domain, 0 that it lies outside the domain, 2 that it lies within the domain and is adjacent to an x-direction thin boundary (e.g. harbour wall), and 3 that it lies within the domain and is adjacent to a y-direction thin boundary. FIND1 (or FIND2) processes the data from DIVE1 (or DIVE2) and produces tables of values that represent the lower and upper boundaries of each row and column in the computational grid, and controls the computation.
DEPTH1 (or DEPTH2) reads the water depth between the bed and mean water level at every grid point.

Once all the necessary information has been specified and transferred to the main program, the solution procedure for the coarse-grid model begins by executing the computations for the first half-timestep, to give the discharge per unit width QXP($=q^{n+\frac{1}{2}}_{xi+\frac{1}{2},j}$), water elevation EP($=\eta^{n+\frac{1}{2}}_{i,j}$) and constituent concentration SP($=S^{n+\frac{1}{2}}_{i,j}$). These upper time values are then re-labelled so that they become the lower time values QX, EM and SM. Similarly at the second half-timestep the solution procedure is repeated to give QYP($=q^{n+1}_{yi,j+\frac{1}{2}}$), EP($=\eta^{n+1}_{i,j}$) and SP($=S^{n+1}_{i,j}$), which in turn are re-labelled to become the lower time values QY, E and SM. At the end of the first timestep the computation switches to the fine-grid model where the boundary conditions are determined by interpolation of the coarse-grid results. Subsequently the solution procedure begins for the fine-grid model, which is identical to that of the coarse-grid model, and is repeated until the number of timesteps reaches the value CF, where CF is the ratio of the coarse-grid time scale

to that of the fine-grid. The computation then switches back to the coarse-grid model where the solution for another timestep is completed before returning to the fine-grid model for another CF number of timesteps. This whole cycle is repeated until the upper time limit is reached.

The Chezy coefficients are updated in the main program, for both coarse- and fine-grid models, at regular time intervals specified by TCHEZS. In addition, at predetermined stages in the computing cycle, tabulated results are obtained.

A listing of the variables used in NESTH1 is given at the beginning of Appendix B.

Hyperbolic Equations			Incompletely Parabolic Equations		
Close Boundaries	Open Boundaries		Close Boundaries	Open Boundaries	
	Inflow	Outflow		Inflow	Outflow
1	2	1	2	3	2

Table 5.1 Number of Boundary Conditions for Two-Dimensional Depth Averaged Flow.

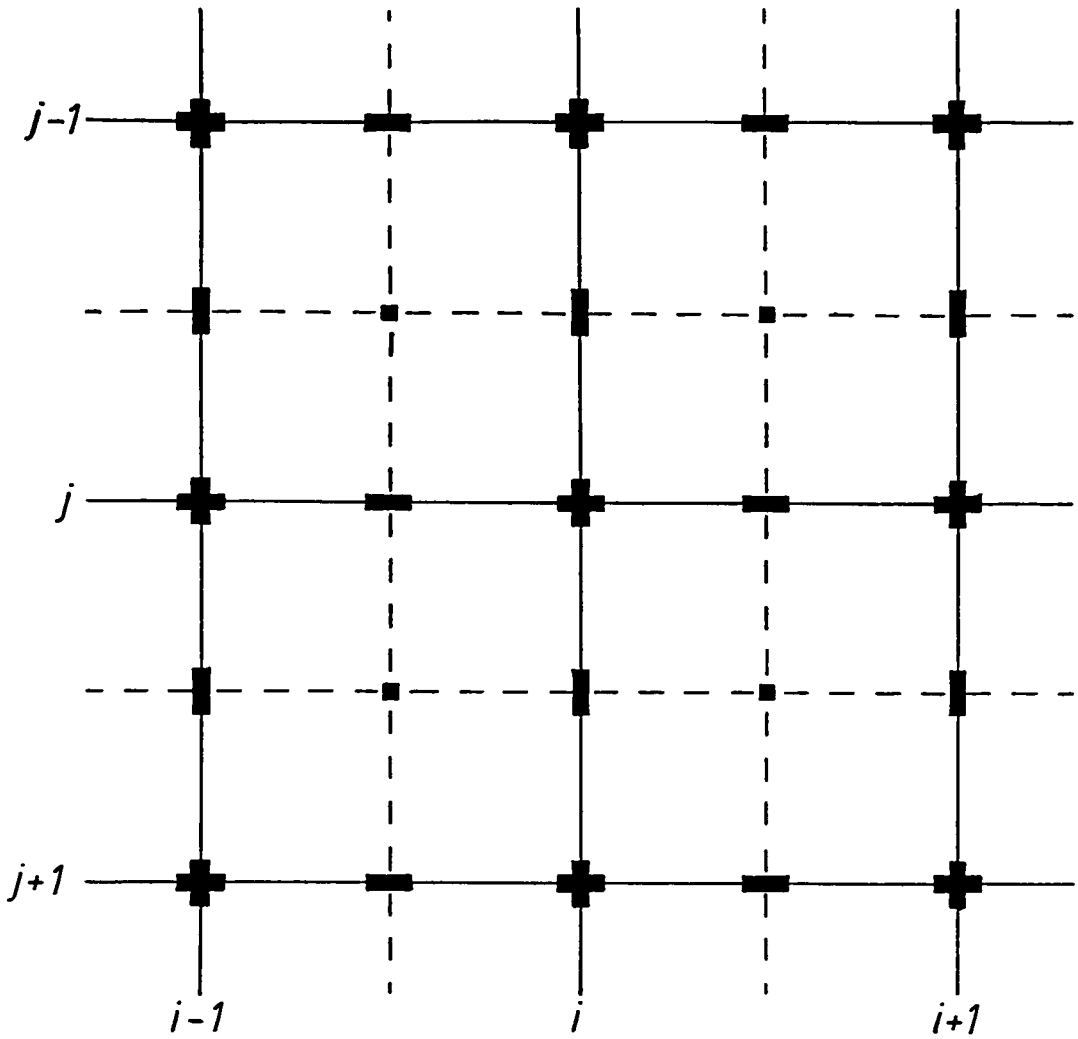

Figure 5.1 The space-staggered finite difference scheme

U

V

h

Calculation Points

η, C , S

i = 1, 2, 3, ...I

j = 1, 2, 3,.....J

CHAPTER 6

APPLICATION A: MODELLING OF TIDAL CIRCULATION AROUND RATTRAY ISLAND

6.1 Introduction

The first application of the model outlined, was to predict the tidal flow field around Rattray Island, Australia, with the main objective being to model the prominent eddy features observed and measured in the lee of the island.

Rattray Island, located just off the east coast of Australia (see fig.(6.1)), is approximately 1.5 km long, 300 m wide and lies in well mixed waters, having a typical depth of about 25 m. Its long axis lies at about 60° into the direction of the dominant semi-diurnal tidal current, and the strong tides flowing past the island give rise to separation at the island tips and generation of large-scale eddies in the lee of the island.

There is, at present, a considerable interest in understanding the flow-mechanisms associated with such eddies, as they are believed to play an important role in the biology and ecology of these shallow shelf waters. In view of the lack of data on eddies shed by such headlands, an intensive and detailed field study of the circulation around Rattray Island was recently undertaken by the Australian Institute of Marine Science. In this study, outlined by Wolanski et al(1984), twenty six current meters were deployed at various sites in the south eastern lee of the island, see fig.(6.2), with time series sea level recordings being taken at several sites around the island. Visual observations of the

island's wake were also made using aerial photography and Landsat imagery, with the surface temperature distribution also being measured at the time of aerial observations. In addition, sail drogues were deployed on occasions and tracked by radar. The recorded tidal ranges were generally about 3 m and a strong south eastwards current was observed and measured during the rising tide. This dominant current gave rise to a strong clockwise rotating eddy in the south eastern lee of the island, which was visible from the air by the high turbidity of the wake waters, see fig.(6.3). The field measurements and observations showed that the eddy was formed after about 1 hr into the rising tide and progressively grew in size throughout the rising tide. The width of the eddy was roughly equal to the length of the island and the length of the eddy was about twice that of the island. In addition the eddy structure was found to be very stable with no signs of Karman vortices. The eddy currents were also of the same order of magnitude as the free stream current. The surface temperature distributions - with the intruding shelf waters of the rising tide being slightly warmer than the waters trapped in the eddy - and the drogue trajectories also confirmed the existence of the eddy. Vertical distributions of temperature and salinity were also measured, with the salinity gradients being negligible. The temperature distribution showed the presence of a weak summer thermocline, with cold water being found in the lee of the island suggesting local upwelling. In all cases the temperature gradients were assumed to be large enough for temperature to be used as a tracer, but small enough for baroclinic effects to be negligible. Vertical variations of horizontal velocities were measured near site 24 (see fig.(6.2)), with no marked vertical gradients being detected. This implied that the flood tide clockwise rotation prevailed throughout the water column. On the ebbing tide,

contrary to the case at rising tide, aerial observations showed the presence of two eddies in the northern wake, with the eddy in the lee of the eastern tip of the island being more pronounced. However, no measurements were made in the northern lee of the island. The field study was performed during periods of calm weather conditions, during the months of November and December 1982, when meteorological forcing was not a significant factor affecting the motion around the island.

The shape of the eddy observed in the island's wake suggests similarity with laboratory observations of two-dimensional flow around obstacles at low values of Re ($=\frac{UD}{\nu}$; U=unperturbed velocity, D=body dimension, ν=kinematic viscosity). For Reynolds numbers of the order of 10-30, a steady wake is observed in laboratory tests, comprising of a vortex pair and a central return flow with only one eddy dominating when the obstacle is inclined into the flow (see Batchelor(1970), Gerrard(1978)). However, a number of discrepancies exist between the laboratory and field data. The velocities in the re-circulation region are of the same magnitude as that of the driving current at Rattray Island while they are about 1% of the free stream velocity in the laboratory (see Keller and Niewstadt(1973)) and, in addition, a distinct upwelling is observed in the island wake. Wolanski et al(1984) and Wolanski(1985), in their attempt to explain these observed phenomena, have proposed a theoretical model of the flow in the wake. This model assumes that the stable eddy is in solid body rotation, except near the sea floor in the boundary layer. In response to pressure gradients set up due to the curvature of the tidal streamlines, a radial flow converging towards the eddy centre is generated near the sea floor and upwelled. This internal eddy circulation also acts as a sediment sorter,

where all particles below the threshold of transport near the bottom are being advected towards the eddy centre, with the fine particles being upwelled and moved away toward the outside of the eddy - hence the turbidity of the wake waters. This mechanism seems to be confirmed by the distribution of fine and coarse sediment around the island, see Wolanski(1985). A similar theoretical model was proposed by Pingree and Maddock(1979) in their study of eddies shed by headlands and tidal bank formation.

6.2 The Numerical Model Applications and Validation

Despite the three-dimensional flow characteristics implied by the internal eddy circulation in the island's wake, the field measurements showed good vertical uniformity of the horizontal eddy features. The use of a two-dimensional numerical model approach in trying to simulate the horizontal circulation around Rattray Island is therefore partially justified.

The computational domain, as shown in fig.(6.2), consisted of a mesh of 60x43 grid squares, with a uniform grid spacing of 200 m, except in the immediate vicinity of the island where a non-uniform grid representation was used. The uniform grid was modified around the island so that the island's boundaries could be represented as accurately as possible. Using the notation given in fig.(6.4) as an example, the first and second derivatives adjacent to the island were represented in the following manner (as cited for the y co-ordinate direction only):

$$\left.\frac{\partial U}{\partial y}\right|_0 = \frac{1}{\Delta x}\left[\frac{1}{\theta_1(1+\theta_1)}U_A - \frac{(1-\theta_1)}{\theta_1}U_0 - \frac{\theta_1}{(1+\theta_1)}U_3\right] \qquad (6.1)$$

$$\left.\frac{\partial^2 U}{\partial y^2}\right|_0 = \frac{1}{\Delta x^2}\left[\frac{2}{\theta_1(1+\theta_1)}U_A + \frac{2}{(1+\theta_1)}U_3 - \frac{2U_0}{\theta_1}\right] \qquad (6.2)$$

The resulting equations have truncation errors of $O(\Delta x^2)$ and $O(\Delta x)$ respectively, see Smith(1978), and are simplified in the model since $U_A=0$ for a no-slip boundary requirement. At the centre of each grid square a representative depth between mean sea level and the bed was required, with the corresponding bathymetric data being provided by the Australian Institute of Marine Science and illustrated in the isoparametric projections of fig.(6.6). However, there were no available data for the bed roughness features and the model simulations were therefore undertaken for an assumed Manning's roughness coefficient of 0.025. This value of n appeared to be a reasonable choice based on Knight's(1981) measurements in the Conwy Estuary, where similar tidal ranges were experienced. In addition, the Coriolis effects have been included with a geographical lattitute of -20°.

The free shear layer turbulence requires a special mention in this case study, in that the mechanism of flow separation can occur at both island tips, thereby making each tip an origin of free shear layer turbulence. Both sources of free shear layer turbulence have been included in the model and were represented by two separate sets of x', y' axes (see fig.(2.3)), having their origins at each tip respectively, with the y' axes pointing in opposite directions into the free stream. Subsequently, the free shear layer stress, given by eqn.(2.43), has been applied to both areas of shear layer dominance.

6.2.1 Open Boundary Conditions

The open boundary conditions for the numerical model were taken from field measured water elevations and velocities recorded over a period of nearly four continuous tidal cycles.

At the north west boundary (see fig.(6.2)) water elevations were specified using linearly interpolated values obtained from data recorded at 10 min intervals around the island. The phase lag between the north west boundary and the island was estimated by approximating the tidal wave celerity to that of a progressive wave, which may be given as $\sqrt{gH_m}$ (H_m being the mean depth between the north west boundary and the island). The time axis for the boundary was corrected accordingly, with the resulting open boundary data being illustrated in fig.(6.5). Although there were no available velocity data at this boundary, the lateral velocity components along the boundary were assumed to be zero. This was thought to be a reasonable assumption, since the velocities measured outside the wake indicated that the tidal currents were predominantly along the north west - south east grid axis (or x-axis). The resulting y-direction momentum equation at this boundary gave rise to a water surface slope along the boundary, as governed by the Coriolis acceleration, i.e.:

$$\frac{\partial \eta}{\partial y} = - \frac{f_c U}{g} \qquad (6.3)$$

In adopting the water surface slope, the water elevation data of fig.(6.5a) were prescribed at the most western elevation grid point, with the water elevations at the other northern boundary grid points being evaluated from eqn.(6.3). In order to test the importance of the water

surface slope along this boundary, a numerical test comparison was made with a horizontal water elevation along the boundary. On comparing the two simulations, the use of a horizontal surface slope gave rise to high and unrealistic velocity gradients at certain phases, introducing a circulatory flow field along the north west boundary, see fig.(6.7). This circulation was not present in the water surface slope simulation given by eqn.(6.3). Hence, the water surface slope given by eqn.(6.3) was deployed in all subsequent numerical model tests. Furthermore, the advective acceleration terms were neglected at this boundary - a common treatment in practical applications of this kind - in order to avoid the occurrence of non-linear instabilities (see Leendertse(1967), Flather and Heaps(1975)).

Along the south east boundary, linearly interpolated velocities were specified from field data recorded at 10 min intervals at site 23 - located very close to the boundary, see fig.(6.2). The data indicated that this position was outside the wake and the velocities were observed to conform to the free stream uni-directional tidal current. Since no other data were available along this boundary, the velocity was assumed to be constant along the boundary and uni-directional, i.e. $U=f(t)$ and $V=0$, with the resulting velocity data being illustrated in fig.(6.5).

The western and eastern boundaries, being parallel to the predominant tidal current direction and outside the island's wake, were assumed to be free-slip walls with only the normal velocity component, V, being zero along these boundaries.

The combination of boundary conditions applied at the lower and upper boundaries of this model, that is the prescription of water elevations and velocities at the north west and south east boundaries respectively, was shown by Thabet et al(1985) to be the most suitable combination for boundary conditions derived from field data. This boundary specification was found to introduce less errors in the computational field than any other combination of boundary conditions.

The model simulations were always started from rest, with the initial mean water elevation across the computational field being coincident with the time of zero velocity along the southernmost boundary. All computations were undertaken for a timestep of 80 s, giving a Courant number of 6.5. A printout of the numerical results was requested at approximately every eighth of the tidal cycle. The program was run on a VAX 11/750 computer under a VAX/VMS operating system and required approximately 12 hr of c.p.u. time to compute the flow field over the four tidal cycles.

6.2.2 Model Tests and Results

In the first of several model simulations, comparisons were made with the field measurements and observations in order to test the validity of the numerical model. Direct comparisons were made between the field measured velocities at the current meter positions shown in fig.(6.2), and the numerically predicted velocities at the grid points closest to these meter positions. Two sets of synoptic maps of field measured velocities on the rising tide, for two different tidal ranges - reproduced from Wolanski et al(1984) - are shown in figs.(6.8) and (6.9) alongside the corresponding numerical model predictions. In comparing

the numerically predicted and field measured results it can be seen that the tidal eddy features predicted in the numerical model have an encouraging degree of similarity with the field measured results. By-and-large the re-circulating velocity magnitudes and directions agree favourably, with the eddy beginning to form in the model after about 1 hr into the rising tide, as confirmed by the field measured results (see Wolanski et al(1984)).

The complete computational flow field is illustrated for three interesting tidal phases in figs.(6.10), (6.11) and (6.12) respectively. In fig.(6.10), which is just after high tide, a well defined clockwise eddy dominates in the lee of the eastern tip of the island. The width of the eddy is a maximum at this tidal phase and is approximately one and a half times the length of the island, and the length of the eddy is about twice that of the island - as noted from aerial observations. Likewise, the velocities in the re-circulation region are of a similar magnitude to the free stream velocities, which is again in agreement with the field measurements. The presence of a second and much weaker eddy is also evident in the lee of the western island tip. Aerial observations did not indicate the existence of this second eddy, but as it is a weaker eddy - according to the numerical predictions - it is possible that the trapped waters were not very turbid, and therefore not visible from the aerial observations. In addition, the majority of the current meters were placed in the region dominated by the large eddy. The current meters 7 and 8 (see fig.(6.2)), however, were in the region of the second eddy and the measured velocities at these positions agree, both in direction and order of magnitude, with the predicted velocities. The current direction is markedly different to that of the neighbouring current meters, see

figs.(6.8) and (6.9), and therefore the presence of this second eddy cannot be excluded from the field data. In fig.(6.11), the tidal circulation around the island is depicted on the falling tide, just before low tide. Although no field measurements were taken in the northern wake, it is interesting to note that the numerical model has predicted two counter-rotating eddies of similar flow features and dimensions. Aerial observations confirm the presence of the two eddies, with the eddy in the lee of the western island tip shown to be less well defined. In fig.(6.12), the stable and progressively growing eddy, produced by the rising tide in the lee of the eastern island tip, is reproduced at about 1 hr before high tide. The eddy again has dimensions and flow characteristics which are in general agreement with the documented field measurements and observations, and shows a strong similarity to the pictorial representation in fig.(6.3) for a similar tidal phase. In the predicted flow field, the presence of the second much weaker eddy is again evident.

From the velocity field predictions, a number of graphical representations have been reproduced, which include the vorticity field, the bed generated shear stress distribution, the free shear layer stress distribution and the bottom friction in the x and y co-ordinate directions respectively. The vorticity distribution of fig.(6.13), which corresponds to the flow field depicted in fig.(6.12), confirms the dominance of the clockwise eddy shed from the eastern island tip, as the lee of the eastern tip includes the largest area of maximum vorticity, giving an indication of its size and direction - with positive vorticity implying a clockwise circulation. On the other hand, the vorticity in the northern wake, during the falling tide, consists of two similar in

size regions of high vorticity, see fig.(6.14). This confirms the existence of the two counter-rotating dominant eddies, with the eddy in the wake of the eastern tip shown to be stronger - a difference not detectable from the flow field representation of fig.(6.11). This observation is in agreement with the aerial observations of the island's wake. The free shear layer stress distribution of the flow field illustrated in fig.(6.12), is shown in fig.(6.15), where the high stress gradients in the mixing zone can be clearly seen. When compared to the bed shear stress distribution, see fig.(6.16), the free shear stress can be seen to dominate completely in the mixing zone. The dominance of the shear layer stress is in line with the analysis of Lean and Weare(1979) - outlined in eqns.(2.46) and (2.49) - where, for Rattray Island, indications are that the free shear layer turbulence dominates in the mixing zone between the limits $50<x'<7600$ m. The bottom frictional stress, depicted in figs.(6.17) and (6.18), relates to infomation about the direction and magnitude of the currents around the island as well as the bathymetry in the area. Comparisons of the two figures shows that the current is predominantly uni-directional except in the lee of the island where the lateral currents give rise to high lateral frictional stresses.

In arriving at the final version of the Rattray Island model described herein, a number of model simulations, each having different features, were also undertaken and compared to the field data. These features include: (a) a different finite difference representation of the island's geometry, (b) a free-slip condition along the island's boundaries, (c) a different representation of the cross-product advective acceleration terms and (d) a coarser grid.

Simulation (a), where the island was represented by a group of grid squares on a regular square mesh, gave very close flow field predictions to the present model, see for example fig.(6.19), with the eddy strength being slightly reduced, as can be seen by comparing the resulting vorticity distribution shown in fig.(6.20) and that of fig.(6.13). Therefore, the numerical representation of the island's shape does not appear to be an important factor in the eddy circulation of the downstream wake. This is in agreement with Wolanski's(1985) analytical model, where it was shown that the eddy size is independent of the island's dimensions. Since, however, the additional computing effort in representing the island's shape more accurately is minimal, it has been adopted in the model.

Simulation (b), included the free-slip condition along the island's boundaries. In view of the complications involved in employing this condition on the irregular grid around the island of the present model, the uniform grid of simulation (a) was used for the comparisons. The results of simulations (a) and (b) were identical, as indicated by comparing the vorticity distributions of figs.(6.20) and (6.21), implying that the no-slip condition was not an essential requirement for vorticity generation in this model study. It is probable that the coarseness of the numerical grid has given rise to this result, in that the velocity gradients associated with the no-slip condition are small because of the large grid spacing. Thus, they have no significant effect on the corresponding flow field.

Simulation (c) involved the representation of the cross-product advection terms of the x- and y- direction momentum equations in terms of $\frac{\partial Vq_x}{\partial y}$ and $\frac{\partial Uq_y}{\partial x}$ respectively, instead of $\frac{\partial Uq_y}{\partial y}$ and $\frac{\partial Vq_x}{\partial x}$ as employed in the present model. The resulting flow field predictions gave rise to high and unrealistic velocity gradients in the close proximity of the island's tips, and in particular for the western tip - see figs.(6.22) and (6.23). As mentioned in Chapter 5, a possible increase in the numerical errors associated with this representation in the finite difference form, as compared to the adopted representation, may be the cause of the unrealistic velocity field predictions in regions where these terms are important.

In simulation (d), a coarser numerical grid was used to predict the flow field around Rattray Island. It consisted of a domain of 40x29 grid points, with a grid spacing of 300 m and a timestep of 120 s, and therefore it was far cheaper to run than the present model. However, the numerical predictions did not share a very close agreement with the field data - see fig.(6.24), where the predicted eddy is noticeably smaller and weaker than the eddy measured and observed in the field. The grid was too coarse to portray accurately the details of the circulatory flow in the wake of the island. In view of the island's size, an even finer grid than the one used at present would be preferable, but c.p.u. time restrictions did not allow further refinement at present. However, the flow field predicted by the present model is in very close agreement with the field data and it is debatable as to whether or not a further increase in the accuracy of the results would justify the increase in the computational costs.

A number of further simulations were performed, with the aim of investigating and assessing the influence of the various terms of the equations of motion on the tidal circulation in the island's wake. They included the investigation of: (a) the Coriolis term, (b) the free shear layer stress, (c) the bed generated shear stress and (d) the bed friction.

In simulation (a), the Coriolis term was excluded throughout the computational domain and the resulting flow field was compared with the corresponding flow field predicted when the Coriolis term was included. The results were very similar, with no detectable differences in the velocity field predictions. The vorticity distributions, however, indicated a small reduction of vorticity and a slight clockwise shift in the regions of high vorticity, as shown by the comparison of the vorticity distributions of figs.(6.25) and (6.14), with the differences being more pronounced at this tidal phase. These observations agree with those of Pingree and Maddock(1980), in that the Coriolis term is a vorticity source and gives rise to an anti-clockwise rotation of circulation patterns (in the southern hemisphere). At this stage, it is useful to consider the scaling parameter Ro, or the Rossby number, to establish the relative importance of the Coriolis term. The Rossby number is defined as the ratio of the inertia effects to the Coriolis effects, and may be approximated to (see Pingree and Maddock(1980)):

$$Ro \sim \frac{\bar{V}}{L\, f_c} \qquad (6.4)$$

where $\bar{V}$ = depth-averaged velocity speed

and L is a characteristic length scale related to the island size

Hence, for Rattray Island, L=1500 m, $f_c=-5\times10^{-5}\ s^{-1}$ and a typical velocity

$\bar{V}$=0.5 m/s gives Ro=6.7. This relatively large Rossby number implies that the effect of the earth's rotation is not very important for this study and that for the bulk of the tidal cycle the flow is therefore dominated by inertia effects - except at high or low tide when the inertia effects are small. The apparent relative unimportance of the Coriolis terms has been confirmed by the numerical model predictions. The exclusion of the Coriolis term at the northern boundary only, however, resulted in a distinctly different flow field prediction, especially at low tide, when the effects of the earth's rotation become more prominent, see fig.(6.7). These results reflect the sensitivity of the computational field to changes in the boundary prescriptions and highlight the importance of the prescription of the correct boundary conditions.

In simulation (b), the free shear layer stress term was excluded from the momentum equations. The resulting circulation strength was slightly reduced, see fig.(6.26), where the reduction in vorticity was more pronounced in the eddy shed by the eastern island tip. Contrary to theoretical expectations, the reduction in the eddy strength was not dramatic, although in some areas of the circulation region the velocities were reduced by as much as 15%. The analysis of Lean and Weare(1979) showed the shear layer mixing to be the dominant momentum transfer mechanism across the streamlines, from the main stream to the eddy, which in mathematical terms is through the lateral gradient of the shear stress - e.g. the term $\frac{\partial}{\partial y}(HT_{xy|f})$ in the x-direction momentum equation. It is apparent, however, that the numerical model is under-predicting the effects of the free shear layer stress term as a result of the discretisation of the horizontal shear gradient and the coarseness of the numerical grid.

In simulation (c), both the free shear layer and bed generated shear stress terms were excluded from the momentum equations, and the results compared to those of simulation (b). The predicted flow fields were almost identical, as can be seen by comparing the vorticity distribution depicted in fig.(6.27) with fig.(6.26), suggesting that the effects of the bed generated shear stress terms were negligible. From earlier comparisons of the shear stress distributions, graphically represented in figs.(6.15) and (6.16), it was expected that the bed generated shear stress term would have less influence on the circulating flow than the free shear layer stress. Its negligible effect on the flow, however, is predominantly caused by the discretisation of the horizontal shear stress gradients on a coarse grid. The reproduction of re-circulation when the lateral shear stress terms are excluded, has also been demonstrated numerically by Lean and Weare(1979), and is a finding in disagreement with the theory, as shown by Flokstra(1977) and illustrated by the vorticity analysis in Chapter 2. The difference between the behaviour of the theoretical solution and the numerical solution has been attributed by Lean and Weare(1979) to the finite grid resolution - inherent in any discretised solution - resulting in numerical dispersion, which may be reduced by the use of a finer grid or a higher-order difference scheme. The numerical tests of Ponce and Yabusaki(1981), on the other hand, indicated that the reproduction of circulation was not a result of numerical dispersion as evidenced by the undiminished presence of the circulation, in spite of increased grid resolution. In a review of accumulated evidence on the generation of circulation in depth-averaged numerical models, Abbott et al(1985) have shown such circulations to be physically realistic despite the exclusion of the lateral shear stresses. The explanation as to how these numerical circulations can arise in a

physically realistic manner remains however to be answered. The numerical grid in this study is relatively coarse, suggesting that numerical dispersion may be contributing to the circulation and ideally the grid resolution should be increased further, but both suggested methods pose difficulties in terms of substantially increasing the computational time requirements.

Finally, the effect of bed friction on the circulating flows in the island's wake were investigated. Two model simulations were undertaken, for different values of Manning's friction coefficient, n. In the first simulation the bed friction was reduced, with n=0.015, and in the second simulation it was increased, with n=0.035, with the resulting flow field predictions being compared with the resulting predictions for n=0.025. As expected, the predicted tidal eddies decreased both in size and strength for the larger value of n (n=0.035) and increased for the lower value of n (n=0.015). The changes were marked, as indicated by the vorticity distribution representations of figs.(6.28) and (6.29), implying that the frictional effects are important in the flow features of the island wake. This conclusion is in agreement with the analytical model of Wolanski(1985), where friction is shown to be an important parameter influencing the size of the eddy. Pingree and Maddock(1980) have shown both numerically and analytically that the use of the quadratic friction law, apart from dissipating vorticity, can give rise to vorticity sources due to bathymetric changes and the quadratic form of friction. To investigate the influence of the bathymetry on the eddy characteristics, the model was run for a horizontal bed and the corresponding results were compared to those of the true bathymetry, see Falconer et al(1985). The resulting flow patterns were very different,

with the model predicting two counter-rotating eddies of similar features in the southern lee for the horizontal bed - as illustrated by the vorticity distribution representation of fig.(6.30) - as compared to the dominant eddy for the true bathymetry. This simulation has shown that there is a strong dependency of the flow field on the bed topography and confirms the scope for vorticity production through the water depth variations. There are therefore clear advantages in using the numerical scheme described by Falconer and Owens(1984), whereby the depth is prescribed at every velocity point, rather than at the corners of each grid square as prescribed in this model (see fig.(5.1)). Such a representation would allow a more accurate representation of the bed topography, since it requires twice as many depth points to be specified in the numerical model. However, the available bathymetric data for the Rattray Island study are sparse and adoption of this refined scheme would involve a great deal of interpolation between known depth points, thereby somewhat defeating the purpose of its adoption.

6.3 Conclusions

The tidal eddy features in the wake of Rattray Island have been successfully modelled, with the agreement between the numerically predicted flow characteristics and field measurements being encouraging.

The effects of the various terms of the governing equations on the flow characteristics have been investigated, with the findings being summarised as: (i) the bed friction, and as a result the bed topography, are important parameters influencing the flow features, (ii) the lateral shear stresses have a small effect on the eddy characteristics, (iii) the free shear stresses have a more marked influence on the flow features

than the bed generated shear stresses, although both effects have been under-predicted as a result of the discretisation of the shear stress gradients and the coarseness of the grid, (iv) contrary to theoretical expectations, re-circulation has been reproduced by the model without the inclusion of the lateral shear stresses, and (v) likewise, the no-slip boundary condition has been shown to be unimportant in this case study - a result partly attributed to the anavoidable coarseness of the grid.

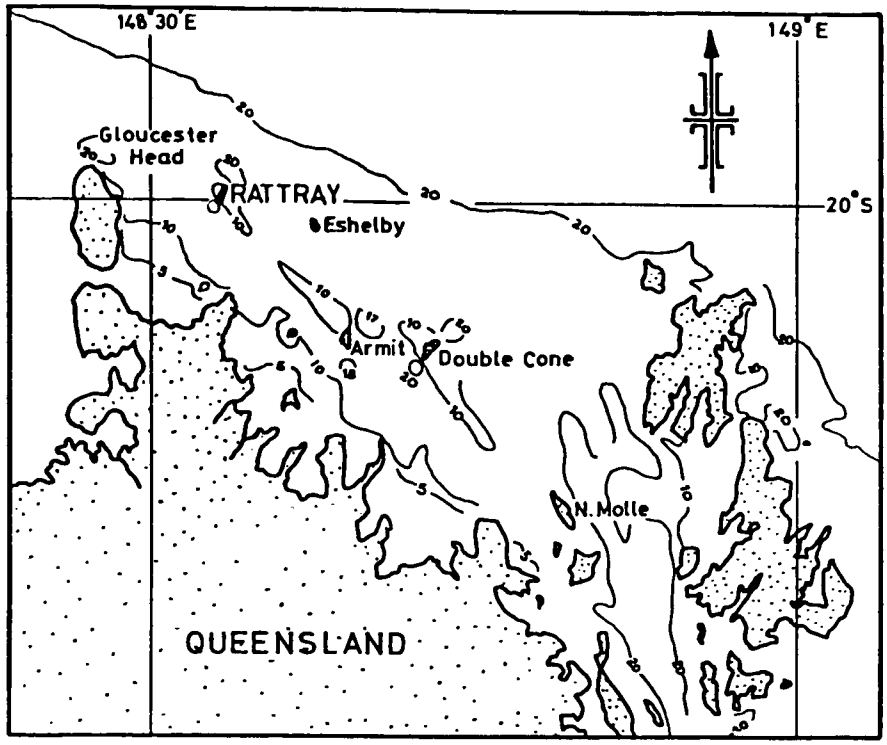

Figure 6.1 Location of Rattray Island and bathymetry (in fathoms)

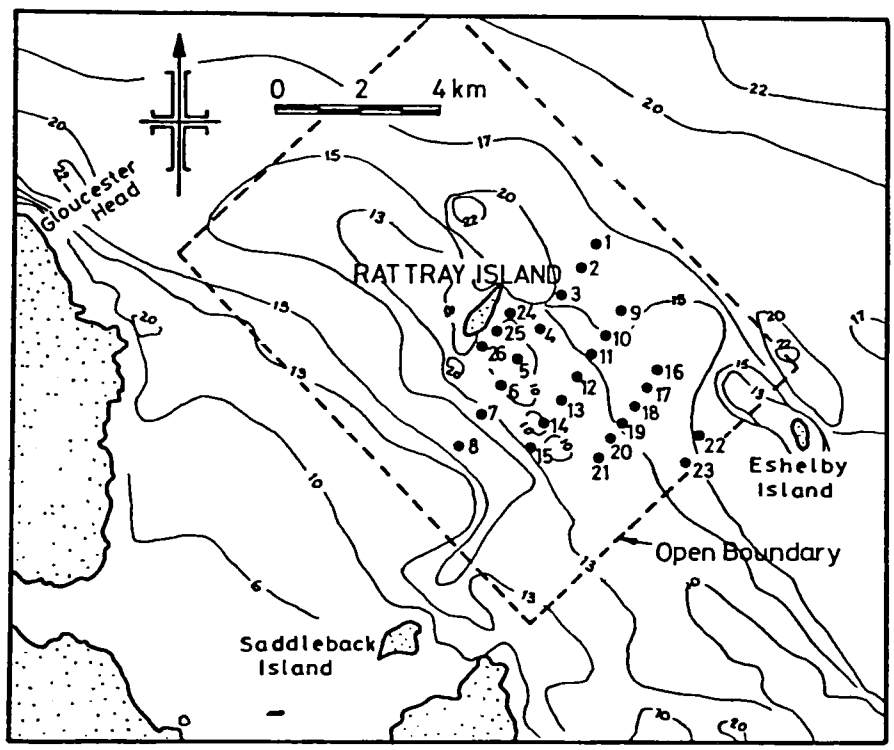

Figure 6.2 Area around Rattray Island showing location of measuring sites and model boundaries

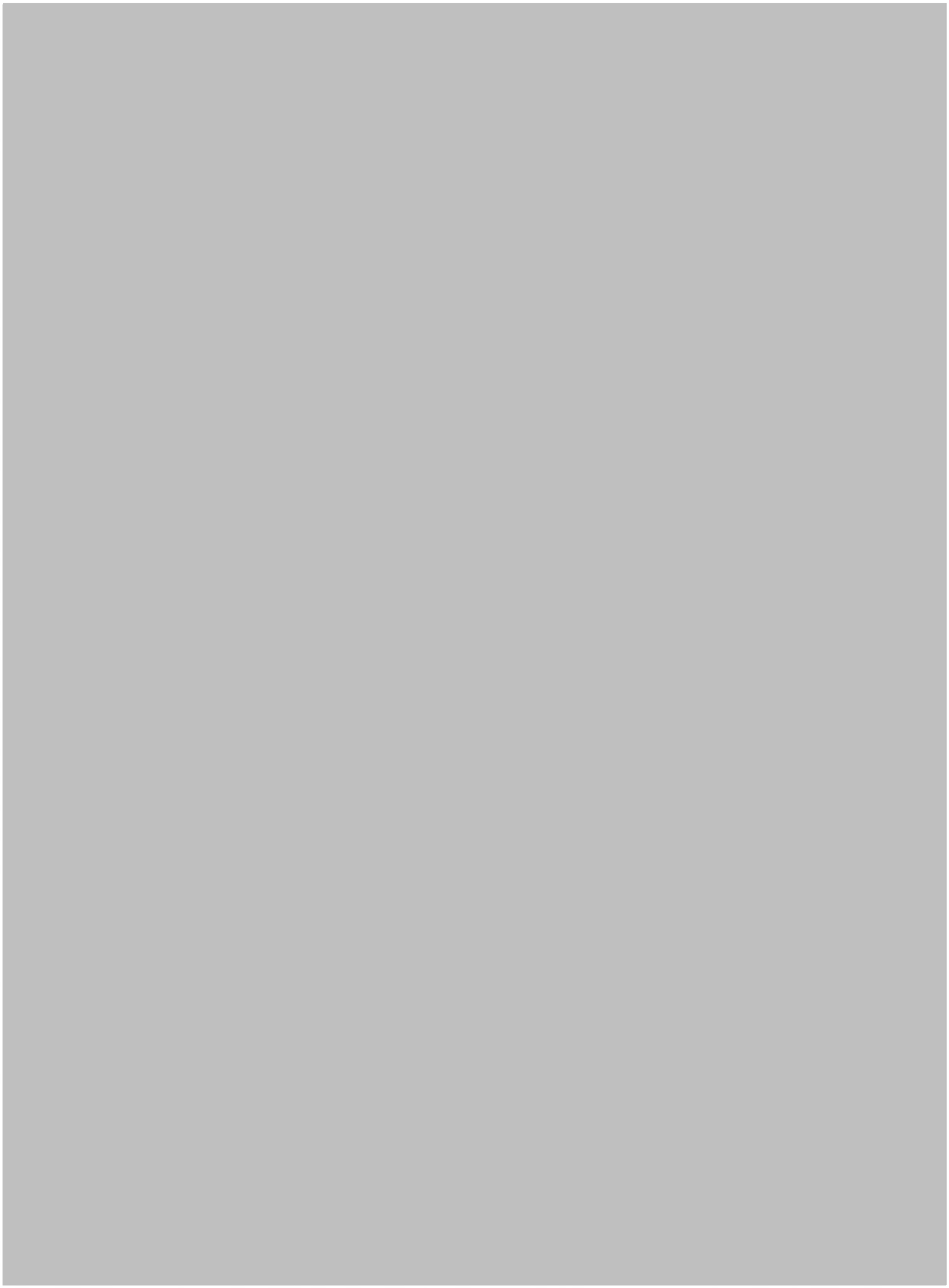

Figure 6.3 Aerial view of Rattray Island from the north, showing dominant tidal eddy in southern wake.

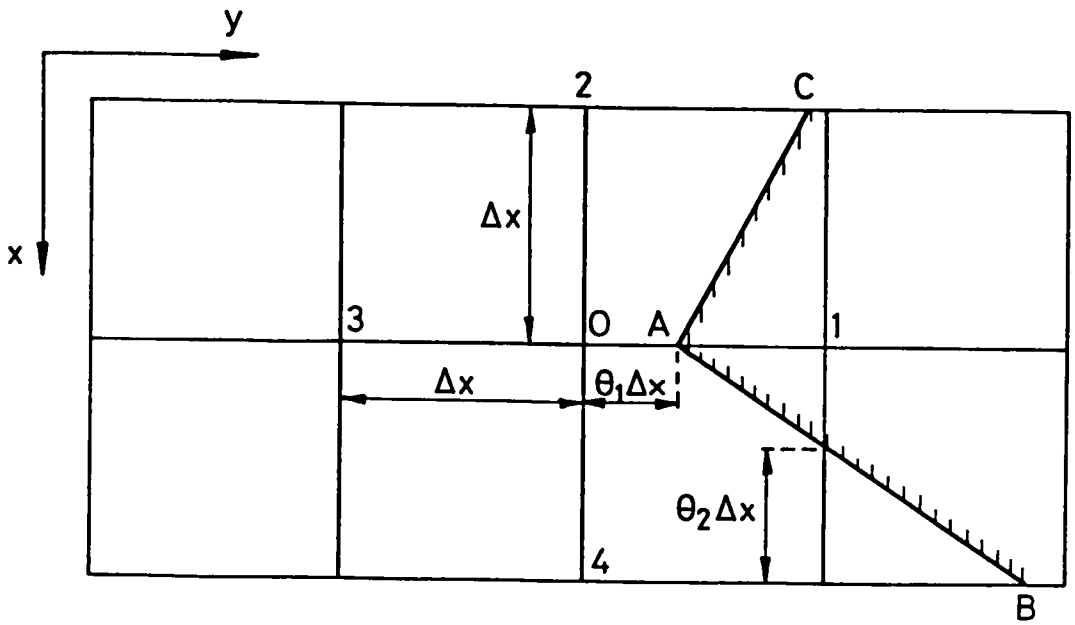

Figure 6.4 Non-uniform grid spacing around headland for more accurate boundary representation

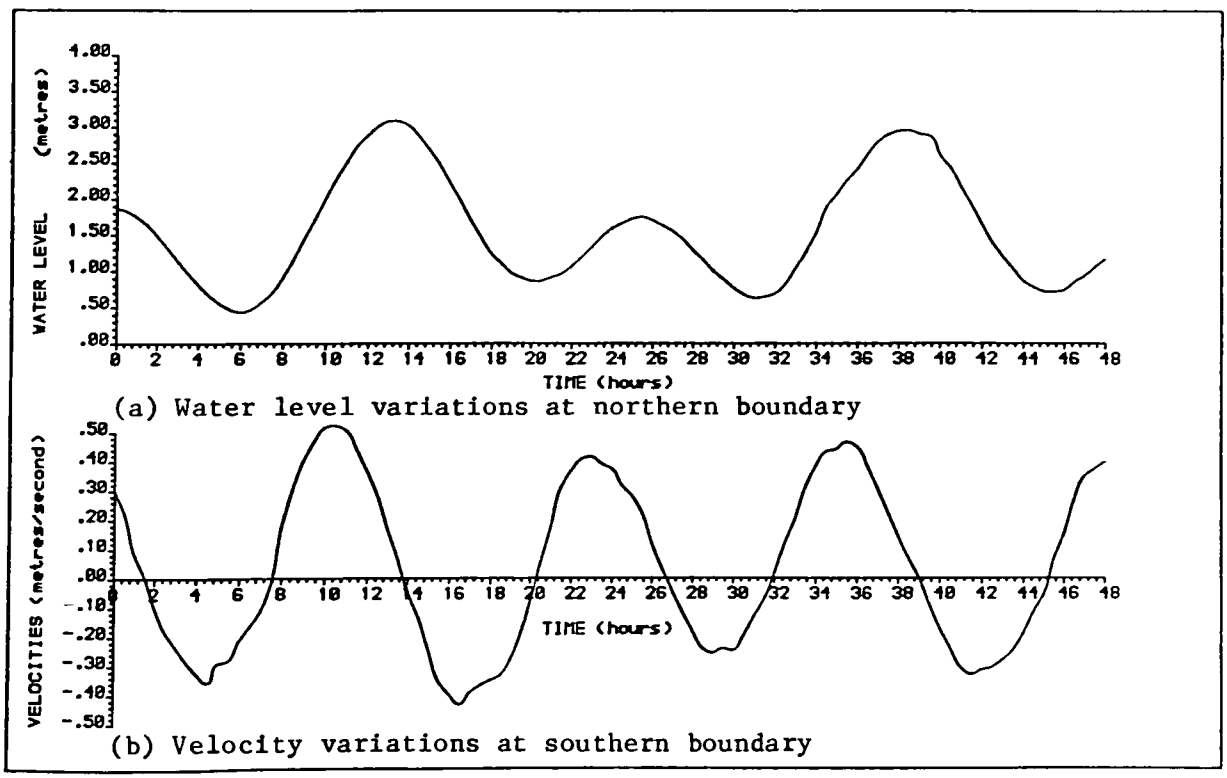

Figure 6.5 Open boundary conditions

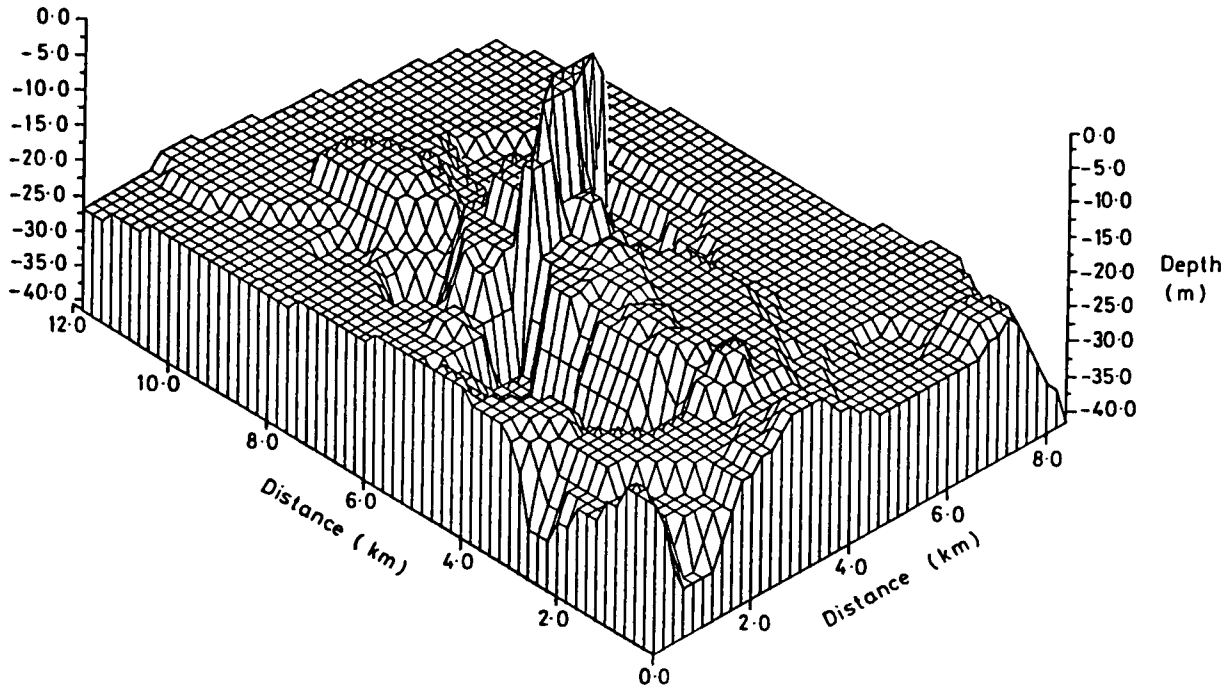

Figure 6.6(a) Isoparametric projection of bathymetry as viewed from the south-west

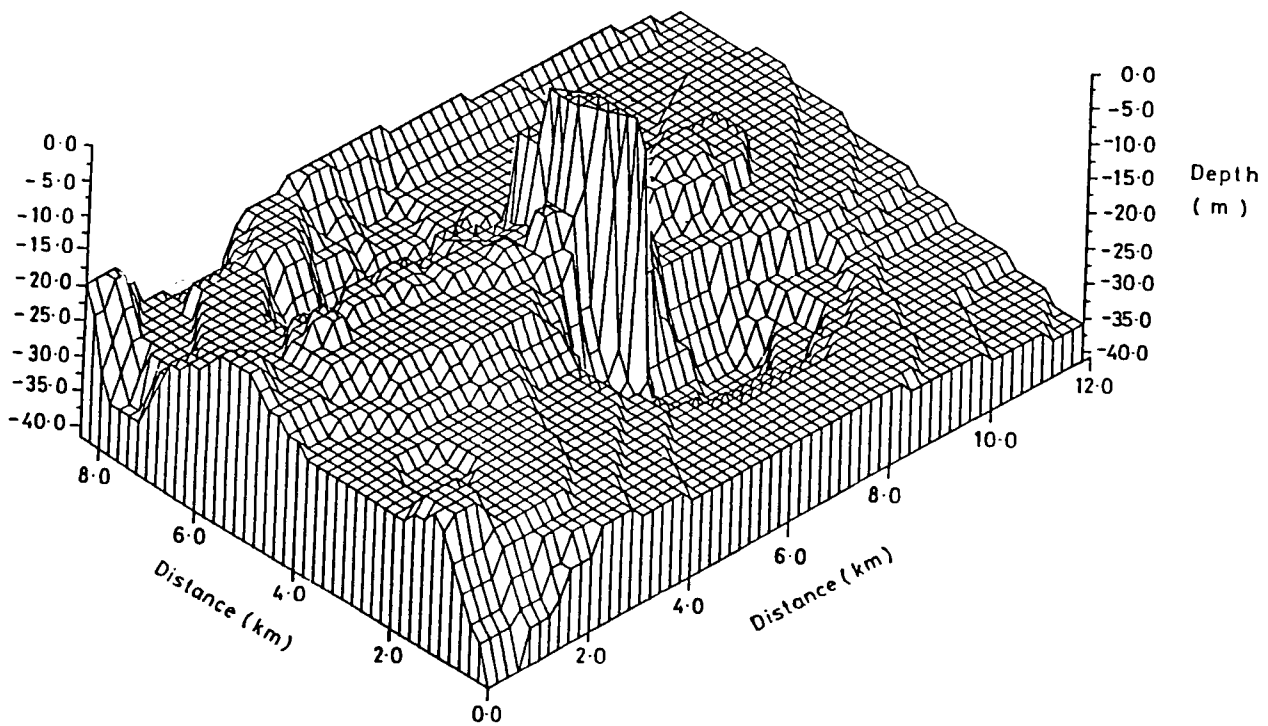

Figure 6.6(b) Isoparametric projection of bathymetry as viewed from the south-east

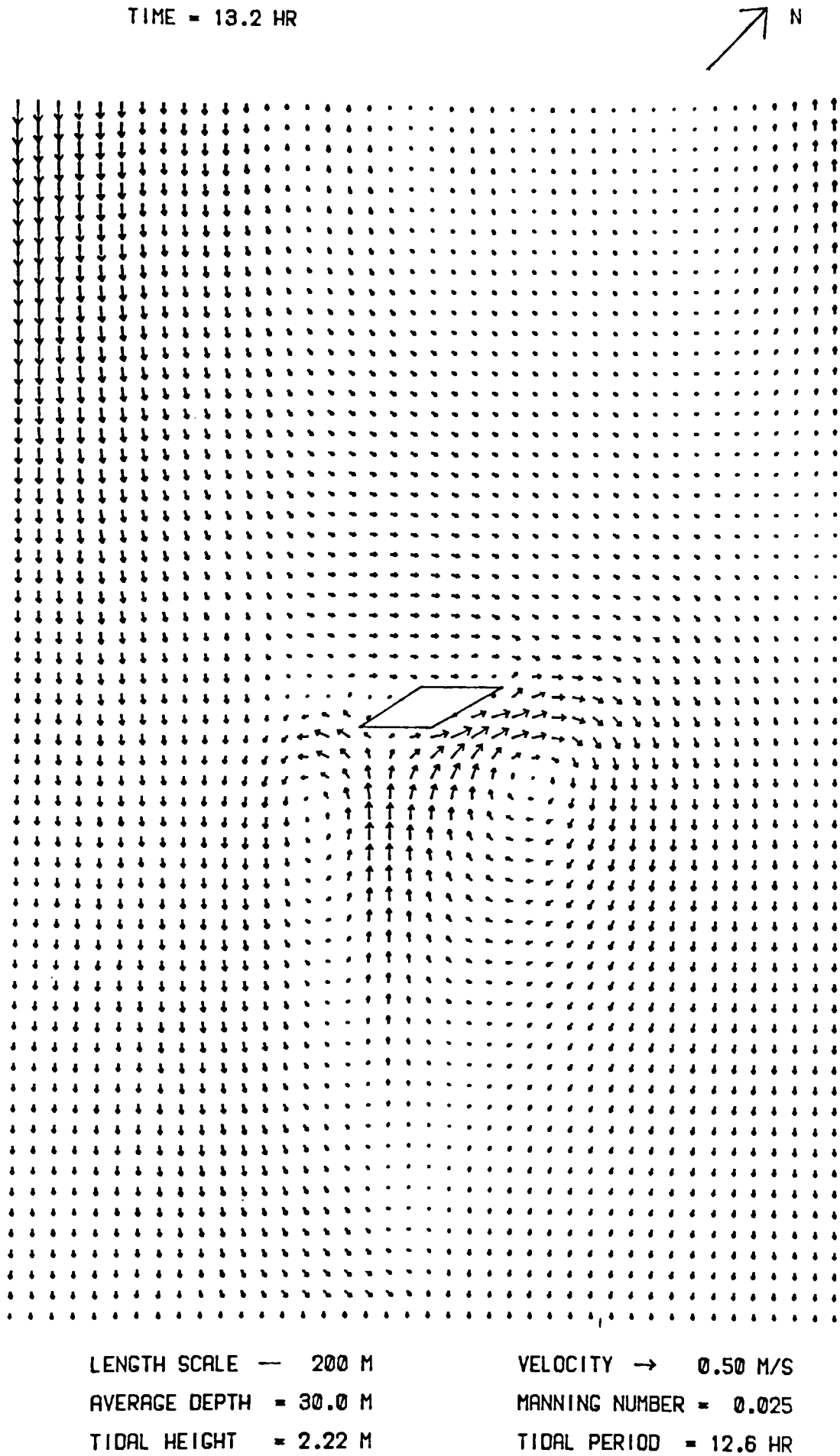

Figure 6.7 Predicted velocity field just after high water level with the omission of the Coriolis term at the northern open boundary

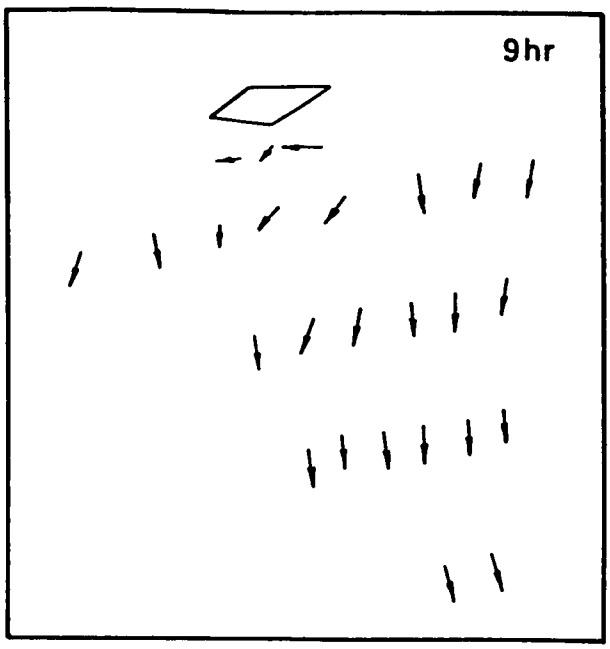

(a) Measured velocities

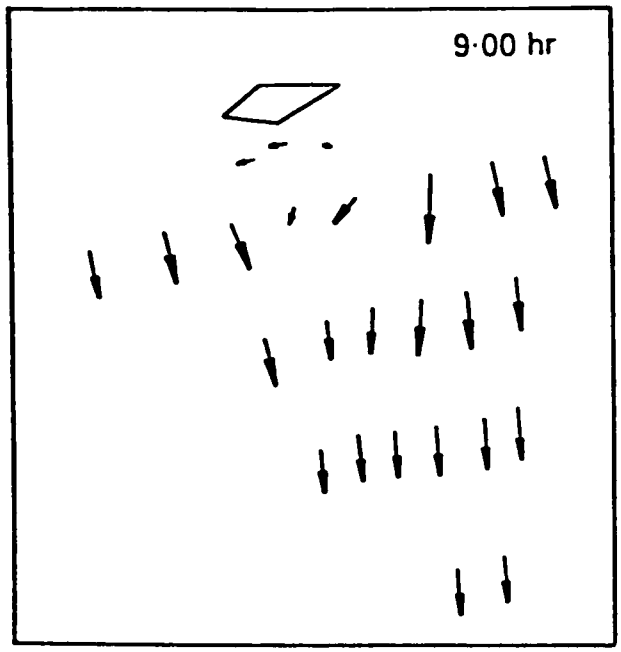

(b) Predicted velocities

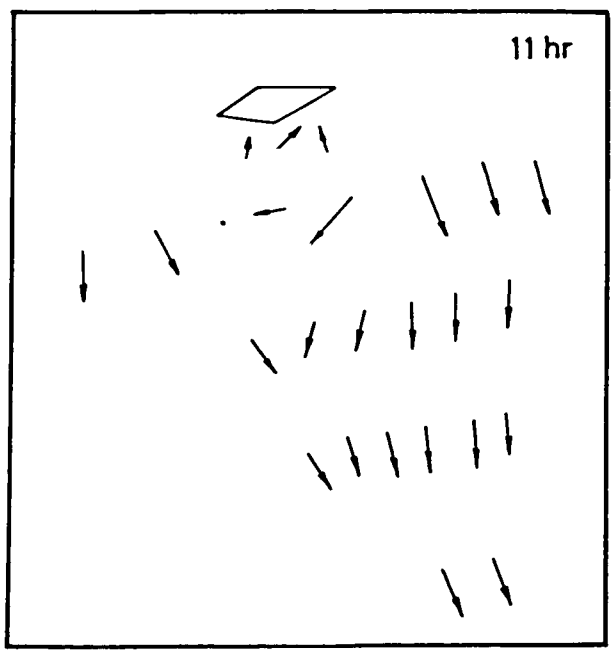

(a) Measured velocities

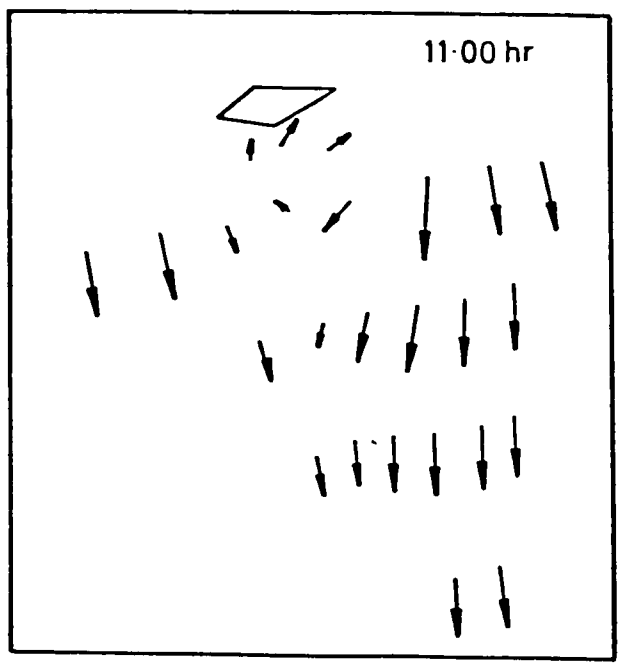

(b) Predicted velocities

Figure 6.8 Comparison of numerically predicted and field measured velocities at measuring sites for three tidal phases and largest tidal range

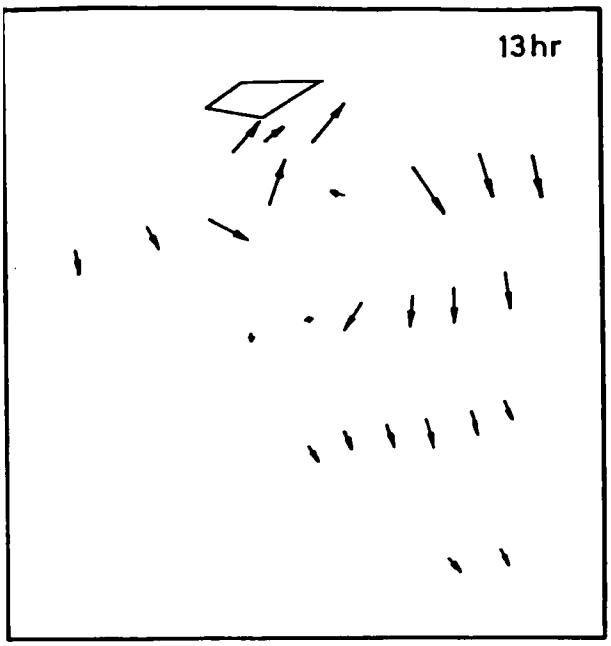

(a) Measured velocities

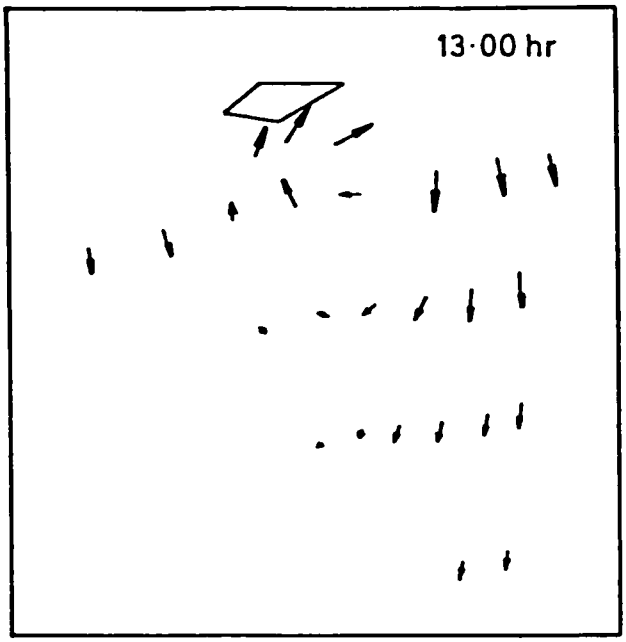

(b) Predicted velocities

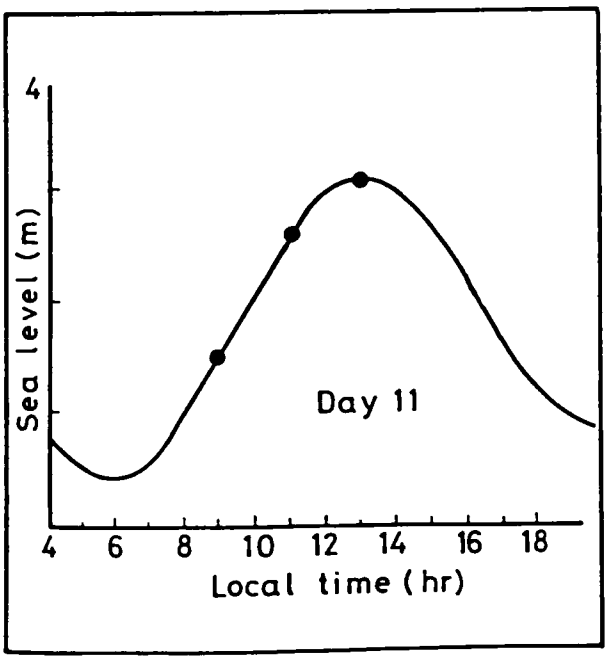

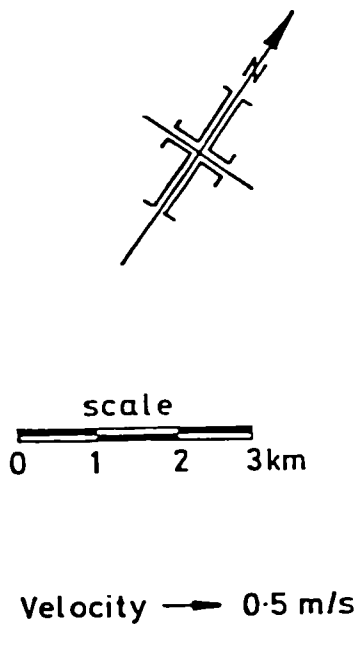

Figure 6.8(cont'd) Comparison of numerically predicted and field measured velocities at measuring sites for three tidal phases and largest tidal range

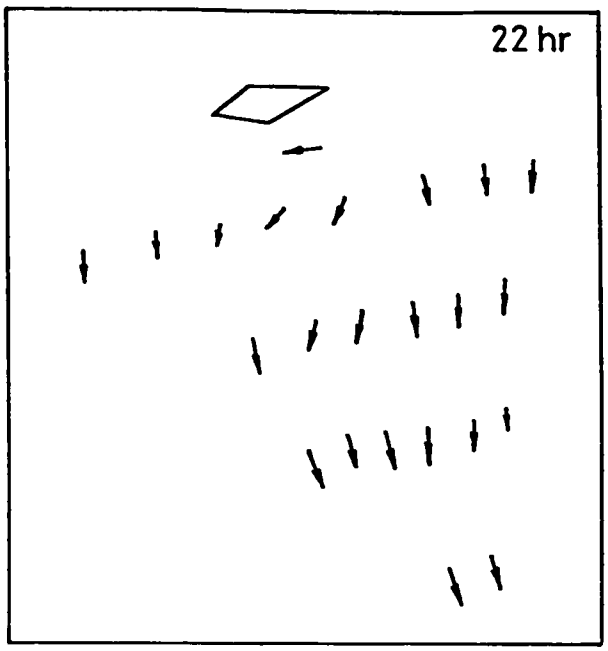

(a) Measured velocities

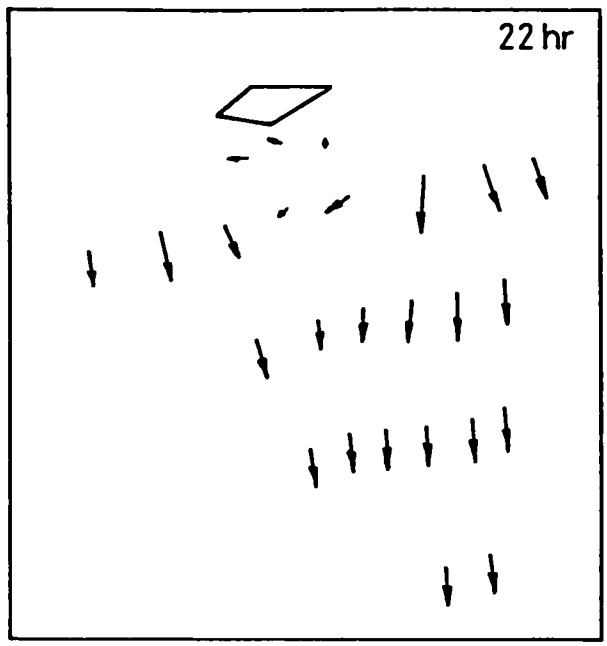

(b) Predicted velocities

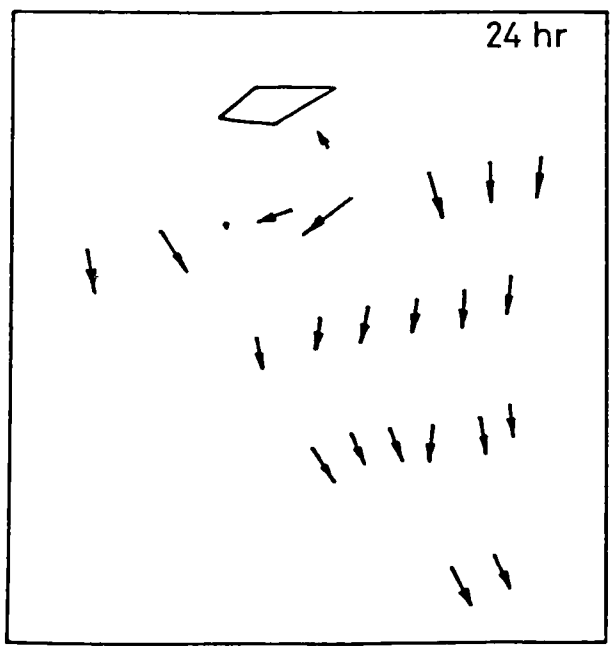

(a) Measured velocities

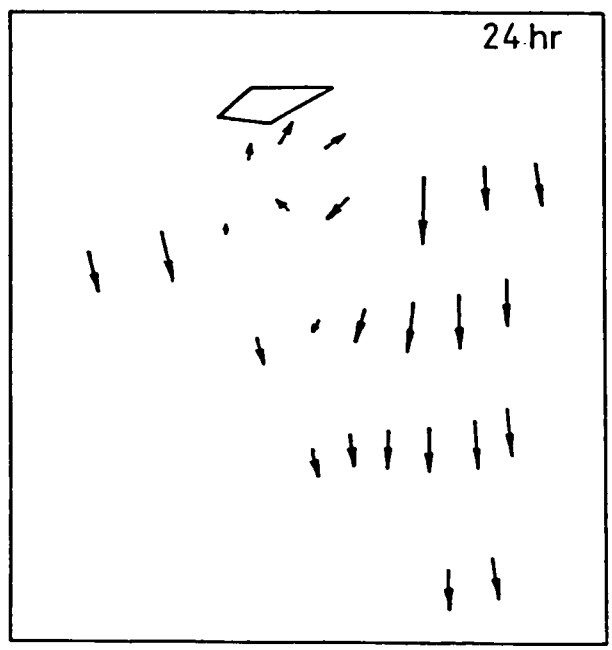

(b) Predicted velocities

Figure 6.9 Comparison of numerically predicted and field measured velocities at measuring sites for three tidal phases and average tidal range

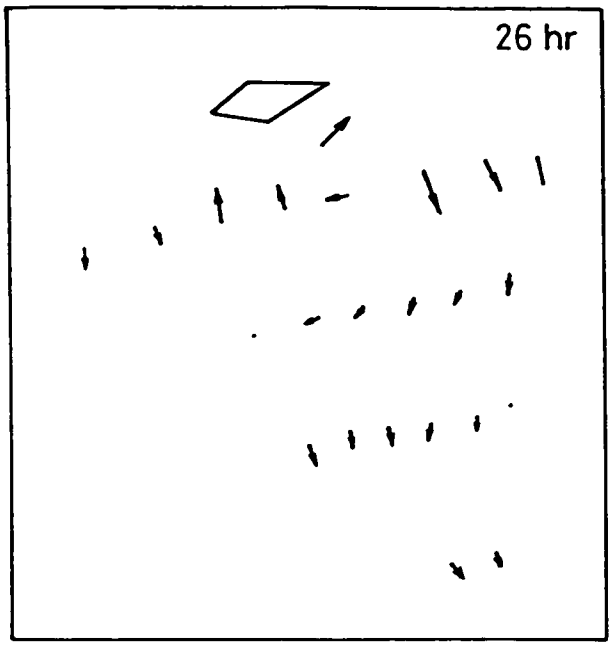

(a) Measured velocities

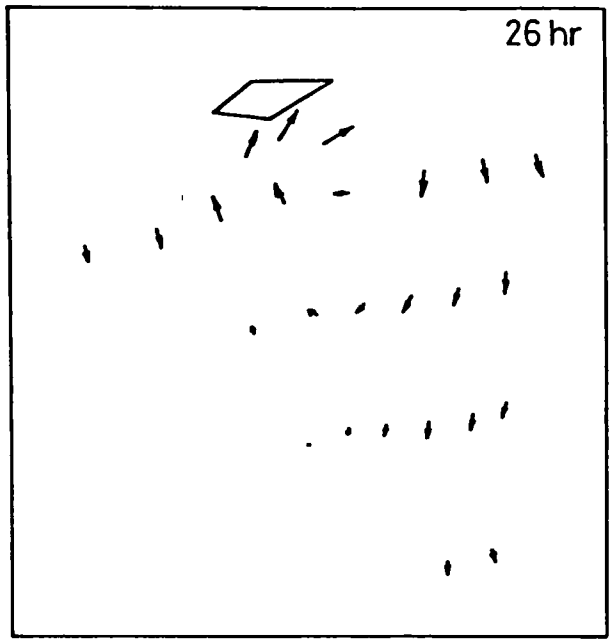

(b) Predicted velocities

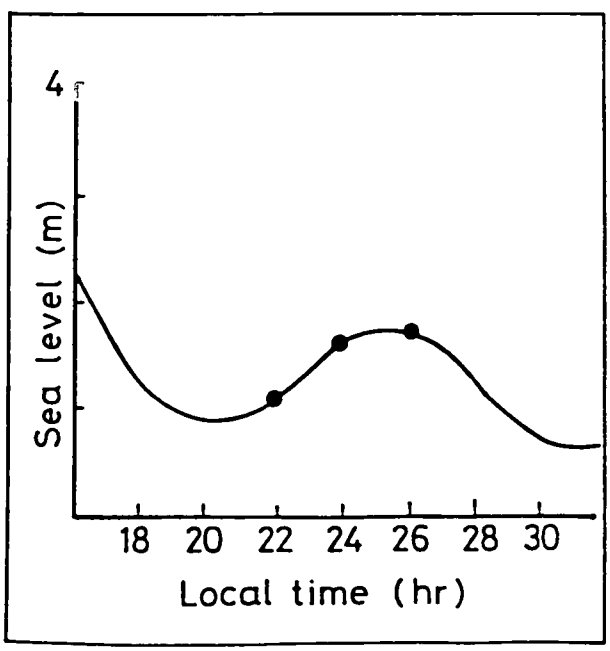

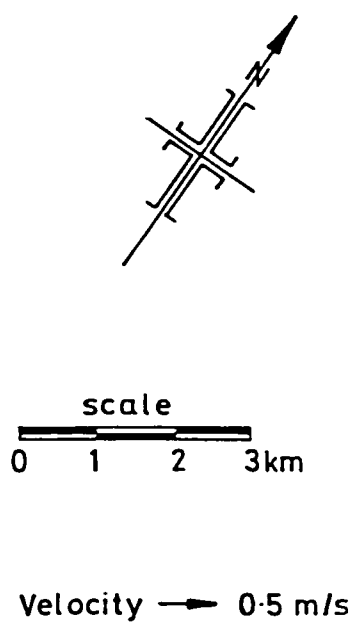

Figure 6.9(cont'd) Comparison of numerically predicted and field measured velocities at measuring sites for three tidal phases and average tidal range

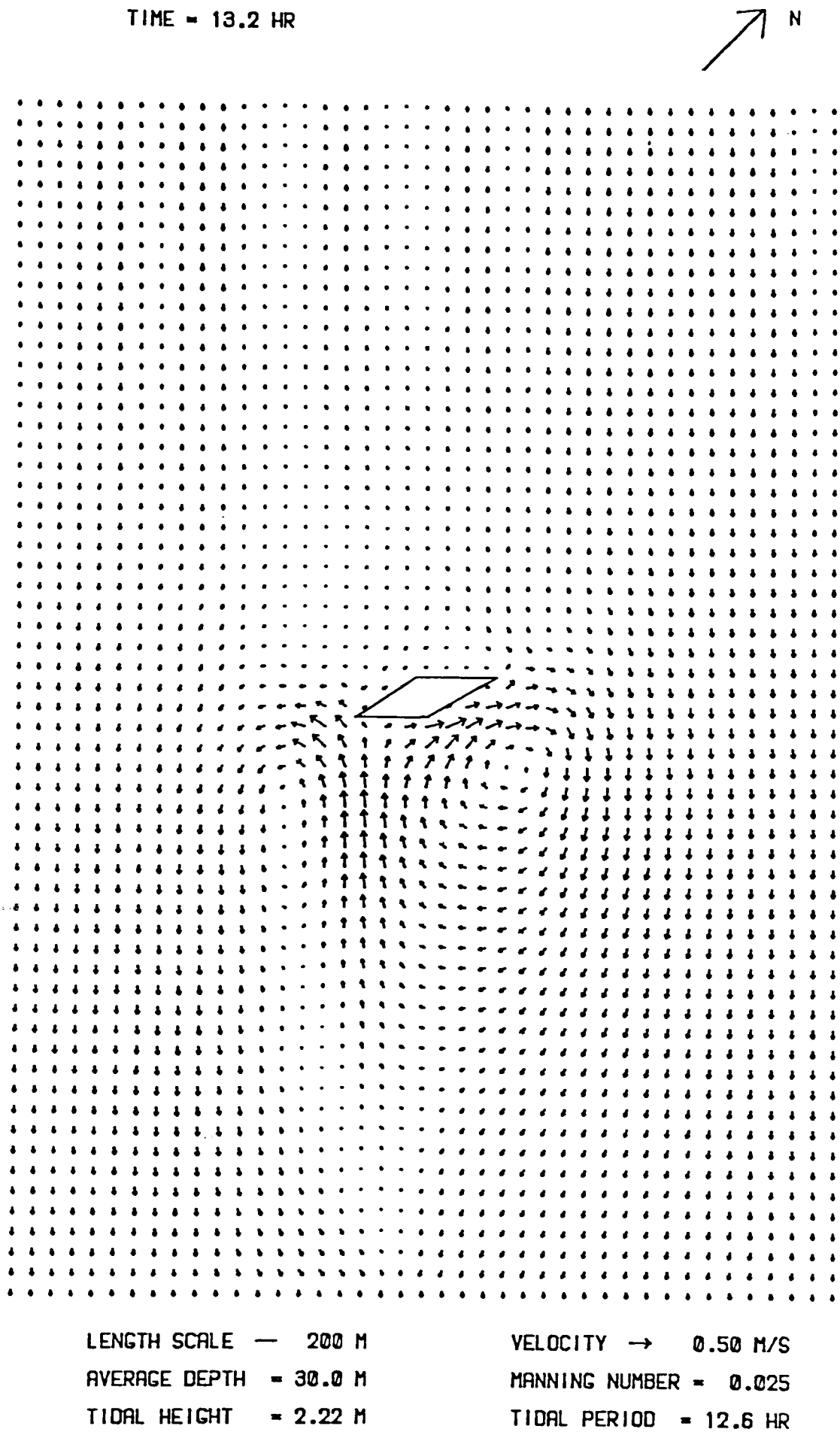

Figure 6.10 Predicted velocity field just after high water level

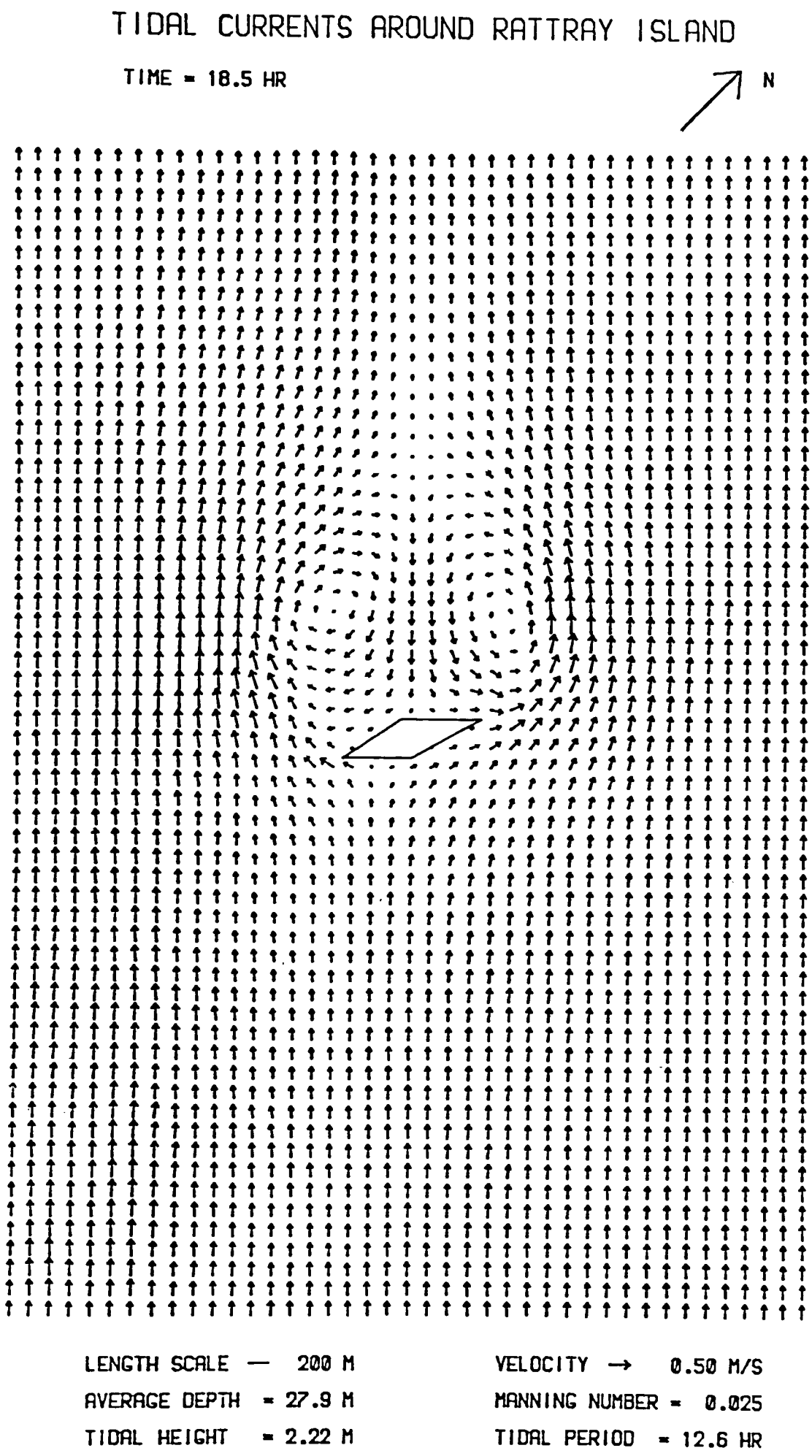

Figure 6.11 Predicted velocity field just before low water level

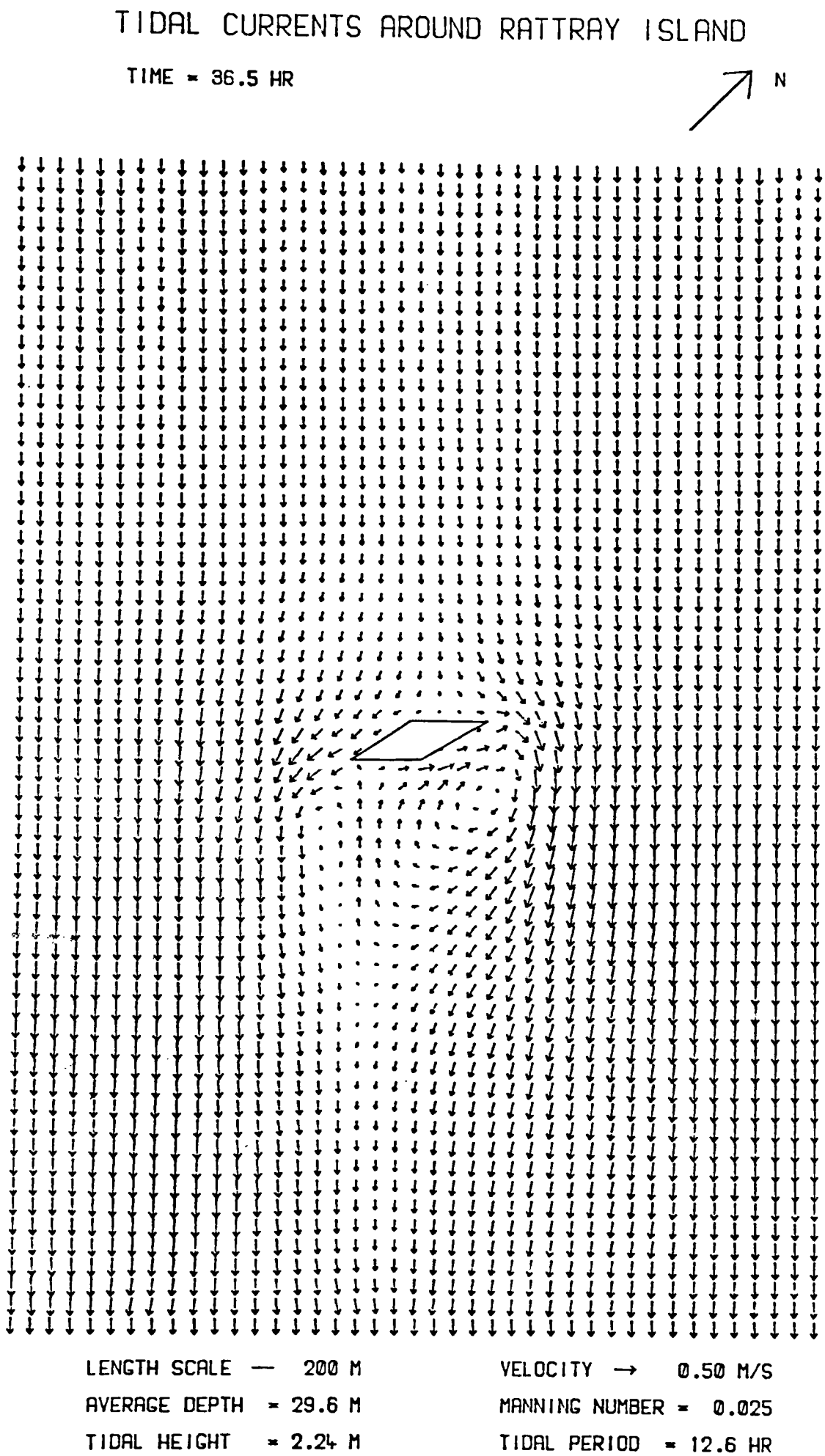

Figure 6.12 Predicted velocity field just before high water level

VORTICITY DISTRIBUTION AROUND RATTRAY ISLAND

TIME = 36.5 HR

N

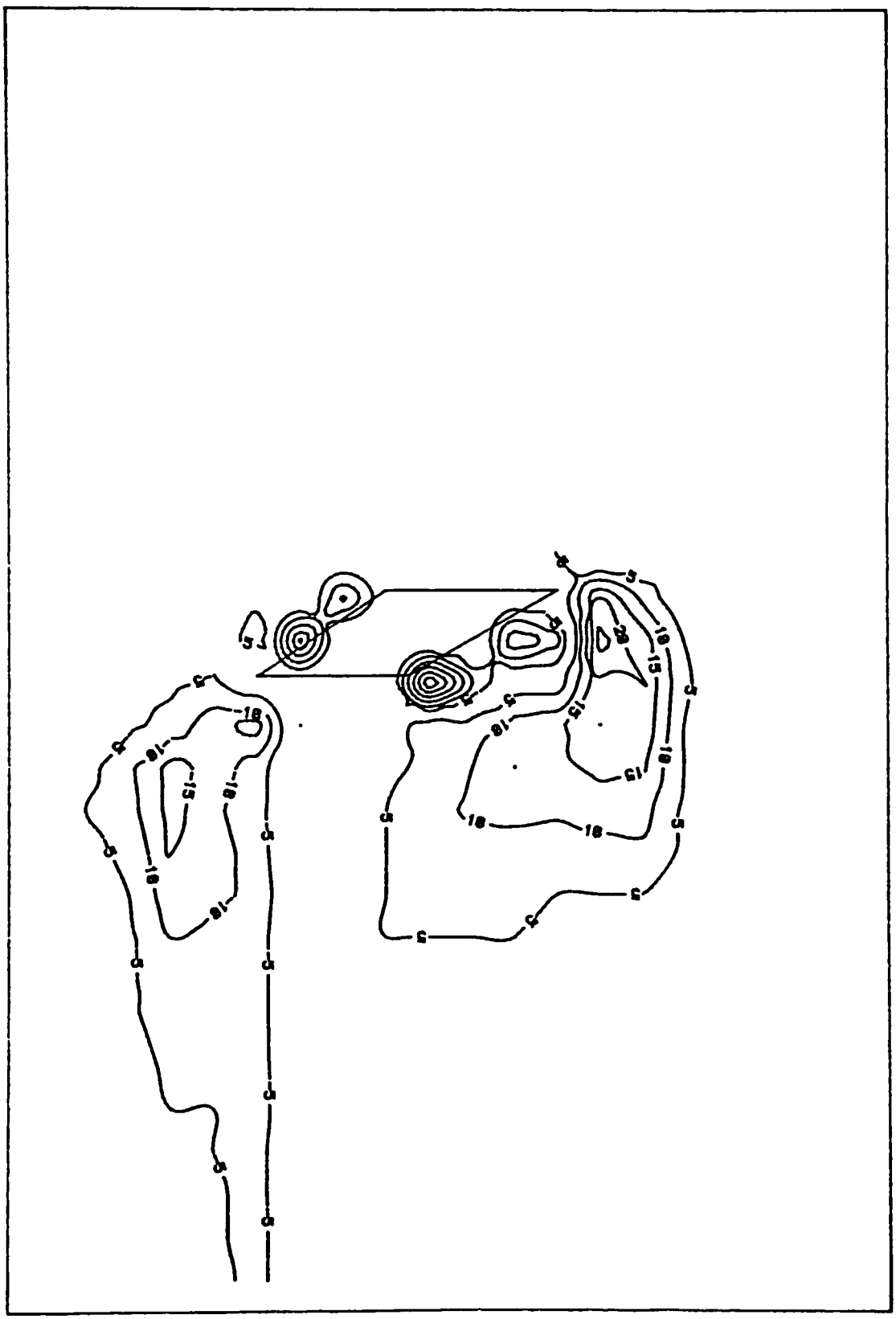

LENGTH SCALE —— 200 M

TIDAL HEIGHT = 2.22 M

TIDAL PERIOD = 12.6 HR

VORTICITY IN 10^{-4} S^{-1}

MANNING NUMBER = 0.025

Figure 6.13 Predicted vorticity distribution just before high water level

VORTICITY DISTRIBUTION AROUND RATTRAY ISLAND

TIME = 18.5 HR

N

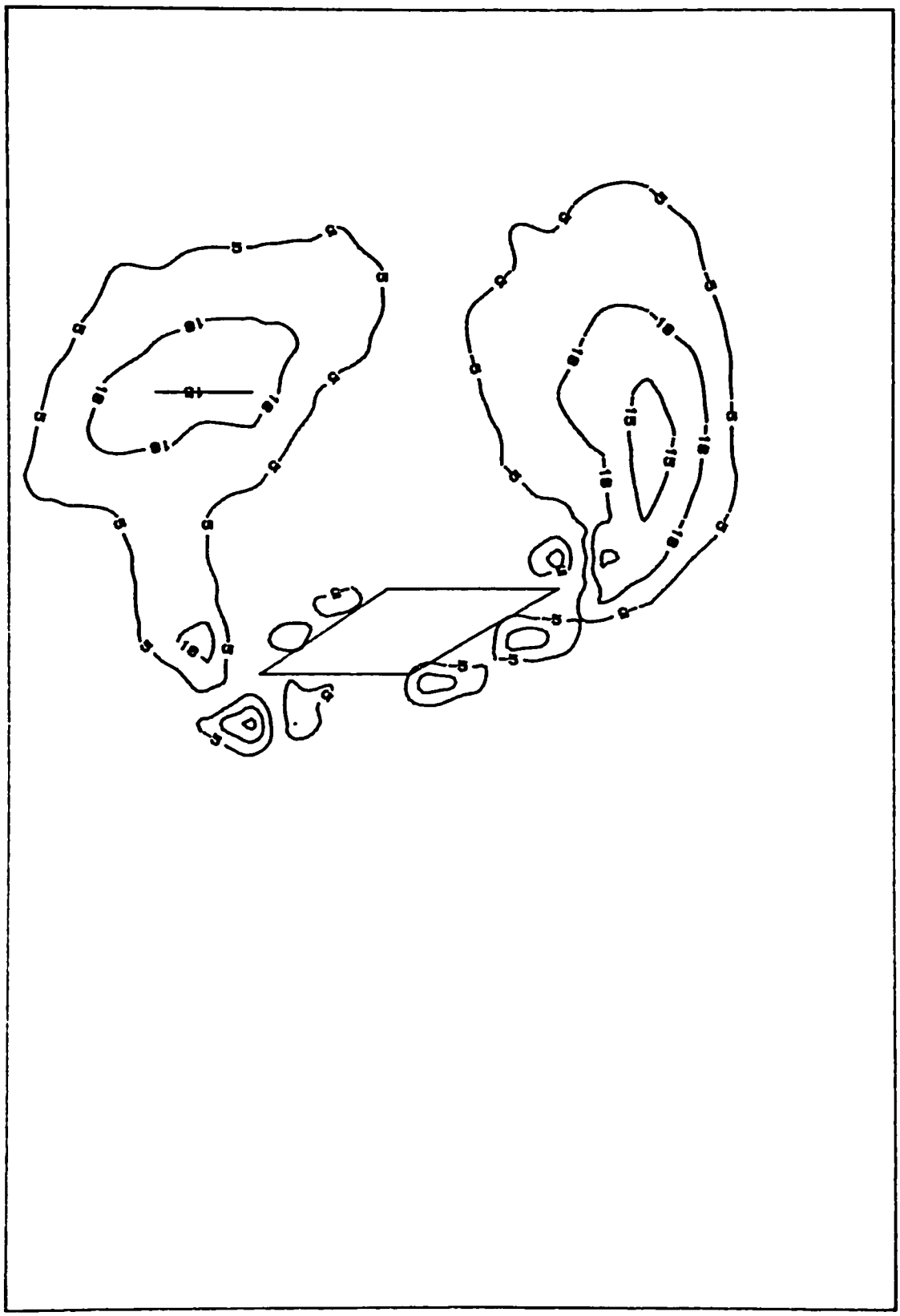

LENGTH SCALE —— 200 M

TIDAL HEIGHT = 2.22 M

TIDAL PERIOD = 12.6 HR

VORTICITY IN 10^{-4} S^{-1}

MANNING NUMBER = 0.025

Figure 6.14 Predicted vorticity distribution just before low water level

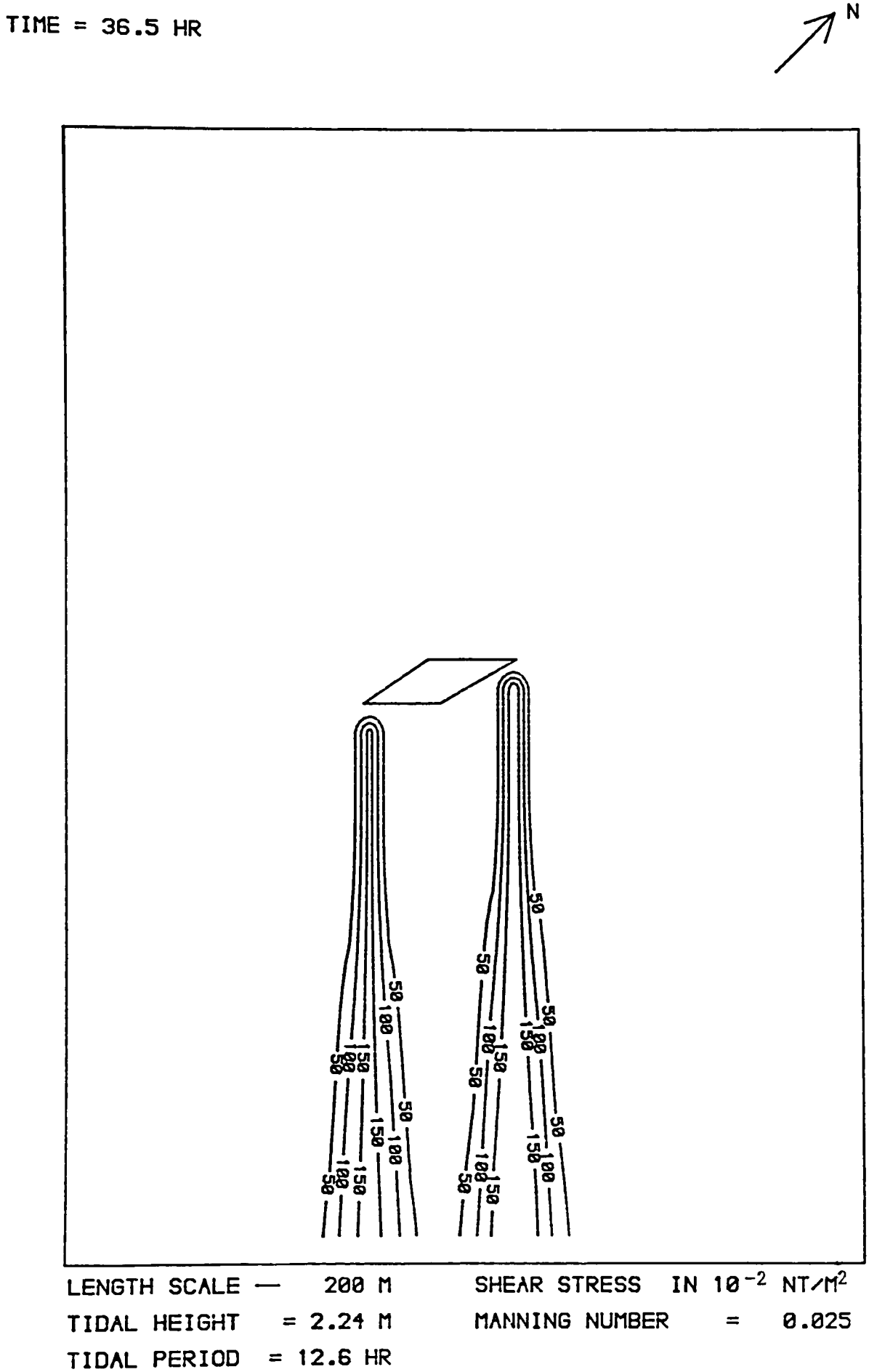

Figure 6.15 Empirically determined free shear layer stress distribution just before high water level

SHEAR STRESS DISTRIBUTION AROUND RATTRAY ISLAND

TIME = 36.5 HR

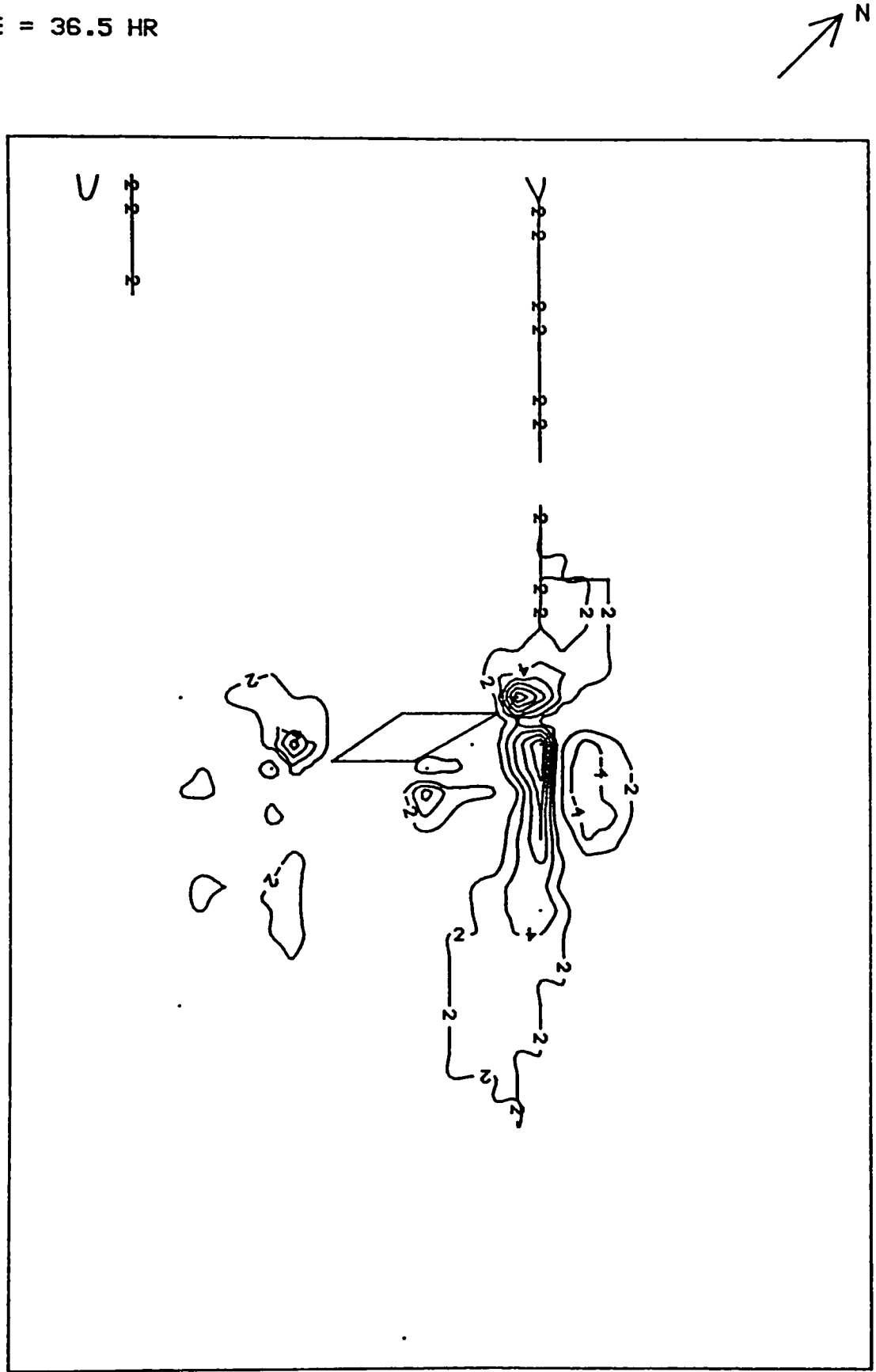

LENGTH SCALE — 200 M

TIDAL HEIGHT = 2.24 M

TIDAL PERIOD = 12.6 HR

SHEAR STRESS IN 10^{-2} NT/M^2

MANNING NUMBER = 0.025

Figure 6.16 Predicted bed generated shear stress distribution just before high water level

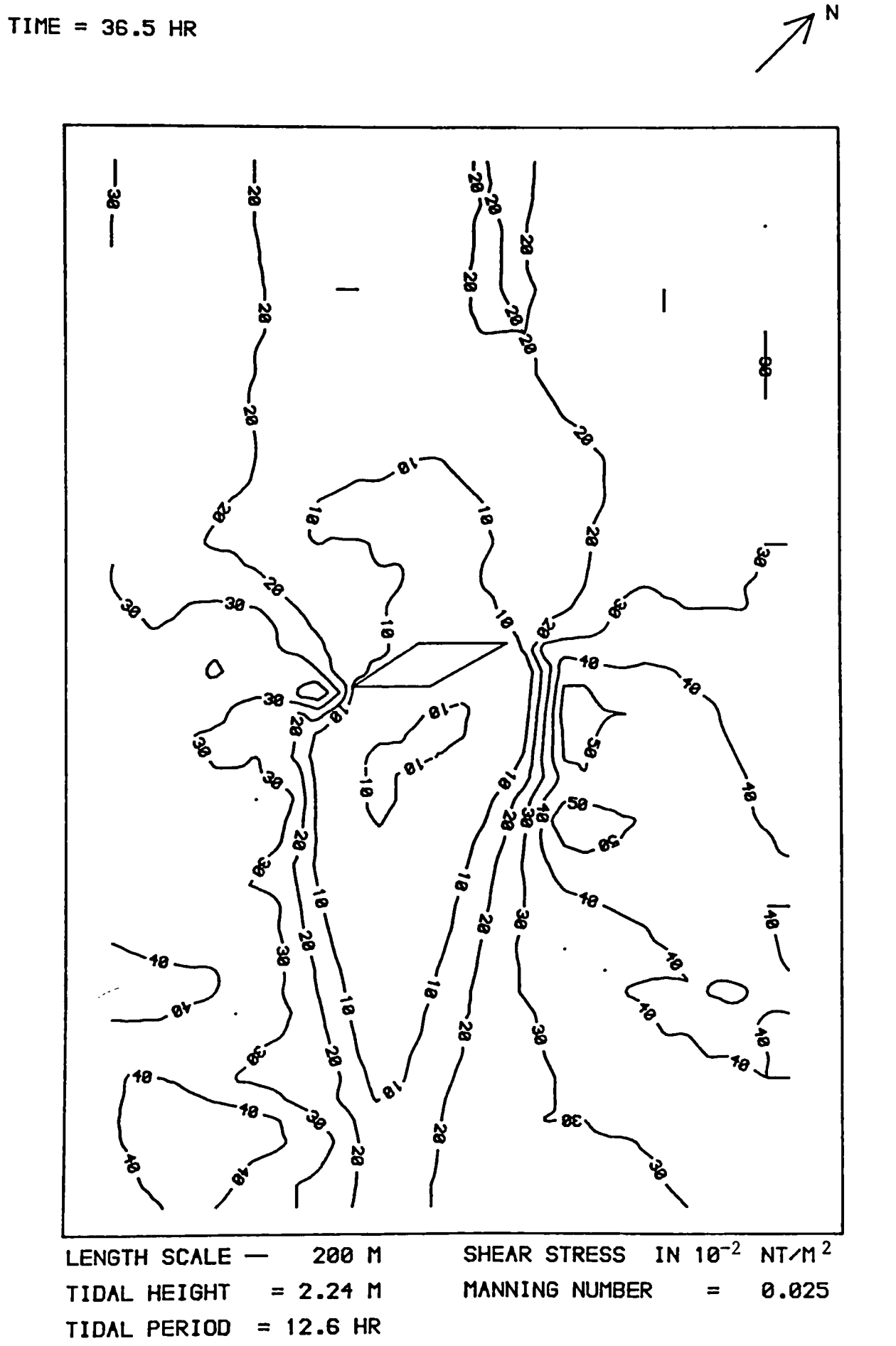

Figure 6.17 Predicted x-direction bed frictional stress distribution just before high water level

BED FRICTIONAL SHEAR STRESS AROUND RATTRAY ISLAND

TIME = 36.5 HR

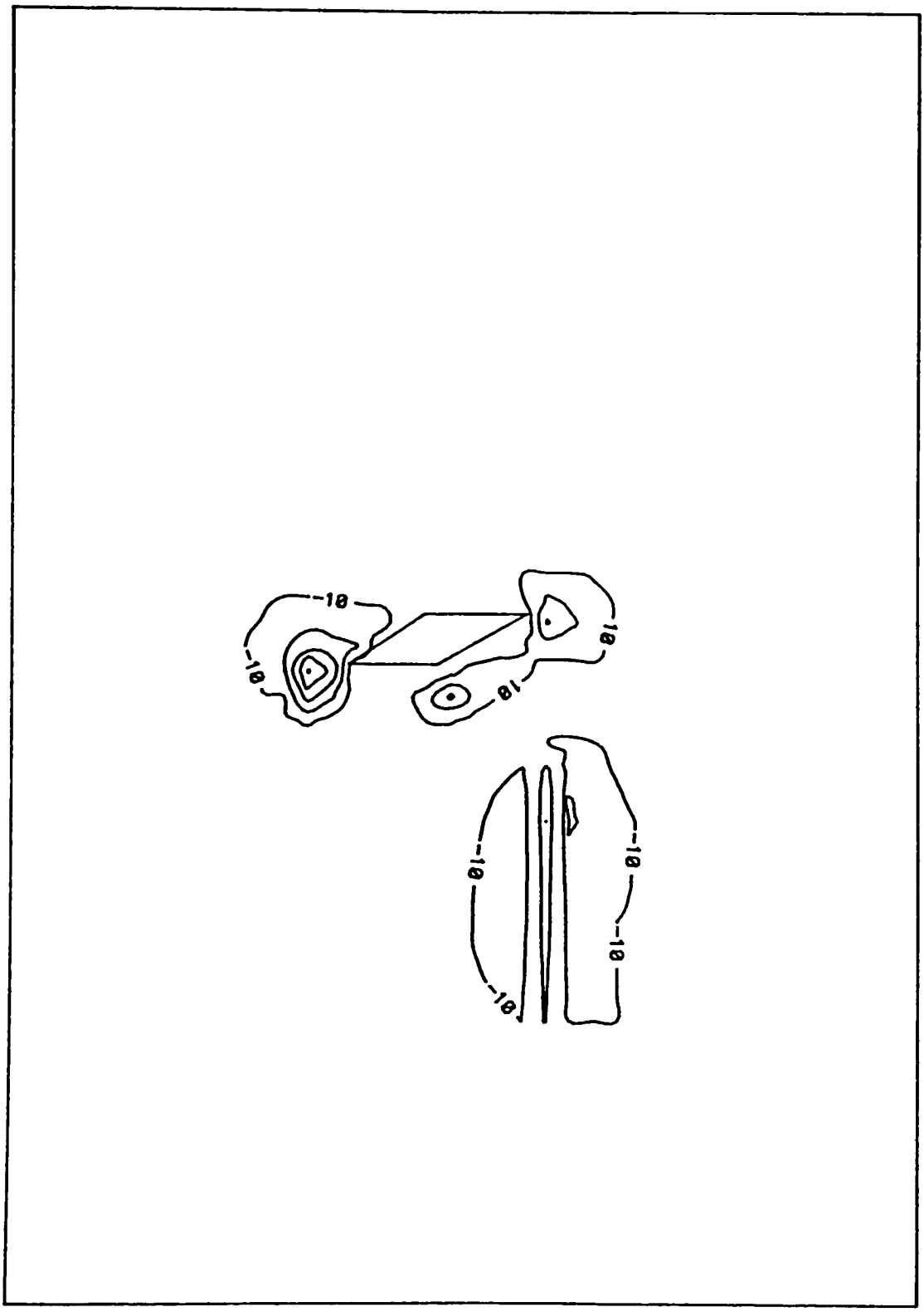

LENGTH SCALE — 200 M SHEAR STRESS IN 10^{-2} NT/M^2

TIDAL HEIGHT = 2.24 M MANNING NUMBER = 0.025

TIDAL PERIOD = 12.6 HR

Figure 6.18 Predicted y-direction bed frictional stress distribution just before high water level

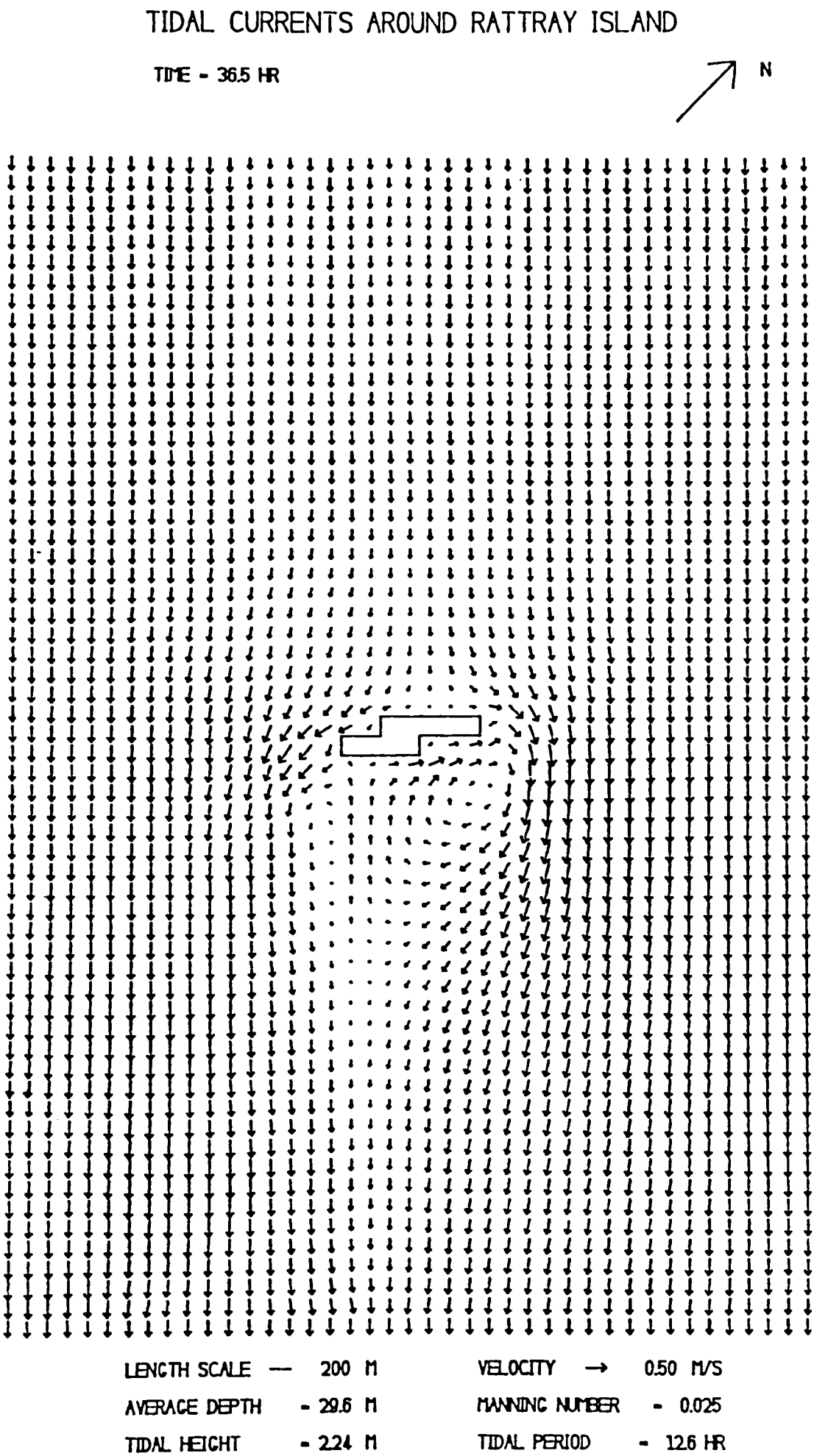

Figure 6.19 Predicted velocity field just before high tide for uniform grid around island

VORTICITY DISTRIBUTION AROUND RATTRAY ISLAND

TIME = 36.5 HR

N

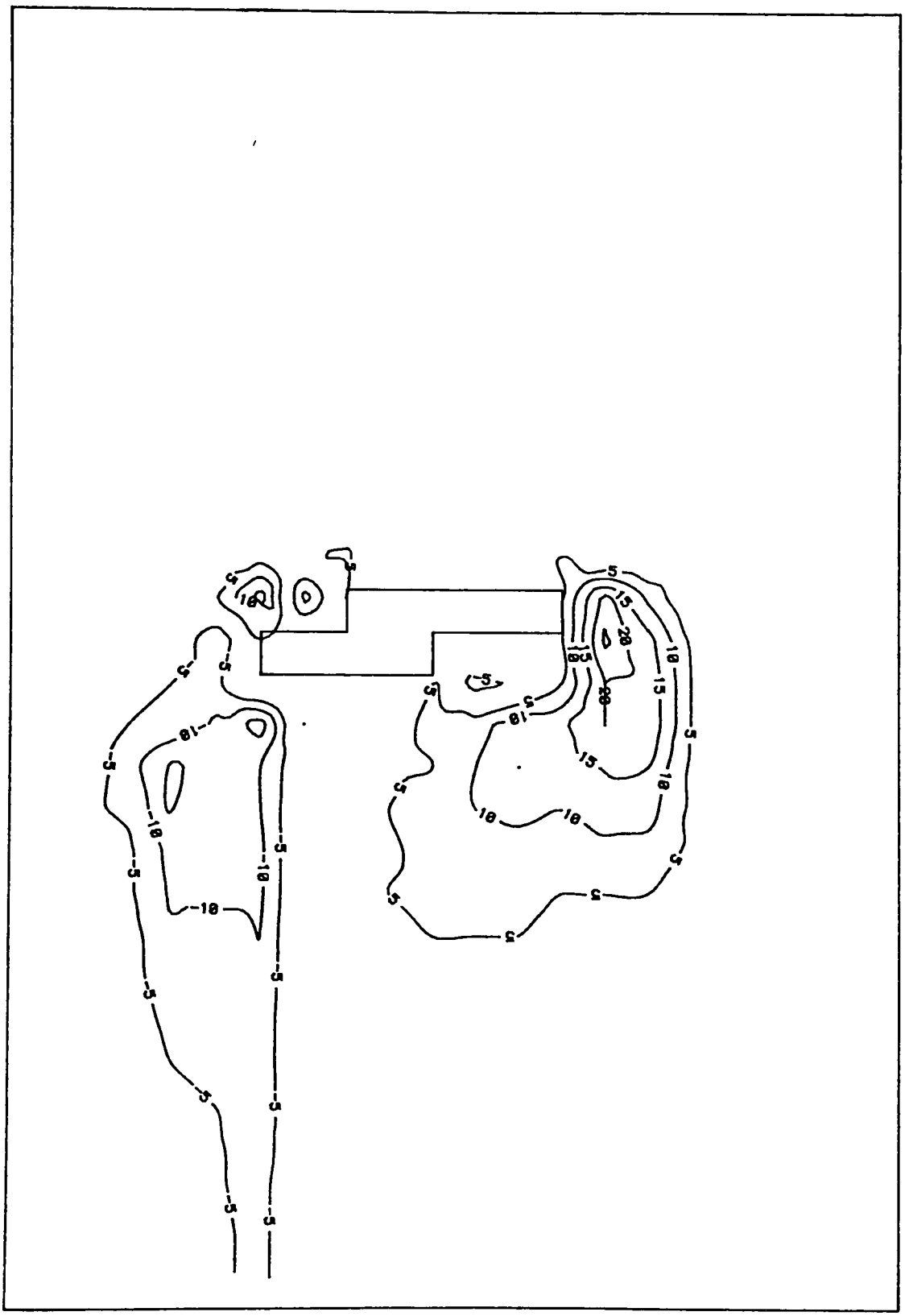

LENGTH SCALE —— 200 M

TIDAL HEIGHT = 2.24 M

TIDAL PERIOD = 12.6 HR

VORTICITY IN 10^{-4} S^{-1}

MANNING NUMBER = 0.025

Figure 6.20 Predicted vorticity distribution just before high water level for uniform grid around island

VORTICITY DISTRIBUTION AROUND RATTRAY ISLAND

TIME = 36.5 HR

N

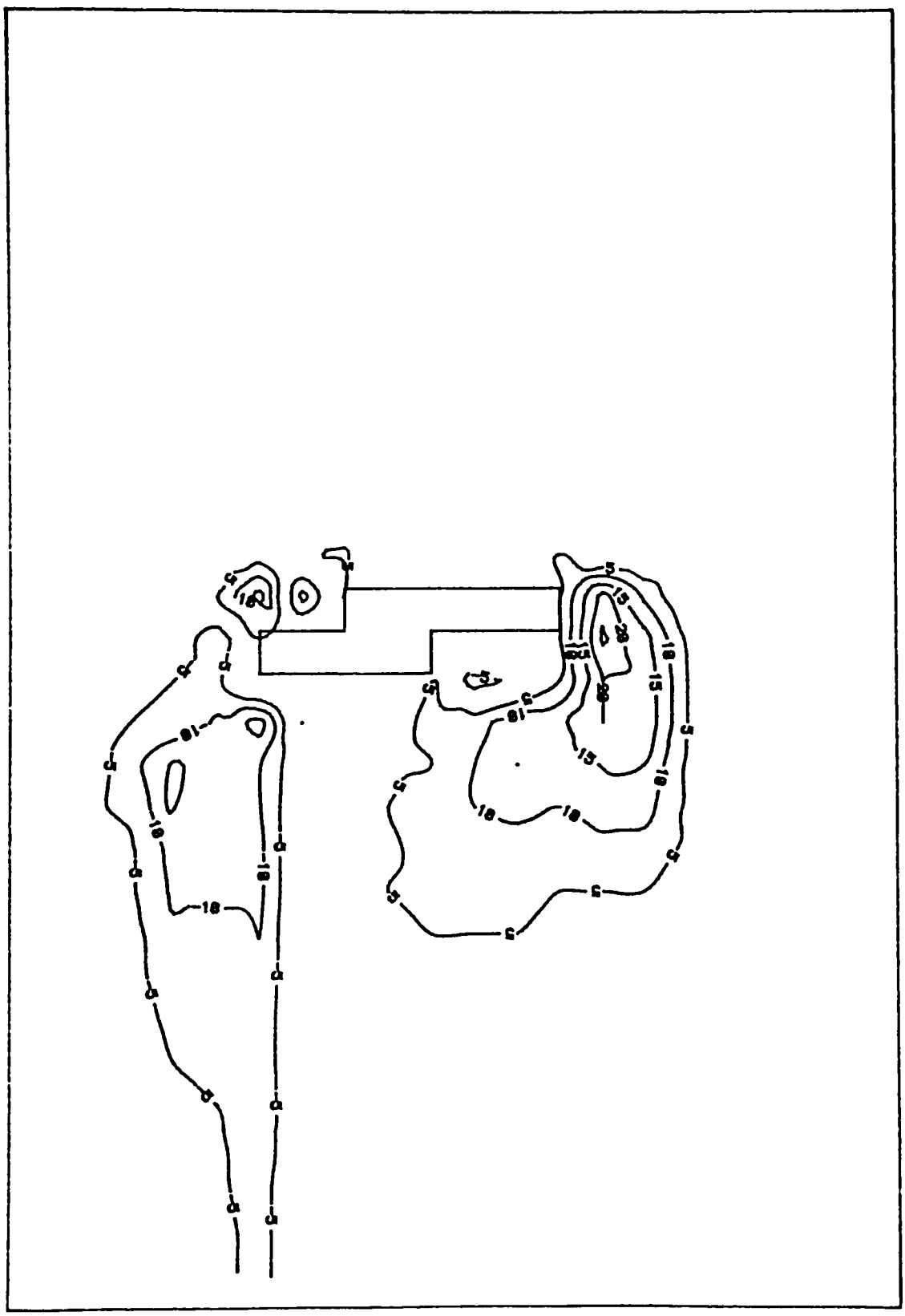

LENGTH SCALE —— 200 M

TIDAL HEIGHT = 2.24 M

TIDAL PERIOD = 12.6 HR

VORTICITY IN 10^{-4} S^{-1}

MANNING NUMBER = 0.025

Figure 6.21 Predicted vorticity distribution just before high water level for uniform grid around island and free-slip boundary condition

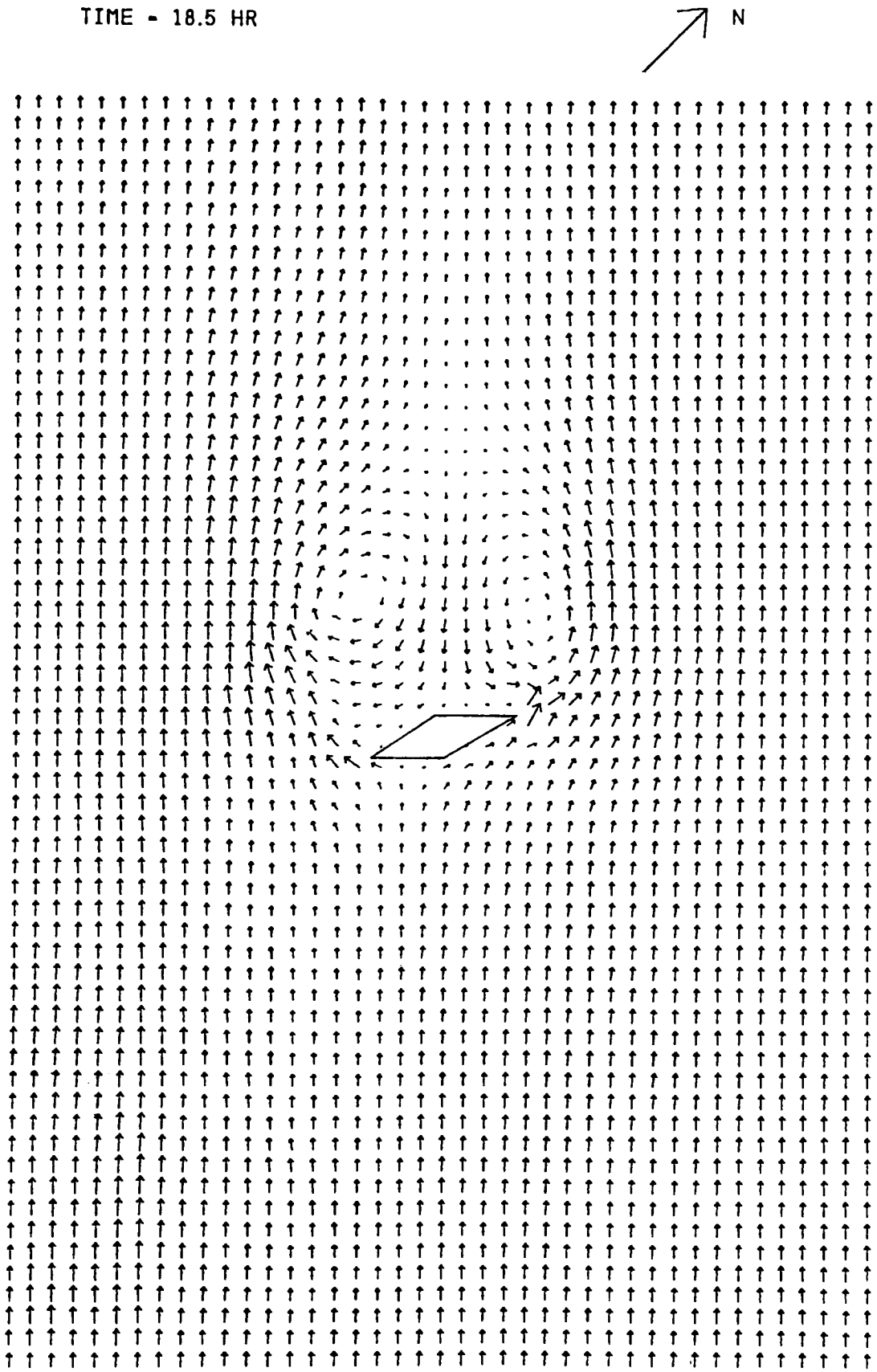

Figure 6.22 Predicted velocity field just before low water level with the cross-product advection terms expressed as $\frac{\partial Vq_x}{\partial y}$ and $\frac{\partial Uq_y}{\partial x}$

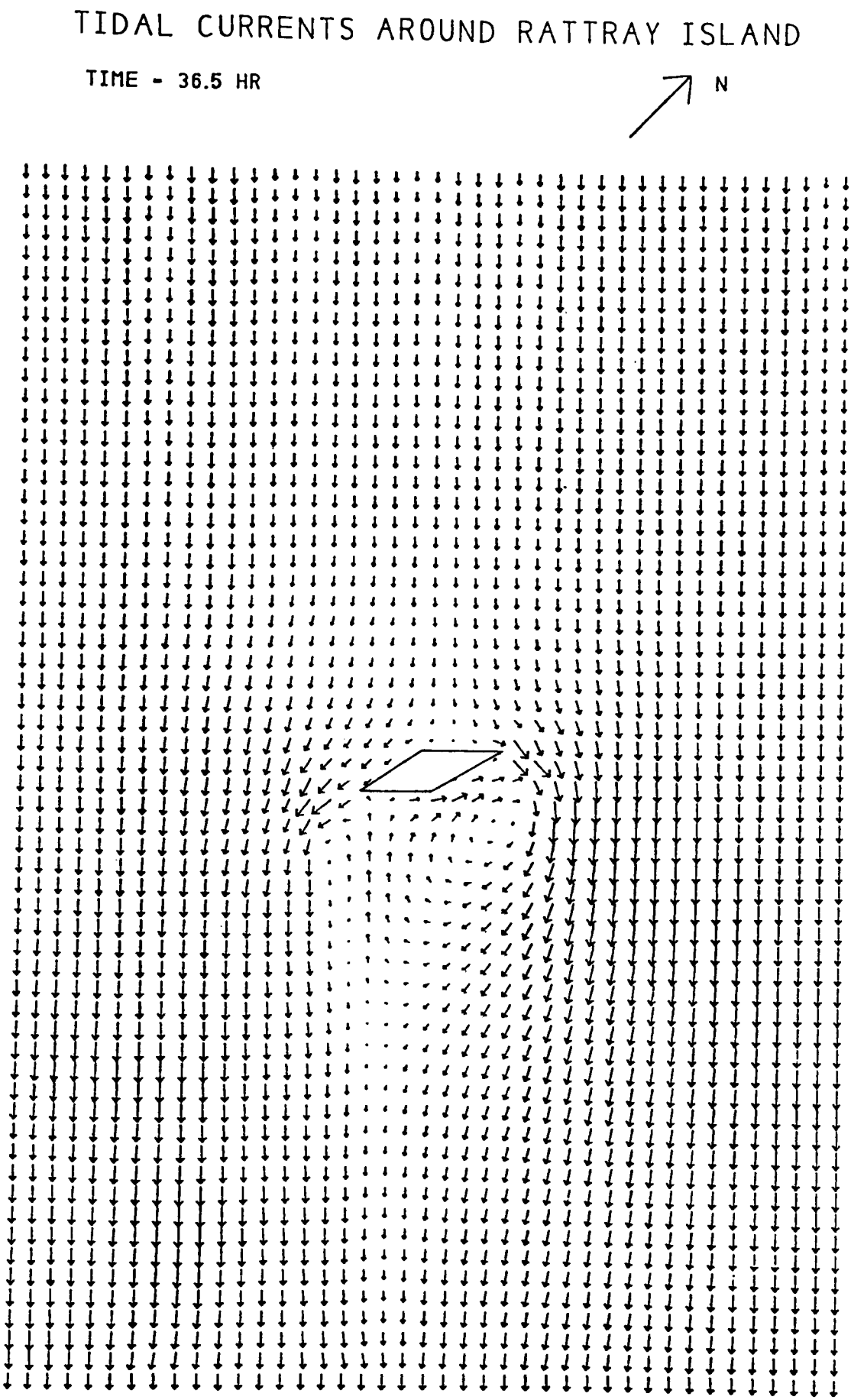

Figure 6.23 Predicted velocity field just before high water level with the cross-product advection terms expressed as $\frac{\partial Vq_x}{\partial y}$ and $\frac{\partial Uq_y}{\partial x}$

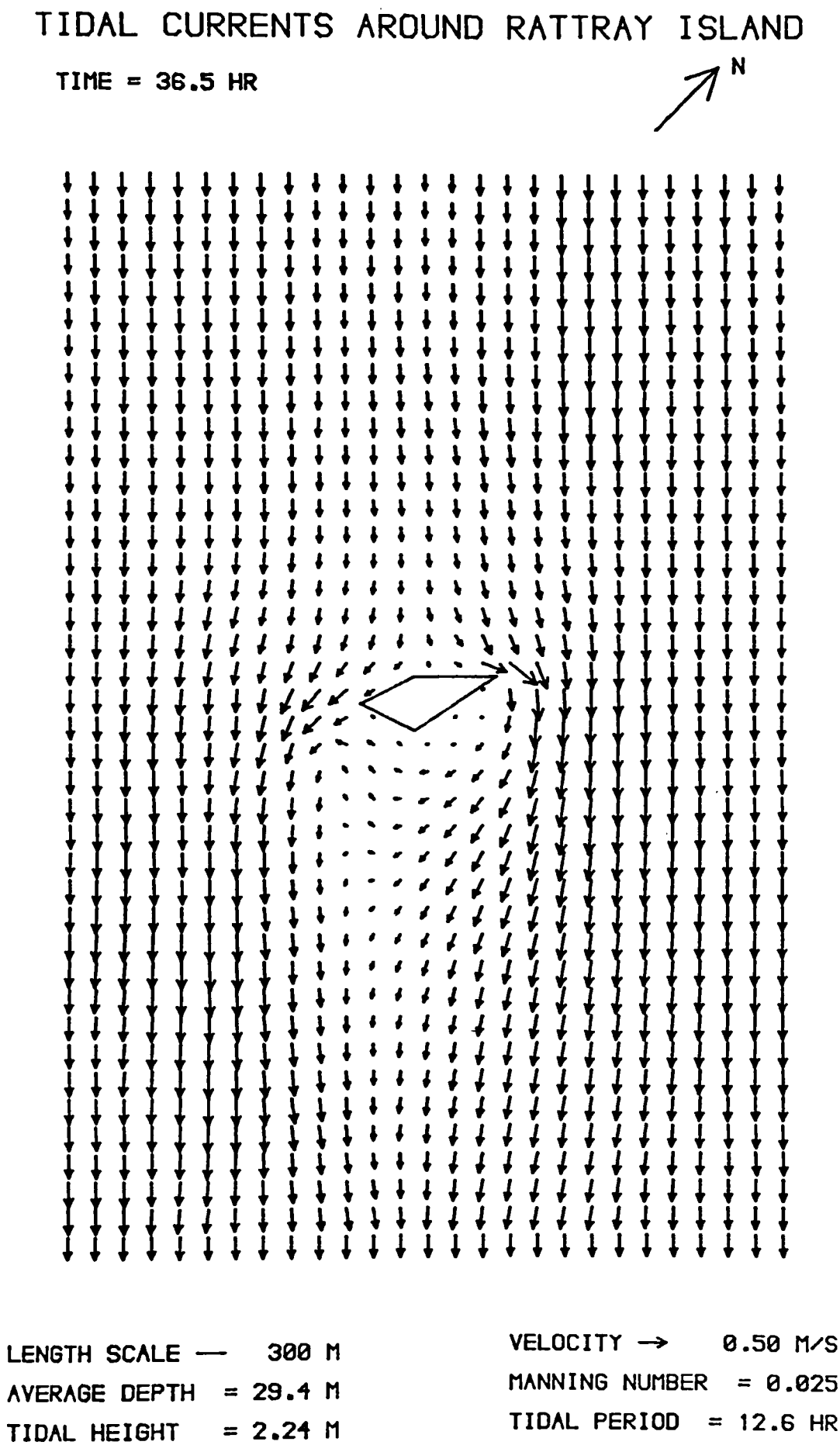

Figure 6.24 Predicted velocity field just before high water level for a coarser grid

VORTICITY DISTRIBUTION AROUND RATTRAY ISLAND

TIME = 18.5 HR

N

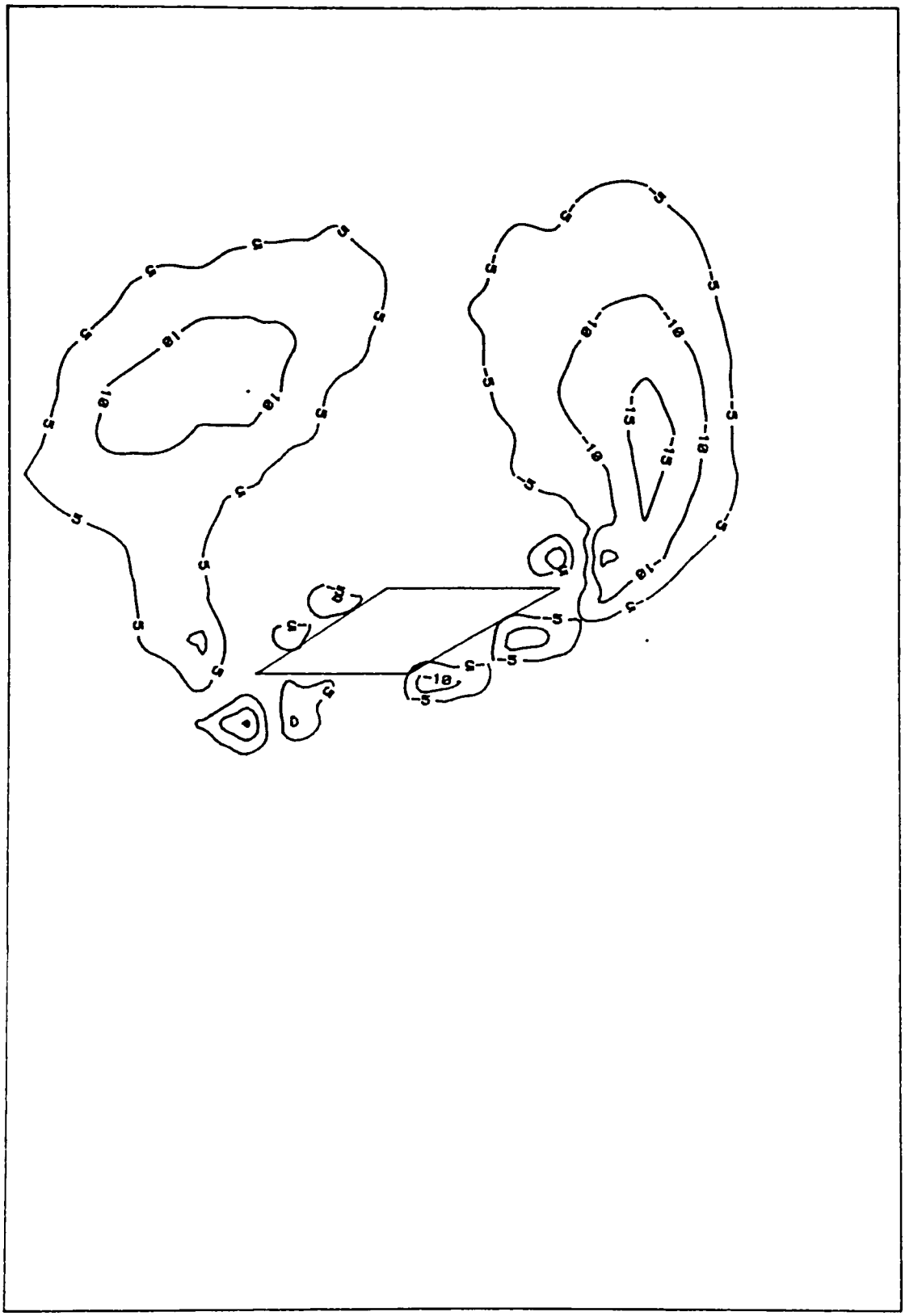

LENGTH SCALE —— 200 M

TIDAL HEIGHT = 2.22 M

TIDAL PERIOD = 12.6 HR

VORTICITY IN 10^{-4} S^{-1}

MANNING NUMBER = 0.025

Figure 6.25 Predicted vorticity distribution just before low water level with the omission of Coriolis effects

VORTICITY DISTRIBUTION AROUND RATTRAY ISLAND

TIME = 36.5 HR

N

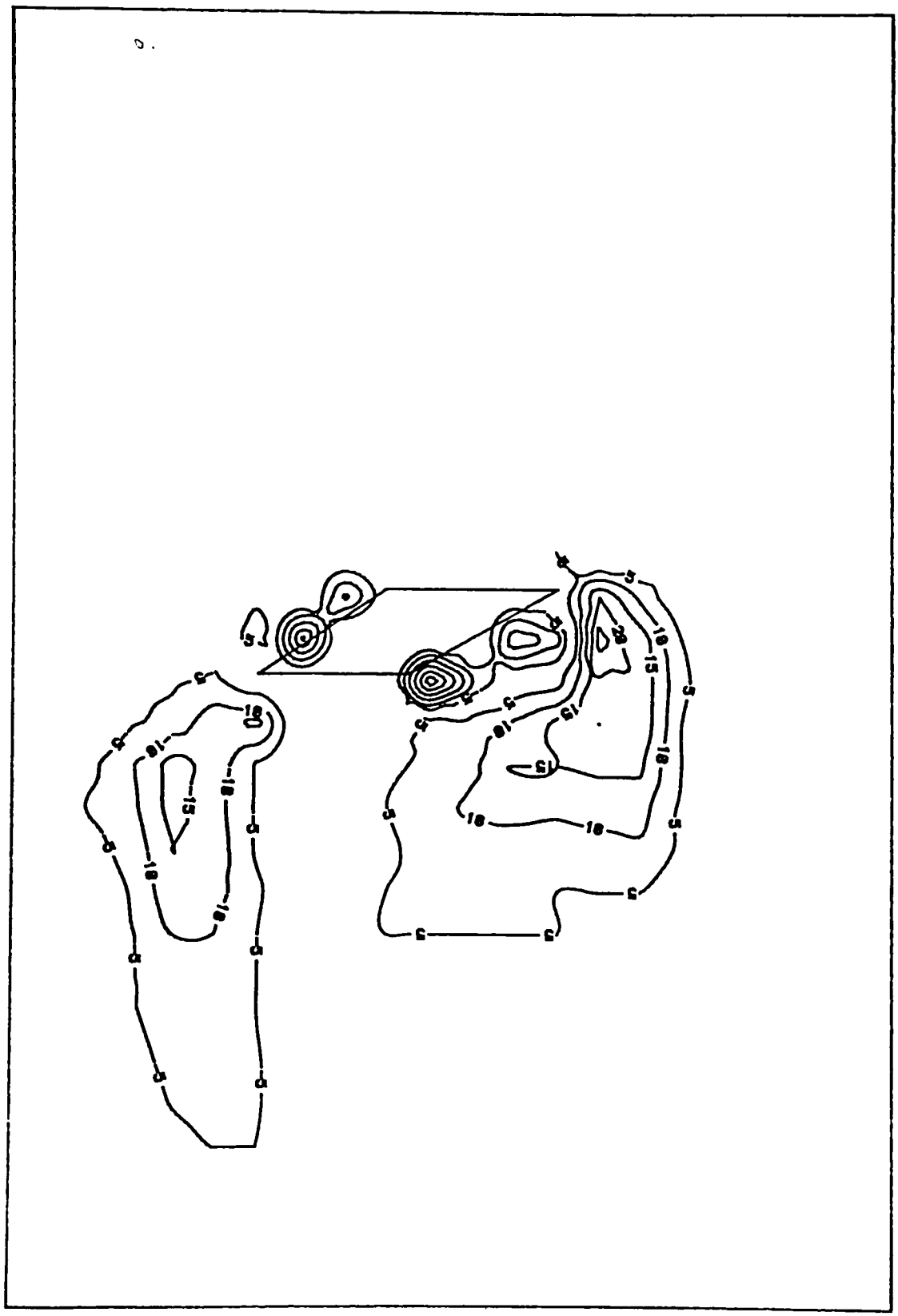

LENGTH SCALE —— 200 M

TIDAL HEIGHT = 2.22 M

TIDAL PERIOD = 12.6 HR

VORTICITY IN 10^{-4} S^{-1}

MANNING NUMBER = 0.025

Figure 6.26 Predicted vorticity distribution just before high water level with the exclusion of free shear layer stresses

VORTICITY DISTRIBUTION AROUND RATTRAY ISLAND

TIME = 36.5 HR

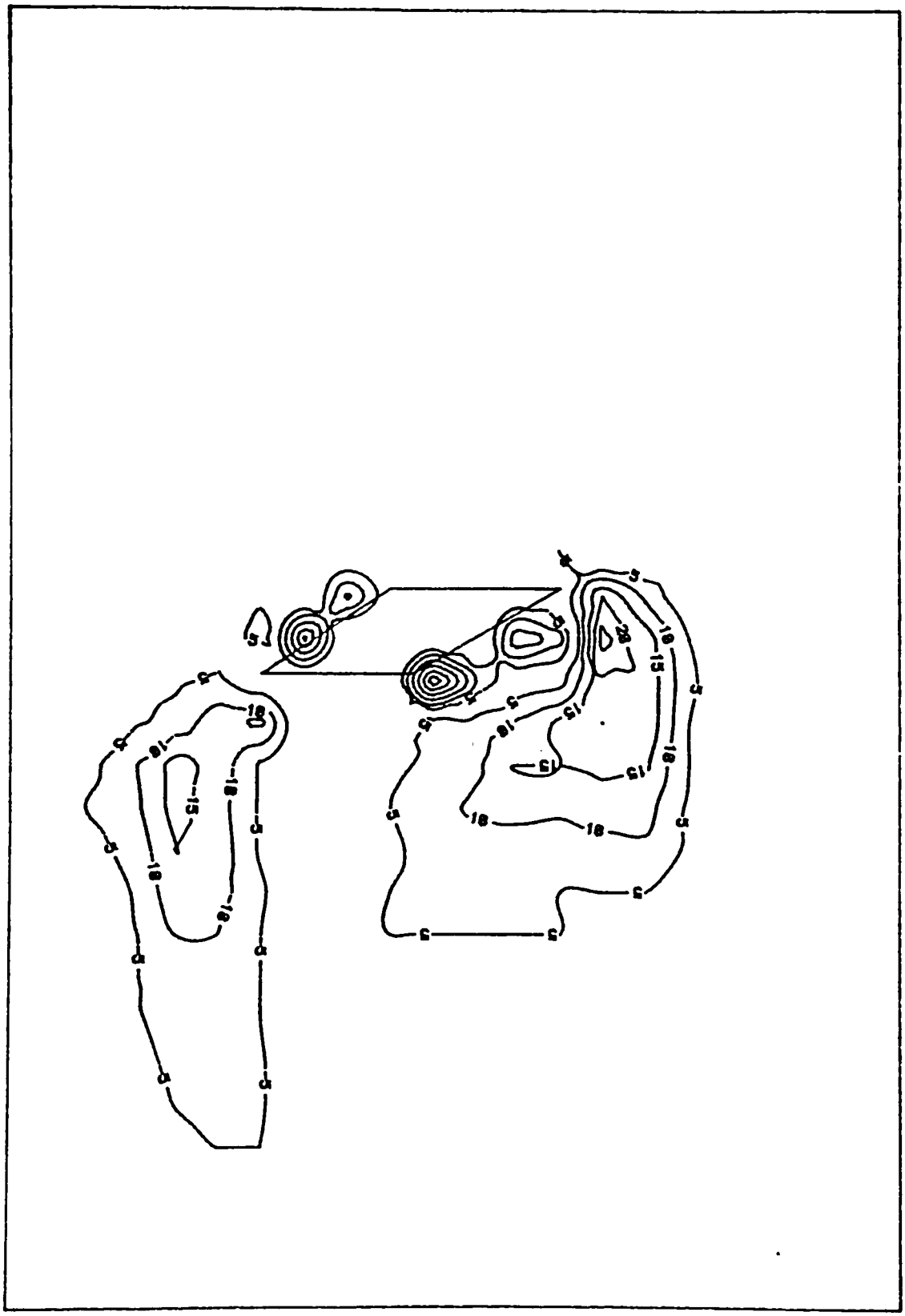

LENGTH SCALE —— 200 M

TIDAL HEIGHT = 2.22 M

TIDAL PERIOD = 12.6 HR

VORTICITY IN 10^{-4} S^{-1}

MANNING NUMBER = 0.025

Figure 6.27 Predicted vorticity distribution just before high water level with the exclusion of all lateral shear stresses

VORTICITY DISTRIBUTION AROUND RATTRAY ISLAND

TIME = 36.5 HR

N

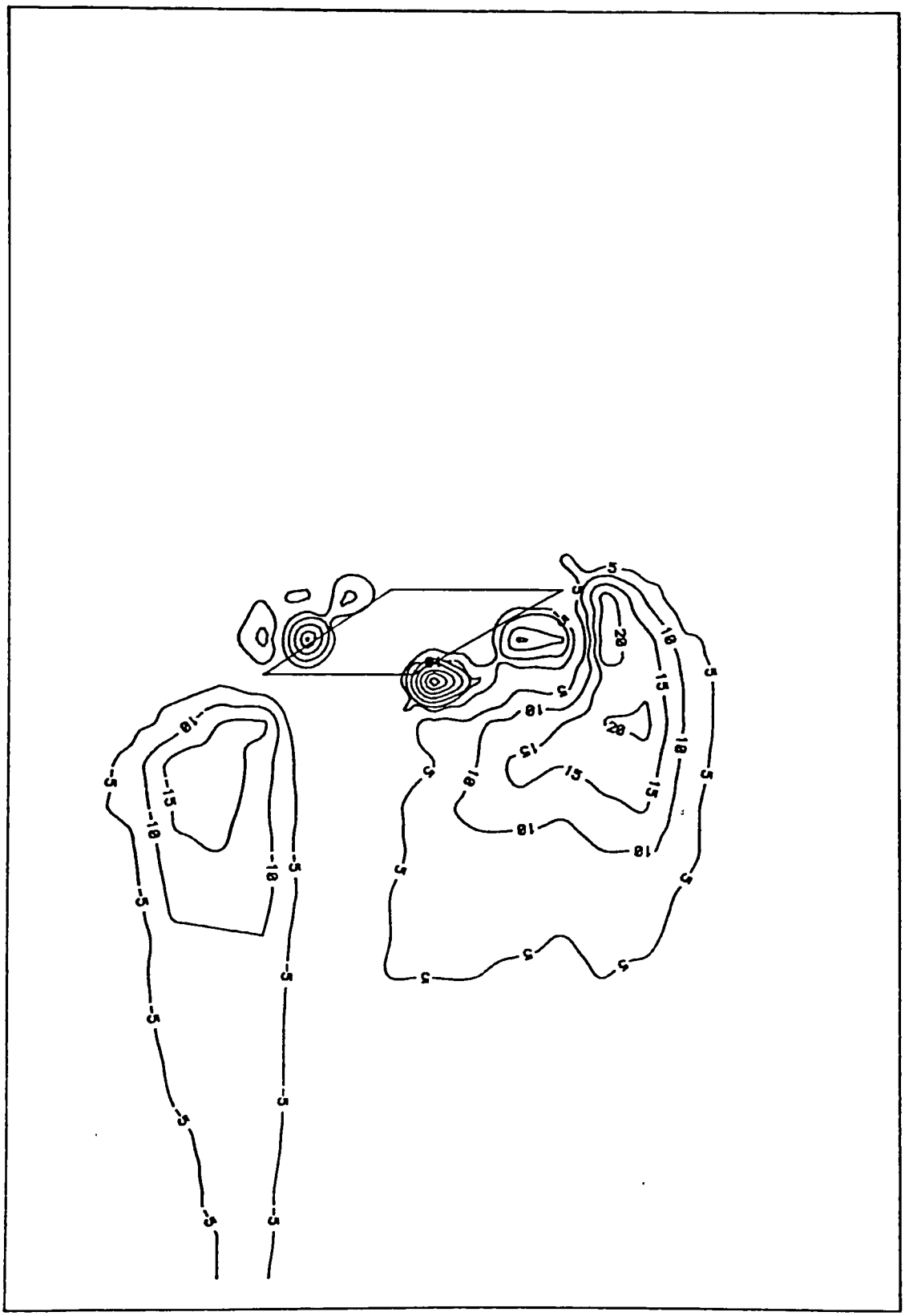

LENGTH SCALE —— 200 M

TIDAL HEIGHT = 2.22 M

TIDAL PERIOD = 12.6 HR

VORTICITY IN 10^{-4} S^{-1}

MANNING NUMBER = 0.015

Figure 6.28 Predicted vorticity distribution just before high tide for Manning coefficient of 0.015

VORTICITY DISTRIBUTION AROUND RATTRAY ISLAND

TIME = 36.5 HR

N

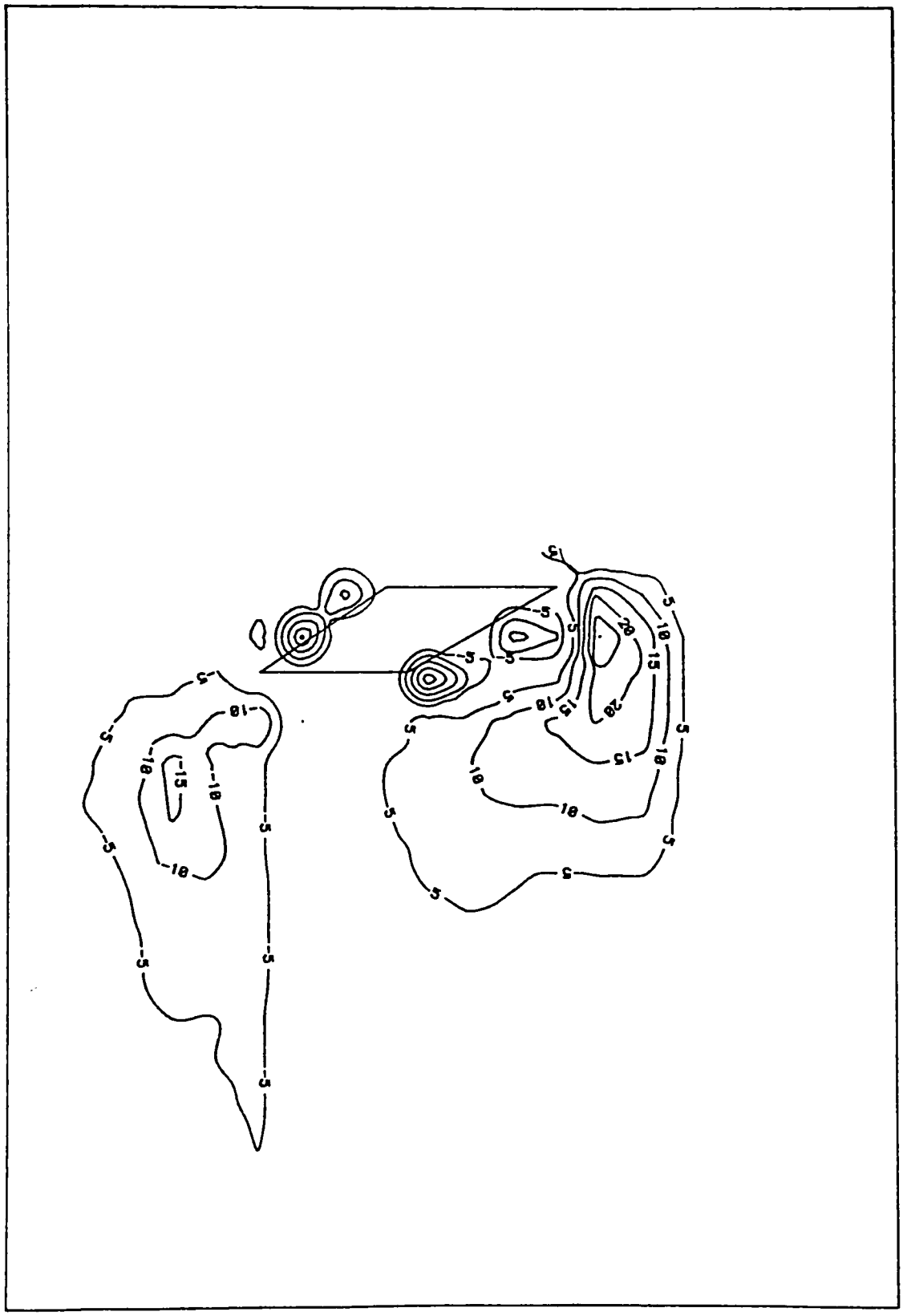

LENGTH SCALE —— 200 M

TIDAL HEIGHT = 2.22 M

TIDAL PERIOD = 12.6 HR

VORTICITY IN 10^{-4} S^{-1}

MANNING NUMBER = 0.035

Figure 6.29 Predicted vorticity distribution just before high tide for Manning coefficient of 0.035

VORTICITY DISTRIBUTION AROUND RATTRAY ISLAND

TIME = 36.5 HR

N

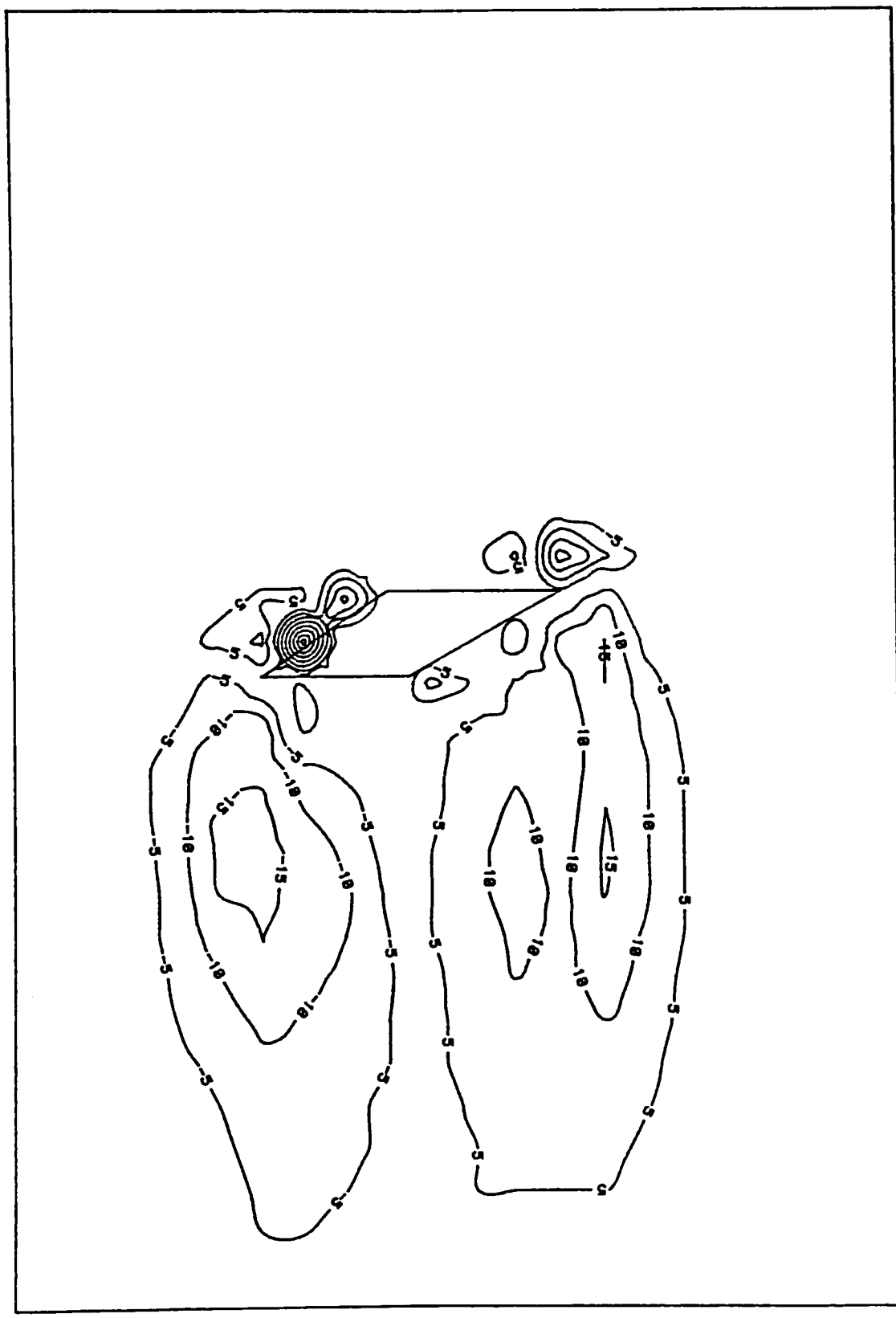

LENGTH SCALE —— 200 M

TIDAL HEIGHT = 2.24 M

TIDAL PERIOD = 12.6 HR

VORTICITY IN 10^{-4} S^{-1}

MANNING NUMBER = 0.025

Figure 6.30 Predicted vorticity distribution just before high tide for horizontal bed

CHAPTER 7

APPLICATION B: MODELLING OF TIDAL CIRCULATION AND FLUSHING IN COASTAL BASINS

7.1 Introduction

The second application of the numerical model was to narrow-entranced harbours having idealised geometries. The main objective has been to simulate the internal tide-induced circulatory velocity fields - established within the basins as a consequence of flow separation at the entrance tip - and the flushing characteristics.

Water quality problems, of considerable importance in the planning and design of harbours as a result of the growing concern as to their environmental impact, are generally assumed to be dependent upon the flow patterns and tidal flushing in such coastal basins. A number of laboratory model studies were recently undertaken by various researchers, either for site specific harbours (see Nece and Richey(1972,1975), Nece et al(1980)) or for idealised harbours (see Nece et al(1976), Jiang and Falconer(1983), Nece(1984)), with the objectives of investigating the influence of various geometric and boundary parameters on the velocity fields and the tidal flushing characteristics. Despite the acknowledged shortcomings of laboratory models, particularly with reference to vertical distortion and low Reynolds numbers and the corresponding improper scaling of diffusion-dispersion processes (see Ippen(1966)), in the absence of field data, they are useful in providing guided indications as to the behaviour of the prototypes.

The laboratory model studies of harbours of idealised geometry, where relative performance has been linked to geometric parameters, have given rise to information that suggests trends in the effects of a number of parameters on the internal circulation and flushing performance of small harbours. In testing the validity of the numerical model, these findings were compared with the numerical model predictions. In addition, a series of laboratory tests were undertaken with the objective of collecting quantitative data on the circulatory velocity fields within such idealised coastal basins, with the aim of undertaking direct comparisons with the corresponding numerical model predictions.

7.2 Laboratory Tests of Idealised Coastal Basins.

All the hydraulic models had a rectangular shape, a flat bottom, vertical sides and an asymmetric entrance, see fig.(7.1). The plan-form area, A, of the model harbours was kept constant throughout the laboratory tests, whereas the length to breadth ratio, L/B, was varied with the resulting model dimensions being similar to those chosen by Jiang and Falconer(1983), thus enabling comparisons to be made with their test results.

The hydraulic models were treated as vertically distorted models of idealised prototype harbours having dimensions and experiencing tidal conditions similar to many small harbours and marinas in Puget Sound, Washington, U.S.A., see Nece et al(1980). The prototype harbour was assumed to have a plan-form area of 0.16 km^2, an entrance width of 100 m, a mean depth of 5.9 m, together with a sinusoidal, semi-diurnal tide of period 12.4 hr and range 5.2 m. Using horizontal and vertical length scale ratios of 1:500 and 1:50 respectively, with a vertical distortion

ratio of 10:1, the corresponding laboratory model scaled dimensions were:

Plan-form area - 0.64 m^2

Entrance width - 200 mm

Mean depth - 118 mm

Tidal range - 104 mm.

Likewise, using a Froude law scaling relationship for dynamic similarity, a conventional approach in the physical modelling of free surface flows (see Henderson(1966)), the corresponding velocity and time scales were 1:7.07 and 1:70.7 respectively, resulting in a model tidal period of 10.52 min.

7.2.1 Experimental Arrangement, Procedure and Results.

The harbour model, constructed primarily of plywood, consisted of a horizontal bed and four sidewalls, two of which were movable. Throughout the tests, the two movable walls were adjusted, enabling the length and breadth dimensions of the model harbour to be varied. The model was positioned at one end of a 5 m x 3 m x 1 m deep PVC tidal tank, with the harbour bed being raised above the tank floor to give the correct depth at the mean water level. The constant amplitude, constant period tides were produced by a tidal generator, situated diametrically opposite the harbour model in the tidal tank. This tidal generator consisted of a vertically oscillating weir driven by a small motor through appropriate gear reducers and an off-set cam, giving simple harmonic motion. The tank was fed by a constant-rate water supply which produced a small overflow over the weir, with the water level within the tank therefore oscillating in phase with the weir. The harmonic motion of the weir produced an oscillatory water surface within the tank which gave rise to nearly sinusoidal model tides. The experimental layout is shown in

fig.(7.2).

A grid was marked on the base of the model, see fig.(7.3), so that the intersection points coincided with every other grid point of the corresponding mathematical model grid representation. To measure the velocities at these grid points drogues were used, which were made of 8 cm long plastic coated drinking straws, sealed and weighted at one end to provide sufficient penetration for the drogues to move with the local depth-averaged velocity. The use of a current meter was considered, but was unsuitable since the velocities within the harbour were generally too small and outside the measurable ranges of the available current meters. A perspex sheet marked with the grid of the harbour basin and resting on top of the sidewalls of the harbour in a horizontal position, was used for tracking the drogue paths, see fig.(7.4).

To check the accuracy with which the drogues measured the water velocity in the harbour models, the following experiment was conducted: In a 600 mm wide flume, a constant discharge was allowed to flow with velocities of magnitudes well within the range of standard current meters. A stretch of 5 m was chosen, and the water velocity was measured at five equidistant points along the centreline of the stretch, at a depth of about 2.5 cm below the surface, using an A.Ott meter of 30 mm diameter. Subsequently, the drogues were positioned on the centre line at the top of the stretch and allowed to travel to the other end while their time of travel was recorded. Their penetration into the flow was about 5 cm. The velocities measured by the drogues were then compared to the average velocity given by the A.Ott meter over the whole stretch. The difference was only of the order of 1-2%, indicating that the drogues' movement closely resembled that of the mean flow. The results

are given in table(7.1).

The tidal generator was first run for two complete tidal cycles, to allow a steady internal circulation pattern to develop before measurements were taken. The drogues were then carefully inserted at fixed points, one minute before the flood and ebb tide mean water levels. The floats were then tracked for the next two minutes with their positions being marked on the perspex sheet every 5 seconds. The procedure was repeated until enough detail had been collected to allow the determination of the velocities, at most of the grid points, at mean water level for both the flood and ebb tides. Parallax errors were reduced in the tracking method by ensuring that an observer sighted down the vertical bore of the straw cylinder, arising as a result of the top of the straw remaining unsealed. Difficulties were encountered in measuring the velocities in some areas near the boundaries of the harbour, where surface tension effects caused the drogues to adhere to the sidewalls. For this reason the velocities at a number of grid points near the sidewalls were not determined. When drogues were inserted at the same time and place, but on different tidal cycles, they yielded pathlines in very close agreement with one another, indicating that the tidal velocity fields were similar.

Three different shapes of harbour were modelled, with L/B ratios of 1.0, 2.0 and 2.833, with the corresponding dimensions being given in table(7.2). The resulting measured velocity fields have been plotted to scale as depicted in figs.(7.5) to (7.9). For the harbour with L/B=2.833 only pathlines were determined on the ebb tide, see fig.(7.10), because the water velocities were very small towards the rear of the harbour and were impossible to measure. In comparing the flow patterns, it can be

seen that, for the square harbour, only one gyre developed in the basin on the flood tide, which subsequently dominated the flow field well into the ebb tide. For the rectangular harbour with L/B = 2.0, one large gyre developed at flood tide with signs of a second small gyre occurring in the rear portion of the harbour. Likewise, for the ratio of L/B = 2.833, this second gyre was found to be more dominant. For the entrance orientation chosen, the dominant gyre was always in the anti-clockwise direction, whereas the second less dominant gyre in the rear of the harbour rotated in a clockwise direction. The gyres occurring for L/B ratios of 2.0 and 2.833 did not dominate during the ebb tide, and it appeared that the angular momentum resulting from the jet-type inflow past the entrance, was being dissipated more positively by the side-wall and bed shear stresses. At the harbour entrance, for all three configurations, the flood tide inflow did not enter as a uniform flow normal to the entrance, but with a momentum component tangential to the harbour entrance, see figs.(7.5), (7.7) and (7.9). This gave rise to a strong contraction of the tidal jet and therefore enhanced its strength. This contraction, clearly seen with the use of a dye, is caused by the inertia of the ambient water flowing along the breakwater and enhanced by the main gyre established within the harbour. Similarly on the ebb tide, the outflow was not normal to the harbour entrance, see figs.(7.6), (7.8) and (7.10). The tangential component arose as a result of the angular momentum of the main gyre, which was not dissipated completely by the side-wall and bed shear stresses.

Finally, water level measurements were taken at the harbour entrance and plotted against time. The resulting experimental tidal curve was then compared to a sinusoidal curve as shown in fig.(7.11). As expected,

both curves were in close agreement and therefore it seemed reasonable to assume that the tidal generator produced sinusoidal tides.

7.3 The Numerical Model Applications and Validation

The numerical model was first applied to the physical model configurations and direct comparisons made between the experimental data and the numerical model predictions, thus enabling the validity of the numerical model to be assessed.

In the initial attempt to simulate numerically the circulatory velocity fields of the physical models, the computational domain was bounded by the harbour physical boundaries, with the harbour entrance being the only open boundary of the numerical model. Considering the application to the square shaped harbour, the computational domain consisted of 20x20 grid points with an equidistant spacing of 40 mm. The bed roughness characteristics were described by a Manning's coefficient of 0.012, such a representation being strictly applicable to fully rough turbulent flows only, see Massey(1979) and Henderson(1966). Although, in practice, for part of the physical model, or part of the tidal cycle, velocities are so low that transitional smooth turbulent or even laminar conditions may prevail, the frictional effects - as outlined later - have been shown to be relatively insignificant on the flow field characteristics of the harbour models. In addition, the Coriolis and wind stress effects were neglected in this and all subsequent physical model simulations, as they were also absent in the laboratory tests.

The open boundary conditions of the asymmetric harbour entrance were described in terms of, firstly, water elevations and, secondly, velocities. The first open boundary representation included a sinusoidal variation in water levels, giving:

$$\eta = a \sin (\omega t + \phi) \tag{7.1}$$

where a = tidal wave amplitude, ω = tidal frequency = $2\pi/T$, T = tidal period and ϕ = phase angle governing the initial conditions. The implementation of this open boundary representation involved, in addition, the omission of the advective accelerations at the open boundary in order to avoid non-linear instabilities, and the assumption that the tangential velocities were zero, i.e. the tidal jet was assumed to be normal to the harbour entrance during both inflow and outflow. The second open boundary representation involved the prescription of the velocity components normal to the entrance, with the assumption being made that the flow was uniform across the entrance width and the tangential velocity components were again zero. The normal velocity components were determined from the continuity equation by equating the flow rate across the harbour entrance with the vertical flow rate within the harbour, see Falconer(1974), giving:

$$U = \frac{LB\ a\ \omega\ \cos(\omega t + \phi)}{W\ (h + a \sin(\omega t + \phi))} \tag{7.2}$$

where W = entrance width.

At the closed boundaries, the no-slip condition was employed and the computational processes started from an initial state of rest, with the initial water elevation being at high tide everywhere. The model was run

for two tidal cycles and a timestep of 0.4 s, giving a Courant number of about 10.8. Earlier tests with a timestep of 0.2 s, corresponding to a Courant number of 5.4, resulted in velocity field predictions which were very close to the predictions that arose from the timestep of 0.4 s.

In comparing the velocity field predictions for the two open boundary representations with the experimental data, it appeared that the water elevation condition imposed at the open boundary was unsatisfactory, giving rise to distorted and unrealistic circulation patterns, see fig.(7.12). The prescription of the normal velocity components at the open boundary, on the other hand, gave a closer though not a particularly good agreement with the experimental results, see figs.(7.13) and (7.14). The numerically predicted gyres were smaller in size, with a different centre of rotation and smaller velocity magnitudes than those measured experimentally.

The above numerical tests have portrayed the sensitivity of the circulatory field within the harbour basins to the description of the flow characteristics at the harbour entrance. Both open boundary representations employed above, involved an over-simplification of the entrance flow conditions, as it was observed from laboratory measurements that the tidal flow through the harbour entrance was neither uniform nor normal to the entrance. However, since the circulatory flow field is induced by the flow conditions (separation mechanism) at the entrance, the accurate description of these open boundary flow conditions is clearly necessary. If the small-sized model domain described above were to be used, the knowledge of detailed and accurate flow data would be required, usually not available in practice as detailed measurements can be costly. It therefore appeared preferable to undertake the study on a

large-sized domain where the flow field sensitivity to the description of the boundary conditions would be reduced in the area of flow interest, by making the boundaries remote from this region. However, the expansion of the computational domain appeared to be inconsistent with the high accuracy required by the local study. A reconciliation of such requirements can be achieved by the use of nested grid models which, by combining grids of different scales, can improve the model resolution in the vicinity of the local study without requiring the fine resolution over the whole domain.

A distinguishing feature of nested grid models is the nature of the interaction between the grid scales, that is, how the information passes between two grids of different scales. One-way interaction models involve the initial computation of the overall coarse-grid model which in turn provides the boundary conditions for the independent computation of the small-sized fine-grid model. Two-way interaction models, on the other hand, require the simultaneous computation of both grids, thus enabling the regions of different spacings to be dynamically inter-linked. The latter method therefore allows the response of the coarse-grid domain to small-scale processes occurring within the fine-grid to be taken into account, giving rise to more coherent results over the computational domain. The dynamic coupling of the nested grids, however, requires a more complex computational code, see Elsberry(1978). On the contrary, in one-way interaction models it is inherently assumed that the large-scale motion of the coarse grid determines the small scale motion in the fine grid, without being affected by small-scale processes occurring within the fine grid. The imposed boundary conditions at the open boundaries of the fine grid, responding only to changes predicted in

the coarse grid, may therefore introduce errors to the fine-grid solution when interactions between the two regions of different scales is large (see Elsberry(1978)). However, one-way interaction models have been widely and successfully used, see Fisher(1981), Leendertse(1984) and Thabet et al(1985). Because of its relative simplicity, as opposed to the two-way interaction, the one-way interaction method has been considered and applied to the harbour simulations in this study.

7.3.1 The Nested Model

The overall coarse-grid domain was chosen to cover the whole plan-form area of the tidal tank and consisted of 27x34 grid points, of uniform grid spacing of 100 mm, and with the tidal tank bathymetry being as depicted in fig.(7.15). At the open boundary, water elevations were prescribed (as given by eqn.(7.1)), in the same manner as described previously, that is, with the omission of the advective acceleration terms and the assumption of zero tengential velocities along the boundary. Since the tidal flow entered and exited the tidal tank as a uniform flow and in a direction normal to the open boundary, such a boundary representation was justified in this study. At the closed boundaries, on the other hand, the no-slip boundary condition was implemented. A timestep of 0.84 s was used in the model, giving rise to a Courant number of about 9.0. Although the Courant number was relatively high, earlier simulations on the non-nested model for Courant numbers of 10.8 and 5.4 indicated little variation in the predicted velocity fields.

The domain of the fine-grid model covered the plan-form area of the model and extended beyond the harbour entrance - as illustrated by the shaded area in fig.(7.15) for the square harbour configuration. The open boundaries of the fine-grid model were required to be located well beyond the harbour entrance, so that the small inaccuracies at the fine-grid open boundaries did not disturb the internal flow field predictions (see Elsberry(1978)). The ratio of the grid scales between the coarse and fine grids in such models is arbitrary, although in practice it has been suggested that the ratio should be kept below about 5 (see Thabet et al(1985)). In this study the ratio of both the grid and time scales between the two nested grids has been chosen to be a factor of 3, giving rise to a Courant number of the order of 9 in both grids. The decrease in the grid size and, as a consequence, in the timestep of the fine-grid model required both the time and space interpolation of the coarse-grid model predictions in order to provide proper boundary conditions at the appropriate points along the open boundaries of the fine-grid model. In the interpolation process, linear variations of both velocities and elevations have been assumed throughout in both time and space.

Concerning the open boundary conditions of the fine-grid model, no guidelines were available as to the most suitable representation. Tests were therefore undertaken to determine the most appropriate combination of the open boundary conditions for this particular case study. The following combinations of open boundary conditions were tested at the four open boundaries of the fine-grid model (see fig.(7.16)) for the square harbour configuration:

(a) Water elevations and tangential velocity components at the lower boundaries, LB1 and LB2, and normal and tangential velocity components at

the upper boundaries, UB1 and UB2,

(b) normal and tangential velocity components at the lower boundaries, LB1 and LB2, and water elevations and tangential velocity components at the upper boundaries, UB1 and UB2, and

(c) normal and tangential velocity components at all four open boundaries.

All three combinations gave similar velocity field predictions within the harbour, with some discrepancies at the open boundaries. Combination (a) yielded the worst flow field predictions at the boundaries, where unrealistic circulation patterns were predicted along the water elevation boundaries, as illustrated by fig.(7.17). The strength of the gyre inside the harbour was also weaker than that given by the combinations (b) and (c). In combination (b), the water elevation boundary UB1 predicted a distorted "wiggly" velocity field at this boundary at certain tidal phases, as shown in fig.(7.18). However, this boundary disturbance did not seem to affect the velocity field inside the harbour. The prescription of velocities at all open boundaries, combination (c), yielded the best velocity field predictions in the areas under the direct influence of the open boundaries, as depicted by figs.(7.19) and (7.20) for the mean water flood and ebb tide respectively. However, this combination gave rise to a poor reproduction of water elevations - a result not detected for any of the other combinations. This finding was in agreement with Boulot (see Fisher(1981)) and Verboom(1985), and is attributed by Boulot to the relative short distance between inflow and outflow boundaries, with the inflows and outflows being of similar magnitude. Since the variation in water elevation depends on the difference between inflows and outflows, a

small relative error at each boundary may involve a substantial error on the variation of water elevation. Such errors may arise from the interpolation of the coarse-grid model results at such boundaries. The treatment employed by Verboom(1985) has therefore been considered and adopted in the nested model described herein, this being the prescription of velocities at all but one boundary at which water elevations were prescribed to control the variation in water elevations in the computational domain. The open boundary UB2 was chosen for the prescription of water elevations, as the distortion of the velocity field at the other boundaries was greater when water elevations were prescribed at these boundaries. The similarity in the flow field predictions within the harbour for all the above combinations have indicated that the choice of the position of the open boundaries in the fine-grid model was appropriate, in that disturbances at the boundaries did not affect the prediction of the flow characteristics at the harbour entrance, and therefore the harbour interior, to any significant degree. At the close boundaries of the fine-grid model, like for the corse-grid model, the no-slip boundary condition was employed.

The bed roughness characteristics were represented, in both the coarse- and fine-grid models, in terms of the Colebrook equation (see Henderson(1966)):

$$\frac{1}{\sqrt{f}} \left(= \frac{C}{\sqrt{8g}} \right) = -\ 2\ \log_{10} \left(\frac{k_s}{12R} + \frac{2.5}{Re\sqrt{f}} \right) \qquad (7.3)$$

where k_s = length parameter characteristic of bed roughness

$\cong$ 0.00061 (for the plywood surface, see Henderson(1966))

Re = Reynolds number = $4UR/\nu$

R = hydraulic radius

$\cong H$ (for shallow water flows)

ν = kinematic viscosity

Equation(7.3) describes the friction factor over a range of flows - from smooth to rough turbulent - prevailing over different tidal phases or regions in the harbour model with the influence of Re on f decreasing as Re and the turbulence intensity increase. For the determination of f from eqn.(7.3), the Newton-Raphson iterative method has been used.

The computational procedure adopted in the solution of the nested grid has already been described in Section 5.5 and involved the interactive execution of the computations in the two grids, with the grids remaining dynamically de-coupled. The model simulations were always started from an initial state of rest, with the initial water elevation being at low tide throughout the computational domain. The simulations were run and executed for two complete tidal cycles, with printouts of the velocity and elevation fields being requested at every quarter of the tidal cycle.

7.3.1.1 The Flow Field Simulations.

In the first series of simulations, the flow field predictions of the fine-grid model were compared with the coarse-grid model results and subsequently with the experimental results for the various rectangular harbour configurations. Although the main part of the study took place in the region of the fine-grid model, comparisons with the coarse-grid model yielded information on the usefulness of nested modelling. The L/B ratios of the harbours modelled for this set of comparisons were 1.0, 1.833 and 2.6, with the two rectangular harbour configurations being

slightly different to those modelled in the laboratory. This discrepancy occurred because the laboratory model configurations did not fit precisely into the uniform grids chosen for the nested models - a problem not envisaged at the time of the laboratory tests. The L/B ratios adopted in the nested models were as close as possible to the laboratory model ratios for the same plan-form area A and, since the difference in the ratios was relatively small it was considered reasonable to make direct comparisons between the numerical and experimental results for all three harbour model configurations.

Apart from the predictions of small-scale processes like the corner eddies, permitted by the finer resolution of the fine-grid model, large differences in the gross flow characteristics were apparent between the coarse- and fine-grid model predictions at various tidal phases. On the flood tide, a stronger circulation was predicted by the fine-grid model, which, for L/B ratios of 1.833 and 2.6, did not occupy the entire harbour basin. There were also obvious signs of the presence of a secondary, and much weaker, gyre at the rear of the harbour which was more pronounced at high tide. However, only one main gyre was predicted in the coarse-grid model, with the gyre occupying the entire basin - for example see figs.(7.21) and (7.22). On the ebb tide, the fine-grid models predicted a weakening circulation, becoming almost non-existent at low tide. This was contrary to the coarse-grid model prediction where a strong circulation dominating throughout the ebb tide was apparent - such differences are depicted in figs.(7.23) and (7.24).

In physical terms and in comparison with the laboratory model results, the fine-grid model predictions were more meaningful. The gyre strength reached a maximum at high tide, as a result of the continuing influx of angular momentum during the flood tide, and subsequently decayed throughout the ebb tide to reach a minimum at low tide, with the outflow jet inducing a net "torque" that opposed the circulation (see Falconer(1974)). In addition, the corner eddies were a result of the adverse pressure gradients that were present along the upstream sidewalls, giving rise to boundary layer separation and return flow.

Since the open boundaries of the fine-grid model were governed by the coarse-grid flow predictions, it was desirable to determine whether or not the unrealistic re-circulation within the harbour, predicted by the coarse-grid model, adversely affected the flow characteristics at these boundaries. The harbour circulation was therefore suppressed in the coarse-grid model by setting the advective accelerations to zero within the harbour basins only, as illustrated in fig.(7.25). From the resulting fine-grid predictions it was apparent that the suppression of this re-circulation did not affect the fine-grid model predictions to any appreciable degree, as can be seen by comparing figs.(7.26) and (7.24). It therefore appeared that the fine-grid model predictions of the flow patterns within the harbours were not noticeably influenced by the physically unrealistic re-circulation predicted by the coarse-grid model. This unrealistic re-circulation could be primarily attributed to the coarseness of the grid.

In comparing the velocity field predictions of the fine-grid models, depicted in figs.(7.27) to (7.32), with the corresponding measured velocity fields from the laboratoty tests, illustrated in figs.(7.5) to (7.10), the general agreement was encouraging for all three harbour configurations.

For the square harbour, the numerically predicted gyre was about the same size, at both flood and ebb mean water level, as the observed in the laboratory model, with the location of the centre of rotation being similar in both studies. The numerically predicted and measured velocities were of similar magnitudes, with the peak velocities being along the harbour perimeter. However, the observed gyre was slightly stronger on the whole, especially on the flood tide. The corner eddies predicted by the numerical model, though not observed in the corresponding physical model results, coincided with the regions where no velocity measurements were taken and have been observed by other investigators in similar physical model studies, including: Falconer(1974), Jiang and Falconer(1983), and Nece(1984). At the harbour entrance, the numerically predicted curvature of the streamlines was in good agreement with observations for the ebb tide, whereas on the flood tide the observed contraction of the incoming jet was far more pronounced in the physical model. A consequence of the stronger contraction of the incoming jet in the laboratory model, was the greater angular momentum input, giving rise to a stronger internal circulation to that predicted numerically.

For the rectangular harbour with an L/B ratio of 1.833, the agreement between the numerically predicted and measured velocity fields was not particularly good at mean water level for the flood tide. While observations for the physical model showed that the main gyre extended across the whole of the harbour interior, with signs of a small counter-rotating gyre in the vicinity of the rearmost corner to the entrance, the numerically predicted gyre was slightly weaker, smaller in size and did not extend to the rear of the harbour. Although no signs of a second gyre were detectable from the velocity field prediction at flood tide mean water level, see fig.(7.29), it appeared to develop as the tide progressed, and became more prominant at high tide - though much weaker than the main gyre. On the other hand, at mean water level for the ebb tide, both the numerically predicted and observed flow fields illustrated the weakening of the main gyre, with the respective flow patterns being in good agreement and having velocities of similar magnitudes. As for the square harbour, at the harbour entrance the similarity between the predicted and measured flow characteristics was greater on the ebb tide, with the flood tide jet contraction again being less pronounced in the numerical model .

Finally, the numerically predicted flow patterns for the rectangular harbour with an L/B ratio of 2.6 were very similar to those predicted for the harbour with an L/B ratio of 1.833. At mean water level on the flood tide, the predicted gyre was similar in size to the main gyre observed in the physical model, although the gyre was relatively weaker in the numerical model. However, contrary to the observed presence of a dominant second gyre, no appreciable circulation was predicted in the rear portion of the harbour at this tidal phase, although it was

predicted at a later stage on the flood tide and became more pronounced at high tide, see fig.(7.22). At mean water level on the ebb tide, both the predicted and observed flow, showed the weakening circulation in the harbour interior, and the general agreement between the respective flow patterns was encouraging.

Possible factors contributing towards the disparities between the numerical predictions and the laboratory results include:

(a) errors in the laboratory measurements, as the method employed is subject to gross inaccuracies and vulnerable to human errors,

(b) the difference in the representation of the harbour entrance, with the numerical model entrance represented as a gap in the breakwater, while in the physical model a small projection on the breakwater end existed which may have enhanced the tidal jet contraction and, as a consequence, the circulation strength,

(c) errors from improper boundary conditions at the open boundaries of the fine-grid model, as a result of the one-way interaction between the nested grids,

(d) errors in the numerical representation of the bed friction or of flow processes such as the turbulent momentum transfer.

From the fine-grid model flow field predictions for the square harbour, graphical representations have been produced for the free shear layer and bed generated shear stress distributions in an attempt to determine their relative significance in relation to the flow field. The free shear layer stress distribution at flood tide mean water level is illustrated in fig.(7.33), where the shear layer stresses attain their maximum value in the harbour interior. When compared to the corresponding bed generated shear stress distribution, depicted in

fig.(7.34), it can be seen that they are of a similar magnitude. However, the gradients of the shear layer stress in the mixing zone are greater, suggesting that their contribution to the transfer of momentum from the tidal jet to the circulation is greater, which is in line with the theory. In investigating further the influence of the free shear layer and bed generated shear stresses on the tidal circulation within the harbour, two specific test simulations were undertaken. In the first simulation, the free shear layer stress term was excluded from the equations of motion and the resulting flow field compared to the corresponding flow field predicted when the free shear layer stresses were included. The exclusion of the free shear layer stress has given rise to a small reduction in the circulation strength, as indicated by comparing the vorticity distributions for the respective flows, see figs.(7.35) and (7.36), suggesting that shear layer mixing is an important momentum transfer mechanism. The second simulation involved the exclusion of both the free shear layer and bed generated shear stresses and, as a consequence, the no-slip boundary condition since its explicit representation is included in the bed generated shear stress term. As for the Rattray Island case study, as outlined in Chapter 6, the numerical predictions of this simulation are in disagreement with theoretical expectations (see Flokstra(1977)), with a strong internal circulation being predicted despite the exclusion of the shear stress terms and the no-slip boundary condition. The increase in the circulation strength, as illustrated by comparing the vorticity distribution of fig.(7.37) with fig.(7.35), appeared to be predominantly due to the exclusion of the no-slip condition. This conclusion was confirmed by the results of a simulation on the rectangular harbour of L/B=2.6, where the free-slip boundary condition was imposed on the

harbour wall boundaries. This simulation predicted a strong single gyre occupying the whole of the harbour interior and dominating throughout the edd tide, as illustrated in fig.(7.38). The pronounced differences between experimental observations and the corresponding numerically predicted flow fields with a free-slip boundary condition, imply that the wall boundary layer was a dominant factor in contributing to the flow characteristics in the harbour models. This confirmed the importance of including the no-slip boundary condition in this study, and as a concequence, the bed generated shear stress.

Finally, in order to determine the sensitivity of the predicted flow patterns on the bed friction, a simulation was undertaken for the rectangular harbour of L/B=2.6, involving a constant Manning number (n=0.012) instead of the Colebrook eqn.(7.3). The resulting flow field was not dissimilar to the flow field predicted using the Colebrook equation in determining the bed friction, as illustrated by comparing the respective vorticity distributions given in figs.(7.39) and (7.40). This numerical test therefore suggested that the bed frictional effects were relatively unimportant in the flow field predictions for these particular harbour model studies.

7.3.1.2 The Tidal Flushing Simulations.

In analysing and investigating the tidal flushing characteristics for the model rectangular harbour configurations, the advective-diffusion equation was also included in the nested models, with the solution procedure described in Chapter 5 being employed.

At the open boundary of the coarse-grid model, the boundary condition was included in the manner described in section 5.4, during outflow, i.e. the boundary concentrations were obtained from values computed within the numerical domain as described in eqn.(5.7). Likewise, on the flooding tide the inflow was assumed to be clean water, i.e. zero concentration, which was in line with the physical model studies undertaken by Jiang and Falconer(1983) and performed in the same tidal tank. At the open boundaries of the fine-grid model, the concentration values were extrapolated from the coarse-grid model for both inflow and outflow.

The model simulations were always started from a state of rest at low tide, with an assumed constant initial concentration of 10 ppm existing within the model harbour. This condition was identical to that at the start of physical model studies as performed by Jiang and Falconer(1983) and Nece(1984), thereby allowing comparisons between the numerical and experimental model results. The low water definition for the starting time was chosen - in contrast to earlier studies performed by Nece and Richey(1972,1975) and Falconer(1974) - because at this tidal phase, residual currents rarely occurred in such physical models. The advantage in commencing the model at low tide was that the local conditions were more likely to be repeated from one cycle to another, as compared with starting at high tide when residual circulation was much more evident. However, in comparing the results obtained over a period of three tidal cycles from tests starting at both the low and high tide, Jiang and Falconer(1983) found that the gross flushing characteristics were very similar. All model simulations were executed for a period of two tidal cycles, with printouts of velocity, water elevation and

concentration fields being requested at every quarter of the tidal cycle. Such simulations required approximately 20 hrs of c.p.u. time on a VAX-11/750 computer.

The nested model was also applied to the rectangular harbour configurations, with L/B ratios of 1/1.833 and 1/2.6, thus a wider range of L/B ratios was considered, with the range being in line with the physical model studies of Jiang and Falconer(1983) and Nece(1984). The velocity field predictions for the harbour models with L/B ratios of 1/1.833 and 1/2.6 were similar to the velocity fields predicted for the harbour models with L/B ratios of 1.833 and 2.6 respectively, as illustrated in figs.(7.29) to (7.32). A local discontinuity occurred in the numerical model at the start of the computation of the constituent concentration fields in both nested grids for all harbour configurations. This discontinuity arose at the harbour entrance as a result of the sharp decrease in concentration from So in the harbour interior to zero everywhere outside the harbour. Finite difference schemes of the type employed in this study, are only strictly applicable to smoothly varying variables and, as outlined by Leendertse(1970), such discontinuities cannot be adequately represented by these computational schemes because their Fourier decomposition has many short period waves which cannot be resolved within the finite numerical grid. The effect is that a spatial disturbance is generated locally by the computation, which in this particular study often resulted in negative concentrations in the vicinity of the harbour entrance. In general, though, this effect is only local and mass conservation still applies, with the overall solution being unaffected, see Leendertse(1970). In a study on temperature distributions by Falconer(1981), however, the disturbances were not

confined to the locality of the discontinuity and gave rise to rather ambiguous results. A number of approaches may be taken in attempting to overcome this problem, which include among others (see Roache(1976)): (a) upstream differencing of the advective terms and (b) treating the discontinuity as a shock wave and thereby introducing just sufficient artificial diffusion to counteract the disturbances caused by the discontinuity itself. Both methods, however, smooth out the disturbances at the expense of accuracy as they may introduce sufficient numerical diffusion to undermine the actual physical diffusion and dispersion. In this particular study, the disturbance appeared at the early stages of the computation only and therefore no modifications to the original central difference representation of the advective-diffusion equation appeared necessary.

A useful and frequently adopted method in assessing and comparing the flushing efficiencies of different harbours is the determination of the average per cycle exchange coefficient, E. This indicates the fraction of water in the basin which is exchanged with the external flow field during each tidal cycle, and is defined as (see Nece and Richey(1975)):

$$E = 1 - (S_i/S_o)^{1/i} \qquad (7.4)$$

where So = initial spatially averaged concentration

S_i = final spatially averaged concentration after i tidal cycles

Equation(7.4) assumes identical, repetitive tides, with similar velocity fields and mixing patterns being reproduced from one tidal cycle to the next.

The exchange ratio E may also be estimated using the tidal prism method, which assumes that the water within the basin at low tide is thouroughly mixed with the external flow field during flood tide. The ratio is defined as:

$$TPR = \frac{\text{Basin Volume at High Tide} - \text{Basin Volume at Low Tide}}{\text{Basin Volume at High Tide}} \qquad (7.5)$$

where TPR is known as the tidal prism ratio. Use of the simple tidal prism ratio, despite its acknowledged shortcomings, is useful for comparing the flushing characteristics of small harbours which communicate directly with ambient waters and are not subject to fresh water inflows (see Nece and Richey(1975)). Knowing the tidal prism ratio, the flushing efficiency can then be evaluated using the established definition (see Nece et al(1976)):

$$\eta = \frac{E}{TPR} \times 100\% \qquad (7.6)$$

and compares measured water exchanges with those predicted by the simple tidal prism theory.

A statistical measure of the uniformity of mixing in the harbour basin was also used in this analysis, and for this purpose the standard deviation of the constituent concentration within the basin, SD, was evaluated according to the following definition (see Chatfield(1978)):

$$SD = \sqrt{\frac{\sum_{i=1}^{N} (S_i - \bar{S})^2}{(N-1)}} \qquad (7.7)$$

where $\bar{S}$ = spatially averaged concentration in the harbour interior

S_i = concentration for the ith grid square within the harbour

N = number of grid squares within the harbour

The standard deviation provides an indication of the uniformity of mixing within the basin, with the smaller values indicating a more uniformly mixed basin.

The numerically predicted concentration results have been assessed and are summarised, for the final tidal cycle, in table(7.3). Graphical representations of the exchange coefficient E, assumed to be related to the overall water quality characteristics within the harbours, and the standard deviation SD over the range of L/B ratios considered are shown in fig.(7.42) for the fine-grid model predictions.

In interpreting the results of fig.(7.42) in some detail, a few observations are apparent. A marked reduction is depicted in the exchange coefficient E and the uniformity of mixing for L/B ratios of less than approximately 1/2 and greater than 2. The general trends of the E curve are in agreement with the physical model results of Falconer(1974), Jiang and Falconer(1983) and Nece(1984). Over the range of L/B ratios from approximately 1/2 to 2, the variation in the exchange coefficient E and standard deviation SD is small, with the numerical model predicting that the square harbour configuration is the ideal shape for maximum overall flushing characteristics. This observation is not in agreement with the physical model results of Jiang and Falconer(1983), illustrated in fig.(7.43), from a study performed on physical model harbours with similar geometric and flow characteristics, where there is a noticeable dip in the exchange coefficient near the L/B value of unity. Nece et al(1976) and Nece(1984) have also indicated this phenomenon in similar physical model studies, which has been linked to the angular

momentum of the flow within the harbour. From a simple angular momentum control volume analysis performed by Falconer(1974), it was deduced that the square harbour would be the optimum rectangular harbour configuration for maximizing the interior velocity field since for a constant plan-form geometry the perimeter, which governs the wall shear forces is a minimum. Since however the square harbour has the minimum boundary perimeter, there is the greatest possibility in such small harbours that the ambient water, entering as a two-dimensional jet, will be able to circumnavigate the basin with a velocity component along the breakwater side as it approaches the entrance from within. If this jet reaches the entrance at about high tide, some of it is reflected back into the basin and some leaves the harbour without accomplishing a significant exchange. It is believed that the dips on the E curves near L/B=1.0 could reflect this phenomenon. Possible causes of the discrepancy in the model predictions may include:

(a) the "front" of the tidal jet not reaching the entrance at high tide, with the tidal jet being slower in the numerical model than in the physical model, and as a result more effective mixing is achieved during the ebb tide, (b) the errors introduced at the fine-grid model open boundaries as a result of the one-way interaction between the nested grids, for both the hydrodynamic and mass transport processes.

Another discrepancy between the model predictions and the physical model results of Jiang and Falconer(1983) was that the latter gave rise to exchange coefficients which were larger than the TPR, i.e. $\eta > 100\%$. However, Nece et al(1976) and Nece(1984) found that the exchange coefficients were less than the TPR for a similar tidal range and TPR, with the flushing efficiencies increasing and exceeding 100% as the tidal

range decreased. The increased efficiency for a decreasing tidal range, was attributed to the slower tidal jet associated with lower tidal ranges, which may not circumnavigate the entire harbour but rather move unmixed basin water into a position where it leaves the harbour on the subsequent ebb tide. This situation may give rise to an exchange coefficient E that exceeds the TPR, i.e. $\eta > 100\%$, as predicted by assuming full mixing on the flood tide. Figure(7.42) also suggests that for rectangular harbours outside the L/B range of 1/2 ~ 2, the harbour configurations with L/B<1 - that is when the long axis parallels the seaward-side breakwater - have better flushing characteristics than the harbour configurations of L/B>1. This observation is in line with the results of Jiang and Falconer(1983), see fig.(7.43), and of Nece(1984) for similar geometric and flow characteristics. This phenomenon probably reflects the effects of a much weaker adverse pressure gradient arising from the sidewall diametrically opposite the entrance, in the case of L/B<1, and thereby resulting in a larger gyre - as illustrated in the comparison of figs.(7.41) and(7.31). Nece(1984) also found that a wider entrance gave rise to the opposite result, with rectangular harbours with L/B>1 having better overall flushing characteristics. This phenomenon may be the result of insufficient contraction of the tidal jet inflow at the entrance for harbour configurations with L/B<1. For an increasing entrance width, the breakwater length becomes smaller, and hence the ambient water currents along the breakwater become weaker, thereby reducing the contraction of the tidal jet at the entrance.

Finally, graphical representations of the spatial distribution of constituent concentration have been produced, as illustrated in figs.(7.44) to (7.48) for the fine-grid model predictions at the end of

one tidal cycle. Information on the local water exchange and uniformity of mixing can be obtained from such plots, and regions of poor local exchange - potential "hot spots" - can be identified. The concentration contour plots of figs.(7.44) to (7.48) indicate that the harbour corners are regions of poor local exchange, and can be eliminated by the rounding of the interior corners as illustrated by Nece(1984). It can also be seen from comparisons of such plots that the harbours with L/B ratios of 1/2.6 and 2.6 have the worst flushing characteristics, with the latter possessing slightly larger regions of high constituent concentration.

7.4 Numerical Tests on Prototype Rectangular Harbours.

With the numerical predictions and laboratory measurements agreeing reasonably well for the physical model harbours, the nested model has finally been applied to the equivalent prototypes. The main objective of this exercise was to model directly the physical processes associated with the tidal action in such harbours, thus analysing the influence of scaling in the physical model simulations. A comparison of the prototype and physical model predictions was therefore undertaken in an attempt to highlight their differences.

The nested model was geometrically similar to that of the physical model tests, whose geometric and bathymetric features are illustrated in fig.(7.15). The harbour dimensions and tidal flow characteristics were outlined in section 7.2, with a Froude law similarity being assumed between the prototype and physical models. In addition, the earth's rotation was included in the prototype simulations, for a geographical latitude of 51.5°, and the bed roughness characteristics were described by using a Manning representation and a coefficient of 0.025.

The boundary conditions of the coarse- and fine-grid models were the same as those deployed in the physical model tests, with the exception of the coarse-grid model open boundary where the inclusion of the Coriolis term required the introduction of a water surface slope along this boundary - as described by eqn.(6.3) and employed in the Rattray Island study. All model simulations were executed from an initial state of rest, at low tide, with a timestep of 60 s in the coarse-grid model and 20 s in the fine-grid model - giving rise to a Courant number of 9 in both models. The computations were performed for two tidal cycles, with printouts of the velocity, elevation, and concentration fields being again requested at every quarter of the tidal cycle.

7.4.1 The Flow Field Simulations

In comparing the flow field predictions for the prototype harbours with their respective physical model predictions, the following observations were made:

While the coarse-grid model flow patterns for the prototype and physical model harbours bear distinct similarities, as illustrated by comparing figs.(7.49) and (7.23) for the square harbour configuration, the fine-grid model velocity field predictions vary greatly. In the fine-grid model a single gyre was predicted for all prototype harbour configurations. During flood tide, the gyre extended over the entire basin, as shown in fig.(7.50) for the rectangular harbour with L/B=2.6, in comparison with the presence of two gyres in the corresponding physical model flow field of fig.(7.22). During the ebb tide the single gyre, although weaker, was still well defined at mean water level, see fig.(7.51), unlike the corresponding physical model predictions where the

gyre had almost disappeared at the same tidal phase, see fig.(7.32).

A comparison of the free shear layer and bed generated shear stress distributions within the prototype harbours at the time of flood tide mean water level - where free shear layer mixing attains its maximum strength - has shown that the free shear layer stress dominates completely within the mixing zone, as illustrated in figs.(7.52) and (7.53) for the square harbour configuration. However, similar comparisons for the physical model simulation have shown that the two stress distributions are of similar magnitudes. The exclusion of the free shear layer stress terms from the equations of motion gave rise to a small reduction in the circulation strength as for the physical model simulations - as indicated by comparing the vorticity distributions of figs.(7.54) and (7.55), given for the square harbour configuration. Likewise, the exclusion of both the free shear layer and bed generated shear stresses did not suppress the circulation, as indicated by the vorticity distribution in fig.(7.56). In addition, the inclusion of the free-slip condition gave rise to an increased circulation and shifted the centre of rotation towards the rear of the basin, as shown by comparing figs.(7.57) and (7.50). This implied that the no-slip boundary condition, which represents the effects of the wall boundary layer, noticeably influences the flow characteristics.

Finally, an increase in the Manning coefficient (from 0.025 to 0.035) noticeably reduced the circulation strength, as illustrated by comparing the respective vorticity distributions of figs.(7.58) and (7.59), suggesting that frictional effects were important in the flow features within the prototype harbours. On the contrary, the flow field predicted by the physical model simulations appeared to be relatively

insensitive to the bottom friction.

In attempting to establish the possible causes for the differences between the prototype and physical model simulations, the equations of motion have been expressed in a dimensionless form in order to identify the dimensionless scaling coefficients and determine the degree of scaling of the various terms in the physical model. Considering the x-direction momentum eqn(2.27), it can be expressed in a dimensionless form, giving:

$$\frac{\partial(U^*H^*)}{\partial t^*} + \frac{\partial(U^{*2}H^*)}{\partial x^*} + \frac{\partial(U^*V^*H^*)}{\partial y^*} - E_c\, V^*H^* + \frac{1}{Fr^2} H^* \frac{\partial \eta^*}{\partial x^*} + \lambda\, U^* \sqrt{U^{*2}+V^{*2}}$$

$$- \delta\, R_e\, U^*\, H^{*2} \frac{\partial U^*}{\partial y^*} - \frac{1}{2\sqrt{2\pi R}}\, U_1^{*2}\, H^* \frac{\partial}{\partial y^*} \left(e^{-\frac{R}{2}\left(\frac{y'}{x'}\right)^2} \right) = 0 \qquad (7.8)$$

with the non-dimensional variables being defined as:

$U^*=U/Uo$; $V^*=V/Uo$; $H^*=H/d$; $\eta^*=\eta/d$; $t^*=(Uo/L)t$; $x^*=x/L$; $y^*=y/L$; $U_1^*=U_1/Uo$

and where L = any representative horizontal length in the harbour

Uo= any representative velocity length in the harbour

d = any representative vertical length in the harbour

δ = a constant

The scaling coefficients of eqn.(7.8) have been defined as:

E_c = Coriolis scaling number = f_cL/Uo

Fr = Froude scaling number = $Uo/\sqrt{gd}$

λ = Friction scaling number = fL/d

R_e = Bed generated turbulence scaling number = $\sqrt{f}d/L$

For the Froude law scaling relationship existing between the prototype and physical model for dynamic similarity, the prototype/model ratios of the various scaling factors were, as depicted in Table(7.4). It can be

seen from Table(7.4) that the physical model under-estimates the magnitude of frictional dissipation in the harbour by a factor of about 9 and over-estimates the rate of transfer of momentum by bed generated turbulence by a factor of about 10.5. These scaling effects have been reflected in the comparisons of the numerical model predictions.

7.4.2 The Tidal Flushing Simulations

In simulating the tidal flushing characteristics of the prototype harbour configurations an interesting problem was encountered. The disturbances caused by the discontinuity, present at the harbour entrance at the start of the computation as the constituent concentration decreased abruptly from So in the harbour basin to zero in the ambient water, persisted throughout the computation and spread across the computational domain. This observation suggested that the constituent transport was governed predominantly by advection in the prototype simulations, with the dispersion terms of the advective-diffusion eqn.(2.64) having little effect on smoothing out these disturbances. In contrast, in the physical model simulations the disturbances caused by the discontinuity were smoothed out by the numerical model at an early stage in the computation. This implied that there was sufficient diffusion in the numerical model to smooth out such disturbances, and suggested that the dispersion term played a more important role in the advective-diffusion processes in the physical model.

The question of mass-transport similitude in the physical model, has also been approached by expressing the advective-diffusion eqn.(2.64) in a dimensionless form, with the dimensionless scaling parameters being identified as follows:

$$\frac{\partial(S^*H^*)}{\partial t^*} + \frac{\partial(H^*U^*S^*)}{\partial x^*} + \frac{\partial(H^*V^*S^*)}{\partial y^*} = R_s \left\{ \frac{\partial}{\partial x^*} \left[H^* D^*_{xx} \frac{\partial S^*}{\partial x^*} + H^* D^*_{xy} \frac{\partial S^*}{\partial y^*} \right] \right.$$

$$\left. + \frac{\partial}{\partial y^*} \left[H^* D^*_{yx} \frac{\partial S^*}{\partial x^*} + H^* D^*_{yy} \frac{\partial S^*}{\partial y^*} \right] \right\} \qquad (7.9)$$

with the non-dimensional variables being:

$$U^* = U/Uo;\ V^* = V/Uo;\ S^* = S/So;\ H^* = H/d;\ x^* = x/L;\ y^* = y/L;\ t^* = (Uo/L)t$$

$$D^*_{xx} = \gamma \frac{k_\ell U^{*2} + k_t V^{*2}}{\sqrt{U^{*2} + V^{*2}}} H^* \qquad D^*_{yy} = \gamma \frac{k_\ell V^{*2} + k_t U^{*2}}{\sqrt{U^{*2} + V^{*2}}} H^*$$

$$D^*_{xy} = D^*_{yx} = \gamma \frac{(k_\ell - k_t)\, U^*V^*}{\sqrt{U^{*2} + V^{*2}}} H^*$$

γ = a constant

where Uo, So, L and d are representative parameters for the flow characteristics in the harbour. The scaling coefficient R_s is defined as the dispersive scaling number and is equal to $\sqrt{f}d/L$. The dispersion scaling number R_s is equal to the bed generated scaling number R_e, and as illustrated in Table(7.4), the physical model over-estimates the dispersion process by a factor of 10.5.

In extending the comparisons between the tidal flushing characteristics for the prototype harbour configurations and the respective physical model results, the discontinuity was modelled by using upstream differencing for the advection terms of the advective-diffusion eqn.(2.64). This technique has been adopted despite its adverse effects on accuracy, see Taylor and Morgan(1981), because of its relatively simple implementation. Accuracy has not been considered to be of paramount importance, because of the relatively small grid spacing, and furthermore the objective of the study was to determine

trends rather than accurately represent the flushing characteristics. The results for the final tidal cycle have been summarised in Table(7.5) and graphical representations of the exchange coefficient E and standard deviation SD, over a range of L/B ratios, are depicted in fig.(7.60).

In interpreting the results of fig.(7.60), a few observations are apparent. Over the range of L/B ratios considered, the variation in the exchange coefficient E and the standard deviation SD was small. However, there is a noticeable dip in the E curve near the L/B ratio of unity, a phenomenon also shown in the laboratory model results, see fig.(7.43), but not predicted by the numerical model in the physical model simulations, see fig.(7.42). The flushing efficiency was shown to be maximum at the L/B=2.6, with a further simulation for L/B=4.0 indicating a deterioration as the L/B ratio was increased further. In contrast to the physical model predictions, the flushing efficiency was marginally better for L/B=2.6 than L/B=1/2.6. However, it was thought that the direction of the outflow tidal jet on the ebb tide was the main cause of this effect. The tangential velocity of the tidal jet at the harbour entrance, during the ebb tide, was larger when the harbour's longest dimension was parallel to the entrance, as a result of the combination of the angular momentum of the main gyre and the inertia of the flow along the breakwater from within the harbour. This was particularly so in the prototype model, where a single gyre was predicted over the entire basin, as compared with the physical model predictions where the main gyre was nearest to the entrance with the tidal jet exiting the harbour at a smaller inclination to the entrance. Comparisons showed that the larger the inclination to the entrance of the outflow tidal jet, the larger the size of the circulation cell developed in the ambient waters, as

illustrated by comparing the velocity field of figs.(7.61) and (7.49). This exterior circulation cell occurred as a result of separation at the entrance and enhanced by the presence of the tank wall boundaries which were relatively close to the harbours. The larger exterior cell subsequently transported the polluted waters further away from the entrance and mixed with ambient waters over a larger area causing a more pronounced dilution. However, the physical model predictions did not reflect this phenomenon which was probably undermined by the existence of multiple cells within the harbour. In addition, due to the vertical distortion in the physical model, the ramp to the platform (as shown in fig.(7.15)) was consequently much steeper than the corresponding slope in the prototype and, as shown by Pingree and Maddock(1980), and illustrated in eqn.(2.57), such gradients in the bathymetry give rise to vorticity production. The greater circulation in the physical model ambient waters, caused by the steeper bathymetric gradients, might therefore have resulted in more polluted water being returned to the basin on the subsequent flood tide. A further observation was that the comparisons of the SD curves showed that mixing in the prototype harbours was more uniform, which may have been caused by the existence of a single gyre which distributed the constituent more uniformly over the harbour.

7.5 Conclusions

In general, the one-way interaction nesting technique has been applied successfully to the tidal processes in physical models of idealised prototype harbours, with the agreement between laboratory measurements and numerical model predictions being encouraging.

The differences in the numerical results of prototype harbours and their respective physical models have highlighted the problems associated with physical model studies and have raised questions as to the suitability of distorted physical models.

The vertical distortion and Froude law scaling for dynamic similarity between prototype and physical models has resulted in an over-estimation of dispersion-diffusion processes and momentum transfer by bed generated turbulence, and an under-estimation of the effects of bed friction. These differences were reflected in the comparisons of the velocity and concentration field predictions for the prototype and scaled physical model harbours.

Regarding the effects of the various terms of the governing equations on the flow characteristics, the following conclusions have been drawn: (1) The turbulent shear stresses and consequently the no-slip boundary condition have been shown to have a marked effect on the circulatory flows in both the prototype and physical model harbours, and (2) the exclusion of the lateral shear stresses did not suppress the circulation, in either the prototype or physical model, although this was contrary to theoretical expectations.

A.Ott Meter	Position 1	Position 2	Position 3	Position 4	Position 5
1st Reading 2nd Reading (m/s)	0.2156 0.2136	0.2156 0.2074	0.2136 0.2198	0.2115 0.2115	0.2136 0.2095
Average Velocity (m/s)	0.2146	0.2115	0.2167	0.2115	0.2115
U_1 (m/s) (average of 5 positions)	0.213				
Drogues	Drogue 1		Drogue 2		
1st Reading 2nd Reading 3rd Reading (sec)	24.0 23.0 23.2		24.4 23.8 23.2		
Average Time (sec)	23.4		23.8		
U_2 (m/s) (distance/time distance= 5 m)	0.214		0.210		
$\frac{U_1 - U_2}{U_1} \times 100\%$	-0.5		+1.4		

Table 7.1 Velocity Measurements Using Drogues and the A.Ott Meter

L/B	Model Dimensions			Prototype Dimensions		
	L(mm)	B(mm)	A(m^2)	L(m)	B(m)	A(km^2)
1.00	800	800	0.640	400	400	0.160
2.00	1120	560	0.627	560	280	0.157
2.833	1360	480	0.653	680	240	0.163

Table 7.2 Model and Prototype Harbour Dimensions

L/B Ratios	1/2.600	1/1.833	1.000	1.833	2.600
$\bar{S}$ - Average Concentration (ppm)	2.750	2.047	1.555	2.169	3.478
SD - Standard Deviation (ppm)	0.690	0.447	0.281	0.704	1.798
E - Exchange Coefficient	0.476	0.548	0.606	0.534	0.410
η - Flushing Efficiency	77.8%	89.5%	99.0%	87.3%	67.0%

Table 7.3 Numerical Predictions on Constituent Concentration Field in Physical Model Harbours at End of 2nd Tidal Cycle.

Scaling Parameters	Model/Prototype
Horizontal Scale (L)	1/500
Vertical Scale (d)	1/50
Fr ($Uo/\sqrt{gd}$)	1/1
Velocity Scale (Uo)	1/7.07
Time scale (L/Uo)	1/70.71
f ($8g/C^2$)	~ 0.03/0.027
λ (fL/d)	~ 1/9.0
R_e ($\sqrt{f}d/L$)	~ 10.5/1

Table 7.4 Scale Ratios

L/B Ratios	1/2.600	1/1.833	1.000	1.833	2.600	4.000
$\bar{S}$ - Average Concentration (ppm)	1.782	1.627	2.083	1.761	1.410	1.745
SD - Standard Deviation (ppm)	0.391	0.131	0.204	0.172	0.179	1.819
E - Exchange Coefficient	0.578	0.597	0.544	0.580	0.624	0.582
η - Flushing Efficiency	94.4%	97.5%	88.9%	94.8%	102.0%	95.1%

Table 7.5 Numerical Predictions on Constituent Concentration Field in Prototype Harbours at End of 2nd Tidal Cycle.

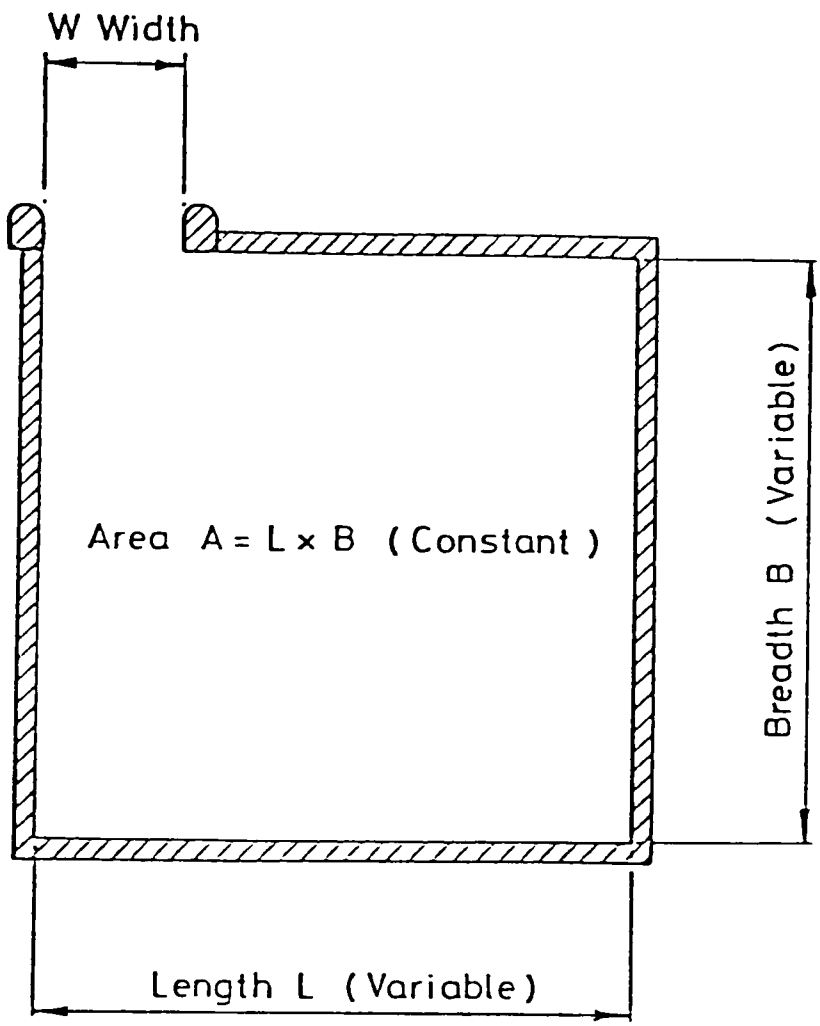

Figure 7.1 Plan view of idealised rectangular harbour

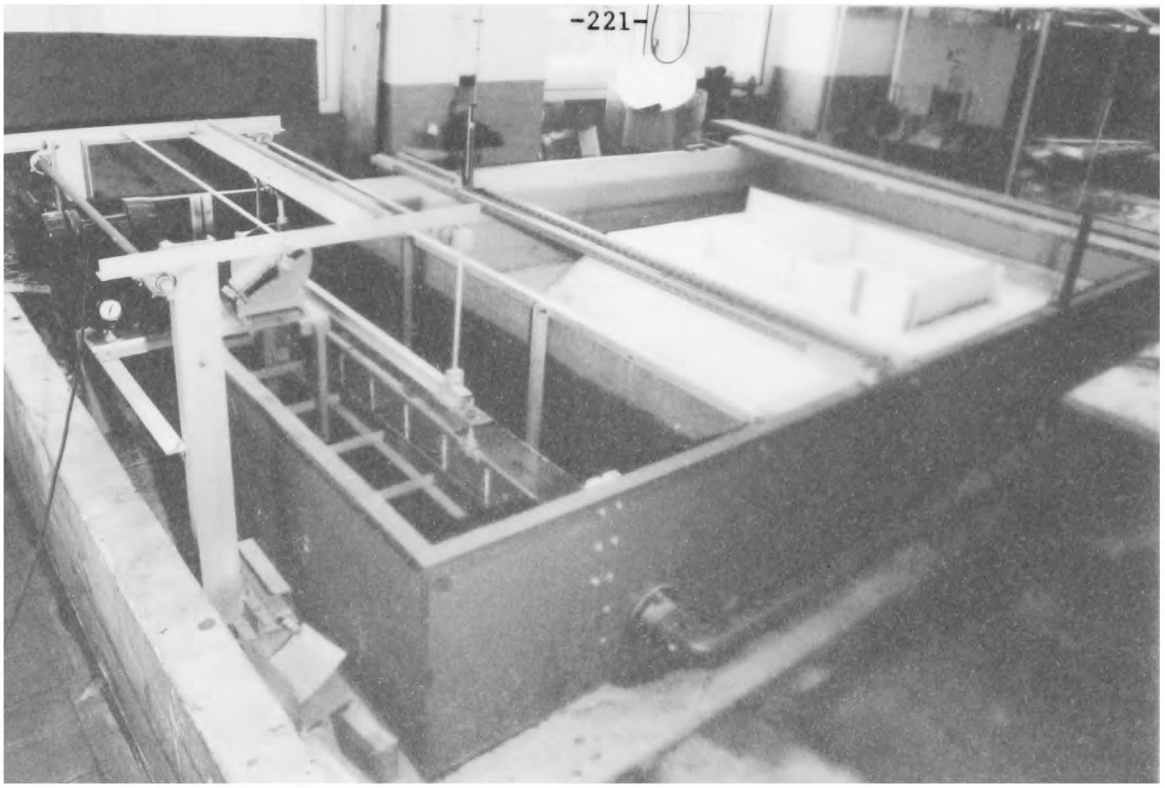

Figure 7.2 The laboratory tidal tank and location of the harbour model.

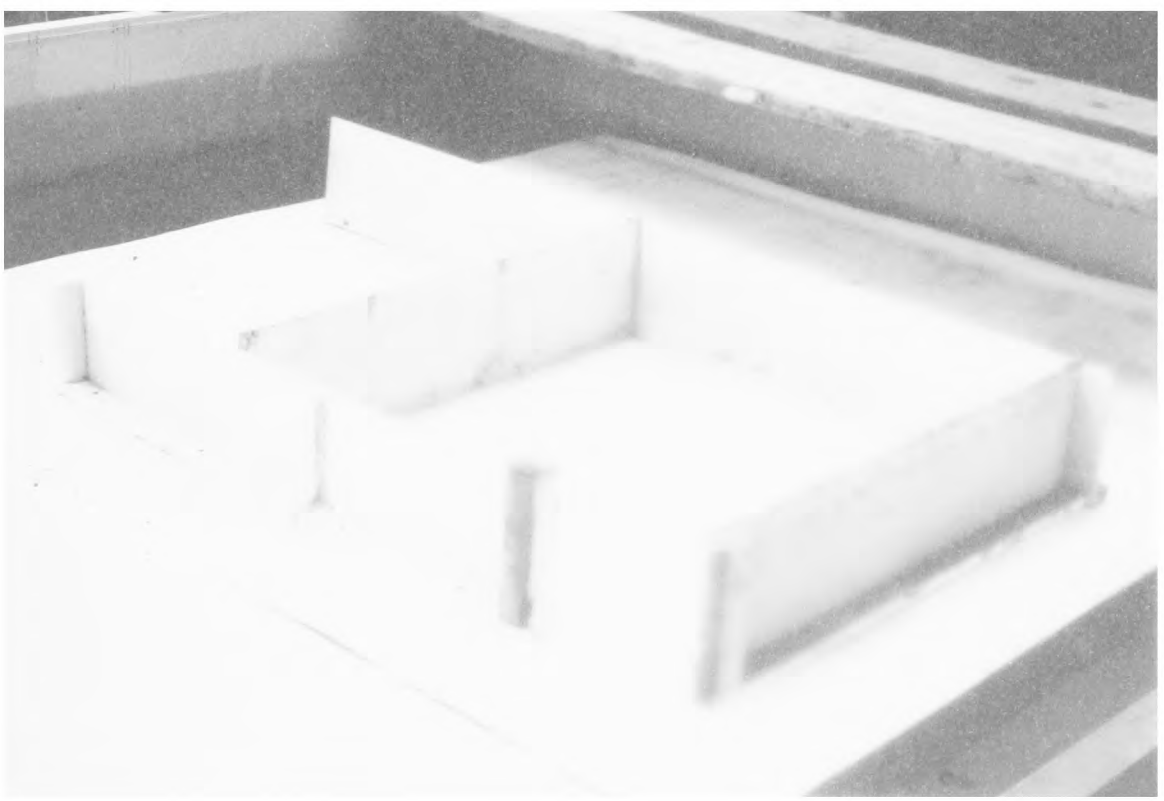

Figure 7.3 The harbour model with the grid marked on the bed.

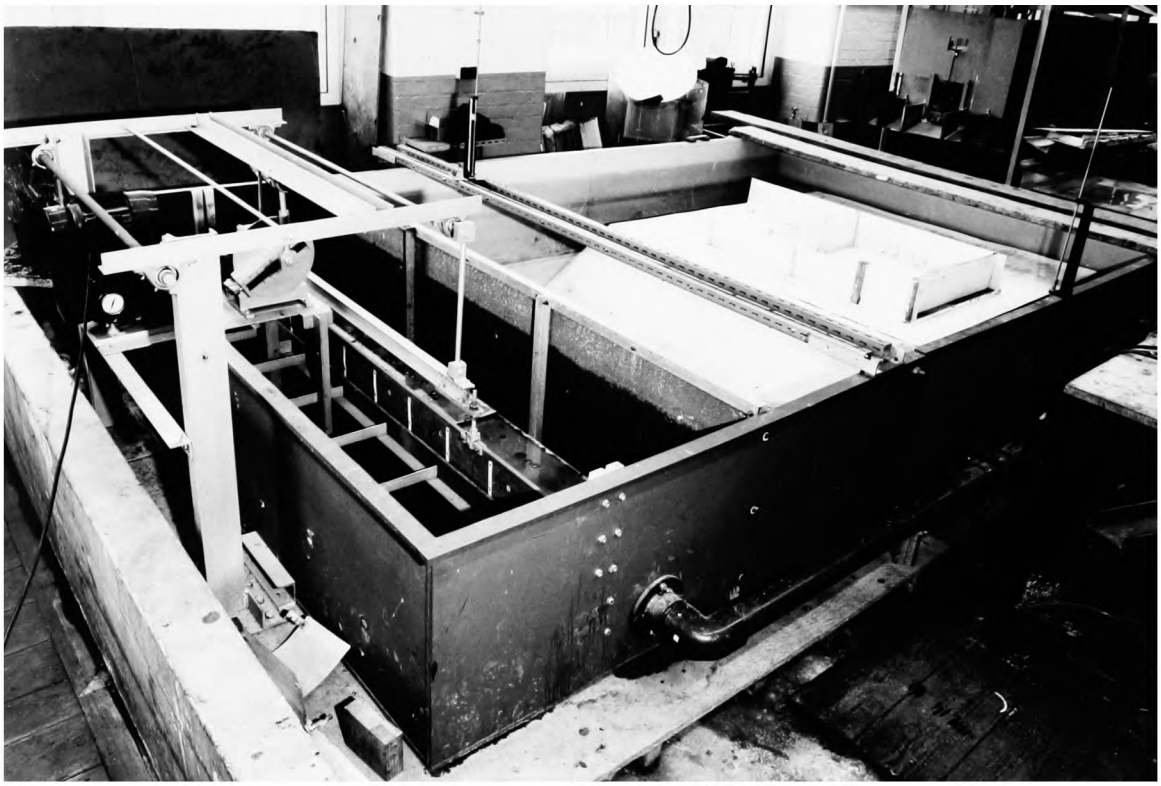

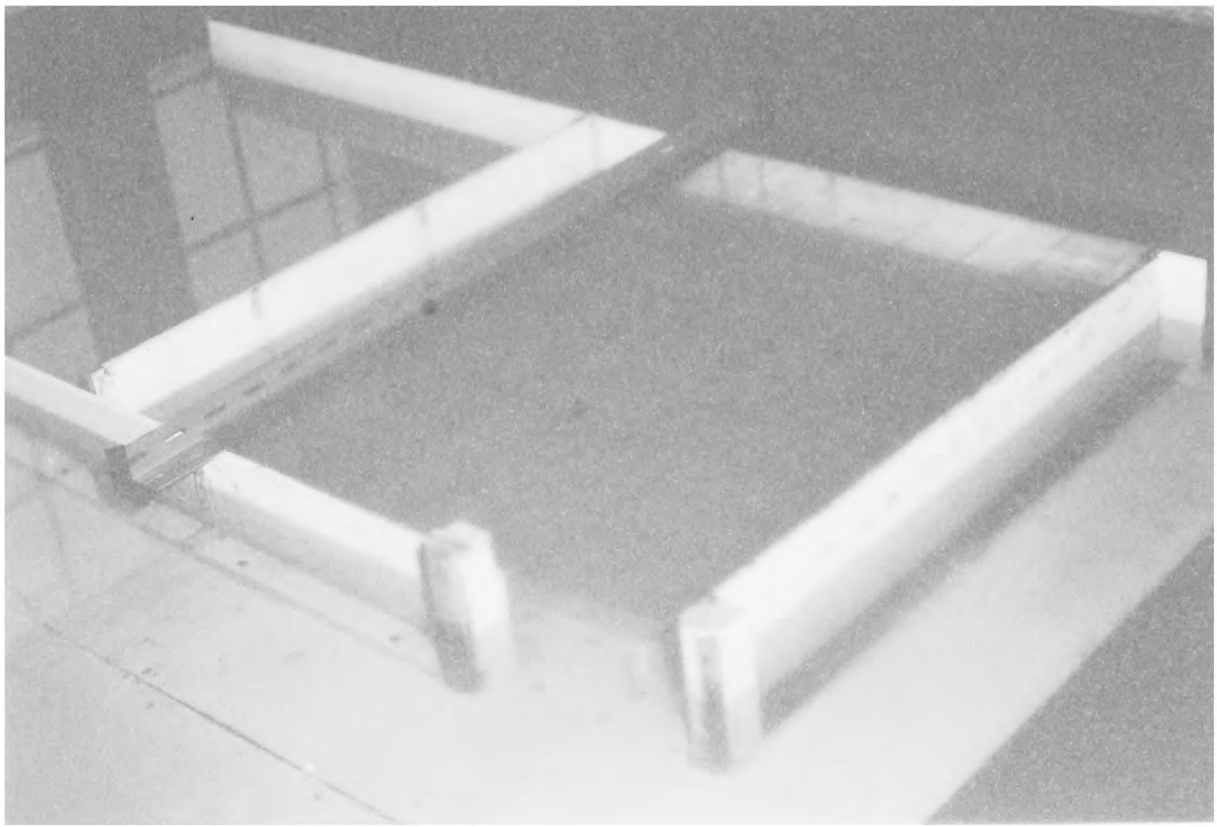

Figure 7.4 Experimental arrangement for velocity measurements.

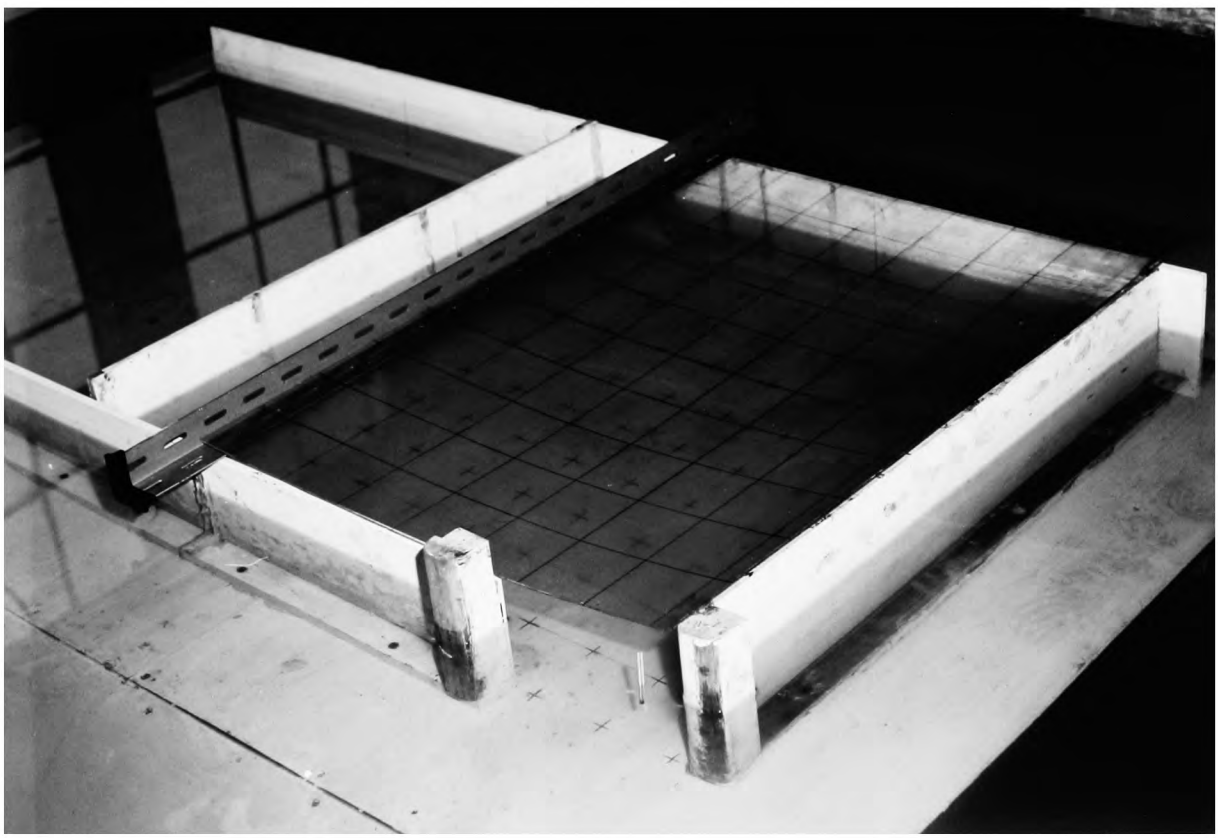

TIDAL VELOCITIES IN A HARBOUR

L/B = 1.0

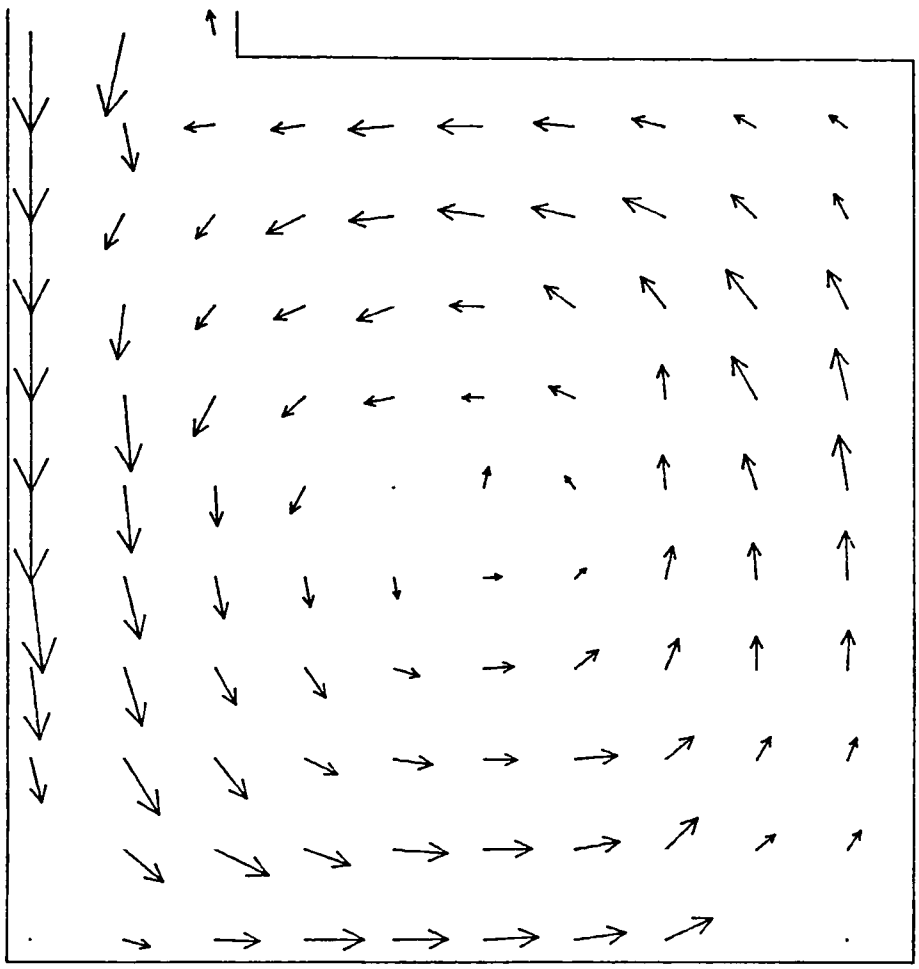

LENGTH SCALE ——— 0.080 M VELOCITY ⟶ 0.030 M/S

TIDAL HEIGHT = 0.104 M TIDAL PERIOD = 632.0 S

MEAN WATER LEVEL = 0.118 M

Figure 7.5 Experimentally measured velocities at mean water level on the flood tide for L/B=1.0

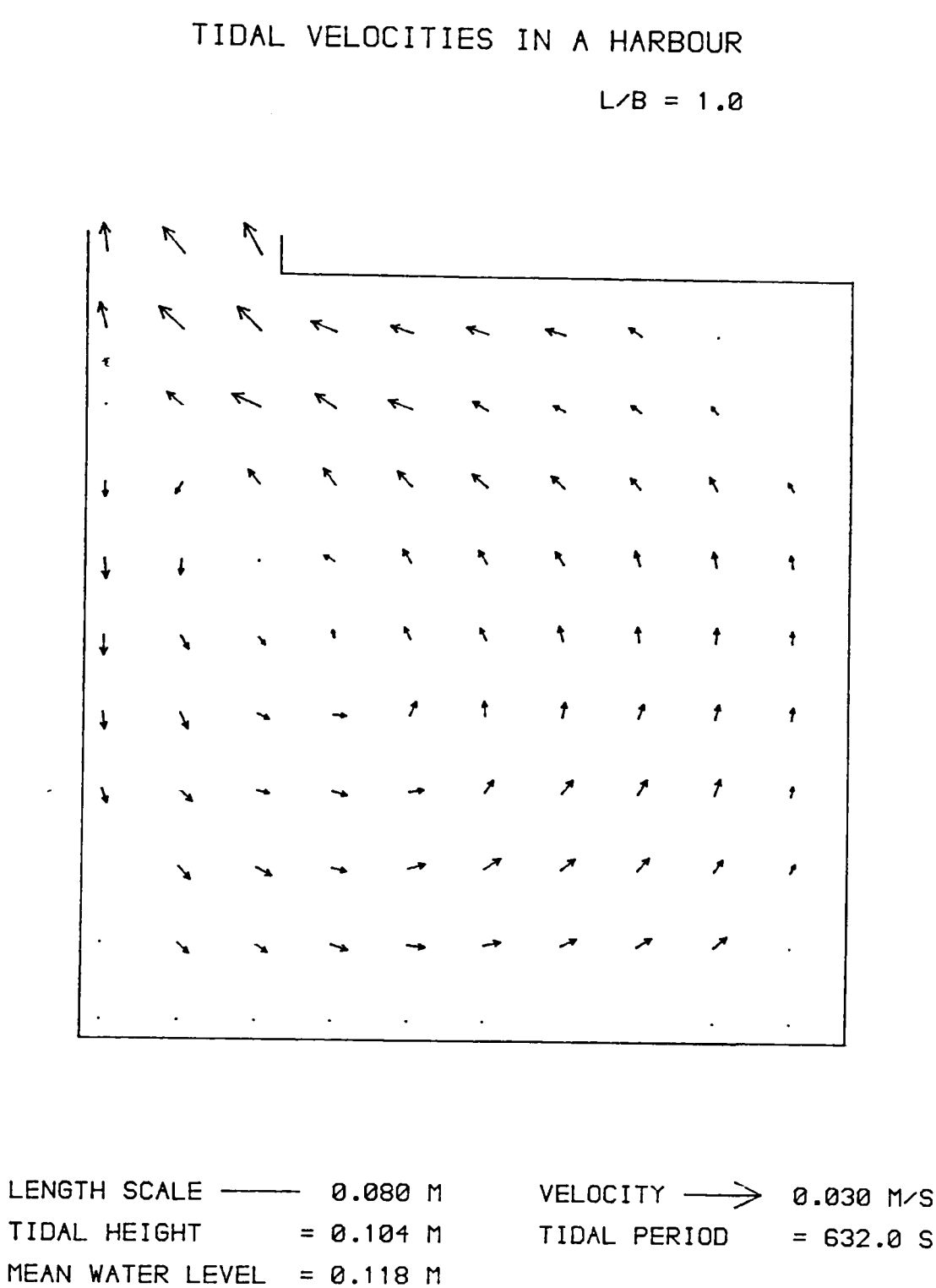

Figure 7.6 Experimentally measured velocities at mean water level on the ebb tide for L/B=1.0

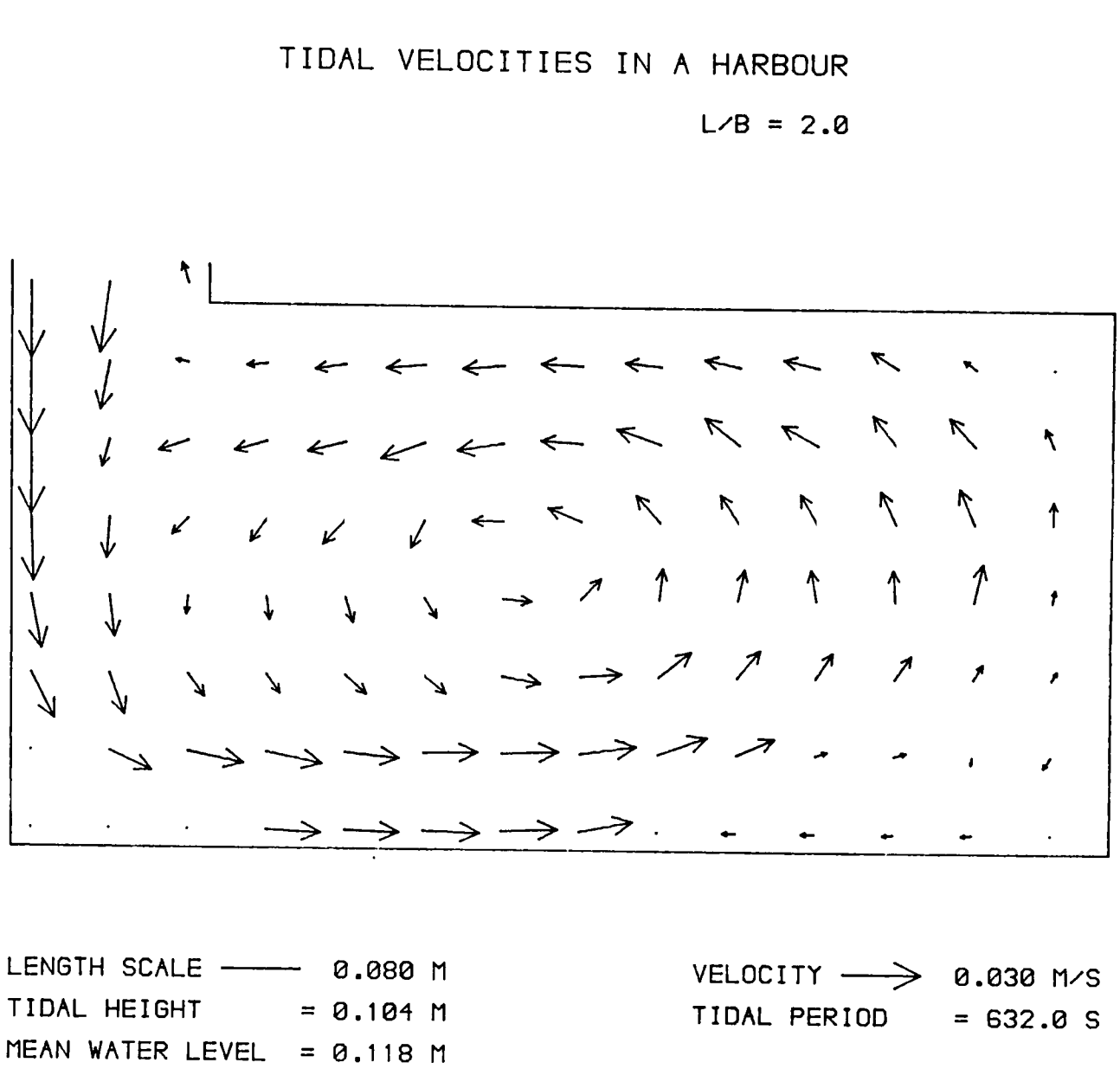

Figure 7.7 Experimentally measured velocities at mean water level on the flood tide for L/B=2.0

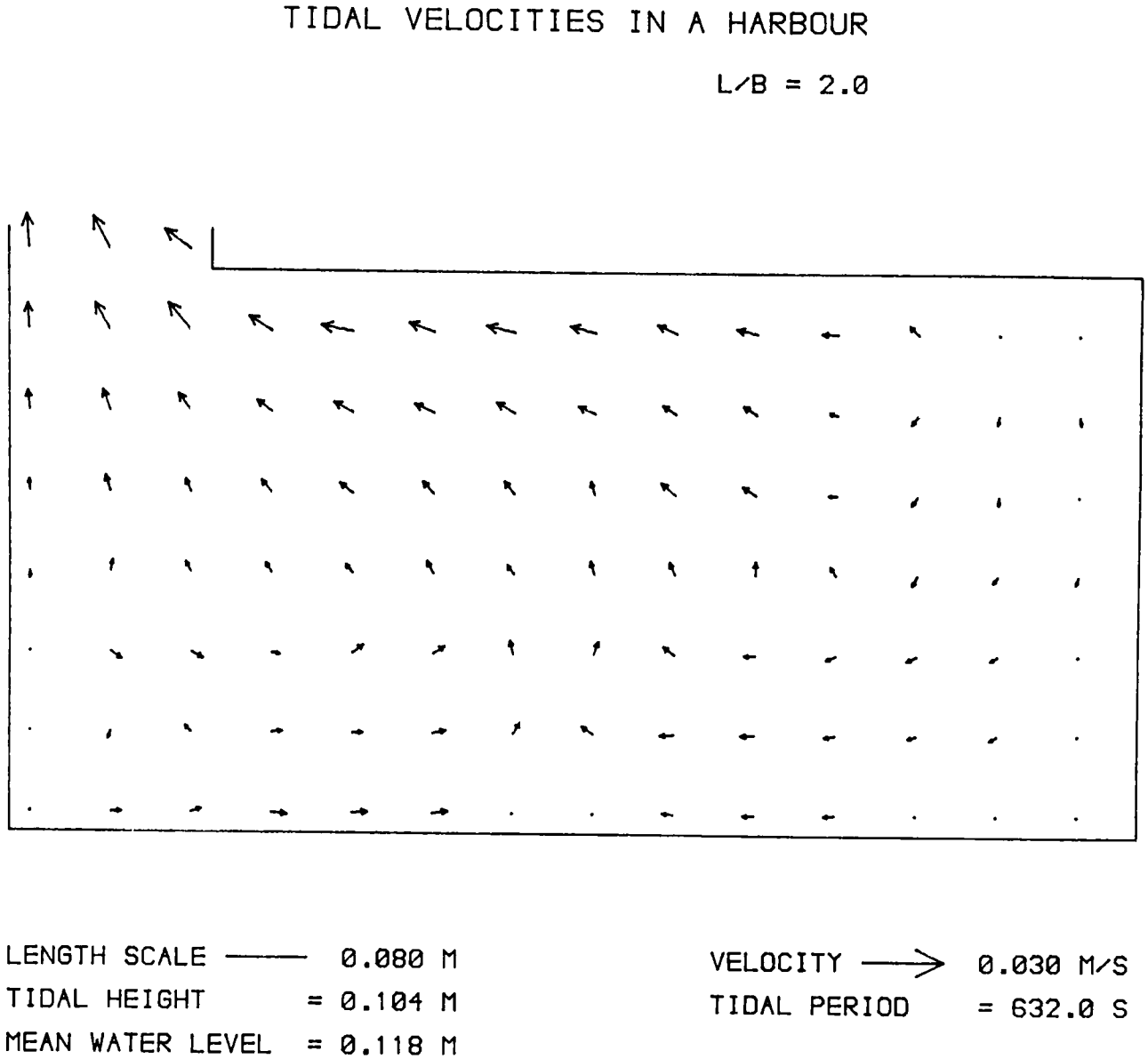

Figure 7.8 Experimentally measured velocities at mean water level on the ebb tide for L/B=2.0

TIDAL VELOCITIES IN A HARBOUR

L/B = 2.8

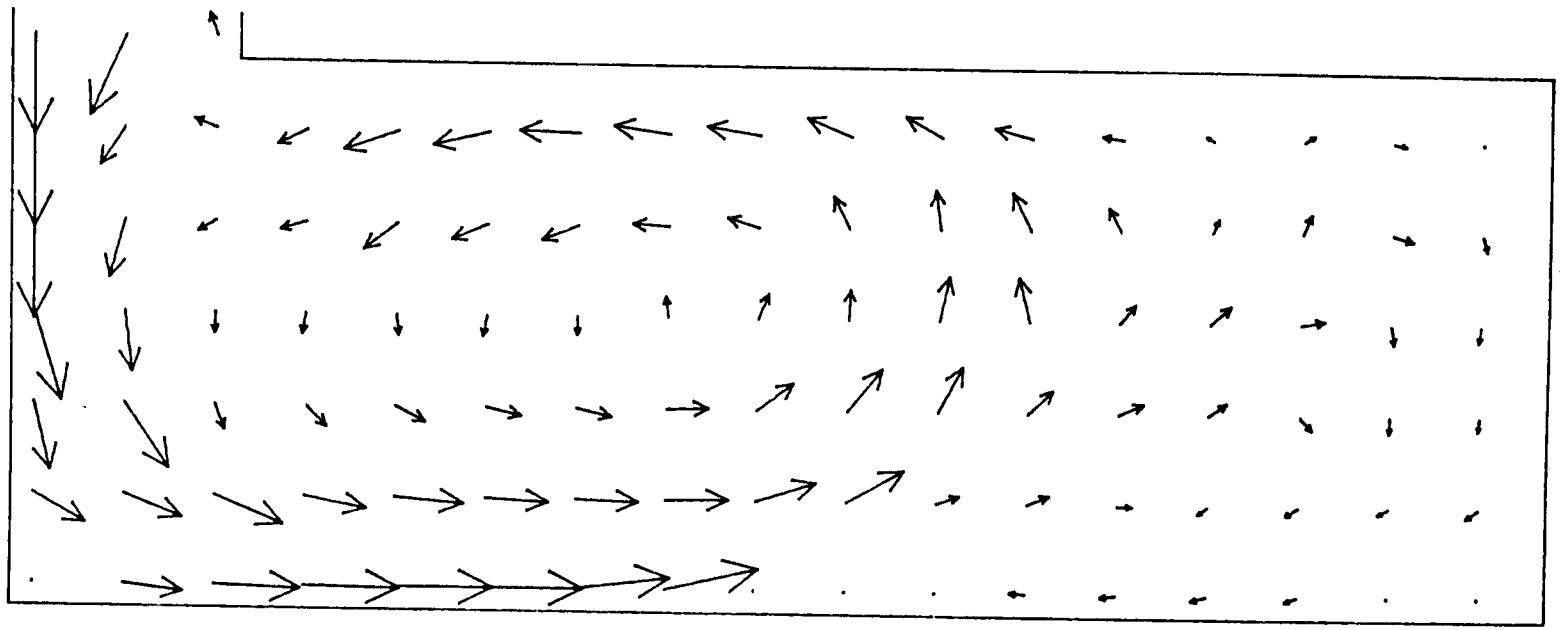

LENGTH SCALE ——— 0.080 M
TIDAL HEIGHT = 0.104 M
MEAN WATER LEVEL = 0.118 M

VELOCITY ⟶ 0.030 M/S
TIDAL PERIOD = 632.0 S

Figure 7.9 Experimentally measured velocities at mean water level on the flood tide for L/B=2.833

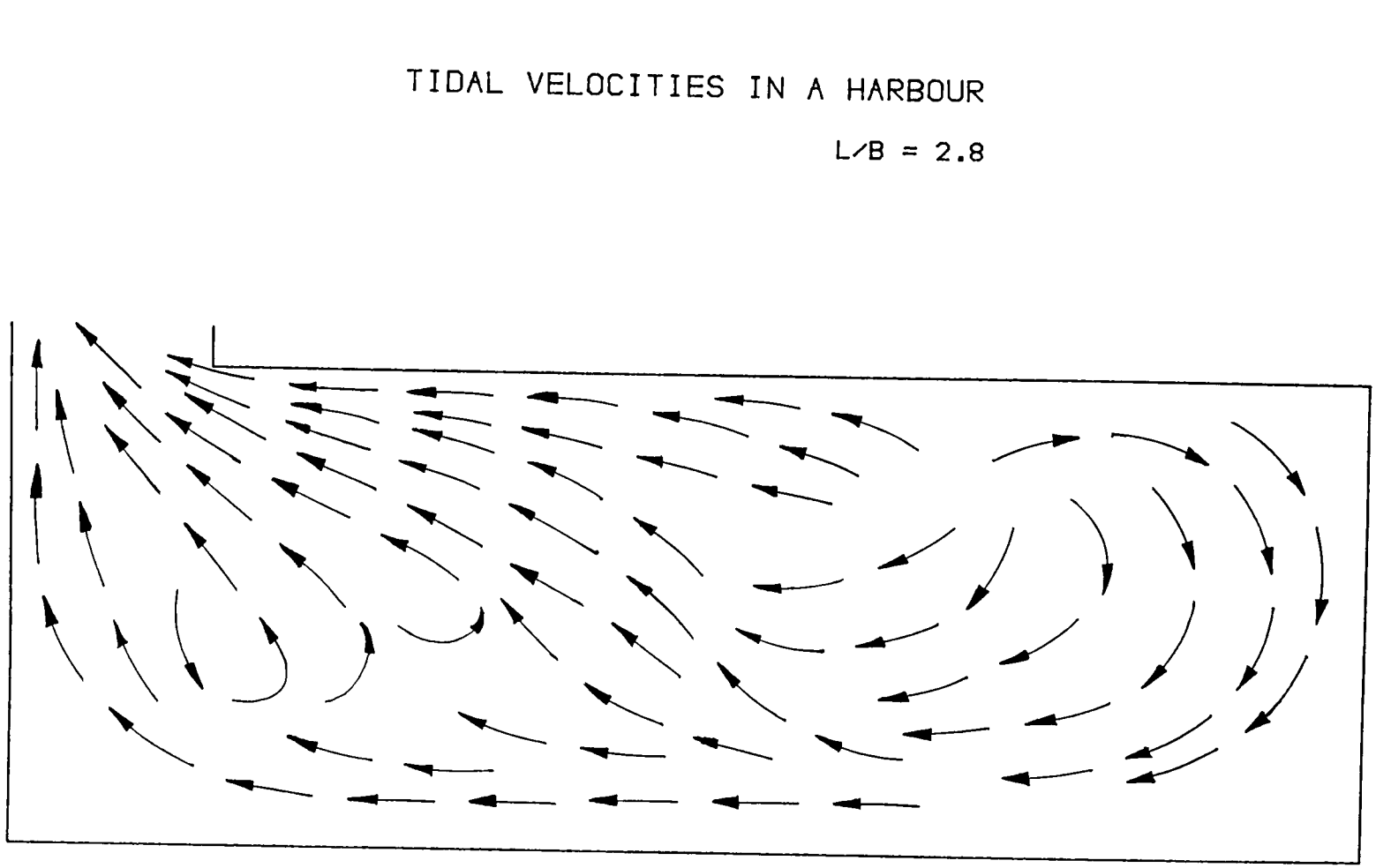

Figure 7.10 Observed pathlines at mean water level on the ebb tide for L/B=2.833

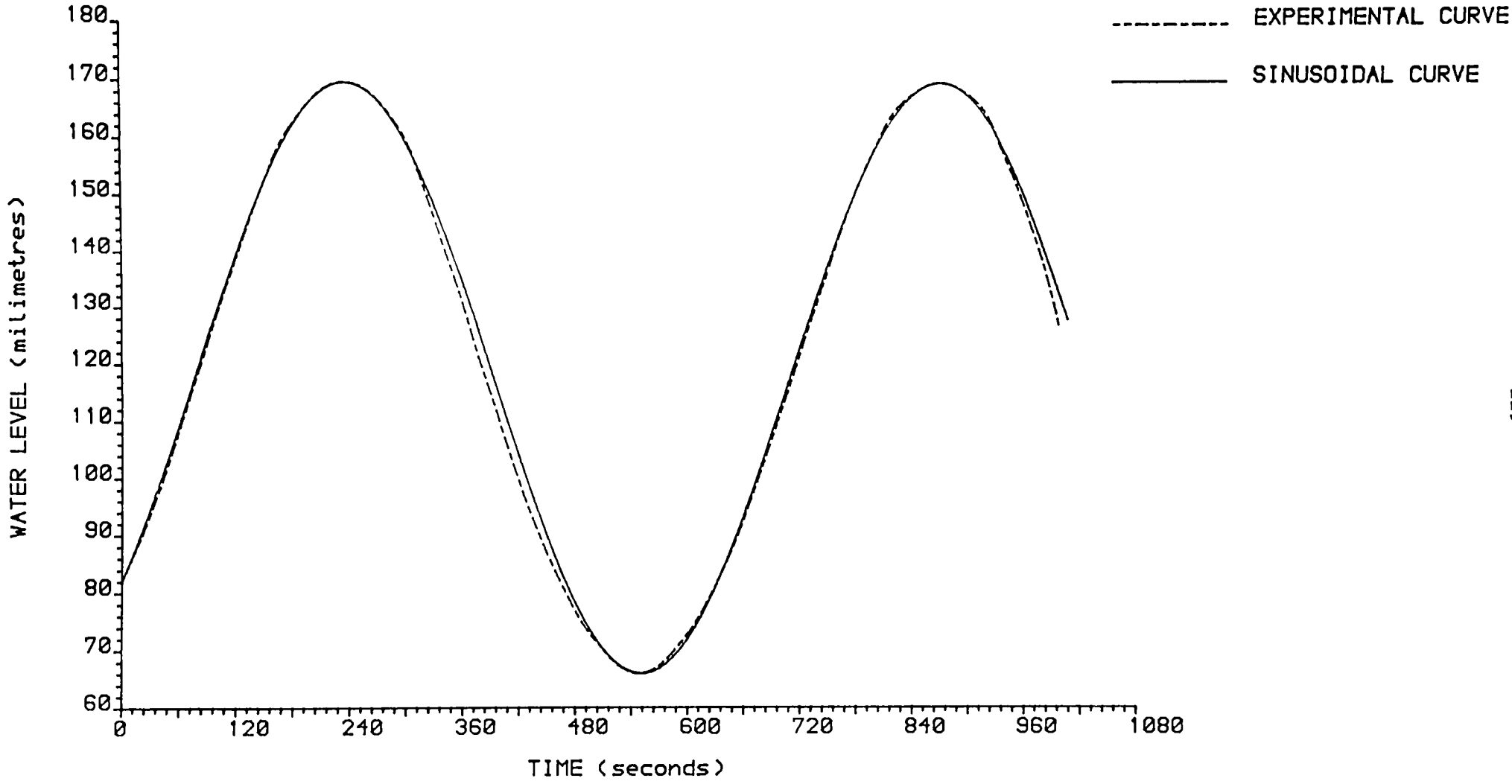

Figure 7.11 Comparison between the wave produced by the tidal generator and a sinusoidal wave

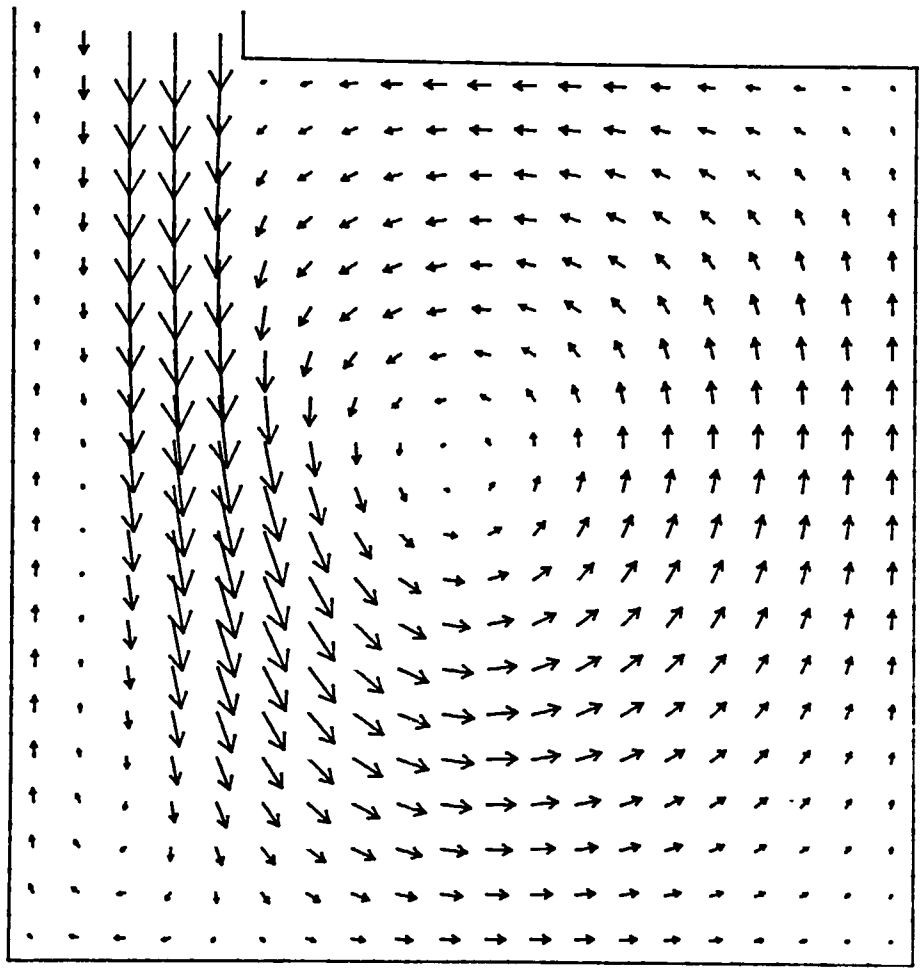

Figure 7.12 Predicted velocity field at mean water flood tide for a water level open boundary and non-nested grid

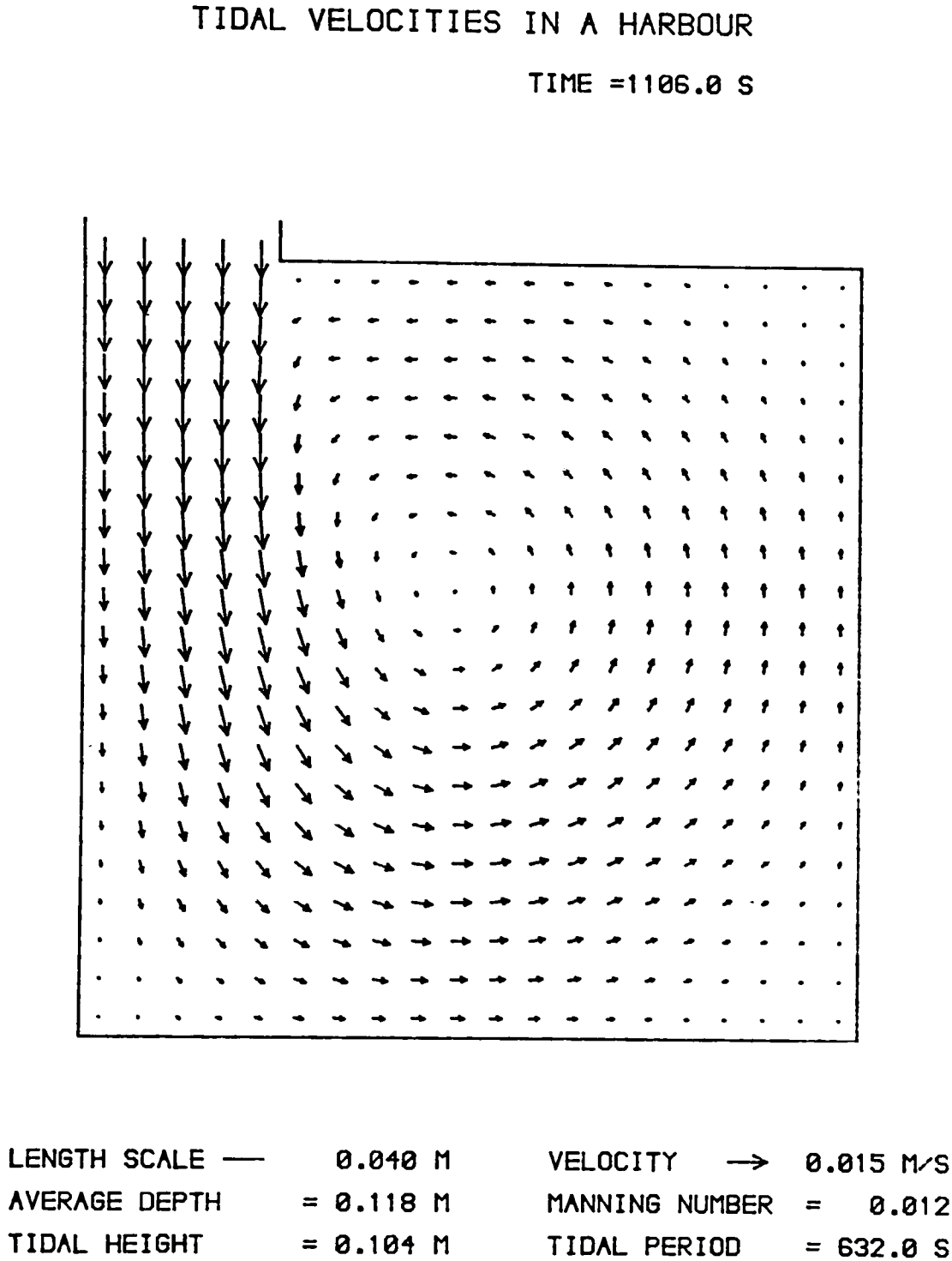

Figure 7.13 Predicted velocity field at mean water flood tide for a velocity open boundary and a non-nested grid

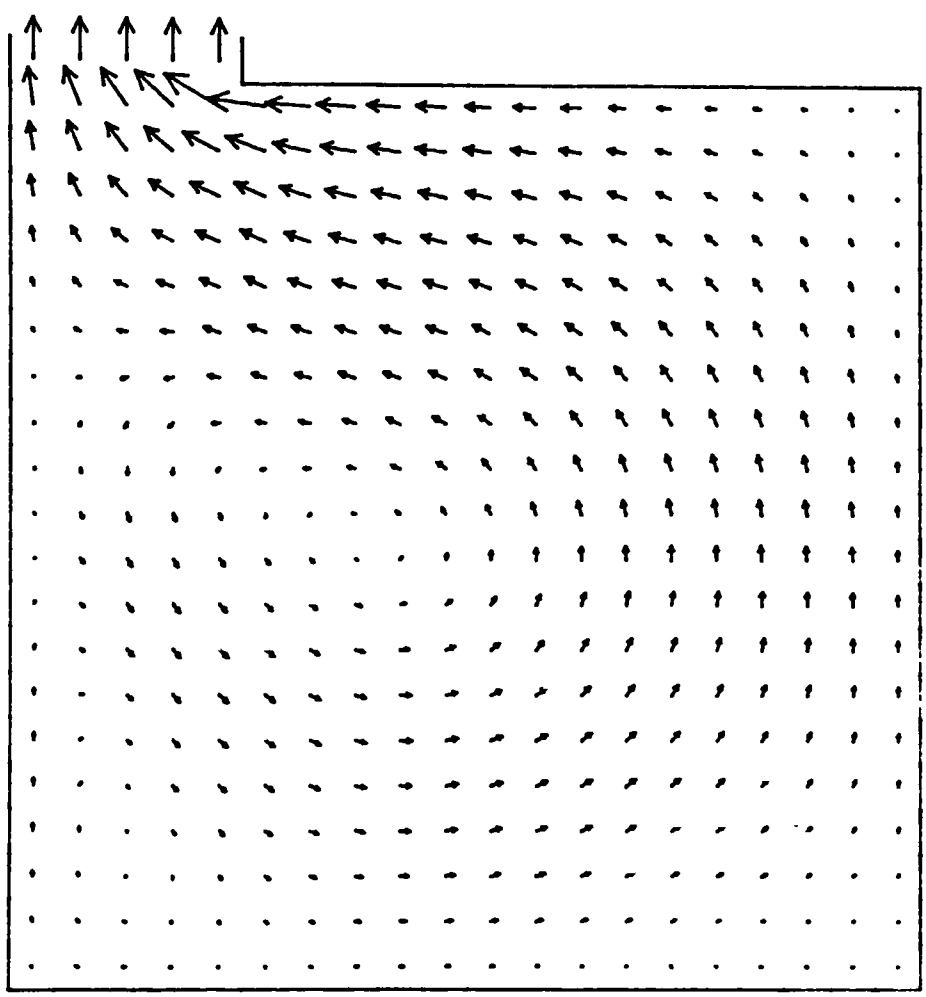

Figure 7.14 Predicted velocity field at mean water ebb tide for a velocity open boundary and a non-nested grid

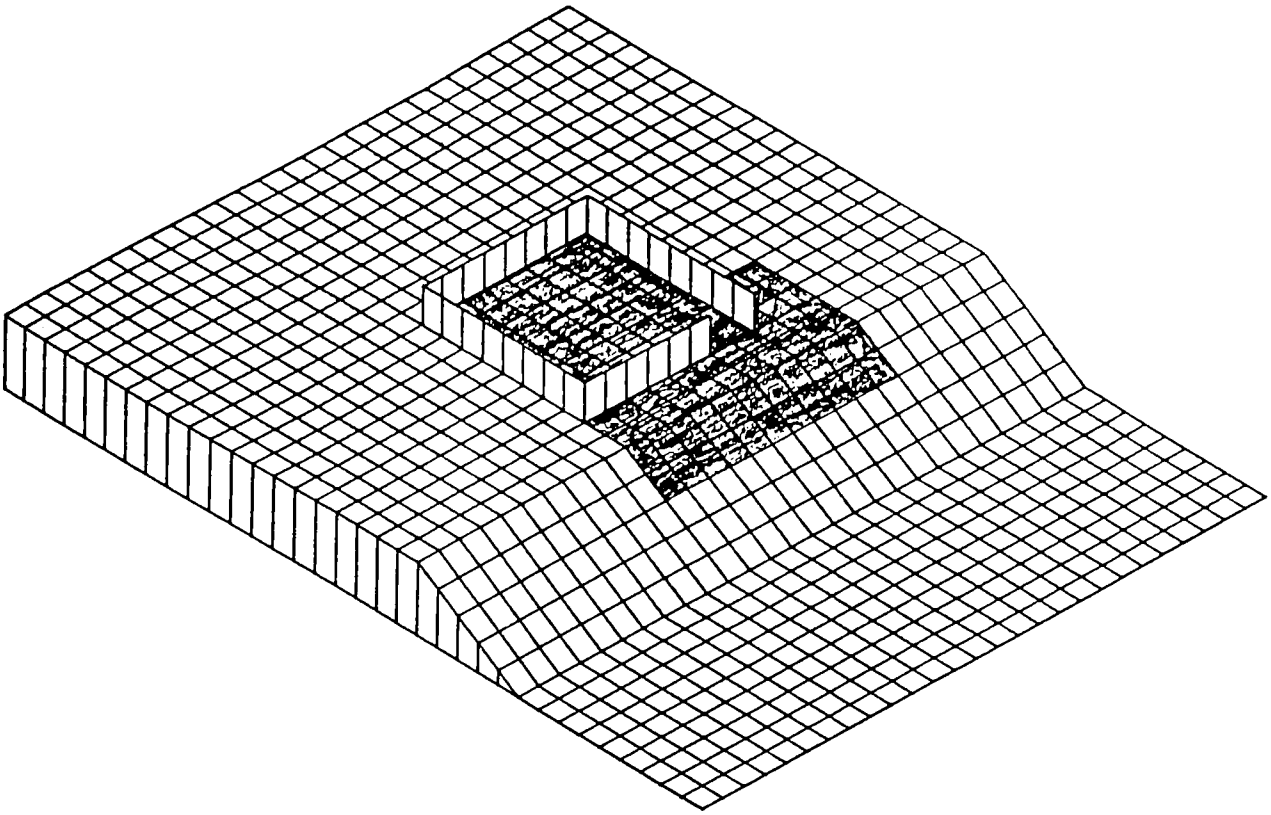

Figure 7.15 Isoparametric projection of the tidal tank bathymetry showing the extend of the nested grid domain

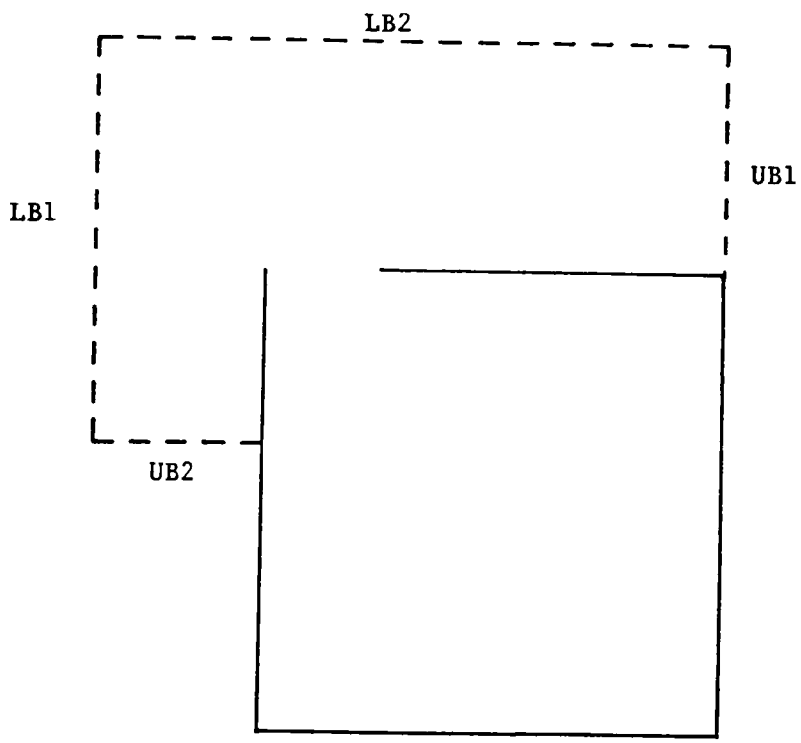

Figure 7.16 Schematic illustration of the fine-grid open boundaries

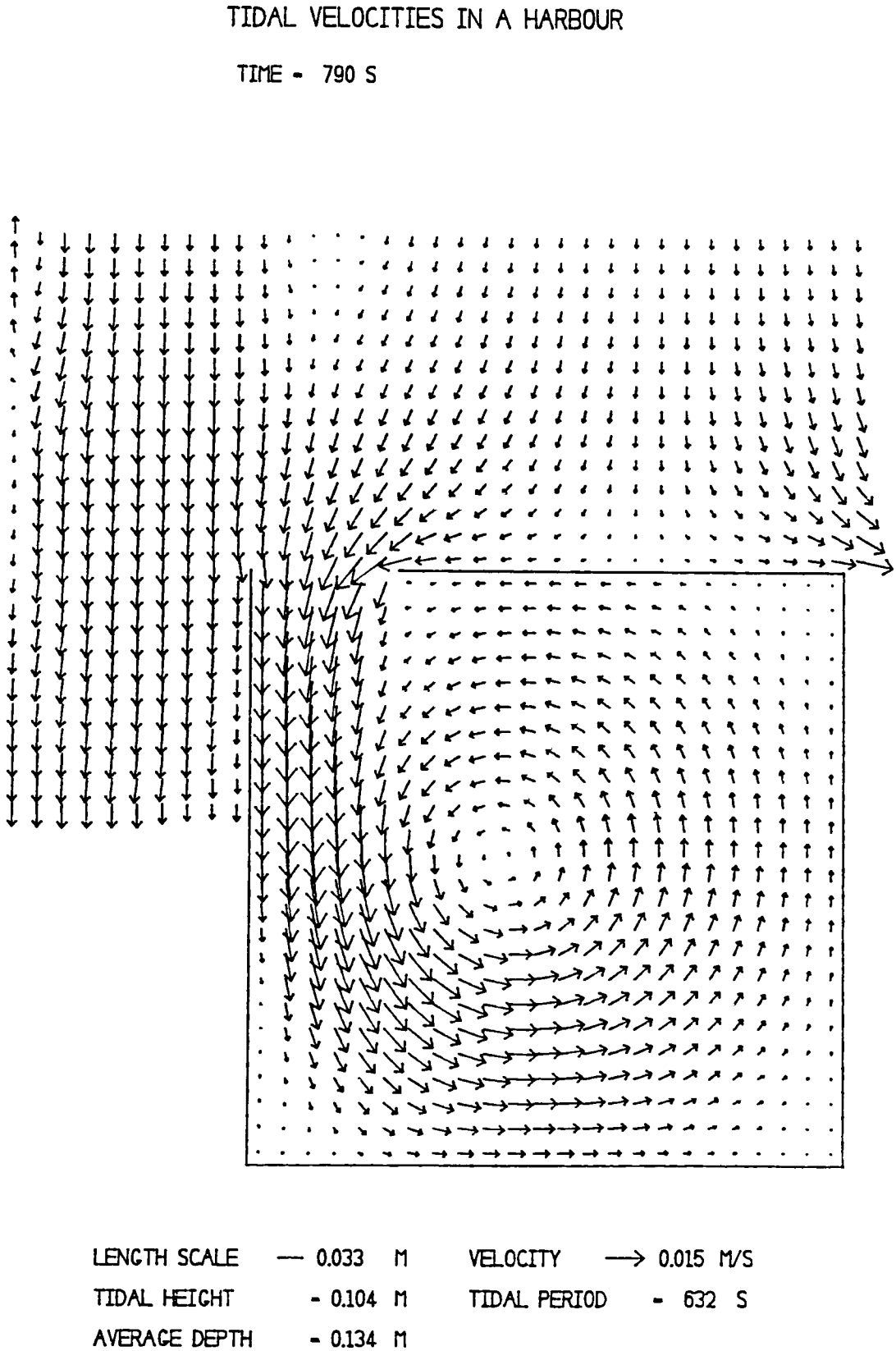

Figure 7.17 Predicted velocity field by fine-grid model at mean water flood tide for the combination of water elevations and velocities at lower and upper open boundaries respectively

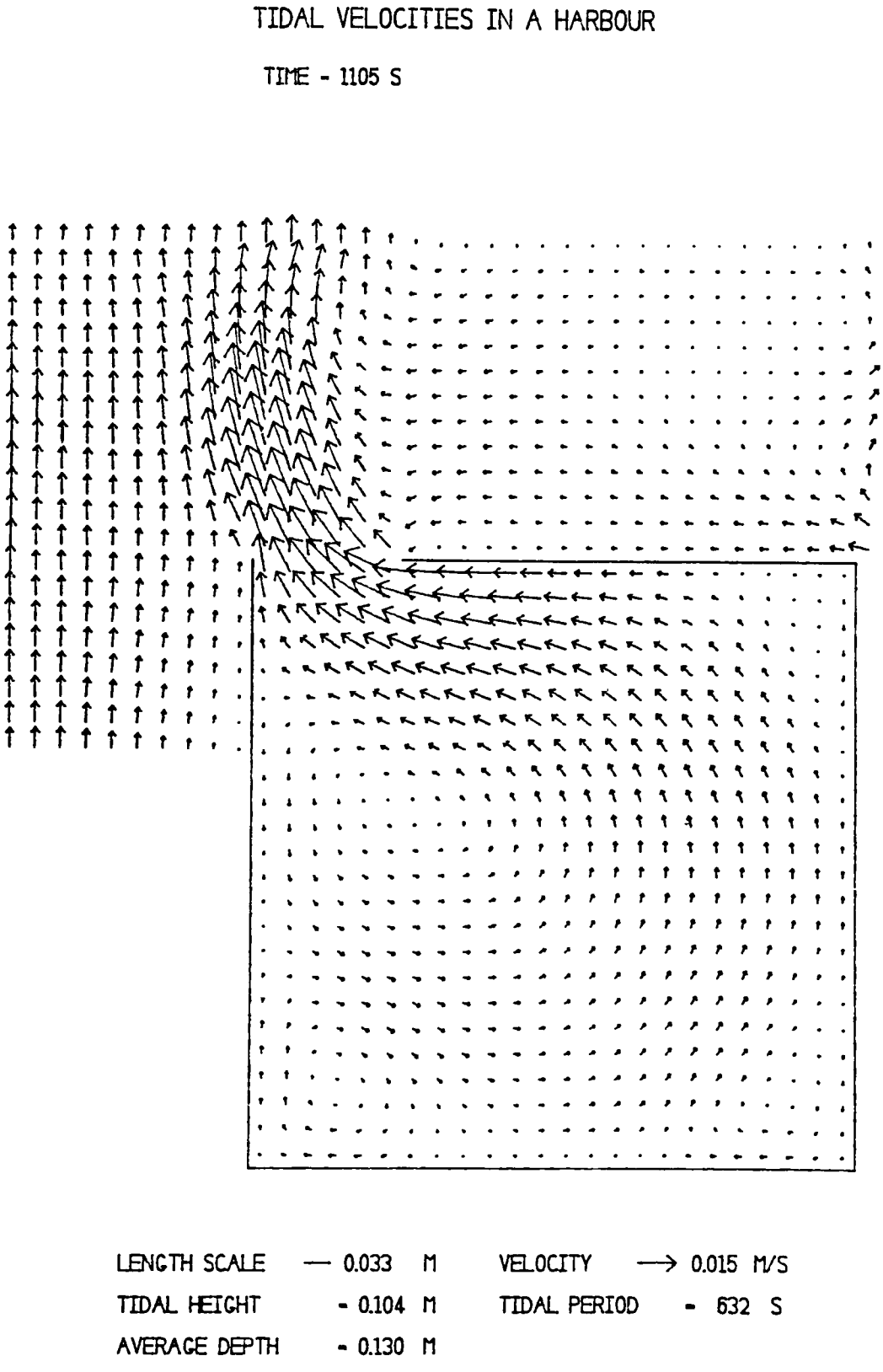

Figure 7.18 Predicted velocity field by fine-grid model at mean water ebb tide for the combination of velocities and water elevations elevations at lower and upper open boundaries respectively

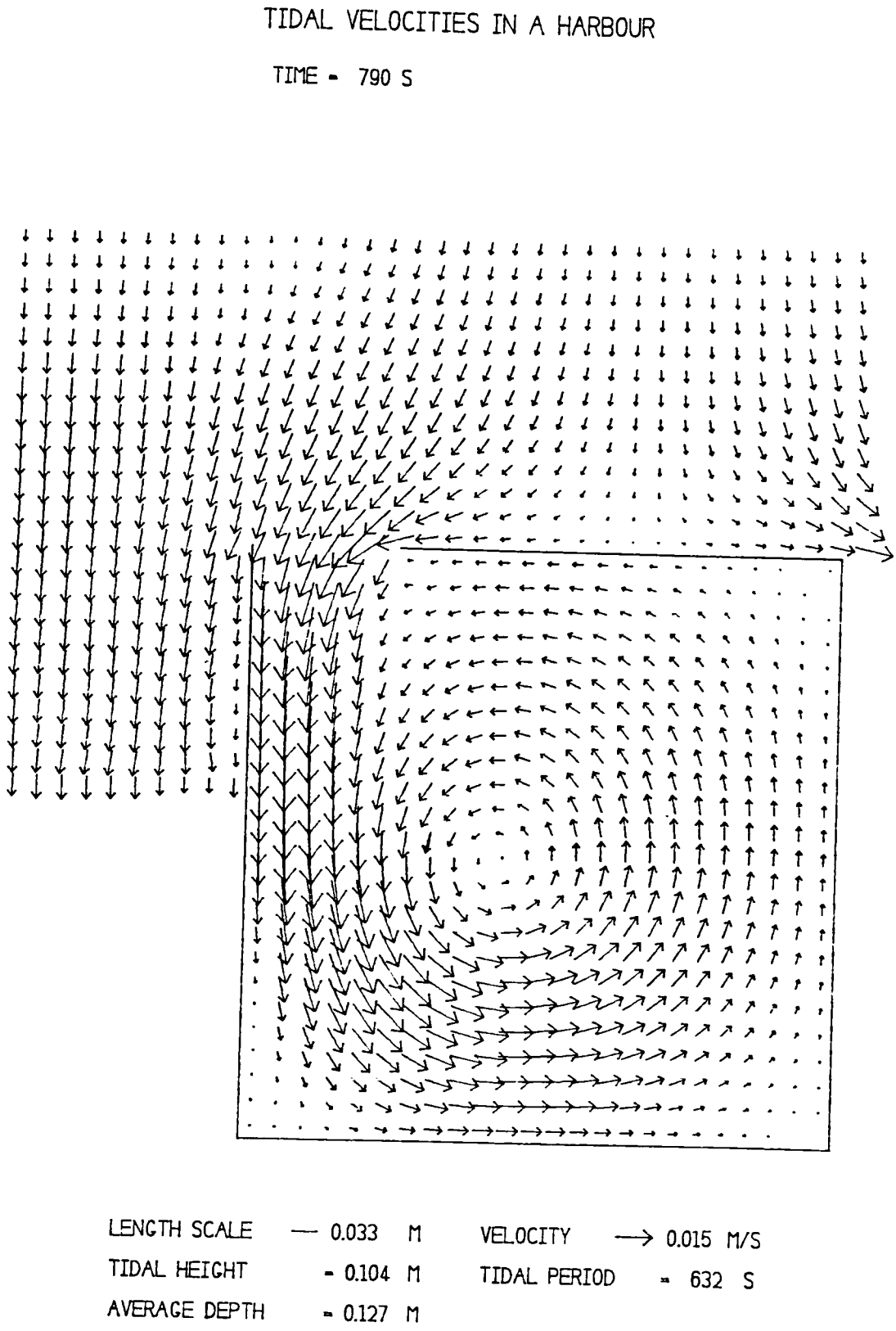

Figure 7.19 Predicted velocity field by fine-grid model at mean water flood tide for velocities at all open boundaries

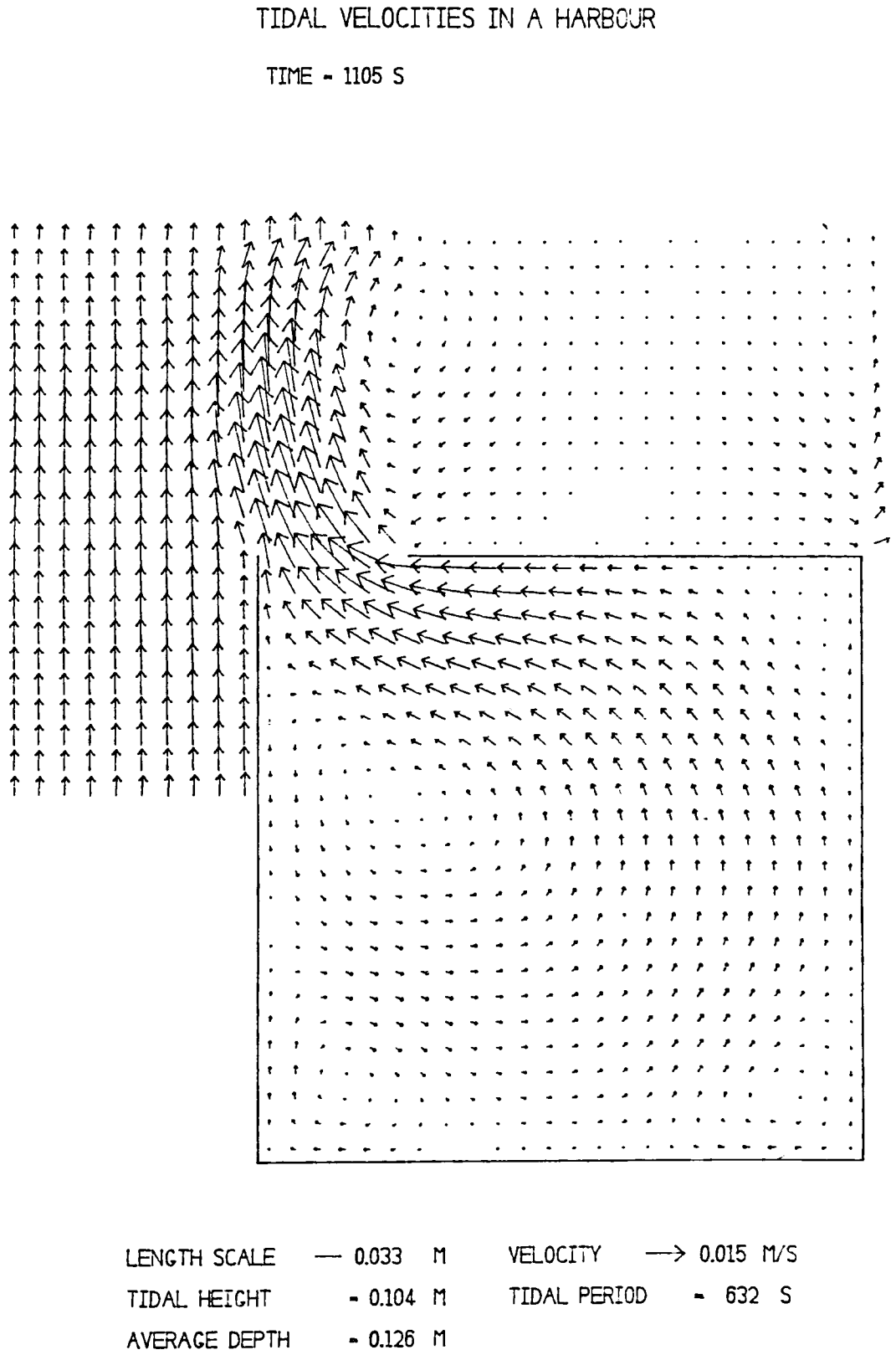

Figure 7.20 Predicted velocity field by fine-grid model at mean water ebb tide for velocities at all open boundaries

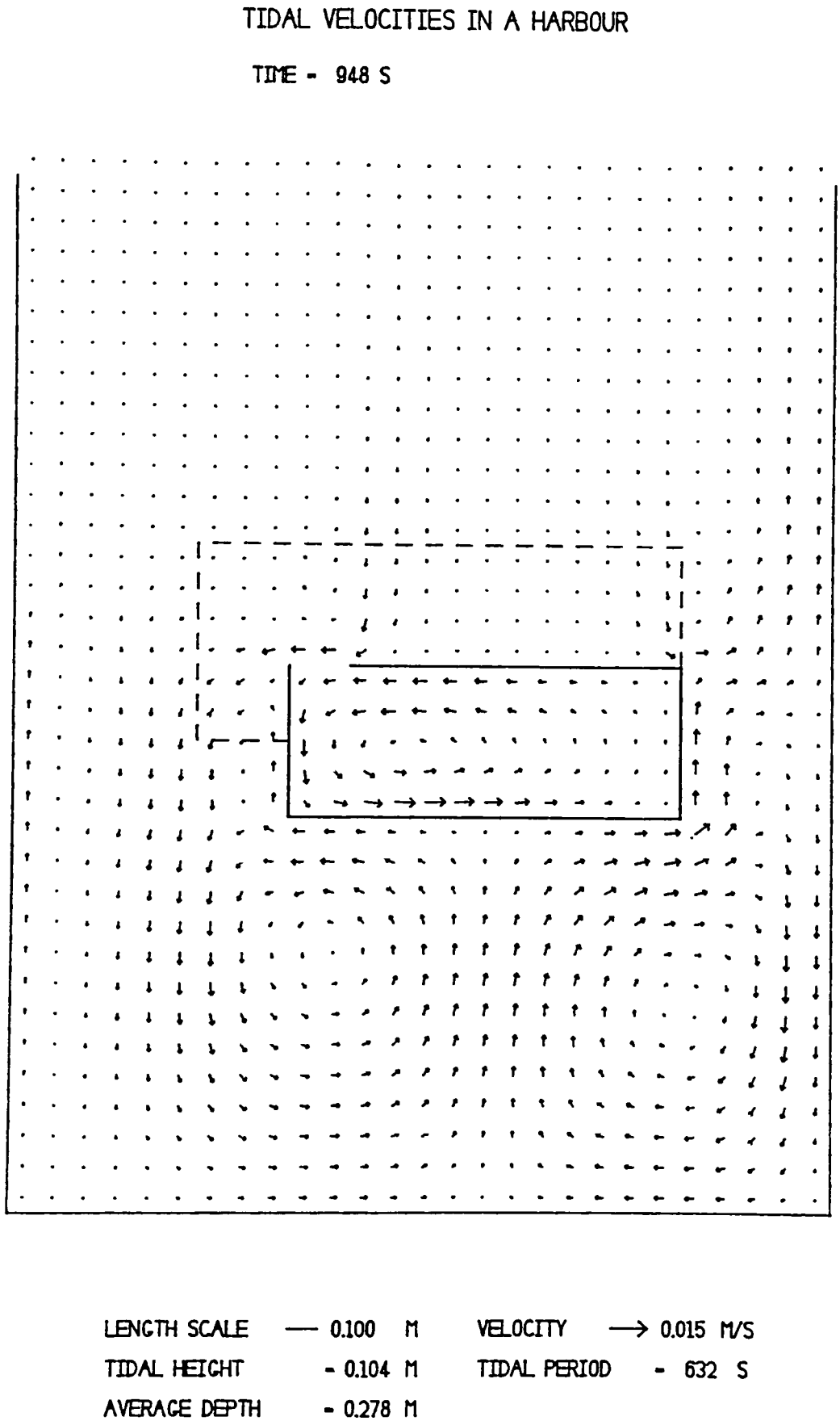

Figure 7.21 Predicted velocity field by coarse-grid model at high tide for L/B=2.6

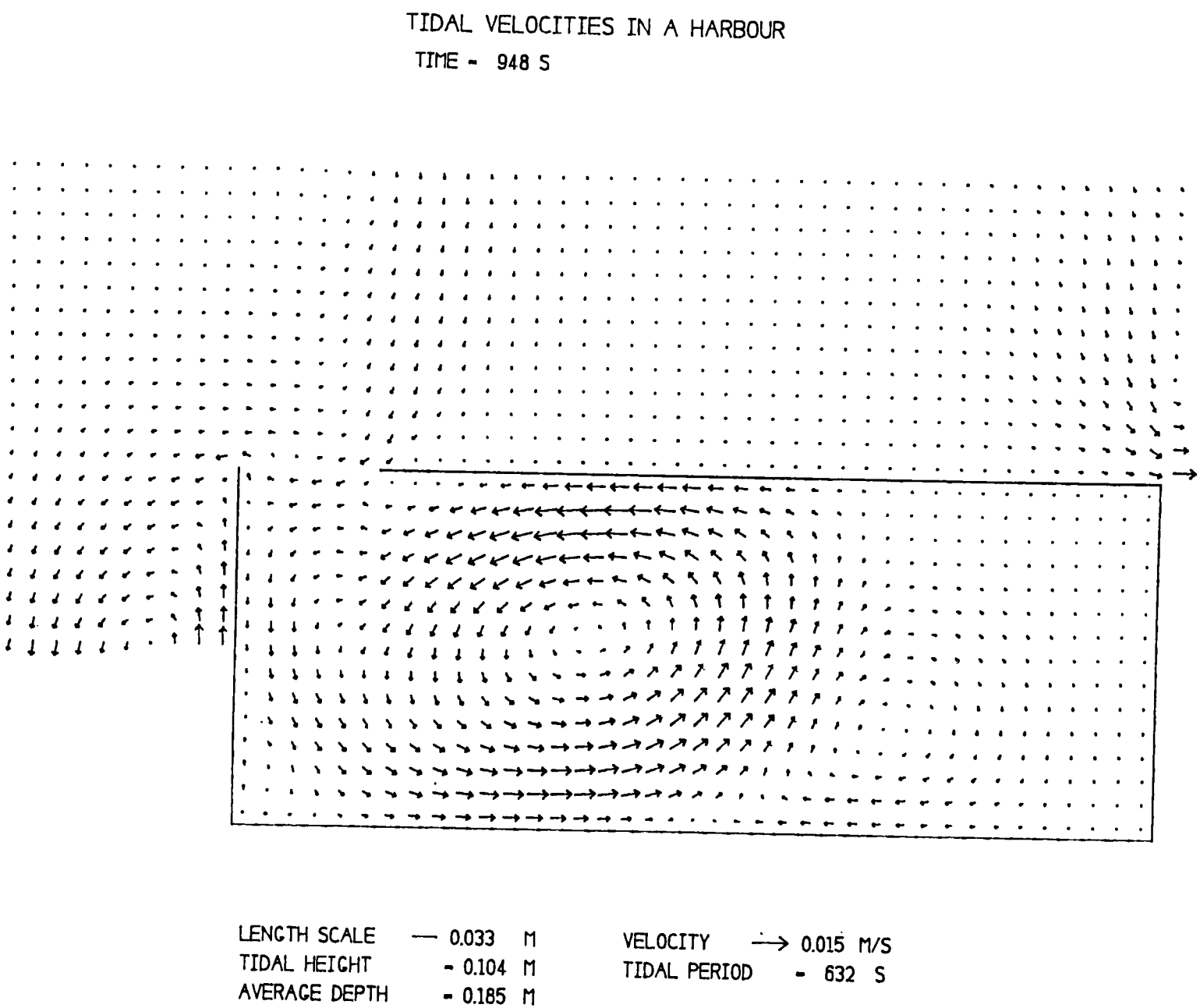

Figure 7.22 Predicted velocity field by fine-grid model at high tide for L/B=2.6

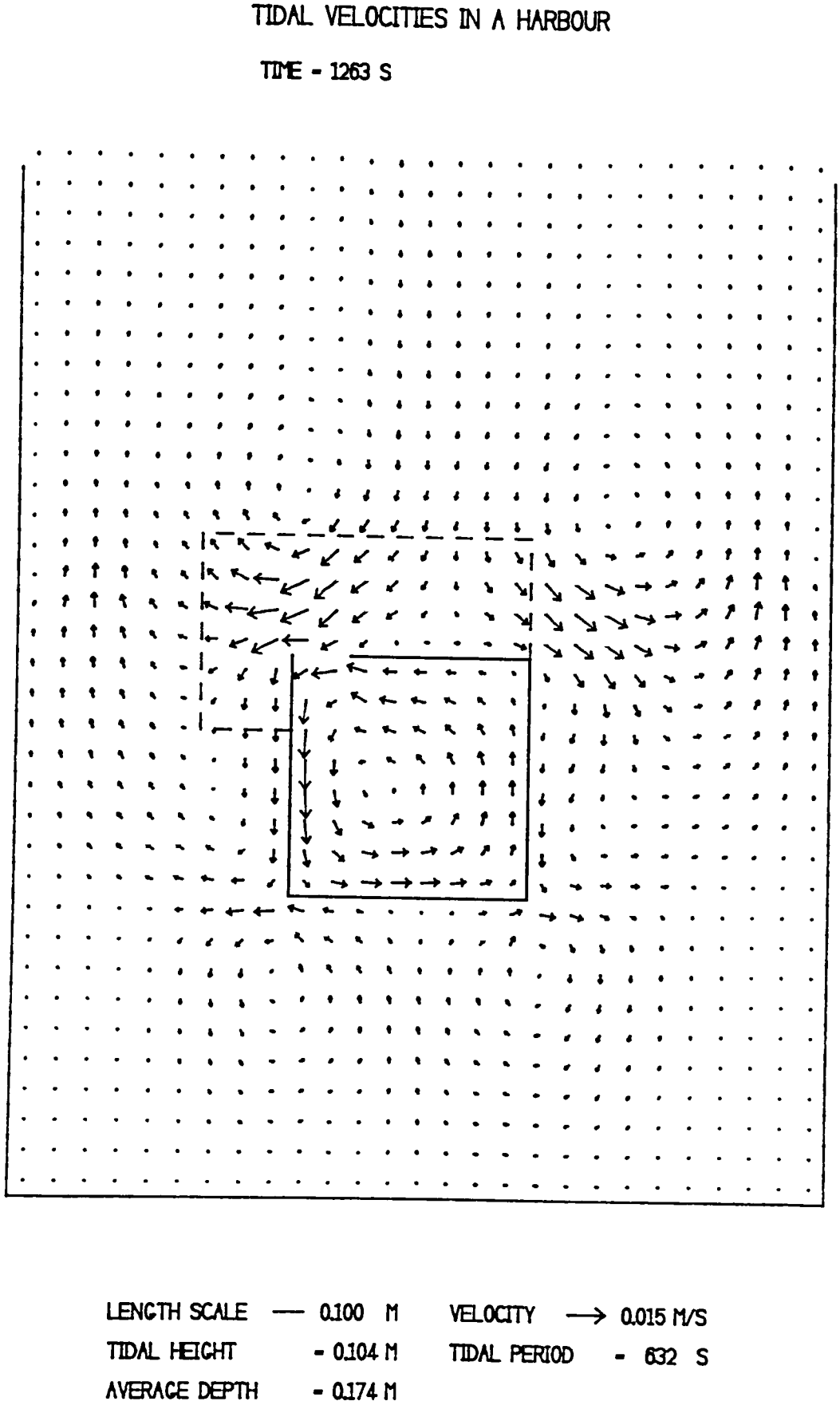

Figure 7.23 Predicted velocity field by coarse-grid model at low tide for L/B=1.0

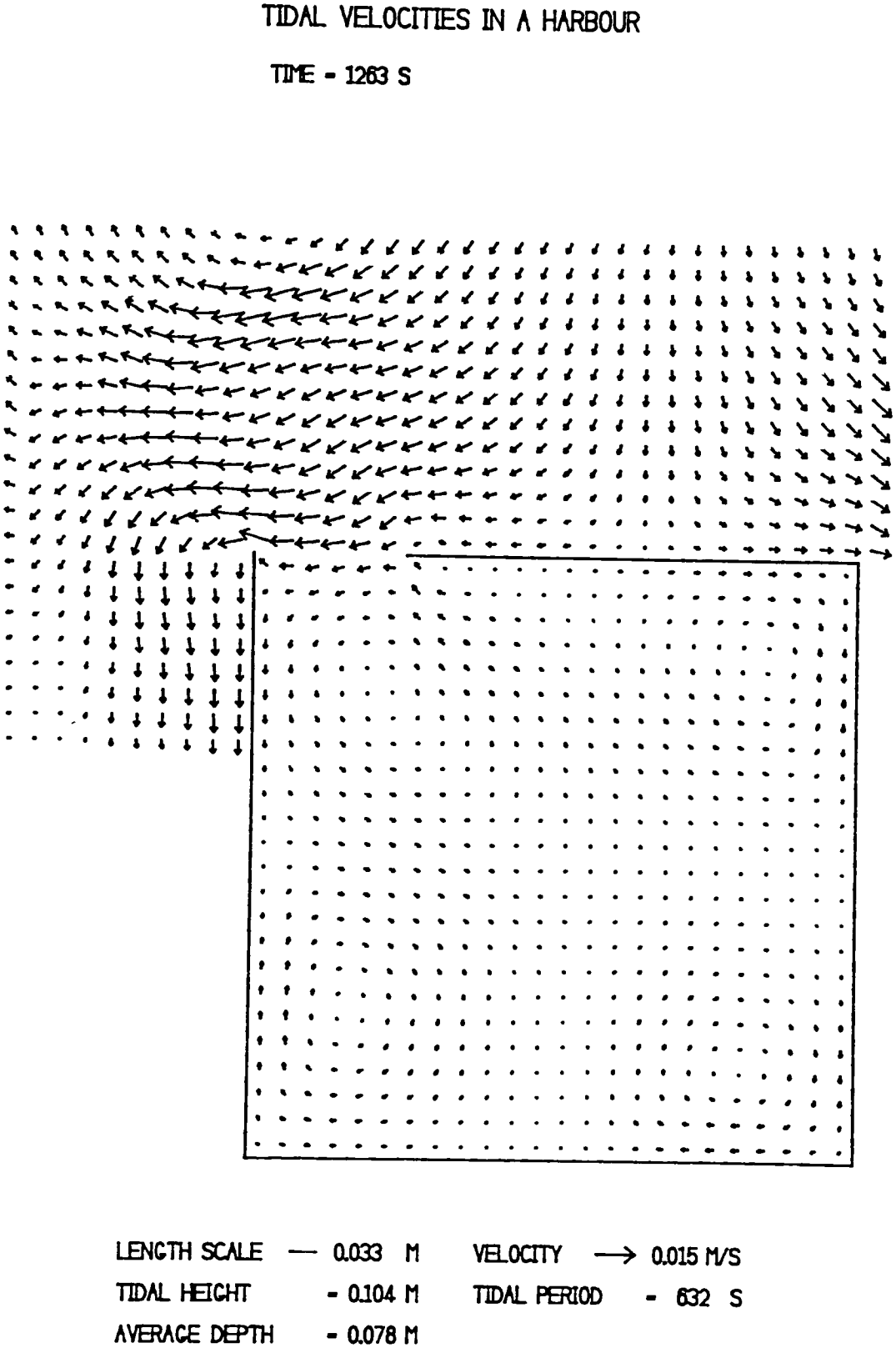

Figure 7.24 Predicted velocity field by fine-grid model at low tide for L/B=1.0

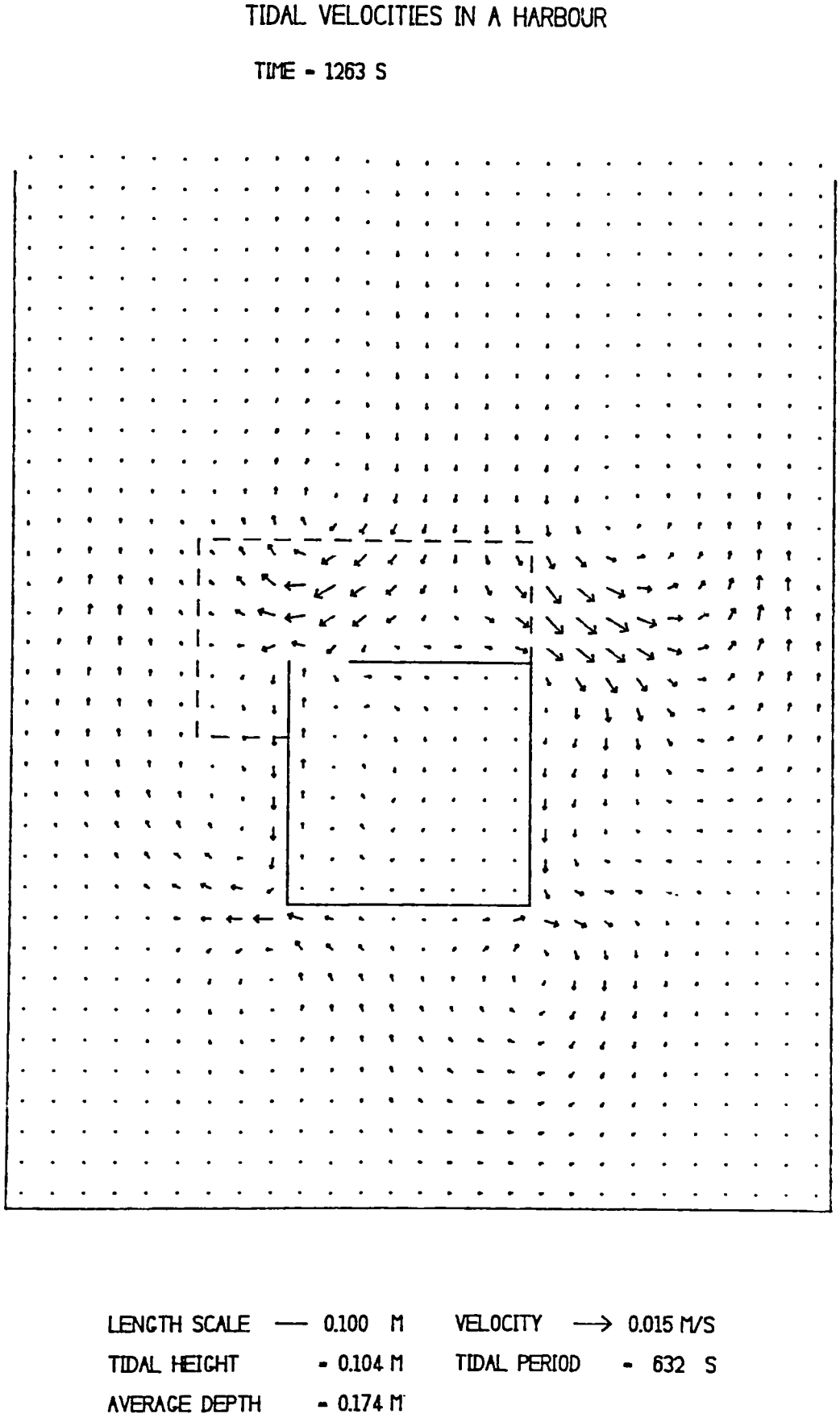

Figure 7.25 Predicted velocity field by coarse-grid model at low tide for L/B=1.0, with the exclusion of the advective acceleration terms within the harbour

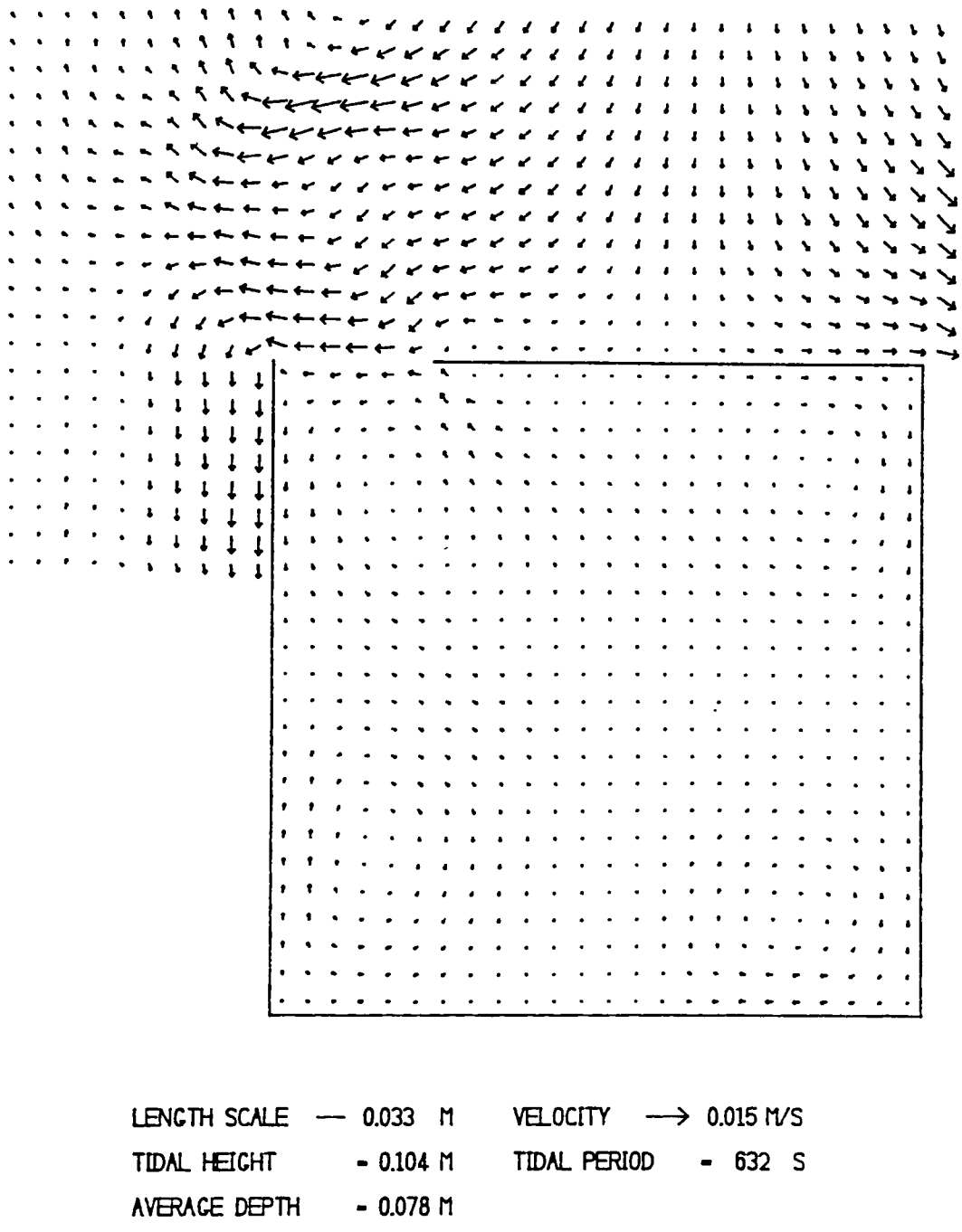

Figure 7.26 Predicted velocity field by fine-grid model at low tide for L/B=1.0, as a result of the suppression of circulation in the coarse-grid model

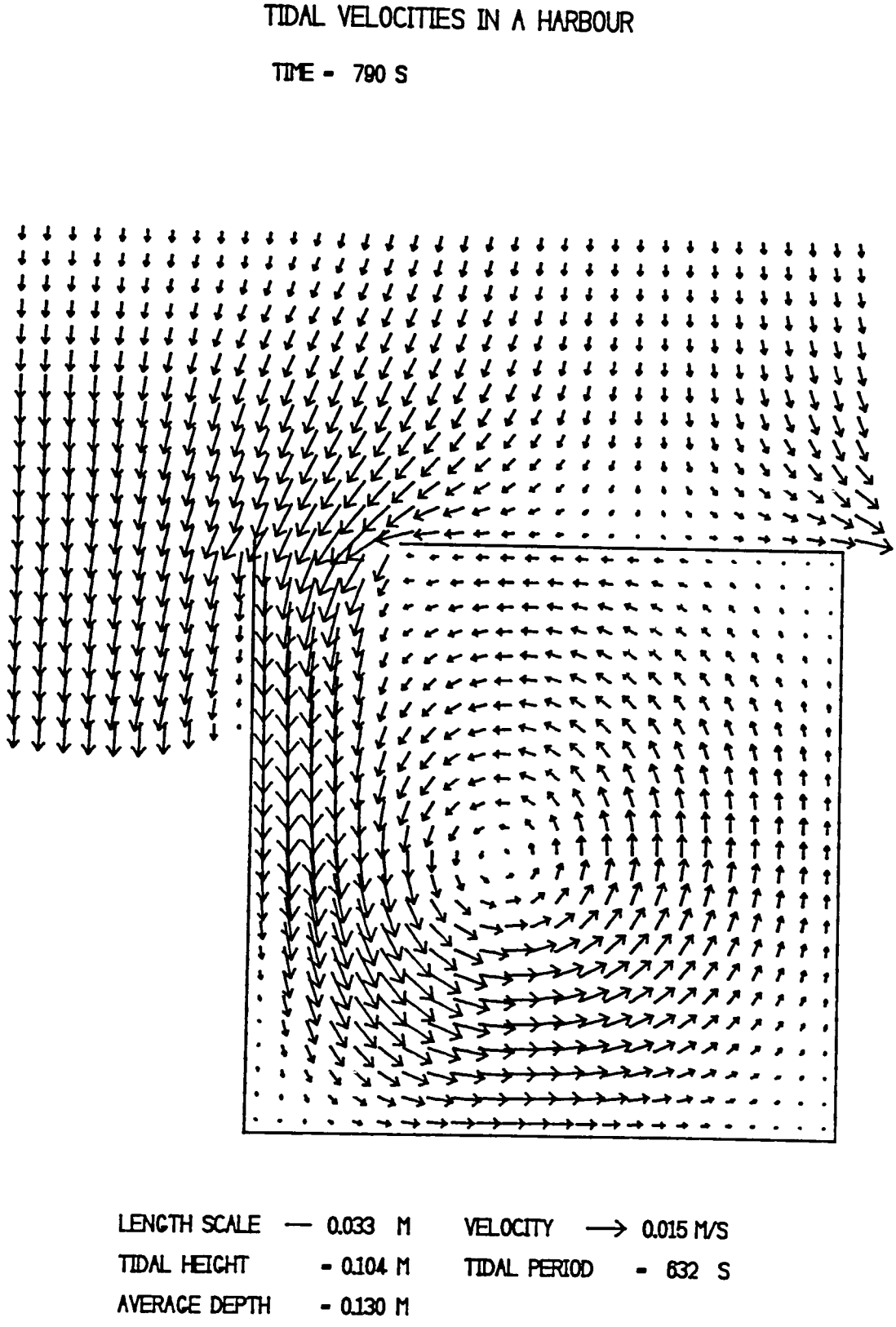

Figure 7.27 Predicted velocity field by fine-grid model at mean water flood tide for L/B=1.0

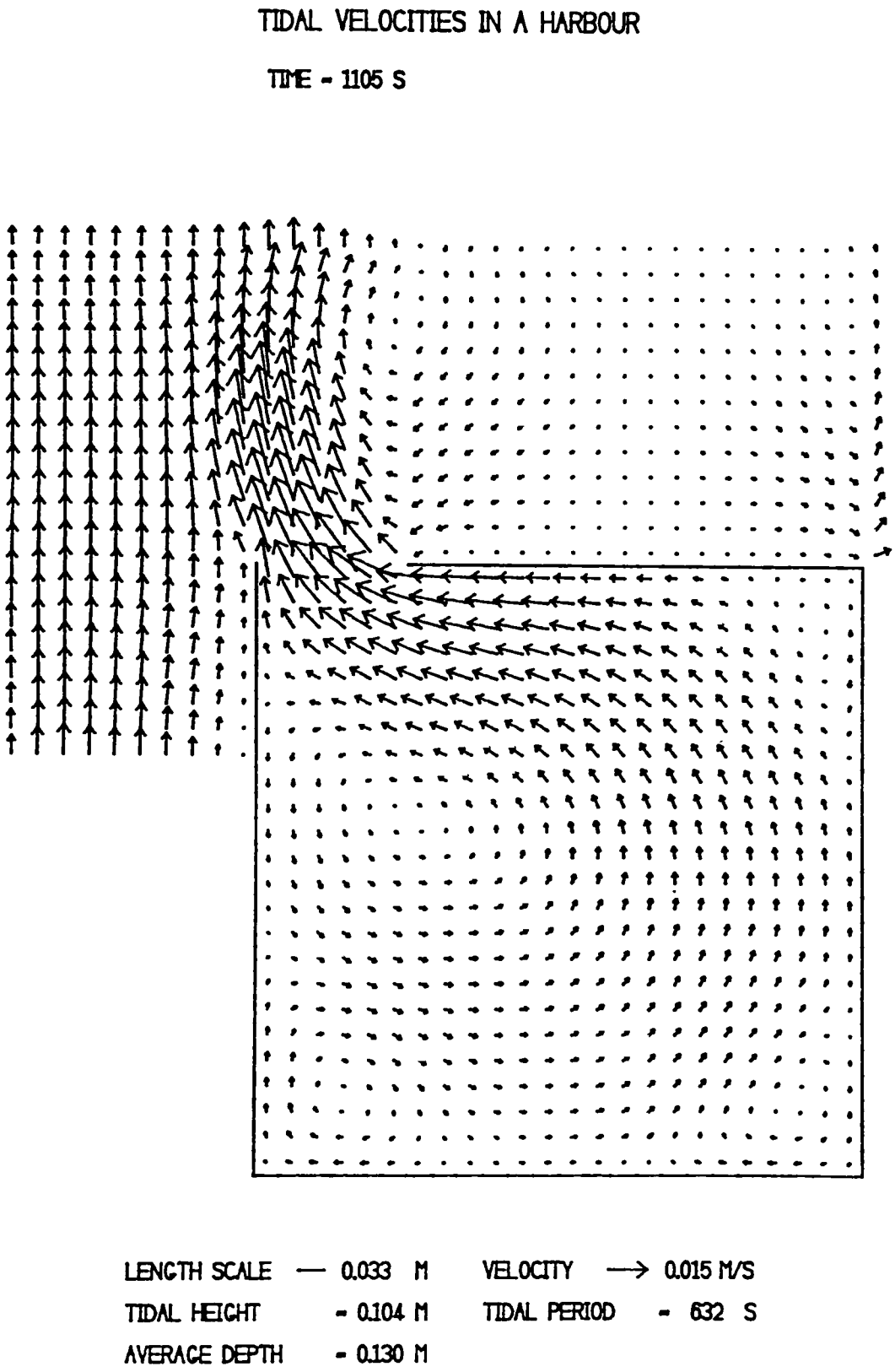

Figure 7.28 Predicted velocity field by fine-grid model at mean water ebb tide for L/B=1.0

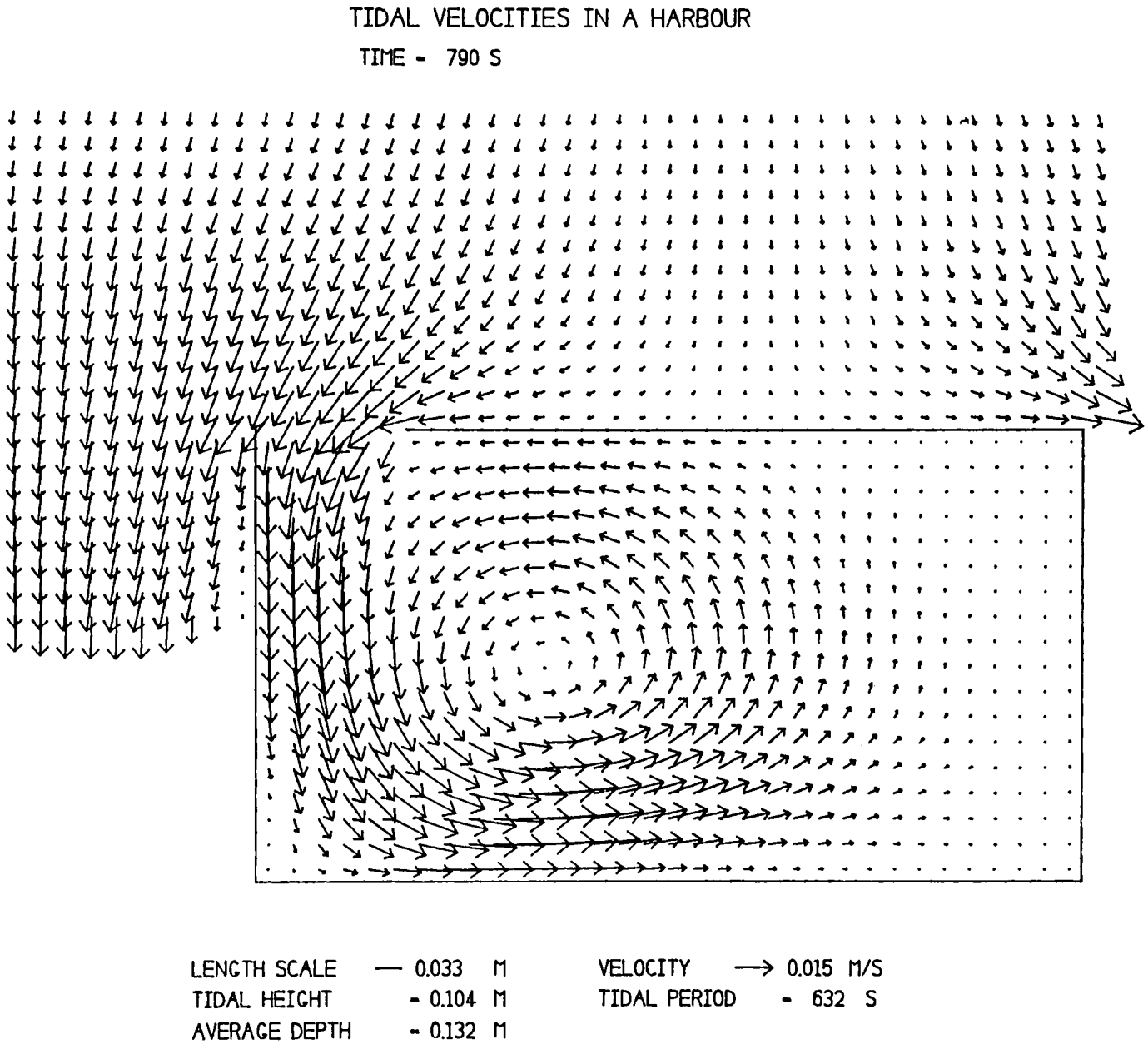

Figure 7.29 Predicted velocity field by fine-grid model at mean water flood tide for L/B=1.833

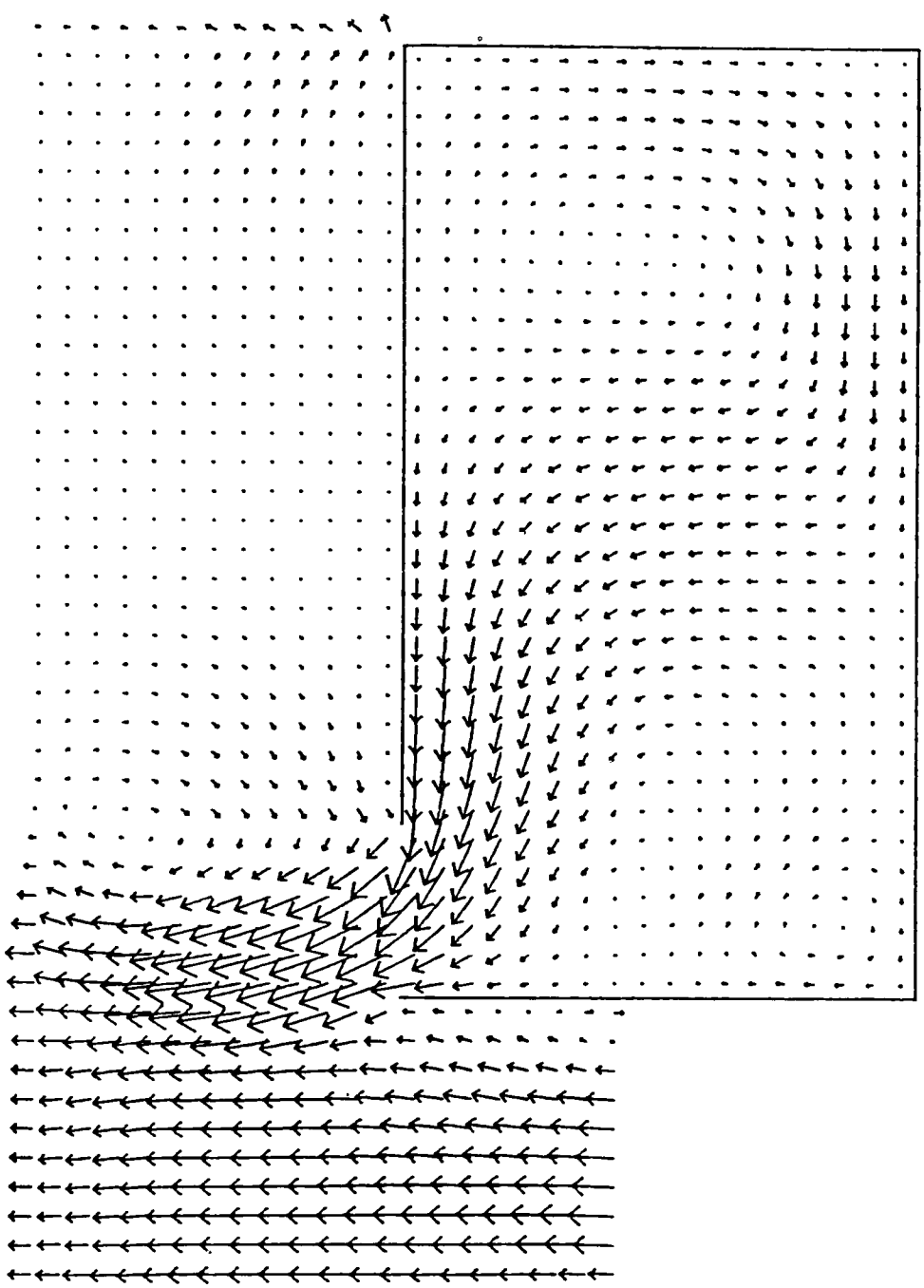

Figure 7.30 Predicted velocity field by fine-grid model at mean water ebb tide for L/B=1.833

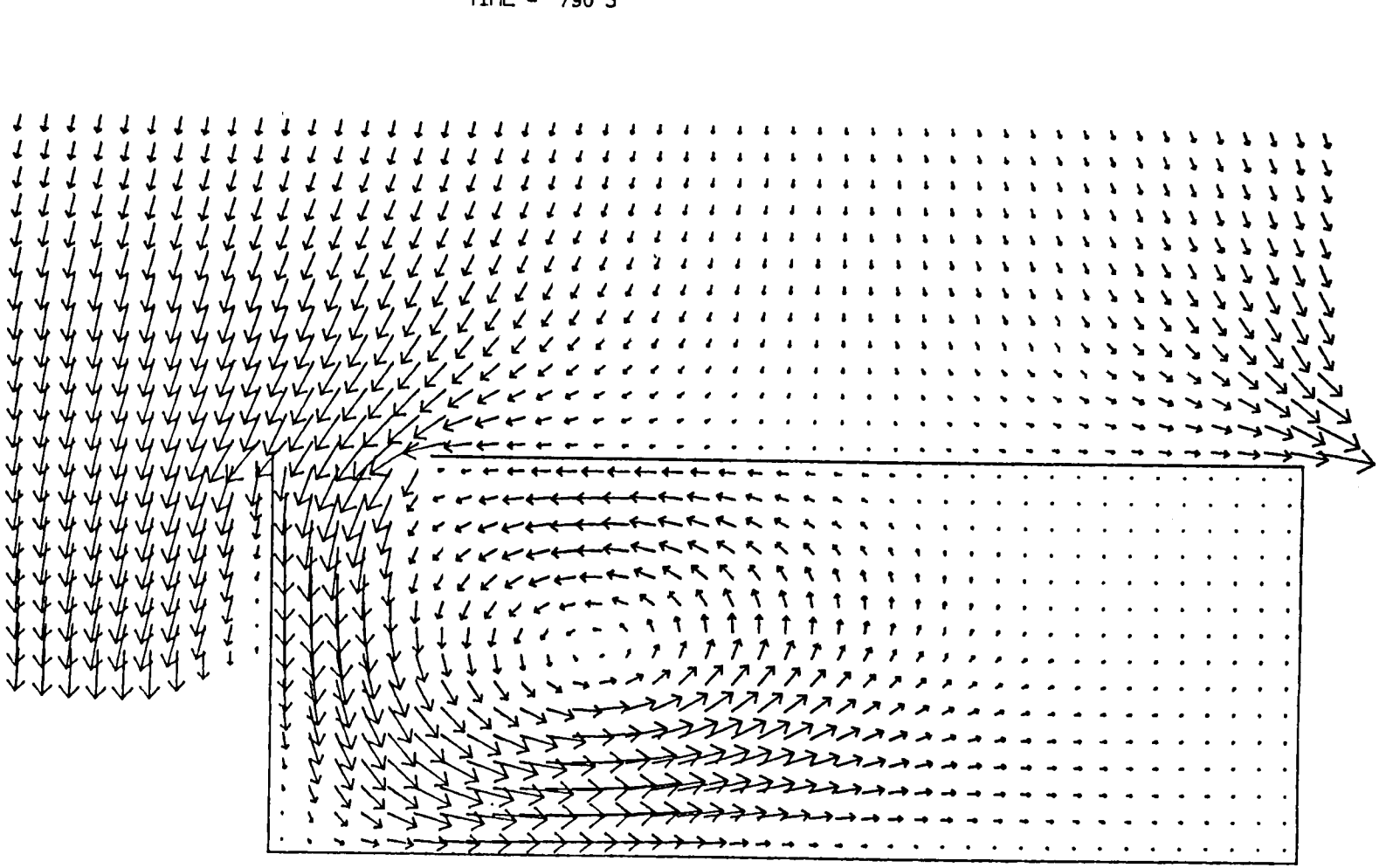

Figure 7.31 Predicted velocity field by fine-grid model at mean water flood tide for L/B=2.6

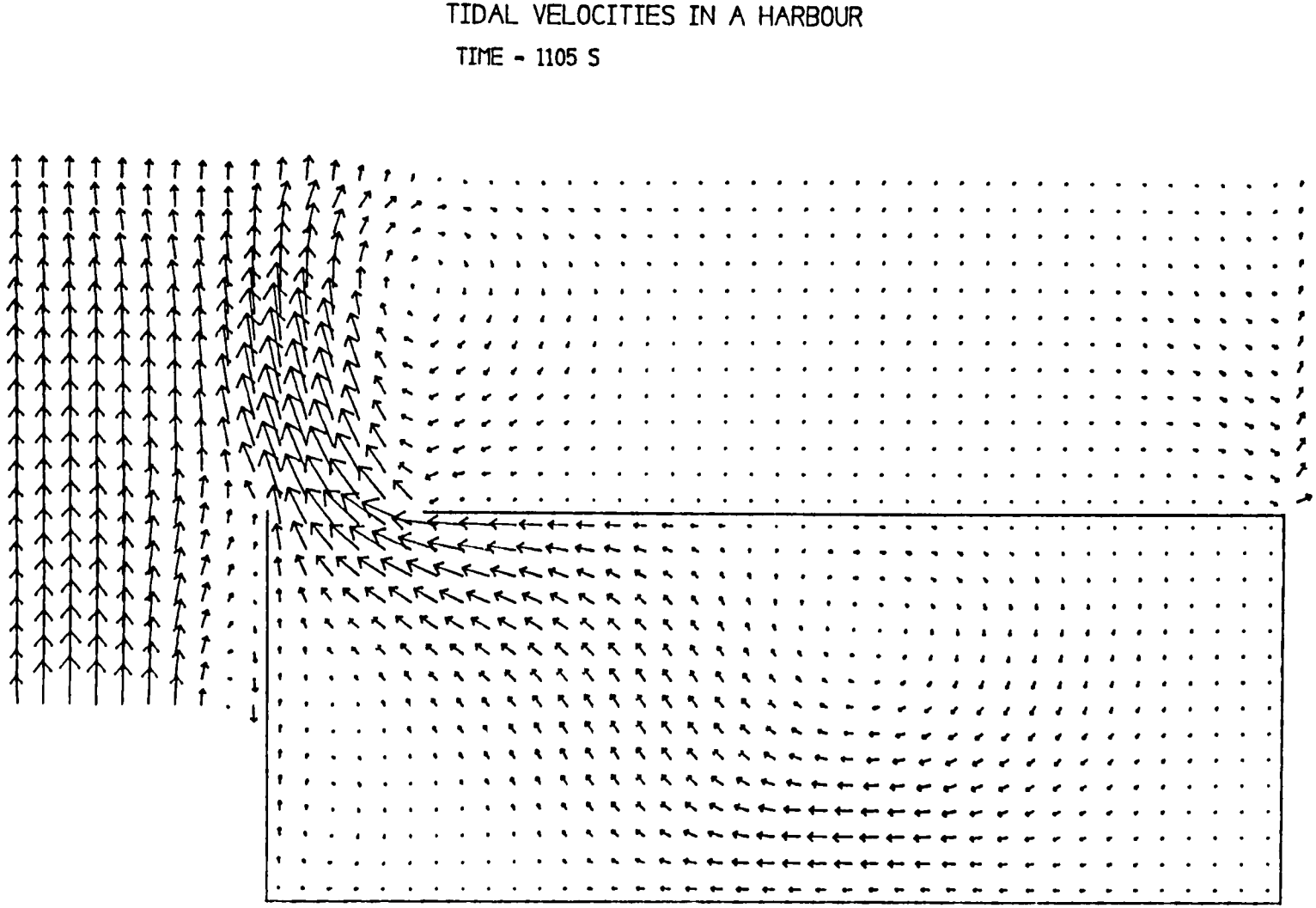

Figure 7.32 Predicted velocity field by fine-grid model at mean water ebb tide for L/B=2.6

SHEAR STRESS DISTRIBUTION IN A HARBOUR

TIME = 790 S

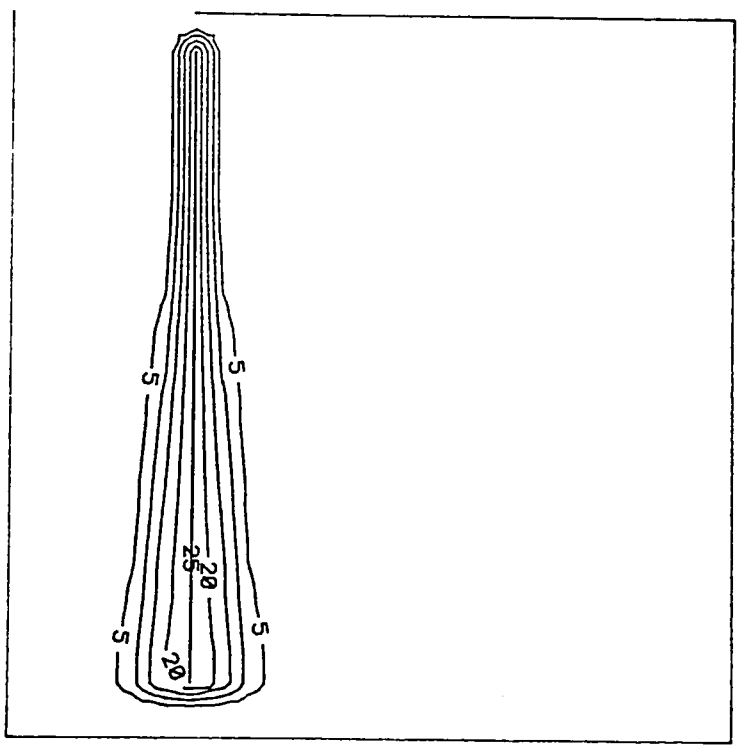

LENGTH SCALE — 0.033 M SHEAR STRESS IN 10^{-4} NT/M^2

TIDAL HEIGHT = 0.104 M TIDAL PERIOD = 632 S

Figure 7.33 Empirically determined free shear layer stress distribution at mean water flood tide for L/B=1.0

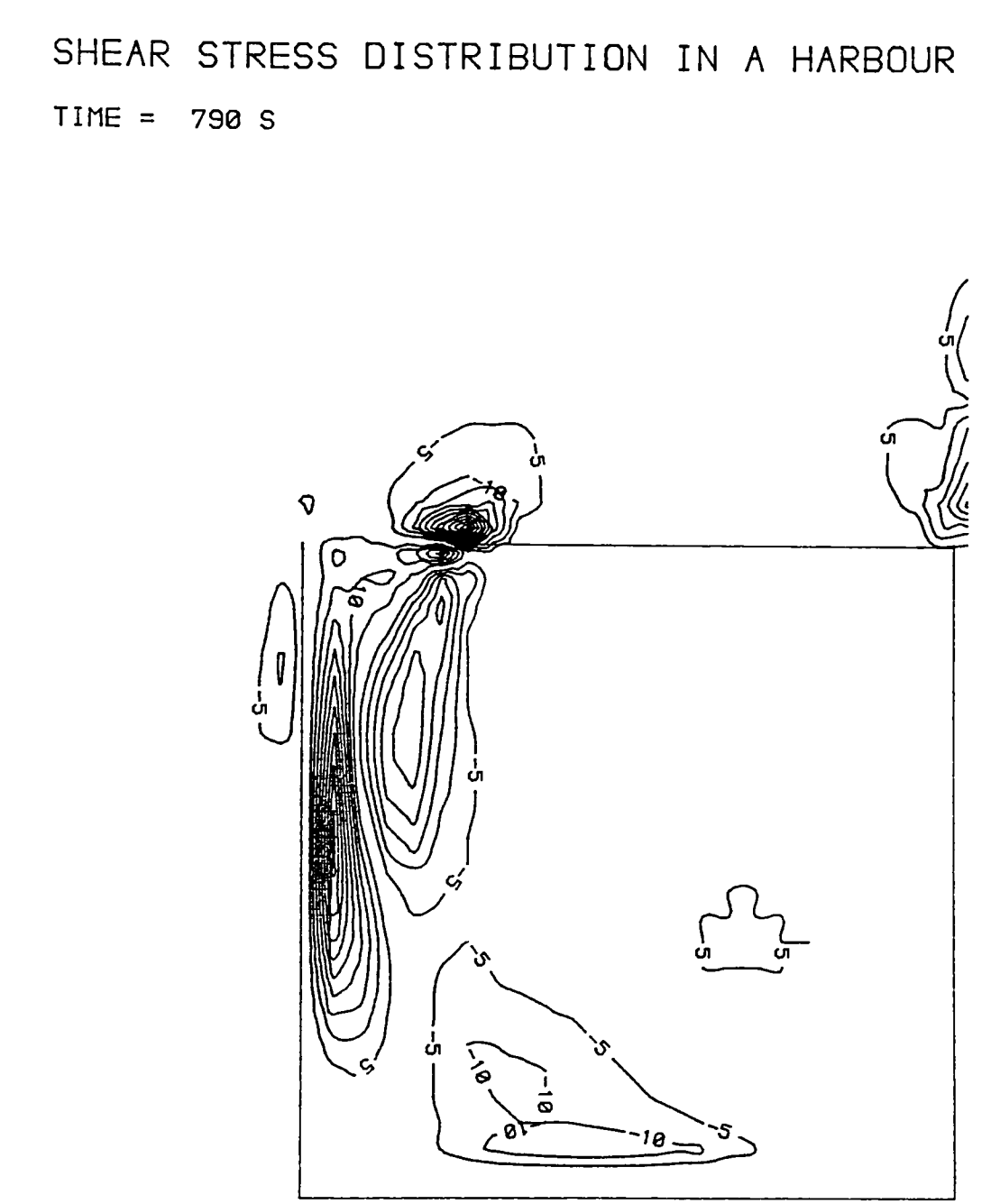

Figure 7.34 Predicted bed generated shear stress distribution at mean water flood tide for L/B=1.0

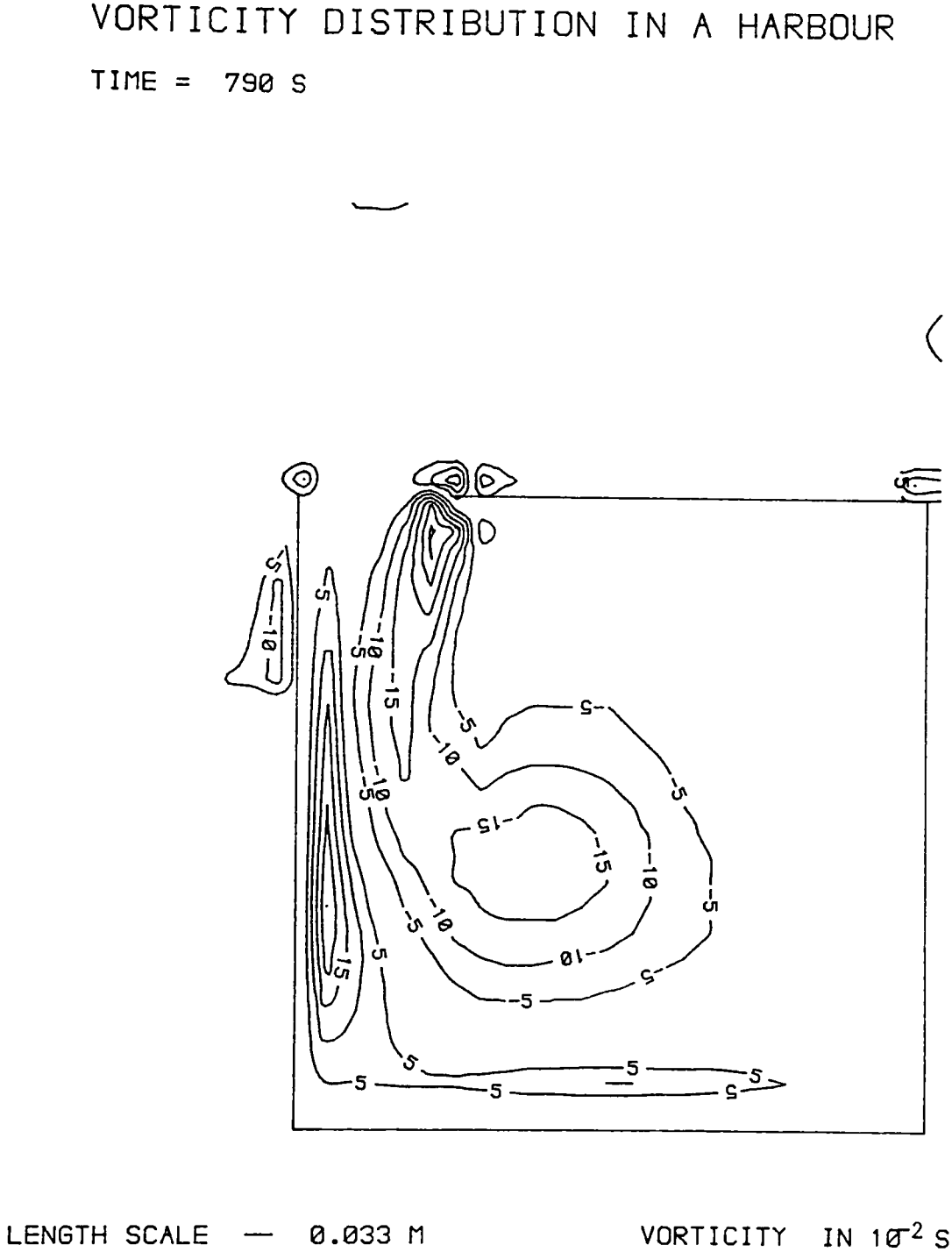

Figure 7.35 Predicted vorticity distribution at mean water flood tide for L/B=1.0

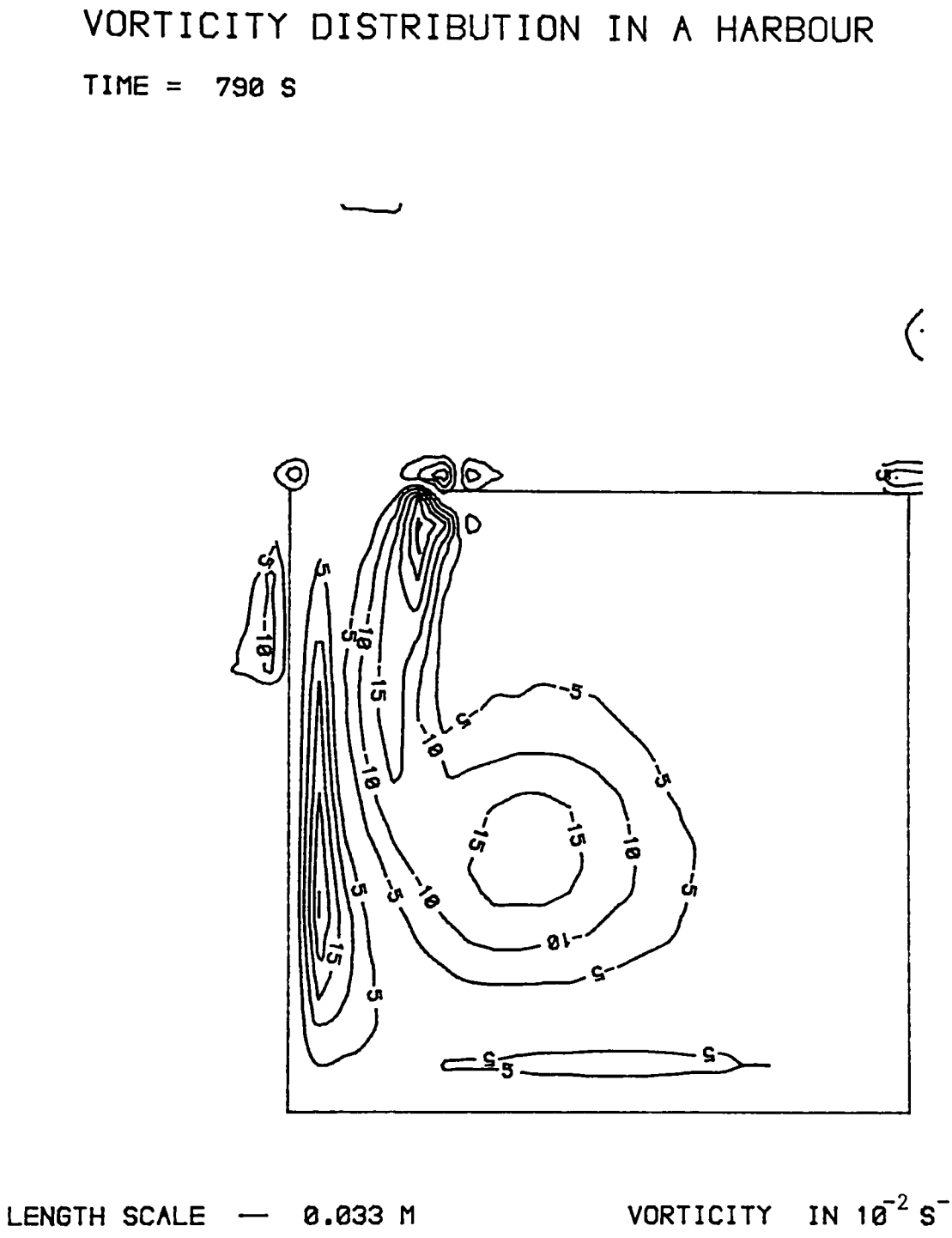

Figure 7.36 Predicted vorticity distribution at mean water flood tide for L/B=1.0, with the exclusion of free shear layer stress

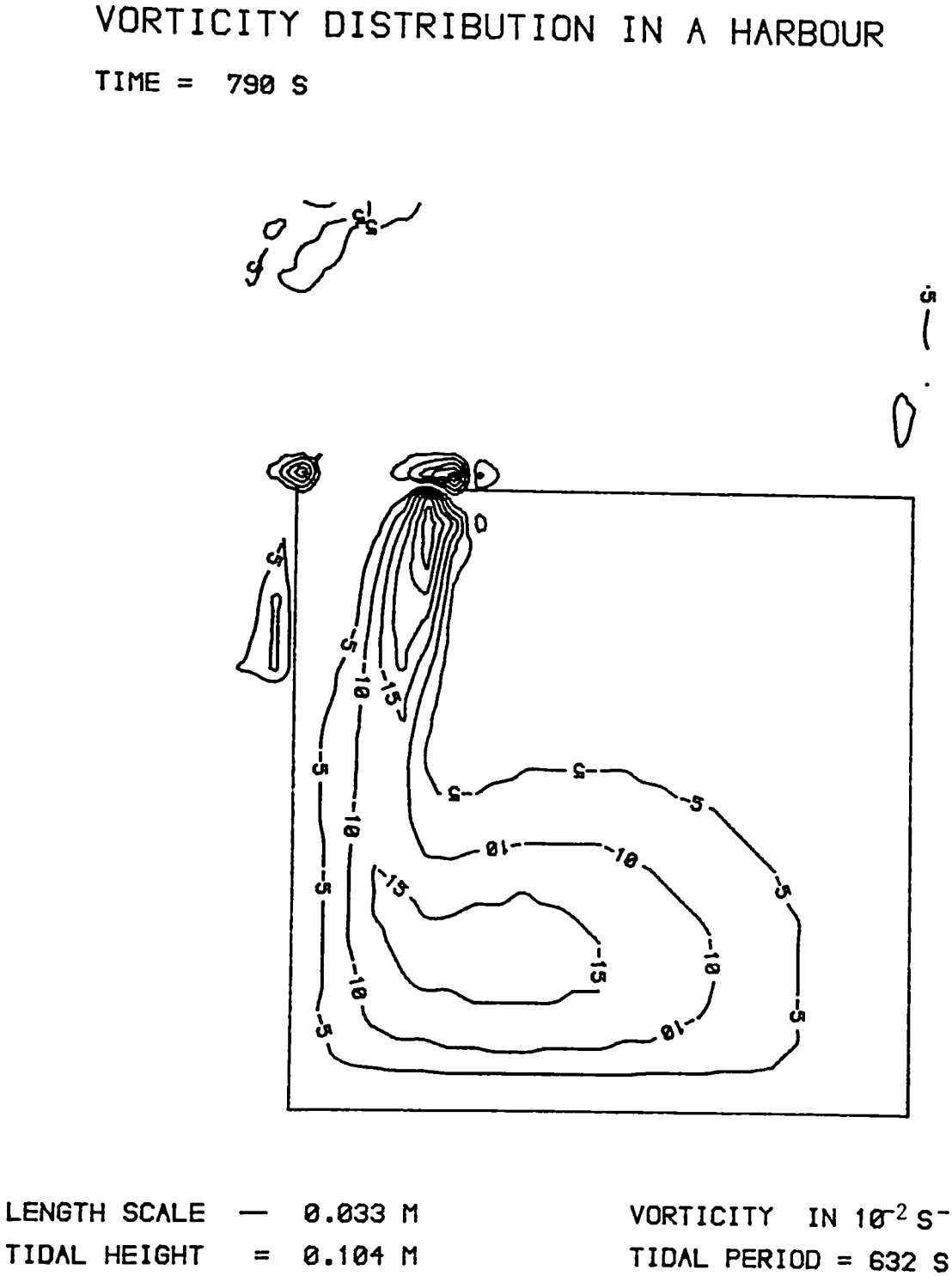

Figure 7.37 Predicted vorticity distribution at mean water flood tide for L/B=1.0, with the exclusion of all lateral shear stresses

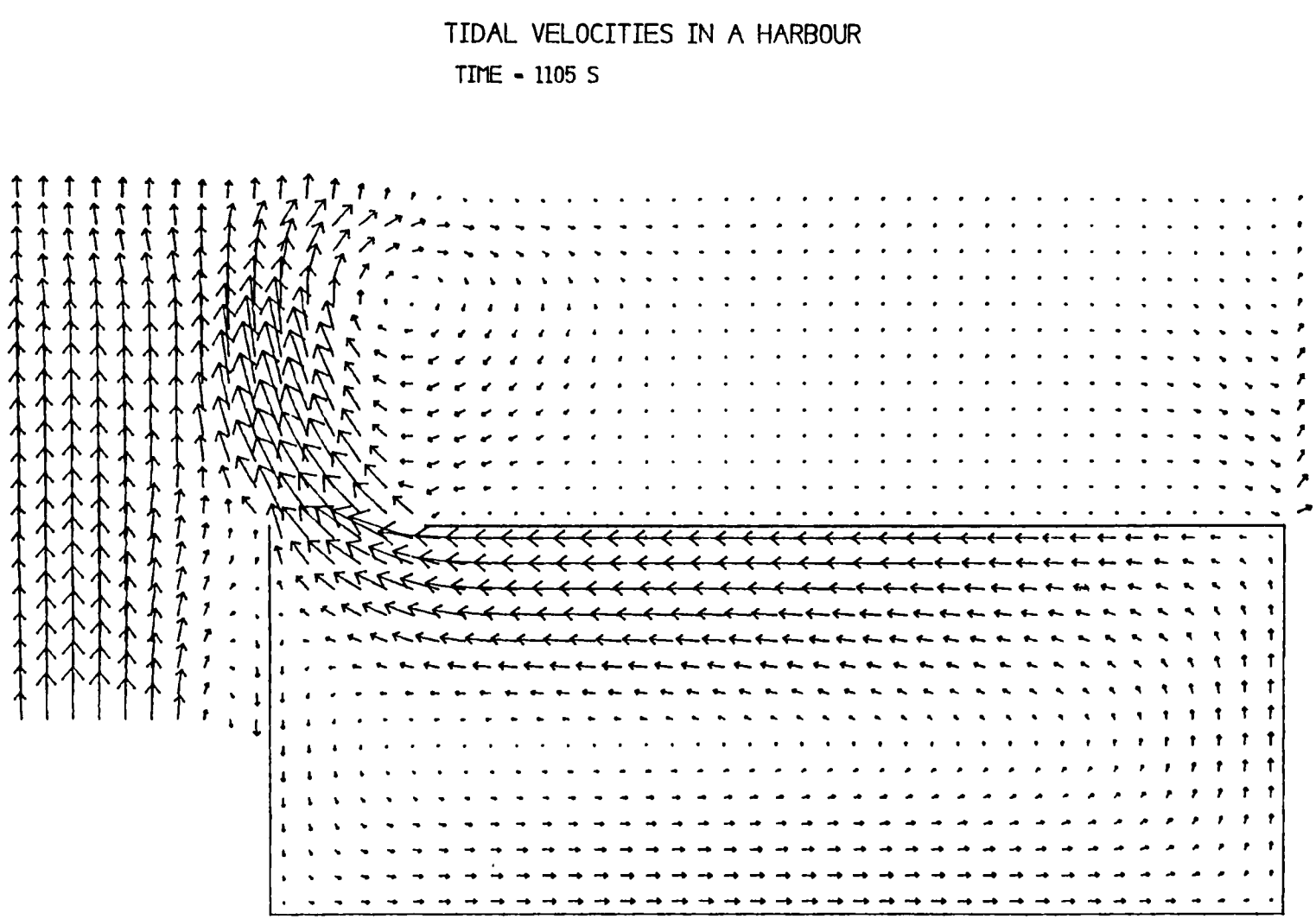

Figure 7.38 Predicted velocity field at mean water ebb tide for L/B=2.6, for the free-slip boundary condition

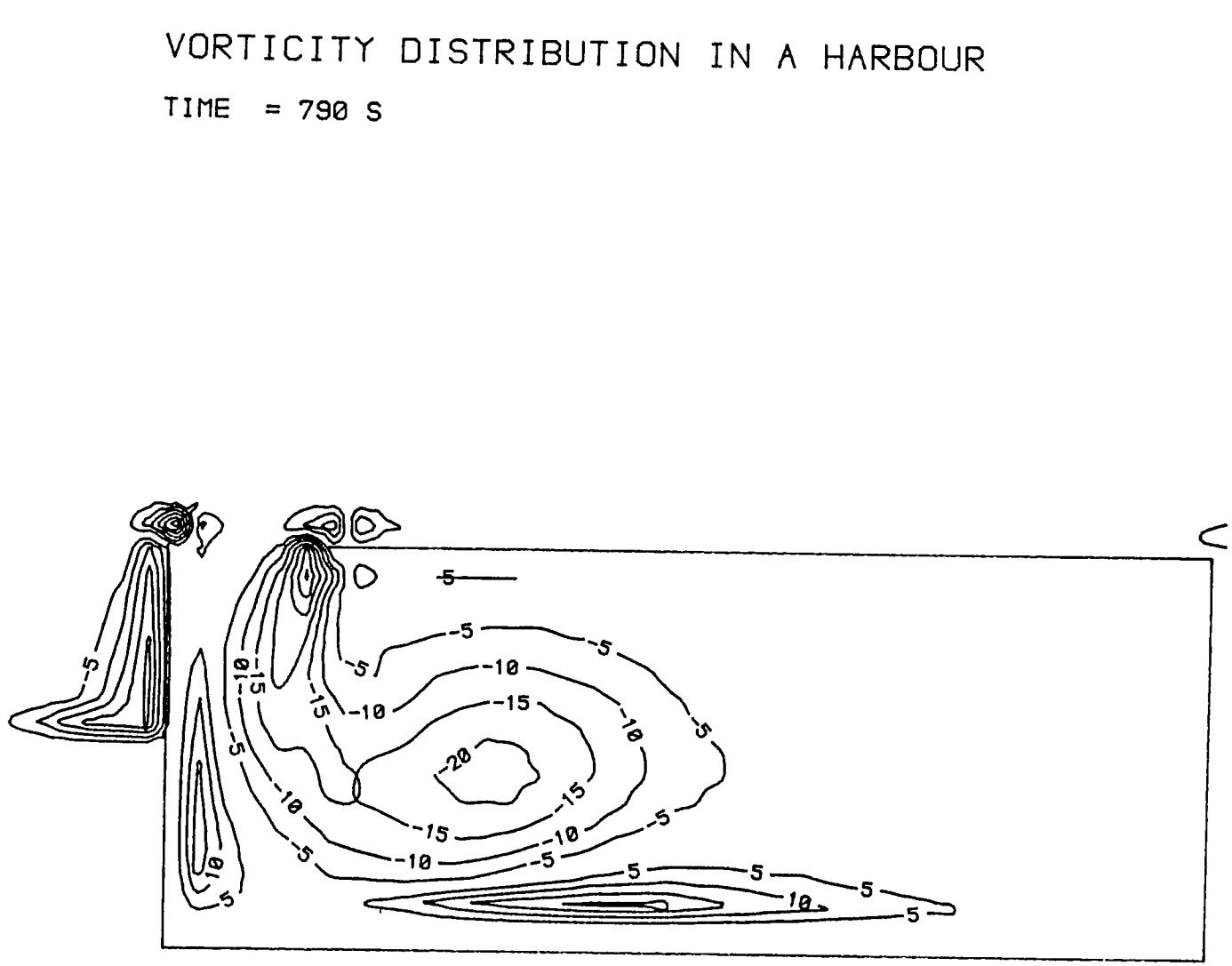

Figure 7.39 Predicted vorticity distribution at mean water ebb tide for L/B=2.6

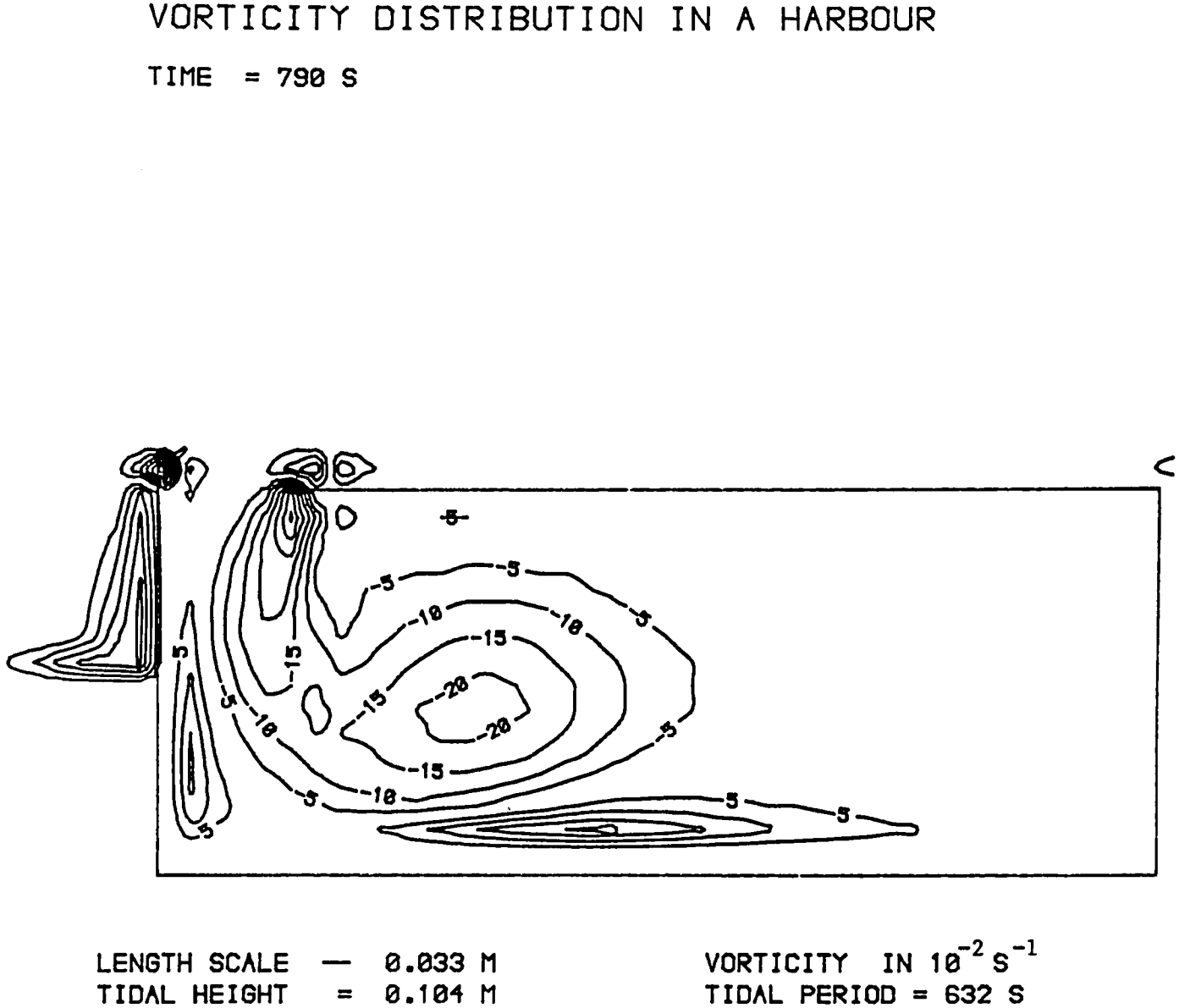

Figure 7.40 Predicted vorticity distribution at mean water ebb tide for L/B=2.6 for a constant Manning coefficient of 0.012

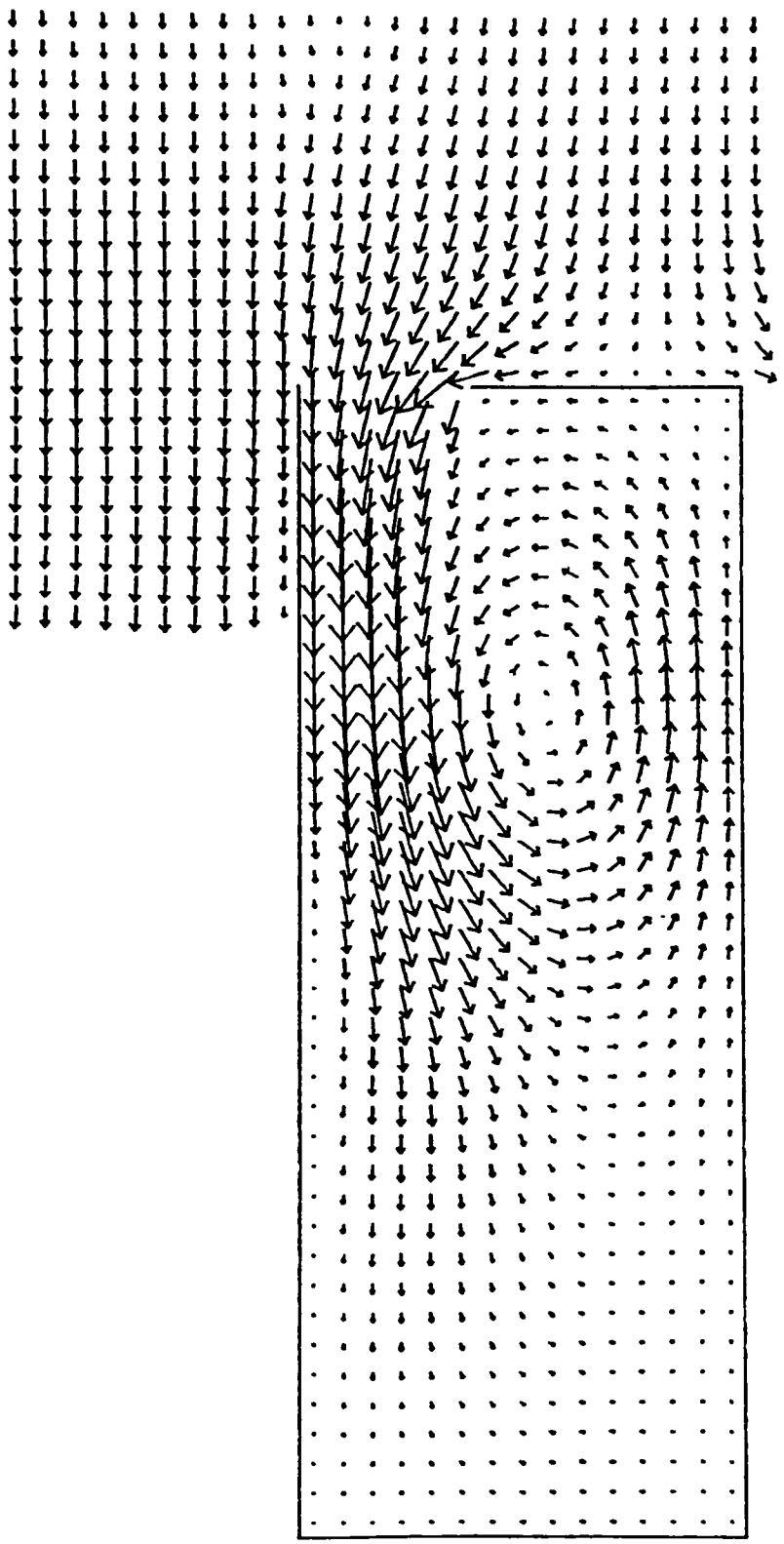

Figure 7.41 Predicted velocity field at mean water flood tide for L/B=1/2.6

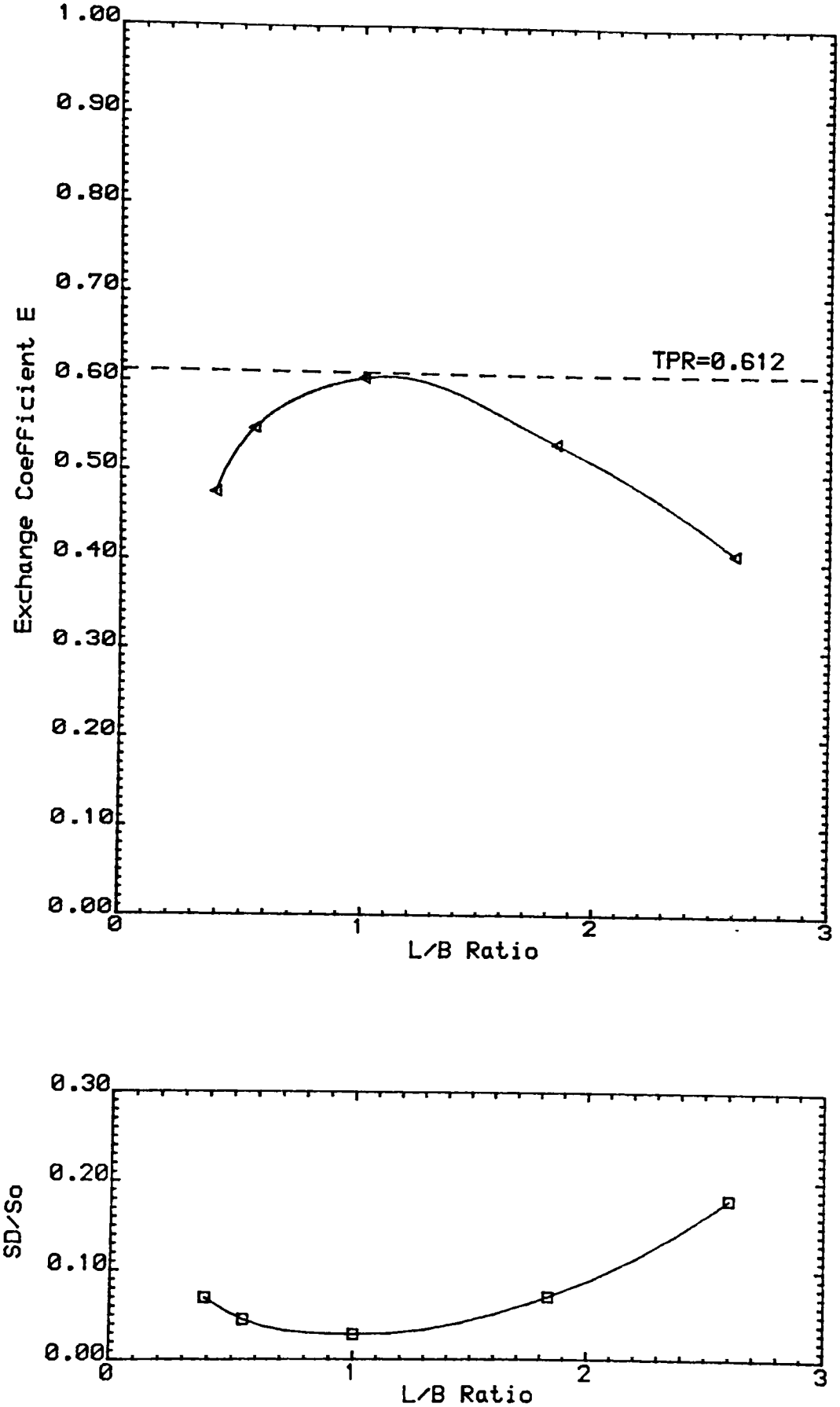

Figure 7.42 Predicted variation of exchange coefficient E and standard deviation SD with L/B ratio

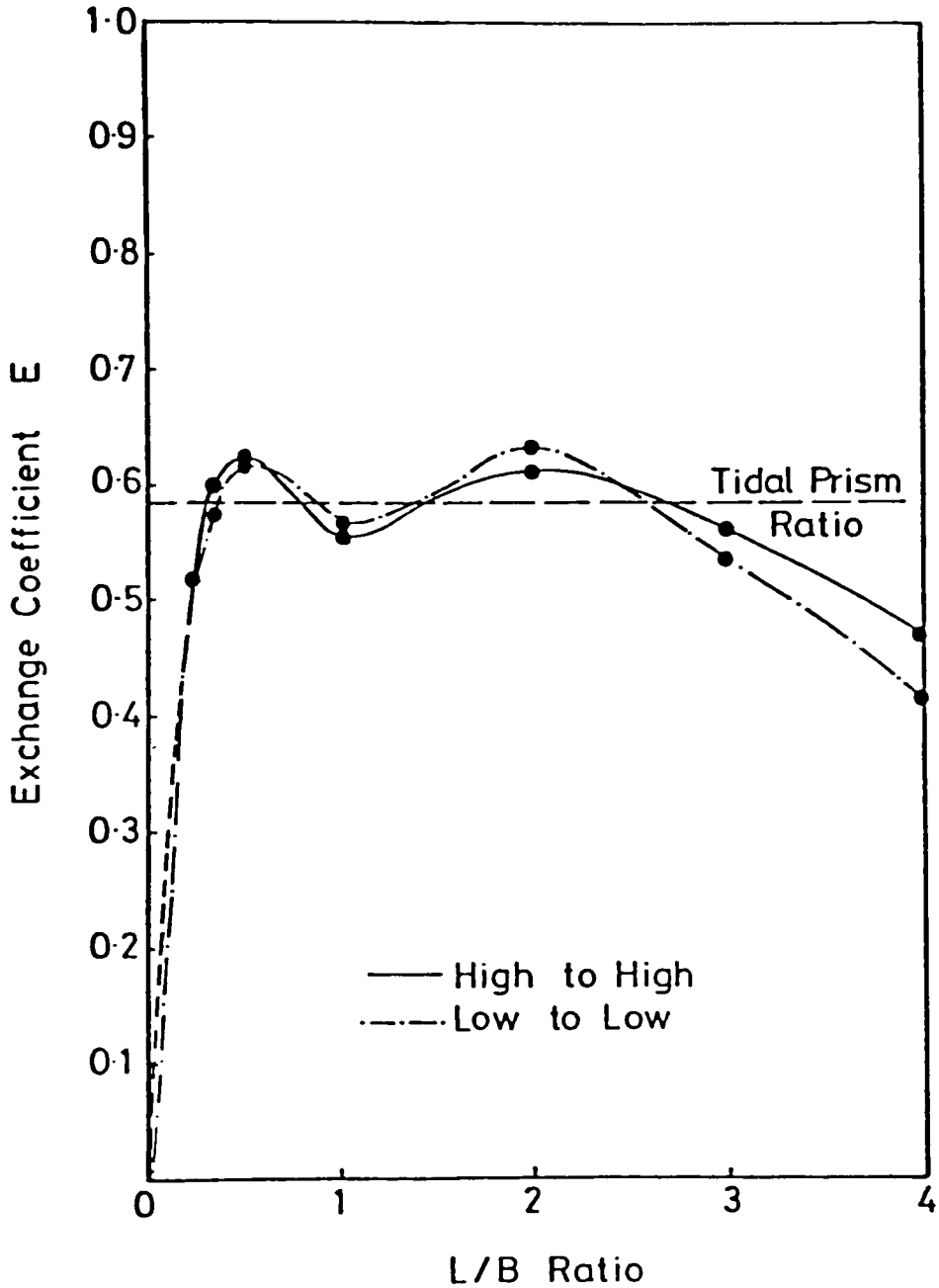

Figure 7.43 Variation of exchange coefficient E with L/B ratio for prototype tidal range of 5.0 m, from laboratory tests

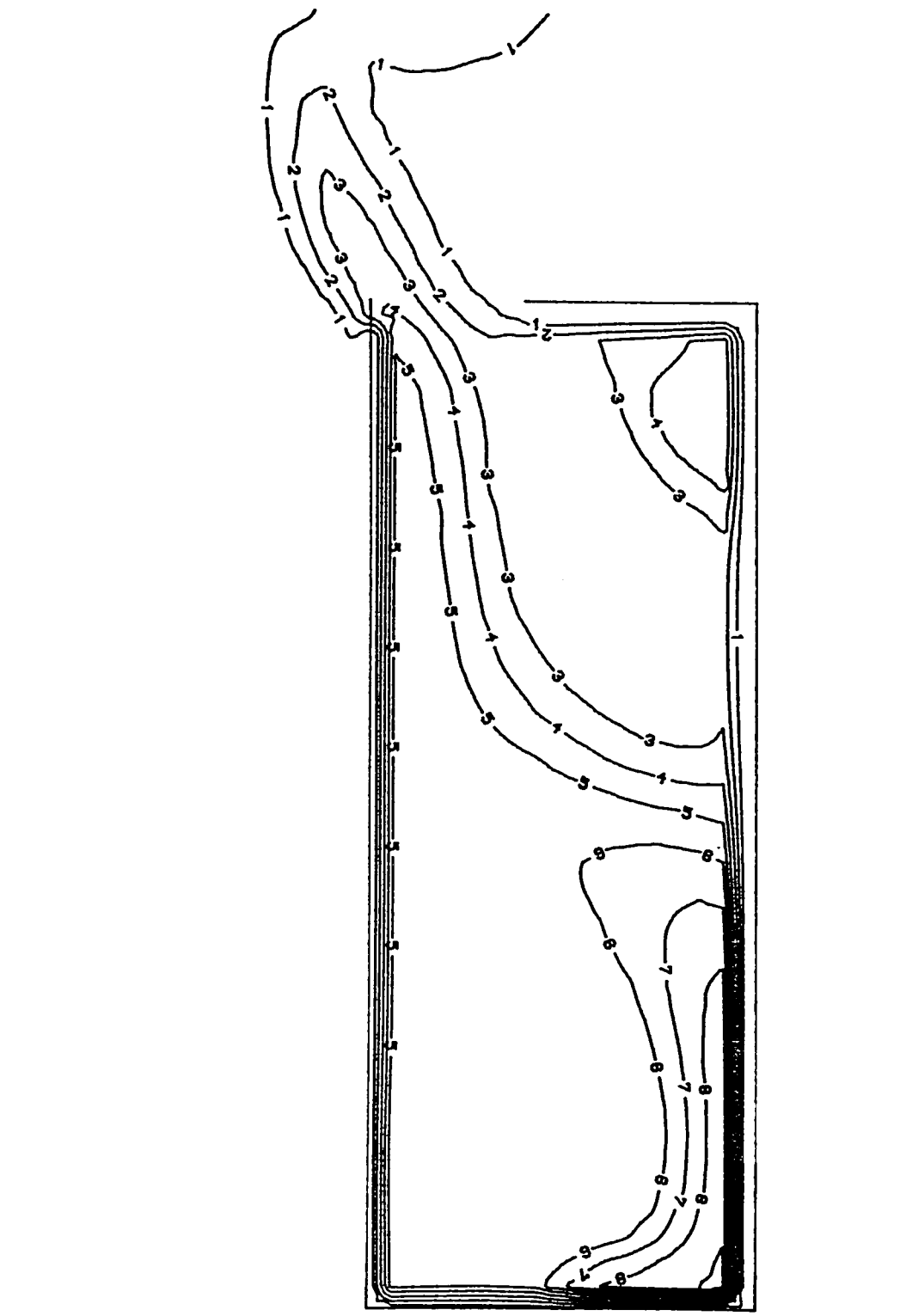

Figure 7.44 Predicted concentration distribution at end of first tidal cycle for L/B=1/2.6

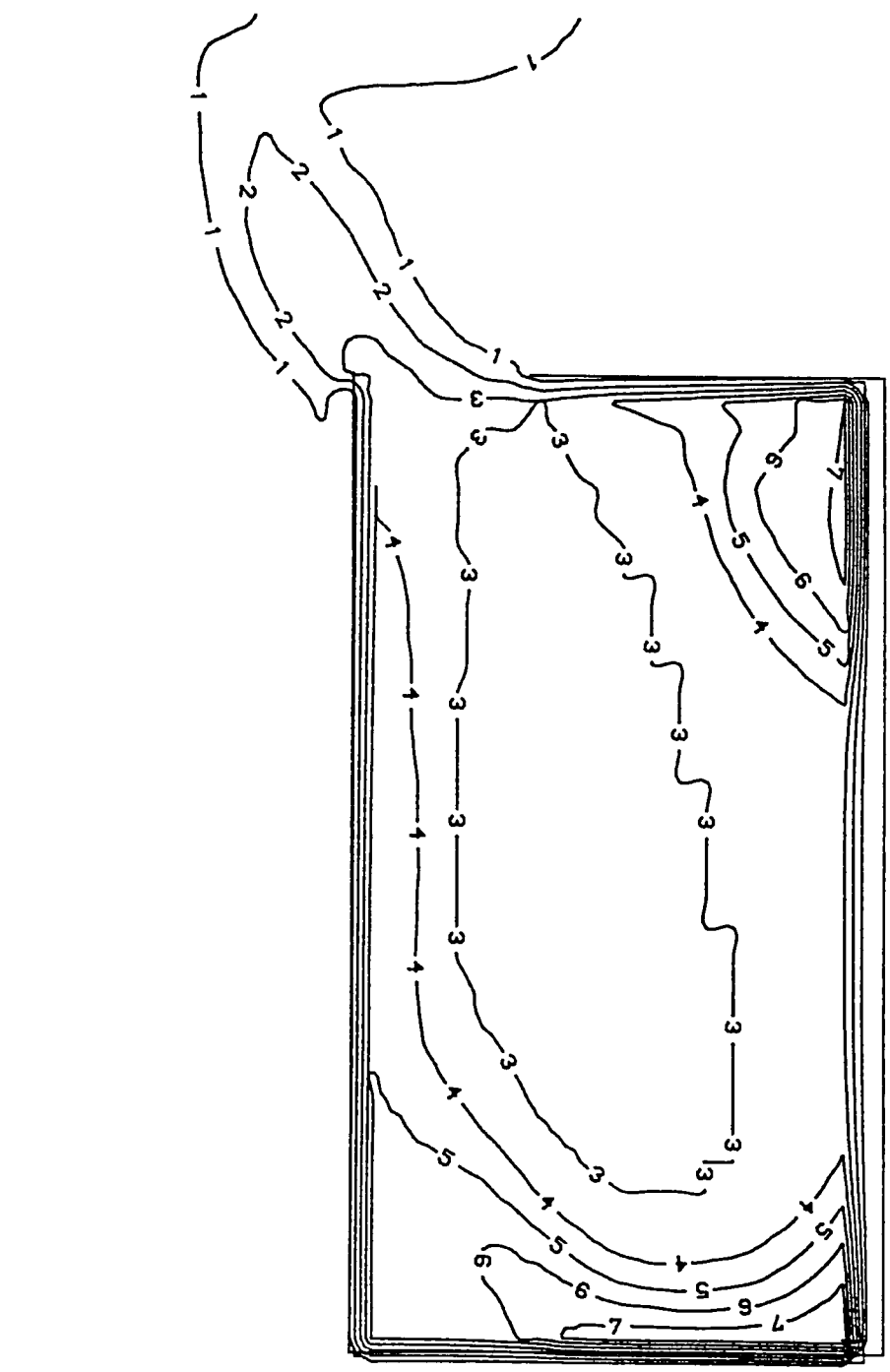

Figure 7.45 Predicted concentration distribution at end of first tidal cycle for L/B=1/1.833

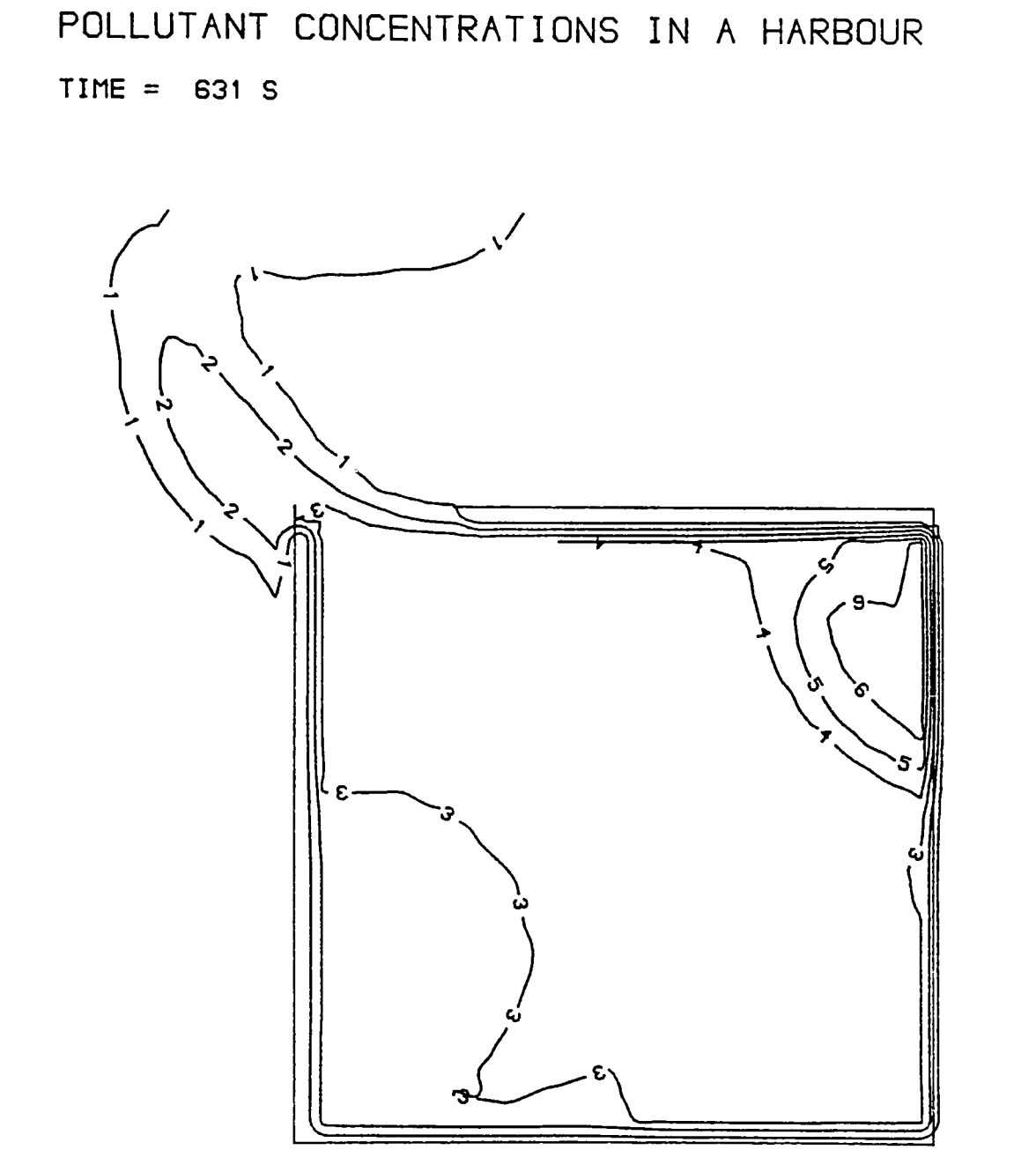

Figure 7.46 Predicted concentration distribution at end of first tidal cycle for L/B=1.0

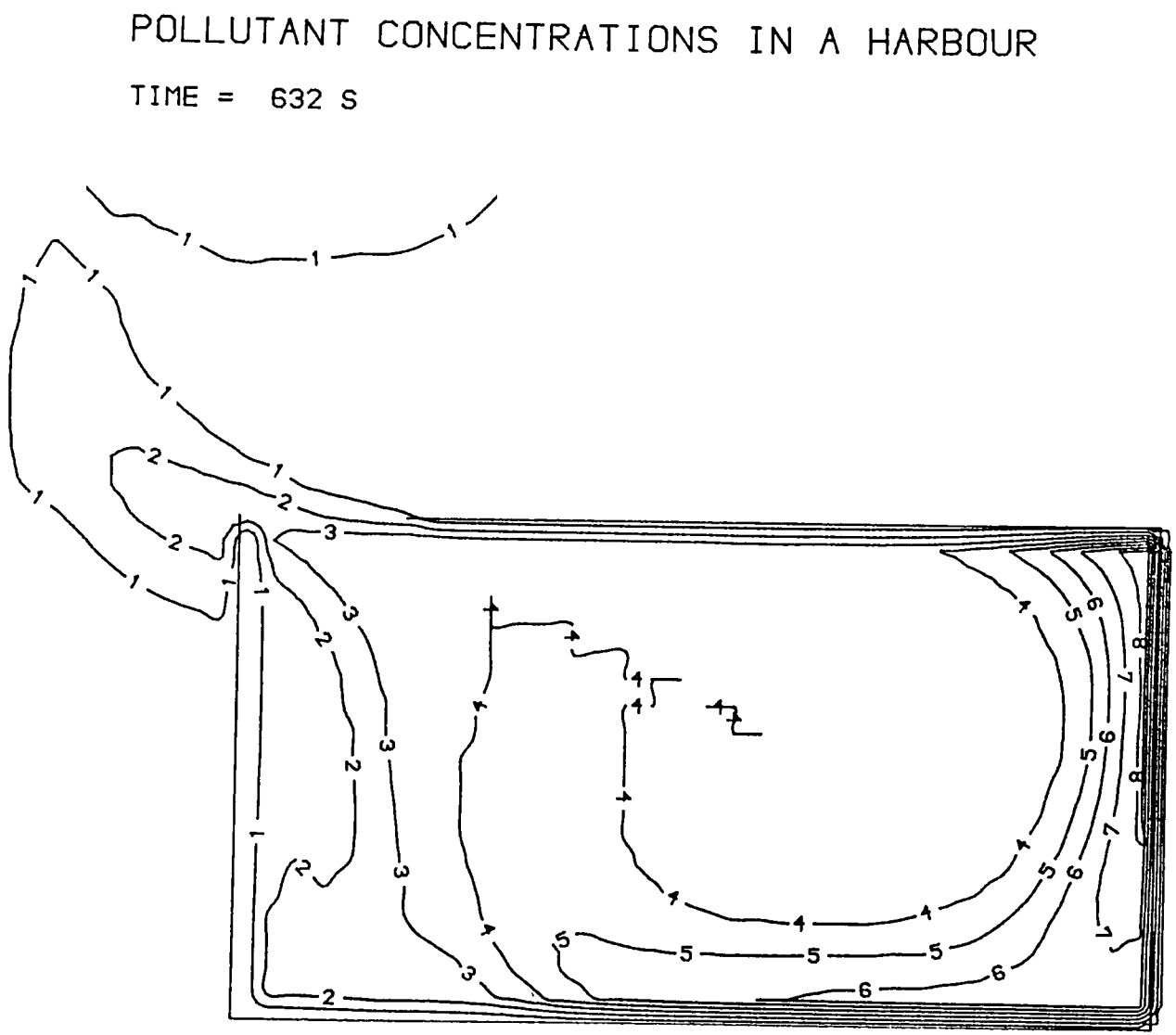

Figure 7.47 Predicted concentration distribution at end of first tidal cycle for L/B=1.833

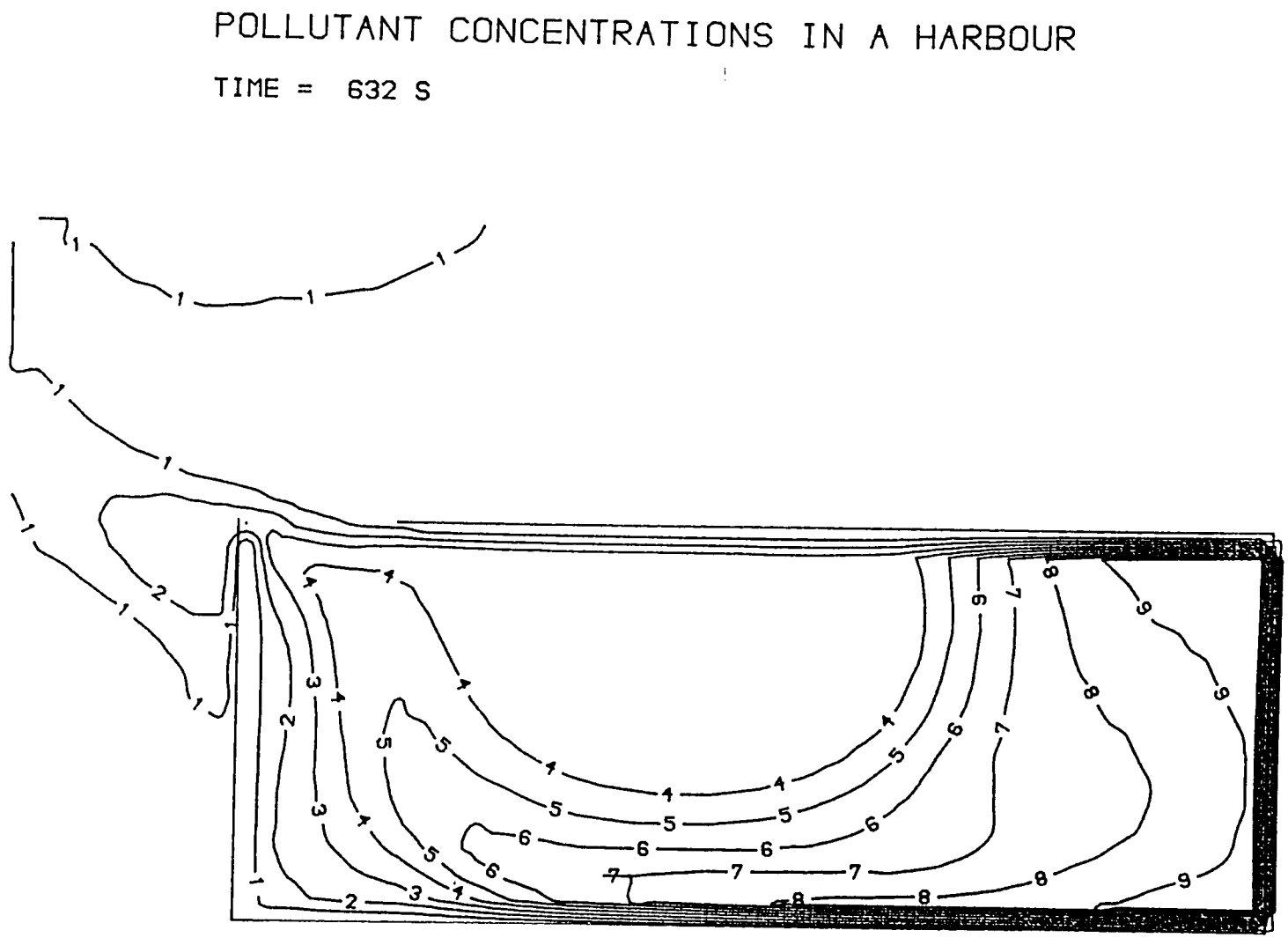

Figure 7.48 Predicted concentration distribution at end of first tidal cycle for L/B=2.6

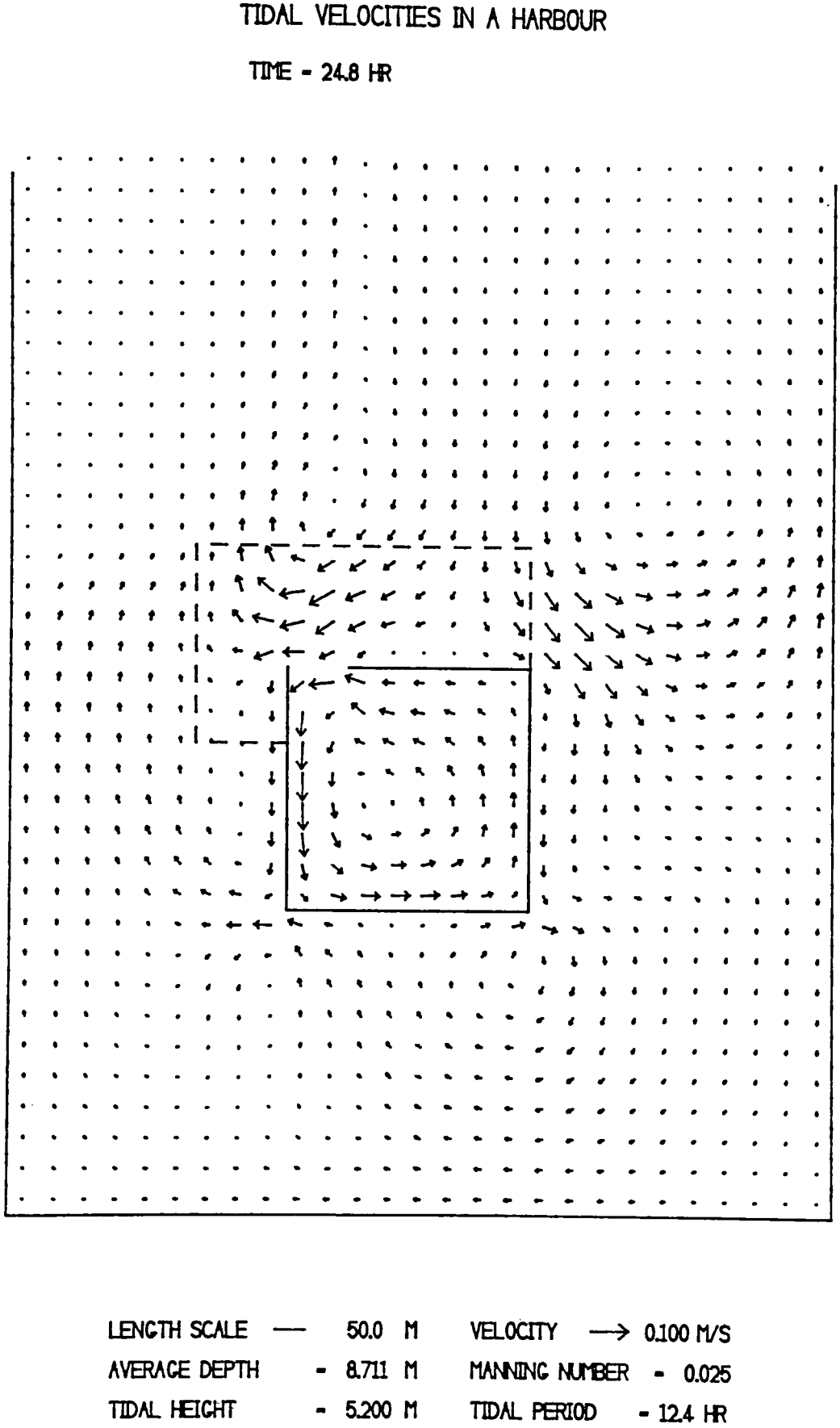

Figure 7.49 Predicted velocity field by coarse-grid model at low tide for prototype harbour with L/B=1.0

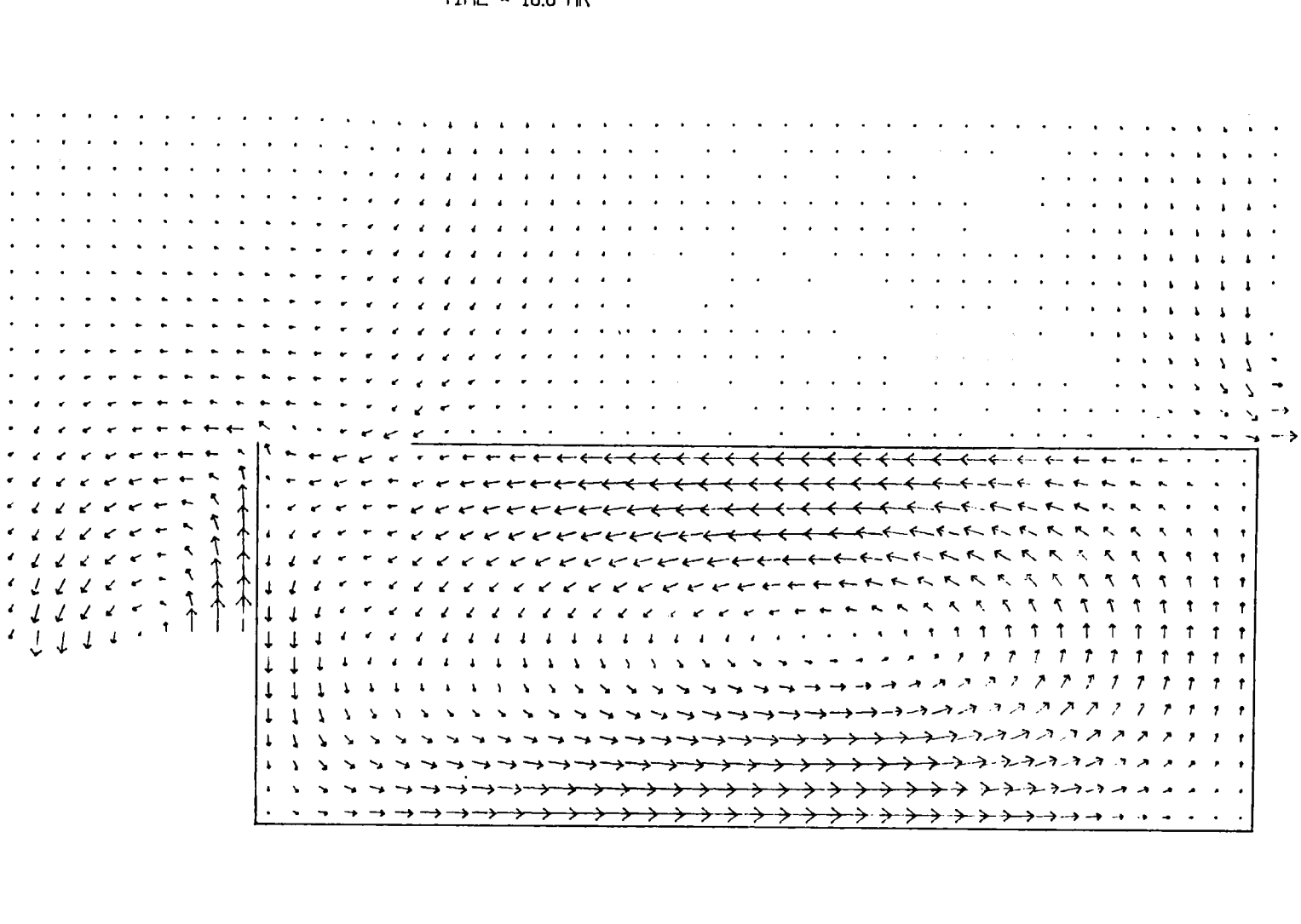

Figure 7.50 Predicted velocity field by fine-grid model at high tide for prototype harbour with L/B=2.6

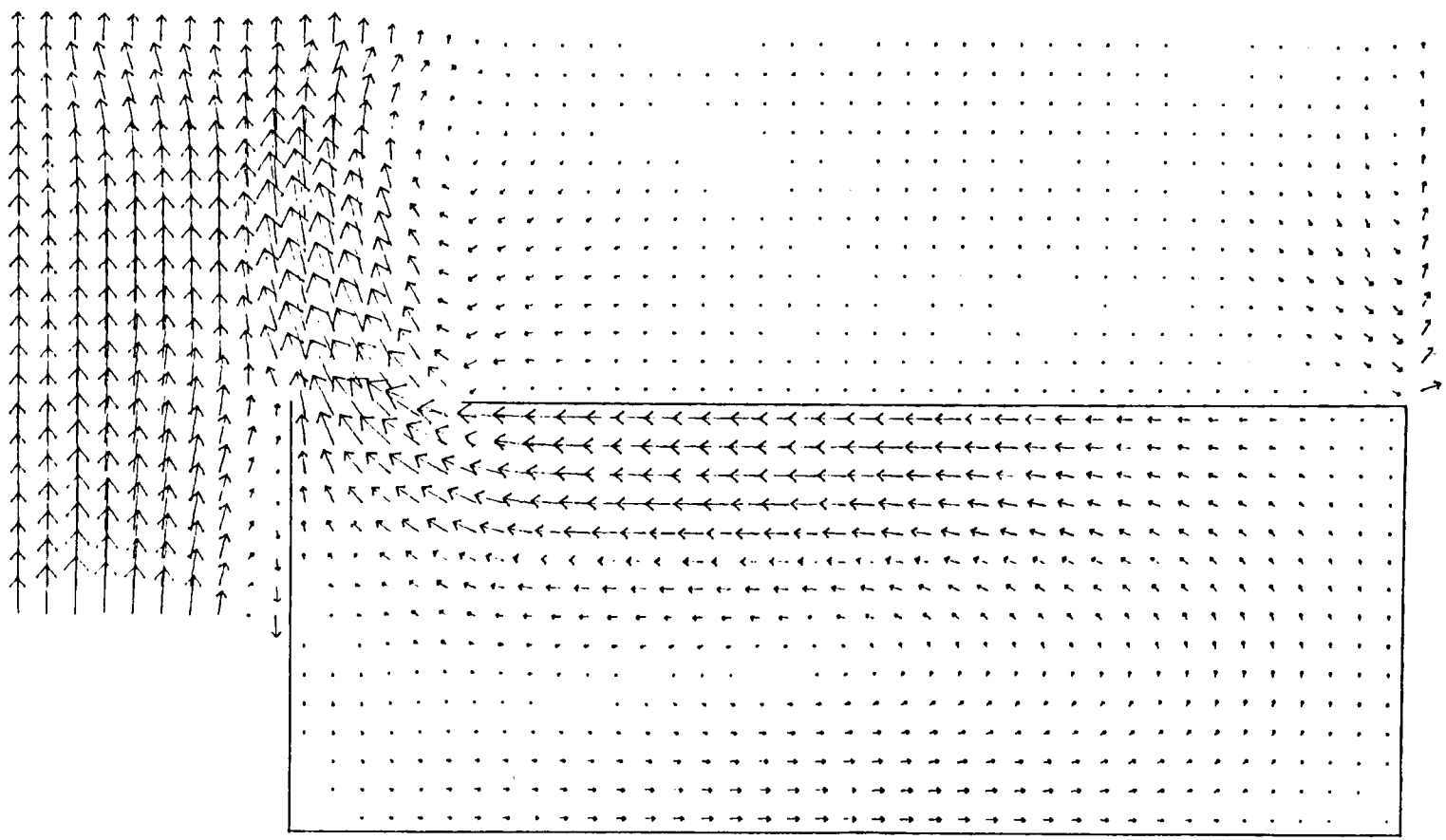

Figure 7.51 Predicted velocity field by fine-grid model at mean water ebb tide for prototype harbour with L/B=2.6

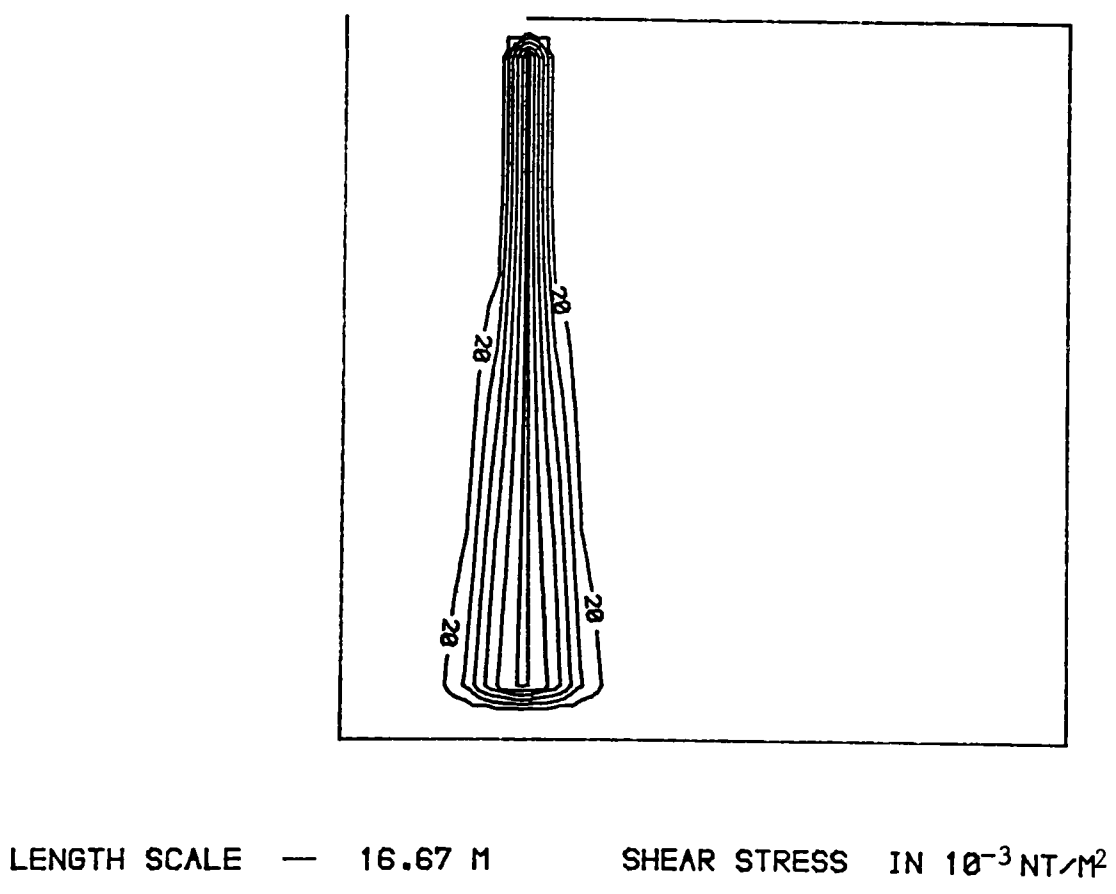

Figure 7.52 Empirically determined free shear layer stress distribution at mean water flood tide for prototype harbour with L/B=1.0

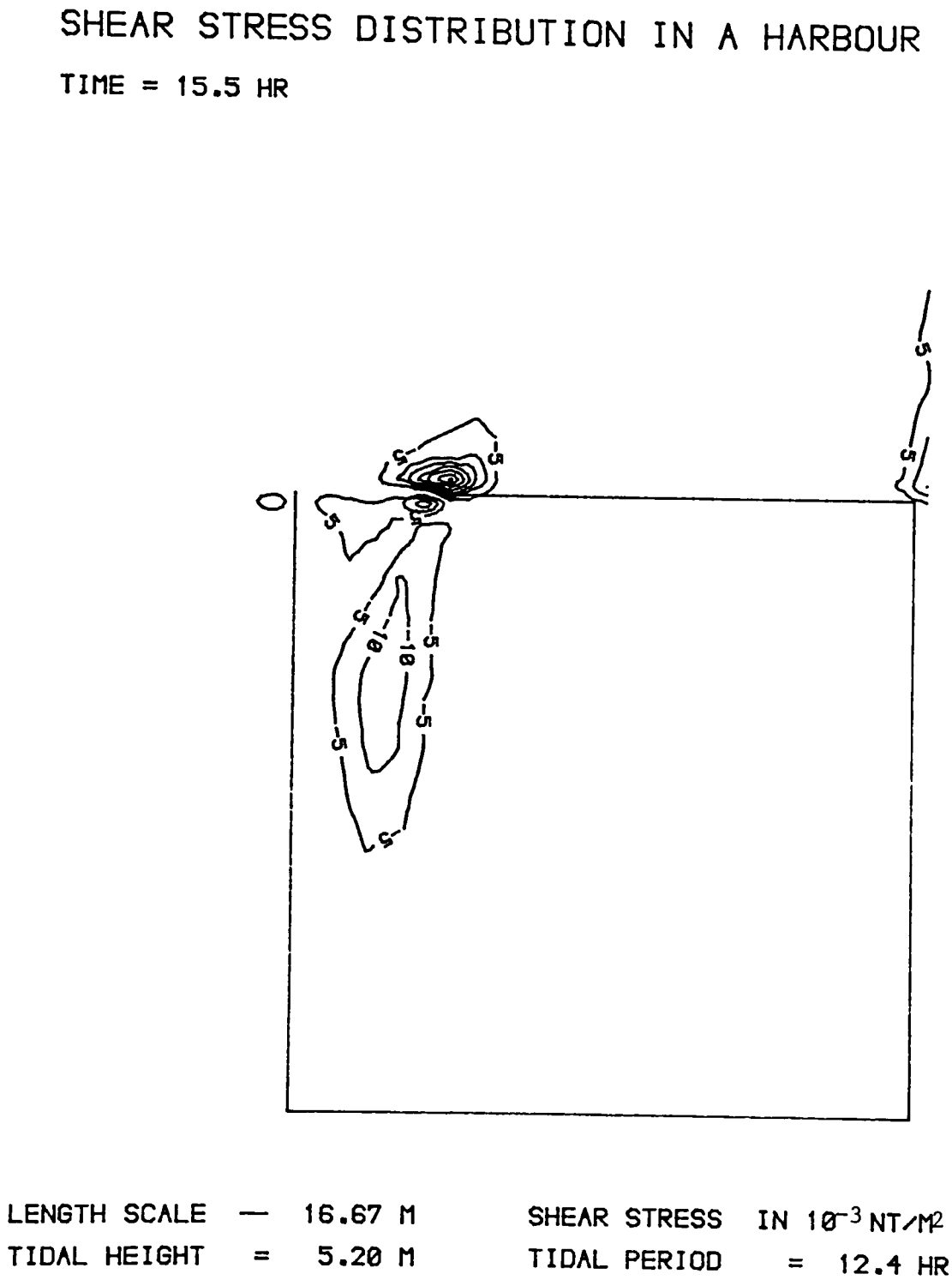

Figure 7.53 Predicted bed generated shear stress distribution at mean water flood tide for prototype harbour with L/B=1.0

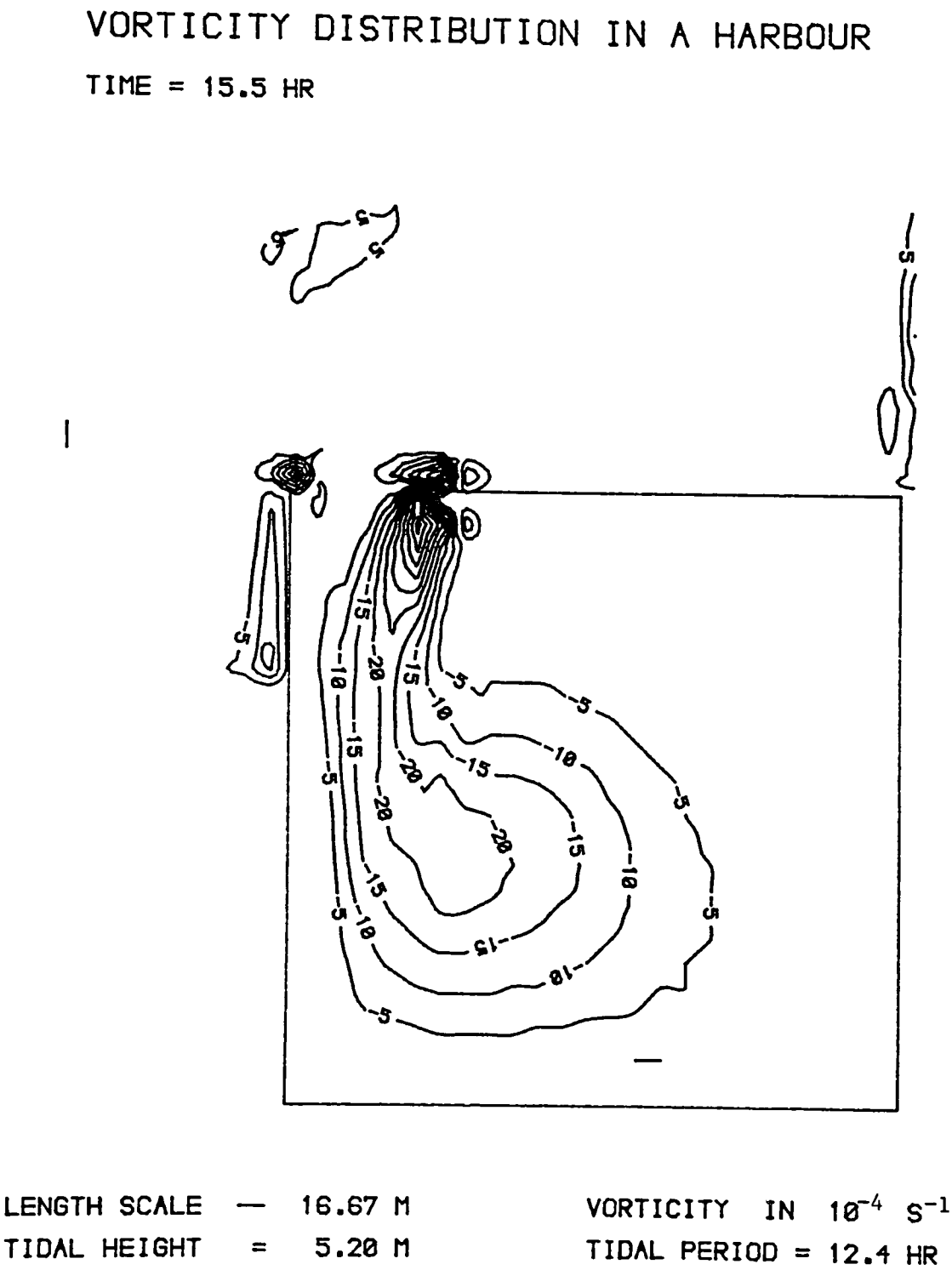

Figure 7.54 Predicted vorticity distribution at mean water flood tide for prototype harbour with L/B=1.0

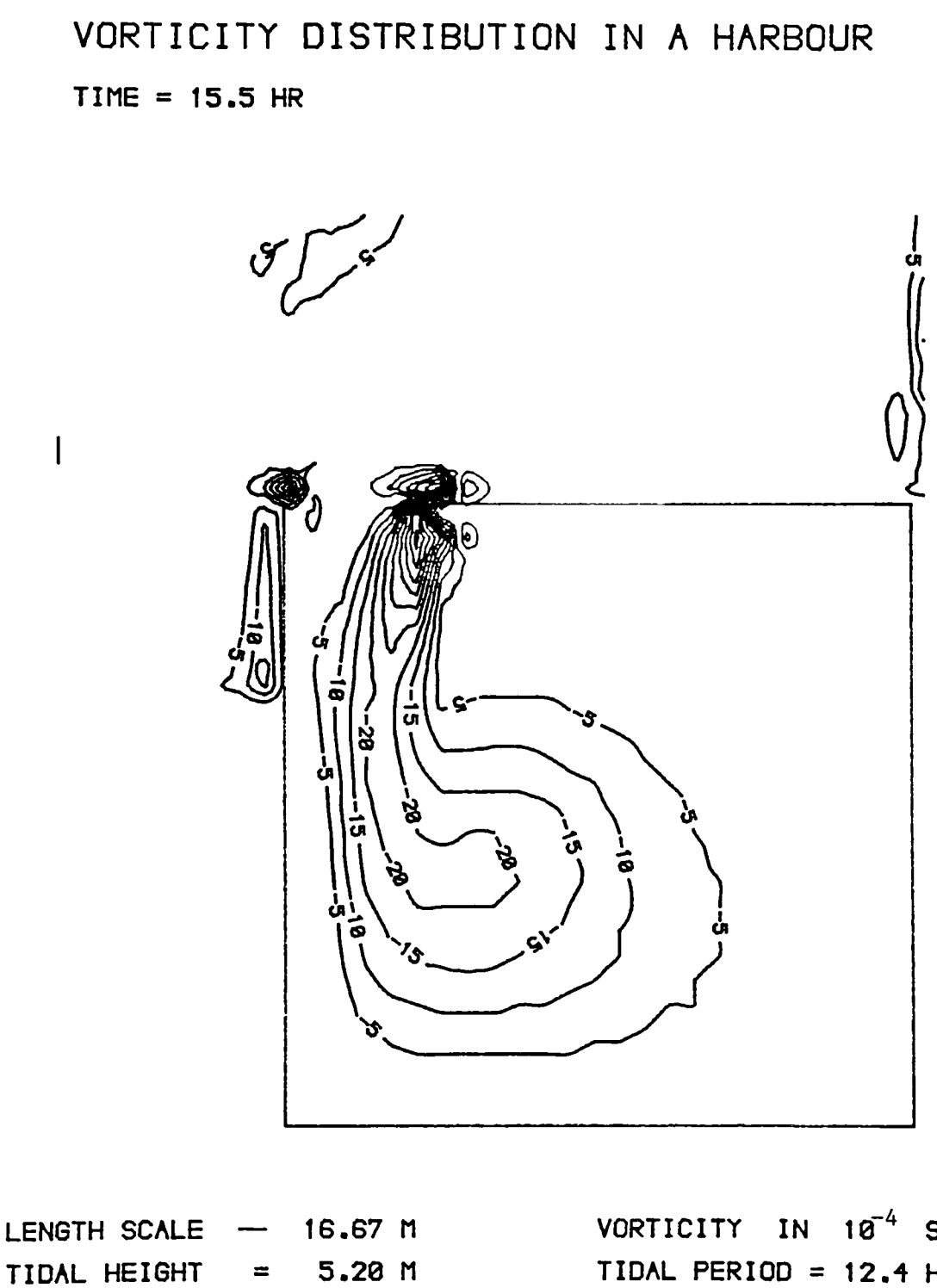

Figure 7.55 Predicted vorticity distribution at mean water flood tide for prototype harbour with L/B=1.0, with the exclusion of free shear layer stresses

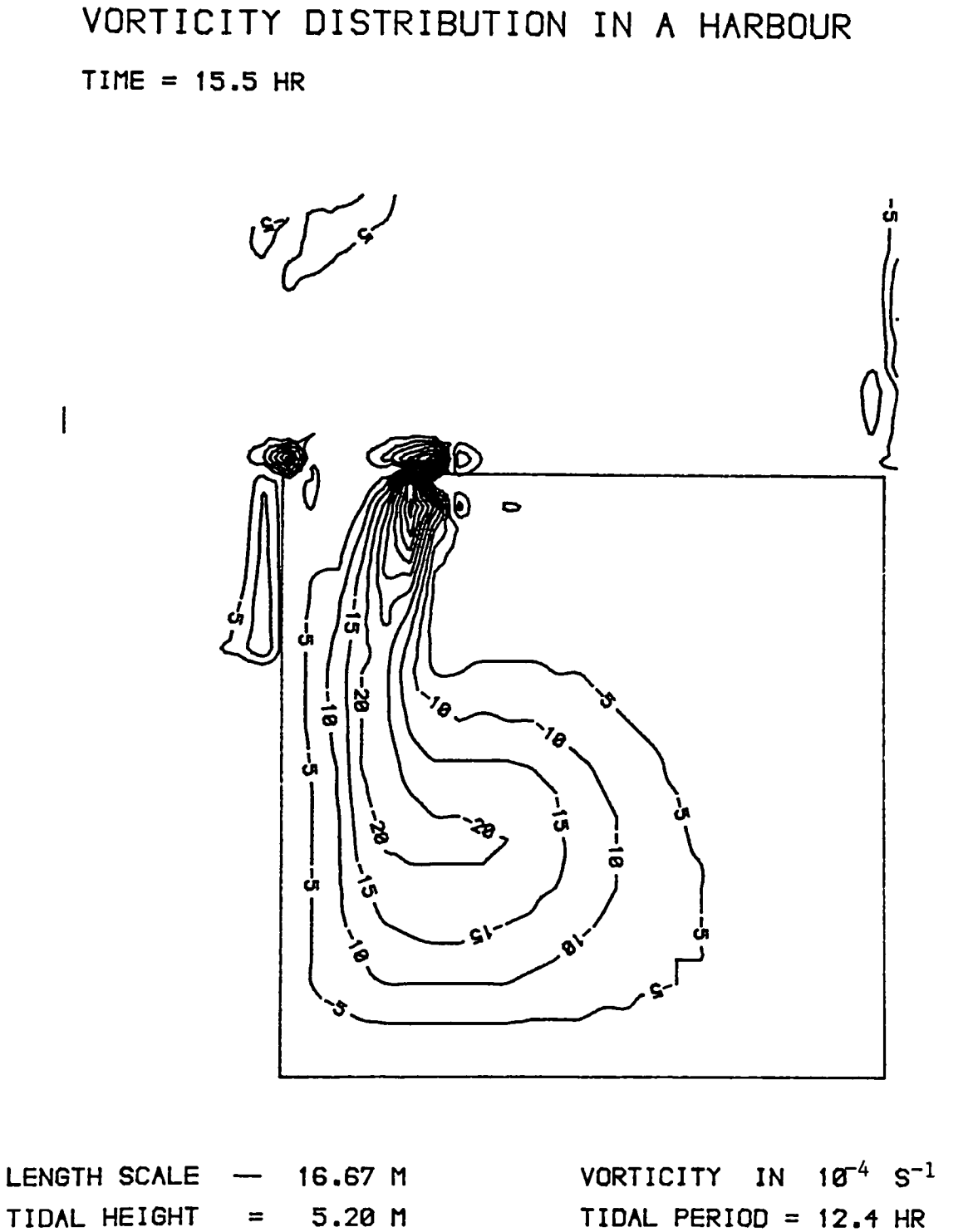

Figure 7.56 Predicted vorticity distribution at mean water flood tide for prototype harbour with L/B=1.0, with the exclusion of all lateral shear stresses

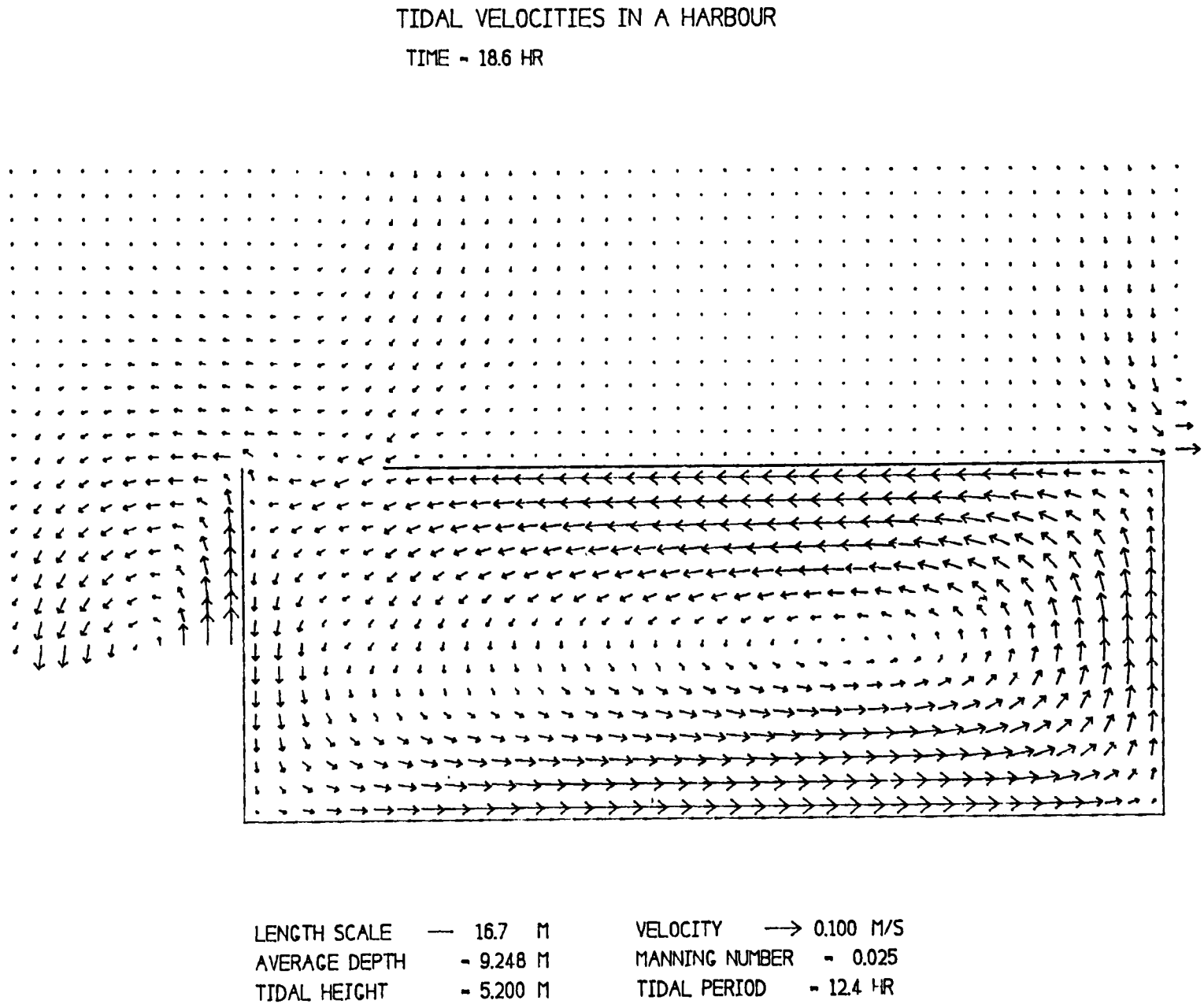

Figure 7.57 Predicted velocity field at high tide for prototype harbour with L/B=2.6, for free-slip boundary condition

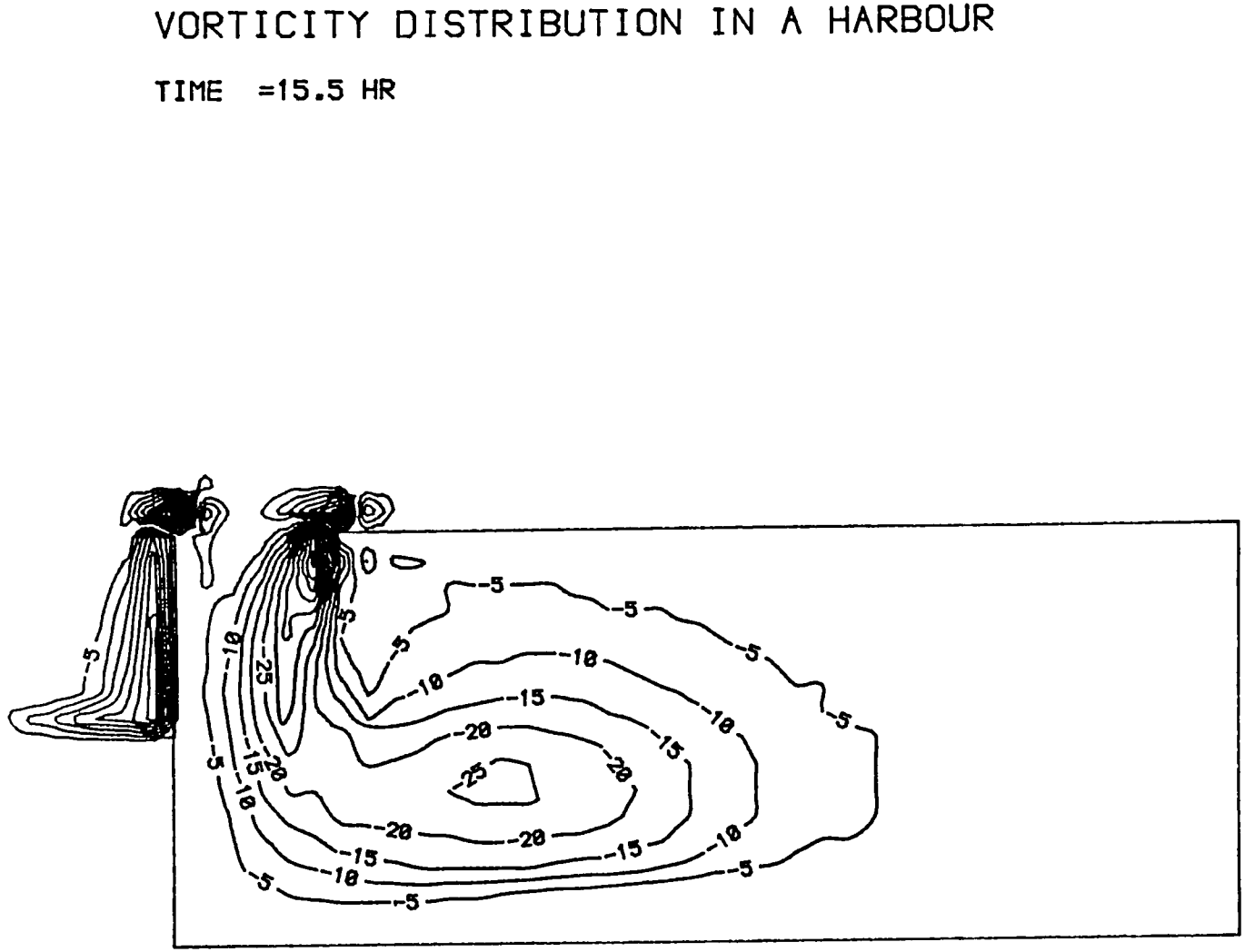

Figure 7.58 Predicted vorticity distribution at mean water flood tide for prototype harbour with L/B=2.6

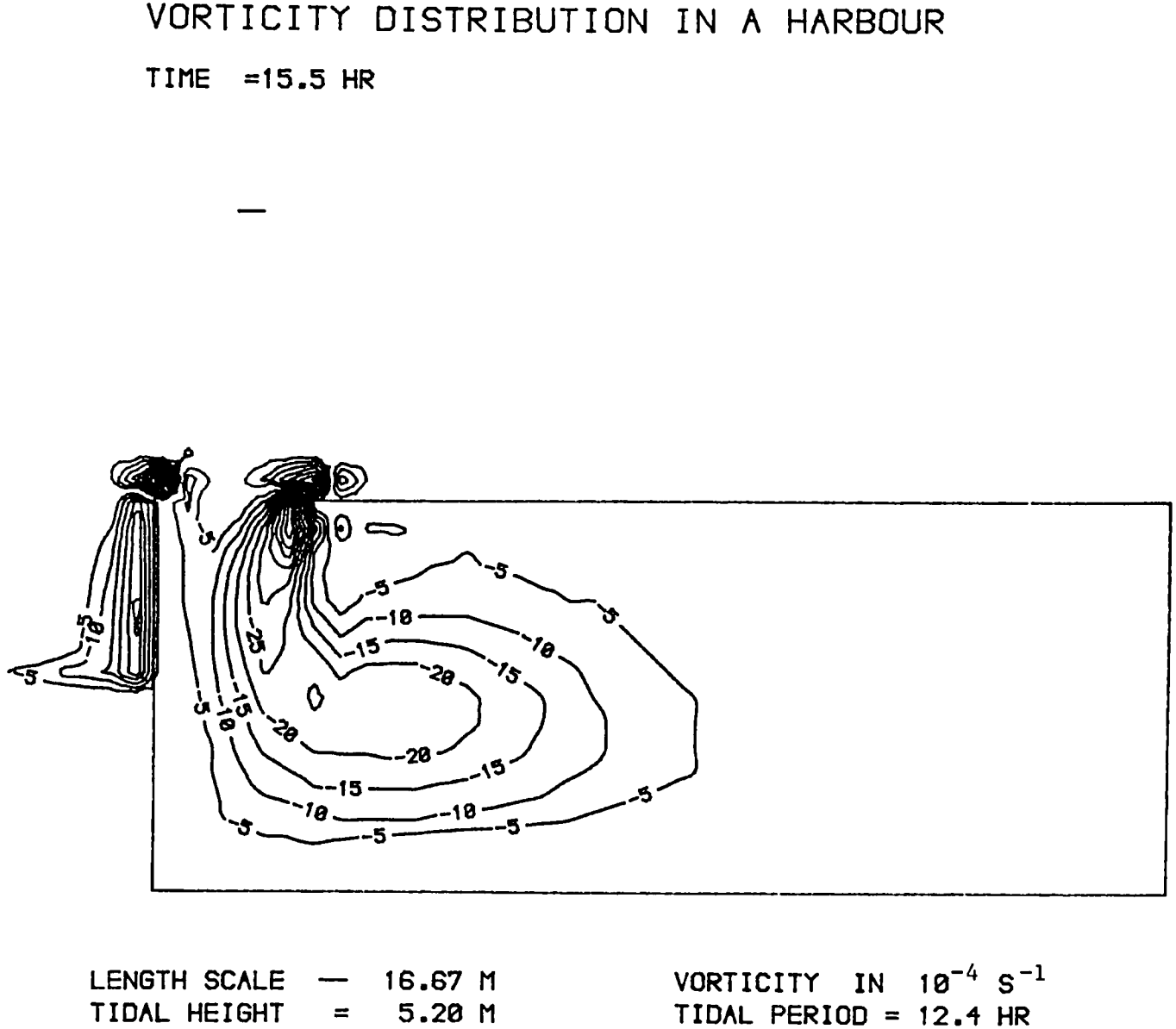

Figure 7.59 Predicted vorticity distribution at mean water flood tide for prototype harbour with L/B=2.6, for Manning coefficient of 0.035

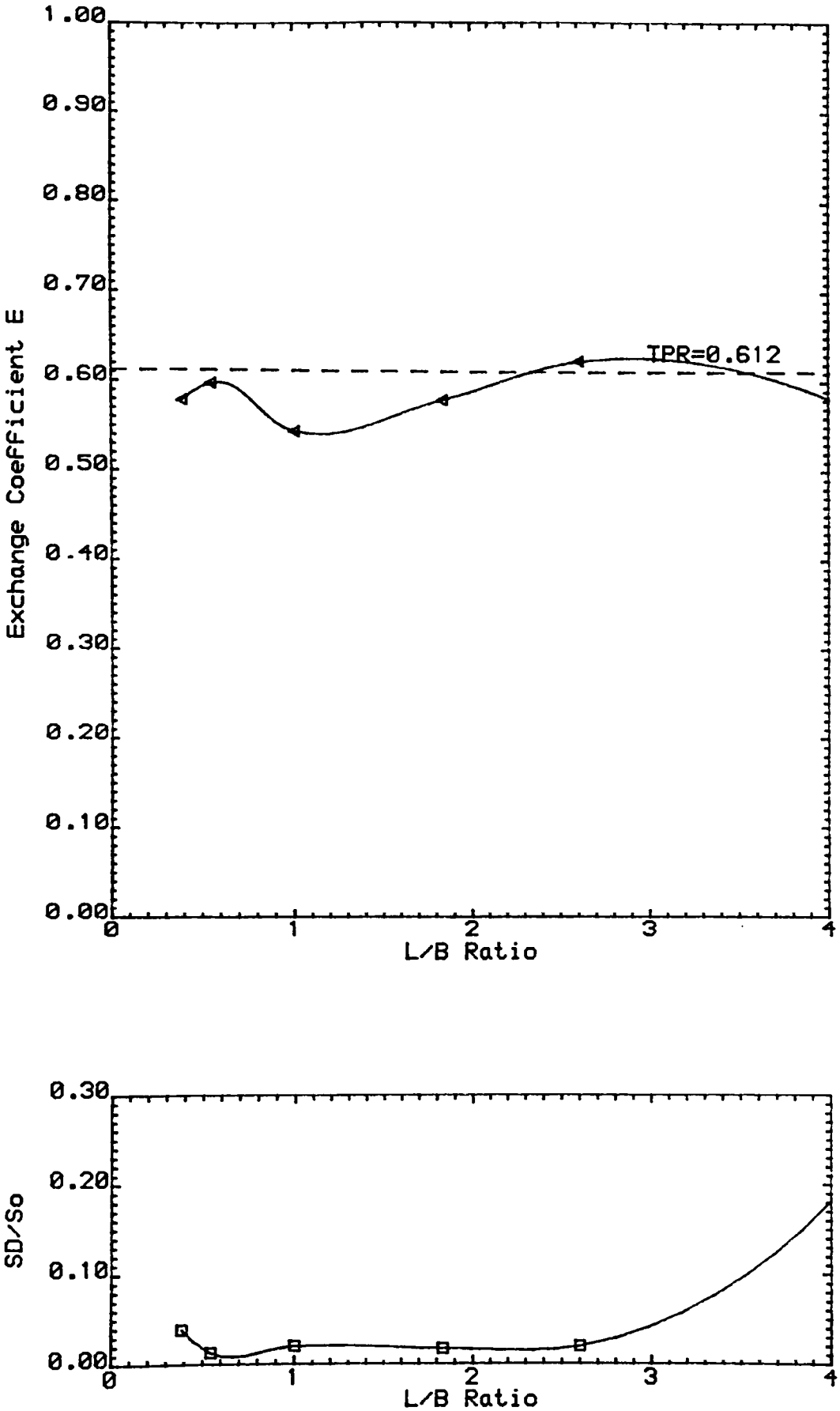

Figure 7.60 Predicted variation of exchange coefficient E and standard deviation SD with L/B ratio for prototype harbours

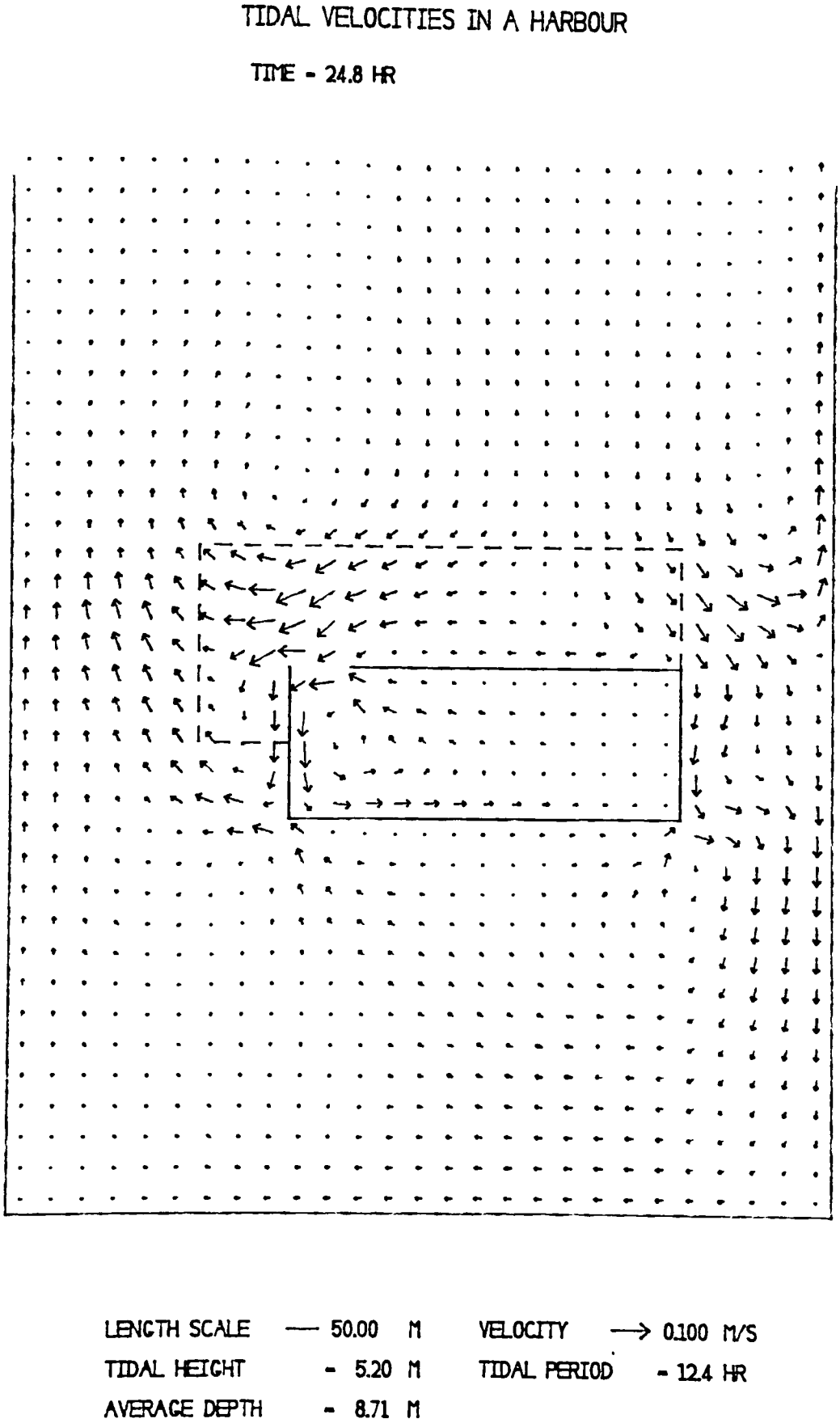

Figure 7.61 Predicted velocity field by coarse-grid model at low tide for prototype harbour with L/B=2.6

CHAPTER 8

CONCLUSIONS AND RECOMMENDATIONS FOR FURTHER WORK

8.1 Conclusions

A finite difference computational model has been enhanced and refined to simulate tide-induced circulatory flows, with special reference to eddies shed in the lee of headlands and to tidal circulation and flushing in narrow entranced coastal basins. The model is of the two-dimensional depth-integrated type and includes a relatively simple "zero-equation" turbulence model. In the turbulence model particular emphasis has been placed on the representation of shear layer turbulence, occurring in the mixing zone of eddying flows. This component of the turbulence structure has been expressed in terms of a constant eddy viscosity across the shear layer and a semi-empirical lateral velocity distribution.

The model has been tested against field measurements from around Rattray Island - off the east coast of Australia - and laboratory model studies of idealised rectangular harbours. The agreement between numerical predictions and measurements proved to be encouraging in both cases, thereby implying that the numerical model was adequately reproducing the depth-mean flow properties and physical processes involved in such circulatory flow fields.

The need to formulate the finite difference equations in a stable and accurate manner was of particular importance. A study of the basic properties of four first order finite difference schemes and a series of numerical tests were undertaken to determine the most suitable finite

difference representation of the governing equations. This was shown to be a fully centred implicit scheme with a double iteration that explicitly expressed the advective and diffusive terms of the momentum equations in a time-centred form.

The sensitivity of the flow field predictions on the open boundary conditions was demonstrated in both case studies. In the Rattray Island study, a water surface slope along the water elevation boundary, governed by the Coriolis acceleration, was found to be necessary in order to avoid unrealistic flow patterns in the vicinity of this boundary. Likewise, in the study of the idealised rectangular harbours, the accurate description of the entrance flow conditions proved to be a pre-requisite for realistic re-circulating flow fields within the harbours. The one-way interaction nesting technique, which overcame the problem of having to prescribe detailed and accurate flow data along the sensitive flow boundaries, was adopted and applied with success to the idealised harbour simulation studies.

The tidal eddy features in the wake of Rattray Island were mainly governed by advection, bed friction and bathymetric features. The lateral shear stresses, theoretically shown to be the dominant momentum transfer mechanism, appeared to have a small effect on the eddy characteristics and, contrary to theoretical expectations, circulation was predicted even when these terms were excluded from the model. The free shear layer stress had a more marked influence on the eddy features than the bed generated shear stress, as anticipated by the theoretical analysis of the shear stresses in eddying zones. Both shear stresses, however, were under-predicted as a result of discretisation on a coarse grid. Likewise, the no-slip boundary condition was shown to have

negligible influence on the flow.

In the model application to the rectangular harbours, a range of physical models and prototypes were simulated. The discrepancies in the predicted flow field and tidal flushing characteristics between the prototypes and their respective physical models, highlighted the problems associated with scaling effects in distorted physical models. Vertically distorted models, using a Froude law scaling criteria, can be shown to over-estimate the dispersion processes and the momentum transfer by bed generated turbulence and under-estimate the bed frictional effects on the flow. Such scaling effects were reflected in the numerical model predictions. Regarding the shear layer stresses, they were properly scaled in the physical models and had a noticeable effect on the circulation of both the prototype and physical model basins. In addition, the no-slip boundary condition was shown to be an important parameter in the flow field predictions, reinforcing the view that such parameters were under-predicted in the Rattray Island study as a result of the coarseness of the numerical grid - an anavoidable inaccuracy in the modelling of large water bodies. Finally, as for the Rattray Island study, the exclusion of the shear stresses did not supress the circulation.

8.2 Recommendations for Further Work

Turbulence Model

The use of a semi-empirical formulation in the representation of the free shear layer turbulence has enabled this turbulence mechanism to be included in the numerical model without the need to resort to more complex turbulence models. However, this representation has the

disadvantage that regions of shear layer turbulence are required to be identified in advance, which is not always an easy task. This constraint may be removed when more universal turbulence models are introduced, like the "k-ε" model, where shear layer turbulence would be inherently described - though at the expense of complexity and cost.

Nesting Technique

The one-way interaction nested model, employed in the harbour model simulations, appears to have successfully simulated the flow field and tidal flushing characteristics. However, there were some discrepancies between the numerical predictions and the physical model measurements. Such discrepancies may be attributed to errors introduced at the fine-grid model open boundaries which, in such a modelling technique, respond only to changes predicted in the coarse-grid model. It would therefore be of interest to repeat and compare the predictions for the harbour model study using the two-way interaction technique, where the nested grids would be dynamically inter-linked, thereby allowing the fine-grid model open boundaries to respond to changes predicted within the fine-grid.

Treatment of a Discontinuity

It is acknowledged that the method adopted in the prototype harbour applications to treat the discontinuity in the constituent concentration field is inadequate as a predictive tool. The first-order upwind differencing of the advection terms in the advective-diffusion equation, gives rise to pronounced numerical diffusion. This influences the model representation of the physical diffusion terms and undermines the accuracy of the numerical model predictions.

It would therefore be desirable to improve on the treatment of discontinuities before the model is applied to practical engineering flows. It has deen demonstrated by Leonard (see Taylor and Morgan(1981)) that a third-order upwind differencing of the advection terms combines inherent stability and accuracy, a method worth considering as a potential discontinuity treatment. The flux-corrected transport technique, where the first order upwind differencing solution is corrected by a flux-corrected anti-diffusion term, is another method worth considering. This technique was shown by Boris and Book(1976) to possess a high degree of accuracy.

Residual Flows

The numerical model may be expanded to include the prediction of residual flows resulting from tidal action. Residual tidal circulations arise as a result of the non-linear character of tidal flow systems, where vorticity is transferred from the tidal oscillating flow field to the mean residual field (see Pingree and Maddock(1977), Ziemmerman(1981), Imasats(1983)). Knowledge of residual velocity fields is of great importance because of their influence on such processes as sediment and pollutant transport, with implications on the bed morphology and sitings of waste outfalls. The computation of residual flows may be included in the numerical model by tidally averaging the velocity field over a complete tidal cycle.

Further Experimental Work

The laboratory tidal tank in which the harbour model tests were performed in this study and also by Jiang and Falconer(1983), appears to have been relatively small. The sidewalls of this tank were very close to the harbour models and interfered with the exterior flow field, giving rise to strong circulation in the immediate vicinity of the harbour. Such a circulatory exterior flow field may have affected appreciably the flow and tidal flushing characteristics of the harbour models. It would therefore be desirable to perform more tests in a larger laboratory basin. In addition, the harbour models were relatively small and, as a result the currents within the harbours were weak and could not be measured by the available current meters. Hence, it would be preferable to perform tests on larger harbour models, where the velocity field could be measured with greater accuracy. Further and more detailed laboratory studies on the tidal flushing characteristics of the harbour models are also needed, as there appears to be some disagreement amongst researchers - as indicated by comparing the results presented by Jiang and Falconer(1983) with Nece(1984).

REFERENCES

1. Abbott, M.B. (1979). "Computational Hydraulics", Pitman Publication.

2. Abbott, M.B. and Cunge, J.A. (Editors) (1982). "Engineering Applications of Computational Hydraulics, Volume I", Pitman Publication.

3. Abbott, M.B., Larsen, J. and Jianhua, T. (1985). "Modelling Circulations in Depth-Integrated Flows. Part 1: The Accumulation of the Evidence", Journal of Hydraulic Research, Vol.23, No.4.

4. Abramowitz, M. and Stegun, I.A. (1966). "Handbook of Mathematical Functions", National Bureau of Standards, Applied Mathematics, Series 55, U.S. Department of Commerce (5th printing).

5. Ames, W.F. (1969). "Numerical Methods for Partial Differential Equations", Thomas Nelson & Sons Ltd.

6. Aziz, K. and Hellums, J.D. (1967). "Numerical Solution of the Three-Dimensional Equations of Motion for Laminar Natural Convection", Physics of Fluids, Vol.10, No.2, pp.314-324.

7. Batchelor, G.K. (1970). "An Introduction to Fluid Dynamics", Cambridge University Press.

8. Benque', J.P., Hauguel, A. and Viollet, P.L. (Editors) (1982). "Engineering Applications of Computational Hydraulics", Vol.II, Pitman Publication.

9. Boris, J.P. and Book, D.L. (1976). "Flux-Corrected Transport. III. Minimal-Error FCT Algorithms", Journal of Computational Physics, Vol.20, pp.397-431.

10. Bradshaw, P., Ferriss, D.H. and Atwell, N.P. (1967). "Calculation of Boundary Layer Development Using the Turbulent Energy Equation", Journal of Fluid Mechanics, Vol.28, No.3, pp.593-616.

11. Chatfield, C. (1978). "Statistics for Technology", Chapman and Hall Publication.

12. Chatwin, P. and Allen, C.M. (1985). "Mathematical Models of Dispersion in Rivers and Estuaries", Annual Review of Fluid Mechenics, Vol.17, pp.119-149.

13. Chiu, S.S. and van de Kreeke, J. (1980). "Finite Difference Solution to the Two-Dimensional Horizontal Long Wave Equations", Rosentiel School of Marine & Atmospheric Science, University of Miami, TR80-1.

14. Cox, I.C.S. (1981). "The Numerical Modelling of Vertical Circulation in Lakes and Estuaries", M.Sc.(Qual.) Thesis, University of Birmingham, Birmingham.

15. Dronkers, J.J. (1964). "Tidal Computations in Rivers and Coastal Waters", North-Holland Publishing Company.

16. Edwards, N.A. (1983) Private Communications.

17. Edwards, N.A., Please, C.P. and Preston, R.W. (1983). "Some Observations on Boundary Conditions for the Shallow-Water Equations in Two Space Dimensions", IMA Journal of Applied Mathematics, Vol.30, pp.161-172.

18. Edwards, N.A. and Preston, R.W. (1985). "Grid Scale Oscillation in 'Flow'-the CERL Shallow Water Solver", Report No. TPRD/L/2779/N84, Central Electricity Research Laboratorie, CEGB, Leatherhead.

19. Elder, J.W. (1959). "The Dispersion of Marked Fluid in Turbulent Shear Flow", Journal of Fluid Mechanics, Vol.5, No.4, pp.544-560.

20. Elsberry, R.L. (1978). "Prediction of Atmospheric Flows on Nested Grids", Computational Techniques for Interface Problems, ASME, AMD Vol.30, pp.67-85.

21. Elvius, T. and Sundstrom, A. (1973). "Computationally Efficient Schemes and Boundary Conditions for a Fine-Mesh Barotropic Model based on the Shallow Water Equations", Tellus, Vol.25, pp.132-156.

22. Engquist, B. and Majda, A. (1977). "Absorbing Boundary Conditions for the Numerical Simulation of Waves", Mathematics of Computation, Vol.31, No.139, pp.629-651.

23. Falconer, R.A. (1974). "Tidal Circulation Effects in Rectangular Harbours", M.Sc. Thesis, University of Washington, Seattle, Washington.

24. Falconer, R.A. (1977). "Mathematical Modelling of Jet-Forced Circulation in Reservoirs and Harbours", Ph.D. Thesis, Imperial College, University of London, London.

25. Falconer, R.A. (1981). "Numerical Model Study of Temperature Distributions in Poole Harbour and Holes Bay", Internal Report, Department of Civil Engineering, University of Birmingham, Birmingham.

26. Falconer, R.A. (1983). "Numerical Model Study of Nutrient Levels in Poole Harbour and Holes Bay", Internal Report, Department of Civil Engineering, University of Birmingham, Birmingham.

27. Falconer, R.A. (1984). "Temperature Distributions in Tidal Flow Field", Journal of Environmental Engineering, ASCE, Vol.110, No.6, pp.1099-1116.

28. Falconer, R.A. and Owens, P.H. (1984). "Mathematical Modelling of Tidal Currents in the Humber Estuary", Journal of the Insitution of Water Engineers and Scientists, Vol.38, No.6, pp.528-542.

29. Falconer, R.A., Wolanski, E. and Mardapitta-Hadjipandeli, L. (1984). "Numerical Simulation of Secondary Circulation in the Lee of Headlands", Proceedings of the 19th International Conference of Coastal Engineering, ASCE, Houston, U.S.A., Vol.III, pp.2414-2433.

30. Falconer, R.A., Wolanski, E., and Mardapitta-Hadjipandeli, L. (1985). "Modelling of Tidal Circulation in an Island's Wake", Journal of Waterway, Port, Coastal and Ocean Engineering, ASCE, (in press).

31. Fisher, H.B. (1973). "Longitudinal Dispersion and Turbulent Mixing in Open Channel Flow", Annual Review of Fluid Mechanics, Vol.5, pp.59-78.

32. Fisher, H.B. (1976). "Some Remarks on Computer Modelling of Coastal Flows", Journal of Waterways, Harbours and Coastal Engineering Division, ASCE, Vol.102, No. WW4, pp.395-406.

33. Fisher, H.B. (1978). "On the Tensor Form of the Bulk Dispersion Coefficient in a Bounded Skewed Shear Flow", Journal of Geophysical Research, Vol.83, No. C5, pp.2373-2375.

34. Fisher, H.B. (Editor) (1981). "Transport Models for Inland and Coastal Waters", Academic Press.

35. Flather, R.A. and Heaps, N.S. (1975). "Tidal Computations for Morecombe Bay", Geophysical Journal of the Royal Astronomical Society, Vol.42, pp.489-517.

36. Flokstra, C. (1977). "The Closure Problem for Depth-Averaged Two-Dimensional Flow", Paper 106, 17th International Association for Hydraulic Research Congress, Baden-Baden, Germany, pp.247-256.

37. Gawain, T.H. and Pritchett, J.W. (1970). "A Unified Heuristic Model of Fluid Turbulence", Journal of Computational Physics, 5, pp.383-405.

38. Gerrard, T.H. (1978). "The Wake of Cylindrical Bluff Bodies at Low Reynolds Number", Philosophical Transactions of the Royal Society of London, 288, pp.351-382.

39. Goldstein, S. (1938). "Modern Developments in Fluid Mechanics", Vol.1, Oxford University Press.

40. Gustaffsson, B. and Sundstrom, A. (1978). "Incompletely Parabolic Problems in Fluid Dynamics", SIAM Journal of Applied Mathematics, Vol.35, No.2, pp.343-357.

41. Hanjalic, K. and Launder, B.E. (1972). "A Reynolds Stress Model and its Application in Thin Shear Flows", Journal of Fluid Mechanics, 52, pp.609-638

42. Harlow, F.M. and Nakayama, P.I. (1967). "Turbulence Transport Equations", Physics of Fluids, Vol.10, pp.2323-2332.

43. Henderson, F.M. (1966). "Open Channel Flow", Macmillan Publishing Company.

44. Hinze, J.O. (1975). "Turbulence", McGraw-Hill Inc., 2nd Edition.

45. H.R.S. (1980). "Harwich Harbour Numerical Model Studies", Report No. EX939, Hydraulics Research Station, Wallingford.

46. Imasats, N. (1983). "What is Tide-Induced Residual Current?", Journal of Physical Oceanography, Vol.13, No.7, pp.1307-1317.

47. Ippen, A.T. (Editor) (1966). "Estuary and Coastline Hydrodynamics", McGraw-Hill Inc.

48. Jiang, J. and Falconer, R.A. (1983). "On the Tidal Exchange Characteristics of Model Rectangular Harbours", Proceedings of the Institution of Civil Engineers, Part 2, Vol.75, pp.475-489.

49. Jones, W.P. and Launder, B.E. (1972). "The Prediction of Laminarization with a Two-Equation Model of Turbulence", Intenational Journal of Heat and Mass Transfer, Vol.15, pp.301-314.

50. Keller, H.B. and Niewstadt, F. (1973). "Viscous FLow Past Circular Cylinders", Computers of Fluids, 1, pp.59-71.

51. Knight, D.W. (1973a). "Theoretical Studies of Long Wave Propagation in Estuaries of Finite Length", International Association for Hydraulics Research, International Symposium on River Mechanics, Bankok, Thailand, pp.C28.1-12.

52. Knight, D.W. (1973b). "Long Wave Propagation in Idealised Estuaries", Journal of the Hydraulics Division, ASCE, Vol.99, No. HY7, pp.993-1007.

53. Knight, D.W. (1981). "Some Field Measurements Concerned with the Behaviour of Resistance Coefficients in a Tidal Channel", Estuarine, Coastal and Shelf Science, Vol.12, pp.303-322.

54. Kolmogorov, A.N. (1942). "Equations of Turbulent Motion of an Incompressible Fluid", Izv, Akad. Nauk. SSR, Seria fizicheska Vi., No.1-2, pp.56-58, (English translation: Imperial College, Mechanical Engineering Department, Report ON/6 (1968)).

55. Kuipers, J. and Vreugdenhil, C.B. (1973). "Calculations of Two-Dimensional Horizontal Flow", Delft Hydraulics Laboratory, Report S163-1.

56. Lamb, H. (1932). "Hydrodynamics", 6th Edition, Cambridge University Press.

57. Launder, B.E. and Spalding, D.B. (1972). "Mathematical Models in Turbulence", Academic Press.

58. Launder, B.E. and Spalding, D.B. (1974). "The Numerical Computation of Turbulent Flow", Computer Methods in Applied Mechanics & Engineering, Vol.3, pp.269-289.

59. Launder, B.E., Reece, G.J. and Rodi, W. (1975). "Progress in the Development of a Reynolds Stress Turbulence Closure", Journal of Fluid Mechanics, Vol.68, pp.537-566.

60. Lean, G.H. and Weare, T.J. (1979). "Modelling Two-Dimensional Circulating Flow", Journal of the Hydraulics Division, ASCE, Vol.105, No. HY1, pp.17-26.

61. Leendertse, J.J. (1967). "Aspects of a Computational Model for Long-Period Water-Wave Propagation", The Rand Corporation, RM-4122-APRA.

62. Leendertse, J.J. (1970). "A Water-Quality Simulation Model for Well-Mixed Estuaries and Coastal Seas:Vol.I, Principles of Computation", The Rand Corporation, RM-6230-RC.

63. Leendertse, J.J. and Gritton, E.C. (1971). "A Water-Quality Simulation Model for Well-Mixed Estuaries and Coastal Seas:Vol.II, Computation Procedures", The Rand Corporation, R-708-NYC.

64. Leendertse, J.J. (1984). "Verification of a Model of the Eastern Scheldt", The Rand Corporation, R-3108-NETH.

65. Liepmann, H.W. and Laufer, J. (1947). "Investigations of Free Turbulent Mixing", Technical Notes, National Advisory on Aeronautics, Washington, TN1257.

66. Lynch, D.R. and Gray, W.G. (1978). "Analytical Solutions for Computer Flow Model Testing", Journal of the Hydraulics Division, ASCE, Vol.104, No. HY10, pp.1409-1428.

67. McDowell, D.M. and O'Connor, B.A. (1977). "Hydraulic Behaviour of Estuaries", The Macmillan Press.

68. McGuirk, J.J. and Rodi, W. (1978). "A Depth-Averaged Mathematical Model for the Near Field of Side Discharges into Open Channel Flow", Journal of Fluid Mechanics, Vol.86, No.4, pp.761-781.

69. Mahmood, K. and Yevjevich, V. (Editors) (1975). "Unsteady Flow in Open Channels", Water Resources Publications, Fort Collins, Colorado.

70. Massey, B.S. (1979). "Mechanics of Fluids", 4th Edition, Van Nostrand Reinhold Company.

71. Naot, D. and Rodi, W. (1982). "Calculation of Secondary Currents in Channel Flow", Journal of the Hydraulics Division, ASCE, Vol.108, No. HY8, pp.948-968.

72. Nece, R.E. (1984). "Planform Effects on Tidal Flushing of Marinas", Journal of Waterway, Port, Coastal and Ocean Engineering, ASCE, Vol.110, No.2, pp.251-269.

73. Nece, R.E. and Richey, E.P. (1972). "Flushing Characteristics of Small-Boat Marinas", Proceedings of the 13th Coastal Engineering Conference, ASCE, Vancouver, Canada, pp.2499-2512.

74. Nece, R.E. and Richey, E.P. (1975). "Application of Physical Tidal Models in Harbor and Marina Design", Proceedings of the Symposium on Modelling Techniques, ASCE, San Francisco, California, pp.783-801.

75. Nece, R.E., Smith, H.N. and Richey, E.P. (1980). "Tidal Circulation and Flushing in Five Western Washington Marinas", Charles W. Harris Hydraulics Laboratory Technical Report No.63, University of Washington, Seattle, Washington.

76. Nece, R.E., Falconer, R.A. and Tsutsumi, T. (1976). "Planform Influence on Flushing and Circulation in Small Harbours", Proceedings of the 15th Coastal Engineering Conference, ASCE, Hawaii, U.S.A., pp.3471-3486.

77. Neumman, G. ang Pierson, W.J. (1966). "Principles of Physical Oceanography", Prentice Hall Inc.

78. Ng, K.H. and Spalding, D.B. (1972). "Turbulence Model for Boundary Layer near Walls", Physics of Fluids, Vol.15, pp.20-30.

79. O'Brien, G.G., Hyman, M.A. and Kaplan, S. (1951). "A Study of the Numerical Solution of Partial Differential Equations", Journal of Mathematics and Physics, vol.29, pp.223-251.

80. Oliger, J. and Sundstrom, A. (1978). "Theoretical and Practical Aspects of some Initial-Boundary Value Problems in Fluid Dynamics", SIAM Journal of Applied Mathematics, Vol.35, No.2, pp.419-446.

81. Pearson, C.E. (1965). "A Computational Method for Viscous Flow Problems", Journal of Fluid Mechanics, Vol.21, No.4, pp.611-612.

82. Phillips, N.A. (1959). "An Example of Non-Linear Computational Instability", The Atmosphere and Sea Motion, Rockefeller Institute Press.

83. Pingree, R.D. and Maddock, L.(1977). "Tide Residuals in the English Channel", Journal of the Marine Biological Association of the United Kingdom, 57, pp.339-354.

84. Pingree, R.D. and Maddock, L. (1979). "Tidal Physics of Headland Flows and Offshore Tidal Bank Formation", Marine Geology, 32, pp.269-289.

85. Pingree, R.D. and Maddock, L. (1980). "The Effects of Bottom Friction and Earth's Rotation in an Island's Wake", Journal of Marine Biological Association of the United Kingdom, 60, pp.499-508.

86. Ponce, V.M. and Yabusaki, S.B. (1981). "Modelling Circulation in Depth-Averaged Flow", Journal of the Hydraulics Division, ASCE, Vol.107, No. HY11, pp.1501-1518.

87. Prandle, D. and Rahman, M. (1980). "Tidal Response in Estuaries", Journal of Physical Oceanography, Vol.10, No.10, pp.1552-1573.

88. Prandtl, L. (1945). "Uber ein neves Formlsystem fur die ausgebildete Turbulez", Narchr. Akad. Wiss., Gottingen, Math-Phys., Klasse, pp.6-19.

89. Preston, R.W. (1985). "The Representation of Dispersion in Two-Dimensional Water Flow", Report No. TPRD/L/2783/N84, Central Electricity Research Laboratories, CEGB, Leatherhead.

90. Proudman, J. (1955a). "The Propagation of Tide and Surge in an Estuary", Proceedings of the Royal Society A, 231. pp.8-21.

91. Proudman, J. (1955b). "The Effect of Friction on a Progressive Wave of Tide and Surge in an Estuary", Proceedings of the Royal Society A, 233, pp.407-418.

92. Proudman, J. (1957). "Oscillations of Tide and Surge in an Estuary of Finite Length", Journal of Fluid Mechanics, Vol.2, pp.371-382.

93. Ramming, H.-G. and Kowalik, Z. (1980). "Numerical Modelling of Marine Hydrodynamics", Elsevier Oceanography Series, 26, Elsevier Scientific Publishing Company.

94. Rastogi, A.K. and Rodi, W. (1978). "Predictions of Heat and Mass Transfer in Open Channels", Journal of the Hydraulics Division, ASCE, Vol.104, No. HY3, pp.397-420.

95. Reynolds, A.J. (1974). "Turbulent Flows in Engineering", Wiley-Interscience Publication.

96. Richtmyer, R.D. and Morton, K.W. (1967). "Difference Methods of Initial-Value Problems", 2nd Edition, Interscience Publishers, J. Wiley & Sons.

97. Roache, P.J. (1976). "Computational Fluid Dynamics", Hermosa Publishers.

98. Rodi, W. (1980). "Turbulence Models and their Application in Hydraulics", A State of Art Review Publication, International Association of Hydraulics Research, Delft, The Netherlands.

99. Rodi, W. and Spalding, D.B. (1970). "A Two Parameter Model of Turbulence and its Application to Free Jets", Warme and Stoffubertragung, Vol.3, pp.85-95.

100. Schlichting, H. (1960). "Boundary-Layer Theory", (Translated by Kestin, J.), 4th Edition, McGraw-Hill Book Company.

101. Singhal, A.K. and Spalding, D.B. (1975). "Prediction of Two-Dimensional Boundary Layers with the Aid of the $k-\varepsilon$ Model of Turbulence", Imperial College, Mechanical Engineering, Report HTS/75.

102. Smith, G.D. (1978). "Numerical Solution of Partial Differential Equations: Finite Difference Methods", 2nd Edition, Oxford University Press.

103. Sokolnikoff, I.S. and Redheffer, R.M. (1966). "Mathematics of Physics and Modern Engineering", McGraw-Hill Inc.

104. Spalding, D.B. (1967). "Heat Transfer from Turbulent Separated Flows", Journal of Fluid Mechanics, Vol.27, No.1, pp.97-109.

105. Stephenson, P.L. (1976). "Theoretical Study of Heat Transfer in Two-Dimensional Turbulent Flow in a Circular Pipe and between Parallel Diverging Plates", International Journal of Heat and Mass Transfer, Vol.19, pp.413-423.

106. Taylor, C. and Morgan, K. (Editors) (1981). "Computational Techniques in Transient and Turbulent Flow", Vol.2, Pineridge Press Ltd.

107. Tennekes, H. and Lumley, J. (1977). "A First Course in Turbulence", 4th Edition, MIT Press.

108. Thabet, R.A.H., Verboom, G.K. and Akkerman, G.J. (1985). "Two Dimensional Modelling of Tidal Motion for Harbours Studies", Proceedings of the International Conference on Numerical Modelling of Ports and Harbours", Birmingham, England, pp.23-32.

109. Tong, G.D. (1982). "Computation of Turbulent Recirculating Flow", Ph.D. Thesis, University College of Swansea, University of Wales, Swansea.

110. Townsend, A.A. (1956). "The Structure of Turbulent Shear Flow", Cambridge University Press.

111. Vager, B.G. and Kagan, B.A. (1971). "Vertical Structure and Turbulence in a Stratified Layer of a Tidal Flow", Atmospheric and Oceanic Physics, Vol.7, No.7, pp.516-522.

112. Verboom, G.K. (1985). Private Communications.

113. Verboom, G.K. and Slob, A. (1984). "Weakly-Reflective Boundary Conditions for Two-Dimensional Shallow Water Flow Problems", Advances in Water Resources, Vol.7, pp.192-197.

114. Vreugdenhill, C.B. and Voogt, J. (1975). "Hydrodynamic Transport Phenomena in Estuaries and Coastal Waters: Scope of Mathematical Models", Proceedings of the Symposium on Modelling Techniques, Waterways, Harbours and Coastal Engineering Division of ASCE, San Francisco, pp.690-708.

115. Wallis, S.G. (1982). "The Simulation of Tidal Flows in Natural and Idealised Estuaries", Ph.D. Thesis, University of Birmingham, Birmingham.

116. Weare, T.J. (1975). "Computational Models in Coastal Harbour Engineering", Lecture Notes: Stability and Accuracy of Finite Difference Schemes, University of Southampton.

117. Weare, T.J. (1976). "Instability of Tidal Flow Computational Schemes", Journal of the Hydraulics Division, ASCE, Vol.105, HY5, pp.569-580.

118. Weatherburn, C.E. (1966). "Advanced Vector Analysis", G.Bell and Sons Ltd.

119. Welch, J.E., Harlow, F.H., Shannon, J.P. and Daly, B.J. (1966). "The MAC Method. A Computing Technique for Solving Viscous, Incompressible, Transient Fluid-Flow Problems Involving Free Surfaces", Los Alamos Scientific Laboratory of the University of California.

120. Williams, J.M. and Holmes, D.W. (1974). "Marker-and-Cell Technique", Hydraulics Research Station, Report INT134, Wallingford.

121. Wolanski, E., Imberger, J. and Heron, M. (1984). "Islands Wakes in Shallow Coastal Waters", Journal of Geophysical Research, Vol.89, No.C6, pp.10553-10569.

122. Wolanski, E. (1985). "Water Circulation in a Topographically Complex Environment", Australian Institute of Marine Science, Internal report, Townsville, Australia.

123. Zeldorich, Y.B. and Myskis, A.D. (1976). "Elements of Applied Mathematics", Mir Publishers.

124. Zimmerman, J.T.F. (1981). "Dynamics, Diffusion and Geomorphological Significance of Tidal Residual Eddies", Nature, Vol.290, pp.549-555.

APPENDIX A

APPENDIX A

THE METHOD OF GAUSS ELIMINATION AND BACK SUBSTITUTION

A.1 Solution of the Shallow Water Wave Equations.

The finite difference eqns.(5.1) to (5.4) may be solved using the method of Gauss elimination and back substitution. To use this method it is first necessary to separate the unknown implicit terms from the known explicit and constant terms. The continuity and momentum eqns.(5.1) and (5.2) can therefore be respectively re-written in the following form:

$$- r_{i-\frac{1}{2}} \, q^{n+\frac{1}{2}}_{xi-\frac{1}{2},j} + \eta^{n+\frac{1}{2}}_{i,j} + r_{i+\frac{1}{2}} \, q^{n+\frac{1}{2}}_{xi+\frac{1}{2},j} = A^{n}_{i,j} \tag{A.1}$$

$$- s_{i} \, \eta^{n+\frac{1}{2}}_{i,j} + s_{i+\frac{1}{2}} \, q^{n+\frac{1}{2}}_{xi+\frac{1}{2},j} + s_{i+1} \, \eta^{n+\frac{1}{2}}_{i+1,j} = B^{n}_{i+\frac{1}{2},j} \tag{A.2}$$

where

$$r_{i-\frac{1}{2}} = r_{i+\frac{1}{2}} = \frac{\Delta t}{2\Delta x}$$

$$A^{n}_{i,j} = \eta^{n}_{i,j} - \frac{\Delta t}{2\Delta x} \left(q^{n}_{yi,j+\frac{1}{2}} - q^{n}_{yi,j-\frac{1}{2}} \right)$$

$$s_{i} = s_{i+1} = g \frac{\Delta t}{2\Delta x} \left(\underline{h}^{y}_{i+\frac{1}{2},j} + \underline{\eta}^{x}_{i+\frac{1}{2},j} \right)$$

$$s_{i+\frac{1}{2}} = 1 + \frac{g\Delta t \left[(QXM_{i+\frac{1}{2},j})^{2} + (\bar{g}^{n}_{yi+\frac{1}{2},j})^{2} \right]^{\frac{1}{2}}}{2 \left(\underline{h}^{y}_{i+\frac{1}{2},j} + \underline{\eta}^{x}_{i+\frac{1}{2},j} \right)^{2} \left(\underline{C}^{x}_{i+\frac{1}{2},j} \right)^{2}}$$

and

$$B^{n}_{i+\frac{1}{2},j} = q^{n-\frac{1}{2}}_{xi+\frac{1}{2},j} - \alpha\frac{\Delta t}{\Delta x}\left(\frac{x}{UM}_{i+1,j}\,\frac{x}{QXM}_{i+1,j} - \frac{x}{UM}_{i,j}\,\frac{x}{QXM}_{i,j}\right) -$$

$$\alpha\frac{\Delta t}{\Delta x}\left(\frac{x}{q}^{n}_{yi+\frac{1}{2},j+\frac{1}{2}}\,UM_{i+\frac{1}{2},r} - \frac{x}{q}^{n}_{yi+\frac{1}{2},j-\frac{1}{2}}\,UM_{i+\frac{1}{2},s}\right) - \frac{g\Delta t}{2\Delta x}\left(\frac{y}{h}_{i+\frac{1}{2},j} + \frac{x}{\eta}^{n}_{i+\frac{1}{2},j}\right)$$

$$\left(\eta^{n-\frac{1}{2}}_{i+1,j} - \eta^{n-\frac{1}{2}}_{i,j}\right) + f\,\bar{q}^{n}_{yi+\frac{1}{2},j} - \frac{g\Delta t\; q^{n-\frac{1}{2}}_{xi+\frac{1}{2},j}\left[(QXM_{i+\frac{1}{2},j})^{2} + (\bar{q}^{n}_{yi+\frac{1}{2},j})^{2}\right]^{\frac{1}{2}}}{2\left(\frac{y}{h}_{i+\frac{1}{2},j} + \frac{x}{\eta}^{n}_{i+\frac{1}{2},j}\right)^{2}\left(\frac{x}{C}_{i+\frac{1}{2},j}\right)^{2}}$$

$$+ \frac{\Delta t\; B\;\sqrt{g}\left[(QXM_{i+\frac{1}{2},j})^{2} + (\bar{q}^{n}_{yi+\frac{1}{2},j})^{2}\right]^{\frac{1}{2}}}{\Delta x^{2}\;\frac{x}{C}_{i+\frac{1}{2},j}}\left(\frac{y}{h}_{i+\frac{1}{2},j} + \frac{x}{\eta}^{n}_{i+\frac{1}{2},j}\right)$$

$$\left(UM_{i+\frac{1}{2},j+1} - 2\,UM_{i+\frac{1}{2},j} + UM_{i+\frac{1}{2},j+1}\right) + C_{f}\,\Delta t\left[\frac{y}{h}_{i+\frac{1}{2},j} + \frac{x}{\eta}^{n}_{i+\frac{1}{2},j}\right]$$

$$\left[\left(\frac{T_{xy|f}}{\rho}\right)^{n}_{i+\frac{1}{2},j+\frac{1}{2}} - \left(\frac{T_{xy|f}}{\rho}\right)^{n}_{i+\frac{1}{2},j-\frac{1}{2}}\right]$$

By applying eqns.(A.1) and (A.2) to all the grid points - from 1 to I - along the row j, a set of simultaneous equations evolve which can be represented in the following tri-diagonal matrix form:

$$\begin{bmatrix}
1 & r_{3/2} & 0 & \cdots & & & & 0 \\
-s_1 & s_{3/2} & s_2 & 0 & \cdots & & & \\
0 & -r_{3/2} & 1 & r_{5/2} & 0 & \cdots & & \\
0 & 0 & -s_2 & s_{5/2} & s_3 & \cdots & & \\
\vdots & & & & & & & \\
0 & & & & -s_{I-1} & s_{I-\frac{1}{2}} & s_I & \\
0 & 0 & 0 & 0 & 0 & -r_{I-\frac{1}{2}} & 1 &
\end{bmatrix}
\begin{bmatrix} \eta_1 \\ q_{x3/2} \\ \eta_2 \\ q_{x5/2} \\ \eta_3 \\ \vdots \\ q_{xI-1/2} \\ \eta_I \end{bmatrix}^{n+\frac{1}{2}}
=
\begin{bmatrix} A_1 \\ B_{3/2} \\ A_2 \\ B_{5/2} \\ A_3 \\ \vdots \\ B_{I-1/2} \\ A_I \end{bmatrix}^{n}
+
\begin{bmatrix} r_{\frac{1}{2}}q_{x\frac{1}{2}} \\ 0 \\ 0 \\ \vdots \\ 0 \\ -r_{I+\frac{1}{2}}q_{xI+\frac{1}{2}} \end{bmatrix}^{n+\frac{1}{2}}$$

(A.3)

where $q_{x\frac{1}{2}}^{n+\frac{1}{2}}$ and $q_{xI+\frac{1}{2}}^{n+\frac{1}{2}}$ are known values of discharge per unit width at the lower and upper boundaries respectively. With the boundary conditions prescribed, it is possible to determine the matrix components $[\eta_1, q_{x\frac{3}{2}}, \eta_2, \ldots\ldots, \eta_I]^{n+\frac{1}{2}}$ by a process of elimination of unknowns. Starting with the first equation of the matrix, the water elevation can be written as:

$$\eta_1^{n+\frac{1}{2}} = -P_1 \, q_{x\frac{3}{2}}^{n+\frac{1}{2}} + Q_1 \qquad (A.4)$$

where $P_1 = r_{\frac{3}{2}}$

and $Q_1 = A_1^n + r_{\frac{1}{2}} \, q_{x\frac{1}{2}}^{n+\frac{1}{2}}$

Equation (A.4) can now be substituted into the second equation of the matrix to eliminate the water elevation $\eta_1^{n+\frac{1}{2}}$, giving:

$$q_{x\frac{3}{2}}^{n+\frac{1}{2}} = -R_1 \, \eta_2^{n+\frac{1}{2}} + S_1 \qquad (A.5)$$

where $R_1 = \dfrac{s_2}{(s_{\frac{3}{2}} + s_1 P_1)}$

and $S_1 = \dfrac{B_{\frac{3}{2}}^n + s_1 Q_1}{(s_{\frac{3}{2}} + s_1 P_1)}$

Similarly eqn.(A.5) can be used to eliminate $q_{x\frac{3}{2}}^{n+\frac{1}{2}}$ from the third matrix equation to give:

$$\eta_2^{n+\frac{1}{2}} = -P_2 \, q_{x\frac{3}{2}}^{n+\frac{1}{2}} + Q_2 \qquad (A.6)$$

where $$P_2 = \frac{r_{\frac{5}{2}}}{(1 + r_{\frac{3}{2}} R_1)}$$

and $$Q_2 = \frac{A_2^n + r_{\frac{3}{2}} S_1}{(1 + r_{\frac{3}{2}} R_1)}$$

This process of substitution and elimination can be continued along the row j until the upper bound is reached. The recursion formulae for the values $q_{xi+\frac{1}{2}}^{n+\frac{1}{2}}$ and $\eta_i^{n+\frac{1}{2}}$ can therefore be written in general as:

$$q_{xi+\frac{1}{2}}^{n+\frac{1}{2}} = - R_i \eta_{i+1}^{n+\frac{1}{2}} + S_i \qquad (A.7)$$

$$\eta_i^{n+\frac{1}{2}} = - P_i q_{xi+\frac{1}{2}}^{n+\frac{1}{2}} + Q_i \qquad (A.8)$$

where $$R_i = \frac{s_{i+1}}{(s_{i+\frac{1}{2}} + s_i P_i)}$$

$$S_i = \frac{B_{i+\frac{1}{2}}^n + s_i Q_i}{(s_{i+\frac{1}{2}} + s_i P_i)}$$

$$P_i = \frac{r_{i+\frac{1}{2}}}{(1 + r_{i-\frac{1}{2}} R_{i-1})}$$

and $$Q_i = \frac{A_i^n + r_{i-\frac{1}{2}} S_{i-1}}{(1 + r_{i-\frac{1}{2}} R_{i-1})}$$

where i refers to any non-boundary grid point. When the penultimate equation from matrix (A.3) is used to eliminate $q_{xI-\frac{1}{2}}^{n+\frac{1}{2}}$ from the last equation, the resulting equation involves only one unknown, $\eta_I^{n+\frac{1}{2}}$, which can be calculated directly. This value is then substituted into the previous equation for $q_{xI-\frac{1}{2}}^{n+\frac{1}{2}}$ - of the form of eqn.(A.6) - which then becomes the only unknown in the equation. This process of back substitution, when continued thus yields all the components of the vector

$[\eta_I, q_{xI-\frac{1}{2}}, \ldots, \eta_2, q_{x\frac{3}{2}}, \eta_1]^{n+\frac{1}{2}}$. This solution procedure can now be repeated for the row j+1 and so on, until all the J rows parallel to the x-axis have been solved, and the values of $\eta^{n+\frac{1}{2}}$ and $q_x^{n+\frac{1}{2}}$ are known throughout the domain. In the second iteration the whole procedure of elimination and back substitution is repeated to give a second and final estimate of $\eta^{n+\frac{1}{2}}$ and $q_x^{n+\frac{1}{2}}$.

During the second operation, from time $(n+\frac{1}{2})\Delta t$ to $(n+1)\Delta t$, the water levels η^{n+1} and discharges per unit width q_y^{n+1} are determined in the same way as described for eqns.(5.1) and (5.2). Firstly, eqns.(5.3) and (5.4) are applied to all the grid points along the row i, parallel to the y-axis, with the resulting set of simultaneous equations being expressed in a matrix form as before. From the resulting matrix equation similar recursion formulae are developed for $q_{yj+\frac{1}{2}}^{n+1}$ and η_j^{n+1}, giving:

$$q_{yj+\frac{1}{2}}^{n+1} = -R_j \, \eta_{j+1}^{n+1} + S_j \tag{A.9}$$

$$\eta_j^{n+1} = -P_j \, q_{yj+\frac{1}{2}}^{n+1} + Q_j \tag{A.10}$$

where

$$R_j = \frac{s_{j+1}}{(s_{j+\frac{1}{2}} + s_j P_j)}$$

$$S_j = \frac{B_{j+\frac{1}{2}}^{n+\frac{1}{2}} + s_j Q_j}{(s_{j+\frac{1}{2}} + s_j P_j)}$$

$$P_j = \frac{r_{j+\frac{1}{2}}}{(1 + r_{j-\frac{1}{2}} R_{j-1})}$$

$$Q_j = \frac{A_j^{n+\frac{1}{2}} + r_{j-\frac{1}{2}} S_{j-1}}{(1 + r_{j-\frac{1}{2}} R_{j-1})}$$

$$A_{i,j}^{n+\frac{1}{2}} = \eta_{i,j}^{n+\frac{1}{2}} - \frac{\Delta t}{2\Delta x} \left(q_{xi+\frac{1}{2},j}^{n+\frac{1}{2}} - q_{xi-\frac{1}{2},j}^{n+\frac{1}{2}}\right)$$

$$r_{j-\frac{1}{2}} = r_{j+\frac{1}{2}} = \frac{\Delta t}{2\Delta x}$$

$$s_i = s_{i+1} = g\frac{\Delta t}{\Delta x}\left(\frac{x}{h}_{i,j+\frac{1}{2}} + \frac{y}{\eta}^{n+\frac{1}{2}}_{i,j+\frac{1}{2}}\right)$$

$$s_{i+\frac{1}{2}} = 1 + \frac{g\Delta t\left[\left(\bar{q}^{n+\frac{1}{2}}_{xi,j+\frac{1}{2}}\right)^2 + \left(QYM_{i,j+\frac{1}{2}}\right)^2\right]^{\frac{1}{2}}}{2\left(\frac{x}{h}_{i,j+\frac{1}{2}} + \frac{y}{\eta}^{n+\frac{1}{2}}_{i,j+\frac{1}{2}}\right)^2 \left(\frac{y}{C}_{i,j+\frac{1}{2}}\right)^2}$$

and

$$B^{n+\frac{1}{2}}_{i,j+\frac{1}{2}} = q^n_{yi,j+\frac{1}{2}} - \alpha\frac{\Delta t}{\Delta x}\left(\frac{y}{q}^{n+\frac{1}{2}}_{xi+\frac{1}{2},j+\frac{1}{2}} VM_{p,j+\frac{1}{2}} - \frac{y}{q}^{n+\frac{1}{2}}_{xi-\frac{1}{2},j+\frac{1}{2}} VM_{t,j+\frac{1}{2}}\right) - \alpha\frac{\Delta t}{\Delta x}$$

$$\left(\frac{y}{VM}_{i,j+1}\frac{y}{QYM}_{i,j+1} - \frac{y}{VM}_{i,j}\frac{y}{QYM}_{i,j}\right) - \frac{g\Delta t}{2\Delta x}\left(\frac{x}{h}_{i,j+\frac{1}{2}} + \frac{y}{\eta}^{n+\frac{1}{2}}_{i,j+\frac{1}{2}}\right)\left(\eta^n_{i,j+1} - \eta^n_{i,j}\right)$$

$$- f\,\bar{q}^{n+\frac{1}{2}}_{xi,j+\frac{1}{2}} - \frac{g\Delta t\, q^n_{yi,j+\frac{1}{2}}\left[\left(\bar{q}^{n+\frac{1}{2}}_{xi,j+\frac{1}{2}}\right)^2 + \left(QYM_{i,j+\frac{1}{2}}\right)^2\right]^{\frac{1}{2}}}{2\left(\frac{x}{h}_{i,j+\frac{1}{2}} - \frac{y}{\eta}^{n+\frac{1}{2}}_{i,j+\frac{1}{2}}\right)^2\left(\frac{y}{C}_{i,j+\frac{1}{2}}\right)^2} + \left(\frac{x}{h}_{i,j+\frac{1}{2}} + \frac{y}{\eta}^{n+\frac{1}{2}}_{i,j+\frac{1}{2}}\right)$$

$$\frac{\Delta t\, B\sqrt{g}\left[\left(\bar{q}^{n+\frac{1}{2}}_{xi,j+\frac{1}{2}}\right)^2 + \left(QYM_{i,j+\frac{1}{2}}\right)^2\right]^{\frac{1}{2}}}{\Delta x^2\,\frac{y}{C}_{i,j+\frac{1}{2}}}\left(VM_{i+1,j+\frac{1}{2}} - 2\,VM_{i,j+\frac{1}{2}} + VM_{i-1,j+\frac{1}{2}}\right)$$

$$+ C_f\,\Delta t\left(\frac{x}{h}_{i,j+\frac{1}{2}} + \frac{y}{\eta}^{n+\frac{1}{2}}_{i,j+\frac{1}{2}}\right)\left[\left(\frac{T_{xy|f}}{\rho}\right)^{n+\frac{1}{2}}_{i+\frac{1}{2},j+\frac{1}{2}} - \left(\frac{T_{xy|f}}{\rho}\right)^{n+\frac{1}{2}}_{i-\frac{1}{2},j+\frac{1}{2}}\right]$$

Having specified the lower and upper boundaries, the values of η^{n+1} and q^{n+1}_y can be determined throughout the domain as before.

The solution procedure illustrated above assumes that the open boundaries are described by discharges per unit width - the terms $q^{n+\frac{1}{2}}_{x\,\frac{1}{2}}$ and $q^{n+\frac{1}{2}}_{xI+\frac{1}{2}}$ of the matrix eqn.(A.3). In order to accommodate the water elevations as open boundary data, the model boundary has to occur at an integral value of i or j as defined in fig.(5.1). For a lower x-direction open boundary, the boundary should be moved from $i=\frac{3}{2}$ to i=1 and as a result a momentum equation would be the first equation of matrix (A.3), and $q^{n+\frac{1}{2}}_{x\,\frac{1}{2}}$ would be replaced by $\eta^{n+\frac{1}{2}}_1$.

A.2 Solution of the Advective-Diffusion Equation

The procedure followed for the solution of the finite difference advective-diffusion eqns.(5.5) and (5.6) is no different to that followed for the solution of the shallow water equations, described in section A.1. During the first operation (from time $n\Delta t$ to $(n+\frac{1}{2})\Delta t$), after the solution of the shallow water eqns.(5.1) and (5.2) and the calculation of $\eta^{n+\frac{1}{2}}$ and $q_x^{n+\frac{1}{2}}$, the advective-diffusion eqn.(5.5) is solved to determine the constituent concentration $S^{n+\frac{1}{2}}$. Firstly, the unknown implicit terms are separated from the known terms and eqn.(5.5) becomes of the following form:

$$-P_i\, S^{n+\frac{1}{2}}_{i-1,j} + Q_i\, S^{n+\frac{1}{2}}_{i,j} + R_i\, S^{n+\frac{1}{2}}_{i+1,j} = E^n_{i,j} \qquad \text{(A.11)}$$

where

$$P_i = \frac{\Delta t}{4\Delta t}\, q^{n+\frac{1}{2}}_{xi-\frac{1}{2},j} + \frac{\Delta t}{2\Delta x^2}\left(\underline{\underline{h}}^{x}_{i-\frac{1}{2},j} + \eta^{x\,n+\frac{1}{2}}_{i-\frac{1}{2},j}\right) D^{n+\frac{1}{2}}_{xxi-\frac{1}{2},j}$$

$$Q_i = \left(\underline{\underline{h}}_{i,j} + \eta^{n+\frac{1}{2}}_{i,j}\right) + \frac{\Delta t}{4\Delta x}\left(q^{n+\frac{1}{2}}_{xi+\frac{1}{2},j} - q^{n+\frac{1}{2}}_{xi-\frac{1}{2},j}\right) + \frac{\Delta t}{2\Delta x^2}\left[\left(\underline{h}^{y}_{i+\frac{1}{2},j} + \underline{\eta}^{x\,n+\frac{1}{2}}_{i+\frac{1}{2},j}\right)\right.$$

$$\left. D^{n+\frac{1}{2}}_{xxi+\frac{1}{2},j} - \left(\underline{h}^{y}_{i-\frac{1}{2},j} + \underline{\eta}^{x\,n+\frac{1}{2}}_{i-\frac{1}{2},j}\right) D^{n+\frac{1}{2}}_{xxi-\frac{1}{2},j}\right]$$

$$R_i = \frac{\Delta t}{4\Delta x}\, q^{n+\frac{1}{2}}_{xi+\frac{1}{2},j} - \frac{\Delta t}{2\Delta x^2}\left(\underline{h}^{y}_{i+\frac{1}{2},j} + \underline{\eta}^{x\,n+\frac{1}{2}}_{i+\frac{1}{2},j}\right) D^{n+\frac{1}{2}}_{xxi+\frac{1}{2},j}$$

and

$$E^n_{i,j} = \left(\bar{h}_{i,j} + \eta^n_{i,j}\right) S^n_{i,j} - \frac{\Delta t}{2\Delta x}\left(\underline{\bar{S}}^{\,y\,n}_{i,j+\frac{1}{2}}\, q^n_{yi,j+\frac{1}{2}} - \underline{\bar{S}}^{\,y\,n}_{i,j-\frac{1}{2}}\, q^n_{yi,j-\frac{1}{2}}\right)$$

$$+ \frac{\Delta t}{2\Delta x^2}\left[\left(S^n_{i,j+1} - S^n_{i,j}\right)\left(\underline{\bar{h}}^{\,x}_{i,j+\frac{1}{2}} + \underline{\eta}^{\,y\,n}_{i,j+\frac{1}{2}}\right) D^n_{yyi,j+\frac{1}{2}} - \left(S^n_{i,j} - S^n_{i,j-1}\right)\right.$$

$$\left(\underline{\bar{h}}^{\,x}_{i,j-\frac{1}{2}} + \underline{\eta}^{\,y}_{n\,i,j-\frac{1}{2}}\right) D^n_{yyi,j-\frac{1}{2}} + \left(\bar{\bar{S}}^n_{i+\frac{1}{2},j+\frac{1}{2}} - \bar{\bar{S}}^n_{i+\frac{1}{2},j-\frac{1}{2}}\right)\left(\underline{\bar{h}}^{\,y}_{i+\frac{1}{2},j} + \underline{\eta}^{\,x\,n+\frac{1}{2}}_{i+\frac{1}{2},j}\right) D^{n+\frac{1}{2}}_{xyi+\frac{1}{2},j}$$

$$- \left(\bar{\bar{S}}^n_{i-\frac{1}{2},j+\frac{1}{2}} - \bar{\bar{S}}^n_{i-\frac{1}{2},j-\frac{1}{2}}\right)\left(\underline{\bar{h}}^{\,y}_{i-\frac{1}{2},j} + \underline{\eta}^{\,x\,n+\frac{1}{2}}_{i-\frac{1}{2},j}\right) D^{n+\frac{1}{2}}_{xyi-\frac{1}{2},j} + \left(\bar{\bar{S}}^n_{i+\frac{1}{2},j+\frac{1}{2}} - \bar{\bar{S}}^n_{i-\frac{1}{2},j+\frac{1}{2}}\right)$$

$$\left.\left(\underline{\bar{h}}^{\,x}_{i,j+\frac{1}{2}} + \underline{\eta}^{\,y\,n}_{i,j+\frac{1}{2}}\right) D^n_{yxi,j+\frac{1}{2}} - \left(\bar{\bar{S}}^n_{i+\frac{1}{2},j-\frac{1}{2}} - \bar{\bar{S}}^n_{i-\frac{1}{2},j-\frac{1}{2}}\right)\left(\underline{\bar{h}}^{\,x}_{i,j-\frac{1}{2}} + \underline{\eta}^{\,y\,n}_{i,j-\frac{1}{2}}\right) D^n_{yxi,j-\frac{1}{2}}\right]$$

By applying eqn.(A.11) to all grid points - from 1 to I - along the row j, a set of simultaneous equations evolve which can be represented in the following tri-diagonal matrix form:

$$\begin{bmatrix} Q_2 & R_2 & 0 & 0 & \cdots & 0 \\ -P_3 & Q_3 & R_3 & 0 & \cdots & 0 \\ 0 & -P_4 & Q_4 & R_4 & \cdots & \cdot \\ \cdot & \cdot & \cdot & \cdot & \cdot & \cdot \\ \cdot & \cdot & \cdot & \cdot & \cdot & \cdot \\ \cdot & \cdot & \cdot & \cdot & \cdot & \cdot \\ \cdot & \cdot & \cdot & \cdot & \cdot & \cdot \\ \cdot & \cdot & \cdot & \cdot & -P_I & Q_I \end{bmatrix} \begin{bmatrix} S_2 \\ S_3 \\ S_4 \\ \cdot \\ \cdot \\ \cdot \\ S_I \end{bmatrix}^{n+\frac{1}{2}} = \begin{bmatrix} E_2 \\ E_3 \\ E_4 \\ \cdot \\ \cdot \\ \cdot \\ E_I \end{bmatrix}^{n} + \begin{bmatrix} +P_2\, S_1 \\ 0 \\ \cdot \\ \cdot \\ \cdot \\ \cdot \\ -R_I\, S_{I+1} \end{bmatrix}^{n+\frac{1}{2}} \qquad \text{(A.12)}$$

where $S_1^{n+\frac{1}{2}}$ and $S_{I+1}^{n+\frac{1}{2}}$ are the known values of concentration at the lower and upper boundaries. Knowing the boundary conditions, it is possible to determine the vector components $[S_1, S_2, \ldots, S_I]^{n+\frac{1}{2}}$ by the process of elimination of unknowns, similar to that described in section A.1. The resulting recursion formulae for $S_i^{n+\frac{1}{2}}$ are given as:

$$S_i^{n+\frac{1}{2}} = -A_i \, S_{i+1}^{n+\frac{1}{2}} + B_i \qquad (A.13)$$

where $A_i = R_i/(Q_i + P_i A_{i-1})$

and $B_i = (E_i^n + P_i B_{i-1})/(Q_i + P_i A_{i-1})$

where i refers to any non-boundary grid point. The process of elimination is carried down to the last equation of matrix (A.12) with the resulting equation involving only one unknown, $S_I^{n+\frac{1}{2}}$, which can be calculated directly. The process of back substitution follows, resulting in the determination of all components of the vector $[S_I, \ldots, S_4, S_3, S_2]^{n+\frac{1}{2}}$. This solution procedure is repeated for the row j+1 and so on, until all the J rows, parallel to the x-axis, have been solved, and the concentration values $S^{n+\frac{1}{2}}$ are known throughout the domain.

During the second operation, from time $(n+\frac{1}{2})\Delta t$ to $(n+1)\Delta t$, the whole procedure of elimination and back substitution is repeated to give the concentration values S^{n+1} over the computational domain.

APPENDIX B

LIST OF SYMBOLS

AG	Gravitational acceleration
ALPHA	Coefficient in advective acceleration terms
AMP	Tidal wave amplitude
AT, DT	Half timestep in coarse or fine grid
AX, DX	Grid spacing in coarse or fine grid
A, B, P, Q, R, S	Gauss elimination factors
BETA	Coefficient in eddy viscosity term
C, CN	Chezy coefficient in coarse or fine grid
C1,C2,C3,C4,C5,C6	Constants in coarse grid
CSX, CSY	Total depth at velocity points U and V respectively in coarse grid
CNX, CNY	Total depth at velocity points U and V respectively in fine grid
DELTA	Constant in longitudinal dispersion coefficient
DEP	Total depth at an elevation grid point
DXX, DXY, DYX, DYY	Dispersion coefficients in coarse grid
DNXX, DNXY, DNYX, DNYY	Dispersion coefficients in fine grid
E, EM, EP	Water elevation in timestep n, $n+\frac{1}{2}$ and n+1 respectively in coarse grid
EN, ENM, ENP	Water elevation in timestep n, $n+\frac{1}{2}$ and n+1 respectively in fine grid
E2, E5	Constants in coarse grid
EDDY	Coefficient of eddy viscosity
EINT	Initial value of water elevation
EMAX, EMIN	Maximum and minimum values of water elevation
ENLEN	Harbour entrance width
EPVAL	Open boundary water elevation value in coarse grid
FRN	Friction factor

F1, F2, F3, F4, F5	Constants in fine grid
GAMMA	Constant in transverse dispersion coefficient
G2, G5	Constants in fine grid
HT, HNT	Mean water depth in coarse or fine grid
H, HN	Parameter defining calculation domain in coarse or fine grid
I, J	Grid point of the x- or y- axis in coarse grid
IS, JS	Grid co-ordinates of entrance tip in coarse grid
IBD, JBD	Computational control parameters which define the extend of the computational domain in the I and J direction respectively in coarse grid
ICOL, NCOL	Number of columns in results tables in coarse or fine grid
IIND, JIND	Counters for I or J
IINDO, JINDO	Number of open boundaries in the x- and y-directions in coarse grid
ILEF, MLEF	Left-hand boundary position in coarse or fine grid
IMAX, JMAX	Maximum value of I or J
IOBD, JOBD	Define the position of the open boundaries in coarse grid
IP, MI, MP, LI	Counters
IRIG, MRIG	Right-hand boundary position in coarse or fine grid
ISRCH, JSRCH	Part of IBD or JBD which indicates the presence of an open boundary
ISTEP, NSTEP	Half timestep operation counter in coarse or fine grid
JB, JT	Bottom and top boundary positions in coarse grid
KONVRT	Array used to hold results during printout
MAXST, IMAXST	Maximum number of timesteps to be used in coarse or fine grid

M, N	Grid point of the x- or y- axis in fine grid
MC, NC	Grid co-ordinates of entrance tip in fine grid
MBD, NBD	Computational control parameters which define the extend of the computational domain in the M and N direction respectively in fine grid
MIND, NIND	Counters for M or N
MINDO, NINDO	Number of open boundaries in the x- and y-directions in fine grid
MMAX, NMAX	Maximum value of M or N
MOBD, NOBD	Define the position of the open boundaries in fine grid
MSRCH, NSRCH	Part of MBD or NBD which indicates the presence of an open boundary
MBOT, MTOP	Bottom and top boundary position in fine grid
NCARD, ICARD	Number of timesteps in tidal cycle for coarse or fine grid
NITER	Interation counter
NPRINC, IPRINC	Number of timesteps between printouts in coarse or fine grid
NSECT, ISECT	Number of calculation selections in coarse or fine grid domain
NST, MST	Timestep counter in coarse or fine grid
NOBGP	Number of grid points across harbour entrance
NUM	Counter
PHA	Phase difference
PI	π
PLANA	Plan-form area
QX, QXP	Discharge per unit width of timestep $n-\frac{1}{2}$ and $n+\frac{1}{2}$ in the x-direction for coarse grid
QNX, QNXP	Discharge per unit width of timestep $n-\frac{1}{2}$ and $n+\frac{1}{2}$ in the x-direction for fine grid
QY, QYP	Discharge per unit width at timestep n

	and n+1 in the y-direction for coarse grid
QNY, QNYP	Discharge per unit width at timestep n and n+1 in the y-direction for fine grid
RKS	Bed roughness parameter
RR	Constant in free shear layer stress terms
REN	Reynolds number
SIG	Wave frequency
SINV	Initial value of constituent concentration
SM, SP	Concentration at lower or upper timestep in coarse grid
SNM, SNP	Concentration at lower or upper timestep in fine grid
SPMEAN	Spatially avaraged concentration
SPDEV	Standard deviation of concentration
TAW, TNW	Free shear layer stress in coarse or fine grid
TCHEZS	Defines time between up-datings of Chezy coefficient
TIMES	Time in seconds from the start of the simulation
TITL	Heading printed out with every results table
UM, VM	Velocity in the x- or y-direction at the intermediate time level in coarse grid
UNM, VNM	Velocity in the x- or y-direction at the intermediate time level in fine grid
VIS	Kinematic viscosity
V1	Free stream velocity
XIA	Array of water elevation values at open boundary of coarse grid, defined at every half timestep over a tidal cycle
XLEN, YLEN	Length of harbour in the x- or y-direction

```
C       ***********************************************
C       *                                             *
C       *                   NESTH1                    *
C       *                                             *
C       * PREDICTION OF TIDAL CIRCULATION AND FLUSHING *
C       *         IN NARROW ENTRANCED HARBOURS        *
C       *          BY THE USE OF NESTED GRIDS         *
C       ***********************************************
C
C
      DIMENSION A(38),B(38),P(38),Q(38),R(38),S(38),KONVRT(38),
     1NPRINT(20),IPRINT(20),CINE(38),CINQ(35,38)
      COMMON TITL(18),XIA(1490),ICOL(29),H(29,36),IBD(60),JBD(60)
     1,IOBD(3),JOBD(3),QX(29,36),QXP(29,36),QY(29,36),QYP(29,36)
     2,E(29,36),EM(29,36),EP(29,36),C(29,36),UM(29,36),VM(29,36)
     3,CSX(29,36),TAW(29,36),CSY(29,36),HT(29,36),
     4HN(35,38),MBD(90),NBD(90),MOBD(3),NOBD(3),QNX(35,38)
     5,QNXP(35,38),QNY(35,38),QNYP(35,38),EN(35,38),ENM(35,38),
     6ENP(35,38),CN(35,38),UNM(35,38),VNM(35,38),CNX(35,38),
     7CNY(35,38),HNT(35,38),TNW(35,38),NCOL(32),
     8SM(29,36),SP(29,36),DXX(29,36),DYY(29,36),DXY(29,36),
     9DYX(29,36),SNM(35,38),SNP(35,38),DNXX(35,38),DNYY(35,38)
     1,DNXY(35,38),DNYX(35,38)
C
C         THE COARSE GRID
C
      IMAX=29
      JMAX=36
      AT=0.42
      AX=0.1
      ALPHA=1.016
      BETA=0.15
      GAMMA=5.93
      DELTA=0.15
      PI=4.0*ATAN(1.0)
      AMP=0.052
      EINT=-AMP
      SINV=10.0
      AG=9.80665
      TIS=AT*1504.0
C
C         CHANGE CHEZY COEFFICIENT EVERY 12 TIMESTEPS
C
      TCHEZS=12.0*2.0*AT
      PHA=180.0
      VIS=1.0E-6
      RKS=0.00061
      RR=288.0
      IS=12
      JS=17
      NCARD=NINTEG(TIS/AT)
      JOBD(1)=0102280
      IINDO=1
      JINDO=2
      NSECT=60
      MAXST=2*752
      NPRINC=188
      IP=1
      MI=1
      READ(5,11) (TITL(J),J=1,18)
      READ(5,11) (ICOL(J),J=1,18)
      READ(5,11) (ICOL(J),J=19,29)
      READ(5,11) (NCOL(J),J=1,18)
      READ(5,11) (NCOL(J),J=19,36)
      READ(5,11) (NCOL(J),J=37,32)
11    FORMAT(18A4)
C
C         SET OPEN BOUNDS AS FUNCTIONS OF XIA(K) VALUES-
C         (K) IS THE HALF TIMESTEP
C
      CALL BOUND(IMAX,JMAX,AX,AT,PI,TIS,NCARD,AMP,THT,PHA,TI)
      GO TO 87
89    CONTINUE
      TNOW=FLOAT(N)
      TIMES=TNOW*AT
      IF(TIMES.GT.TIS) GO TO 75
      EPVAL=XIA(N)
      MIMAX=N
      GO TO 76
75    IF(MI.GT.MIMAX) MI=1
      EPVAL=XIA(MI)
      MI=MI+1
76    DO 72 I=2,IMAX-1
72    EP(I,1)=EPVAL
```

```
      IF(ISTEP.EQ.1) GO TO 96
      GO TO 199
C
C          SET OPEN BOUNDS FOR POLLUTANT CONCENTRATION
C
99    CONTINUE
      DO 71 I=2,IMAX-1
      IF(QYP(I,1).LE.0.0) GO TO 83
      SP(I,1)=0.0
      GO TO 71
83    II=I-1
      SP(I,1)=SM(I,1)-(2.0*QYP(I,1)/(HT(I,1)+HT(II,1)+EP(I,2)
     1+EP(I,1)))*(SM(I,2)-SM(I,1))*AT/AX
71    CONTINUE
      IF(ISTEP.EQ.1) GO TO 208
      GO TO 308
87    CONTINUE
      NST=0
      C1=AT/AX
      C2=(AG*AT)/AX
      C3=AG*AT
      C4=2.0*AT*FC
      C5=2.0*AT/(AX**2)
      E2=0.5*AT/AX
      E5=AT/(AX**2)
      DO 400 I=1,IMAX
      DO 400 J=1,JMAX
      QX(I,J)=0.0
      UM(I,J)=0.0
      QXP(I,J)=0.0
      QY(I,J)=0.0
      VM(I,J)=0.0
      QYP(I,J)=0.0
      E(I,J)=0.0
      EM(I,J)=0.0
      EP(I,J)=0.0
      C(I,J)=0.0
      HT(I,J)=0.0
      H(I,J)=0.0
      CSX(I,J)=0.0
      CSY(I,J)=0.0
      TAW(I,J)=0.0
      SM(I,J)=0.0
      SP(I,J)=0.0
      DXX(I,J)=0.0
      DXY(I,J)=0.0
      DYY(I,J)=0.0
      DYX(I,J)=0.0
400   CONTINUE
C
C          READ IN LOCATIONS OF WATER LEVEL COMPUTATIONS
C
      CALL DIVE1(IMAX,JMAX)
C
C          SET THE IBD(N) AND JBD(N) VALUES
C
      CALL FIND1(IIND,JIND,IMAX,JMAX,IINDO,JINDO,NSECT)
C
C          READ IN WATER DEPTHS
C
      CALL DEPTH1(IMAX,JMAX)
      NSUM=0
      DO 25 N=1,20
      NSUM=NSUM+NPRINC
      NPRINT(N)=NSUM
25    CONTINUE
      NUM=1
7     IF(NUM.EQ.IIND) GO TO 3
      ISRCH=IBD(NUM)/1000000
      I=IBD(NUM)/10000-ISRCH*100
      JBOT=IBD(NUM)/100-ISRCH*10000-I*100
      JTOP=IBD(NUM)-ISRCH*1000000-I*10000-JBOT*100
      II=I-1
      DO 2 J=JBOT,JTOP
      JJ=J-1
      E(1,J)=EINT
      EM(1,J)=EINT
      EP(1,J)=EINT
      DEP=E(1,J)+0.25*(HT(I,J)+HT(I,JJ)+HT(II,J)+HT(II,JJ))
      FRN=1.0/(-2.0*ALOG10(RKS/(12.0*DEP)))**2
      C(I,J)=SQRT(8.0*AG/FRN)
      CSX(I,J)=0.5*(HT(I,J)+HT(I,JJ))+EINT
      CSY(I,J)=0.5*(HT(I,J)+HT(II,J))+EINT
2     CONTINUE
      IF(I.LT.11.OR.I.GT.18) GO TO 322
```

```
      DO 323 J=18,25
      SN(I,J)=SINV
      SP(I,J)=SINV
323   CONTINUE
322   NUM=NUM+1
      GO TO 7
3     CONTINUE
      NA=1
31    IF(NA.EQ.JINDO) GO TO 32
      J=JOBD(NA)/100000
      ILEF=JOBD(NA)/1000-J*100
      IRIG=JOBD(NA)/10-J*10000-ILEF*100
      JJ=J-1
      IF(J.EQ.1) JJ=1
      DO 33 I=ILEF,IRIG
      II=I-1
      E(I,J)=EINT
      EN(I,J)=EINT
      EP(I,J)=EINT
      DEP=E(I,J)+0.5*(HT(I,J)+HT(II,J))
      FRN=1.0/(-2.0*ALOG10(RKS/(12.0*DEP)))**2
      C(I,J)=SQRT(8.0*AG/FRN)
      CSX(I,J)=0.5*(HT(I,J)+HT(I,JJ))+EINT
      CSY(I,J)=0.5*(HT(I,J)+HT(II,J))+EINT
33    CONTINUE
      NA=NA+1
      GO TO 31
32    CONTINUE
      NA=1
41    IF(NA.EQ.IINDO) GO TO 42
      I=IOBD(NA)/100000
      JBOT=IOBD(NA)/1000-I*100
      JTOP=IOBD(NA)/10-I*10000-JBOT*100
      II=I-1
      IF(I.EQ.1) II=1
      DO 43 J=JBOT,JTOP
      JJ=J-1
      E(I,J)=EINT
      EN(I,J)=EINT
      EP(I,J)=EINT
      DEP=E(I,J)+0.5*(HT(I,J)+HT(I,JJ))
      FRN=1.0/(-2.0*ALOG(RKS/(12.0*DEP)))**2
      C(I,J)=SQRT(8.0*AG/FRN)
      CSX(I,J)=0.5*(HT(I,J)+HT(I,JJ))+EINT
      CSY(I,J)=0.5*(HT(I,J)+HT(II,J))+EINT
43    CONTINUE
      NA=NA+1
      GO TO 41
42    CONTINUE
C
C          SET UP PRINT INSTRUCTIONS
C
      ISTEP=2
      TIMES=0.0
      CTIMES=0.0
      GO TO 500
C
C          COMPUTE QXP AND EP ON ROW J (FIRST HALF TIMESTEP)
C
88    ISTEP=1
      NST=NST+1
      N=2*NST-1
      IF(NST.GT.MAXST) STOP
C
C          SET OPEN BOUNDS
C
      NITER=1
      GO TO 89
96    NUM=1
5     IF(NUM.EQ.JIND) GO TO 10
      JSRCH=JBD(NUM)/1000000
      J=JBD(NUM)/10000-JSRCH*100
      ILEF=JBD(NUM)/100-JSRCH*10000-J*100
      IRIG=JBD(NUM)-JSRCH*1000000-J*10000-ILEF*100
      IL=ILEF
      ILL=IL-1
      ILLL=IL+1
      IR=IRIG
      IRR=IR-1
      IRRR=IR+1
      JJ=J-1
      JJJ=J+1
      R(ILL)=0.0
      S(ILL)=QXP(ILL,J)
      DO 100 I=IL,IR
```

```
      II=I-1
      III=I+1
      A(I)=E(I,J)-C1*(QY(I,J)-QY(I,JJ))
      P(I)=C1/(1.0+C1*R(II))
      Q(I)=(A(I)+C1*S(II))/(1.0+C1*R(II))
101   CONTINUE
      IF(I.EQ.IR) GO TO 100
      TEMP1=UM(I,J)*CSX(I,J)
      TEMP2=0.25*(QY(I,J)+QY(III,J)+QY(I,JJ)+QY(III,JJ))
      TEMP3=SQRT(TEMP1**2+TEMP2**2)
      TEMP4=0.5*(C(I,J)+C(III,J))
      TEMP11=C2*CSX(I,J)
      EDDY=BETA*SQRT(AG)*TEMP3/TEMP4
      TEMP12=1.0+(C3*TEMP3)/(CSX(I,J)**2*TEMP4**2)
      TEMP13=TEMP11*P(I)+TEMP12
      DX1=UM(III,J)*CSX(III,J)
      DX2=UM(I,J)*CSX(I,J)
      DX3=UM(II,J)*CSX(II,J)
      TEMP17=UM(I,JJJ)
      TEMP18=UM(I,JJ)
      IF((QY(I,JJ)+QY(III,JJ)).LT.0.0) TEMP18=UM(I,J)
      IF((QY(I,J)+QY(III,J)).GT.0.0) TEMP17=UM(I,J)
      TEMP40=UM(I,JJJ)
      TEMP41=UM(I,JJ)
      IF(UM(I,JJJ).EQ.0.0) GO TO 49
      IF(H(III,JJJ).NE.2.0.AND.H(I,JJJ).NE.2.0) GO TO 51
49    TEMP40=-UM(I,J)
      TEMP17=0.0
51    IF(H(I,J).NE.2.0.AND.H(III,J).NE.2.0) GO TO 52
      TEMP41=-UM(I,J)
      TEMP18=0.0
52    CONTINUE
      TEMP14=0.25*((DX1+DX2)*(UM(III,J)+UM(I,J))-(DX2+DX3)*
     1(UM(I,J)+UM(II,J)))
      TEMP15=0.5*((QY(III,J)+QY(I,J))*TEMP17-(QY(III,JJ)+QY(I,JJ))*
     1TEMP18)
      D2=1.0
      B(I)=QX(I,J)+C2*CSX(I,J)*(UM(I,J)-UM(III,J))
     1-(C3*QX(I,J)*TEMP3)/(CSX(I,J)**2*TEMP4**2)-C4*TEMP2
     2-2.0*C1*ALPHA*TEMP14-2.0*C1*ALPHA*TEMP15
     3+C5*EDDY*(TEMP40-2.0*UM(I,J)+TEMP41)*CSX(I,J)
     4+20*C1*D2*(TAW(I,J)-TAW(I,JJ))
      R(I)=TEMP11/TEMP13
      S(I)=(B(I)+TEMP11*Q(I))/TEMP13
100   CONTINUE
      QXP(IR,J)=0.0
      DO 262 N=ILLL,IR
      I=IR+ILLL-N
      II=I-1
      EP(I,J)=-P(I)*QXP(I,J)+Q(I)
      QXP(II,J)=-R(II)*EP(I,J)+S(II)
262   CONTINUE
      EP(IL,J)=-P(IL)*QXP(IL,J)+Q(IL)
      NUM=NUM+1
      GO TO 5
10    CONTINUE
      NITER=NITER+1
      IF(NITER.GT.2) GO TO 990
      DO 117 I=1,IMAX
      DO 117 J=1,JMAX
      IF(CSX(I,J).EQ.0.0) GO TO 117
      UM(I,J)=0.5*(QXP(I,J)+QX(I,J))/CSX(I,J)
117   CONTINUE
      GO TO 96
990   CONTINUE
C
C          COMPUTE SP ON ROW J (FIRST HALF TIMESTEP)
C
      NUM=1
      GO TO 99
208   IF(NUM.EQ.JIND) GO TO 290
      JSRCH=JBD(NUM)/1000000
      J=JBD(NUM)/10000-JSRCH*100
      IL=JBD(NUM)/100-JSRCH*10000-J*100
      IR=JBD(NUM)-JSRCH*1000000-J*10000-IL*100
      ILL=IL-1
      ILLL=IL+1
      IRR=IR-1
      IRRR=IR+1
      JJ=J-1
      JJJ=J+1
      A(ILL)=0.0
      B(ILL)=SP(ILL,J)
      P(IL)=0.0
      DXX(ILL,J)=0.0
```

```
      DXY(ILL,J)=0.0
      IF(JSRCH.NE.1.AND.JSRCH.NE.3) GO TO 201
      TEMP16=0.5*(HT(ILL,J)+HT(ILL,JJ)+EP(ILL,J)+EP(IL,J))
      IF(QXP(ILL,J).EQ.0.0) GO TO 350
      TEMP19=0.25*(QY(ILL,J)+QY(IL,J)+QY(ILL,JJ)+QY(IL,JJ))
      TEMP30=SQRT(QXP(ILL,J)**2+TEMP19**2)
      TEMP31=0.5*(C(ILL,J)+C(IL,J))
      TEMP32=SQRT(AG)/(TEMP30*TEMP31)
      DXX(ILL,J)=TEMP16*((GAMMA*QXP(ILL,J)**2+DELTA*TEMP19**2)*TEMP32)
      DXY(ILL,J)=TEMP16*(GAMMA-DELTA)*QXP(ILL,J)*TEMP19*TEMP32
      IF(QY(IL,J).EQ.0.0) DXY(ILL,J)=0.0
      IF(QY(IL,JJ).EQ.0.0) DXY(ILL,J)=0.0
350   P(IL)=E2*QXP(ILL,J)+E5*DXX(ILL,J)
201   R(IR)=0.0
      DXX(IR,J)=0.0
      DXY(IR,J)=0.0
      IF(JSRCH.NE.2.AND.JSRCH.NE.3) GO TO 203
      TEMP16=0.5*(HT(IR,J)+HT(IR,JJ)+EP(IR,J)+EP(IRR,J))
      IF(QXP(IR,J).EQ.0.0) GO TO 361
      TEMP19=0.25*(QY(IR,J)+QY(IRR,J)+QY(IR,JJ)+QY(IRR,JJ))
      TEMP30=SQRT(QXP(IR,J)**2+TEMP19**2)
      TEMP31=0.5*(C(IR,J)+C(IRR,J))
      TEMP32=SQRT(AG)/(TEMP30*TEMP31)
      DXX(IR,J)=TEMP16*((GAMMA*QXP(IR,J)**2+DELTA*TEMP19**2)*TEMP32)
      DXY(IR,J)=TEMP16*(GAMMA-DELTA)*QXP(IR,J)*TEMP19*TEMP32
      IF(QY(IR,J).EQ.0.0) DXY(IR,J)=0.0
      IF(QY(IR,JJ).EQ.0.0) DXY(IR,J)=0.0
361   R(IR)=E2*QXP(IR,J)-E5*DXX(IR,J)
203   DO 202 I=IL,IR
      II=I-1
      III=I+1
      A(I)=0.0
      B(I)=0.0
      IF(I.EQ.IL) GO TO 204
      P(I)=E2*QXP(II,J)+E5*DXX(II,J)
204   DXX(1,J)=0.0
      DXY(1,J)=0.0
      IF(I.EQ.IR) GO TO 205
      TEMP16=0.5*(HT(I,J)+HT(1,JJ)+EP(I,J)+EP(III,J))
      IF(QXP(I,J).EQ.0.0) GO TO 362
      TEMP19=0.25*(QY(1,J)+QY(III,J)+QY(I,JJ)+QY(III,JJ))
      TEMP30=SQRT(QXP(I,J)**2+TEMP19**2)
      TEMP31=0.5*(C(I,J)+C(III,J))
      TEMP32=SQRT(AG)/(TEMP30*TEMP31)
      DXX(I,J)=TEMP16*((GAMMA*QXP(I,J)**2+DELTA*TEMP19**2)*TEMP32)
      DXY(I,J)=TEMP16*(GAMMA-DELTA)*QXP(I,J)*TEMP19*TEMP32
      IF(QY(I,J).EQ.0.0.OR.QY(III,J).EQ.0.0) DXY(I,J)=0.0
      IF(QY(I,JJ).EQ.0.0.OR.QY(III,JJ).EQ.0.0) DXY(I,J)=0.0
      IF(H(III,JJJ).EQ.3.0) DXY(I,J)=0.0
362   R(I)=E2*QXP(I,J)-E5*DXX(I,J)
205   Q(I)=(EP(I,J)+0.25*(HT(I,J)+HT(II,J)+HT(I,JJ)+HT(II,JJ)))+E2*
     1(QXP(I,J)-QXP(II,J))+E5*(DXX(I,J)+DXX(II,J))
      S(I)=SM(I,J)*(E(I,J)+0.25*(HT(I,J)+HT(II,J)+HT(I,JJ)+HT(II,JJ))
     1)-E2*(QY(I,J)*(SM(I,J)+SM(I,JJJ))-QY(I,JJ)*(SM(I,J)+SM(I,JJ)))
     2+E5*((SM(I,JJJ)-SM(I,J))*DYY(I,J)-(SM(I,J)-SM(I,JJ))*DYY(I,JJ))
     3+0.25*E5*((SM(1,JJJ)+SM(III,JJJ)-SM(I,JJ)-SM(III,JJ))*DXY(I,J)
     4-(SM(I,JJJ)+SM(II,JJJ)-SM(I,JJ)-SM(II,JJ))*DXY(II,J)+(SM(III,J)
     5+SM(III,JJJ)-SM(II,J)-SM(II,JJJ))*DYX(I,J)-(SM(III,J)+SM(III,JJ)
     6-SM(II,J)-SM(II,JJ))*DYX(I,JJ))
      A(I)=R(I)/(Q(I)+P(I)*A(II))
      B(I)=(S(I)+P(I)*B(II))/(Q(I)+P(I)*A(II))
202   CONTINUE
      DO 206 N=1LLL,IRRR
      I=ILLL+IRRR-N
      II=I-1
      SP(II,J)=-A(II)*SP(I,J)+B(II)
206   CONTINUE
      NUM=NUM+1
      GO TO 208
290   CONTINUE
      DO 300 I=1,IMAX
      II=I-1
      III=I+1
      IF(I.EQ.1) II=1
      IF(I.EQ.IMAX) III=IMAX
      DO 300 J=1,JMAX
      IF(C(I,J).EQ.0.0) GO TO 92
      JJ=J-1
      JJJ=J+1
      IF(J.EQ.1) JJ=1
      IF(J.EQ.JMAX) JJJ=JMAX
      CSX(I,J)=0.5*(HT(I,J)+HT(I,JJ)+EP(I,J)+EP(III,J))
      UM(I,J)=QXP(I,J)/CSX(I,J)
      CSY(I,J)=0.5*(HT(I,J)+HT(II,J)+EP(I,J)+EP(I,JJJ))
92    CONTINUE
```

```
      QX(I,J)=QXP(I,J)
      EM(I,J)=LP(I,J)
      SM(I,J)=SP(I,J)
300   CONTINUE
C
C          PRINT INSTRUCTIONS
C
500   IF(ISTEP-2) 297,296,297
296   CONTINUE
      IF(TIMES.LT.CTIMES) GO TO 46
      IF(CTIMES.EQ.0.0) GO TO 1445
      DO 44 I=1,IMAX
      II=I-1
      IF(I.EQ.1) II=1
      DO 44 J=1,JMAX
      IF(C(I,J).EQ.0.0) GO TO 44
      JJ=J-1
      IF(J.EQ.1) JJ=1
      DEP=E(I,J)+0.25*(HT(I,J)+HT(I,JJ)+HT(II,J)+HT(II,JJ))
      REN=2.0*DEP*SQRT((UM(I,J)+UM(II,J))**2+(VM(I,J)+VM(I,JJ))**2)/VIS
      FRN=8.0*AG/(C(I,J)**2)
47    FRNOLD=FRN
      XOLD=1.0/SQRT(FRNOLD)
      FXOLD=XOLD+2.0*ALOG10(RKS/(12.0*DEP)+2.5*XOLD/REN)
      FDXOLD=1.0+5.0/((RKS/(12.0*DEP)+2.5*XOLD/REN)*REN*ALOG(10.0))
      XNEW=XOLD-FXOLD/FDXOLD
      FRN=1.0/(XNEW**2)
      IF(ABS(FRN-FRNOLD).GT.1.0E-3) GO TO 47
      C(I,J)=SQRT(8.0*AG/FRN)
44    CONTINUE
1445  CTIMES=CTIMES+TCHEZS
46    CONTINUE
      IF(NST.NE.NPRINT(IP)) GO TO 297
      IP=IP+1
      NSUM=0
      SPTOT=0.0
      VOLTOT=0.0
      DO 168 I=II,18
      II=I-1
      DO 168 J=18,25
      JJ=J-1
      DEP=E(I,J)+0.25*(HT(I,J)+HT(I,JJ)+HT(II,J)+HT(II,JJ))
      VOL=DEP*AX*AX
      SPTOT=SPTOT+SM(I,J)*VOL
      VOLTOT=VOLTOT+VOL
      NSUM=NSUM+1
168   CONTINUE
      SPMEAN=SPTOT/VOLTOT
      VLMEAN=VOLTOT/FLOAT(NSUM)
      NUM=0
      SVAR=0.0
      DO 169 I=11,18
      II=I-1
      DO 169 J=18,25
      JJ=J-1
      DEP=E(I,J)+0.25*(HT(I,J)+HT(I,JJ)+HT(II,J)+HT(II,JJ))
      VOL=DEP*AX*AX
      SVAR=SVAR+(SM(I,J)*VOL-SPMEAN*VLMEAN)**2
      NUM=NUM+1
169   CONTINUE
      SVAR=SVAR/FLOAT(NUM)
      SDEV=SQRT(SVAR)
      SPDEV=SDEV/VLMEAN
      WRITE(6,107) SPMEAN,SPDEV
107   FORMAT(1X,2F7.4)
1674  WRITE(6,5020) (TITL(J),J=1,18),NST,TIMES
5020  FORMAT(1H1/18A4//10X,42HWATER ELEVATIONS IN  10TH MMS  AT TIMESTEP
     1,I5,20X,17HTIME IN SECONDS =,F7.1/)
      WRITE(6,20) (ICOL(J),J=1,29)
20    FORMAT(/3X,29A4/2X,1HJ)
      DO 6000 J=1,JMAX
      DO 6006 I=1,IMAX
6006  KONVRT(I)=NINTEG(E(I,J)*10000.0)
6000  WRITE(6,6001) J,(KONVRT(I),I=1,IMAX)
6001  FORMAT(/1X,I2,30I4)
      WRITE(6,5026) (TITL(J),J=1,18),NST,TIMES
5026  FORMAT(1H1/18A4//10X,45HU VELOCITIES IN  MILLIMETRES/SEC  AT TIMES
     1TEP,I5,20X,17HTIME IN SECONDS =,F7.1/)
      WRITE(6,20) (ICOL(J),J=1,29)
      DO 6004 J=1,JMAX
      DO 6008 I=1,IMAX
      KONVRT(1)=0
      KONVRT(I)=NINTEG(UM(I,J)*1000.0)
6008  CONTINUE
6004  WRITE(6,6001) J,(KONVRT(I),I=1,IMAX)
```

```
      WRITE(6,5021) (TITL(J),J=1,18),NST,TIMES
5021  FORMAT(1H1/18A4//10X,45HV VELOCITIES IN  MILLIMETRES/SEC  AT TIMES
     1TEP,I5,20X,17HTIME IN SECONDS =,F7.1/)
      WRITE(6,20) (ICOL(J),J=1,29)
      DO 6003 J=1,JMAX
      DO 6007 I=1,IMAX
      KONVRT(I)=0
      KONVRT(I)=NINTEG(VM(I,J)*1000.0)
6007  CONTINUE
6003  WRITE(6,6001) J,(KONVRT(I),I=1,IMAX)
      WRITE(6,6015) (TITL(J),J=1,18),NST,TIMES
6015  FORMAT(1H1/18A4//10X,47HCONCENTRATIONS IN PARTS PER MILLION AT
     1 TIMESTEP,I5,10X,17HTIME IN SECONDS -,F7.1/)
      WRITE(6,20) (ICOL(J),J=1,29)
      DO 6016 J=1,JMAX
      DO 6017 I=1,IMAX
      KONVRT(I)=0
      KONVRT(I)=NINTEG(SM(I,J))
6017  CONTINUE
6016  WRITE(6,6001) J,(KONVRT(I),I=1,IMAX)
297   IF(ISTEP.EQ.2) GO TO 88
      ISTEP=2
      N=2*NST
C
C         SET OPEN BOUNDS
C
      NITER=1
      GO TO 89
C
C          COMPUTE QYP AND EP ON COLUMN I (SECOND HALF TIMESTEP)
C
199   NUM=1
      V1=0.5*(VM(II,17)+VM(I2,17))
      CONST=(V1**2)/(2.0*SQRT(2.0*PI*kR))
15    IF(NUM.EQ.IIND) GO TO 110
      ISRCH=IBD(NUM)/1000000
      I=IBD(NUM)/10000-ISRCH*100
      JBOT=IBD(NUM)/100-ISRCH*10000-I*100
      JTOP=IBD(NUM)-ISRCH*1000000-I*10000-JBOT*100
      JB=JBOT
      JBB=JB-1
      JBBB=JB+1
      JT=JTOP
      JTT=JT-1
      JTTT=JT+1
      II=I-1
      III=I+1
      R(JBB)=0.0
      S(JBB)=QYP(I,JBB)
      IF(ISRCH.NE.1.AND.ISRCH.NE.3) GO TO 268
      TEMP1=VM(I,JBB)*CSY(I,JBB)
      TEMP2=0.25*(QX(I,JBB)+QX(I,JB)+QX(II,JBB)+QX(II,JB))
      TEMP3=SQRT(TEMP2**2+TEMP1**2)
      TEMP4=0.5*(C(I,JB)+C(I,JBB))
      EDDY=BETA*SQRT(AG)*TEMP3/TEMP4
      TEMP12=1.0+(C3*TEMP3)/(CSY(I,JBB)**2*TEMP4**2)
      TEMP40=VM(III,JBB)
      TEMP41=VM(II,JBB)
      IF(C(III,JBB).GT.0.0) GO TO 53
      TEMP40=-VM(I,JBB)
53    IF(C(II,JBB).GT.0.0) GO TO 54
      TEMP41=-VM(I,JBB)
54    CONTINUE
      B(JBB)=QY(I,JBB)-C2*CSY(I,JBB)*(E(1,JB)-E(I,JBB))
     1-(C3*QY(1,JBB)*TEMP3)/(CSY(I,JBB)**2*TEMP4**2)+C4*TEMP2
     2+C5*EDDY*(TEMP40-2.0*VM(I,JBB)+TEMP41)*CSY(I,JBB)
      S(JBB)=(B(JBB)+C2*CSY(I,JBB)*EP(I,JBB))/TEMP12
      R(JBB)=(C2*CSY(I,JBB))/(TEMP12)
268   DO 200 J=JB,JT
      JJ=J-1
      JJJ=J+1
      A(J)=EM(I,J)-C1*(QX(I,J)-QX(II,J))
      P(J)=C1/(1.0+C1*R(JJ))
      Q(J)=(A(J)+C1*S(JJ))/(1.0+C1*R(JJ))
      IF(J.EQ.JT) GO TO 200
      TEMP1=VM(I,J)*CSY(I,J)
      TEMP2=0.25*(QX(I,J)+QX(I,JJJ)+QX(II,J)+QX(II,JJJ))
      TEMP3=SQRT(TEMP2**2+TEMP1**2)
      TEMP4=0.5*(C(I,JJJ)+C(I,J))
      TEMP11=C2*CSY(I,J)
      EDDY=BETA*SQRT(AG)*TEMP3/TEMP4
      TEMP12=1.0+(C3*TEMP3)/(CSY(I,J)**2*TEMP4**2)
      TEMP13=TEMP11*P(J)+TEMP12
      DY1=VM(I,JJJ)*CSY(I,JJJ)
      DY2=VM(I,J)*CSY(I,J)
```

```
      DY3=VM(I,JJ)*CSY(I,JJ)
      TEMP17=VM(III,J)
      TEMP18=VM(II,J)
      IF((QX(II,J)+QX(II,JJJ)).LT.0.0) TEMP18=VM(I,J)
      IF((QX(I,J)+QX(I,JJJ)).GT.0.0) TEMP17=VM(I,J)
      TEMP40=VM(III,J)
      TEMP41=VM(II,J)
      IF(VM(III,J).EQ.0.0) GO TO 48
      IF(H(III,J).NE.3.0.AND.H(III,JJJ).NE.3.0) GO TO 57
48    TEMP40=-VM(I,J)
      TEMP17=0.0
57    IF(VM(II,J).EQ.0.0) GO TO 147
      IF(H(I,J).NE.3.0.AND.H(I,JJJ).NE.3.0) GO TO 58
147   TEMP41=-VM(I,J)
      TEMP18=0.0
58    CONTINUE
      TEMP14=0.25*((DY1+DY2)*(VM(I,JJJ)+VM(I,J))-(DY2+DY3)*
     1(VM(I,J)+VM(I,JJ)))
      TEMP15=0.5*((QX(I,JJJ)+QX(I,J))*TEMP17-(QX(II,JJJ)+QX(II,J))*
     1TEMP18)
      D2=1.0
      IF(D2.EQ.0.0) GO TO 356
      IF(V1.LT.0.0) GO TO 351
      IF(J.LE.JS.OR.J.GT.22) GO TO 355
      IF(I.LT.11.OR.I.GT.23) GO TO 355
      XS=FLOAT(J-JS)*AX
      YS=FLOAT(IS-I)*AX
      TEMP50=CONST
      GO TO 354
351   IF(J.GE.JS) GO TO 355
      XS=FLOAT(JS-J)*AX
      YS=FLOAT(IS-1)*AX
      TEMP50=-CONST
354   TEMP51=HT(I,J)+0.25*(EM(I,J)+EM(I,JJJ)+EM(III,J)+EM(III,JJJ))
      TAW(I,J)=TEMP50*EXP(-0.5*RR*((YS/XS)**2))*TEMP51
      GO TO 356
355   D2=0.0
356   B(J)=QY(I,J)-C2*CSY(I,J)*(E(I,JJJ)-E(I,J))
     1-(C3*QY(I,J)*TEMP3)/(CSY(I,J)**2*TEMP4**2)+C4*TEMP2
     2-2.0*C1*ALPHA*TEMP14-2.0*C1*ALPHA*TEMP15
     3+C5*EDDY*(TEMP40-2.0*VM(I,J)+TEMP41)*CSY(I,J)
     4+2.0*C1*D2*(TAW(I,J)-TAW(II,J))
      R(J)=TEMP11/TEMP13
      S(J)=(B(J)+TEMP11*Q(J))/TEMP13
200   CONTINUE
      QYP(I,JT)=0.0
      DO 333 N=JBBB,JT
      J=JT+JBBB-N
      JJ=J-1
      EP(I,J)=-P(J)*QYP(I,J)+Q(J)
      QYP(I,JJ)=-R(JJ)*EP(I,J)+S(JJ)
333   CONTINUE
      EP(I,JB)=-P(JB)*QYP(I,JB)+Q(JB)
      IF(ISRCH.NE.1.AND.ISRCH.NE.3) GO TO 229
      QYP(I,JBB)=-R(JBB)*EP(I,JB)+S(JBB)
229   NUM=NUM+1
      GO TO 15
110   CONTINUE
      NITER=NITER+1
      IF(NITER.GT.2) GO TO 813
      DO 852 I=1,IMAX
      DO 852 J=1,JMAX
      IF(CSY(I,J).EQ.0.0) GO TO 852
      VM(I,J)=0.5*(QYP(I,J)+QY(I,J))/CSY(I,J)
852   CONTINUE
      GO TO 199
813   CONTINUE
C
C          COMPUTE SP ON COLUMN I (SECOND HALF TIMESTEP)
C
      NUM=1
      GO TO 99
308   IF(NUM.EQ.IIND) GO TO 390
      ISRCH=IBD(NUM)/1000000
      I=IBD(NUM)/10000-ISRCH*100
      JB=IBD(NUM)/100-ISRCH*10000-I*100
      JT=IBD(NUM)-ISRCH*1000000-I*10000-JB*100
      JBB=JB-1
      JBBB=JB+1
      JTT=JT-1
      JTTT=JT+1
      II=I-1
      III=I+1
      A(JBB)=0.0
      B(JBB)=SP(I,JBB)
```

```
      P(JB)=0.0
      DYY(I,JBB)=0.0
      DYX(I,JBB)=0.0
      IF(ISRCH.NE.1.AND.ISRCH.NE.3) GO TO 301
      TEMP16=0.5*(HT(I,JBB)+HT(II,JBB)+EP(I,JBB)+EP(I,JB))
      IF(QYP(I,JBB).EQ.0.0) GO TO 363
      TEMP19=0.25*(QX(I,JBB)+QX(I,JB)+QX(II,JBB)+QX(II,JB))
      TEMP30=SQRT(QYP(I,JBB)**2+TEMP19**2)
      TEMP31=0.5*(C(I,JBB)+C(I,JB))
      TEMP32=SQRT(AG)/(TEMP30*TEMP31)
      DYY(I,JBB)=TEMP16*((GAMMA*QYP(I,JBB)**2+DELTA*TEMP19**2)*TEMP32)
      DYX(I,JBB)=TEMP16*(GAMMA-DELTA)*QYP(I,JBB)*TEMP19*TEMP32
      IF(QX(I,JB).EQ.0.0) DYX(I,JBB)=0.0
      IF(QX(II,JB).EQ.0.0) DYX(I,JBB)=0.0
363   P(JB)=E2*QYP(I,JBB)+E5*DYY(I,JBB)
301   R(JT)=0.0
      DYY(I,JT)=0.0
      DYX(I,JT)=0.0
      IF(ISRCH.NE.2.AND.ISRCH.NE.3) GO TO 303
      TEMP16=0.5*(HT(I,JT)+HT(II,JT)+EP(I,JT)+EP(I,JTTT))
      IF(QYP(I,JT).EQ.0.0) GO TO 364
      TEMP19=0.25*(QX(I,JT)+QX(I,JTTT)+QX(II,JT)+QX(II,JTTT))
      TEMP30=SQRT(QYP(I,JT)**2+TEMP19**2)
      TEMP31=0.5*(C(I,JT)+C(I,JTTT))
      TEMP32=SQRT(AG)/(TEMP30*TEMP31)
      DYY(I,JT)=TEMP16*((GAMMA*QYP(I,JT)**2+DELTA*TEMP19**2)*TEMP32)
      DYX(I,JT)=TEMP16*(GAMMA-DELTA)*QYP(I,JT)*TEMP19*TEMP32
      IF(QX(I,JT).EQ.0.0) DYX(I,JT)=0.0
      IF(QX(II,JT).EQ.0.0) DYX(I,JT)=0.0
364   R(JT)=E2*QYP(I,JT)-E5*DYY(I,JT)
303   DO 302 J=JB,JT
      JJ=J-1
      JJJ=J+1
      A(J)=0.0
      B(J)=0.0
      IF(J.EQ.JB) GO TO 304
      P(J)=E2*QYP(I,JJ)+E5*DYY(I,JJ)
304   DYY(I,J)=0.0
      DYX(I,J)=0.0
      IF(J.EQ.JT) GO TO 305
      TEMP16=0.5*(HT(I,J)+HT(II,J)+EP(I,J)+EP(I,JJJ))
      IF(QYP(I,J).EQ.0.0) GO TO 365
      TEMP19=0.25*(QX(I,J)+QX(I,JJJ)+QX(II,J)+QX(II,JJJ))
      TEMP30=SQRT(QYP(I,J)**2+TEMP19**2)
      TEMP31=0.5*(C(I,J)+C(I,JJJ))
      TEMP32=SQRT(AG)/(TEMP30*TEMP31)
      DYY(I,J)=TEMP16*((GAMMA*QYP(I,J)**2+DELTA*TEMP19**2)*TEMP32)
      DYX(I,J)=TEMP16*(GAMMA-DELTA)*QYP(I,J)*TEMP19*TEMP32
      IF(QX(I,J).EQ.0.0.OR.QX(I,JJJ).EQ.0.0) DYX(I,J)=0.0
      IF(QX(II,J).EQ.0.0.OR.QX(II,JJJ).EQ.0.0) DYX(I,J)=0.0
      IF(H(III,JJJ).EQ.2.0) DYX(I,J)=0.0
365   R(J)=E2*QYP(I,J)-E5*DYY(I,J)
305   Q(J)=(EP(I,J)+0.25*(HT(I,J)+HT(II,J)+HT(I,JJ)+HT(II,JJ)))+E2*
     1(QYP(I,J)-QYP(I,JJ))+E5*(DYY(I,J)+DYY(I,JJ))
      S(J)=SM(I,J)*(EM(I,J)+0.25*(HT(I,J)+HT(II,J)+HT(I,JJ)+HT(II,JJ))
     1)-E2*(QX(I,J)*(SM(I,J)+SM(III,J))-QX(II,J)*(SM(I,J)+SM(II,J)))
     2+E5*((SM(III,J)-SM(I,J))*DXX(I,J)-(SM(I,J)-SM(II,J))*DXX(II,J))
     3+0.25*E5*((SM(I,JJJ)+SM(III,JJJ)-SM(I,JJ)-SM(III,JJ))*DXY(I,J)
     4-(SM(I,JJJ)+SM(II,JJJ)-SM(I,JJ)-SM(II,JJ))*DXY(II,J)+(SM(III,J)
     5+SM(III,JJJ)-SM(II,J)-SM(II,JJJ))*DYX(I,J)-(SM(III,J)+SM(III,JJ)
     6-SM(II,J)-SM(II,JJ))*DYX(I,JJ))
      A(J)=R(J)/(Q(J)+P(J)*A(JJ))
      B(J)=(S(J)+P(J)*B(JJ))/(Q(J)+P(J)*A(JJ))
302   CONTINUE
      DO 306 N=JBBB,JTTT
      J=JBBB+JTTT-N
      JJ=J-1
      SP(I,JJ)=-A(JJ)*SP(I,J)+B(JJ)
306   CONTINUE
      NUM=NUM+1
      GO TO 308
390   CONTINUE
      DO 116 I=1,IMAX
      II=I-1
      III=I+1
      IF(I.EQ.1) II=1
      IF(I.EQ.IMAX) III=IMAX
      DO 116 J=1,JMAX
      IF(C(I,J).EQ.0.0) GO TO 658
      JJ=J-1
      JJJ=J+1
      IF(J.EQ.1) JJ=1
      IF(J.EQ.JMAX) JJJ=JMAX
      CSX(I,J)=0.5*(HT(I,J)+HT(I,JJ)+EP(I,J)+EP(III,J))
      CSY(I,J)=0.5*(HT(I,J)+HT(II,J)+EP(I,J)+EP(I,JJJ))
```

```
      VM(I,J)=QYP(I,J)/CSY(I,J)
  658 CONTINUE
      QY(I,J)=QYP(I,J)
      E(I,J)=EP(I,J)
      SM(I,J)=SP(I,J)
  116 CONTINUE
      GO TO 500
C
C          THE FINE GRID
C
  453 IF(NST.GT.1) GO TO 388
      MMAX=35
      NMAX=38
      DT=AT/3.0
      DX=AX/3.0
      TNCHEZ=TCHEZS
      ICARD=NINTEG(TIS/DT)
      MOBD(1)=0102200
      MOBD(2)=3502131
      NOBD(1)=0102340
      NOBD(2)=2102101
      MINDO=3
      NINDO=3
      ISECT=90
      IMAXST=2*2256
      IPRINC=564
      MC=16
      NC=13
      MP=1
      LI=1
      GO TO 287
C
C          SET OPEN BOUNDS
C
  289 CONTINUE
      TNOW=FLOAT(K)
      HTIMES=TNOW*DT
      IF(NSTEP.EQ.2) GO TO 376
      M=1
      I=7
      DO 1702 N=2,20
      J=IFIX(FLOAT(N+1)/3.0+0.5)+13
      KD=N-3*(J-14)
      VNUM=FLOAT(KD)
      IF(KD.EQ.3) GO TO 578
      QP3=QX(I,J-1)+VNUM*(QX(I,J)-QX(I,J-1))/3.0
     1-(UM(I,J)*((4.0-VNUM)*(HT(I,J)-HT(I,J-1))
     2+(2.0-VNUM)*(HT(I,J-1)-HT(I,J-2)))-UM(I,J-1)*
     3((VNUM-1.0)*(HT(I,J)-HT(I,J-1))+(VNUM+1.0)*
     4(HT(I,J-1)-HT(I,J-2))))/18.0
      GO TO 579
  578 QP3=QX(I,J)
  579 IF(MST.EQ.(3*NST-2)) CINQ(M,N)=(QP3-QNX(M,N))/2.0
      QNXP(M,N)=QNX(M,N)+CINQ(M,N)
 1702 CONTINUE
      M=MMAX-1
      I=IFIX(FLOAT(M-1)/3.0+0.5)+7
      DO 1700 N=2,12
      J=IFIX(FLOAT(N+1)/3.0+0.5)+13
      KD=N-3*(J-14)
      VNUM=FLOAT(KD)
      IF(KD.EQ.3) GO TO 573
      QP3=QX(I,J-1)+VNUM*(QX(I,J)-QX(I,J-1))/3.0
     1-(UM(I,J)*((4.0-VNUM)*(HT(I,J)-HT(I,J-1))
     2+(2.0-VNUM)*(HT(I,J-1)-HT(I,J-2)))-UM(I,J-1)*
     3((VNUM-1.0)*(HT(I,J)-HT(I,J-1))+(VNUM+1.0)*
     4(HT(I,J-1)-HT(I,J-2))))/18.0
      GO TO 574
  573 QP3=QX(I,J)
  574 IF(MST.EQ.(3*NST-2)) CINQ(M,N)=(QP3-QNX(M,N))/2.0
      QNXP(M,N)=QNX(M,N)+CINQ(M,N)
 1700 CONTINUE
      N=13
      QNXP(M,N)=2.0*QNXP(M,N-1)-QNXP(M,N-2)
      N=21
      J=IFIX(FLOAT(N)/3.0+0.5)+13
      DO 1704 M=1,10
      I=IFIX(FLOAT(M)/3.0+0.5)+7
      VNUM=FLOAT(M-1-3*(I-8))
      QP3=QX(I-1,J)+VNUM*(QX(I,J)-QX(I-1,J))/3.0
      IF(MST.EQ.(3*NST-2)) CINQ(M,N)=(QP3-QNX(M,N))/2.0
      QNXP(M,N)=QNX(M,N)+CINQ(M,N)
 1704 CONTINUE
      N=1
      J=14
```

```
      DO 1705 M=1,MMAX
      I=IFIX(FLOAT(M)/3.0+0.5)+7
      VNUM=FLOAT(M-1-3*(I-8))
      UM1I=2.0*(HT(I-1,J)-HT(I-1,J-1))*(UM(I-1,J)-UM(I-1,J-1))/3.0
      UM1=2.0*(HT(I,J)-HT(I,J-1))*(UM(I,J)-UM(I,J-1))/3.0
      QP3=(2.0*QX(I-1,J-1)+QX(I-1,J)-UM1I)/3.0+VNUM*((2.0*QX(I,J-1)+
     1QX(I,J)-UM1)-(2.0*QX(I-1,J-1)+QX(I-1,J)-UM1I))/9.0
      IF(MST.EQ.(3*NST-2)) CINQ(M,N)=(QP3-QNX(M,N))/2.0
      QNXP(M,N)=QNX(M,N)+CINQ(M,N)
1705  CONTINUE
      GO TO 396
376   N=1
      J=13
      DO 1703 M=2,MMAX-1
      I=IFIX(FLOAT(M+1)/3.0+0.5)+7
      VNUM=FLOAT(M-3*(I-8))
      QP3=QY(I-1,J)+VNUM*(QY(I,J)-QY(I-1,J))/3.0
      QNYP(M,N)=QNY(M,N)+(QP3-QNY(M,N))/FLOAT(3*NST+1-MST)
1703  CONTINUE
      N=21
      J=IFIX(FLOAT(N-1)/3.0+0.5)+13
      DO 1701 M=1,9
      I=IFIX(FLOAT(M+1)/3.0+0.5)+7
      VNUM=FLOAT(M-3*(I-8))
      EP3=E(I-1,J)+VNUM*(E(I,J)-E(I-1,J))/3.0
      ENP(M,N)=EN(M,N)+(EP3-EN(M,N))/FLOAT(3*NST+1-MST)
1701  CONTINUE
      M=10
      ENP(M,N)=ENP(M-1,N)-0.5*FC*(QNYP(M-1,N-1)+QNYP(M,N-1))/
     1(AG*CNX(M-1,N))
      M=MMAX
      I=IFIX(FLOAT(M+1)/3.0+0.5)+7
      DO 1706 N=1,12
      J=IFIX(FLOAT(N)/3.0+0.5)+13
      VNUM=FLOAT(N-I-3*(J-14))
      QYJJ=(QY(I-1,J-1)+2.0*QY(I,J-1))/3.0
      QYJ=(QY(I-1,J)+2.0*QY(I,J))/3.0
      VMJJ=(VM(I-1,J-1)+2.0*VM(I,J-1))/3.0
      VMJ=(VM(I-1,J)+2.0*VM(I,J))/3.0
      QP3=QYJJ+VNUM*(QYJ-QYJJ)/3.0
     1-2.0*(VMJ-VMJJ)*(HT(I,J)-HT(I,J-1))/9.0
      QNYP(M,N)=QNY(M,N)+(QP3-QNY(M,N))/FLOAT(3*NST+1-MST)
1706  CONTINUE
      M=1
      I=8
      DO 1707 N=1,21
      J=IFIX(FLOAT(N)/3.0+0.5)+13
      VNUM=FLOAT(N-1-3*(J-14))
      QYJJ=(2.0*QY(I-1,J-1)+QY(I,J-1))/3.0
      QYJ=(2.0*QY(I-1,J)+QY(I,J))/3.0
      VMJJ=(2.0*VM(I-1,J-1)+VM(I,J-1))/3.0
      VMJ=(2.0*VM(I-1,J)+VM(I,J))/3.0
      QP3=QYJJ+VNUM*(QYJ-QYJJ)/3.0
     1-2.0*(HT(I-1,J)-HT(I-1,J-1))*(VMJ-VMJJ)/9.0
      QNYP(M,N)=QNY(M,N)+(QP3-QNY(M,N))/FLOAT(3*NST+1-MST)
1707  CONTINUE
      GO TO 699
C
C           SET OPEN BOUNDS FOR POLLUTANT CONCENTRATIONS
C
799   CONTINUE
      N=1
      I=8
      DO 781 N=1,21
      J=IFIX(FLOAT(N+1)/3.0+0.5)+13
      VNUM=FLOAT(N-3*(J-14))
      SP3=(2.0*SN(I-1,J-1)+SN(I,J-1))/3.0+VNUM*((2.0*SN(I-1,J)+SN(I,J))
     1-(2.0*SN(I-1,J-1)+SN(I,J-1)))/9.0
      SNP(M,N)=SNM(M,N)+(SP3-SNM(M,N))/FLOAT(6*NST+1-KHF)
781   CONTINUE
      M=MMAX
      I=IFIX(FLOAT(M)/3.0+0.5)+7
      DO 782 N=1,12
      J=IFIX(FLOAT(N+1)/3.0+0.5)+13
      VNUM=FLOAT(N-3*(J-14))
      SP3=(SN(I-1,J-1)+2.0*SN(I,J-1))/3.0+VNUM*((SN(I-1,J)+2.0*SN(I,J))
     1-(SN(I-1,J-1)+2.0*SN(I,J-1)))/9.0
      SNP(M,N)=SNM(M,N)+(SP3-SNM(M,N))/FLOAT(6*NST+1-KHF)
782   CONTINUE
      N=13
      SNP(M,N)=2.0*SNP(M,N-1)-SNP(N,N-2)
      N=1
      J=14
      DO 783 M=2,MMAX-1
      I=IFIX(FLOAT(M+1)/3.0+0.5)+7
```

```
      VNUM=FLOAT(N-3*(I-8))
      SP3=(2.0*SM(I-1,J-1)+SM(I-1,J))/3.0+VNUM*((2.0*SM(I,J-1)+SM(I,J))
     1-(2.0*SM(I-1,J-1)+SM(I-1,J)))/9.0
      SNP(M,N)=SNM(M,N)+(SP3-SNM(M,N))/FLOAT(6*NST+1-KHF)
  783 CONTINUE
      N=21
      J=IFIX(FLOAT(N)/3.0+0.5)+13
      DO 784 M=2,9
      I=IFIX(FLOAT(M+1)/3.0+0.5)+7
      VNUM=FLOAT(N-3*(I-8))
      SP3=SM(I-1,J)+VNUM*(SM(I,J)-SM(I-1,J))/3.0
      SNP(M,N)=SNM(M,N)+(SP3-SNM(M,N))/FLOAT(6*NST+1-KHF)
  784 CONTINUE
      M=10
      SNP(M,N)=2.0*SNP(M-1,N)-SNP(M-2,N)
      IF(NSTEP.EQ.1) GO TO 408
      GO TO 508
  287 CONTINUE
      MST=0
      F1=DT/DX
      F2=(AG*DT)/DX
      F3=AG*DT
      F4=2.0*DT*FC
      F5=2.0*DT/(DX**2)
      G2=0.5*DT/DX
      G5=DT/(DX**2)
      DO 440 M=1,MMAX
      DO 440 N=1,NMAX
      QNX(M,N)=0.0
      UNM(M,N)=0.0
      QNXP(M,N)=0.0
      QNY(M,N)=0.0
      VNM(M,N)=0.0
      QNYP(M,N)=0.0
      EN(M,N)=0.0
      ENM(M,N)=0.0
      ENP(M,N)=0.0
      CN(M,N)=0.0
      HNT(M,N)=0.0
      HN(M,N)=0.0
      CNX(M,N)=0.0
      CNY(M,N)=0.0
      TNW(M,N)=0.0
      CINQ(M,N)=0.0
      SNM(M,N)=0.0
      SNP(M,N)=0.0
      DNXX(M,N)=0.0
      DNYY(M,N)=0.0
      DNXY(M,N)=0.0
      DNYX(M,N)=0.0
  440 CONTINUE
C
C          READ IN LOCATIONS OF WATER LEVEL COMPUTATIONS
C
      CALL DIVE2(MMAX,NMAX)
C
C          SET THE MBD(N) AND NBD(N) VALUES
C
      CALL FIND2(MIND,NIND,MMAX,NMAX,MINDO,NINDO,ISECT)
C
C          READ IN WATER DEPTHS
C
      CALL DEPTH2(MMAX,NMAX)
      NSUM=0
      DO 225 N=1,20
      NSUM=NSUM+IPRINC
      IPRINT(N)=NSUM
  225 CONTINUE
      NUM=1
   27 IF(NUM.EQ.MINDO) GO TO 23
      MSRCH=MBD(NUM)/1000000
      M=MBD(NUM)/10000-MSRCH*100
      NBOT=MBD(NUM)/100-MSRCH*10000-M*100
      NTOP=MBD(NUM)-MSRCH*1000000-M*10000-NBOT*100
      MM=M-1
      DO 22 N=NBOT,NTOP
      NN=N-1
      EN(M,N)=EINT
      ENM(M,N)=EINT
      ENP(M,N)=EINT
      DEP=EN(M,N)+0.25*(HNT(M,N)+HNT(M,NN)+HNT(MM,N)+HNT(MM,NN))
      FRN=1.0/(-2.0*ALOG10(RKS/(12.0*DEP)))**2
      CN(M,N)=SQRT(8.0*AG/FRN)
      CNX(M,N)=0.5*(HNT(M,N)+HNT(M,NN))+EINT
      CNY(M,N)=0.5*(HNT(M,N)+HNT(MM,N))+EINT
```

```
 22    CONTINUE
       IF(N.LT.11) GO TO 621
       DO 622 N=14,NMAX-1
       SNM(M,N)=SINV
       SNP(M,N)=SINV
 622   CONTINUE
 621   NUM=NUM+1
       GO TO 27
 23    CONTINUE
       NA=1
 331   IF(NA.EQ.NINDO) GO TO 332
       N=NOBD(NA)/100000
       NLEF=NOBD(NA)/1000-N*100
       NRIG=NOBD(NA)/10-N*10000-NLEF*100
       ML=NLEF-1
       MR=NRIG+1
       NN=N-1
       IF(N.EQ.1) NN=1
       IF(HN(MR,N).EQ.3.0) MR=NRIG
       DO 533 M=ML,MR
       MM=M-1
       IF(M.EQ.1) MM=1
       EN(M,N)=EINT
       ENM(M,N)=EINT
       ENP(M,N)=EINT
       DEP=EN(M,N)+0.5*(HNT(M,N)+HNT(MM,N))
       FRN=1.0/(-2.0*ALOG10(RKS/(12.0*DEP)))**2
       CN(M,N)=SQRT(8.0*AG/FRN)
       CNX(M,N)=0.5*(HNT(M,N)+HNT(M,NN))+EINT
       IF(N.EQ.1) CNX(M,N)=0.27+EINT
       CNY(M,N)=0.5*(HNT(M,N)+HNT(MM,N))+EINT
 533   CONTINUE
       NA=NA+1
       GO TO 331
 332   CONTINUE
       NA=1
 341   IF(NA.EQ.MINDO) GO TO 342
       M=MOBD(NA)/100000
       NBOT=MOBD(NA)/1000-M*100
       NTOP=MOBD(NA)/10-M*10000-NBOT*100
       MM=M-1
       IF(M.EQ.1) MM=1
       DO 343 N=NBOT,NTOP
       NN=N-1
       EN(M,N)=EINT
       ENM(M,N)=EINT
       ENP(M,N)=EINT
       DEP=EN(M,N)+0.5*(HNT(M,N)+HNT(M,NN))
       FRN=1.0/(-2.0*ALOG10(RKS/(12.0*DEP)))**2
       CN(M,N)=SQRT(8.0*AG/FRN)
       CNX(M,N)=0.5*(HNT(M,N)+HNT(M,NN))+EINT
       CNY(M,N)=0.5*(HNT(M,N)+HNT(MM,N))+EINT
 343   CONTINUE
       NA=NA+1
       GO TO 341
 342   CONTINUE
C
C          SET UP PRINT INSTRUCTIONS
C
       NSTEP=2
       HTIMES=0.0
       CHTIMES=0.0
       GO TO 550
C
C          COMPUTE QNXP AND ENP ON ROW J (FIRST HALF TIMESTEP)
C
 288   IF(MST.EQ.(3*NST)) GO TO 500
 388   NSTEP=1
       MST=MST+1
       K=2*MST-1
       IF(MST.GT.IMAXST) STOP
C
C          SET OPEN BOUNDS
C
       NITER=1
       GO TO 289
 396   NUM=1
 35    IF(NUM.EQ.NINB) GO TO 171
       NSRCH=NBD(NUM)/1000000
       N=NBD(NUM)/10000-NSRCH*100
       NLEF=NBD(NUM)/100-NSRCH*10000-N*100
       NRIG=NBD(NUM)-NSRCH*1000000-N*10000-NLEF*100
       NL=NLEF
       NLL=NL-1
       NLLL=NL+1
```

```
      MR=MR1G
      MRR=MR-1
      MRRR=MR+1
      NN=N-1
      NNN=N+1
      R(MLL)=0.0
      S(MLL)=QNXP(MLL,N)
      DO 172 M=ML,MR
      MM=M-1
      MMM=M+1
      A(M)=EN(M,N)-F1*(QNY(M,N)-QNY(M,NN))
      P(M)=F1/(1.0+F1*R(MM))
      Q(M)=(A(M)+F1*S(MM))/(1.0+F1*R(MM))
      IF(M.EQ.MR) GO TO 172
      TEMP1=UNM(M,N)*CNX(M,N)
      TEMP2=0.25*(QNY(M,N)+QNY(MMM,N)+QNY(M,NN)+QNY(MMM,NN))
      TEMP3=SQRT(TEMP1**2+TEMP2**2)
      TEMP4=0.5*(CN(M,N)+CN(MMM,N))
      TEMP11=F2*CNX(M,N)
      EDDY=BETA*SQRT(AG)*TEMP3/TEMP4
      TEMP12=1.0+(F3*TEMP3)/(CNX(M,N)**2*TEMP4**2)
      TEMP13=TEMP11*P(M)+TEMP12
      DX1=UNM(MMM,N)*CNX(MMM,N)
      DX2=UNM(M,N)*CNX(M,N)
      DX3=UNM(MM,N)*CNX(MM,N)
      TEMP17=UNM(M,NNN)
      TEMP18=UNM(M,NN)
      IF((QNY(M,NN)+QNY(MMM,NN)).LT.0.0) TEMP18=UNM(M,N)
      IF((QNY(M,N)+QNY(MMM,N)).GT.0.0) TEMP17=UNM(M,N)
      TEMP40=UNM(M,NNN)
      TEMP41=UNM(M,NN)
      IF(UNM(M,NNN).EQ.0.0) GO TO 149
      IF(HN(MMM,NNN).NE.2.0.AND.HN(M,NNN).NE.2.0) GO TO 357
149   TEMP40=-UNM(M,N)
      TEMP17=0.0
357   IF(UNM(M,NN).EQ.0.0) GO TO 148
      IF(HN(MMM,N).NE.2.0.AND.HN(M,N).NE.2.0) GO TO 352
148   TEMP41=-UNM(M,N)
      TEMP18=0.0
352   CONTINUE
      TEMP14=0.25*((DX1+DX2)*(UNM(MMM,N)+UNM(M,N))-(DX2+DX3)*
     1(UNM(M,N)+UNM(MM,N)))
      TEMP15=0.5*((QNY(MMM,N)+QNY(M,N))*TEMP17-(QNY(MMM,NN)+QNY(M,NN))*
     1TEMP18)
      D2=1.0
      B(M)=QNX(M,N)+F2*CNX(M,N)*(ENM(M,N)-ENM(MMM,N))
     1-(F3*QNX(M,N)*TEMP3)/(CNX(M,N)**2*TEMP4**2)-F4*TEMP2
     2-2.0*F1*ALPHA*TEMP14-2.0*F1*ALPHA*TEMP15
     3+F5*EDDY*(TEMP40-2.0*UNM(M,N)+TEMP41)*CNX(M,N)
     4+2.0*F1*D2*(TNW(M,N)-TNW(M,NN))
      R(M)=TEMP11/TEMP13
      S(M)=(B(M)+TEMP11*Q(M))/TEMP13
172   CONTINUE
      DO 178 K=MLLL,MR
      M=MR+MLLL-K
      MM=M-1
      ENP(M,N)=-P(M)*QNXP(M,N)+Q(M)
      QNXP(MM,N)=-R(MM)*ENP(M,N)+S(MM)
178   CONTINUE
      ENP(ML,N)=-P(ML)*QNXP(ML,N)+Q(ML)
      IF(NSRCH.NE.2.AND.NSRCH.NE.3) GO TO 1673
      QNXP(MRRR,N)=2.0*QNXP(MR,N)-QNXP(MRR,N)
1673  NUM=NUM+1
      GO TO 35
171   CONTINUE
      NITER=NITER+1
      IF(NITER.GT.2) GO TO 999
      DO 1177 M=1,MMAX
      DO 1177 N=1,NMAX
      IF(CNX(M,N).EQ.0.0) GO TO 1177
      UNM(M,N)=0.5*(QNXP(M,N)+QNX(M,N))/CNX(M,N)
1177  CONTINUE
      GO TO 396
999   CONTINUE
      DO 732 N=2,20
732   ENP(1,N)=2.0*ENP(2,N)-ENP(3,N)
      DO 734 M=1,MMAX-1
734   ENP(M,1)=2.0*ENP(M,2)-ENP(M,3)
      DO 735 M=1,10
735   ENP(M,21)=2.0*ENP(M,20)-ENP(M,19)
      DO 736 N=1,13
736   ENP(MMAX,N)=2.0*ENP(MMAX-1,N)-ENP(MMAX-2,N)
C
C          COMPUTE SNP ON ROW N (FIRST HALF TIMESTEP)
C
```

```
      KHF=2*MST-1
      NUM=1
      GO TO 799
408   IF(NUM.EQ.NIND) GO TO 490
      NSRCH=NBD(NUM)/1000000
      N=NBD(NUM)/10000-NSRCH*100
      ML=NBD(NUM)/100-NSRCH*10000-N*100
      MR=NBD(NUM)-NSRCH*1000000-N*10000-ML*100
      MLL=ML-1
      MLLL=ML+1
      MRR=MR-1
      MRRR=MR+1
      NN=N-1
      NNN=N+1
      A(MLL)=0.0
      B(MLL)=SNP(MLL,N)
      P(ML)=0.0
      DNXX(MLL,N)=0.0
      DNXY(MLL,N)=0.0
      IF(NSRCH.NE.1.AND.NSRCH.NE.3) GO TO 401
      TEMP16=0.5*(HNT(MLL,N)+HNT(MLL,NN)+ENP(MLL,N)+ENP(ML,N))
      IF(QNXP(MLL,N).EQ.0.0) GO TO 366
      TEMP19=0.25*(QNY(MLL,N)+QNY(ML,N)+QNY(MLL,NN)+QNY(ML,NN))
      TEMP30=SQRT(QNXP(MLL,N)**2+TEMP19**2)
      TEMP31=0.5*(CN(MLL,N)+CN(ML,N))
      TEMP32=SQRT(AG)/(TEMP30*TEMP31)
      DNXX(MLL,N)=TEMP16*((GAMMA*QNXP(MLL,N)**2+DELTA*TEMP19**2)*
     1TEMP32)
      DNXY(MLL,N)=TEMP16*(GAMMA-DELTA)*QNXP(MLL,N)*TEMP19*TEMP32
      IF(QNY(ML,N).EQ.0.0) DNXY(MLL,N)=0.0
      IF(QNY(ML,NN).EQ.0.0) DNXY(MLL,N)=0.0
366   P(ML)=G2*QNXP(MLL,N)+G5*DNXX(MLL,N)
401   R(MR)=0.0
      DNXX(MR,N)=0.0
      DNXY(MR,N)=0.0
      IF(NSRCH.NE.2.AND.NSRCH.NE.3) GO TO 403
      TEMP16=0.5*(HNT(MR,N)+HNT(MR,NN)+ENP(MR,N)+ENP(MRRR,N))
      IF(QNXP(MR,N).EQ.0.0) GO TO 367
      TEMP19=0.25*(QNY(MR,N)+QNY(MRRR,N)+QNY(MR,NN)+QNY(MRRR,NN))
      TEMP30=SQRT(QNXP(MR,N)**2+TEMP19**2)
      TEMP31=0.5*(CN(MR,N)+CN(MRRR,N))
      TEMP32=SQRT(AG)/(TEMP30*TEMP31)
      DNXX(MR,N)=TEMP16*((GAMMA*QNXP(MR,N)**2+DELTA*TEMP19**2)*TEMP32)
      DNXY(MR,N)=TEMP16*(GAMMA-DELTA)*QNXP(MR,N)*TEMP19*TEMP32
      IF(QNY(MR,N).EQ.0.0) DNXY(MR,N)=0.0
      IF(QNY(MR,NN).EQ.0.0) DNXY(MR,N)=0.0
367   R(MR)=G2*QNXP(MR,N)-G5*DNXX(MR,N)
403   DO 402 M=ML,MR
      MM=M-1
      MMM=M+1
      A(M)=0.0
      B(M)=0.0
      IF(M.EQ.ML) GO TO 404
      P(M)=G2*QNXP(MM,N)+G5*DNXX(MM,N)
404   DNXX(M,N)=0.0
      DNXY(M,N)=0.0
      IF(M.EQ.MR) GO TO 405
      TEMP16=0.5*(HNT(M,N)+HNT(M,NN)+ENP(M,N)+ENP(MMM,N))
      IF(QNXP(M,N).EQ.0.0) GO TO 368
      TEMP19=0.25*(QNY(M,N)+QNY(MMM,N)+QNY(M,NN)+QNY(MMM,NN))
      TEMP30=SQRT(QNXP(M,N)**2+TEMP19**2)
      TEMP31=0.5*(CN(M,N)+CN(MMM,N))
      TEMP32=SQRT(AG)/(TEMP30*TEMP31)
      DNXX(M,N)=TEMP16*((GAMMA*QNXP(M,N)**2+DELTA*TEMP19**2)*TEMP32)
      DNXY(M,N)=TEMP16*(GAMMA-DELTA)*QNXP(M,N)*TEMP19*TEMP32
      IF(QNY(M,N).EQ.0.0.OR.QNY(MMM,N).EQ.0.0) DNXY(M,N)=0.0
      IF(QNY(M,NN).EQ.0.0.OR.QNY(MMM,NN).EQ.0.0) DNXY(M,N)=0.0
      IF(HN(MMM,NNN).EQ.3.0) DNXY(M,N)=0.0
368   R(M)=G2*QNXP(M,N)-G5*DNXX(M,N)
405   Q(M)=(ENP(M,N)+0.25*(HNT(M,N)+HNT(MM,N)+HNT(M,NN)+HNT(MM,NN)))+G2*
     1(QNXP(M,N)-QNXP(MM,N))+G5*(DNXX(M,N)+DNXX(MM,N))
      S(M)=SNN(M,N)*(EN(M,N)+0.25*(HNT(M,N)+HNT(MM,N)+HNT(M,NN)+HNT(MM,
     1NN)))-G2*(QNY(M,N)*(SNM(M,N)+SNM(M,NNN))-QNY(M,NN)*(SNM(M,N)+SNM(
     2M,NN)))+G5*((SNM(M,NNN)-SNM(M,N))*DNYY(M,N)-(SNM(M,N)-SNM(M,NN))*
     3DNYY(M,NN))+0.25*G5*((SNM(M,NNN)+SNM(MMM,NNN)-SNM(M,NN)-SNM(MMM,
     4NN))*DNXY(M,N)-(SNM(M,NNN)+SNM(MM,NNN)-SNM(M,NN)-SNM(MM,NN))*
     5DNXY(MM,N)+(SNM(MMM,N)+SNM(MMM,NNN)-SNM(MM,N)-SNM(MM,NNN))*
     6DNYX(M,N)-(SNM(MMM,N)+SNM(MMM,NN)-SNM(MM,N)-SNM(MM,NN))*DNYX(M,NN
     7))
      A(M)=R(M)/(Q(M)+P(M)*A(MM))
      B(M)=(S(M)+P(M)*B(MM))/(Q(M)+P(M)*A(MM))
402   CONTINUE
      DO 406 K=MLLL,MRRR
      M=MLLL+MRRR-K
      MM=M-1
```

```
      SNP(MM,N)=-A(MM)*SNP(M,N)+B(MM)
  406 CONTINUE
      NUM=NUM+1
      GO TO 408
  490 CONTINUE
      DO 317 M=1,MMAX
      MM=M-1
      MMM=M+1
      IF(M.EQ.1) MM=1
      IF(M.EQ.MMAX) MMM=MMAX
      DO 317 N=1,NMAX
      IF(CN(M,N).EQ.0.0) GO TO 392
      NN=N-1
      NNN=N+1
      IF(N.EQ.1) NN=1
      IF(N.EQ.NMAX) NNN=NMAX
      CNX(M,N)=0.5*(HNT(M,N)+HNT(M,NN)+ENP(M,N)+ENP(MMM,N))
      IF(N.EQ.1) CNX(M,N)=0.27+0.5*(ENP(M,N)+ENP(MMM,N))
      UNM(M,N)=QNXP(M,N)/CNX(M,N)
      CNY(M,N)=0.5*(HNT(M,N)+HNT(MM,N)+ENP(M,N)+ENP(M,NNN))
  392 CONTINUE
      QNX(M,N)=QNXP(M,N)
      ENM(M,N)=ENP(M,N)
      SNM(M,N)=SNP(M,N)
  317 CONTINUE
C
C          PRINT INSTRUCTIONS
C
  550 IF(NSTEP-2) 197,196,197
  196 CONTINUE
      IF(HTIMES.LT.CHTIMES) GO TO 746
      IF(CHTIMES.EQ.0.0) GO TO 748
      DO 744 M=1,MMAX
      MM=M-1
      IF(M.EQ.1) MM=1
      DO 744 N=1,NMAX
      IF(CN(M,N).EQ.0.0) GO TO 744
      NN=N-1
      IF(N.EQ.1) NN=1
      DEP=EN(M,N)+0.25*(HNT(M,N)+HNT(M,NN)+HNT(MM,N)+HNT(MM,NN))
      REN=2.0*DEP*SQRT((UNM(M,N)+UNM(MM,N))**2+(VNM(M,N)+VNM(M,NN))
     1**2)/VIS
      FRN=8.0*AG/(CN(M,N)**2)
  747 FRNOLD=FRN
      XOLD=1.0/SQRT(FRNOLD)
      FXOLD=XOLD+2.0*ALOG10(RKS/(12.0*DEP)+2.5*XOLD/REN)
      FDXOLD=1.0+5.0/((RKS/(12.0*DEP)+2.5*XOLD/REN)*REN*ALOG(10.0))
      XNEW=XOLD-FXOLD/FDXOLD
      FRN=1.0/(XNEW**2)
      IF(ABS(FRN-FRNOLD).GT.1.0E-3) GO TO 747
      CN(M,N)=SQRT(8.0*AG/FRN)
  744 CONTINUE
  748 CHTIMES=CHTIMES+TNCHEZ
  746 CONTINUE
      IF(MST.NE.IPRINT(MP)) GO TO 197
      MP=MP+1
      NSUM=0
      SPTOT=0.0
      VOLTOT=0.0
      DO 768 M=11,MMAX-1
      MM=M-1
      DO 768 N=14,NMAX-1
      NN=N-1
      DEP=EN(M,N)+0.25*(HNT(M,N)+HNT(M,NN)+HNT(MM,N)+HNT(MM,NN))
      VOL=DEP*AX*AX
      SPTOT=SPTOT+SNM(M,N)*VOL
      VOLTOT=VOLTOT+VOL
      NSUM=NSUM+1
  768 CONTINUE
      SPMEAN=SPTOT/VOLTOT
      VLMEAN=VOLTOT/FLOAT(NSUM)
      NUM=0
      SVAR=0.0
      DO 269 M=11,MMAX-1
      MM=M-1
      DO 269 N=14,NMAX-1
      NN=N-1
      DEP=EN(M,N)+0.25*(HNT(M,N)+HNT(M,NN)+HNT(MM,N)+HNT(MM,NN))
      VOL=DEP*AX*AX
      SVAR=SVAR+(SNM(M,N)*VOL-SPMEAN*VLMEAN)**2
      NUM=NUM+1
  269 CONTINUE
      SVAR=SVAR/FLOAT(NUM-1)
      SDEV=SQRT(SVAR)
      SPDEV=SDEV/VLMEAN
```

```
      WRITE(6,207) SPMEAN,SPDEV
207   FORMAT(1X,2F7.4)
2764  WRITE(6,7020) (TITL(J),J=1,18),MST,HTIMES
7020  FORMAT(1H1/18A4//10X,42HWATER ELEVATIONS IN  10TH MMS  AT TIMESTEP
     1,I5,20X,17HTIME IN SECONDS =,F7.1/)
      WRITE(6,70) (NCOL(J),J=1,32)
70    FORMAT(/3X,32A4/2X,11HN)
      DO 7000 N=1,NMAX
      DO 7006 M=4,MMAX
7006  KONVRT(M)=NINTEG(EN(M,N)*10000.0)
7000  WRITE(6,7001) N,(KONVRT(M),M=4,MMAX)
7001  FORMAT(/1X,I2,32I4)
      WRITE(6,7022) (TITL(J),J=1,18),MST,HTIMES
7022  FORMAT(1H1/18A4//10X,45HU VELOCITIES IN  MILLIMETRES/SEC  AT TIM
     1ESTEP,I5,20X,17HTIME IN SECONDS =,F7.1/)
      WRITE(6,70) (NCOL(J),J=1,32)
      DO 7004 N=1,NMAX
      DO 7008 M=4,MMAX
      KONVRT(M)=0
      KONVRT(M)=NINTEG(UNM(M,N)*1000.0)
7008  CONTINUE
7004  WRITE(6,7001) N,(KONVRT(M),M=4,MMAX)
      WRITE(6,7021) (TITL(J),J=1,18),MST,HTIMES
7021  FORMAT(1H1/18A4//10X,45HV VELOCITIES IN  MILLIMETRES/SEC  AT TIM
     1ESTEP,I5,20X,17HTIME IN SECONDS =,F7.1/)
      WRITE(6,70) (NCOL(J),J=1,32)
      DO 7003 N=1,NMAX
      DO 7007 M=4,MMAX
      KONVRT(M)=0
      KONVRT(M)=NINTEG(VNM(M,N)*1000.0)
7007  CONTINUE
7003  WRITE(6,7001) N,(KONVRT(M),M=4,MMAX)
      WRITE(6,7026) (TITL(J),J=1,18),MST,HTIMES
7026  FORMAT(1H1/18A4//10X,47HCONCENTRATIONS IN PARTS PER MILLION AT
     1 TIMESTEP,I5,10X,17HTIME IN SECONDS =,F7.1/)
      WRITE(6,70) (NCOL(J),J=1,32)
      DO 7027 N=1,NMAX
      DO 7028 M=4,MMAX
      KONVRT(M)=0
      KONVRT(M)=NINTEG(SNM(M,N))
7028  CONTINUE
7027  WRITE(6,7001) N,(KONVRT(M),M=4,MMAX)
197   IF(NSTEP.EQ.2) GO TO 288
      NSTEP=2
      K=2*MST
C
C         SET OPEN BOUNDS
C
      NITER=1
      GO TO 289
C
C          COMPUTE QNYP AND ENP ON COLUMN I (SECOND HALF TIMESTEP)
C
699   NUM=1
      V1=0.25*(VNM(12,13)+VNM(13,13)+VNM(14,13)+VNM(15,13))
      CONST=(V1**2)/(2.0*SQRT(2.0*PI*RR))
65    IF(NUM.EQ.NIND) GO TO 610
      MSRCH=MBD(NUM)/1000000
      M=MBD(NUM)/10000-MSRCH*100
      NBOT=MBD(NUM)/100-MSRCH*10000-M*100
      NTOP=MBD(NUM)-MSRCH*1000000-M*10000-NBOT*100
      NB=NBOT
      NBB=NB-1
      NBBB=NB+1
      NT=NTOP
      NTT=NT-1
      NTTT=NT+1
      MM=M-1
      MMM=M+1
      R(NBB)=0.0
      S(NBB)=QNYP(M,NBB)
      DO 600 N=NB,NT
      NN=N-1
      NNN=N+1
      A(N)=ENM(M,N)-F1*(QNX(M,N)-QNX(MM,N))
      P(N)=F1/(1.0+F1*R(NN))
      Q(N)=(A(N)+F1*S(NN))/(1.0+F1*R(NN))
      IF(CN(M,NNN).EQ.0.0.OR.HN(M,NNN).EQ.2.0) GO TO 600
      TEMP1=VNM(M,N)*CNY(M,N)
      TEMP2=0.25*(QNX(M,N)+QNX(M,NNN)+QNX(MM,N)+QNX(MM,NNN))
      TEMP3=SQRT(TEMP2**2+TEMP1**2)
      TEMP4=0.5*(CN(M,NNN)+CN(M,N))
      TEMP11=F2*CNY(M,N)
      EDDY=BETA*SQRT(AG)*TEMP3/TEMP4
      TEMP12=1.0+(F3*TEMP3)/(CNY(M,N)**2*TEMP4**2)
```

```
      TEMP13=TEMP11*P(N)+TEMP12
      DY1=VNM(M,NNN)*CNY(M,NNN)
      DY2=VNM(M,N)*CNY(M,N)
      DY3=VNM(M,NN)*CNY(M,NN)
      TEMP17=VNM(MMM,N)
      TEMP18=VNM(MM,N)
      IF((QNX(MM,N)+QNX(MM,NNN)).LT.0.0) TEMP18=VNM(M,N)
      IF((QNX(M,N)+QNX(M,NNN)).GT.0.0) TEMP17=VNM(M,N)
      TEMP40=VNM(MMM,N)
      TEMP41=VNM(MM,N)
      IF(VNM(MMM,N).EQ.0.0) GO TO 249
      IF(HN(MMM,NNN).NE.3.0.AND.HN(MMM,N).NE.3.0) GO TO 765
 249  TEMP40=-VNM(M,N)
      TEMP17=0.0
 765  IF(VNM(MM,N).EQ.0.0) GO TO 248
      IF(HN(M,NNN).NE.3.0.AND.HN(M,N).NE.3.0) GO TO 766
 248  TEMP41=-VNM(M,N)
      TEMP18=0.0
 766  CONTINUE
      TEMP14=0.25*((DY1+DY2)*(VNM(M,NNN)+VNM(M,N))-(DY2+DY3)*
     1(VNM(M,N)+VNM(M,NN)))
      TEMP15=0.5*((QNX(M,NNN)+QNX(M,N))*TEMP17-(QNX(MM,NNN)+QNX(MM,N))*
     1TEMP18)
      IF(N.NE.NT) GO TO 1774
      TEMP14=0.0
      TEMP15=0.0
 1774 D2=1.0
      IF(D2.EQ.0.0) GO TO 656
      IF(V1.LT.0.0) GO TO 651
      IF(N.LE.NC)GO TO 655
      IF(M.LT.11) GO TO 655
      XS=FLOAT(N-NC)*DX
      YS=FLOAT(MC-M)*DX
      TEMP50=CONST
      GO TO 654
 651  IF(N.GE.NC) GO TO 655
      XS=FLOAT(NC-N)*DX
      YS=FLOAT(MC-M)*DX
      TEMP50=-CONST
 654  TEMP51=HNT(M,N)+0.25*(ENM(M,N)+ENM(M,NNN)+ENM(MMM,N)+ENM(MMM,NNN))
      TNW(M,N)=TEMP50*EXP(-0.5*RR*((YS/XS)**2))*TEMP51
      GO TO 656
 655  D2=0.0
 656  B(N)=QNY(M,N)-F2*CNY(M,N)*(EN(M,NNN)-EN(M,N))
     1-(F3*QNY(M,N)*TEMP3)/(CNY(M,N)**2*TEMP4**2)+F4*TEMP2
     2-2.0*F1*ALPHA*TEMP14-2.0*F1*ALPHA*TEMP15
     3+F5*EDDY*(TEMP40-2.0*VNM(M,N)+TEMP41)*CNY(M,N)
     4+2.0*F1*D2*(TNW(M,N)-TNW(MM,N))
      R(N)=TEMP11/TEMP13
      S(N)=(B(N)+TEMP11*Q(N))/TEMP13
 600  CONTINUE
      IF(MSRCH.NE.2.AND.MSRCH.NE.3) GO TO 2763
      QNYP(M,NT)=-R(NT)*ENP(M,NTTT)+S(NT)
 2763 CONTINUE
      DO 633 K=NBBB,NT
      N=NT+NBBB-K
      NN=N-1
      ENP(M,N)=-P(N)*QNYP(M,N)+Q(N)
      QNYP(M,NN)=-R(NN)*ENP(M,N)+S(NN)
 633  CONTINUE
      ENP(M,NB)=-P(NB)*QNYP(M,NB)+Q(NB)
      IF(MSRCH.NE.2.AND.MSRCH.NE.3) GO TO 2767
      QNYP(M,NTTT)=2.0*QNYP(M,NT)-QNYP(M,NTT)
 2767 NUM=NUM+1
      GO TO 65
 610  CONTINUE
      NITER=NITER+1
      IF(NITER.GT.2) GO TO 6813
      DO 6852 M=1,MMAX
      DO 6852 N=1,NMAX
      IF(CNY(M,N).EQ.0.0) GO TO 6852
      VNM(M,N)=0.5*(QNYP(M,N)+QNY(M,N))/CNY(M,N)
 6852 CONTINUE
      GO TO 699
 6813 CONTINUE
      DO 1732 M=2,MMAX-1
 1732 ENP(M,1)=2.0*ENP(M,2)-ENP(M,3)
      DO 1734 N=1,20
 1734 ENP(1,N)=2.0*ENP(2,N)-ENP(3,N)
      DO 1735 N=1,13
 1735 ENP(MMAX,N)=2.0*ENP(MMAX-1,N)-ENP(MMAX-2,N)
C
C          COMPUTE SNP ON COLUMN M (SECOND HALF TIMESTEP)
C
      KHF=2*MST
```

```
      NUM=1
      GO TO 799
  508 IF(NUM.EQ.MIND) GO TO 590
      MSRCH=MBD(NUM)/1000000
      M=MBD(NUM)/10000-MSRCH*100
      NB=MBD(NUM)/100-MSRCH*10000-M*100
      NT=MBD(NUM)-MSRCH*1000000-M*10000-NB*100
      NBB=NB-1
      NBBB=NB+1
      NTT=NT-1
      NTTT=NT+1
      MM=M-1
      MMM=M+1
      A(NBB)=0.0
      B(NBB)=SNP(M,NBB)
      P(NB)=0.0
      DNYY(M,NBB)=0.0
      DNYX(M,NBB)=0.0
      IF(MSRCH.NE.1.AND.MSRCH.NE.3) GO TO 501
      TEMP16=0.5*(HNT(M,NBB)+HNT(MM,NBB)+ENP(M,NBB)+ENP(M,NB))
      IF(QNYP(M,NBB).EQ.0.0) GO TO 369
      TEMP19=0.25*(QNX(M,NBB)+QNX(M,NB)+QNX(MM,NBB)+QNX(MM,NB))
      TEMP30=SQRT(QNYP(M,NBB)**2+TEMP19**2)
      TEMP31=0.5*(CN(M,NBB)+CN(M,NB))
      TEMP32=SQRT(AG)/(TEMP30*TEMP31)
      DNYY(M,NBB)=TEMP16*((GAMMA*QNYP(M,NBB)**2+DELTA*TEMP19**2)
     1*TEMP32)
      DNYX(M,NBB)=TEMP16*(GAMMA-DELTA)*QNYP(M,NBB)*TEMP19*TEMP32
      IF(QNX(M,NB).EQ.0.0) DNYX(M,NBB)=0.0
      IF(QNX(MM,NB).EQ.0.0) DNYX(M,NBB)=0.0
  369 P(NB)=G2*QNYP(M,NBB)+G5*DNYY(M,NBB)
  501 R(NT)=0.0
      DNYY(M,NT)=0.0
      DNYX(M,NT)=0.0
      IF(MSRCH.NE.2.AND.MSRCH.NE.3) GO TO 503
      TEMP16=0.5*(HNT(M,NT)+HNT(MM,NT)+ENP(M,NT)+ENP(M,NTTT))
      IF(QNYP(M,NT).EQ.0.0) GO TO 370
      TEMP19=0.25*(QNX(M,NT)+QNX(M,NTTT)+QNX(MM,NT)+QNX(MM,NTTT))
      TEMP30=SQRT(QNYP(M,NT)**2+TEMP19**2)
      TEMP31=0.5*(CN(M,NT)+CN(M,NTTT))
      TEMP32=SQRT(AG)/(TEMP30*TEMP31)
      DNYY(M,NT)=TEMP16*((GAMMA*QNYP(M,NT)**2+DELTA*TEMP19**2)*TEMP32)
      DNYX(M,NT)=TEMP16*(GAMMA-DELTA)*QNYP(M,NT)*TEMP19*TEMP32
      IF(QNX(M,NT).EQ.0.0) DNYX(M,NT)=0.0
      IF(QNX(MM,NT).EQ.0.0) DNYX(M,NT)=0.0
  370 R(NT)=G2*QNYP(M,NT)-G5*DNYY(M,NT)
  503 DO 502 N=NB,NT
      NN=N-1
      NNN=N+1
      A(N)=0.0
      B(N)=0.0
      IF(N.EQ.NB) GO TO 504
      P(N)=G2*QNYP(M,NN)+G5*DNYY(M,NN)
  504 DNYY(M,N)=0.0
      DNYX(M,N)=0.0
      IF(N.EQ.NT) GO TO 505
      TEMP16=0.5*(HNT(M,N)+HNT(MM,N)+ENP(M,N)+ENP(M,NNN))
      IF(QNYP(M,N).EQ.0.0) GO TO 371
      TEMP19=0.25*(QNX(M,N)+QNX(M,NNN)+QNX(MM,N)+QNX(MM,NNN))
      TEMP30=SQRT(QNYP(M,N)**2+TEMP19**2)
      TEMP31=0.5*(CN(M,N)+CN(M,NNN))
      TEMP32=SQRT(AG)/(TEMP30*TEMP31)
      DNYY(M,N)=TEMP16*((GAMMA*QNYP(M,N)**2+DELTA*TEMP19**2)*TEMP32)
      DNYX(M,N)=TEMP16*(GAMMA-DELTA)*QNYP(M,N)*TEMP19*TEMP32
      IF(QNX(M,N).EQ.0.0.OR.QNX(M,NNN).EQ.0.0) DNYX(M,N)=0.0
      IF(QNX(MM,N).EQ.0.0.OR.QNX(MM,NNN).EQ.0.0) DNYX(M,N)=0.0
      IF(IIN(MMM,NNN).EQ.2.0) DNYX(M,N)=0.0
  371 R(N)=G2*QNYP(M,N)-G5*DNYY(M,N)
  505 Q(N)=(ENP(M,N)+0.25*(HNT(M,N)+HNT(MM,N)+HNT(M,NN)+HNT(MM,NN)))+G2*
     1(QNYP(M,N)-QNYP(M,NN))+G5*(DNYY(M,N)+DNYY(M,NN))
      S(N)=SNM(M,N)*(ENM(M,N)+0.25*(HNT(M,N)+HNT(MM,N)+HNT(M,NN)+HNT(MM,
     1NN)))-G2*(QNX(M,N)*(SNM(M,N)+SNM(MMM,N))-QNX(MM,N)*(SNM(M,N)+SNM(
     2MM,N)))+G5*((SNM(MMM,N)-SNM(M,N))*DNXX(M,N)-(SNM(M,N)-SNM(MM,N))*
     3DNXX(MM,N))+0.25*G5*((SNM(M,NNN)+SNM(MMM,NNN)-SNM(M,NN)-SNM(MMM,NN
     4))*DNXY(M,N)-(SNM(M,NNN)+SNM(MM,NNN)-SNM(M,NN)-SNM(MM,NN))*DNXY(MM
     5,N)+(SNM(MMM,N)+SNM(MMM,NNN)-SNM(MM,N)-SNM(MM,NNN))*DNYX(M,N)-(SNM
     6(MMM,N)+SNM(MMM,NN)-SNM(MM,N)-SNM(MM,NN))*DNYX(M,NN))
      A(N)=R(N)/(Q(N)+P(N)*A(NN))
      B(N)=(S(N)+P(N)*B(NN))/(Q(N)+P(N)*A(NN))
  502 CONTINUE
      DO 506 K=NBBB,NTTT
      N=NBBB+NTTT-K
      NN=N-1
      SNP(M,NN)=-A(NN)*SNP(M,N)+B(NN)
  506 CONTINUE
```

```
      NUM=NUM+1
      GO TO 508
590   CONTINUE
      DO 6116 M=1,MMAX
      MM=M-1
      MMM=M+1
      IF(M.EQ.1) MM=1
      IF(M.EQ.MMAX) MMM=MMAX
      DO 6116 N=1,NMAX
      IF(CN(M,N).EQ.0.0) GO TO 6658
      NN=N-1
      NNN=N+1
      IF(N.EQ.1) NN=1
      IF(N.EQ.NMAX) NNN=NMAX
      CNX(M,N)=0.5*(HNT(M,N)+HNT(M,NN)+ENP(M,N)+ENP(MMM,N))
      IF(N.EQ.1) CNX(M,N)=0.27+0.5*(ENP(M,N)+ENP(MMM,N))
      CNY(M,N)=0.5*(HNT(M,N)+HNT(MM,N)+ENP(M,N)+ENP(M,NNN))
      VNM(M,N)=QNYP(M,N)/CNY(M,N)
6658  CONTINUE
      QNY(M,N)=QNYP(M,N)
      EN(M,N)=ENP(M,N)
      SNM(M,N)=SNP(M,N)
6116  CONTINUE
      GO TO 550
      END
C
C          FUNCTION TO CONVERT VARIABLE A TO NEAREST INTEGER
C
      FUNCTION NINTEG(A)
      IF(A) 1,2,3
1     NINTEG=IFIX(A-0.5)
      GO TO 4
2     NINTEG=IFIX(A)
      GO TO 4
3     NINTEG=IFIX(A+0.5)
4     CONTINUE
      RETURN
      END
C
C           SUBROUTINE BOUND HANDLES THE READING OF ALL
C           TABLE VALUES OF THE OPEN BOUNDARIES IN STORAGE
C
      SUBROUTINE BOUND(IMAX,JMAX,AX,AT,PI,TIS,NCARD,AMP,THT,PHA,TI)
      COMMON TITL(18),XIA(1490),ICOL(29),H(29,36),IBD(60),JBD(60)
     1,IOBD(3),JOBD(3),QX(29,36),QXP(29,36),QY(29,36),QYP(29,36)
     2,E(29,36),EM(29,36),EP(29,36),C(29,36),UM(29,36),VM(29,36)
     3,CSX(29,36),TAW(29,36),CSY(29,36),HT(29,36),
     4HN(35,38),MBD(90),NBD(90),NOBD(3),NOBD(3),QNX(35,38)
     5,QNXP(35,38),QNY(35,38),QNYP(35,38),EN(35,38),ENM(35,38),
     6ENP(35,38),CN(35,38),UNM(35,38),VNM(35,38),CNX(35,38),
     7CNY(35,38),HNT(35,38),TNW(35,38),NCOL(47),
     8SN(29,36),SP(29,36),DXX(29,36),DYY(29,36),DXY(29,36),
     9DYX(29,36),SNM(35,38),SNP(35,38),DNXX(35,38),DNYY(35,38)
     1,DNXY(35,38),DNYX(35,38)
      NOBGP=2
      SIG=2.0*PI/TIS
      XLEN=13.0*AX
      YLEN=5.0*AX
      ENLEN=AX*FLOAT(NOBGP)
      EMAX=-100.0
      EMIN=100.0
      T=AT
      DO 100 N=1,NCARD
      XIB=AMP*COS(SIG*T-2.0*PI*PHA/360.0)
      IF(XIB.GT.EMAX)  EMAX=XIB
      IF(XIB.LT.EMIN)  EMIN=XIB
      XIA(N)=XIB
      T=T+AT
100   CONTINUE
      THT=EMAX-EMIN
      WRITE(6,10) (TITL(J),J=1,18)
      WRITE(6,20) XLEN,YLEN,ENLEN,AMP,TI
      WRITE(6,30)
      WRITE(6,40) (N,XIA(N),N=1,NCARD)
10    FORMAT(1H1/18A4//10X,32HELEVATIONS AT BOUNDARY IN METRES//)
20    FORMAT(10X,10HX LENGTH =,F6.1,5X,10HY LENGTH =,F6.1,5X,16HENTRANCE
     1 WIDTH =,F6.1,5X,11HAMPLITUDE =,F6.3,5X,8HPERIOD =,F8.1//)
30    FORMAT((3X,9(13H    K   XIA  )))
40    FORMAT((3X,9(15,1X,F6.3,1X)))
      RETURN
      END
C
C           SUBROUTINE DIVE1 READS IN LOCATIONS OF WATER
C           LEVEL COMPUTATIONS FOR COARSE GRID
C
```

```
      SUBROUTINE DIVE1(IMAX,JMAX)
      COMMON TITL(18),XIA(1490),ICOL(29),H(29,36),IBD(60),JBD(60)
     1,IOBD(3),JOBD(3),QX(29,36),QXP(29,36),QY(29,36),QYP(29,36)
     2,E(29,36),EM(29,36),EP(29,36),C(29,36),UM(29,36),VM(29,36)
     3,CSX(29,36),TAW(29,36),CSY(29,36),HT(29,36),
     4HN(35,38),MBD(90),NBD(90),MOBD(3),NOBD(3),QNX(35,38)
     5,QNXP(35,38),QNY(35,38),QNYP(35,38),EN(35,38),ENM(35,38),
     6ENP(35,38),CN(35,38),UNM(35,38),VNM(35,38),CNX(35,38),
     7CNY(35,38),HNT(35,38),TNW(35,38),CNOL(32),
     8SM(29,36),SP(29,36),DXX(29,36),DYY(29,36),DXY(29,36),
     9DYX(29,36),SNM(35,38),SNP(35,38),DNXX(35,38),DNYY(35,38)
     1,DNXY(35,38),DNYX(35,38)
      WRITE(6,10) (TITL(J),J=1,18)
      WRITE(6,20) (ICOL(J),J=1,29)
      DO 1 J=1,JMAX
      READ(5,30) (IBD(I),I=1,IMAX)
      WRITE(6,40) J,(IBD(I),I=1,IMAX)
      DO 1 I=1,IMAX
1     H(I,J)=FLOAT(IBD(I))
      RETURN
10    FORMAT(1H1/18A4//10X,21HWATER LEVELS IN FIELD///)
20    FORMAT(3X,29A4/2X,1HJ)
30    FORMAT(30I2)
40    FORMAT(/1X,I2,30I4)
      END
C
C          SUBROUTINE FIND1 PROCESSES DIVE DATA AND THE IOBD
C          AND JOBD VALUES GIVING TWO TABLES (IBD AND JBD)
C          WHICH ARE USED TO CONTROL THE COMPUTATION
C
      SUBROUTINE FIND1(IIND,JIND,IMAX,JMAX,IINDO,JINDO,NSECT)
      LOGICAL START
      COMMON TITL(18),XIA(1490),ICOL(29),H(29,36),IBD(60),JBD(60)
     1,IOBD(3),JOBD(3),QX(29,36),QXP(29,36),QY(29,36),QYP(29,36)
     2,E(29,36),EM(29,36),EP(29,36),C(29,36),UM(29,36),VM(29,36)
     3,CSX(29,36),TAW(29,36),CSY(29,36),HT(29,36),
     4HN(35,38),MBD(90),NBD(90),MOBD(3),NOBD(3),QNX(35,38)
     5,QNXP(35,38),QNY(35,38),QNYP(35,38),EN(35,38),ENM(35,38),
     6ENP(35,38),CN(35,38),UNM(35,38),VNM(35,38),CNX(35,38),
     7CNY(35,38),HNT(35,38),TNW(35,38),NCOL(47),
     8SM(29,36),SP(29,36),DXX(29,36),DYY(29,36),DXY(29,36),
     9DYX(29,36),SNM(35,38),SNP(35,38),DNXX(35,38),DNYY(35,38)
     1,DNXY(35,38),DNYX(35,38)
      DO I N=1,NSECT
      IBD(N)=0
1     JBD(N)=0
      IIND=1
      JIND=1
      DO 2 I=2,IMAX
      START=.TRUE.
      DO 3 J=2,JMAX
      IF(.NOT.START) GO TO 4
      IF(H(I,J).EQ.0.0.OR.H(I,J).EQ.2.0) GO TO 3
      IBD(IIND)=J*100+IBD(IIND)
      IF(H(I,J-1).EQ.2.0) IBD(IIND)=IBD(IIND)-1*100
      START=.FALSE.
      GO TO 3
4     IF(H(I,J).NE.0.0.AND.H(I,J).NE.2.0) GO TO 5
      IBD(IIND)=J-1+IBD(IIND)+10000*I
      GO TO 6
5     IF(J.NE.JMAX) GO TO 3
      IBD(IIND)=J+IBD(IIND)+10000*I
6     IIND=IIND+1
      START=.TRUE.
3     CONTINUE
2     CONTINUE
      DO 12 J=2,JMAX
      START=.TRUE.
      DO 13 I=2,IMAX
      IF(.NOT.START) GO TO 14
      IF(H(I,J).EQ.0.0.OR.H(I,J).EQ.3.0) GO TO 13
      JBD(JIND)=I*100+JBD(JIND)
      IF(H(I-1,J).EQ.3.0) JBD(JIND)=JBD(JIND)-1*100
      START=.FALSE.
      GO TO 13
14    IF(H(I,J).NE.0.0.AND.H(I,J).NE.3.0) GO TO 15
      JBD(JIND)=I-1+JBD(JIND)+10000*J
      GO TO 16
15    IF(I.NE.IMAX) GO TO 13
      JBD(JIND)=I+JBD(JIND)+10000*J
16    JIND=JIND+1
      START=.TRUE.
13    CONTINUE
12    CONTINUE
      NUM=1
```

```
  100   IF(NUM.EQ.IIND) GO TO 300
        I=IBD(NUM)/10000
        JF=IBD(NUM)/100-I*100
        L=IBD(NUM)-I*10000-JF*100
        JFBOT=JF-1
        LTOP=L+1
        NA=1
  200   IF(NA.EQ.JINDO) GO TO 210
        J=JOBD(NA)/100000
        ILEF=JOBD(NA)/1000-J*100
        IRIG=JOBD(NA)/10-J*10000-ILEF*100
        IBERN=JOBD(NA)-J*100000-ILEF*1000-IRIG*10
        IF(I.GE.ILEF.AND.I.LE.IRIG.AND.JFBOT.EQ.J) IBD(NUM)=IBD(NUM)
       1+1000000
        IF(I.GE.ILEF.AND.I.LE.IRIG.AND.LTOP.EQ.J) IBD(NUM)=IBD(NUM)
       2+2000000
        NA=NA+1
        GO TO 200
  210   NUM=NUM+1
        GO TO 100
  300   CONTINUE
        NUM=1
  101   IF(NUM.EQ.JIND) GO TO 301
        J=JBD(NUM)/10000
        IFL=JBD(NUM)/100-J*100
        L=JBD(NUM)-J*10000-IFL*100
        IFLEF=IFL-1
        LRIG=L+1
        NA=1
  201   IF(NA.EQ.IINDO) GO TO 211
        I=IOBD(NA)/100000
        JBOT=IOBD(NA)/1000-I*100
        JTOP=IOBD(NA)/10-I*10000-JBOT*100
        JBERN=IOBD(NA)-I*100000-JBOT*1000-JTOP*10
        IF(J.GE.JBOT.AND.J.LE.JTOP.AND.IFLEF.EQ.I) JBD(NUM)=JBD(NUM)
       1+1000000
        IF(J.GE.JBOT.AND.J.LE.JTOP.AND.LRIG.EQ.I) JBD(NUM)=JBD(NUM)
       2+2000000
        NA=NA+1
        GO TO 201
  211   NUM=NUM+1
        GO TO 101
  301   CONTINUE
        WRITE(6,20) (TITL(J),J=1,18)
        WRITE(6,21) (N,IBD(N),JBD(N),N=1,NSECT)
        RETURN
   20   FORMAT((1H1/18A4//4X,4(29H    NUM        IBD        JBD)))
   21   FORMAT((///4X,4(3X,14,3X,18,3X,18)))
        END
C
C           SUBROUTINE DEPTH1 READS THE WATER LEVELS FOR COARSE GRID
C
        SUBROUTINE DEPTH1(IMAX,JMAX)
        COMMON TITL(18),XIA(1490),ICOL(29),H(29,36),IBD(60),JBD(60)
       1,IOBD(3),JOBD(3),QX(29,36),QXP(29,36),QY(29,36),QYP(29,36)
       2,E(29,36),EM(29,36),EP(29,36),C(29,36),UM(29,36),VM(29,36)
       3,CSX(29,36),TAW(29,36),CSY(29,36),HT(29,36),
       4HN(35,38),MBD(90),NBD(90),MOBD(3),NOBD(3),QNX(35,38)
       5,QNXP(35,38),QN(35,38),QNYP(35,38),EN(35,38),ENM(35,38),
       6ENP(35,38),CN(35,38),UNM(35,38),VNM(35,38),CNX(35,38),
       7CNY(35,38),HNT(35,38),TNW(35,38),NCOL(47),
       8SM(29,36),SP(29,36),DXX(29,36),DYY(29,36),DXY(29,36),
       9DYX(29,36),SNM(35,38),SNP(35,38),DNXX(35,38),DNYY(35,38)
       1,DNXY(35,38),DNYX(35,38)
        NO=15
        IF(IMAX.LT.NO)  NO=IMAX
        DO 10 J=1,JMAX
        READ(5,5) (HT(I,J),I=1,NO)
  10    CONTINUE
        IF(IMAX.LE.NO) GO TO 12
        NQ=NO+1
        DO 11 J=1,JMAX
        READ(5,5) (HT(I,J),I=NQ,IMAX)
  11    CONTINUE
  12    CONTINUE
        WRITE(6,20) (TITL(J),J=1,18)
        WRITE(6,30) (ICOL(J),J=1,29)
        DO 13 J=1,JMAX
  13    WRITE(6,40) J,(HT(I,J),I=1,IMAX)
        RETURN
   5    FORMAT(15(F5.3))
  20    FORMAT(1H1/18A4//10X,44HMEAN INITIAL WATER DEPTHS IN FIELD IN METR
       1ES/)
  30    FORMAT(/3X,29A4/2X,1HJ)
  40    FORMAT(/1X,I2,30F4.2)
```

```
      END
C
C          SUBROUTINE FIND2 PROCESSES DIVE DATA AND THE MOBD
C          AND NOBD VALUES GIVING TWO TABLES (MBD AND NBD)
C          WHICH ARE USED TO CONTROL THE COMPUTATION
C
      SUBROUTINE FIND2(MIND,NIND,MMAX,NMAX,MINDO,NINDO,ISECT)
      LOGICAL START
      COMMON TITL(18),XIA(1490),ICOL(29),H(29,36),IBD(60),JBD(60)
     1,IOBD(3),JOBD(3),QX(29,36),QXP(29,36),QY(29,36),QYP(29,36)
     2,E(29,36),EM(29,36),EP(29,36),C(29,36),UM(29,36),VM(29,36)
     3,CSX(29,36),TAW(29,36),CSY(29,36),HT(29,36),
     4HN(35,38),MBD(90),NBD(90),MOBD(3),NOBD(3),QNX(35,38)
     5,QNXP(35,38),QNY(35,38),QNYP(35,38),EN(35,38),ENM(35,38),
     6ENP(35,38),CN(35,38),UNM(35,38),VNM(35,38),CNX(35,38),
     7CNY(35,38),HNT(35,38),TNW(35,38),NCOL(47),
     8SM(29,36),SP(29,36),DXX(29,36),DYY(29,36),DXY(29,36),
     9DYX(29,36),SNM(35,38),SNP(35,38),DNXX(35,38),DNYY(35,38)
     1,DNXY(35,38),DNYX(35,38)
      DO 1 N=1,ISECT
      MBD(N)=0
1     NBD(N)=0
      MIND=1
      NIND=1
      DO 2 M=2,MMAX
      START=.TRUE.
      DO 3 N=2,NMAX
      IF(.NOT.START) GO TO 4
      IF(HN(M,N).EQ.0.0.OR.HN(M,N).EQ.2.0) GO TO 3
      MBD(MIND)=N*100+MBD(MIND)
      IF(HN(M,N-1).EQ.2.0) MBD(MIND)=MBD(MIND)-1*100
      START=.FALSE.
      GO TO 3
4     IF(HN(M,N).NE.0.0.AND.HN(M,N).NE.2.0) GO TO 5
      MBD(MIND)=N-1+MBD(MIND)+10000*M
      GO TO 6
5     IF(N.NE.NMAX) GO TO 3
      MBD(MIND)=N+MBD(MIND)+10000*M
6     MIND=MIND+1
      START=.TRUE.
3     CONTINUE
2     CONTINUE
      DO 12 N=2,NMAX
      START=.TRUE.
      DO 13 M=2,MMAX
      IF(.NOT.START) GO TO 14
      IF(HN(M,N).EQ.0.0.OR.HN(M,N).EQ.3.0) GO TO 13
      NBD(NIND)=M*100+NBD(NIND)
      IF(HN(M-1,N).EQ.3.0) NBD(NIND)=NBD(NIND)-1*100
      START=.FALSE.
      GO TO 13
14    IF(HN(M,N).NE.0.0.AND.HN(M,N).NE.3.0) GO TO 15
      NBD(NIND)=M-1+NBD(NIND)+10000*N
      GO TO 16
15    IF(M.NE.MMAX) GO TO 13
      NBD(NIND)=M+NBD(NIND)+10000*N
16    NIND=NIND+1
      START=.TRUE.
13    CONTINUE
12    CONTINUE
      NUM=1
100   IF(NUM.EQ.MIND) GO TO 300
      M=MBD(NUM)/10000
      NF=MBD(NUM)/100-M*100
      L=MBD(NUM)-M*10000-NF*100
      NFBOT=NF-1
      LTOP=L+1
      NA=1
200   IF(NA.EQ.NINDO) GO TO 210
      N=NOBD(NA)/100000
      MLEF=NOBD(NA)/1000-N*100
      MRIG=NOBD(NA)/10-N*10000-MLEF*100
      MBERN=NOBD(NA)-N*100000-MLEF*1000-MRIG*10
      IF(M.GE.MLEF.AND.M.LE.MRIG.AND.NFBOT.EQ.N) MBD(NUM)=MBD(NUM)
     1+1000000
      IF(M.GE.MLEF.AND.M.LE.MRIG.AND.LTOP.EQ.N) MBD(NUM)=MBD(NUM)
     2+2000000
      NA=NA+1
      GO TO 200
210   NUM=NUM+1
      GO TO 100
300   CONTINUE
      NUM=1
101   IF(NUM.EQ.NIND) GO TO 301
      N=NBD(NUM)/10000
```

```
      MFL=NBD(NUM)/100-N*100
      L=NBD(NUM)-N*10000-MFL*100
      MFLEF=MFL-1
      LRIG=L+1
      NA=1
  201 IF(NA.EQ.MINDO) GO TO 211
      N=MOBD(NA)/100000
      NBOT=MOBD(NA)/1000-N*100
      NTOP=MOBD(NA)/10-N*10000-NBOT*100
      NBERN=MOBD(NA)-N*100000-NBOT*1000-NTOP*10
      IF(N.GE.NBOT.AND.N.LE.NTOP.AND.MFLEF.EQ.M) NBD(NUM)=NBD(NUM)
     1+1000000
      IF(N.GE.NBOT.AND.N.LE.NTOP.AND.LRIG.EQ.M) NBD(NUM)=NBD(NUM)
     2+2000000
      NA=NA+1
      GO TO 201
  211 NUM=NUM+1
      GO TO 101
  301 CONTINUE
      WRITE(6,20) (TITL(J),J=1,18)
      WRITE(6,21) (N,MBD(N),NBD(N),N=1,ISECT)
      RETURN
   20 FORMAT((1H1/18A4//4X,4(29H    NUM         MBD         NBD)))
   21 FORMAT((///4X,4(3X,I4,3X,I8,3X,I8)))
      END
C
C          SUBROUTINE DEPTH2 READS THE WATER LEVELS FOR FINE GRID
C
      SUBROUTINE DEPTH2(MMAX,NMAX)
      COMMON TITL(18),XIA(1490),ICOL(29),H(29,36),IBD(60),JBD(60)
     1,IOBD(3),JOBD(3),QX(29,36),QXP(29,36),QY(29,36),QYP(29,36)
     2,E(29,36),EM(29,36),EP(29,36),C(29,36),UM(29,36),VM(29,36)
     3,CSX(29,36),TAW(29,36),CSY(29,36),HT(29,36),
     4HN(35,38),NBD(90),NBD(90),MOBD(3),NOBD(3),QNX(35,38)
     5,QNXP(35,38),QNY(35,38),QNYP(35,38),EN(35,38),ENM(35,38),
     6ENP(35,38),CN(35,38),UNM(35,38),VNM(35,38),CNX(35,38),
     7CNY(35,38),HNT(35,38),TNW(35,38),NCOL(47),
     8SM(29,36),SP(29,36),DXX(29,36),DYY(29,36),DXY(29,36),
     9DYX(29,36),SNM(35,38),SNP(35,38),DNXX(35,38),DNYY(35,38)
     1,DNXY(35,38),DNYX(35,38)
      NO=15
      IF(MMAX.LT.NO)  NO=MMAX
      DO 10 N=1,NMAX
   10 READ(5,5) (HNT(M,N),M=1,NO)
      IF(MMAX.LE.NO) GO TO 12
      NQ=NO+1
      NO=2*NO
      IF(MMAX.LT.NO) NO=MMAX
      DO 11 N=1,NMAX
   11 READ(5,5) (HNT(M,N),M=NQ,NO)
      IF(MMAX.LE.NO) GO TO 12
      NQ=NO+1
      NO=NO+15
      IF(MMAX.LT.NO) NO=MMAX
      DO 15 N=1,NMAX
   15 READ(5,5) (HNT(M,N),M=NQ,NO)
      IF(MMAX.LE.NO) GO TO 12
      NQ=NO+1
      DO 14 N=1,NMAX
   14 READ(5,5) (HNT(N,N),M=NQ,MMAX)
   12 CONTINUE
      WRITE(6,20) (TITL(J),J=1,18)
      WRITE(6,30) (NCOL(J),J=1,32)
      DO 13 N=1,NMAX
   13 WRITE(6,40) N,(HNT(M,N),M=4,MMAX)
      RETURN
    5 FORMAT(15(F5.3))
   20 FORMAT(1H1/18A4//10X,44HMEAN INITIAL WATER DEPTHS IN FIELD IN METR
     1ES/)
   30 FORMAT(/3X,32A4/2X,1HN)
   40 FORMAT(/1X,I2,32F4.2)
      END
C
C          SUBROUTINE DIVE2 READS IN LOCATIONS OF WATER
C          LEVEL COMPUTATIONS FOR FINE GRID
C
      SUBROUTINE DIVE2(MMAX,NMAX)
      COMMON TITL(18),XIA(1490),ICOL(29),H(29,36),IBD(60),JBD(60)
     1,IOBD(3),JOBD(3),QX(29,36),QXP(29,36),QY(29,36),QYP(29,36)
     2,E(29,36),EM(29,36),EP(29,36),C(29,36),UM(29,36),VM(29,36)
     3,CSX(29,36),TAW(29,36),CSY(29,36),HT(29,36),
     4HN(35,38),NBD(90),NBD(90),MOBD(3),NOBD(3),QNX(35,38)
     5,QNXP(35,38),QNY(35,38),QNYP(35,38),EN(35,38),ENM(35,38),
     6ENP(35,38),CN(35,38),UNM(35,38),VNM(35,38),CNX(35,38),
     7CNY(35,38),HNT(35,38),TNW(35,38),NCOL(47),
```

```
     8SM(29,36),SP(29,36),DXX(29,36),DYY(29,36),DXY(29,36),
     9DYX(29,36),SNM(35,38),SNP(35,38),DNXX(35,38),DNYY(35,38)
     1,DNXY(35,38),DNYX(35,38)
      WRITE(6,10) (TITL(J),J=1,18)
      WRITE(6,20) (NCOL(J),J=1,32)
      DO 1 N=1,NMAX
      READ(5,30) (MBD(M),M=1,MMAX)
      WRITE(6,40) N,(MBD(M),M=4,MMAX)
      DO 1 M=1,MMAX
1     HN(M,N)=FLOAT(MBD(M))
      RETURN
10    FORMAT(1H1/18A4//10X,21HWATER LEVELS IN FIELD//)
20    FORMAT(3X,32A4/2X,1HN)
30    FORMAT(1X,35I2)
40    FORMAT(/1X,I2,32I4)
      END
```

```
              TIDE INDUCED CIRCULATION IN A RECTANGULAR HARBOUR
I  1   2   3   4   5   6   7   8   9  10  11  12  13  14  15  16  17  18
  19  20  21  22  23  24  25  26  27  28  29
M  4   5   6   7   8   9  10  11  12  13  14  15  16  17  18  19  20  21
  22  23  24  25  26  27  28  29  30  31  32  33  34  35
 0 0 0 0 0 0 0 0 0 0 0 0 0 0 0 0 0 0 0 0 0 0 0 0 0 0 0 0 0
 0 1 1 1 1 1 1 1 1 1 1 1 1 1 1 1 1 1 1 1 1 1 1 1 1 1 1 1 0
 0 1 1 1 1 1 1 1 1 1 1 1 1 1 1 1 1 1 1 1 1 1 1 1 1 1 1 1 0
 0 1 1 1 1 1 1 1 1 1 1 1 1 1 1 1 1 1 1 1 1 1 1 1 1 1 1 1 0
 0 1 1 1 1 1 1 1 1 1 1 1 1 1 1 1 1 1 1 1 1 1 1 1 1 1 1 1 0
 0 1 1 1 1 1 1 1 1 1 1 1 1 1 1 1 1 1 1 1 1 1 1 1 1 1 1 1 0
 0 1 1 1 1 1 1 1 1 1 1 1 1 1 1 1 1 1 1 1 1 1 1 1 1 1 1 1 0
 0 1 1 1 1 1 1 1 1 1 1 1 1 1 1 1 1 1 1 1 1 1 1 1 1 1 1 1 0
 0 1 1 1 1 1 1 1 1 1 1 1 1 1 1 1 1 1 1 1 1 1 1 1 1 1 1 1 0
 0 1 1 1 1 1 1 1 1 1 1 1 1 1 1 1 1 1 1 1 1 1 1 1 1 1 1 1 0
 0 1 1 1 1 1 1 1 1 1 1 1 1 1 1 1 1 1 1 1 1 1 1 1 1 1 1 1 0
 0 1 1 1 1 1 1 1 1 1 1 1 1 1 1 1 1 1 1 1 1 1 1 1 1 1 1 1 0
 0 1 1 1 1 1 1 1 1 1 1 1 1 1 1 1 1 1 1 1 1 1 1 1 1 1 1 1 0
 0 1 1 1 1 1 1 1 1 1 1 1 1 1 1 1 1 1 1 1 1 1 1 1 1 1 1 1 0
 0 1 1 1 1 1 1 1 1 1 1 1 1 1 1 1 1 1 1 1 1 1 1 1 1 1 1 1 0
 0 1 1 1 1 1 1 1 1 1 1 1 1 1 1 1 1 1 1 1 1 1 1 1 1 1 1 1 0
 0 1 1 1 1 1 1 1 1 1 1 1 1 1 1 1 1 1 1 1 1 1 1 1 1 1 1 1 0
 0 1 1 1 1 1 1 1 1 1 3 1 2 2 2 2 2 2 3 1 1 1 1 1 1 1 1 1 0
 0 1 1 1 1 1 1 1 1 1 3 1 1 1 1 1 1 1 3 1 1 1 1 1 1 1 1 1 0
 0 1 1 1 1 1 1 1 1 1 3 1 1 1 1 1 1 1 3 1 1 1 1 1 1 1 1 1 0
 0 1 1 1 1 1 1 1 1 1 3 1 1 1 1 1 1 1 3 1 1 1 1 1 1 1 1 1 0
 0 1 1 1 1 1 1 1 1 1 3 1 1 1 1 1 1 1 3 1 1 1 1 1 1 1 1 1 0
 0 1 1 1 1 1 1 1 1 1 3 1 1 1 1 1 1 1 3 1 1 1 1 1 1 1 1 1 0
 0 1 1 1 1 1 1 1 1 1 3 1 1 1 1 1 1 1 3 1 1 1 1 1 1 1 1 1 0
 0 1 1 1 1 1 1 1 1 1 3 1 1 1 1 1 1 1 3 1 1 1 1 1 1 1 1 1 0
 0 1 1 1 1 1 1 1 1 1 2 2 2 2 2 2 2 2 1 1 1 1 1 1 1 1 1 1 0
 0 1 1 1 1 1 1 1 1 1 1 1 1 1 1 1 1 1 1 1 1 1 1 1 1 1 1 1 0
 0 1 1 1 1 1 1 1 1 1 1 1 1 1 1 1 1 1 1 1 1 1 1 1 1 1 1 1 0
 0 1 1 1 1 1 1 1 1 1 1 1 1 1 1 1 1 1 1 1 1 1 1 1 1 1 1 1 0
 0 1 1 1 1 1 1 1 1 1 1 1 1 1 1 1 1 1 1 1 1 1 1 1 1 1 1 1 0
 0 1 1 1 1 1 1 1 1 1 1 1 1 1 1 1 1 1 1 1 1 1 1 1 1 1 1 1 0
 0 1 1 1 1 1 1 1 1 1 1 1 1 1 1 1 1 1 1 1 1 1 1 1 1 1 1 1 0
 0 1 1 1 1 1 1 1 1 1 1 1 1 1 1 1 1 1 1 1 1 1 1 1 1 1 1 1 0
 0 1 1 1 1 1 1 1 1 1 1 1 1 1 1 1 1 1 1 1 1 1 1 1 1 1 1 1 0
 0 1 1 1 1 1 1 1 1 1 1 1 1 1 1 1 1 1 1 1 1 1 1 1 1 1 1 1 0
 0 0 0 0 0 0 0 0 0 0 0 0 0 0 0 0 0 0 0 0 0 0 0 0 0 0 0 0 0
0.4380.4380.4380.4380.4380.4380.4380.4380.4380.4380.4380.4380.4380.4380.438
0.4380.4380.4380.4380.4380.4380.4380.4380.4380.4380.4380.4380.4380.4380.438
0.4380.4380.4380.4380.4380.4380.4380.4380.4380.4380.4380.4380.4380.4380.438
0.4380.4380.4380.4380.4380.4380.4380.4380.4380.4380.4380.4380.4380.4380.438
0.4380.4380.4380.4380.4380.4380.4380.4380.4380.4380.4380.4380.4380.4380.438
0.4380.4380.4380.4380.4380.4380.4380.4380.4380.4380.4380.4380.4380.4380.438
0.4380.4380.4380.4380.4380.4380.4380.4380.4380.4380.4380.4380.4380.4380.438
0.4380.4380.4380.4380.4380.4380.4380.4380.4380.4380.4380.4380.4380.4380.438
0.4380.4380.4380.4380.4380.4380.4380.4380.4380.4380.4380.4380.4380.4380.438
0.4380.4380.4380.4380.4380.4380.4380.4380.4380.4380.4380.4380.4380.4380.438
0.3740.3740.3740.3740.3740.3740.3740.3740.3740.3740.3740.3740.3740.3740.374
0.3100.3100.3100.3100.3100.3100.3100.3100.3100.3100.3100.3100.3100.3100.310
0.2460.2460.2460.2460.2460.2460.2460.2460.2460.2460.2460.2460.2460.2460.246
0.1820.1820.1820.1820.1820.1820.1820.1820.1820.1820.1820.1820.1820.1820.182
0.1180.1180.1180.1180.1180.1180.1180.1180.1180.1180.1180.1180.1180.1180.118
0.1180.1180.1180.1180.1180.1180.1180.1180.1180.1180.1180.1180.1180.1180.118
0.1180.1180.1180.1180.1180.1180.1180.1180.1180.1180.1180.1180.1180.1180.118
0.1180.1180.1180.1180.1180.1180.1180.1180.1180.1180.1180.1180.1180.1180.118
0.1180.1180.1180.1180.1180.1180.1180.1180.1180.1180.1180.1180.1180.1180.118
0.1180.1180.1180.1180.1180.1180.1180.1180.1180.1180.1180.1180.1180.1180.118
0.1180.1180.1180.1180.1180.1180.1180.1180.1180.1180.1180.1180.1180.1180.118
0.1180.1180.1180.1180.1180.1180.1180.1180.1180.1180.1180.1180.1180.1180.118
0.1180.1180.1180.1180.1180.1180.1180.1180.1180.1180.1180.1180.1180.1180.118
0.1180.1180.1180.1180.1180.1180.1180.1180.1180.1180.1180.1180.1180.1180.118
0.1180.1180.1180.1180.1180.1180.1180.1180.1180.1180.1180.1180.1180.1180.118
0.1180.1180.1180.1180.1180.1180.1180.1180.1180.1180.1180.1180.1180.1180.118
0.1180.1180.1180.1180.1180.1180.1180.1180.1180.1180.1180.1180.1180.1180.118
0.1180.1180.1180.1180.1180.1180.1180.1180.1180.1180.1180.1180.1180.1180.118
0.1180.1180.1180.1180.1180.1180.1180.1180.1180.1180.1180.1180.1180.1180.118
0.1180.1180.1180.1180.1180.1180.1180.1180.1180.1180.1180.1180.1180.1180.118
0.1180.1180.1180.1180.1180.1180.1180.1180.1180.1180.1180.1180.1180.1180.118
0.1180.1180.1180.1180.1180.1180.1180.1180.1180.1180.1180.1180.1180.1180.118
0.1180.1180.1180.1180.1180.1180.1180.1180.1180.1180.1180.1180.1180.1180.118
0.1180.1180.1180.1180.1180.1180.1180.1180.1180.1180.1180.1180.1180.1180.118
0.1180.1180.1180.1180.1180.1180.1180.1180.1180.1180.1180.1180.1180.1180.118
0.0000.0000.0000.0000.0000.0000.0000.0000.0000.0000.0000.0000.0000.0000.000
0.4380.4380.4380.4380.4380.4380.4380.4380.4380.4380.4380.4380.4380.000
0.4380.4380.4380.4380.4380.4380.4380.4380.4380.4380.4380.4380.4380.000
0.4380.4380.4380.4380.4380.4380.4380.4380.4380.4380.4380.4380.4380.000
0.4380.4380.4380.4380.4380.4380.4380.4380.4380.4380.4380.4380.4380.000
0.4380.4380.4380.4380.4380.4380.4380.4380.4380.4380.4380.4380.4380.000
0.4380.4380.4380.4380.4380.4380.4380.4380.4380.4380.4380.4380.4380.000
0.4380.4380.4380.4380.4380.4380.4380.4380.4380.4380.4380.4380.4380.000
```

```
0.4380.4380.4380.4380.4380.4380.4380.4380.4380.4380.4380.4380.4380.000
0.4380.4380.4380.4380.4380.4380.4380.4380.4380.4380.4380.4380.4380.000
0.4380.4380.4380.4380.4380.4380.4380.4380.4380.4380.4380.4380.4380.000
0.3740.3740.3740.3740.3740.3740.3740.3740.3740.3740.3740.3740.3740.000
0.3100.3100.3100.3100.3100.3100.3100.3100.3100.3100.3100.3100.3100.000
0.2460.2460.2460.2460.2460.2460.2460.2460.2460.2460.2460.2460.2460.000
0.1820.1820.1820.1820.1820.1820.1820.1820.1820.1820.1820.1820.1820.000
0.1180.1180.1180.1180.1180.1180.1180.1180.1180.1180.1180.1180.1180.000
0.1180.1180.1180.1180.1180.1180.1180.1180.1180.1180.1180.1180.1180.000
0.1180.1180.1180.1180.1180.1180.1180.1180.1180.1180.1180.1180.1180.000
0.1180.1180.1180.1180.1180.1180.1180.1180.1180.1180.1180.1180.1180.000
0.1180.1180.1180.1180.1180.1180.1180.1180.1180.1180.1180.1180.1180.000
0.1180.1180.1180.1180.1180.1180.1180.1180.1180.1180.1180.1180.1180.000
0.1180.1180.1180.1180.1180.1180.1180.1180.1180.1180.1180.1180.1180.000
0.1180.1180.1180.1180.1180.1180.1180.1180.1180.1180.1180.1180.1180.000
0.1180.1180.1180.1180.1180.1180.1180.1180.1180.1180.1180.1180.1180.000
0.1180.1180.1180.1180.1180.1180.1180.1180.1180.1180.1180.1180.1180.000
0.1180.1180.1180.1180.1180.1180.1180.1180.1180.1180.1180.1180.1180.000
0.1180.1180.1180.1180.1180.1180.1180.1180.1180.1180.1180.1180.1180.000
0.1180.1180.1180.1180.1180.1180.1180.1180.1180.1180.1180.1180.1180.000
0.1180.1180.1180.1180.1180.1180.1180.1180.1180.1180.1180.1180.1180.000
0.1180.1180.1180.1180.1180.1180.1180.1180.1180.1180.1180.1180.1180.000
0.1180.1180.1180.1180.1180.1180.1180.1180.1180.1180.1180.1180.1180.000
0.1180.1180.1180.1180.1180.1180.1180.1180.1180.1180.1180.1180.1180.000
0.1180.1180.1180.1180.1180.1180.1180.1180.1180.1180.1180.1180.1180.000
0.1180.1180.1180.1180.1180.1180.1180.1180.1180.1180.1180.1180.1180.000
0.1180.1180.1180.1180.1180.1180.1180.1180.1180.1180.1180.1180.1180.000
0.1180.1180.1180.1180.1180.1180.1180.1180.1180.1180.1180.1180.1180.000
0.0000.0000.0000.0000.0000.0000.0000.0000.0000.0000.0000.0000.0000.000
 0 0 0 0 0 0 0 0 0 0 0 0 0 0 0 0 0 0 0 0 0 0 0 0 0 0 0 0 0 0 0 0 0 0 0
 0 1 1 1 1 1 1 1 1 1 1 1 1 1 1 1 1 1 1 1 1 1 1 1 1 1 1 1 1 1 1 1 1 1 0
 0 1 1 1 1 1 1 1 1 1 1 1 1 1 1 1 1 1 1 1 1 1 1 1 1 1 1 1 1 1 1 1 1 1 0
 0 1 1 1 1 1 1 1 1 1 1 1 1 1 1 1 1 1 1 1 1 1 1 1 1 1 1 1 1 1 1 1 1 1 0
 0 1 1 1 1 1 1 1 1 1 1 1 1 1 1 1 1 1 1 1 1 1 1 1 1 1 1 1 1 1 1 1 1 1 0
 0 1 1 1 1 1 1 1 1 1 1 1 1 1 1 1 1 1 1 1 1 1 1 1 1 1 1 1 1 1 1 1 1 1 0
 0 1 1 1 1 1 1 1 1 1 1 1 1 1 1 1 1 1 1 1 1 1 1 1 1 1 1 1 1 1 1 1 1 1 0
 0 1 1 1 1 1 1 1 1 1 1 1 1 1 1 1 1 1 1 1 1 1 1 1 1 1 1 1 1 1 1 1 1 1 0
 0 1 1 1 1 1 1 1 1 1 1 1 1 1 1 1 1 1 1 1 1 1 1 1 1 1 1 1 1 1 1 1 1 1 0
 0 1 1 1 1 1 1 1 1 1 1 1 1 1 1 1 1 1 1 1 1 1 1 1 1 1 1 1 1 1 1 1 1 1 0
 0 1 1 1 1 1 1 1 1 1 1 1 1 1 1 1 1 1 1 1 1 1 1 1 1 1 1 1 1 1 1 1 1 1 0
 0 1 1 1 1 1 1 1 1 1 1 1 1 1 1 1 1 1 1 1 1 1 1 1 1 1 1 1 1 1 1 1 1 1 0
 0 1 1 1 1 1 1 1 1 1 1 1 1 1 1 1 1 1 1 1 1 1 1 1 1 1 1 1 1 1 1 1 1 1 0
 0 1 1 1 1 1 1 1 1 1 3 1 1 1 1 1 2 2 2 2 2 2 2 2 2 2 2 2 2 2 2 2 2 2 0
 0 1 1 1 1 1 1 1 1 1 3 1 1 1 1 1 1 1 1 1 1 1 1 1 1 1 1 1 1 1 1 1 1 1 0
 0 1 1 1 1 1 1 1 1 1 3 1 1 1 1 1 1 1 1 1 1 1 1 1 1 1 1 1 1 1 1 1 1 1 0
 0 1 1 1 1 1 1 1 1 1 3 1 1 1 1 1 1 1 1 1 1 1 1 1 1 1 1 1 1 1 1 1 1 1 0
 0 1 1 1 1 1 1 1 1 1 3 1 1 1 1 1 1 1 1 1 1 1 1 1 1 1 1 1 1 1 1 1 1 1 0
 0 1 1 1 1 1 1 1 1 1 3 1 1 1 1 1 1 1 1 1 1 1 1 1 1 1 1 1 1 1 1 1 1 1 0
 0 1 1 1 1 1 1 1 1 1 3 1 1 1 1 1 1 1 1 1 1 1 1 1 1 1 1 1 1 1 1 1 1 1 0
 0 0 0 0 0 0 0 0 0 0 3 1 1 1 1 1 1 1 1 1 1 1 1 1 1 1 1 1 1 1 1 1 1 1 0
 0 0 0 0 0 0 0 0 0 0 1 1 1 1 1 1 1 1 1 1 1 1 1 1 1 1 1 1 1 1 1 1 1 1 0
 0 0 0 0 0 0 0 0 0 0 1 1 1 1 1 1 1 1 1 1 1 1 1 1 1 1 1 1 1 1 1 1 1 1 0
 0 0 0 0 0 0 0 0 0 0 1 1 1 1 1 1 1 1 1 1 1 1 1 1 1 1 1 1 1 1 1 1 1 1 0
 0 0 0 0 0 0 0 0 0 0 1 1 1 1 1 1 1 1 1 1 1 1 1 1 1 1 1 1 1 1 1 1 1 1 0
 0 0 0 0 0 0 0 0 0 0 1 1 1 1 1 1 1 1 1 1 1 1 1 1 1 1 1 1 1 1 1 1 1 1 0
 0 0 0 0 0 0 0 0 0 0 1 1 1 1 1 1 1 1 1 1 1 1 1 1 1 1 1 1 1 1 1 1 1 1 0
 0 0 0 0 0 0 0 0 0 0 1 1 1 1 1 1 1 1 1 1 1 1 1 1 1 1 1 1 1 1 1 1 1 1 0
 0 0 0 0 0 0 0 0 0 0 1 1 1 1 1 1 1 1 1 1 1 1 1 1 1 1 1 1 1 1 1 1 1 1 0
 0 0 0 0 0 0 0 0 0 0 1 1 1 1 1 1 1 1 1 1 1 1 1 1 1 1 1 1 1 1 1 1 1 1 0
 0 0 0 0 0 0 0 0 0 0 1 1 1 1 1 1 1 1 1 1 1 1 1 1 1 1 1 1 1 1 1 1 1 1 0
 0 0 0 0 0 0 0 0 0 0 1 1 1 1 1 1 1 1 1 1 1 1 1 1 1 1 1 1 1 1 1 1 1 1 0
 0 0 0 0 0 0 0 0 0 0 1 1 1 1 1 1 1 1 1 1 1 1 1 1 1 1 1 1 1 1 1 1 1 1 0
 0 0 0 0 0 0 0 0 0 0 1 1 1 1 1 1 1 1 1 1 1 1 1 1 1 1 1 1 1 1 1 1 1 1 0
 0 0 0 0 0 0 0 0 0 0 1 1 1 1 1 1 1 1 1 1 1 1 1 1 1 1 1 1 1 1 1 1 1 1 0
 0 0 0 0 0 0 0 0 0 0 1 1 1 1 1 1 1 1 1 1 1 1 1 1 1 1 1 1 1 1 1 1 1 1 0
 0 0 0 0 0 0 0 0 0 0 1 1 1 1 1 1 1 1 1 1 1 1 1 1 1 1 1 1 1 1 1 1 1 1 0
 0 0 0 0 0 0 0 0 0 0 1 1 1 1 1 1 1 1 1 1 1 1 1 1 1 1 1 1 1 1 1 1 1 1 0
 0 0 0 0 0 0 0 0 0 0 0 0 0 0 0 0 0 0 0 0 0 0 0 0 0 0 0 0 0 0 0 0 0 0 0
0.2460.2460.2460.2460.2460.2460.2460.2460.2460.2460.2460.2460.2460.2460.246
0.2250.2250.2250.2250.2250.2250.2250.2250.2250.2250.2250.2250.2250.2250.225
0.2030.2030.2030.2030.2030.2030.2030.2030.2030.2030.2030.2030.2030.2030.203
0.1820.1820.1820.1820.1820.1820.1820.1820.1820.1820.1820.1820.1820.1820.182
0.1610.1610.1610.1610.1610.1610.1610.1610.1610.1610.1610.1610.1610.1610.161
0.1390.1390.1390.1390.1390.1390.1390.1390.1390.1390.1390.1390.1390.1390.139
0.1180.1180.1180.1180.1180.1180.1180.1180.1180.1180.1180.1180.1180.1180.118
0.1180.1180.1180.1180.1180.1180.1180.1180.1180.1180.1180.1180.1180.1180.118
0.1180.1180.1180.1180.1180.1180.1180.1180.1180.1180.1180.1180.1180.1180.118
0.1180.1180.1180.1180.1180.1180.1180.1180.1180.1180.1180.1180.1180.1180.118
0.1180.1180.1180.1180.1180.1180.1180.1180.1180.1180.1180.1180.1180.1180.118
0.1180.1180.1180.1180.1180.1180.1180.1180.1180.1180.1180.1180.1180.1180.118
0.1180.1180.1180.1180.1180.1180.1180.1180.1180.1180.1180.1180.1180.1180.118
0.1180.1180.1180.1180.1180.1180.1180.1180.1180.1180.1180.1180.1180.1180.118
0.1180.1180.1180.1180.1180.1180.1180.1180.1180.1180.1180.1180.1180.1180.118
0.1180.1180.1180.1180.1180.1180.1180.1180.1180.1180.1180.1180.1180.1180.118
0.1180.1180.1180.1180.1180.1180.1180.1180.1180.1180.1180.1180.1180.1180.118
0.1180.1180.1180.1180.1180.1180.1180.1180.1180.1180.1180.1180.1180.1180.118
```

```
0.1180.1180.1180.1180.1180.1180.1180.1180.1180.1180.1180.1180.1180.1180.118
0.1180.1180.1180.1180.1180.1180.1180.1180.1180.1180.1180.1180.1180.1180.118
0.1180.1180.1180.1180.1180.1180.1180.1180.1180.1180.1180.1180.1180.1180.118
0.1180.1180.1180.1180.1180.1180.1180.1180.1180.1180.1180.1180.1180.1180.118
0.1180.1180.1180.1180.1180.1180.1180.1180.1180.1180.1180.1180.1180.1180.118
0.1180.1180.1180.1180.1180.1180.1180.1180.1180.1180.1180.1180.1180.1180.118
0.1180.1180.1180.1180.1180.1180.1180.1180.1180.1180.1180.1180.1180.1180.118
0.1180.1180.1180.1180.1180.1180.1180.1180.1180.1180.1180.1180.1180.1180.118
0.1180.1180.1180.1180.1180.1180.1180.1180.1180.1180.1180.1180.1180.1180.118
0.1180.1180.1180.1180.1180.1180.1180.1180.1180.1180.1180.1180.1180.1180.118
0.1180.1180.1180.1180.1180.1180.1180.1180.1180.1180.1180.1180.1180.1180.118
0.1180.1180.1180.1180.1180.1180.1180.1180.1180.1180.1180.1180.1180.1180.118
0.1180.1180.1180.1180.1180.1180.1180.1180.1180.1180.1180.1180.1180.1180.118
0.1180.1180.1180.1180.1180.1180.1180.1180.1180.1180.1180.1180.1180.1180.118
0.1180.1180.1180.1180.1180.1180.1180.1180.1180.1180.1180.1180.1180.1180.118
0.1180.1180.1180.1180.1180.1180.1180.1180.1180.1180.1180.1180.1180.1180.118
0.1180.1180.1180.1180.1180.1180.1180.1180.1180.1180.1180.1180.1180.1180.118
0.1180.1180.1180.1180.1180.1180.1180.1180.1180.1180.1180.1180.1180.1180.118
0.1180.1180.1180.1180.1180.1180.1180.1180.1180.1180.1180.1180.1180.1180.118
0.0000.0000.0000.0000.0000.0000.0000.0000.0000.0000.0000.0000.0000.0000.000
0.2460.2460.2460.2460.2460.2460.2460.2460.2460.2460.2460.2460.2460.2460.246
0.2250.2250.2250.2250.2250.2250.2250.2250.2250.2250.2250.2250.2250.2250.225
0.2030.2030.2030.2030.2030.2030.2030.2030.2030.2030.2030.2030.2030.2030.203
0.1820.1820.1820.1820.1820.1820.1820.1820.1820.1820.1820.1820.1820.1820.182
0.1610.1610.1610.1610.1610.1610.1610.1610.1610.1610.1610.1610.1610.1610.161
0.1390.1390.1390.1390.1390.1390.1390.1390.1390.1390.1390.1390.1390.1390.139
0.1180.1180.1180.1180.1180.1180.1180.1180.1180.1180.1180.1180.1180.1180.118
0.1180.1180.1180.1180.1180.1180.1180.1180.1180.1180.1180.1180.1180.1180.118
0.1180.1180.1180.1180.1180.1180.1180.1180.1180.1180.1180.1180.1180.1180.118
0.1180.1180.1180.1180.1180.1180.1180.1180.1180.1180.1180.1180.1180.1180.118
0.1180.1180.1180.1180.1180.1180.1180.1180.1180.1180.1180.1180.1180.1180.118
0.1180.1180.1180.1180.1180.1180.1180.1180.1180.1180.1180.1180.1180.1180.118
0.1180.1180.1180.1180.1180.1180.1180.1180.1180.1180.1180.1180.1180.1180.118
0.1180.1180.1180.1180.1180.1180.1180.1180.1180.1180.1180.1180.1180.1180.118
0.1180.1180.1180.1180.1180.1180.1180.1180.1180.1180.1180.1180.1180.1180.118
0.1180.1180.1180.1180.1180.1180.1180.1180.1180.1180.1180.1180.1180.1180.118
0.1180.1180.1180.1180.1180.1180.1180.1180.1180.1180.1180.1180.1180.1180.118
0.1180.1180.1180.1180.1180.1180.1180.1180.1180.1180.1180.1180.1180.1180.118
0.1180.1180.1180.1180.1180.1180.1180.1180.1180.1180.1180.1180.1180.1180.118
0.1180.1180.1180.1180.1180.1180.1180.1180.1180.1180.1180.1180.1180.1180.118
0.1180.1180.1180.1180.1180.1180.1180.1180.1180.1180.1180.1180.1180.1180.118
0.1180.1180.1180.1180.1180.1180.1180.1180.1180.1180.1180.1180.1180.1180.118
0.1180.1180.1180.1180.1180.1180.1180.1180.1180.1180.1180.1180.1180.1180.118
0.1180.1180.1180.1180.1180.1180.1180.1180.1180.1180.1180.1180.1180.1180.118
0.1180.1180.1180.1180.1180.1180.1180.1180.1180.1180.1180.1180.1180.1180.118
0.1180.1180.1180.1180.1180.1180.1180.1180.1180.1180.1180.1180.1180.1180.118
0.1180.1180.1180.1180.1180.1180.1180.1180.1180.1180.1180.1180.1180.1180.118
0.1180.1180.1180.1180.1180.1180.1180.1180.1180.1180.1180.1180.1180.1180.118
0.1180.1180.1180.1180.1180.1180.1180.1180.1180.1180.1180.1180.1180.1180.118
0.1180.1180.1180.1180.1180.1180.1180.1180.1180.1180.1180.1180.1180.1180.118
0.1180.1180.1180.1180.1180.1180.1180.1180.1180.1180.1180.1180.1180.1180.118
0.1180.1180.1180.1180.1180.1180.1180.1180.1180.1180.1180.1180.1180.1180.118
0.1180.1180.1180.1180.1180.1180.1180.1180.1180.1180.1180.1180.1180.1180.118
0.1180.1180.1180.1180.1180.1180.1180.1180.1180.1180.1180.1180.1180.1180.118
0.1180.1180.1180.1180.1180.1180.1180.1180.1180.1180.1180.1180.1180.1180.118
0.1180.1180.1180.1180.1180.1180.1180.1180.1180.1180.1180.1180.1180.1180.118
0.1180.1180.1180.1180.1180.1180.1180.1180.1180.1180.1180.1180.1180.1180.118
0.0000.0000.0000.0000.0000.0000.0000.0000.0000.0000.0000.0000.0000.0000.000
0.2460.2460.2460.2460.246
0.2250.2250.2250.2250.225
0.2030.2030.2030.2030.203
0.1820.1820.1820.1820.182
0.1610.1610.1610.1610.161
0.1390.1390.1390.1390.139
0.1180.1180.1180.1180.118
0.1180.1180.1180.1180.118
0.1180.1180.1180.1180.118
0.1180.1180.1180.1180.118
0.1180.1180.1180.1180.118
0.1180.1180.1180.1180.118
0.1180.1180.1180.1180.118
0.1180.1180.1180.1180.000
0.1180.1180.1180.1180.000
0.1180.1180.1180.1180.000
0.1180.1180.1180.1180.000
0.1180.1180.1180.1180.000
0.1180.1180.1180.1180.000
0.1180.1180.1180.1180.000
0.1180.1180.1180.1180.000
0.1180.1180.1180.1180.000
0.1180.1180.1180.1180.000
0.1180.1180.1180.1180.000
0.1180.1180.1180.1180.000
0.1180.1180.1180.1180.000
0.1180.1180.1180.1180.000
```

0.1180.1180.1180.1180.000
0.1180.1180.1180.1180.000
0.1180.1180.1180.1180.000
0.1180.1180.1180.1180.000
0.1180.1180.1180.1180.000
0.1180.1180.1180.1180.000
0.1180.1180.1180.1180.000
0.1180.1180.1180.1180.000
0.1180.1180.1180.1180.000
0.1180.1180.1180.1180.000
0.0000.0000.0000.0000.000
****